Modelling the evaporation of cryogenic liquids in storage tanks

Felipe Huerta Pérez

Thesis submitted for the degree of

PhD

Department of Earth Science and Engineering

Imperial College London

July 2021

Abstract

Cryogenic liquids are substances with a normal boiling point below -150°C. Recently, the interest in cryogenic liquids has skyrocketed because of their role in the energy transition, particularly for LNG and liquid hydrogen. Cryogenic liquids are stored in highly insulated tanks, which are nevertheless subject to heat ingress from the surroundings. The heat ingress drives thermal stratification, natural convection, pressure build-up and evaporation. Managing the evaporated cryogen, denominated boil-off gas (BOG), pose techno-economic, safety and environmental challenges. To facilitate the design and operation of cryogenic storage tanks, new models for cryogenic liquids evaporation have been developed.

For isobaric storage, a 1-D model has been developed. The model includes wall heating, heat conduction and advection in the vapour phase. The model shows that advection dominates vapour heat transfer. A 2-D CFD model has been developed to validate the assumptions of the 1-D model. The CFD model validates the 1-D model assumption of one-dimensional advective flow. Additionally, the CFD model shows that thermal stratification dampens natural convection in the vapour. Analytical solutions of the 1-D model valid for the pseudo-steady state have been developed. The analytical solutions constitute an easy-to-use tool for practitioners to improve BOG management.

For non-isobaric storage, a 1-D model that considers wall heating, heat conduction and wall boiling has been developed. The 1-D model demonstrates that wall boiling is relevant even for low heat fluxes. The 1-D model predictions were in good agreement with experimental pressure and vapour temperature profiles. The assumptions of the 1-D model have been validated by developing a new single-phase CFD model. A multiphase model has been developed to investigate interfacial transport phenomena. It shows that interfacial momentum transfer slightly enhances liquid heat transfer, and that vapour heating dominates pressure build-up at the beginning of the storage period.

Statement of originality

I declare that this thesis is my own work, unless appropriately referenced within the text.

Copyright declaration

Acknowledgements

I thank Velisa Vesovic for being an outstanding supervisor, excellent mentor, and human being. I am grateful for his example of integrity in research, which will endlessly fuel my determination to contribute to society from academia. Our fascination for modelling transport phenomena made every meeting an exciting and challenging scientific discussion.

I thank my parents, Sandra and Leonel. I feel honestly fortunate for all the love, care and attention that they put into my upbringing. I would have to live ten lives to reciprocate 1% of all what they have done for me. Thank you for showing me that what makes a good person are their ethics and compassion. Thank you for instilling in me your relentless determination, which has helped me to bounce back during difficult times of my life.

I would also like to thank all the people who were the right "initial and boundary conditions" for my life over these last four years. I am grateful for my girlfriend, Antonia, who has provided me with love, support, positive energy and excellent cakes. Her passion for fluid mechanics and transport phenomena was an extra motivation to run the extra mile. I am grateful for José Álamos, a great friend from Chile and now living in Hamburg. His support during these years has been invaluable. I thank Ridwanur Chowdhury (Rid) for being there through thick and thin. May London remembers us taking the Piccadilly Line back home at 3 am on a Friday and then going back to Imperial the day after to run simulations. I thank Andrea Gayon for her friendship, our great philosophical discussions and for being an example of excellence in research. I thank Samuel Brooke-Barnett (Sam) for his friendship, wise advice and for running Fribes together in 2017-2018. I thank Anouk L'Hermitte, for being a great friend and being an example of determination. I thank Lior Suchoy and Kartikeya Sangwan for their great friendship and philosophical discussions.

I thank my friends and colleagues from DECODED. They have shown me that it is always worth investing time, energy and effort in mentoring our learners. In particular, I am grateful to Tor Njamo, Jonathan Costa, Marina Jutzet and Vanisha Taylor. I thank my learners in the context of the Data Fellowship. They were an example

of perseverance and hard work. Thanks to Lloyd Greensite, James Falshaw, Karl Merisalu, Sam Berry, Natalie Harding, Sophie Shervington and Christine Vargas.

I thank my closest friends from Chile. Thanks to Matías Vargas and Sebastían Salata for our Sunday calls full of deep reflections, great conversations and video games. Thanks to Felipe Pizarro, Felipe Salce, Claudio Díaz, Fabrizio Moletto, Alejandro Meyer and Pablo Bahamonde for our weekly video calls, which have kept our friendship fresh. Thanks to Guillermo Moreno, Raúl Ponce, Gonzalo Cárcamo, Valentina Vallés, George Wenzel, Benjamín Maluenda, and Pablo Faúndez, for being always willing to meet every time I go back to Chile. Thanks to Andrés Pérez, Verónica Puga and Daniela Valenzuela for reaching out and being always hopeful and ambitious with their careers.

I thank everyone who had a positive impact on my development as a researcher. I am grateful to Catalina Pino for our scientific discussions about transport phenomena. Her support was crucial in several graduate courses that we took together. Thanks to Jorge Ávalos, Leandro Perao and Hannah Moran for joining our OpenFOAM Code Reviews. Special thanks to Hannah for agreeing to have weekly thesis writing sessions, which provided me with extra support and accountability. Thanks to all the members of the Research Software and Engineering Community (RSE) at Imperial. I particularly thank Jeremy Cohen, Stefano Galvan, Simon Clifford and Chris Cave-Ayland for joining our weekly RSE coffees. My software engineering skills have improved thanks to them.

Finally, I thank ANID Chile for funding this PhD. I also want to recognise the role of my MSc supervisor, José Ricardo Pérez, for guiding me in my first steps as a researcher and enabling me to find this PhD opportunity.

Table of Contents

List of Figures

List of Tables

Chapter 1

Introduction

1.1 Climate change and energy transition

The economic progress of global society since industrialisation has primarily relied on the use of fossil fuels as an energy source. The usage of fossil fuels produces carbon dioxide (CO_2) and other greenhouse gases, which accumulate in the atmosphere and produce global warming. Global warming, defined as the increase of average surface temperature of the planet [1] is driven by the combination of natural processes and human activity. Anthropogenic global warming corresponds to the fraction of global warming induced by humans [2]. Anthropogenic global warming is estimated to have produced an increase of 1.0°C in surface temperature since pre-industrial levels [1]. This constitutes nearly the totality of the observed global warming since pre-industrial levels, demonstrating that human activities are the main driver of global warming [1].

Global warming drives climate change, which is defined as the change in the state of the climate that can be identified by change in the mean, and/or in the variability, of its properties and that persists for an extended period [2]. Impacts of climate change are already observable, like the loss of sea ice, accelerated sea rise level, longer and more intense heat waves [3]. Some of the impacts of a global warming of 2°C will be long-lasting or irreversible, such as the loss of biodiversity [3]. In the scenario of global warming of 1.5°C or higher, climate related risks are disproportionally high for the most disadvantaged and vulnerable populations [3]. Food access, mortality, poverty and inequality are expected to significantly increase with climate change in the least developed countries, particularly in Africa and Asia [3]. Thus, there is an urgency on achieving net zero emissions as soon as possible.

The International Panel for Climate Change (IPCC) has suggested limiting global warming to 1.5°C to significantly reduce the impact of climate change [1]. To maximize the likelihood of achieving this goal, global CO_2 emissions need to decrease sharply in

the next decades aiming to reach net zero by 2040. Carbon dioxide reduction (CDR) technologies, such as carbon dioxide capture, utilization and storage (CCUS), are not by their own a sustainable solution [4]. The upscaling of CDR will have significant impacts on land, energy and water. Therefore, to minimize the reliance on CDR to achieve net zero emissions by 2040, global CO_2 emissions must start to decrease now.

A sharp reduction of global CO_2 emissions will require fast, incremental and disruptive transformations of the energy system, such as decarbonisation and an increased share of renewable energy in the global energy mix. In order to limit global warming to 1.5°C, renewable energy should supply a share of 52-67% of primary energy pathways, while coal must be practically eradicated (1-7%) [4]. In this scenario, all remaining fossil fuels decrease their share from 2018, -13% to -62% for gas and -39 to -77% for oil [4]. The energy transition is defined as the transformations in the energy mix required to significantly reduce CO2 emissions.

The urgent requirement for an energy transition is driving an unprecedented change in the global energy sector to limit global warming. This change is challenging, particularly in an environment of increasing worldwide energy consumption mainly driven by the development of non-OECD countries [5]. In sharp contrast with the IPCC recommendation, the energy transition is not happening fast enough to limit global warming to 1.5°C. Although in 2020 global CO_2 emissions decreased slightly, in 2021 CO_2 emissions are heading for their second-largest annual increase level [6]. Furthermore, the demand for all fossil fuels is set to grow significantly in 2021 [6]. Strikingly, the supply of the most contaminant fossil fuel, coal, is expected to rebound significantly in 2021 approaching to its 2014 peak [6]. Therefore, limiting global warming to 1.5°C – 2°C in the current scenario of fossil fuel growth seems extremely unlikely. Thus, it would seem that the energy transition is being slow, despite an increase in share and reduction in costs of renewable energy [6]. In this thesis, the slow energy transition is defined as the scenario in which the energy transition fails to limit global warming to 1.5°C.

1.2 Role of natural gas in the scenario of a slow energy transition

In the absence of drastic changes in international regulations of fossil fuels production and utilisation, a complete transition will take around a century [7]. In a slow energy transition scenario, public and private stakeholders are increasingly opting for natural gas owing to its competitive cost and lower emissions when compared to other fossil fuels [8]. For instance, natural gas demand increased 3% in 2017 alone [9], and its supply is expected to increase by 45% from 2016 to 2040 [8]. Among fossil fuels, natural gas demand will experience the biggest growth, set to grow 3.2% in 2021 [6].

Natural gas (NG) is predominantly a hydrocarbon mixture consisting mainly of methane, lower amounts of other n-alkanes and small inorganic molecules. Natural gas can be distributed to the users through two pathways, depending mainly on the location of the users. If the users are near the natural gas source, NG can be distributed directly through pressurized pipelines. If the users are located far from the source, it is more convenient to apply a liquefaction process to NG to produce liquefied natural gas (LNG). LNG then can be distributed through marine transportation to large storage facilities and regasification terminal. In the regasification terminals, LNG is typically vaporized to match seasonal energy demands, and then it is distributed through pressurized pipelines. The regasification of LNG generates large amounts of energy, which had led to new processes and technologies to exploit this so called “cold energy” [10-14] .

An increasing number of users are opting for LNG compelled by concerns around the security of supply and the location of natural gas fields [15]. Furthermore, LNG is not only becoming the preferred way to transport natural gas, but also finding a use as marine and heavy-duty vehicle fuel [16-19]. In some instances, LNG is economically superior to traditional marine fuel and even marine gas oil [20]. Nevertheless, there remain some concerns about the environmental impact of the increase in LNG trading [21]. Although LNG is demonstratable a cleaner alternative to coal in terms of reduction of greenhouse emissions, methane leakages may significantly counterweigh or even negate the environmental benefits of natural gas [22]. The interested reader is referred to GIIGNL white paper [23] for a comprehensive description of the LNG supply chain.

1.2.1 LNG weathering in large scale storage

LNG is industrially stored in highly insulated tanks at cryogenic temperatures below -160°C, which corresponds to its saturation point at typical operating pressures slightly above the atmospheric pressure. Although the tanks are highly insulated, the large temperature gradients between the LNG and the surrounding air or sea water drive heat ingress from the surroundings. The heat ingress leads to the preferential evaporation of LNG with the most volatile components, methane and nitrogen, predominantly ending in the vapour phase. For isobaric storage, a cryogenic compressor is used to remove the produced vapour to keep the tank pressure constant. The removed vapour is denominated as boil-off gas (BOG). The heat ingress and BOG removal produce weathering of the remaining LNG. LNG weathering is defined as the change in composition of the LNG during its storage owing to the continuous BOG removal.

LNG weathering can induce safety hazards such as rollover, limits the NG marketability and has a high environmental impact. In several storage scenarios, such as road transportation and marine transportation in old vessels, the BOG is directly vented to the atmosphere. It has been identified that the LNG supply chain, and particularly the storage stages, are a super-emitters of methane [22]. In normal industrial operations, accurate quantitative knowledge of weathering is essential in the allocation of LNG cargoes to storage tanks. This allows to ensure grid suitability of the delivered natural gas in terms of its heating value and anticipating the consequences of loading a new batch of LNG. The weathering of LNG at large scale is an isobaric evaporation of a cryogenic multicomponent mixture. Therefore, developing theoretical understanding of the transport phenomena during LNG weathering is crucial for the energy transition. In particular, it will allow to optimise the design of storage tanks and regasification processes. This consequently will provide economic benefits, improve process safety and reduce methane emissions.

1.2.2 LNG for freight transport

Recently, the use of LNG as a cleaner alternative to fossil fuels in transportation has received substantial attention. Life-cycle analysis demonstrate that LNG produces fewer CO_2 emissions than other fossil fuels [24]. Furthermore, LNG produces less

emissions than some sustainable carriers such as methanol and dimethyl ether for short term storage associated with transport [24]. In road and marine vehicles, LNG is often stored under non-isobaric conditions to minimize BOG generation. In marine vehicles powered by natural gas, the large-scale cargo containment system (CCS) is often connected to the vehicle engine. As the working pressure range in large scale CCS is typically narrow (100 ~ 120 kPa), the overall storage process is nearly isobaric. Although this constitutes a cycle of pressurization and depressurization stages, the process is typically regarded as isobaric as the liquid thermal stratification is less than 0.1 K [25]. Nevertheless, recent evidence shows that the change in vapour temperature during pressurization stages may be significant owing to the absence of BOG removal in that period [26].

In road-transportation, LNG is typically stored in highly insulated, horizontally oriented cylindrical tanks. The capacity of these storage tanks ranges from 0.24 to 0.43 m^3 for typical LNG powered trucks, such as the Volvo-FH LNG [27]. In the Volvo-FH LNG, the operating pressure ranges from 0.4 to 1.0 MPa, while the MAWP is 1.6 MPa. This yields to holding times between 5 and 10 days for 25% and 90% initial liquid filling, respectively [27]. Volvo recommends parking the Volvo-FH LNG with full tank and frequent use to completely avoid venting methane [27]. This industrial evidence shows that for low liquid fillings in small tanks, the pressure build-up happens faster than for high liquid fillings. Owing to weight and size limitations and a lower volume to surface ratio, the insulation performance in small tanks is significantly worse than for large storage tanks. Although the usage of LNG in trucks is still in early days, truck drivers are interested in purchasing LNG trucks if tax reductions are implemented [28].

Although methane and LNG are highly flammable, LNG-powered vehicles have proven extremely safe, as no serious incidents have been reported up to date [29]. The usage of LNG in road transportation is growing exponentially. In China, the number of LNG-powered vehicles increased from 50,000 to almost 400,000 between 2012 and 2018 [30]. Similarly, in Europe the LNG powered vehicles are expected to grow from 5,000 on 2018 to up to 500,000 by 2025 [31]. Therefore, improving the understanding of the physical phenomena during the non-isobaric storage of LNG will provide environmental and economic benefits to society during the energy transition.

1.3 Green hydrogen as an energy carrier for a sustainable future

As limiting global warming is urgent, the share in the energy mix of renewable energy with a low carbon footprint must increase at a faster pace [6]. Although a slow energy transition will not limit global warming to 1.5-2°C, the transition has been progressively accelerating in the last decade. This is a consequence of an increased investment in research and development of renewable energies, which has increased their techno-economic feasibility [6]. It is worth noting that not all types of renewable energy produce low CO_2 emissions. Life-cycle emissions of wind and solar power are 3.5-12 gCO_2 eq KWh^{-1}, much smaller than ~ 100 gCO_2 eq KWh^{-1} for hydropower and bioenergy [32]. Therefore, research and development in energy production, storage and utilisation related to wind and solar power will increase the likelihood of a faster energy transition.

Hydrogen is positioning itself as a key energy carrier and energy storage technology for intermittent renewable energy in the energy transition. Nowadays, 96% of the hydrogen is produced using fossil fuels as a feedstock, while only 4% is produced from renewable sources by electrolysis [33]. Hydrogen produced from fossil fuels without carbon capture utilization and storage (CCUS) is labelled as grey hydrogen. The mainstream technology in the production of grey hydrogen is steam methane reforming (SMR) [34]. As SMR produces high quantities of CO_2, the hydrogen produced by this route is not suitable for an energy transition unless a CCUS unit is integrated in the process [33]. If the CO_2 emissions during SMR are captured, the produced hydrogen is denominated blue hydrogen. On the other hand, the cleanest hydrogen comes from renewable electrolysis, where solar or wind power is used to electrolyse water [34]. The hydrogen produced from renewable sources without CO_2 emissions is denominated green hydrogen.

Hanley et al. [33] reviewed the future role of hydrogen in the energy transition using integrated energy systems modelling for potential hydrogen pathways. Figure 1.1 summarizes the potential pathways that Hanley et al. [33] simulated, and also provides an overview of the hydrogen supply chain. As it can be observed in Figure 1.1, hydrogen is produced from different energy resources and by a variety of production methods. Hydrogen must be stored across the storage, transport and consumption stages of the

LH_2 pathways depicted in Figure 1.1. Unlike liquid fuels such as diesel or oil, liquid hydrogen is a cryogenic liquid with a boiling point of -253 °C at 1 atmosphere. Owing to its very low boiling temperature, density and specific heat, the LH_2 storage poses much greater engineering challenges, than LNG storage, mainly due to a much larger heat ingress [34, 35]. The larger temperature gradient between the surrounding air and the stored liquid hydrogen produces a higher boil-off and faster pressure build-up compared to LNG.

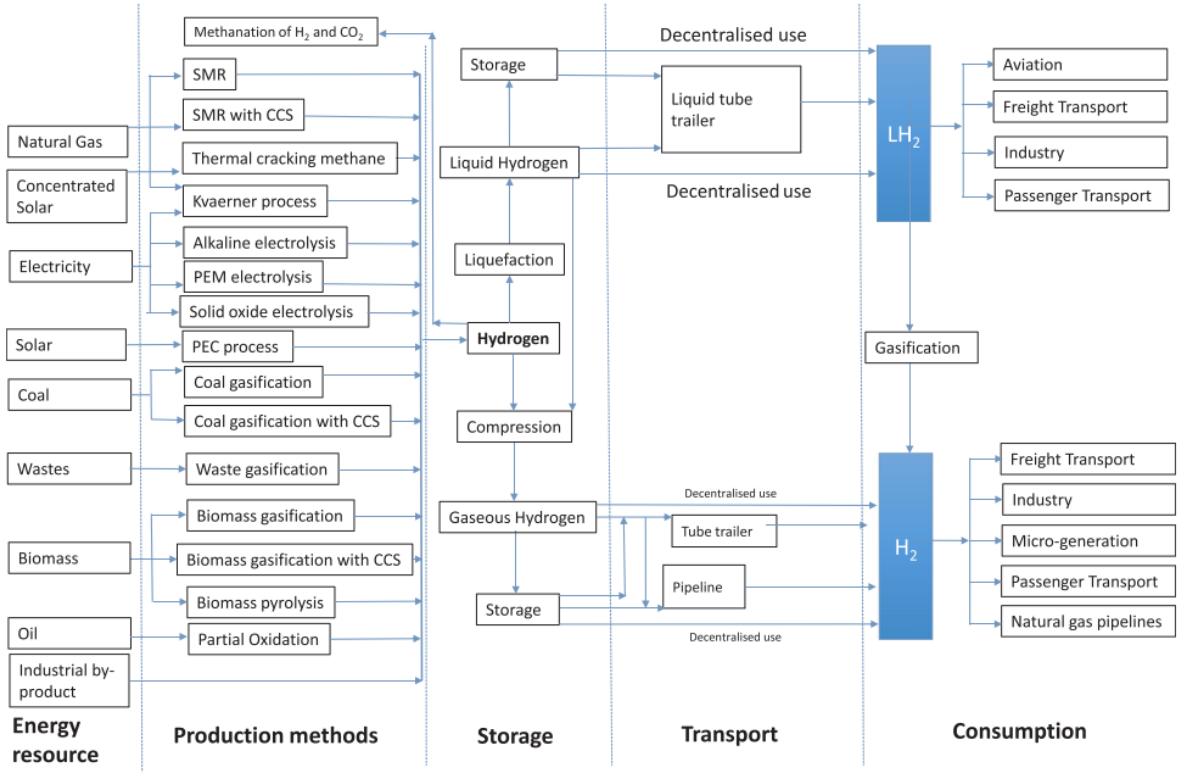

Fig. 1. Potential hydrogen pathways towards 2050.

Figure 1.1: Hydrogen supply chain and potential pathways by 2050. Reprinted from "The role of hydrogen in low carbon energy futures – A review of existing perspectives" by Hanley et al. 2018, Renewable and Sustainable Energy Reviews, 82: 3027-3045.

The biggest challenge on the use of hydrogen as an energy vector is its storage [34, 35]. Hanley et al. [33] concluded that the most economically viable pathways at the moment consider the storage of hydrogen as a compressed gas. Although compressed and liquefied hydrogen are the most traditional hydrogen storage technologies, a number of new technologies are being investigated or in early stages of development. Table 1.1 summarizes Rivard et al. recent review [35] that compares hydrogen storage technologies for mobility applications. In Table 1.1, metal organic frameworks (MOF) and carbon nanostructures are physical storage technologies based in the adsorption of

hydrogen in a solid matrix. Metal hydrides, metal borohydrides, Kubas-type and liquid organic hydrogen carriers (LOHC) and chemical hydrogen as ammonia (NH_3) are types of chemical storage of hydrogen. In contrast to physical storage, in chemical storage hydrogen is stored in a larger molecule as a product of a chemical reaction. For a detailed description of physical and chemical hydrogen storage technologies, the reader is referred to Rivard et al. review [35].

Table 1.1: Storage methods overview, reprinted from Rivard, E. et al. (2019) "Hydrogen Storage for Mobility: A Review.", *Materials*, 12:12-22. The unit for the gravimetric energy density is defined as wt % = ρ[kg m^{-3}]/1000 × 100. For instance, the gravimetric energy density of liqud hydrogen is 75 kg m^{-3}.

Method	Gravimetric Energy Density (wt %)	Volumetric Energy Density (MJ/L)	Temperature (K)	Pressure (barg)	Remarks
Compressed	5.7	4.9	293	700	Current industry standard
Liquid	7.5	6.4	20	0	Boil-off constitues major disadvantage
Cold/cryo compressed	5.4	4.0	40–80	300	Boil-off constitues major disadvantage
MOF	4.5	7.2	78	20–100	Attractive densities only at very low temperatures.
Carbon nanostructures	2.0	5.0	298	100	Volumetric density based on powder density of 2.1 g/mL and 2.0 wt % storage capacity.
Metal hydrides	7.6	13.2	260–425	20	Requires thermal management system.
Metal borohydrides	14.9–18.5	9.8–17.6	130	105	Low temperature, high pressure thermal management required
Kubas-type	10.5	23.6	293	120	
LOHC	8.5	7	293	0	Highly endo/exothermal requires processing plant and catalyst. Not suitable for mobility
Chemical	15.5	11.5	298	10	Requires SOFC fuel cell.

Rivard et al. [35] concluded that compressed gas is the most feasible hydrogen storage technology, in agreement with Hanley et al. [33]. Nevertheless, liquid hydrogen storage has a number of applications in the aerospace industry [36] and is a niche of active current research and commercial developments. For instance, cold/cryo-compressed hydrogen is a promising technology in which hydrogen is stored as a liquid-vapour mixture to minimize boil-off rates (BOR) in mobility applications [37, 38].

The advantages of liquid hydrogen are its reasonably high gravimetric energy density, and its larger volumetric energy density when compared against compressed hydrogen [35]. The main economic challenge of LH_2 is the high cost of liquefaction (USD 1.00/ kgH_2) [39]. This produces a low energy storage efficiency, achieving just 70% in the most efficient liquefaction plant in the US as of today [40]. The main practical

challenge of the usage of LH_2 as a vehicle fuel is its low boiling point and high boil-off rates [35]. We will focus the rest of this section on describing LH_2 storage in stationary tanks for scenarios relevant to industrial applications.

A traditional application of liquid hydrogen is as a fuel for space shuttles [2]. In this application, LH_2 is stored under non-isobaric conditions in medium-sized storage tanks both at the launch pad and in the rocket fuel tank. Minimizing the boil-off of LH_2 during its storage has been identified as a determinant factor for the success of space exploration missions [41, 42]. The boil-off of LH_2 is mainly determined by the tank insulation performance, in a similar way to LNG storage as it was discussed in section 2.1. A good insulation performance requires to achieve a low overall heat transfer coefficient of the multi-layer insulation (MLI) system of the tank. This design objective is still relevant for novel, state of the art actively cooled cryogenic storage tanks. For instance, in zero-boil off systems the evaporation of LH_2 is prevented by a refrigeration cycle [43, 44]. Ultimately, although those systems prevent the venting of LH_2, LH_2 is required in the refrigeration cycle in a quantity proportional to the refrigeration load. As an example, Figure 1.2 shows a 2,033 m^3 cylindrical hydrogen storage tank used in NASA's deep space rocket Space Launch System.

Figure 1.2: NASA 2,033 m^3 liquid hydrogen tank. This tank is a part of the space launch system (SLS) in the Marshall Space Flight Center in Huntsville, Alabama, U.S.A. Reprinted from NASA, 2019, from: https://www.nasa.gov/exploration/systems/sls/nasa-engineers-break-sls-test-tank-on-purpose-to-test-extreme-limits.html

As liquid hydrogen can constitute a renewable energy carrier, its applications are rapidly increasing to achieve the carbon neutrality by 2050 following the Paris Climate Agreement. Recently, the international interest on increasing the viability of large-scale storage and marine transportation of liquid hydrogen has increased dramatically. For instance, the first marine transportation of LH_2 in a pilot cargo ship will happen between Australia and Japan [6] is scheduled for 2021. The infrastructure around this project includes the development of stationary above-ground liquid hydrogen storage tanks [7].

Figure 1.3 shows an industrial scale implementation of a liquid hydrogen spherical storage tank developed by Kawasaki Heavy Industries, Ltd. [45]. On December 24, 2020, Kawasaki announced the construction of a 2,500 m^3 liquid hydrogen storage tank at Kobe Port Island, Japan. The spherical geometry of the tank has been justified as the one that minimizes the heat ingress from the surroundings. The spherical tank is insulated through a double-shell vacuum-insulation structure. In this structure, a vacuum sealed insulation is located between the inner and outer shells to minimize the heat ingress from the surroundings and hence boil-off rates (BOR). The manufacturer reports a BOR of 0.1 %/d for this tank, intended to be installed in receiving and loading terminals. Therefore, the models developed in this thesis for isobaric and non-isobaric conditions are applicable to the storage of liquid hydrogen in realistic, economically viable scenarios.

Figure 1.3: 2,500 m^3 LH_2 spherical storage tank built by Kawasaki on Kobe Airport Island, Japan. Reprinted from Japan Times, 2020. From https://www.japantimes.co.jp/news/2020/11/04/business/japanese-new-hydrogen-project/.

1.4 Relevance of cryogenic liquids for the energy transition

LNG and LH_2 belong to a family of cryogenic liquids that are traditionally classified as substances with a normal boiling point below -150°C. Cryogenic liquids are expected to play a pivotal role in the energy transition regardless of the pace of the transition. They are widely used as energy carriers [46-48], refrigerants [49] and rocket propellants [50]. Novel applications of cryogenic liquids involve power generation [51] and CO2 storage by cryogenic separation [52-54]. As discussed previously, both natural gas and hydrogen can be efficiently stored as LNG and LH_2, respectively, to facilitate their shipping and improve their volumetric energy density. The main techno-economical challenge in the supply chain of LNG, LH_2 and in general for any cryogenic liquid is their storage.

Owing to their low normal boiling point, cryogenic liquids are stored in highly insulated vessels. During their storage, cryogenic liquids are subject to heat ingress driven by the large temperature difference between the surroundings and the stored cryogen. As discussed in sections 1.2 - 1.3, the heat intrusion drives several complex transport phenomena within a cryogen. These phenomena include natural convection, evaporation/condensation, thermal stratification and liquid thermal expansion, which raise engineering, safety, economic and environmental challenges. The predominance of these transport phenomena will depend on the operating conditions of the storage tank. For large-scale storage, cryogenic liquids undergo isobaric evaporation as the boil-off gas (BOG) is removed, as it is generated to keep the tank pressure constant. For small and mid-scale storage cryogenic liquids undergo non-isobaric evaporation as venting the cryogen is neither economical nor safe.

1.4.1 Transport phenomena during the storage of cryogenic liquids

For the isobaric evaporation of cryogenic liquids, the dominant transport phenomena are evaporation, vapour thermal stratification and buoyancy driven flow in the vapour [55]. In contrast, the non-isobaric evaporation is much more complex. The pressure build-up drives an increase in saturation temperature which happens faster than the physical time scale of thermal diffusion in the liquid. This drives the thermal stratification of the liquid. As the liquid is no longer isothermal, heat ingress drives

natural convection in the liquid, and potentially wall boiling at moderate heat fluxes [56]. The dominant phase change mechanism will depend on the rate of pressure change, wall boiling and the interfacial energy balance. Therefore, for non-isobaric evaporation of cryogens liquid thermal stratification and buoyancy driven flow are significant in both phases. Wall boiling may occur, and the dominant phase change mechanism cannot be determined a priori.

1.5 Research gap and objective of this thesis

In a context of energy transition and a rapid growth of the utilisation of cryogenic liquids, realistic models for cryogenic liquids storage are becoming increasingly necessary. Although these models have been developed for more than 60 years [50, 57], several transport phenomena during the evaporation are still not well understood. Even for the simpler isobaric evaporation scenario, the accurate modelling of the vapour phase transport phenomena is not straightforward. With the increase of computational power and advances in computational physics, computational fluid dynamics (CFD) models are proliferating as a prominent tool in engineering. Although computational fluid dynamics (CFD) models may allow a highly detailed simulation of the evaporation of cryogens, their industrial application is limited. This is a consequence of long simulation times, of the magnitude of days and weeks, and because of excessive model complexity in many scenarios. From a scientific point of view, CFD models in isolation rarely allow progress in theoretical understanding of transport phenomena. Nevertheless, CFD models are an invaluable tool for researchers for: (i) observing the evolution of system variables in scales unfeasible or impractical in experiments, and (ii) validating the assumptions of simpler models.

1.5.1 Research objectives

The **objective** of this research is to develop and implement realistic models for the evaporation of cryogenic liquids. For the isobaric evaporation of cryogens, three objectives are established:

1. To develop a realistic 1-D heat transfer model for the vapour phase applicable to the storage of pure cryogenic liquids and the weathering of LNG. This model must include heat conduction, advection and vapour heating through the walls. Additionally, the model must accurately model the displacement of the vapour-liquid interface in a finite domain. The model is expected to accurately predict all operating variables, in particular the BOG rate and vapour temperatures. Additionally, the model should be capable to run simulations in less than 30 seconds of computational time. Low simulation times will allow the model to be applicable in real-time control and complex optimisations for BOG management.
2. To derive analytical solutions for the developed 1-D model. The analytical solutions must constitute an easy-to-use tool for practitioners to estimate liquid volumes, evaporation rates, BOG rates and the vapour temperature profile during cryogen storage. Additionally, the solutions must be suitable to validate the 1-D model for limiting scenarios.
3. To develop a CFD model that allows the accurate prediction of the velocity and temperature profiles in the vapour phase during the isobaric storage of cryogens. The CFD model must resolve vapour phase fluid flow and heat transfer, so that quantification of the effect of natural convection and turbulence on temperature profiles and BOG rates can be established. Additionally, the CFD model must allow for validation of the 1-D model and its range of applicability.

For the non-isobaric evaporation of cryogens, three different objectives are set:

1. To develop a realistic 1-D non-equilibrium model that includes heat conduction and wall heating in both phases, advection in the vapour and wall boiling. The 1-D model should allow the practitioner a quick estimation of the pressure build-up and thermal stratification.
2. To develop a single-phase CFD model for the liquid phase that must accurately resolve liquid-phase velocity and temperature profiles in the presence of wall boiling. The developed CFD model should accurately

quantify the effect of natural convection on liquid thermal stratification and pressurization rates. Additionally, the CFD model will allow us to verify the assumptions made, for the liquid phase, in the 1-D model.

3. To develop a multiphase CFD model using the two-fluid approach. This approach considers vapour and liquid as an interpenetrating continuum, and it is suitable for modelling wall boiling. The multiphase model will allow us to quantify the effect of interfacial heat and momentum transfer on pressurization rates and thermal stratification. Additionally, the multiphase model will allow for the verification of the assumptions of the simpler 1-D and single-phase CFD models and establish their range of applicability.

1.5.2 Research impact

The models developed in this thesis are divided in two sub-categories depending on the storage scenario: isobaric and non-isobaric evaporation models. The new isobaric evaporation models developed as part of current research [55, 58] are applicable to any pure cryogenic liquid [55, 58], and for the weathering of LNG mixture [59]. They are currently being actively used by LNG researchers in close contact with industry [26, 60]. For the much more complex, non-isobaric evaporation scenario, the models presented in this thesis are in active development.

From an industrial point of view, the developed models allow for the optimal design and operation of cryogenic liquid storage tanks. For isobaric storage, the accurate prediction of BOG rates, BOG temperature and liquid volume allow for a better characterization and improvements in process safety and in reducing costs. In particular for LH_2 storage, the models provide further theoretical understanding that can potentially allow a more reliable assessment of the energy efficiency of hydrogen energy pathways that considers LH_2 storage. This impact is crucial, as life-cycle analyses are highly valued by energy policymakers and investors. In contrast, the non-isobaric evaporation models will be a valuable tool in the research of development in a number of emerging applications in the transport sector. In particular, in LH_2 and LNG fuelling stations, road and space vehicles.

1.5.3 Thesis outline

This thesis is organized in a total of nine chapters. We start with the Introduction and Literature Review chapters, which are common to all scenarios of cryogenic storage. Thereafter, the core research chapters are divided in two parts: (i) for isobaric evaporation (Chapters 3-5) and (ii) non-isobaric evaporation (Chapter 6-8) models. Finally, the Conclusions chapter comprises and summarizes the results for isobaric and non-isobaric evaporation. An outline of each chapter is given below:

- Chapter 1 justifies the relevance of the storage of cryogenic liquids in the context of the energy transition. Several engineering applications are presented, emphasising the complex array of transport phenomena relevant to the storage of cryogenic liquids.
- Chapter 2 consists of a comprehensive literature review of experimental, theoretical and numerical studies of cryogenic liquids storage. The originality of this review is its broad scope, that comprises isobaric and non-isobaric evaporation of several cryogenic liquids under different tank geometries and heat fluxes.
- Chapter 3 presents the development of three isobaric evaporation models: a CFD model for the vapour phase, a 1-D non-equilibrium model and an LNG weathering model. Additionally, analytical solutions for the 1-D evaporation model for pure cryogens are derived and presented.
- Chapter 4 provides a comprehensive verification of the isobaric evaporation model, including grid independence studies and order of accuracy analyses.
- Chapter 5 presents the results obtained with the isobaric evaporation models. The 1-D non-equilibrium model is validated against the analytical solutions derived in this work [58]. Additionally, the assumptions used in the development of the 1-D non-equilibrium model are computationally validated against the CFD model.
- Chapter 6 presents the development of three new, non-isobaric evaporation models: 1-D, single phase CFD and multiphase CFD models.
- Chapter 7 provides a brief verification of the models developed in Chapter 6, with an emphasis on grid independence studies. The aim of this chapter is to verify

the correct computational implementation of the non-isobaric evaporation models, which are more complex than the isobaric evaporation models.

- Chapter 8 presents the results obtained with the non-isobaric evaporation models. The non-isobaric evaporation models are comprehensively validated against two experimental datasets [61, 62]. Additionally, the new non-isobaric evaporation models are compared for the storage of liquid nitrogen in an 8 m^3 tank filled to 30% and 97% of its capacity.
- Chapter 9 provides the conclusions of this thesis, summarizing the main findings for the isobaric and non-isobaric evaporation of cryogenic liquids and proposing suggestions for future work.

1.6 References

[1] V. Masson-Delmotte *et al.*, *Global warming of 1.5 C: an IPCC special report on the impacts of global warming of 1.5° C above pre-industrial levels and related global greenhouse gas emission pathways, in the context of strengthening the global response to the threat of climate change, sustainable development, and efforts to eradicate poverty*. World Meteorological Organization Geneva, Switzerland, 2018.

[2] V. Masson-Delmotte, P. Zhai, H.-O. Pörtner, D. Roberts, J. Skea, P.R.Shukla, A.Pirani, W. Moufouma-Okia, C. Péan, R. Pidcock, S. Connors, J.B.R. Matthews, Y.Chen, X.Zhou, M.I.Gomis, E. Lonnoy, T. Maycock, M.Tignor, and T. Waterfield (eds.), "IPCC, 2018: Annex I: Glossary [Matthews, J.B.R. (ed.)]. In: Global Warming of 1.5°C. An IPCC Special Report on the impacts of global warming of 1.5°C above pre-industrial levels and related global greenhouse gas emission pathways, in the context of strengthening the global response to the threat of climate change, sustainable development, and efforts to eradicate poverty," IPCC, 2018.

[3] M. R. Allen *et al.*, "Framing and Context in Global Warming of 1.5 C: An IPCC Special Report on the impacts of global warming of 1.5 C above pre-industrial levels and related global greenhouse gas emission pathways, in the context of strengthening the global response to the threat of climate change, sustainable development, and efforts to eradicate poverty," *Sustainable Development, and Efforts to Eradicate Poverty'.(Eds V Masson-Delmotte, P Zhai, HO Pörtner, D Roberts, J Skea, PR Shukla, A Pirani, W Moufouma-Okia, C Péan, R Pidcock, S Connors, JBR Matthews, Y Chen, X Zhou, MI Gomis, E Lonnoy, T Maycock, M Tignor, T Waterfield) pp,* pp. 41-91, 2018.

[4] J. Rogelj *et al.*, "Mitigation pathways compatible with 1.5 C in the context of sustainable development," in *Global warming of 1.5° C*: Intergovernmental Panel on Climate Change, 2018, pp. 93-174.

[5] "International energy outlook 2017," U.S. Energy Information Administration, Washington, DC 20585, 2017.

[6] International Energy Agency, "Global Energy Review 2021," IEA, Paris, 2021. [Online]. Available: https://www.iea.org/reports/global-energy-review-2021

[7] K. J. Warner and G. A. Jones, "The climate-independent need for renewable energy in the 21st century," *Energies,* vol. 10, no. 8, Aug 2017, Art no. 1197, doi: 10.3390/en10081197.

[8] "World energy outlook 2017," International Energy Agency, France, 2017.

[9] "Global energy and CO2 status report," International Energy Agency, Paris, France, 2018.

[10] I. Lee, J. Park, and I. Moon, "Conceptual design and exergy analysis of combined cryogenic energy storage and LNG regasification processes: Cold and power integration," *Energy,* vol. 140, pp. 106-115, 2017/12/01/ 2017, doi: https://doi.org/10.1016/j.energy.2017.08.054.

[11] G. Ma, H. Lu, G. Cui, and K. Huang, "Multi-stage Rankine cycle (MSRC) model for LNG cold-energy power generation system," *Energy,* vol. 165, pp. 673-688, 2018/12/15/ 2018, doi: https://doi.org/10.1016/j.energy.2018.09.203.

[12] L. Pattanayak and B. N. Padhi, "Thermodynamic analysis of combined cycle power plant using regasification cold energy from LNG terminal," *Energy,* vol. 164, pp. 1-9, Dec 2018, doi: 10.1016/j.energy.2018.08.187.

[13] S. Le, J.-Y. Lee, and C.-L. Chen, "Waste cold energy recovery from liquefied natural gas (LNG) regasification including pressure and thermal energy," *Energy,* vol. 152, pp. 770-787, 2018/06/01/ 2018, doi: https://doi.org/10.1016/j.energy.2018.03.076.

[14] T. He, Z. R. Chong, J. Zheng, Y. Ju, and P. Linga, "LNG cold energy utilization: Prospects and challenges," *Energy,* vol. 170, pp. 557-568, 2019/03/01/ 2019, doi: https://doi.org/10.1016/j.energy.2018.12.170.

[15] "BP Energy outlook 2018," BP, London, 2018.

[16] D. Lowell, H. Wang, and N. Lutsey, "Assessment of the fuel cycle impact of liquefied natural gas as used in international shipping," The International Council on Clean Transportation, Final report, 2013.

[17] F. Burel, R. Taccani, and N. Zuliani, "Improving sustainability of maritime transport through utilization of Liquefied Natural Gas (LNG) for propulsion," *Energy,* vol. 57, pp. 412-420, Aug 2013, doi: 10.1016/j.energy.2013.05.002.

[18] H. Q. Song, X. M. Ou, J. H. Yuan, M. X. Yu, and C. Wang, "Energy consumption and greenhouse gas emissions of diesel/LNG heavy-duty vehicle fleets in China based on a bottom-up model analysis," *Energy,* vol. 140, pp. 966-978, Dec 2017, doi: 10.1016/j.energy.2017.09.011.

[19] D. H. Kwak, J. H. Heo, S. H. Park, S. J. Seo, and J. K. Kim, "Energy-efficient design and optimization of boil-off gas (BOG) re-liquefaction process for liquefied natural gas (LNG)-fuelled ship," *Energy,* vol. 148, pp. 915-929, Apr 2018, doi: 10.1016/j.energy.2018.01.154.

[20] B. Y. Yoo, "Economic assessment of liquefied natural gas (LNG) as a marine fuel for CO2 carriers compared to marine gas oil (MGO)," *Energy,* vol. 121, pp. 772-780, Feb 2017, doi: 10.1016/j.energy.2017.01.061.

[21] A. Q. Gilbert and B. K. Sovacool, "US liquefied natural gas (LNG) exports: Boom or bust for the global climate?," *Energy,* vol. 141, pp. 1671-1680, Dec 2017, doi: 10.1016/j.energy.2017.11.098.

[22] A. R. Brandt *et al.*, "Methane Leaks from North American Natural Gas Systems," *Science,* vol. 343, no. 6172, pp. 733-735, 2014-02-14 2014, doi: 10.1126/science.1247045.

[23] GIIGNL, "LNG Information paper No. 2 the LNG process chain," The International Group of Liquefied Natural Gas Importers (GIIGNL), Neuilly'sur'Seine, France, 2009.

[24] M. Al-Breiki and Y. Bicer, "Comparative life cycle assessment of sustainable energy carriers including production, storage, overseas transport and utilization," *Journal of Cleaner Production,* vol. 279, p. 123481, 2021-01-01 2021, doi: 10.1016/j.jclepro.2020.123481.

[25] R. N. Krikkis, "A thermodynamic and heat transfer model for LNG ageing during ship transportation. Towards an efficient boil-off gas management," *Cryogenics,* vol. 92, pp. 76-83, 2018/06/01/ 2018, doi: https://doi.org/10.1016/j.cryogenics.2018.04.007.

[26] R. N. Krikkis, B. Wang, and S. Niotis, "An analysis of the ballast voyage of an LNG Carrier. The significance of the loading and discharging cycle," *Appl. Therm. Eng.,* vol. 194, p. 117092, 2021/07/25/ 2021, doi: https://doi.org/10.1016/j.applthermaleng.2021.117092.

[27] Volvo Truck Corporation, "Fact sheet gas tank LGAS205." [Online]. Available: https://stpi.it.volvo.com/STPIFiles/Volvo/FactSheet/LGAS155,%20LGAS205_Eng_02_3120592 28.pdf

[28] A. C. Rodrigues Teixeira, P. G. Machado, R. R. Borges, T. L. Felipe Brito, E. Moutinho Dos Santos, and D. Mouette, "The use of liquefied natural gas as an alternative fuel in freight transport – Evidence from a driver's point of view," *Energy Policy,* vol. 149, p. 112106, 2021-02-01 2021, doi: 10.1016/j.enpol.2020.112106.

[29] T. Banaszkiewicz *et al.*, "Liquefied Natural Gas in Mobile Applications—Opportunities and Challenges," *Energies,* vol. 13, no. 21, p. 5673, 2020-10-30 2020, doi: 10.3390/en13215673.

[30] H. Hao, Z. Liu, F. Zhao, and W. Li, "Natural gas as vehicle fuel in China: A review," *Renew. Sust. Energ. Rev,* vol. 62, pp. 521-533, 2016-09-01 2016, doi: 10.1016/j.rser.2016.05.015.

[31] T. O. I. f. E. Studies., "A Review of Prospects for Natural Gas as a Fuel in Road Transport," 2019. Accessed: 22 June 2021.

[32] M. Pehl, A. Arvesen, F. Humpenöder, A. Popp, E. G. Hertwich, and G. Luderer, "Understanding future emissions from low-carbon power systems by integration of life-cycle assessment and integrated energy modelling," *Nature Energy,* vol. 2, no. 12, pp. 939-945, 2017-12-01 2017, doi: 10.1038/s41560-017-0032-9.

[33] E. S. Hanley, J. P. Deane, and B. P. Ó. Gallachóir, "The role of hydrogen in low carbon energy futures–A review of existing perspectives," *Renew. Sust. Energ. Rev,* vol. 82, pp. 3027-3045, 2018/02/01/ 2018, doi: https://doi.org/10.1016/j.rser.2017.10.034.

[34] L. Van Hoecke, L. Laffineur, R. Campe, P. Perreault, S. W. Verbruggen, and S. Lenaerts, "Challenges in the use of hydrogen for maritime applications," *Energy & Environmental Science,* 10.1039/D0EE01545H vol. 14, no. 2, pp. 815-843, 2021, doi: 10.1039/D0EE01545H.

[35] E. Rivard, M. Trudeau, and K. Zaghib, "Hydrogen Storage for Mobility: A Review," (in English), *Materials,* Review vol. 12, no. 12, p. 22, Jun 2019, Art no. 1973, doi: 10.3390/ma12121973.

[36] R. Elliot, "Rocket Propellant and Pressurizaition Systems," ed: Prentice Hall., Inc., Englewood Cliffs, NJ–1964.–404 p, 1964.

[37] S. M. Aceves *et al.*, "High-density automotive hydrogen storage with cryogenic capable pressure vessels," *Int. J. Hydrogen Energy,* vol. 35, no. 3, pp. 1219-1226, 2010/02/01/ 2010, doi: https://doi.org/10.1016/j.ijhydene.2009.11.069.

[38] J. Moreno-Blanco, G. Petitpas, F. Espinosa-Loza, F. Elizalde-Blancas, J. Martinez-Frias, and S. M. Aceves, "The fill density of automotive cryo-compressed hydrogen vessels," *Int. J. Hydrogen Energy,* vol. 44, no. 2, pp. 1010-1020, 2019/01/08/ 2019, doi: https://doi.org/10.1016/j.ijhydene.2018.10.227.

[39] US Drive "Hydrogen Delivery Technical Team Roadmap July 2017," 2017.

[40] S. Krasae-in, J. H. Stang, and P. Neksa, "Development of large-scale hydrogen liquefaction processes from 1898 to 2009," *Int. J. Hydrogen Energy,* vol. 35, no. 10, pp. 4524-4533, 2010/05/01/ 2010, doi: https://doi.org/10.1016/j.ijhydene.2010.02.109.

[41] S. M. Aceves, G. D. Berry, and G. D. Rambach, "Insulated pressure vessels for hydrogen storage on vehicles," *Int. J. Hydrogen Energy,* vol. 23, no. 7, pp. 583-591, Jul 1998, doi: 10.1016/s0360-3199(97)00079-7.

[42] Z. Liu, Y. Li, and G. Zhou, "Study on thermal stratification in liquid hydrogen tank under different gravity levels," *Int. J. Hydrogen Energy,* vol. 43, no. 19, pp. 9369-9378, 2018/05/10/ 2018, doi: https://doi.org/10.1016/j.ijhydene.2018.04.001.

[43] A. Hofmann, "Theory to boil-off gas cooled shields for cryogenic storage vessels," *Cryogenics,* vol. 44, no. 3, pp. 159-165, 2004, doi: 10.1016/j.cryogenics.2003.09.003.

[44] Z. Q. Zuo, P. J. Sun, W. B. Jiang, X. J. Qin, P. Li, and Y. H. Huang, "Thermal stratification suppression in reduced or zero boil-off hydrogen tank by self-spinning spray bar," *Int. J. Hydrogen Energy,* vol. 44, no. 36, pp. 20158-20172, 2019/07/26/ 2019, doi: https://doi.org/10.1016/j.ijhydene.2019.05.241.

[45] L. Kawasaki Heavy Industries. "Kawasaki Completes Basic Design for World's Largest Class (11,200-cubic-meter) Spherical Liquefied Hydrogen Storage Tank." https://global.kawasaki.com/en/corp/newsroom/news/detail/?f=20201224_8018 (accessed 4th of June, 2021).

[46] M. Voldsund, K. Jordal, and R. Anantharaman, "Hydrogen production with CO2 capture," *Int. J. Hydrogen Energy,* vol. 41, no. 9, pp. 4969-4992, Mar 2016, doi: 10.1016/j.ijhydene.2016.01.009.

[47] T. Zhang, L. J. Chen, X. L. Zhang, S. W. Mei, X. D. Xue, and Y. Zhou, "Thermodynamic analysis of a novel hybrid liquid air energy storage system based on the utilization of LNG cold energy," *Energy,* vol. 155, pp. 641-650, Jul 2018, doi: 10.1016/j.energy.2018.05.041.

[48] M. Aneke and M. Wang, "Energy storage technologies and real life applications – A state of the art review," *Appl. Energy,* vol. 179, pp. 350-377, 2016/10/01/ 2016, doi: https://doi.org/10.1016/j.apenergy.2016.06.097.

[49] Y. Yildiz and M. Nalbant, "A review of cryogenic cooling in machining processes," *Int. J. Mach. Tool. Manu.,* vol. 48, no. 9, pp. 947-964, Jul 2008, doi: 10.1016/j.ijmachtools.2008.01.008.

[50] R. W. Arnett and R. O. Voth, "A computer program for the calculation of thermal stratification and self-pressurization in a liquid hydrogen tank," National Aeronautics and Space Administration, 1972. [Online]. Available: <Go to WoS>://WOS:000345232900026

[51] Y. Liu and K. Guo, "A novel cryogenic power cycle for LNG cold energy recovery," *Energy,* vol. 36, no. 5, pp. 2828-2833, 2011.

[52] B. Sreenivasulu, D. V. Gayatri, I. Sreedhar, and K. V. Raghavan, "A journey into the process and engineering aspects of carbon capture technologies," *Renew. Sust. Energ. Rev.,* vol. 41, pp. 1324-1350, Jan 2015, doi: 10.1016/j.rser.2014.09.029.

[53] Y. N. Wang, J. M. Pfotenhauer, X. Q. Zhi, L. M. Qiu, and J. F. Li, "Transient model of carbon dioxide desublimation from nitrogen-carbon dioxide gas mixture," *Int. J. Heat Mass Transfer,* vol. 127, pp. 339-347, Dec 2018, doi: 10.1016/j.ijheatmasstransfer.2018.07.068.

[54] C. Song, Q. Liu, S. Deng, H. Li, and Y. Kitamura, "Cryogenic-based CO2 capture technologies: State-of-the-art developments and current challenges," *Renew. Sust. Energ. Rev,* vol. 101, pp. 265-278, 2019/03/01/ 2019, doi: https://doi.org/10.1016/j.rser.2018.11.018.

[55] F. Huerta and V. Vesovic, "CFD modelling of the isobaric evaporation of cryogenic liquids in storage tanks," *Int. J. Heat Mass Transfer,* vol. 176, p. 121419, 2021/09/01/ 2021, doi: https://doi.org/10.1016/j.ijheatmasstransfer.2021.121419.

[56] J. Ren, H. Zhang, M. Bi, J. Yu, and S. Sun, "Numerical investigation of the coupled heat transfer of liquefied gas storage tanks," *Int. J. Hydrogen Energy,* vol. 42, no. 38, pp. 24222-24228, 2017, doi: 10.1016/j.ijhydene.2017.07.155.

[57] S. W. Churchill, "Heat leakage and wall temperature profiles for above ground low-temperature storage tanks," *Chem. Eng. Prog.,* vol. 58, no. 11, pp. 55-60, 1962.

[58] F. Huerta and V. Vesovic, "Analytical solutions for the isobaric evaporation of pure cryogens in storage tanks," *Int. J. Heat Mass Transfer,* vol. 143, p. 118536, 2019/11/01/ 2019, doi: https://doi.org/10.1016/j.ijheatmasstransfer.2019.118536.

[59] F. Huerta and V. Vesovic, "A realistic vapour phase heat transfer model for the weathering of LNG stored in large tanks," *Energy,* vol. 174, pp. 280-291, 2019/05/01/ 2019, doi: https://doi.org/10.1016/j.energy.2019.02.174.

[60] Z. Duan, H. Xue, X. Gong, and W. Tang, "A thermal non-equilibrium model for predicting LNG boil-off in storage tanks incorporating the natural convection effect," *Energy,* p. 121162, 2021/06/07/ 2021, doi: https://doi.org/10.1016/j.energy.2021.121162.

[61] M. Seo and S. Jeong, "Analysis of self-pressurization phenomenon of cryogenic fluid storage tank with thermal diffusion model," *Cryogenics,* vol. 50, no. 9, pp. 549-555, Sep 2010, doi: 10.1016/j.cryogenics.2010.02.021.

[62] M. Kang, J. Kim, H. You, and D. Chang, "Experimental investigation of thermal stratification in cryogenic tanks," *Exp. Therm. Fluid Sci.,* vol. 96, pp. 371-382, 2018/09/01/ 2018, doi: https://doi.org/10.1016/j.expthermflusci.2017.12.017.

Chapter 2

Literature review

This chapter provides a review of the technological and scientific development of the storage of cryogenic liquids. The aim of this review is to highlight the complexity of the transport phenomena that arise during the storage of liquid cryogens. Section 2.1, provides a review of experimental and theoretical work on cryogen evaporation and LNG weathering under isobaric conditions. Section 2.1 deals with isobaric storage only and sets the background for chapters 3-5 of this thesis. Section 2.2 provides a review of experimental and theoretical work on non-isobaric evaporation models of cryogenic liquids. Section 2.2 deal with the more complex non-isobaric storage scenario and sets the background for chapters 6-8 of this thesis. For the sake of conciseness, the review of heat transfer, turbulence and boiling sub-models has been deferred to chapter 3 and 6.

Although 129 years have passed since the invention of the Dewar's cryogenic storage vessel [1], experimental data regarding cryogenic liquid storage is still limited. This is a consequence of the safety and practical challenges on setting up experiments with cryogenic liquids. As a result of these experimental challenges, most research has been focused on developing theoretical and computational models. Nevertheless, the scarce experimental results have been pivotal to the development of theoretical and computational models. This chapter provides a detailed description of experimental research, while only the main assumptions, results and modelling approaches are highlighted for computational and theoretical research.

2.1 Storage of cryogenic liquids under isobaric conditions

Most research on the isobaric evaporation of pure cryogens has been carried out to investigate LNG weathering [2, 3]. These studies have been focused on LNG storage

in large tanks during long storage periods typical of marine transportation and peak-shaving facilities. Several studies have been focused on predicting LNG rollover, which is a safety hazard that arise from the rapid mixing of a stratified LNG and sudden vapour release [4-12]. In this review, LNG rollover will not be addressed in detail. This thesis will focus on the storage of cryogenic liquids assuming that the storage process is free from safety hazards. The weathering of LNG occurs in storage stages through the LNG supply chain such as in LNG cargoes and peak shaving facilities. Owing to the engineering challenges posed by cryogenic liquids and the market-sensitivity of industrial data, few experimental data on weathering under isobaric conditions is available in the open literature [13]. Another early research niche for isobaric evaporation was the storage of liquid hydrogen as a rocket propellant in auxiliary storage tanks at launch pads [14]. Recently, zero boil-off technologies (ZBOT) such as vapour cooled shields [15] or jet mixing [16, 17] have been developed to minimize BOG during the storage of cryogenic liquids. These state-of-the art technologies operate under isobaric conditions. Thus, improving the understanding of transport phenomena during the isobaric evaporation of cryogens in storage tank will aid the aerospace, healthcare, and renewable energy sectors.

In subsection 2.1.1, a review of the scarce experimental evidence on the isobaric evaporation of cryogenic liquids and LNG weathering is provided. In subsection 2.1.2, a review of LNG weathering models that assume thermal equilibrium between vapour and liquid phases is provided. In subsection 2.1.3, a review of non-equilibrium weathering models is provided. Non-equilibrium models have received overwhelming attention in the last 3 years. Finally, in subsection 2.1.4 a review of computational fluid dynamics (CFD) models for the isobaric evaporation of cryogens and LNG weathering is provided.

2.1.1 Experimental evidence

Stochl and Knoll [14] experimentally investigated the performance of a multilayer insulation system (MLI) during the isobaric evaporation of LH_2 in a 4.89 m^3 spherical oblate storage tank initially filled at 95% of its capacity. They found that for wall heat fluxes of 0.3, 1.7 and 3 W $m^{-2}K^{-1}$, the BOR were 0.2%, 1.3% and 2% per day, respectively. This finding experimentally validated, for the first time, the theoretical intuition that

boil-off rates are proportional to wall heat flux during isobaric evaporation. Inside the MLI, conduction dominated heat transfer for the lowest heat flux scenario, while radiation dominated heat transfer in the highest heat flux scenario.

In addition to conduction and convection, heat is transferred by radiation during the storage of cryogenic liquids. Heat radiation occurs between the surroundings and the outer tank shell, between the multi-layered insulation system, and between the internal tank walls and the cryogenic liquid and its vapour. The multi-layered insulation system consists of alternating layers of radiation shields and low conductivity spacer material, such as fibreglass or perlite [18], under a high vacuum. The layers of radiation shields are intended to decrease the radiative heat transfer within the MLI system. This is necessary because of the large temperature difference between the surroundings and the outer tank surface, and between the outer and inner layers. On the other hand, the heat radiation between the inner tank wall, the cryogenic vapour and its liquid has not been studied yet. Radiation will not be studied in this thesis, although it may be significant for scenarios where the vapour is significantly superheated with respect to the liquid. Therefore, more research is needed to quantify radiative heat transfer during the storage of cryogenic liquids.

Belmedani et al. [19] experimentally investigated the isobaric evaporation of LN_2 in a vertically orientated cylindrical tank under high wall heat fluxes (3 and 5 kW m^{-2}). A detailed analysis of the boundary layer near the wall and the thermally stratified layer below the interface was provided. They found that the evaporation rate disrupted the thermally stratified layer, and that the Rayleigh (*Ra*) number increased with the evaporation rate. An inverse relationship between the thermally stratified layer thickness and the evaporation rate was observed. This shows that vigorous evaporation at the interface can remove liquid thermal stratification and improve liquid mixing. Li et al. [20] investigated the effect of liquid filling on heat ingress for the isobaric evaporation of LN_2 in a 180 L vertically orientated cylindrical tank. The experimental results showed that the total heat ingress is partitioned between a constant heat ingress from the bottom and a variable heat ingress through the walls. Additionally, it was concluded that the heat ingress through the walls increases linearly with liquid filling (*LF*).

Lin et al. [21] experimentally investigated the isobaric evaporation of LN_2 in a 1.5 m^3 horizontally orientated cylindrical tank at 7 different liquid fillings between 30% and 60%. Thermocouples at the middle and the top of the tank showed significant vapour thermal stratification. The maximum superheating of the vapour with respect to the liquid was up to 50 K, and it increased with decreasing liquid filling. A heat transfer model augmented with an adjacent fluid layer sub-model between phase boundaries was included to obtain the temperature distribution in the tank. The model required one empirical parameter, the "effective thermal conductivity", to consider convection and multiphase effects. By fitting the effective thermal conductivity to the gathered experimental data, Lin et al. [21] showed that convection contributed less than 10% to BOG generation. For LN_2 isobaric evaporation in a horizontally orientated storage tank, conduction was the dominant heat transfer mechanism in the vapour phase. It was also observed that as the liquid filling decreased from 50% to 40% due to evaporation, the vapour-liquid interface oscillated. Nevertheless, the oscillation of the interface did not de-stratify the vapour phase.

Qu et al. [22] used datasets from an onboard collection platform installed in several LNG cargos for the purpose of model validation. A 160,000 m^3 on board storage tank was considered. The vapour was superheated with respect to the liquid, and its maximum temperature increased from 143 to 173 K in a 62-h ballast (low liquid filling) voyage. In contrast, for a 62-h laden (high liquid filling) voyage, the vapour phase was no more than 4 K superheated with respect to the liquid. Furthermore, the temperature decreased and then increased during the voyage. Based on these results, Qu et al. [22] pointed out that modelling the vapour phase during the isobaric storage of LNG is challenging.

Krikkis [23] presented industrial data of LNG weathering in a membrane LNG carrier with four containment tanks for two voyages of 251 and 320 h. His data showed that boil-off rates follow the fuel requirement from the engine. Liquid thermal stratification was lower than 1 K, while the vapour was superheated up to 90 K with respect to the liquid. This demonstrated that despite the sloshing of the vessel, vapour and liquid phases are not in thermodynamic equilibrium. Krikkis [23] suggested that for the first 50 h of the voyages, the conjugate heat transfer problem between the containment tank

and stored LNG mixture must be solved. Subsequently, Krikkis et al. [24] provided data for a 25,000 m^3 LNG cargo with four cargo containment systems (CCS) for a complete loading and unloading cycle. A non-uniform wall temperature distribution was observed, which led to non-uniform wall heat fluxes to both vapour and liquid phases. Krikkis et al. [24] observed that non-uniform wall heat fluxes drove complex phase change mechanisms within the tank during LNG loading. During the loading process, the ascending liquid enters in contact with a previously superheated wall, driving nucleate boiling, sub-cooled boiling and natural convection at different times. Conjugate heat transfer was relevant for the totality of the loading, laden voyage, unloading and ballast voyage (600 h) cycle. They found that during the ballast voyage, surface evaporation was the dominant evaporation mechanism.

Yu et al. [25] developed a prototype to test dynamic BOG generation in a 40 m^3 horizontally orientated cylindrical LNG container under shipping conditions. The container was filled to 90% of its capacity with a commercial LNG mixture. The effect of ship roll motion was investigated for three different shipping scenarios varying the amplitude and frequency of a sinusoidal periodic motion. For each scenario, an additional experiment under static conditions was performed as a base case. For all scenarios, it was found that the average BOG increased noticeably with the roll motion of the test platform. The maximum increase in BOG rates was 29% for the scenario with the highest roll motion amplitude. They concluded that ship motion enhanced LNG evaporation owing to (i) dynamic wetting and drying of the tank walls as the interface displaces and (ii) viscous dissipation of the kinetic energy from the ship motion. Additionally, the vapour temperature at the top of the tank was 12 K superheated with respect to the liquid temperature for all scenarios. This superheating was stable throughout the whole duration of the tests, indicating that ship roll motion does not produce vapour thermal destratification.

Niu et al. [26] performed experiments for the isobaric evaporation of LN_2 in a 40 m^3 LNG cargo containment system (CCS) designed to operate in floating and regasification storage units. Boil-off rates and ambient temperature were measured through 24 h of evaporation. A conversion technique was developed to relate the experimental results for LN_2 tests to LNG evaporation under the International Gas Code (IGC) conditions. It

was found that the temperature of the internal walls and BOR significantly varied with ambient temperature. Furthermore, for an increase of 1 °C, the BOG rates increased 5%. This result is an order of magnitude higher than Migliore et al. [27] estimation (0.2% increase in BOG for an increase of 1°C of ambient temperature). This disagreement is potentially explained by the much smaller volume (1:4125) of the tank used in Niu et al. [26] experiments.

Recently, liquid nitrogen evaporation [28] and LNG weathering [29] experiments have been carried out with high precision and state of the art instrumentation. Perez et al. [28] developed an experimental system and procedure to measure boil-off gas and thermal stratification during the evaporation of cryogens in storage tanks. A 6.73 L vertically orientated storage tank was heated through the walls by electrical elements installed in an outer copper layer. During the isobaric stage of the experiments, they found that the vapour was thermally stratified and superheated with respect to the liquid. The maximum superheating and thermal stratification increased with decreasing liquid filling. Simultaneously, the liquid temperature profile was spatially homogeneous for all the experimental scenarios. For all experiments, the BOG rates slowly decreased with time as the area of the tank in contact with liquid nitrogen decreased due to evaporation.

Al Ghafri et al. [29] used the same experimental device developed by Perez et al. [28] to experimentally investigate the weathering of a methane-ethane mixture. Seven experiments were performed under different wall heat fluxes, initial liquid fillings and mixture compositions at a pressure set point of 151 kPa for the isobaric stage. They found that mixtures for a methane molar fraction (x_{C1}) higher than 0.82, the BOG was almost pure methane ($y_{C1} > 0.995$). In all scenarios, the vapour was thermally stratified and superheated with respect to the liquid phase, as observed by Perez et al. [28] for LN_2 evaporation in the same system. Both BOG and average vapour temperatures increased significantly with the temperature of the boundary copper can, which in turns determines the wall heat flux. For the experiments with low variations of boundary temperature, the BOG rates were nearly constant. In line with previous experimental research on other systems, BOG rates decreased with initial liquid filling. This suggests

that the vapour phase acts as a resistance to heat transfer from the surroundings to the liquid, which drives evaporation.

2.1.2 Equilibrium models

Early research was focused on developing LNG weathering models under the assumption that the vapour and liquid are at thermal equilibrium. The thermal equilibrium assumption implicitly implies that all the heat ingress to the vapour phase is transferred to the liquid instantaneously. The key strength of equilibrium models is their simplicity. Among weathering equilibrium models, two different approaches can be identified: (i) based on the boil-off ratio (BOR) and (ii) based on heat ingress calculation. BOR based models predict weathering by using a fixed BOR as an empirical model input. The input BOR is obtained from experimental or industrial data for specific storage tanks at typical operating conditions [30-32]. Although BOR based models are frequently used in the industry because of their simplicity, they are not best suited for LNG with high nitrogen content [27]. Additionally, BOR based models are also not appropriate for scenario testing for scenarios where BOR data is not available. On the other hand, models based on heat ingress calculation have firmer theoretical foundations and are more generic. These models calculate the BOR and other industry relevant parameters using a heat transfer model that considers the tank insulation properties. Thus, simulations can be performed by solving mass and energy balances, the heat transfer model and a thermodynamic model that constitute the weathering model. Heat ingress calculation models have been used to simulate weathering and cryogen evaporation across a range of scales and cryogens [13].

The first weathering model was developed in 1962 by Churchill [33], who developed a one-dimensional, steady-state heat transfer model for the tank walls for the isobaric evaporation of pure methane. Although Churchill [33] assumed thermal equilibrium and between the vapour and the liquid, he mentioned the possibility of the vapour to be superheated. In that case, he suggested to examine the non-uniformity of the heat flux to the vapour phase. Three decades later, Shah and Aarts [34] developed the first transient model of weathering which also allowed an arbitrary LNG mixture. The Shah and Arts model was subsequently included as a sub-model in several works which aimed

to improve the thermodynamic model [35-38]. Adom et al. [39] developed a weathering model and explored the effect of operating pressure on BOG rates. They concluded that BOG rates decrease with increasing operating pressure.

Pellegrini et al. [40] developed a weathering model assuming a constant heat ingress and allowed the variation of LNG thermophysical properties during weathering. They simplified the phase equilibrium calculations to linearize the system, which allowed their model to achieve convergence at the expense of accuracy for nitrogen-rich mixtures. Thereafter, Migliore et al. [41] developed a weathering model based on rigorous heat transfer and phase equilibrium sub-models that no longer required the constant heat ingress assumption. They concluded that even small nitrogen concentrations (~ 0.5%) in the LNG mixture have a pronounced effect in BOG rates.

As it was discussed in subsection 2.1.1, vapour thermal stratification has been consistently observed in recent experimental studies. This is theoretically expected owing to the low thermal diffusivity of the LNG vapour [13, 42]. The heating from the vapour through the walls and its cooling at the interface will drive natural convection. Unfortunately, equilibrium models are not able to predict vapour temperature profiles and can only include natural convection in an oversimplified manner. This limits the applicability of equilibrium models, as they overpredict evaporation rates by neglecting the resistance to heat transfer in the vapour phase, and underpredict BOG temperatures [13, 42]. Additionally, equilibrium models underpredict BOG rates at the beginning of the evaporation because of neglecting vapour thermal expansion [13, 43].

2.1.3 Non-equilibrium models

To overcome the limitations of equilibrium models, non-equilibrium models have been developed. Non-equilibrium models allow the vapour phase to be superheated with respect to the liquid by the inclusion of a vapour phase heat transfer sub-model. The key strengths of non-equilibrium models are a better agreement with experimental data [3, 44] and their high computational efficiency [3, 13, 28, 43-45]. To achieve a high computational efficiency, vapour buoyancy driven flow and temperature profiles are modelled instead of solving the momentum, continuity and energy

equations. The variety of the assumptions have led to a significant disagreement in the vapour phase heat transfer sub-models available in the literature [5, 13, 23, 24, 28, 42, 44-47]. The differences among sub-models are significant as they predict radically different vapour temperature profiles and BOG rates.

As early as in 1968, Neill et al. [4] developed a non-equilibrium model as a part of their LNG rollover simulations. This non-equilibrium model included radiation from the surroundings. They suggested that radiation contributed between 12% to 30% to the total heat transfer. However, their model was not able to accurately predict BOR rates. Neill et al. [4] model predicted a thermally stratified vapour, of up to 60 K superheated with respect to the liquid, which was in a good agreement with limited industrial data used for model validation. Afterwards, simpler models were developed in which the vapour temperature profile is not explicitly resolved. Instead, the vapour to liquid heat transfer rate is calculated directly either as a constant fraction of the vapour heat ingress [5, 23], or through assuming pure natural convection [22, 28, 45, 47]. Although these simple models have shown good agreement on steady-state BOG rates, they are unable to predict vapour temperature profiles.

In more complex non-equilibrium models, partial differential equations that govern vapour phase heat transfer are solved in conjunction with ordinary differential equations subsystem from the liquid bulk. Using this approach, Migliore et al. [42] assumed that the vapour phase heat transfer was governed by pure conduction. Their approach was justified by the limited convective heat transfer in the vapour phase due to the stable, negative density gradient. Migliore et al. [42] further assumed that the vapour phase temperature profile was governed by the one-dimensional heat diffusion equation in the vertical coordinate, and used its similarity solution for semi-infinite domains. Huerta and Vesovic [13] expanded this model by adding advection and representing the vapour wall heating as a volumetric source term. We found that for low liquid fillings the equilibrium model [41] in some cases overestimates the BOG rates by as much as 100%. We also found that the vapour phase reached a pseudo-steady state after a transient time proportional to the ratio between the vapour space and the average advective velocity. This led us to develop analytical solutions for the limiting scenario of the isobaric evaporation of pure cryogenic liquids [3].

This paragraph focuses on LNG weathering models in scenarios of marine transportation. Krikkis [23] developed a non-equilibrium model assuming that the vapour was superheated with respect to the liquid, but both phases had a spatially homogeneous temperature. This model was deployed to investigate a carrier which used the evaporated natural gas as a fuel. Krikkis [23] concluded that BOG rates were mainly governed by the carrier power curves and suggested that conjugate heat transfer have a significant effect on BOG rates. This suggestion is in line with Sharafian et al. [48] review for BOG rates generation during non-isobaric storage in a static tank.

Qu et al. [22] published the non-equilibrium thermodynamic model used by Gaztransport & Technigaz to simulate LNG evaporation and weathering in membrane cargo carriers. The vapour and liquid were assumed thermally homogeneous, but at different temperatures. The main contribution of this work was the inclusion of conjugate heat transfer, radiation and sloshing in a simplified manner. The model showed good agreement with experimental data on average vapour temperatures and BOG rates carriers. Recently, Krikkis et al. [24] extended his weathering model to include conjugate heat transfer, and used Huerta and Vesovic [13] vapour phase heat transfer sub-model to model thermal stratification. They suggested that the range of applicability of Huerta and Vesovic [13] model can be extended to non-isobaric conditions using a non-uniform velocity profile. That profile should consider the deceleration of the vapour as it reaches to the top of the tank under non-isobaric conditions.

Wang et al. [45] developed a non-equilibrium model for LNG storage and weathering using a resistance-capacitance network approach. This approach considers conjugate heat transfer and can be applied to dynamic conditions such as the filling and emptying of the storage tank. Wang et al. [45] found that in the absence of dynamic conditions, cylindrical tanks vertically or horizontally orientated have the same performance on minimizing BOG rates. In contrast, under dynamic conditions horizontally orientated storage tanks produce smaller BOG rates than vertically orientated tanks.

Duan et al. [44] developed a non-equilibrium model which features a new liquid phase natural convection sub-model. Natural convection in the liquid was implemented using the integral form of the buoyancy driven flow equations based on the Leibniz rule.

For the vapour phase, they used Huerta and Vesovic [13] heat transfer sub-model. They found excellent agreement on vapour and liquid temperature profiles when validating against Kang et al. [49] steady-state profiles for nitrogen evaporation in small tanks under high liquid fillings. Duan et al. [44] performed the analysis for the evaporation of LNG in a 36,800 m^3 storage tank filled at 90% of its capacity. They found that between 22% and 55% of the heat ingress from the surroundings would go to increasing liquid sensible heat. This finding suggests that models which neglect liquid natural convection would greatly overestimate BOG and evaporation rates. These results contrast with Saleem et al. [50] CFD model, where they concluded that after 20 h more than 99% of the liquid heat ingress go into producing evaporation. Duan et al. [44] model may underestimate evaporation rates because it neglects wall boiling and wall evaporation [51].

Jo et al. [52, 53] developed a non-equilibrium LNG weathering model where the stored LNG was divided in three sub-domains: vapour, upper liquid and lower liquid. Each sub-domain was assumed to have a spatially homogeneous temperature. The weathering under both isobaric ("venting") and non-isobaric ("sealed tank mode") operating conditions were investigated. This approach was taken considering that BOG compressors under isobaric conditions can fail, and a process control system must work reliably for both isobaric and non-isobaric conditions. The evaporation of LNG in a 173,400 m^3 No.96 membrane tank used in industry was investigated for three different initial liquid fillings: 10%, 50% and 94%. For the storage under isobaric conditions, it was found that evaporation was the dominant phase change mechanism. Additionally, the temperature of the upper and lower liquid layers was the same. This implied that the vertical division of the liquid domain was redundant for the storage under isobaric conditions. The rate of vapour heating in isobaric conditions was much slower than in non-isobaric conditions owing to the removal of energy as BOG. This observation shows that scaling for the transient time of vapour heating proposed by Huerta and Vesovic [13] is not applicable for non-isobaric conditions.

Although non-equilibrium models produce more realistic results than equilibrium models, they rely on several assumptions to simplify vapour phase momentum transfer. Furthermore, it is not possible to realistically consider multiphase phenomena near the

tank walls or at the vapour-liquid interface in a non-equilibrium model. CFD models can overcome those limitations by solving a full continuum model of the isobaric evaporation of liquid cryogens. The key strength of CFD models is the detailed description of velocity, temperature and density profiles in the modelled fluid phases.

2.1.4 CFD models

Khelifi-Touhami et al. [54] performed CFD simulations of laminar natural convection ($10^3 < Ra < 10^5$) in a vertical cylindrical cavity. The cavity was heated through the walls, insulated at the bottom, and cooled at the top through an evaporative heat flux. This configuration simulates the liquid phase during the isobaric evaporation of a cryogenic liquid. It was found that the maximum and minimum heat fluxes were located at the wall-liquid contact surface and at the tank axis, respectively. Roh and Son [55] performed CFD simulations for the liquid phase over the same geometry considering simultaneous wall and bottom heating and turbulent natural convection. They observed that the maximum heat flux occurred at the wall-liquid contact surface, generalising Khelifi-Touhami et al. [54] conclusion for turbulent natural convection. Additionally, Roh and Son [55] concluded that the vapour to liquid heat transfer contributed less than 1% of the total heat ingress to the liquid.

Maksimov et al. [56] performed 2-D simulations of natural convection in a liquid enclosed in a rectangular cavity under bottom and wall heating. They used the vorticity-stream function approach, valid for nearly two-dimensional flows. Maksimov et al. [56] concluded that the aspect ratio of the rectangular cavity had a significant effect on thermal stratification in the liquid. Saleem et al. [50] performed multiphase CFD simulations on the isobaric evaporation of pure methane in an onshore cylindrical storage tank. The Volume of Fluid (VoF) method was used to track the vapour liquid interface. It was concluded that surface evaporation was the dominant heat transfer mechanism for typical storage conditions. Furthermore, the transition to nucleate boiling in the liquid bulk required a superheating of 2.5-2.8 K for LNG. That degree of superheating would require an overall heat transfer coefficient in the liquid phase (U_L) of 25 W $m^{-2}K^{-1}$. That value of U_L is three orders of magnitude higher than typical U values for insulated storage tank used in industry. Unfortunately, the vapour temperature

profiles obtained by Saleem et al. [50] model significantly underpredicted the vapour temperature typical of industrial storage conditions. This is a consequence of Saleem et al. [50] choice of the standard k-ϵ turbulence model for a nearly stagnant vapour phase. The k-ϵ model is known to significantly overpredict the turbulent kinetic energy in stagnation and low velocity regions [57]. This leads to an overprediction of the effective thermal diffusivity for cryogenic storage CFD simulations [58].

Wang et al. [59] performed CFD simulations to quantify the impact of mechanical vibrations and heat ingress on BOG rates for LNG storage during on-road transportation. A 40 m^3 cylindrical storage tank horizontally orientated was considered. Wang et al. [59] concluded that heat ingress contributed more than 70% to BOG rates in all scenarios. However, the contribution from vibrations to BOG rates increased rapidly with driving speed, was more than 10% for the slowest driving speed, and cannot be neglected [59]. Jeon [60] developed a multiphase model considering solid conduction and conjugate heat transfer. They successfully validated their model against Lin et al. [21] and Jeong et al. [61] KC-1 containment ship BOG experimental data. In particular, Jeon [60] considered a horizontally orientated cylindrical tank supported by two saddles. In this scenario, nucleate boiling was observed near the saddles. A jet of bubbles drove multiphase natural convection that dominated liquid temperature and velocity profiles. Additionally, a well-mixed layer driven by surface evaporation was observed below the vapour-liquid interface. In the liquid bulk, natural convection was strong at the beginning of the evaporation, and then it was dampened as the temperature profile fully developed.

Recently, Huerta and Vesovic [43] developed a CFD model of the vapour phase during the isobaric evaporation of pure cryogenic liquids. We considered pure methane as the stored cryogen and performed CFD simulations for three scenarios that comprise different liquid fillings and tank sizes. Huerta and Vesovic [43] found that the vapour phase was strongly thermally stratified. The onset of thermal stratification dampened natural convection in all scenarios. Vapour temperature profiles, BOG and evaporation rates were in excellent agreement with Huerta and Vesovic [13] 1-D weathering model. Using CFD as a validation tool, we were able to computationally validate the strongest assumptions in Huerta and Vesovic 1-D model [13]. Namely, for estimating BOG rates

and vapour temperatures, natural convection in the vapour can be accurately represented by an effective, advective, upwards velocity [43].

The main disadvantage of CFD models is they require longer simulation times than non-equilibrium models. Typically, CFD models require between 3 and 5 orders of magnitude more simulation time than non-equilibrium models. This makes CFD models for the evaporation of cryogenic liquids unsuitable for simulating long storage periods. Nevertheless, they offer unprecedented amount of detail on the transport phenomena. Thus, the capabilities of CFD evaporation and weathering models can be best exploited as a validation tool for simpler non-equilibrium and equilibrium models.

2.2 Storage of cryogenic liquids under non-isobaric conditions

The aim of this subsection is to review experimental and theoretical developments for the non-isobaric evaporation of cryogenic liquids in storage tanks. In subsection 2.2.1, the available experimental literature on the non-isobaric storage of cryogenic liquids is reviewed. In section 2.2.2, the simplest models constituting bulk mass and energy balances are reviewed, highlighting the key simplifying assumptions of each model. In section 2.2.3, non-isobaric evaporation models based on more realistic heat transfer and fluid flow sub-models are reviewed. Finally, in subsection 2.2.4 a comprehensive review of the computational fluid dynamic (CFD) models for the non-isobaric evaporation of cryogenic liquids is provided.

2.2.1 Experimental work on non-isobaric storage of cryogenic liquids

In 1963, Anderson and Kolar [62] experimentally investigated the non-isobaric evaporation of a 2:1 mixture of trichloroethane with ethyl alcohol in a 3.42 L vertical container filled at 66% of its capacity. Anderson and Kolar [62] captured Schlieren photographs of the fluid flow and measured liquid temperature profiles over three different heating conditions, namely wall heating, bottom heating and mixed wall and bottom heating. Anderson and Kolar [62] found that under bottom heating only, the liquid temperature was spatially homogeneous and increased with time. For wall heating, a stable thermally stratified layer developed from the interface. For the mixed regime of wall and bottom heating, two regions were formed with the characteristics of

each heating regime. In other words, a thermally stratified layer was observed below the interface, while a well-mixed, liquid bulk region was observed below the stratified layer. The mixed regime was considerably more complex as the thermally stratified layer exchanged heat and mass with the liquid bulk region.

Tatom et al. [63] presented Anderson et al. [62] data in conjunction with additional experimental data for the non-isobaric evaporation of liquid hydrogen. The same wall, bottom and mixed heating conditions were studied for the storage of LH_2 in a 2.27 m^3 vertically orientated cylindrical tank. Tatom et al. [63] concluded that for LH_2 stored in a larger tank, thermal stratification behaviour was analogous to Anderson et al. [62] results. Furthermore, it was observed that for LH_2 storage under mixed heating conditions, the currents driven by bottom heating disrupted the wall boundary layer. The disruption of the wall boundary layer was considered a driver of the enhanced liquid mixing. This phenomena explained the smaller liquid thermal stratification observed for the mixed regime [63] when compared against wall heating only.

In 1964, Ring provided experimental evidence on liquid thermal stratification during the active pressurization of cryogenic liquids in storage tanks [64]. Active pressurization is the process in which an inert gas is injected to a cryogenic storage tank to increase its pressure. In active pressurization, the dominant phase change mechanism is usually condensation, and the timescale of the process is much shorter than for self-pressurization. Ring [64] reported experimental data for both liquid in-ground and in-flight tests of adiabatic active pressurization using helium as the inert gas. For the in-ground test, liquid nitrogen was pressurized in a full-scale in-ground Titan oxidizer tank. For the in-flight test, temperature measurements of liquid oxygen temperature in the storage tank of Vanguard and Titan flights were considered. Ring [64] experimental data showed that for both scenarios, a thermally stratified layer developed below the interface. The warm stratified layer was up to 15 K superheated and partially mixed with the liquid.

Aydelott and Spuckler [65] experimentally investigated the evaporation of liquid hydrogen in a lab-scale spherical tank of 56 cm diameter with its vent closed. Three liquid fillings LF = (30%, 50%, 80%) and heat fluxes (q_w = 60, 63 and 203 Wm^{-2}) were considered. Aydelott and Spuckler [65] observed that the initial liquid filling had a small

effect on pressurization rates. To explain this result, Aydelott and Spuckler [65] suggested that the increase of liquid thermal stratification and the decrease of vapour heating with liquid filling counterbalanced their effects on pressure rise. Additionally, it was concluded that the pressurization rate increased linearly with the wall heat flux. Finally, it was observed that the vapour temperature varied only with height and the isotherms were horizontal. On the basis of these results, Aydelott and Spuckler [65] proposed that natural convection was small and conduction dominated vapour phase heat transfer. Nevertheless, Aydelott and Spuckler [65] pointed out that their conclusions regarding the heat transfer in the vapour were speculative as this phenomena was not yet well understood.

Arnett and Voth [66] reported experimental results for the evolution pressure and vapour temperature during the non-isobaric evaporation of LH_2 for NASA Plum Brook B-2 in ground test. The pressure of the storage tank increased linearly with time. Their results also showed that the vapour phase temperature increased with height, reaching 70 K of maximum superheating 4.5 m above the interface. Lacovic experimental data on liquid hydrogen evaporation during the Centaur C-8 flight reported an analogous behaviour for vapour temperature stratification and pressurization rate [67]. Hasan et al. [68] studied the self-pressurization of liquid-hydrogen in a 4.89 m^3 ellipsoidal tank filled at 95% of its capacity. In contrast to previous studies, Hasan et al. [68] investigated three different, very low heat fluxes: 0.35, 2 and 3.5 W $m^{-2}K^{-1}$. They found that the pressurization rate increased with heat flux, in line with previous studies. In the scenario of highest heat flux, the pressure increased three times faster than theoretical predictions assuming thermal equilibrium between vapour and liquid. The pressure build-up showed an initial transient response where the pressure increased rapidly, followed by a period of nearly constant pressure rise rate. For all experiments, the vapour temperature reached a pseudo-steady state after 4 hours while the liquid temperature kept increased during the totality of the storage period.

Van Dresar et al. [69] investigated the self-pressurization of LH_2 in the same 4.89 m^3 storage tank considered by Stochl and Knoll [14]. Two heat fluxes, 2.0 and 3.5 Wm^{-2}, and three initial different liquid fillings, 29%, 49% and 83%, were tested. The highest pressurization rate was observed for the intermediate liquid filling (49%) because of the

effect of the ellipsoidal geometry on liquid wet area. This shows that the pressurization rate does not increases monotonically with liquid filling, which shows that Aydelott and Spuckler [65] results cannot be generalized for larger spherical tanks. Van Dresar et al. [69] study was the first experimental investigation that demonstrated a potentially non-linear relationship between pressurization rates and liquid filling.

Aszodi et al. [70] performed experiments to measure temperature profiles and void fractions during the storage of water under high heat fluxes representative of exposure to fire. A 12.27 L cylindrical tank vertically orientated filled at 84% of its capacity was subject to a heat flux of 20.4 kWm^{-2} through the side walls. Thermal stratification was observed after 200 s from the beginning of the experiments. The difference between the temperature at the interface and at the bottom of the liquid first increased and then decreased, reaching 50 K after 1000 s. Sub-cooled wall boiling was observed near the wall, where the void fraction reached 20%. A boiling front with high void fraction emerged below the vapour liquid interface, which propagated downwards with time. In that front, the liquid was well mixed and at saturation temperature, while below that front, thermal stratification was observed. Temperature jumps in the thermocouples installed in the tank were found at different times, indicating the progress of the boiling front. Aszodi et al. [70] experiments demonstrated that under high heat fluxes, multiphase heat, mass and momentum transfer enhanced natural convection in the liquid and cannot be neglected.

Gong et al. [71] studied the self-pressurization of liquefied petroleum gas (LPG) in a 60 L vertically orientated cylindrical tank under high heat fluxes. The tank stored liquid propane considering two initial liquid fillings, 50% and 80%, and two heat fluxes, 3 and 5 kW m^{-2}. Gong et al. [71] concluded that heat flux and liquid filling increased the pressurization rate. They argued that the pressurization rate was higher for the higher liquid filling scenarios because of higher liquid thermal stratification. A maximum superheating of 30 K between the interface and the liquid bulk was observed in the high liquid filling, high heat flux experiment. Lin et al. [72] investigated vapour and liquid thermal stratification during the pressurization of LPG subject to high heat fluxes. A 50 L cylindrical tank in vertical configuration was heated through the side walls only by an electric heater. Two liquid fillings (85% and 45%) and heat fluxes (4 kWm^{-2} and 10 kWm^{-}

²) were investigated. The degree of stratification , $\beta = P/P_{sat}$ [73], was used to quantify stratification. where P is the pressure at the interface and P_{sat} the saturation pressure evaluated at the mass averaged liquid temperature. Lin et al. [72] concluded that liquid thermal stratification increased with heat flux but decreased with initial liquid filling, which contrasts with Gong et al. [71] conclusions.

Shi et al. [74] investigated liquid thermal stratification in water stored in a storage tank simulating high heat fluxes representative of fire exposure. The heating of water under different liquid fillings in a 50 L cylindrical tank in vertical configuration was investigated under non-uniform wall heating. The main novelty of Shi et al. [74] study was the use of two different electrical heaters to separately heat the liquid and vapour phases. This allowed the investigation of thermal stratification and pressure build-up in the scenarios of only liquid heating, and homogeneous liquid and vapour heating. It was found that the liquid was thermally homogeneous if only the liquid phase was heated. In contrast, under the scenario of vapour and liquid heating, significant thermal stratification in the liquid developed. Subsequently, these conclusions were confirmed for R22 storage in the same storage tank [75]. This ground-breaking finding demonstrates that for high heat fluxes, liquid thermal stratification is a consequence of the increase of vapour heating only.

Hulsbosch-Dam performed a bonfire test on a horizontally orientated cylindrical tank filled at 66% of its capacity with liquid nitrogen [76]. A bonfire test is a heat load test for a storage tank where it the tank is fully engulfed in flames. Hulsbosch-Dam et al. [76] found an initial slow pressure rise owing to the physical time for heating the tank walls. They developed two simple equilibrium and non-equilibrium models for the pressure rise on the tank during the bonfire test. It was found that the pressure rise was between the predictions of both models during the whole test. Near the end of the bonfire test, it was found that the pressure predicted by the equilibrium model agreed very well with the experimental results.

Das et al. [77] performed a visualization study of natural convection in a two-dimensional rectangular glass enclosure filled with water heated by the side walls. They concluded that in the absence of evaporation and wall boiling, a well-mixed, vortex-like

structure develops below the interface. Below the vortical structure, liquid thermal stratification was observed.

Kanazawa et al. [78] studied heat and fluid flow in a 1.3 L lab-scale rectangular storage tank using electrochemical mass transfer and the Reynolds analogy ($Sh = Nu$) . Only the liquid phase was considered, and the experiments were set to reproduce turbulent natural convection in three heating regimes, namely bottom, wall and mixed heating. These regimes are analogous to the ones considered by Anderson et al. and Tatom et al. experiments [62, 63]. Kanazawa et al. [78] concluded that Sherwood number (Sh) at the bottom decreased in the mixed heating scenario owing to weak flow impingement. In contrast, Sh at the walls was invariant to the heating regime and followed natural convection correlations of laminar flow even when $Ra \sim 10^{13}$. Kanazawa et al. [78] attributed this effect to flow laminarization owing to the weak circulation in the system, but did not discuss edge effects. Owing to the small scale of the geometry, edge effects could be significant enough to invalidate the use of infinite horizontal/vertical plate correlations of natural convection.

Li et al. [79] investigated the self-pressurization of LN_2 in a storage tank subject to accidental loss of vacuum of its multi-layer insulation (MLI) system. The experimental setup comprised a 30 L cylindrical tank in vertical configuration filled at 84% of its capacity. The heat flux was not reported but it was estimated as $q_w \sim O(100\ \mathrm{Wm^{-2}K^{-1}})$. Li et al. [79] found that significant vertical thermal stratification developed in the liquid. The difference between the temperature at the interface and at the liquid bulk increased and then decreased with time. It was also found that the liquid temperature was radially homogeneous everywhere except in a thin region below the vapour-liquid interface.

Ludwig et al. [80] experimentally measured liquid thermal stratification and pressure build-up of LN_2 in a storage tank subject to active pressurization and sloshing. A 40 L cylindrical tank in vertical configuration filled at 70% of its capacity was considered. It was observed that a thermally stratified layer developed below the vapour-liquid interface, but its thickness was higher than the one predicted by the similarity solution for semi-infinite plates. Ludwig et al. [80] argued that this was a consequence of natural convection in the liquid phase driven by wall heating. Subsequently, Ludwig et al. [81] carried out experiments on active pressurization of LN_2

stored in the same tank [80], filled at 68.4% of its capacity, without sloshing. They found that liquid thermal stratification during active pressurization was driven by the increase in saturation temperature at the interface. Furthermore, Ludwig et al. [81] found that the thermally stratified layer thickness in the liquid phase followed the scaling $\delta_{SL} \sim 2\sqrt{\alpha_L t}$, where α_L is the liquid thermal diffusivity and t the time. This implies that for active pressurization with low wall and bottom heat flux, conduction dominates heat transfer below the vapour-liquid interface.

Wang et al. [82] experimentally investigated the active pressurization of liquid oxygen (LO_2) in a 59 m^3 storage tank filled to 90% of its capacity. A cylindrical tank in vertical configuration was considered, and high-temperature helium (600 K) was used as a pressurizing agent. During the experiments, LO_2 was discharged through a valve at the bottom of the tank. The pressurization performances of radial and anti-cone diffusers were compared, and the discharge rate was between 0.158 and 0.152 $m^3\ s^{-1}$, respectively. It was found that the vapour phase was thermally stratified, and the maximum temperature increased with decreasing liquid filling as the tank discharged. On the other hand, no noticeable thermal stratification in the liquid was observed. For both diffusers, it was concluded that the pressurization performance decreased because of heat transfer processes. For the radial diffuser, heat transfer between the vapour and the tank walls decreased pressurization rates, while for the anti-cone diffuser, enhanced vapour to liquid heat transfer decreased pressurization rates.

Ryu et al. [83] performed 12 experiments on thermal stratification during the active pressurization of R290 in a 10.6 L cylindrical tank in vertical configuration. They investigated the effect of pressurizing gas inlet flow, initial liquid filling and initial tank pressure on thermal stratification and pressurization rates. They found that the pressurization rate increased with the enthalpy of the pressurizing gas and the initial internal energy of the liquid. The liquid filling did not affect pressurization rates in the experimental range. For high inlet flowrates, condensation was driven by the pressurizing gas. For low inlet flowrates, the cooling of the vapour through the interface dominated the condensation rate.

Qu et al. [22] reported anonymised pressure build-up data for the self-pressurization of LNG in a large-scale floating storage and regasification unit (FSRU).

Unfortunately, the heating conditions and tank volume was not reported due to confidentiality. Nevertheless, it was found that the normalized pressure showed a rapid increase for $t^* = t/\tau_p$ = 0 – 0.4, where τ_p is the pressurization period. After that period, the normalized pressure increased roughly linearly with the dimensionless time. The normalized pressure showed a three-fold increase at the end of the pressurization period, giving light on the pressure operating ranges in FSRU.

Kassemi et al. [16] (2018) studied the self-pressurization and thermal stratification of Perfluoro-n-Pentane (PnP or C_5F_{12}) at terrestrial gravity, and under microgravity in the international space station (ISS). A 1.65 L cylindrical storage tank in vertical configuration filled at 70% of its capacity was heated uniformly using a vacuum jacket. For the on-ground experiments, a laminar boundary layer driven by natural convection was observed in the liquid near the wall. Simultaneously, Rayleigh-Bénard convection was observed in the liquid region above the tank bottom. On the basis of temperature measurements at 43 different locations, it was concluded that the velocity and temperature profiles were axisymmetric. Under microgravity, it was concluded that thermal conduction was still an important heat transfer mechanism of a similar magnitude to radiation. Thermal conduction was significant when compared to radiation even at high degrees of vacuum of the tank multi layered insulation system.

Imai [84] and Nishida et al. [17] experimentally investigated a pressure control system based on a thermodynamic vent system (TVS) based in jet mixing. LN_2 was stored in a 30.3 L vertically orientated cylindrical tank filled at 52% of its capacity. The pressure setpoint was 300 kPa and it was controlled through a solenoid valve. The experiments were divided in three stages: pressure build-up, BOG venting with no jet, and BOG venting with jet mixing. They concluded that jet mixing can be used to control the tank pressure and reduce BOG generation by 98.1%. A high jet-mixing flowrate and low degree of subcooling was required to ensure that the subcooled injected liquid reached the vapour-liquid interface.

Recent experimental studies on thermal stratification during the self-pressurization of cryogens stored in insulated tanks have been carried out using sophisticated apparatus [28, 29, 49, 85]. In these studies, highly resolved spatial-

temporal pressure and temperature profiles have been reported [28, 29, 49, 85]. Only small cylindrical vessels (V_T ~ 6-13 L) in vertical configuration have been considered.

Seo et al. [85] experimentally investigated the self-pressurization of LN_2 in a 6.75 L vertically orientated cylindrical storage tank in a narrow pressure range (0.1-0.145 MPa). Five different combinations of liquid fillings and wall heat fluxes were tested by modifying the vacuum level of the Dewar surrounding the storage tank. In all scenarios, thermal stratification was observed for both phases. For the vapour phase, a pseudo-steady state was achieved shortly after the beginning of the evaporation. In contrast, the liquid temperature increased continuously driven by the increase in the saturation temperature of the liquid as pressure built up. Thermal stratification was larger under the highest liquid filling (70%) and wall heat flux (27 $Wm^{-2}K^{-1}$), while for the lowest liquid filling (10%), the liquid temperature was spatially homogeneous. Seo et al. [85] observed that the pressure build-up cannot be predicted neither using a 1-D thermal diffusion model nor an equilibrium model.

Kang et al. [49] experimentally investigated thermal stratification during the self-pressurization of LN_2 stored in a 10 L vertically orientated cylindrical storage tank. A broad pressure range was selected (0.1 - 1 MPa). Three different liquid fillings were tested under the same heat flux through the bottom and walls of the tank, while the tank top was insulated. They found that the degree of liquid thermal stratification increased with liquid filling, in agreement with Seo et al. [85] findings. In contrast to Seo et al. [85], the vapour phase did not reach a clear pseudo-steady state. This is a consequence of the 20 times broader pressurization range and 6 times larger aspect ratio (H/D) in Kang et al. [49] experiments. Kang et al. [49] repeated Seo et al. [85] methodology of contrasting the experimental pressure build-up with the predictions obtained by an equilibrium model. They found that for their tested scenarios, the equilibrium model underpredicted holding times, which leads to over-conservative design guidelines. Seo et al. [85] and Kang et al. [49] experimental data on LN_2 evaporation will be used in Chapter 7 to validate non-isobaric evaporation models developed in Chapter 6.

In the previously described LN_2 evaporation experiments performed by Perez et al. [28], the pressure build-up from 100 to 150 kPa was also investigated. The pressure build-up and thermal stratification trends were in qualitative agreement with Seo and Jeong

[85] and Kang et al. [49] experiments. They concluded that an accurate prediction of liquid thermal stratification is necessary to predict evaporation rates during the pressurization stage. Thereafter, Al Ghafri et al. [29] used the same experimental setup to investigate the non-isobaric evaporation of a range of methane-ethane mixtures. This pivotal study constitutes the first measurement in open literature of temperature, pressure, composition and BOG rates for an LNG-like mixture. During the self-pressurization stage, evaporation rates and temperature profiles in both vapour and liquid phases for methane-ethane mixtures followed similar dynamics of a pure cryogen. This is theoretically [86] and computationally [41] expected, as compositional changes in LNG-like mixtures happen through a much longer time-scale than the self-pressurization time-scale.

2.2.2 Reduced models based on bulk mass and energy balances

In subsection 2.2.1, the experimental evidence on the complex interplay between pressure build-up, thermal stratification, phase change and multiphase flow during the non-isobaric storage of cryogenic liquids was reviewed. This subsection focuses on the self-pressurization driven by heat ingress during the non-isobaric storage of cryogens. Self-pressurization is relevant for all cryogenic liquids as during their supply chain there is always a significant storage period between production and use. In contrast, active pressurization is observed in a narrower range of applications, mainly when the cryogenic liquid is used as a vehicle fuel. Rather surprisingly, the modelling of self-pressurization is much more complex than for active pressurization. During self-pressurization, natural convection, heat conduction and multiphase are relevant and of a similar magnitude. In active pressurization, either the rapid increase of vapour temperature or vapour density by the pressurizing gas dominate over other transport phenomena. This allows the successful use of simplifying assumptions and reduced order models, which is not the case for self-pressurization.

In this subsection, attempts on developing reduced models for the self-pressurization of cryogenic liquids during their storage are reviewed. In the context of this thesis, reduced models are defined as models where the vapour and liquid phases are assumed to be bulk phases. Hence, no partial differential equations are solved to

calculate the transport of energy, momentum, or mass. Although the reduced order models developed up to date have a very narrow range of applicability, they are simple to understand and implement. Furthermore, they may provide valuable insight for limiting storage scenarios of industrial interest.

Gursu et al. [87] developed three models for the non-isobaric evaporation of liquid hydrogen in a vertically orientated storage tank. Two of these models were "isothermal" models and fit in the definition of reduced order models: homogeneous and surface evaporation models. The homogeneous or "equilibrium" model considers that vapour and liquid phases are at thermal equilibrium during the whole self-pressurization. In the surface evaporation model, it is assumed that all the heat ingress to the liquid is used to evaporate the liquid. The homogeneous model predicted lower pressures when compared against experiments because it overestimated the amount of sensible heat absorbed by the liquid [88]. On the other hand, the surface evaporation model predicted a higher pressure build-up when compared against experiments. This was expected as the surface evaporation model overestimates the fraction of heat ingress that is used to evaporate the liquid [88]. In contrast to LN_2 and LNG storage, LH_2 undergoes ortho-para conversion, which is an exothermal reaction. Gursu et al. [88] observed that high concentrations of ortho-hydrogen in the stored LH_2 produced a faster pressure build-up.

Chen et al. [89] developed an equilibrium model to predict the pressure build-up during the storage of LNG in a medium-sized storage tank used in a fuelling station. This equilibrium model is equivalent to Gursu et al. equilibrium model [87], augmented with a thermodynamic sub-model to calculate mixture phase equilibrium. The storage tank was subject to frequent emptying as it was used to fuel LNG powered vehicles. A reasonable agreement was obtained with a single point of experimental pressure build-up. This suggests that the effect of a periodic emptying of the tank produced the destratification of the liquid and vapour phases. However, as no temperature measurements were performed, the exact reasons which made the equilibrium model suitable for an LNG storage tank that is periodically emptied remain unknown.

Sharafian et al. [48] developed a non-equilibrium, non-isobaric evaporation model where the vapour was allowed to be superheated with respect to the liquid. They

simulated BOG generation in a 57.2 m^3 subcooled storage tank under non-isobaric conditions. The temperature of each phase was assumed spatially homogeneous, and the vapour to liquid heat transfer rate was calculated through natural convection correlations. It was concluded that LNG could be stored for 3.7 times longer in a subcooled storage tank when compared against a tank under traditional preconditioning. Qu et al. [22] developed a bulk phase non equilibrium model applicable for LNG self-pressurization during marine transportation. This model considers the energy sources of the ship cargo and a simplified sub-model of conjugate heat transfer between the ship structure and the stored LNG. The model was capable of reproducing the industrial data of pressure rise in a voyage. Unfortunately, the exact values for pressure were redacted owing to confidentiality reasons, which limits the scientific value of Qu et al. [22] model.

2.2.3 1-D models and bulk models based on the boundary layer theory

The first models for the non-isobaric evaporation of cryogenic liquids characterised natural convection and thermal stratification in the liquid phase using boundary layer equations. The liquid phase was divided in three subsystems: a thermally homogeneous region in the liquid bulk, a boundary layer near the tank wall, and a thermally stratified layer just below the interface. This approach was based on Eckert and Jackson steady-state boundary layer equations for turbulent natural convection on a flat vertical plate [90]. Arnett and Voth [66] developed the first non-isobaric evaporation model for cryogenic liquids. They used Eckert and Jackson [90] equations for steady state boundary layer flow, and coupled them with a sub-model for the thermally stratified layer growth. An exponential temperature distribution in the thermally stratified layer was assumed, which allowed the calculation of the temperature gradient just below the interface. Arnett and Voth [66] validated their model against Centaur AC-8 flight and Plum Brook B-2 experimental data. They obtained a very good agreement ($\epsilon < 4\%$) on pressure while the temperature profiles in the liquid and vapour phase were not accurately predicted.

Twenty years after Arnett and Voth [66] model, Gursu et al. [87, 88] extended Arnett and Voth [66] model to include LH_2 ortho-para conversion. They found that the

pressure rise was sensitive to the empirical exponent in the power law solution of the boundary layer velocity. The results were largely invariant to small changes in the coefficients of the exponential distribution of temperature in the thermally stratified layer. Gursu et al. [87, 88] validated their model against LH_2 self-pressurization experiments presented by Arnett and Voth [66] and Aydelott et al. [65]. By using appropriate coefficients in the power law velocity profile of the boundary layer, they were able to match temperature and pressure experimental data for LH_2. This demonstrated that it is not possible to choose a realistic velocity profile *a priori* for boundary-layer based non-isobaric evaporation models.

Gong et al. [71] used a very similar approach to Gursu et al. [87] to investigate LPG pressurization under high heat fluxes through the tank walls (3-5 kW m^{-2}) . They used the more realistic velocity and temperature profiles developed by Yu et al. [91] for transient natural convection in a partially filled, vertically orientated 60 L cylindrical tank. Gong et al. [71] obtained an excellent agreement with experimental data on the pseudo-steady state pressurization rate. However, the model was not able to predict the curvature in the pressure profile at the beginning of the evaporation. This was a consequence of assuming a spatially homogeneous temperature in the vapour phase in their model. They concluded that vapour pressurization produced liquid thermal stratification, which further accelerated the pressure build-up, and shortened the holding time when compared against an equilibrium model.

In parallel to the boundary layer approach, non-isobaric evaporation models with a 1-D heat transfer sub-model in the liquid phase have been developed. Tatom et al. [63] developed a 1-D thermal diffusion model for the liquid phase. The model required two experimental parameters, K_0 and K_1, to be fitted. K_0 measured the fraction of the sidewall heating that is considered to go to raising the bulk liquid temperature, while K_1 is a mixing modulus that governs the effect of bottom heating on the thermally stratified layer depth. Tatom et al. [63] obtained excellent agreement with industrial data, although their model has a limited range of applicability owing to its semi-empirical nature. Seo et al. [85] developed a 1-D thermal diffusion model for vapour and liquid phases. They assumed that heat was transported only by heat conduction, and vapour and liquid phases were heated by a spatially homogeneous source term. Seo et al. [85]

model did not predict either the experimental pressure or temperature profiles data well for LN_2 non-isobaric evaporation in a 6.75 L storage tank. They proposed that the lack of agreement was a consequence of neglecting natural convection and thermal expansion in the liquid.

Although the 1-D non-equilibrium models and boundary layer theory based models are more realistic than equilibrium models, they have a narrow range of applicability. This is a consequence of the strict assumptions applied in the construction of each model. To overcome this limitation, CFD models have become the new research paradigm to investigate the self-pressurization of cryogenic liquids in storage tanks [92].

2.2.4 Computational fluid dynamics (CFD) models

Aszodi et al. [70] developed a 2-D CFD model for the liquid phase which was coupled with a bulk-phase model for the vapour. They used vorticity-stream function approach to simplify the calculations and used the model to investigate the pressure build-up in a storage tank filled with water under thermal attack. The model showed a reasonable agreement with experimental liquid temperature profiles, although it slightly overestimated the liquid temperature.

Panzarella et al. [92] developed a 2-D, incompressible CFD model for the liquid phase during the non-isobaric evaporation of liquid cryogens. Natural convection was included through the Boussinesq approximation, and the vapour was assumed a bulk phase. An explicit equation for the vapour pressure evolution, and hence its saturation temperature, was developed to simplify model implementation. Panzarella et al. [92] found that at the end of the storage period, a simple equilibrium model predicted the same pressurization rate as the CFD model. However, they also concluded that equilibrium models underpredicted the pressure obtained with the CFD model because they neglect liquid thermal stratification. Barsi and Kassemi [93] subsequently validated Panzarella et al. [92] model against cryogenic self-pressurization experiments performed in NASA Glenn's K-site facility [14, 68, 94]. These experiments were thoroughly described in subsection 2.2.1 of this literature review.

Kartuzova and Kassemi [95, 96] and Kartuzova et al. [97] improved Panzarella et al. [92] CFD model by including a more accurate description of two key physical phenomena. First, they removed the vapour bulk assumption and developed a multiphase model in which the interface is tracked using the Volume of Fluid (VoF) method [98]. Secondly, they included a conjugate heat transfer sub-model to resolve temperature profiles along the tank wall. Two methods were tested to calculate the interfacial mass transfer rate: the Schrage kinetic equation [99] and an interfacial energy balance. The difference between these phase change methods was negligible, suggesting that these methods and their implementation are robust for the simulation of cryogenic liquid storage. Subsequently, Kassemi and Kartuzova [100] successfully validated their model against NASA Glenn's K-site facility [14, 68, 94] data on LH_2 self-pressurization. They found that an accommodation coefficient close to 1 in the Schrage model [99] provided the best predictions. Furthermore, the model was largely insensitive to the accommodation coefficient when the interface was flat and unperturbed. Finally, Kassemi and Kartuzova [100] found that the k-ε and $k-\omega-SST$ models underpredicted the experimental vapour temperature. This is consistent with the underprediction of vapour superheating obtained by Saleem et al. [50], as a consequence of the overprediction of vapour turbulent thermal diffusivity by the k-ε model in stagnant regions [57], as discussed previously. Kassemi and Kartuzova [100] suggested that more realistic turbulence models were required to accurately capture turbulent heat transfer in the vapour phase.

Kumar et al. [101] implemented a 2-D multiphase CFD model based on the Volume of Fluid (VoF) approach to investigate thermal stratification in liquid hydrogen tanks. A vertically orientated cylindrical tank was considered, and evaporation was implemented using the Lee model [102]. They validated their model against Barnett et al. [103] experiments of the influence of aspect ratio on thermal stratification and self-pressurization rates. In these experiments, liquid nitrogen was heated through the walls only at moderate heat fluxes (25 – 100 Wm^{-2}). It was found that liquid thermal stratification increased with the tank aspect ratio H/D.

Roh et al. [104] developed a 2-D CFD model for the liquid phase during the non-isobaric evaporation of cryogenic liquids in rectangular enclosures. The liquid was

assumed incompressible and natural convection was implemented using the Boussinesq approximation. Based on Roh et al. [55] previous results for isobaric evaporation, the vapour to liquid heat transfer rate was neglected. The vapour phase was thus simplified as a thermally insulated bulk-phase, in which pressure increased only as a consequence of evaporation. Roh et al. [104] used the k-ϵ turbulence model to simulate liquid-phase turbulence. They concluded that evaporation rate can be significantly reduced by increasing the tank operating pressure through active pressurization. Under the self-pressurization scenario, they observed that during the transient period at the beginning of the evaporation, condensation may occur. It is worth noting that the use of the k-ϵ turbulence model for buoyancy driven flows is not advised [58]. Furthermore, a thermally insulated vapour is not a realistic operating scenario. Therefore, although Roh et al. [55] methodology constitutes a valuable contribution to the cryogenic evaporation field, their results cannot be generalised.

Choi et al. [105] implemented two-fluid Euler-Euler simulations for LN_2 and LNG evaporation. They assumed that all the evaporation occurred in the vapour-liquid interface, neglecting wall boiling. The model was partially validated against a subset of Seo and Jeong [85] and Barnett [103] self-pressurization experiments. Choi et al. [105] model produced a reasonable agreement on pressure, but poor agreement on liquid temperatures when validating against Seo and Jeong [85] experiments. However, the agreement on pressure rise and temperature profiles between Choi et al. [105] model and Barnett [103] experiments was excellent.

Ovidi et al. [106] implemented 2-D multiphase CFD model coupled with a bespoke, 1-D steady-state heat transfer model for the tank walls. They used the VoF approach and the Lee model [102] to characterise phase change, in a similar way to Kumar et al. [101]. However, Ovidi et al. [106] allowed both evaporation and condensation to occur, while Kumar et al. [101] assumed that only evaporation occurred. Ovidi et al. [106] validated their model against a single Seo and Jeong [85] experiment: LN_2 self-pressurization in a 6.75 L storage tank filled to 50% of its capacity subject to a wall heat ingress of 1.2 W. Ovidi et al. [106] model predicted the pressure well with an absolute error within 1%, while the model overpredicted vapour temperature by up to 22 K. Ovidi et al. [106] attributed the overprediction of the vapour temperature to their uniform wall heat flux

assumption, as that boundary condition was not detailed by Seo and Jeong [85]. From the results that will be shown in Chapter 8 of this thesis, evidence that supports Ovidi et al. [106] hypothesis will be provided. The lack of agreement on vapour temperature illustrates the importance of considering conjugate heat transfer in the tank walls.

Ovidi et al. [106] used their model to numerically investigate the non-isobaric evaporation of liquid methane and liquid ethane in a vertically orientated 100 m^3 cylindrical storage tank. They explored self-pressurization for intact and damaged insulation systems for three different liquid fillings. For the intact tanks, they observed higher pressurisation for low liquid fillings even if the saturation temperature was slightly lower than for high liquid filling. The vapour superheating was 20 times higher than the liquid superheating in all intact and damaged insulation systems. Ovidi et al. [106] concluded that self-pressurization and vapour heating was higher for ethane than methane. Therefore, storage of liquid ethane posed higher risks than the storage of liquid methane.

Recently, Kassemi et al. [107] presented a comprehensive validation study of their multiphase Volume of Fluid (VoF) models. When validating against Hasan et al. [68] experiments, they found that a k-ϵ turbulence model overestimated the vapour turbulent heat transfer and underestimated vapour temperature. Setting the vapour as a laminar fluid provided a better agreement with the experimental pressure build-up and temperature. Their third validation case considered the 2017 Zero Boil-Off Tank (ZBOT) experiments performed under a microgravity five million times smaller than the terrestrial gravity in a cylindrical vessel in the international space station (ISS) [16]. They found excellent agreement between the CFD model and experimental ullage shape, pressure build-up and temperatures of the vapour, liquid and solid tank. Under microgravity, conduction and radiation were the dominant heat transfer mechanisms.

2.3 Chapter summary

For the isobaric evaporation of cryogenic liquids in storage tanks, the experimental evidence is consistent across a broad range of cryogens, tanks sizes and heat fluxes. The

evaporation and BOG rates are mainly driven by the heat ingress into the liquid phase. The temperature of the surrounding air determines the driving force for heat ingress. Therefore, the heat ingress increases with the temperature of the surrounding air. The vapour phase is superheated with respect to the liquid, whereas the liquid is thermally homogeneous. Owing to the vapour superheating, the vapour acts as an effective resistance to the heat transfer, evaporation rates and BOG generation. For heat fluxes typical of cryogenic storage (0-100 $Wm^{-2}K^{-1}$), conduction is the dominant heat transfer mechanism in the vapour phase. For storage tanks and containers under sloshing or roll motion, BOG rates increase. This increase is a consequence of the disruption of the smooth interface, higher wet area in contact with the liquid walls and the generation of liquid films and droplets. Even for non-static scenarios, vapour thermal stratification quickly develops and constitutes a stable equilibrium against perturbations.

Isobaric evaporation models can be classified in equilibrium, non-equilibrium and CFD models. Among these models, non-equilibrium models are becoming the option of choice for researchers and practitioners as they achieve a good balance between complexity and accuracy. The main challenge in the development of non-equilibrium models is the development of a realistic vapour phase heat transfer sub-model. The vapour phase is superheated with respect to the liquid, and heat is transferred by heat conduction, natural convection and advection. The selection of accurate assumptions to simplify the three-dimensional, coupled fluid and heat flow, to a simpler model, is essential. In this thesis, a non-equilibrium model featuring a 1-D vapour phase heat transfer sub model is developed assuming a spatially homogeneous, one-dimensional advective flow [13]. To validate the assumptions of the non-equilibrium model, a full 2-D CFD model for the vapour phase is developed [43]. Finally, analytical solutions applicable for the storage of pure cryogens are developed to further validate the 1-D model and to provide an easy-to-use tool for practitioners [3].

For the non-isobaric evaporation of pure cryogens stored in tanks, natural convection and thermal stratification are relevant to both vapour and liquid phases. The experimental evidence shows that pressure build-up drives the thermal stratification of the liquid. Tank self-pressurization is driven primarily by vapour heating, while the contribution of liquid evaporation to pressure build-up is much smaller. Non-isobaric

evaporation models developed up to date are classified into bulk phase, 1-D, boundary layer and CFD models. These models have a narrow range of applicability, owing to the complex coupling between interfacial heat and mass transfer with transport phenomena in the bulk of each phase. In this thesis, three models relevant for the non-isobaric evaporation of pure cryogens in closed tanks are developed that consider the effect of wall boiling. Wall boiling has been neglected in previous studies. The simplest model is a 1-D non-equilibrium model that includes heat conduction, wall heating, vapour advection and wall boiling. To validate the assumptions of the non-equilibrium 1-D model, a 2-D CFD model for the liquid phase is developed. Finally, to quantify the effect of interfacial heat and momentum transfer, a multiphase CFD model with adequate sub-models for interfacial transport phenomena is implemented.

2.4 References

[1] V. P. Dawson, *Engines and innovation: Lewis Laboratory and American propulsion technology*. National Aeronautics and Space Administration, Office of Management ..., 1991.

[2] A. Sharafian, H. Talebian, P. Blomerus, O. Herrera, and W. Mérida, "A review of liquefied natural gas refueling station designs," *Renew. Sust. Energ. Rev,* vol. 69, pp. 503-513, 2017, doi: 10.1016/j.rser.2016.11.186.

[3] F. Huerta and V. Vesovic, "Analytical solutions for the isobaric evaporation of pure cryogens in storage tanks," *Int. J. Heat Mass Transfer,* vol. 143, p. 118536, 2019/11/01/ 2019, doi: https://doi.org/10.1016/j.ijheatmasstransfer.2019.118536.

[4] D. T. Neill, H. T. Hashemi, and C. M. Sliepcevich, "Boil-off rates and wall temperatures in above ground LNG storage tanks," presented at the Chem. Eng. Prog. Symp., 1968, 1968.

[5] J. Heestand, C. W. Shipman, and J. W. Meader, "A predictive model for rollover in stratified LNG tanks," *AlChE J.,* vol. 29, no. 2, pp. 199-207, 1983/03/01 1983, doi: 10.1002/aic.690290205.

[6] S. Bates and D. S. Morrison, "Modelling the behaviour of stratified liquid natural gas in storage tanks: A study of the rollover phenomenon," *Int. J. Heat Mass Transfer,* vol. 40, no. 8, pp. 1875-1884, May 1997, doi: 10.1016/s0017-9310(96)00218-9.

[7] W. B. Zimmerman and J. M. Rees, "Rollover instability due to double diffusion in a stably stratified cylindrical tank," *Physics of Fluids,* vol. 19, no. 12, Dec 2007, Art no. 123604, doi: 10.1063/1.2827488.

[8] Y. Li, Z. Li, and W. Wang, "Simulating on rollover phenomenon in LNG storage tanks and determination of the rollover threshold," *Journal of Loss Prevention in the Process Industries,* vol. 37, pp. 132-142, 2015, doi: 10.1016/j.jlp.2015.07.007.

[9] M. Kulitsa and D. A. Wood, "LNG rollover challenges and their mitigation on Floating Storage and Regasification Units: New perspectives in assessing rollover consequences," *Journal of Loss Prevention in the Process Industries,* vol. 54, pp. 352-372, 2018-07-01 2018, doi: 10.1016/j.jlp.2018.04.007.

[10] A. Hubert, S. Dembele, P. Denissenko, and J. Wen, "Predicting Liquefied Natural Gas (LNG) rollovers using Computational Fluid Dynamics," *Journal of Loss Prevention in the Process Industries,* vol. 62, p. 103922, 2019/11/01/ 2019, doi: https://doi.org/10.1016/j.jlp.2019.103922.

[11] A. Saleem, S. Farooq, I. A. Karimi, and R. Banerjee, "CFD Analysis of Stratification and Rollover Phenomena in an Industrial-Scale LNG Storage Tank," *Industrial and Engineering Chemistry Research,* Article vol. 59, no. 31, pp. 14126-14144, 2020, doi: 10.1021/acs.iecr.0c02546.

[12] Z. Wang, F. Han, Y. Liu, and W. Li, "Evolution Process of Liquefied Natural Gas from Stratification to Rollover in Tanks of Coastal Engineering with the Influence of Baffle Structure," *Journal of Marine Science and Engineering,* vol. 9, no. 1, p. 95, 2021.

[13] F. Huerta and V. Vesovic, "A realistic vapour phase heat transfer model for the weathering of LNG stored in large tanks," *Energy,* vol. 174, pp. 280-291, 2019/05/01/ 2019, doi: https://doi.org/10.1016/j.energy.2019.02.174.

[14] R. Stochl and R. Knoll, "Thermal performance of a liquid hydrogen tank multilayer insulation system at warm boundary temperatures of 630, 530, and 152 R," 1991 1991, p. 2400.

[15] A. Hofmann, "Theory to boil-off gas cooled shields for cryogenic storage vessels," *Cryogenics,* vol. 44, no. 3, pp. 159-165, 2004, doi: 10.1016/j.cryogenics.2003.09.003.

[16] M. Kassemi, S. Hylton, and O. V. Kartuzova, "Zero-Boil-Off Tank (ZBOT) Experiment ? Ground-Based Validation of Two ? Phase Self-Pressurization CFD Model & Preliminary Microgravity Results," in *2018 Joint Propulsion Conference*, (AIAA Propulsion and Energy Forum: American Institute of Aeronautics and Astronautics, 2018.

[17] K. Nishida, R. Imai, O. Kawanami, Y. Umemura, and T. Himeno, "Ground-Based Experiment on Reducing Boil-Off Gas by Jet Mixing for Future Cryogenic Propulsion System," *International Journal of Microgravity Science and Application,* vol. 38, no. 1, p. 380102, 2021.

[18] K. D. Timmerhaus, "Cryogenic Process Engineering," in *Encyclopedia of Physical Science and Technology (Third Edition)*, R. A. Meyers Ed. New York: Academic Press, 2003, pp. 13-36.

[19] M. Belmedani, A. Belgacem, and R. Rebiai, "Analysis of Natural convection in liquid nitrogen under storage conditions," *Journal of applied sciences,* vol. 8, no. 14, pp. 2544-2552, 2008.

[20] Y. Li, R. Wang, and C. Wang, "Study on effect of liquid level on the heat leak into vertical cryogenic vessels," *Cryogenics,* vol. 50, no. 6, pp. 367-372, 2010/06/01/ 2010, doi: https://doi.org/10.1016/j.cryogenics.2009.12.009.

[21] Y. Lin, C. Ye, Y. Y. Yu, and S. W. Bi, "An approach to estimating the boil-off rate of LNG in type C independent tank for floating storage and regasification unit under different filling ratio," *Appl. Therm. Eng.*, vol. 135, pp. 463-471, May 2018, doi: 10.1016/j.applthermaleng.2018.02.066.

[22] Y. Qu, I. Noba, X. Xu, R. Privat, and J.-N. Jaubert, "A thermal and thermodynamic code for the computation of Boil-Off Gas – Industrial applications of LNG carrier," *Cryogenics,* vol. 99, pp. 105-113, 2019, doi: 10.1016/j.cryogenics.2018.09.002.

[23] R. N. Krikkis, "A thermodynamic and heat transfer model for LNG ageing during ship transportation. Towards an efficient boil-off gas management," *Cryogenics,* vol. 92, pp. 76-83, 2018/06/01/ 2018, doi: https://doi.org/10.1016/j.cryogenics.2018.04.007.

[24] R. N. Krikkis, B. Wang, and S. Niotis, "An analysis of the ballast voyage of an LNG Carrier. The significance of the loading and discharging cycle," *Appl. Therm. Eng.,* vol. 194, p. 117092, 2021/07/25/ 2021, doi: https://doi.org/10.1016/j.applthermaleng.2021.117092.

[25] P. Yu, Y.-c. Yin, Z.-j. Wei, and Q.-j. Yue, "A prototype test of dynamic boil-off gas in liquefied natural gas tank containers," *Appl. Therm. Eng.,* vol. 180, p. 115817, 2020/11/05/ 2020, doi: https://doi.org/10.1016/j.applthermaleng.2020.115817.

[26] W. C. Niu, J. C. Lin, Y. L. Ju, and Y. Z. Fu, "The daily evaporation rate test and conversion method for a new independent type B LNG mock-up tank," *Cryogenics,* vol. 111, p. 103168, 2020/10/01/ 2020, doi: https://doi.org/10.1016/j.cryogenics.2020.103168.

[27] C. Migliore, C. Tubilleja, and V. Vesovic, "Weathering prediction model for stored liquefied natural gas (LNG)," (in English), *J. Nat. Gas. Sci. Eng.,* vol. 26, pp. 570-580, Sep 2015, doi: 10.1016/j.jngse.2015.06.056.

[28] F. Perez *et al.*, "Measurements of boil-off gas and stratification in cryogenic liquid nitrogen with implications for the storage and transport of liquefied natural gas," *Energy,* vol. 222, p. 119853, 2021/05/01/ 2021, doi: https://doi.org/10.1016/j.energy.2021.119853.

[29] S. Z. S. Al Ghafri *et al.*, "Advanced boil-off gas studies for liquefied natural gas," *Appl. Therm. Eng.,* vol. 189, p. 116735, 2021/05/05/ 2021, doi: https://doi.org/10.1016/j.applthermaleng.2021.116735.

[30] M. Miana, R. Del Hoyo, V. Rodrigálvarez, J. R. Valdés, and R. Llorens, "Calculation models for prediction of Liquefied Natural Gas (LNG) ageing during ship transportation," *Appl. Energy,* vol. 87, no. 5, pp. 1687-1700, 2010, doi: 10.1016/j.apenergy.2009.10.023.

[31] M. Miana, R. Legorburo, D. Díez, and Y. H. Hwang, "Calculation of Boil-Off Rate of Liquefied Natural Gas in Mark III tanks of ship carriers by numerical analysis," *Appl. Therm. Eng.,* vol. 93, pp. 279-296, 2015, doi: 10.1016/j.applthermaleng.2015.09.112.

[32] M. Miana, R. Del Hoyo, and V. Rodrigálvarez, "Comparison of evaporation rate and heat flow models for prediction of Liquefied Natural Gas (LNG) ageing during ship transportation," *Fuel,* vol. 177, pp. 87-106, 2016, doi: 10.1016/j.fuel.2016.02.070.

[33] S. W. Churchill, "Heat leakage and wall temperature profiles for above ground low-temperature storage tanks," *Chem. Eng. Prog.,* vol. 58, no. 11, pp. 55-60, 1962.

[34] J. M. Shah and J. J. Aarts, "Effect of weathering of LNG in storage tanks," presented at the Advances in Cryogenic Engineering, Boston, 1995. [Online]. Available: https://doi.org/10.1007/978-1-4613-9847-9_31.

[35] K. J. Kountz, "Weathering of LNG in on-board storage tanks," Institute of Gas Technology, Chicago, 1999.

[36] A. Aspelund, G. Gjøvåg, P. Nekså, and K. Kolsaker, "LNG—Chain, a calculation tool for natural gas quality in small scale LNG distribution chains," presented at the ICEC-21 International Cryogenic Engineering Conference 2007.

[37] A. Aspelund, T. Gundersen, J. Myklebust, M. P. Nowak, and A. Tomasgard, "An optimization-simulation model for a simple LNG process," *Comput. Chem. Eng.,* vol. 34, no. 10, pp. 1606-1617, Oct 2010, doi: 10.1016/j.compchemeng.2009.10.018.

[38] G. G. Dimopoulos and C. A. Frangopoulos, "A dynamic model for liquefied natural gas evaporation during marine transportation," *Int. J. Thermodyn.,* vol. 11, no. 3, pp. 123-131, 2008, doi: 10.5541/ijot.220.

[39] E. Adom, Z. I. Sheikh, and J. Xianda, "Modelling of boil off gas in LNG tanks: a case study," *IJET,* vol. 2, no. 4, pp. 292-296, 2010.

[40] L. A. Pellegrini, S. Moioli, F. Brignoli, and C. Bellini, "LNG technology: the weathering in above-ground storage tanks," *Ind. Eng. Chem. Res.,* vol. 53, no. 10, pp. 3931-3937, 2014, doi: 10.1021/ie404128d.

[41] C. Migliore Cappello, "Modelling the weathering process of stored liquefied natural gas (LNG)," 2015.

[42] C. Migliore, A. Salehi, and V. Vesovic, "A non-equilibrium approach to modelling the weathering of stored Liquefied Natural Gas (LNG)," *Energy,* vol. 124, pp. 684-692, 2017, doi: 10.1016/j.energy.2017.02.068.

[43] F. Huerta and V. Vesovic, "CFD modelling of the isobaric evaporation of cryogenic liquids in storage tanks," *International Journal of Heat and Mass Transfer,* vol. 176, p. 121419, 2021/09/01/ 2021, doi: https://doi.org/10.1016/j.ijheatmasstransfer.2021.121419.

[44] Z. Duan, H. Xue, X. Gong, and W. Tang, "A thermal non-equilibrium model for predicting LNG boil-off in storage tanks incorporating the natural convection effect," *Energy,* p. 121162, 2021/06/07/ 2021, doi: https://doi.org/10.1016/j.energy.2021.121162.

[45] Z. H. Wang, A. Sharafian, and W. Merida, "Non-equilibrium thermodynamic model for liquefied natural gas storage tanks," *Energy,* vol. 190, Jan 2020, Art no. 116412, doi: 10.1016/j.energy.2019.116412.

[46] M. S. Khan, S. Effendy, I. A. Karimi, and A. Wazwaz, "Improving design and operation at LNG regasification terminals through a corrected storage tank model," *Appl. Therm. Eng.,* vol. 149, pp. 344-353, Feb 2019, doi: 10.1016/j.applthermaleng.2018.12.060.

[47] S. Effendy, M. S. Khan, S. Farooq, and I. A. Karimi, "Dynamic modelling and optimization of an LNG storage tank in a regasification terminal with semi-analytical solutions for N2-free LNG," *Computers & Chemical Engineering,* vol. 99, pp. 40-50, 2017, doi: 10.1016/j.compchemeng.2017.01.012.

[48] A. Sharafian, O. E. Herrera, and W. Mérida, "Performance analysis of liquefied natural gas storage tanks in refueling stations," *J. Nat. Gas. Sci. Eng.,* vol. 36, pp. 496-509, 2016, doi: 10.1016/j.jngse.2016.10.062.

[49] M. Kang, J. Kim, H. You, and D. Chang, "Experimental investigation of thermal stratification in cryogenic tanks," *Experimental Thermal and Fluid Science,* vol. 96, pp. 371-382, 2018/09/01/ 2018, doi: https://doi.org/10.1016/j.expthermflusci.2017.12.017.

[50] A. Saleem, S. Farooq, I. A. Karimi, and R. Banerjee, "A CFD simulation study of boiling mechanism and BOG generation in a full-scale LNG storage tank," *Computers & Chemical Engineering,* vol. 115, pp. 112-120, Jul 2018, doi: 10.1016/j.compchemeng.2018.04.003.

[51] J. L. Ferrín and L. J. Pérez-Pérez, "Numerical simulation of natural convection and boil-off in a small size pressurized LNG storage tank," *Computers & Chemical Engineering,* vol. 138, p. 106840, 2020/07/12/ 2020, doi: https://doi.org/10.1016/j.compchemeng.2020.106840.

[52] Y. Jo, K. Shin, and S. Hwang, "Development of dynamic simulation model of LNG tank and its operational strategy," *Energy,* vol. 223, p. 120060, 2021/05/15/ 2021, doi: https://doi.org/10.1016/j.energy.2021.120060.

[53] Y.-P. Jo, M. S. F. Bangi, S.-H. Son, J. S.-I. Kwon, and S.-W. Hwang, "Dynamic modeling and offset-free predictive control of LNG tank," *Fuel,* vol. 285, p. 119074, 2021/02/01/ 2021, doi: https://doi.org/10.1016/j.fuel.2020.119074.

[54] M. S. Khelifi-Touhami, A. Benbrik, D. Lemonnier, and D. Blay, "Laminar natural convection flow in a cylindrical cavity application to the storage of LNG," *Journal of Petroleum Science and Engineering,* vol. 71, no. 3, pp. 126-132, 2010/04/01/ 2010, doi: https://doi.org/10.1016/j.petrol.2009.12.011.

[55] S. Roh and G. Son, "Numerical study of natural convection in a liquefied natural gas tank," *Journal of Mechanical Science and Technology,* vol. 26, no. 10, pp. 3133-3140, 2012, doi: 10.1007/s12206-012-0820-x.

[56] V. I. Maksimov, T. A. Nagornova, V. P. Glazyrin, and I. A. Shestakov, "Analysis of influence of heat insulation on the thermal regime of storage tanks with liquefied natural gas," presented at the Thermophysical Basis of Energy Technologies 2015, Tomsk, Russia, 2016. [Online]. Available: <Go to ISI>://WOS:000372790500042.

[57] T. J. Craft, L. J. W. Graham, and B. E. Launder, "Impinging jet studies for turbulence model assessment—II. An examination of the performance of four turbulence models," *Int. J. Heat Mass Transfer,* vol. 36, no. 10, pp. 2685-2697, 1993-07-01 1993, doi: 10.1016/s0017-9310(05)80205-4.

[58] M. Kassemi, O. Kartuzova, and S. Hylton, "Validation of two-phase CFD models for propellant tank self-pressurization: Crossing fluid types, scales, and gravity levels," *Cryogenics,* vol. 89, pp. 1-15, 2018/01/01/ 2018, doi: https://doi.org/10.1016/j.cryogenics.2017.10.019.

[59] X. Wang, Y. Xu, S. Wang, Q. Xu, and T. C. Ho, "Comprehensive study on boil-off gas generation from LNG road tankers under simultaneous impacts of heat leakage and transportation vibration," *Fuel,* vol. 275, p. 117876, 2020/09/01/ 2020, doi: https://doi.org/10.1016/j.fuel.2020.117876.

[60] G.-M. Jeon, J.-C. Park, and S. Choi, "Multiphase-thermal simulation on BOG/BOR estimation due to phase change in cryogenic liquid storage tanks," *Appl. Therm. Eng.,* vol. 184, p. 116264, 2021/02/05/ 2021, doi: https://doi.org/10.1016/j.applthermaleng.2020.116264.

[61] J. Hyeon-won and S. W Jaewoo, "Thermal analysis of insulation system for KC-1 membrane LNG tank," *Journal of Ocean Engineering and Technology,* vol. 31, no. 2, pp. 91-102, 2017.

[62] B. H. Anderson and M. J. Kolar, "Experimental investigation of the behavior of a confined fluid subjected to nonuniform source and wall heating," 1963.

[63] J. W. Tatom, W. H. Brown, L. H. Knight, and E. F. Coxe, "Analysis of thermal stratification of liquid hydrogen in rocket propellant tanks," in *Advances in Cryogenic Engineering*: Springer, 1964, pp. 265-272.

[64] R. Elliot, "Rocket Propellant and Pressurizaition Systems," ed: Prentice Hall., Inc., Englewood Cliffs, NJ–1964.–404 p, 1964.

[65] J. C. Aydelott and C. M. Spuckler, "Effect of size on normal-gravity self-pressurization of spherical liquid hydrogen tankage," 1969.

[66] R. W. Arnett and R. O. Voth, "A computer program for the calculation of thermal stratification and self-pressurization in a liquid hydrogen tank," National Aeronautics and Space Administration, 1972. [Online]. Available: <Go to WoS>://WOS:000345232900026

[67] R. F. Lacovic, *Management of cryogenic propellants in a full-scale orbiting space vehicle*. National Aeronautics and Space Administration, 1968.

[68] M. M. Hasan, C. S. Lin, and N. T. Vandresar, "Self-pressurization of a flightweight liquid hydrogen storage tank subjected to low heat flux," 1991.

[69] N. T. Van Dresar, C. S. Lin, and M. M. Hasan, "Self-pressurization of a flightweight liquid hydrogen tank: effects of fill level at low wall heat flux.."

[70] A. Aszodi, E. Krepper, and H. M. Prasser, "Experimental and numerical investigation of one and two phase natural convection in storage tanks," *Heat and Mass Transfer,* vol. 36, no. 6, pp. 497-504, 2000/11/01 2000, doi: 10.1007/s002310000112.

[71] Y. W. Gong, W. S. Lin, A. Z. Gu, and X. S. Lu, "A simplified model to predict the thermal response of PLG and its influence on BLEVE," *Journal of Hazardous Materials,* vol. 108, no. 1, pp. 21-26, 2004/04/30/ 2004, doi: https://doi.org/10.1016/j.jhazmat.2004.01.012.

[72] W. Lin, Y. Gong, T. Gao, A. Gu, and X. Lu, "Experimental studies on the thermal stratification and its influence on BLEVEs," *Exp. Therm. Fluid Sci.,* vol. 34, no. 7, pp. 972-978, 2010/10/01/ 2010, doi: https://doi.org/10.1016/j.expthermflusci.2010.03.001.

[73] A. M. Birk and M. H. Cunningham, "Liquid temperature stratification and its effect on BLEVEs and their hazards," *Journal of Hazardous Materials,* vol. 48, no. 1-3, pp. 219-237, Jun 1996, doi: 10.1016/0304-3894(95)00157-3.

[74] J. Shi, M. Bi, and X. Yang, "Experimental research on thermal stratification of liquefied gas in tanks under external thermal attack," *Exp. Therm. Fluid Sci.,* vol. 41, pp. 77-83, 2012/09/01/ 2012, doi: https://doi.org/10.1016/j.expthermflusci.2012.03.013.

[75] J. Shi, J. Ren, P. Liu, and M. Bi, "Experimental research on the effects of fluid and heater on thermal stratification of liquefied gas," *Exp. Therm. Fluid Sci.,* vol. 50, pp. 29-36, 2013/10/01/ 2013, doi: https://doi.org/10.1016/j.expthermflusci.2013.04.021.

[76] C. Hulsbosch-Dam *et al.*, "Thermodynamic aspects of an LNG tank in fire and experimental validation," presented at the 11th International Conference on Experimental Fluid Mechanics (EFM 2016), Czech Republic, 2017, 2017.

[77] S. P. Das, S. Chakraborty, and P. Dutta, "Studies on thermal stratification phenomenon in LH2 storage vessel," *Heat Transfer Engineering,* vol. 25, no. 4, pp. 54-66, Jun 2004, doi: 10.1080/01457630490443767.

[78] T. Kanazawa, K. Kudo, A. Kuroda, and N. Tsui, "Experimental study on heat and fluid flow in LNG tank heated from the bottom and the sidewalls," *Heat Transfer—Asian Research,* vol. 33, no. 7, pp. 417-430, 2004, doi: 10.1002/htj.20031.

[79] X. Li, G. Xie, and R. Wang, "Experimental and numerical investigations of fluid flow and heat transfer in a cryogenic tank at loss of vacuum," *Heat and Mass Transfer,* vol. 46, no. 4, pp. 395-404, 2010/04/01 2010, doi: 10.1007/s00231-010-0583-9.

[80] C. Ludwig, M. E. Dreyer, and E. J. Hopfinger, "Pressure variations in a cryogenic liquid storage tank subjected to periodic excitations," *Int. J. Heat Mass Transfer,* vol. 66, pp. 223-234, 2013/11/01/ 2013, doi: https://doi.org/10.1016/j.ijheatmasstransfer.2013.06.072.

[81] C. Ludwig and M. E. Dreyer, "Investigations on thermodynamic phenomena of the active-pressurization process of a cryogenic propellant tank," *Cryogenics,* vol. 63, pp. 1-16, 2014/09/01/ 2014, doi: https://doi.org/10.1016/j.cryogenics.2014.05.005.

[82] L. Wang, Y. Z. Li, Y. H. Jin, and Y. Ma, "Experimental investigation on pressurization performance of cryogenic tank during high-temperature helium pressurization process," *Cryogenics,* vol. 66, pp. 43-52, Mar 2015, doi: 10.1016/j.cryogenics.2014.12.001.

[83] J. Ryu, J. Kim, S. Seo, Y. Seo, and D. Chang, "Experimental investigation of condensation performance in pressurised tank during vapour inlet process," *Appl. Therm. Eng.,* vol. 138, pp. 900-912, 2018/06/25/ 2018, doi: https://doi.org/10.1016/j.applthermaleng.2018.04.025.

[84] R. Imai, K. Nishida, O. Kawanami, Y. Umemura, and T. Himeno, "Basic Study on Thermodynamic Vent System in Propulsion System for Future Spacecraft," *Microgravity Science and Technology,* vol. 32, no. 3, pp. 339-348, 2020/06/01 2020, doi: 10.1007/s12217-019-09768-w.

[85] M. Seo and S. Jeong, "Analysis of self-pressurization phenomenon of cryogenic fluid storage tank with thermal diffusion model," *Cryogenics,* vol. 50, no. 9, pp. 549-555, Sep 2010, doi: 10.1016/j.cryogenics.2010.02.021.

[86] C. Conrado and V. Vesovic, "The influence of chemical composition on vaporisation of LNG and LPG on unconfined water surfaces," *Chem. Eng. Sci.,* vol. 55, no. 20, pp. 4549-4562, Oct 2000, doi: 10.1016/s0009-2509(00)00110-x.

[87] S. Gursu, S. A. Sherif, T. N. Veziroglu, and J. W. Sheffield, "Analysis and optimization of thermal stratification and self-pressurization effects in liquid-hydrogen storage-systems - Part 1: Model development.," *J Energ. Resour. ASME,* vol. 115, no. 3, pp. 221-227, Sep 1993, doi: 10.1115/1.2905997.

[88] S. Gursu, S. A. Sherif, T. N. Veziroglu, and J. W. Sheffield, "Analysis and optimization of thermal stratification and self-pressurization effects in liquid-hydrogen storage-systems - Part 2: Model results and conclusions," *J Energ. Resour. ASME,* vol. 115, no. 3, pp. 228-231, Sep 1993, doi: 10.1115/1.2905998.

[89] Q. S. Chen, J. Wegrzyn, and V. Prasad, "Analysis of temperature and pressure changes in liquefied natural gas (LNG) cryogenic tanks," *Cryogenics,* vol. 44, no. 10, pp. 701-709, 2004, doi: 10.1016/j.cryogenics.2004.03.020.

[90] E. R. G. Eckert and T. W. Jackson, "Analysis of turbulent free-convection boundary layer on flat plate," National Advisory Committee for Aeronautics, 1950. [Online]. Available: <Go to WoS>://WOS:A1993LZ87100012

[91] C. M. Yu, N. U. Aydemir, and J. E. S. Venart, "Transient free convection and thermal stratification in uniformly-heated partially-filled horizontal cylindrical and spherical vessels," *Journal of Thermal Science,* vol. 1, no. 2, pp. 114-122, 1992/06/01 1992, doi: 10.1007/BF02650847.

[92] C. H. Panzarella and M. Kassemi, "On the validity of purely thermodynamic descriptions of two-phase cryogenic fluid storage," *J. Fluid Mech.,* vol. 484, pp. 41-68, 2003, doi: 10.1017/s0022112003004002.

[93] S. Barsi and M. Kassemi, "Investigation of Tank Pressurization and Pressure Control—Part II: Numerical Modeling," *Journal of Thermal Science and Engineering Applications,* vol. 5, no. 4, pp. 041006-041006-9, 2013, doi: 10.1115/1.4023892.

[94] N. T. Van Dresar, C. S. Lin, and M. M. Hasan, "Self-pressurization of a flightweight liquid hydrogen tank: effects of fill level at low wall heat flux," presented at the 30th Aerospace Sciences Meeting and Exhibit, Reno, Nevada, Unites States of America., 1992.

[95] O. Kartuzova and M. Kassemi, "Modeling active pressure control in a large scale cryogenic storage tank in normal gravity," 2012, p. 3983.

[96] O. Kartuzova and M. Kassemi, "Modeling interfacial turbulent heat transfer during ventless pressurization of a large scale cryogenic storage tank in microgravity," 2011, p. 6037.

[97] O. V. Kartuzova, M. Kassemi, J. P. Moder, and J. H. Agui, "Self-pressurization and spray cooling simulations of the multipurpose hydrogen test bed (MHTB) ground-based experiment," 2014, p. 3578.

[98] C. W. Hirt and B. D. Nichols, "Volume of fluid (VOF) method for the dynamics of free boundaries," *Journal of Computational Physics,* vol. 39, no. 1, pp. 201-225, 1981/01/01/ 1981, doi: https://doi.org/10.1016/0021-9991(81)90145-5.

[99] R. W. Schrage, *A theoretical study of interphase mass transfer*. Columbia University Press, 1953.

[100] M. Kassemi and O. Kartuzova, "Effect of interfacial turbulence and accommodation coefficient on CFD predictions of pressurization and pressure control in cryogenic storage tank," *Cryogenics,* vol. 74, pp. 138-153, 2016/03/01/ 2016, doi: https://doi.org/10.1016/j.cryogenics.2015.10.018.

[101] S. P. Kumar, B. Prasad, G. Venkatarathnam, K. Ramamurthi, and S. S. Murthy, "Influence of surface evaporation on stratification in liquid hydrogen tanks of different aspect ratios," *Int. J. Hydrogen Energy,* vol. 32, no. 12, pp. 1954-1960, Aug 2007, doi: 10.1016/j.ijhydene.2006.08.052.

[102] W. H. Lee, "Pressure iteration scheme for two-phase flow modeling," *IN" MULTIPHASE TRANSPORT: FUNDAMENTALS, REACTOR SAFETY, APPLICATIONS"*. pp. 407-432, 1980.

[103] D. O. Barnett, "Liquid Nitrogen Stratification Analysis and Experiments in a Partially Filled, Spherical Container," in *Advances in Cryogenic Engineering*, Boston, MA, K. D. Timmerhaus, Ed., 1995// 1995: Springer US, pp. 174-187.

[104] S. Roh, G. Son, G. Song, and J. Bae, "Numerical study of transient natural convection in a pressurized LNG storage tank," *Appl. Therm. Eng.,* vol. 52, no. 1, pp. 209-220, 2013/04/05/ 2013, doi: https://doi.org/10.1016/j.applthermaleng.2012.11.021.

[105] S. W. Choi, W. I. Lee, and H. S. Kim, "Numerical analysis of convective flow and thermal stratification in a cryogenic storage tank," *Numerical Heat Transfer, Part A: Applications,* vol. 71, no. 4, pp. 402-422, 2017/02/16 2017, doi: 10.1080/10407782.2016.1264771.

[106] F. Ovidi, E. Pagni, G. Landucci, and C. Galletti, "Numerical study of pressure build-up in vertical tanks for cryogenic flammables storage," *Appl. Therm. Eng.,* vol. 161, p. 114079, 2019, doi: 10.1016/j.applthermaleng.2019.114079.

[107] M. Kassemi, S. Hylton, and O. Kartuzova, "1G and Microgravity Tank Self-Pressurization: Experiments and CFD Model Validations across Ra and Bo Regimes," *International Journal of Microgravity Science and Application,* vol. 37, no. 1, p. 370103, 2020.

Chapter 3

Model development for the isobaric evaporation of cryogenic liquids in storage tanks

3.1 Introduction

In this chapter, new models for the isobaric evaporation of cryogenic liquids in static storage tanks are presented. The new models take the non-equilibrium weathering model of Migliore et al. [1] as the starting point. For the isobaric evaporation of a pure cryogen, the liquid temperature is assumed to be spatially homogeneous and equal to the saturation temperature of the stored cryogen at the operating pressure. Consequently, the thermophysical and thermodynamic properties of the liquid phase are also spatially homogeneous. As the saturation temperature of a pure cryogen is constant during isobaric evaporation, its liquid thermophysical and thermodynamic properties are also constant. For the weathering of LNG, the assumption of spatially homogeneous thermophysical and thermodynamic properties is also very good. Industrial data of LNG storage under isobaric conditions show that the variation of the LNG temperature is lower than 0.1 K [2]. Thus, the change of liquid temperature owing to spatial changes in composition and hydrostatic pressure during LNG weathering is negligible. The saturation temperature LNG will slowly change as time progresses because of weathering. Nevertheless, for both pure cryogens and LNG, the liquid phase can be modelled as a bulk phase.

There is strong experimental and industrial evidence that shows that the vapour above the cryogen is superheated with respect to the liquid during the storage of cryogenic liquids [2-7]. This superheating is primarily a consequence of three effects. First, the vertical heat transfer enhancement owing to natural convection in the vapour bulk is small [1, 4, 6]. Second, the vapour of a cryogenic liquid has low thermal conductivity at the operating conditions typical of isobaric storage. For instance, k_V =

0.0072 $Wm^{-2}K$ for LN_2 and 0.0143 $Wm^{-2}K$ for liquid methane at P = 100 kPa, that makes the vapour phase an effective resistance to heat transfer. Third, as the BOG is removed through a valve at the tank roof, energy is continuously removed from the vapour phase. The continuous removal of energy with BOG reduces the energy available in the vapour to heat the liquid through the interface [8]. Therefore, the vapour to liquid heat transfer during the isobaric storage is expected to be much smaller than the vapour heat ingress. This more realistic, non-equilibrium modelling approach contrasts with the assumption that all vapour heat ingress is transferred into the liquid, widely used in equilibrium models [9].

In section 3.2, a bulk model for the liquid phase and a computational fluid dynamics (CFD) model for the vapour phase for the isobaric evaporation of cryogenic liquids in storage tanks are developed. On the basis of the dominance of thermal stratification in the vertical direction, a simplified 1-D vapour phase heat transfer model is developed in section 3.3. The coupling of this simplified model to the liquid bulk model constitutes the isobaric 1-D model for pure cryogens. In section 3.4, analytical solutions of the isobaric 1-D model are developed under the assumption of pseudo-steady state vapour heat transfer. Finally, in section 3.5, the isobaric 1-D model is extended by including a thermodynamic equilibrium model for multicomponent mixtures. As the model provides the evolution of the composition of both liquid and vapour phases, it allows the prediction of the weathering of LNG.

3.2 CFD model

The cryogenic storage tank has been modelled as a vertical cylinder with multi-layer insulation (MLI) containing a pure cryogenic liquid. The cryogenic liquid and its vapour are assumed to be separated by a smooth interface, orthogonal to the direction of gravity. The smooth interface assumption is adequate for low heat fluxes representative of industrial tanks, $q_{\text{in}} < 10$ $Wm^{-2}K^{-1}$. For fluxes of that magnitude, Saleem et al. [10] concluded that no boiling was observed. Instead, they observed that surface evaporation was the dominant phase change mechanism in a 201,000 m^3 storage tank. A schematic of the cryogenic storage tank and the heat and mass flows is depicted in Figure 3.1. The difference between the temperature of the surroundings, T_{air}, and the

temperature of the cryogenic liquid, T_L, drives a heat ingress through the walls at a rate $\dot{Q}_{L,in}$. This rate is defined as the liquid heat ingress. The stored liquid is subject to an additional heat ingress from the bottom of the tank at a rate $\dot{Q}_{bot}$. The bottom heat ingress is either driven by the same mechanism of $\dot{Q}_{L,in}$, or by an electrical element to prevent ground freezing. Similarly, the difference between T_{air} and the vapour temperature T_V drives a heat ingress through the walls at a rate $\dot{Q}_{V,in}$, and through the roof at a rate $\dot{Q}_{roof}$.

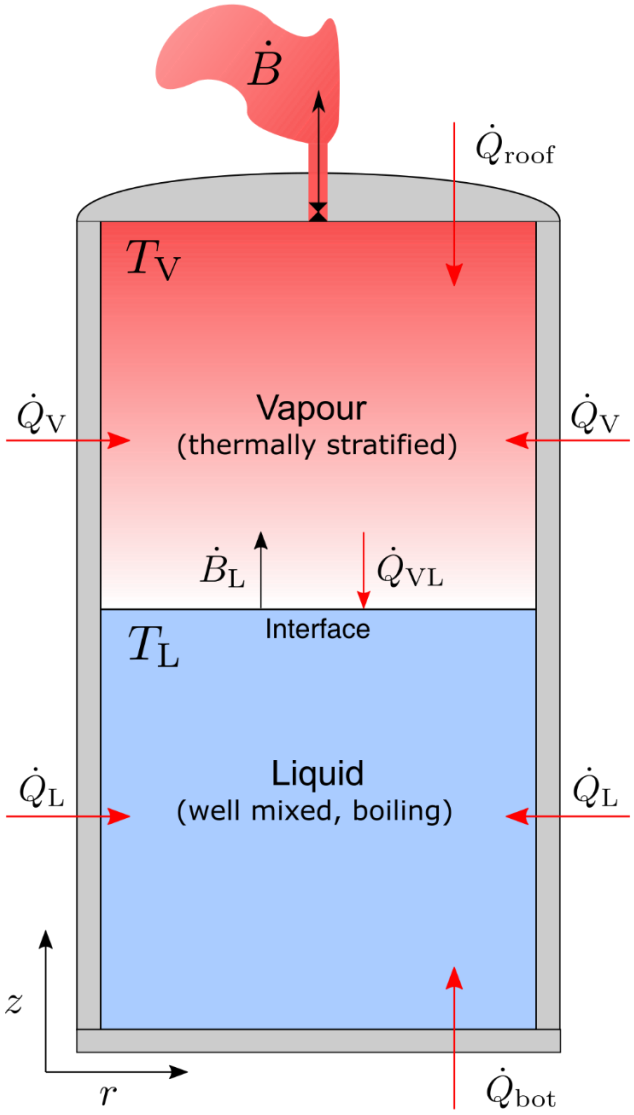

Figure 3.1: Schematic of the cylindrical cryogenic storage tank considered for model development. The vapour is modelled as a 2-D subsystem and the liquid is modelled as a bulk phase. The red and black arrows represent heat and mass flows, respectively. The z and r coordinates represent the vertical and radial directions, respectively.

As the tank operates under isobaric conditions, the pure liquid thermodynamic and thermophysical properties were assumed to be constant and spatially homogeneous. This assumption is reasonable because the increase of hydrostatic pressure with depth is small for the cases studied in this chapter. As a consequence, the change of liquid saturation temperature with depth is negligible (< 2 K). As the evaporation progresses, the vapour heat ingress will increase the vapour temperature. At the vapour liquid-interface, the vapour temperature will remain at the saturation temperature of the cryogen and a vertical temperature gradient will be established in the vapour phase. This gradient will drive a vapour to liquid heat transfer at the rate of $\dot{Q}_{\mathrm{VL}}$, as the vapour will heat the liquid through the interface.

The heat entering the liquid will evaporate the stored cryogen at a rate $\dot{B}_{\mathrm{L}}$. To keep the tank pressure constant, some of the evaporated cryogen is removed as boil-off gas (BOG) at a rate $\dot{B}$. The BOG is removed through a cylindrical vent aligned with the tank vertical axis. As the vapour adjacent to the tank wall is being heated, its density will decrease, and a buoyancy driven flow will be formed in the vapour phase. To capture this phenomenon, the vapour phase has been modelled as a 2-D domain, in the vertical (z) and radial (r) direction. The variation of vapour velocity and temperature in the azimuthal direction was neglected owing to the axial symmetry of the storage tank. Furthermore, the low magnitude of velocities and natural convection expected for the thermally stratified vapour are not likely to induce significant turbulence in the azimuthal direction. In sections 3.2.1 and 3.2.2, the mathematical models for the liquid and vapour phases are presented. The CFD implementation of these models is presented in sections 3.2.3 - 3.2.6.

3.2.1 Liquid phase bulk model

The evaporation rate, $\dot{B}_{\mathrm{L}}$, is calculated from a mass balance over the liquid subsystem,

$$-\dot{B}_{\mathrm{L}} = \frac{d}{dt}(\rho_{\mathrm{L}} V_{\mathrm{L}}) = \rho_{\mathrm{L}} \frac{dV_{\mathrm{L}}}{dt} + V_{\mathrm{L}} \frac{d\rho_{\mathrm{L}}}{dt}, \tag{3.1}$$

where ρ and V are the density and volume of the cryogen and t is the time. The subscripts L and V indicate liquid and vapour phases, respectively. As the evaporation is driven by the total liquid heat ingress $\dot{Q}_{\mathrm{L,tot}}$,

$$\dot{Q}_{\mathrm{L,tot}} = \dot{Q}_{\mathrm{L,in}} + \dot{Q}_{\mathrm{VL}} + \dot{Q}_{\mathrm{bot}}, \tag{3.2}$$

Eq. (3.1) is coupled with an energy balance for the liquid phase,

$$\dot{Q}_{\mathrm{L,tot}} - \dot{B}_{\mathrm{L}} h_{\mathrm{V}}(T_{\mathrm{L}}) = \frac{d}{dt}\left(\rho_{\mathrm{L}} V_{\mathrm{L}} h_{\mathrm{L}}(T_{\mathrm{L}})\right). \tag{3.3}$$

where the quantities h and T are the enthalpy and temperature, respectively. For the isobaric evaporation of pure cryogens at a given pressure P, the saturation temperature of the cryogen remains constant through the evaporation. Assuming that the variation of hydrostatic pressure with depth is negligible, the pressure through the whole liquid phase is spatially homogeneous. In practical isobaric storage scenarios, the cryogen is evaporating at its saturation temperature. Hence, the temperature of the liquid is also spatial-temporally homogeneous and equals to its saturation temperature at the operating pressure, $T_{\mathrm{L}} = T_{\mathrm{sat}}(P)$. As the temperature and pressure of the liquid are constant for this storage scenario, Eqs. (3.1) and (3.3) simplify to:

$$-\dot{B}_{\mathrm{L}} = \rho_{\mathrm{L}} \frac{dV_{\mathrm{L}}}{dt}, \tag{3.4}$$

$$\dot{Q}_{\mathrm{L,tot}} - \dot{B}_{\mathrm{L}} h_{\mathrm{V}}(T_{\mathrm{L}}) = \rho_{\mathrm{L}} h_{\mathrm{L}} \frac{dV_{\mathrm{L}}}{dt}, \tag{3.5}$$

Substituting Eq. (3.4) in Eq. (3.5), the rate of change of liquid volume can be written explicitly,

$$\frac{dV_{\mathrm{L}}}{dt} = \frac{-\dot{Q}_{\mathrm{L,tot}}}{\rho_{\mathrm{L}}\left(h_{\mathrm{V}}(T_{\mathrm{L}}) - h_{\mathrm{L}}(T_{\mathrm{L}})\right)} = \frac{-\dot{Q}_{\mathrm{L,tot}}}{\rho_{\mathrm{L}} \Delta H_{\mathrm{LV}}}. \tag{3.6}$$

where $\Delta H_{\mathrm{LV}} = h_{\mathrm{V}} - h_{\mathrm{L}}$ is the enthalpy of vaporization of the cryogen. Industrial cryogenic storage tanks are normally preconditioned to ensure that the temperature of the inner walls is constant. Hence, steady-state heat transfer is assumed in the solid layers of the tank multi layered insulation (MLI) and heat accumulation in the tank wall is neglected. Under this assumption, the heat ingress through the walls occurs by mixed natural convection and conduction,

$$\dot{Q}_{\psi,\mathrm{in}} = U_{\psi} A_{\psi} \left(T_{\mathrm{air}} - T_{\psi}\right), \quad \psi = \mathrm{L}\ or\ \mathrm{V} \tag{3.7}$$

Where U is the overall heat transfer coefficient based in external area, T_{air} is the temperature of the surrounding air and A_{ψ} is the area of the tank wall in contact with the phase ψ. For a particular multi-layered insulated cylindrical storage tank containing a cryogen, U_{L} can be calculated following the method of Migliore et al [9]. Alternatively, empirical or industrial boil-off data can be used to fit the overall heat transfer coefficient. In this section, U_{L} was fitted from boil-off rate data for the evaporation of liquid nitrogen in an industrial 8 m³ storage tank [11]. The detailed calculation of U_{L} can be found in the Appendix A. Calculating the heat ingresses through the walls using Eq. (3.7) implies that radiation heat transfer has been neglected. This is an excellent approximation methane and LNG storage, as it will only underestimate the total heat ingress by approximately 1.5% [4].

The cylindrical tank has an internal diameter d_{i}, an external diameter d_{o}, a height l and a total volume $V_{\mathrm{T}} = V_{\mathrm{L}} + V_{\mathrm{V}}$. For this geometry, the wet area A_{L} and dry area A_{V} are defined as:

$$A_{\mathrm{L}} = \pi d_{\mathrm{o}} l_{\mathrm{L}} = \pi d_{\mathrm{o}} \left(\frac{V_{\mathrm{L}}}{A_{\mathrm{T}}}\right) = \frac{4 V_{\mathrm{L}} d_{\mathrm{o}}}{d_{\mathrm{i}}^2}, \tag{3.8}$$

$$A_{\mathrm{V}} = \pi d_{\mathrm{o}} l_{\mathrm{V}} = \frac{4(V_{\mathrm{T}} - V_{\mathrm{L}}) d_{\mathrm{o}}}{d_i^2}, \tag{3.9}$$

where d_{i} and d_{o} are the internal and external diameters, respectively, $l_{\psi} = V_{\psi}/A_{\mathrm{T}}$ is the height of the phase ψ and $A_{\mathrm{T}} = \pi d_{\mathrm{i}}^2/4$ is the cross-sectional area of the storage tank. If the bottom of the tank is being heated, the bottom heat transfer rate can be either a model input or calculated through $\dot{Q}_{\mathrm{b}} = U_{\mathrm{L}} A_{\mathrm{T}} (T_{\mathrm{air}} - T_{\mathrm{L}})$. Similarly, if the roof of the tank is being heated, the roof heat transfer rate can be either a model input or calculated through $\dot{Q}_{\mathrm{roof}} = U_{\mathrm{V,roof}} A_{\mathrm{T}} (T_{\mathrm{air}} - T_{\mathrm{V}}(z = l_{\mathrm{V}}))$. The vapour to liquid heat transfer rate is calculated using the Fourier's law at the vapour side of the interface,

$$\dot{Q}_{\mathrm{VL}} = 2\pi k_{\mathrm{V}}(T_{\mathrm{L}}) \int_0^{R_{\mathrm{T}}} \frac{\partial T_{\mathrm{V}}}{\partial z}\Big|_{z=0} r dr, \tag{3.10}$$

where $R_{\mathrm{T}} = d_{\mathrm{i}}/2$ is the internal tank radius and $k_{\mathrm{V}}(T_{\mathrm{L}})$ the vapour thermal conductivity just above the vapour-liquid interface.

Finally, the BOG rate is defined by a mass balance over the whole storage tank,

$$-\dot{B} = \frac{d}{dt}(\rho_{\mathrm{L}} V_{\mathrm{L}} + \bar{\rho}_{\mathrm{V}} V_{\mathrm{V}}) = -\dot{B}_{\mathrm{L}} + \bar{\rho}_{\mathrm{V}} \frac{dV_{\mathrm{V}}}{dt} + V_{\mathrm{V}} \frac{d\bar{\rho}_{\mathrm{V}}}{dt}. \tag{3.11}$$

where $\bar{\rho}_{\mathrm{V}} = 1/V_{\mathrm{V}} \times \int_{\Omega=V_{\mathrm{V}}} \rho_{\mathrm{V}}\, dV$ is the spatially averaged vapour density. The initial condition for the ordinary differential equation (ODE) Eq. (3.6) is given by the initial liquid volume. The initial liquid volume is defined as $V_{\mathrm{L}}(t = 0) = V_{\mathrm{T}} LF$, where LF represents the initial liquid filling of the tank. The liquid bulk model is coupled with the vapour phase model through the vapour to liquid heat transfer, $\dot{Q}_{\mathrm{VL}}$. In section 3.2.2, a 2-D CFD model is presented for the vapour phase. This model provides the vapour temperature profiles required for the calculation of $\dot{Q}_{\mathrm{VL}}$ and $\bar{\rho}_{\mathrm{V}}$, which provides closure to Eq. (3.6).

3.2.2 2-D vapour phase CFD model

The vapour phase has been modelled as a 2-D domain extending in the radial and vertical (r,z) directions, as already discussed. Thus, the domain is defined as the rectangle $\Omega_{\mathrm{V}} = (0,0) \times (R_{\mathrm{T}}, l_{\mathrm{V}}(t))$ where $l_{\mathrm{V}}(t)$ is the vapour height defined as $l_{\mathrm{V}}(t) = V_{\mathrm{V}}/A_{\mathrm{T}}$ where $l_{\mathrm{V}}(t)$ can be obtained from the solution of Eq. (3.6). As $dV_{\mathrm{L}}/dt < 0$, owing to the evaporation of the liquid cryogen, the vapour height will increase with time.

The compressible Navier-Stokes equations govern the vapour pressure and velocity profiles. The continuity equation for a compressible fluid is given by,

$$\frac{\partial \rho_{\mathrm{V}}}{\partial t} + \nabla \cdot (\rho_{\mathrm{V}} \mathbf{v}) = 0\,, \tag{3.12}$$

where $\mathbf{v} = (v_r, v_z)$ is the vapour velocity. The momentum conservation equation for a compressible fluid can be written as:

$$\frac{\partial}{\partial t}(\rho_{\mathrm{V}} \mathbf{v}) = -[\nabla \cdot \rho_{\mathrm{V}} \mathbf{v}\mathbf{v}] - \nabla P + \left[\nabla \cdot \left(\mu_{\mathrm{V}}(\mathbf{v} + \mathbf{v}^{\mathrm{T}}) - \frac{2}{3}\mu_{\mathrm{V}}(\nabla \cdot \mathbf{v})\mathbf{I}\right)\right] + \rho_{\mathrm{V}} \mathbf{g}\,, \tag{3.13}$$

where μ is the dynamic viscosity, $\mathbf{g}$ is the acceleration due to gravity, and $\mathbf{I}$ is the unit tensor. The vapour is assumed an ideal gas governed by the equation $\rho_{\mathrm{V}} = P/RT_{\mathrm{V}}$, where R is the universal gas constant. Assuming that the viscous dissipation is negligible, the heat transfer in the vapour phase is governed by the energy equation,

$$\frac{\partial}{\partial t}\left(\frac{1}{2}\rho_{\mathrm{V}}|\mathbf{v}|^2+\rho_{\mathrm{V}}h_{\mathrm{V}}\right)=-\nabla\cdot\left(\frac{1}{2}\rho_{\mathrm{V}}|\mathbf{v}|^2\mathbf{v}+\rho_{\mathrm{V}}h_{\mathrm{V}}\mathbf{v}\right)+k_{\mathrm{V}}\nabla^2T_{\mathrm{V}}+\rho(\mathbf{v}\cdot\mathbf{g})+\frac{dP}{dt}. \quad (3.14)$$

For an ideal gas, $dh_{\mathrm{V}}=c_{\mathrm{p,V}}dT_{\mathrm{V}}$, where $c_{\mathrm{p,V}}$ is the vapour specific heat capacity at constant pressure and it is assumed constant. This is a good assumption for the pure cryogens considered in this work (methane and nitrogen), as they behave as simple gases where the vibrational contribution to heat capacity is negligible.

To keep the tank pressure constant, the vapour is removed through a cylindrical valve at the top of the tank. The valve is described by the open boundary $\partial\Omega_{\mathrm{valve}}$: $(0\le r\le R_{\mathrm{valve}},\ z=l_{\mathrm{V}})$, where $R_{valve}=0.03\,R_{\mathrm{T}}$. The roof of the tank, $\partial\Omega_{\mathrm{roof}}$: $(R_{\mathrm{valve}}<r\le R_{\mathrm{T}},\ z=l_{\mathrm{V}})$, and the walls, $\partial\Omega_{\mathrm{wall}}:(r=R_{\mathrm{T}},\ 0\le z\le l_{\mathrm{V}})$, are solid boundaries. The vapour-liquid interface, $\partial\Omega_{\mathrm{int}}:(0\le r\le R_{\mathrm{T}},\ z=0)$, is modelled as an open boundary from which the evaporated liquid enters to the vapour domain. The tank axis, $\partial\Omega_{\mathrm{sym}}:(r=0,\ 0\le z\le l_{\mathrm{V}})$, describes the assumption of axis-symmetry in the cylindrical domain. Figure 3.2 depicts the domain for the vapour and its boundaries.

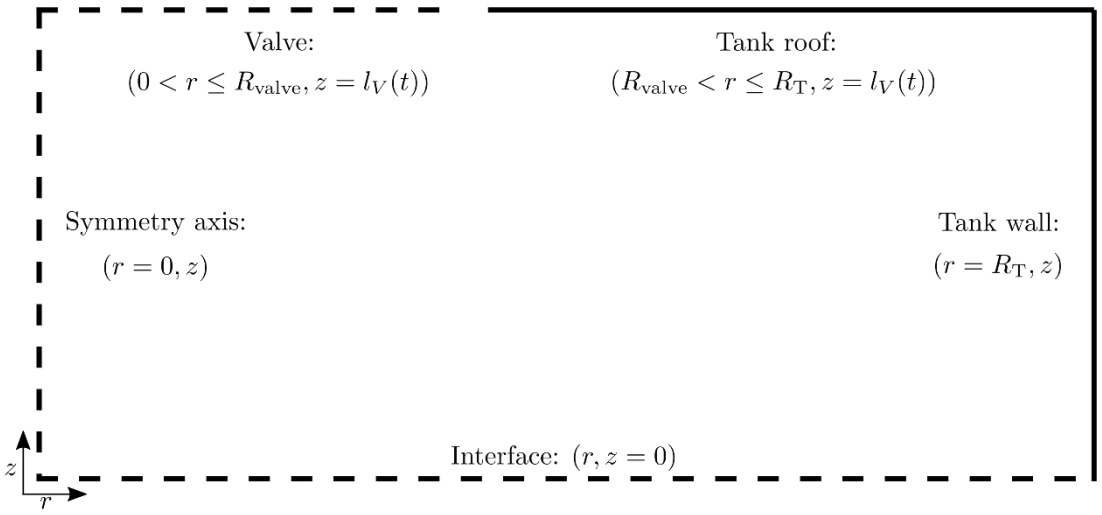

Figure 3.2: Schematic of the vapour domain modelled as a 2-D cylindrical geometry. The interface moves downwards as the evaporation of the stored cryogen progresses. Solid lines represent solid boundaries with no mass transfer through them, while dashed lines represent open boundaries. The radial length of the valve is not at scale.

The pressure boundary condition at the valve is set to a constant value $P=0.1$ MPa. At the tank roof, tank wall and vapour-liquid interface the pressure is calculated to be consistent with the velocity boundary conditions. At the axis of symmetry, the

pressure derivative is set to $\partial P/\partial r|_{r=0,z}$ = 0. The outlet velocity boundary condition is calculated to be consistent with the pressure boundary condition at the valve. No-slip boundary conditions are applied to the velocity at the tank wall and roof, $\mathbf{v}|_{r=R_\mathrm{T},z} = \mathbf{v}|_{R_\mathrm{valve}<r<R_\mathrm{T},z=l_\mathrm{V}} = 0$. At the vapour-liquid interface, the velocity is calculated assuming that the evaporation rate is spatially uniform and orthogonal to the interface. This results in a spatially homogeneous velocity, calculated through dividing the evaporation rate by the product of interfacial area and vapour density at the interface,

$$v_z|_{r,z=0} = \frac{\dot{B}_\mathrm{L}}{\rho_\mathrm{V}(T_\mathrm{L})\pi R_\mathrm{T}^2}\,. \tag{3.15}$$

The vapour model is coupled with the liquid bulk model through Eq. (3.15), as $\dot{B}_\mathrm{L}$ is calculated from Eqs. (3.4) and (3.6).

At the tank roof, two different temperature boundary conditions were investigated. If the roof is assumed to be perfectly insulated, a homogeneous Neumann boundary condition, $\partial T_\mathrm{V}/\partial z|_{r,z=l_\mathrm{V}}$ = 0, defines the vapour temperature. If heat ingresses through the tank roof, a convection-conduction Robin boundary condition is imposed, $k_\mathrm{V}\frac{\partial T_\mathrm{V}}{\partial z}|_{r,z=l_\mathrm{V}} = U_\mathrm{roof}(T_\mathrm{air} - T_\mathrm{V})$, where U_roof is the overall heat transfer coefficient at the roof. To ensure the axis-symmetrical temperature profile at the axis of symmetry, a zero-gradient boundary condition is applied, $\partial T_\mathrm{V}/\partial r|_{r=0,z} = 0$. At the tank walls, a convection-conduction boundary condition is imposed, $k_\mathrm{V}\frac{\partial T_\mathrm{V}}{\partial r}|_{r=R_\mathrm{T},z} = U_\mathrm{V}(T_\mathrm{air} - T_\mathrm{V})$, to account for the heating of the vapour through the walls. Finally, at the vapour-liquid interface thermal equilibrium is assumed, $T_\mathrm{V}|_{r,z=0} = T_\mathrm{L} = T_\mathrm{sat}(P)$.

At the beginning of the evaporation, the system is subject to the following initial conditions,

$$\begin{aligned} P(t=0) &= P_\mathrm{valve} + \rho_\mathrm{V}|\mathbf{g}|(l_\mathrm{V} - z), \\ \mathbf{v}(t=0) &= (0,0)\,, \\ T_\mathrm{V}(t=0) &= T_\mathrm{L} = T_\mathrm{sat}(P)\,. \end{aligned} \tag{3.16}$$

indicating that at the beginning of the evaporation (i) the pressure minus the hydrostatic head is constant and calculated from the pressure boundary condition at

the outlet; (ii) the vapour is stagnant and (iii) the vapour phase is at thermal equilibrium with the liquid. The coupling of the 2-D vapour with the liquid-bulk model will be referred in this thesis as the vapour-CFD model.

3.2.3 CFD implementation in OpenFOAM

The vapour-CFD model has been implemented in the open-source finite volume CFD library OpenFOAM v2006 [12, 13]. The solver overBuoyantPimpleDyMFoam [13] has been selected because it is a solver for compressible flow, compatible with dynamic meshes and suitable for buoyancy driven flows. As the Rayleigh number in all the tested scenarios is higher or close to the transitional regime threshold, $Ra > 7.7 \times 10^8$, the flow regime has been assumed turbulent. Direct numerical simulation is not feasible nor practical owing to the relatively long simulation times of interest for this work, $\tau_{sim} \sim$ 4,800 – 133,000 s. Hence, turbulence modelling is required to solve Eqs. (3.12)-(3.14) in a reasonable mesh for the storage tanks studied, $V_T \sim 8 - 80$ m^3.

Two turbulence models have been tested: k - ω -SST [14] and Large Eddy Simulation (LES). The LES model was implemented using the Smagorinsky model for the sub grid scale turbulent quantities [15] with the Smagorinsky constant set to C_s = 0.21. This value for C_s was suggested by Eidson for Rayleigh Bénard convection [16], and it has been used successfully in different scenarios of turbulent buoyancy driven flow [17]. The use of LES turbulence modelling for the 2-D model is justified by the axial symmetry and low velocities expected during isobaric evaporation. The suitability of this approach will be tested in section 5.1 by comparing the LES model against the k-ω-SST model.

3.2.4 Vapour domain discretization

The 2-D vapour domain was discretised into a structured orthogonal wedge mesh composed by hexahedra and prisms using Gmsh 4.5.6 [18]. The domain was partitioned into two uniform meshes: (i) a region below the roof, and (ii) a region below the valve. In the region below the valve, a higher radial mesh resolution was required to reduce the numerical errors produced by the large velocity gradients. The mesh resolution was

controlled by the radial and vertical grid spacing, Δr and Δz. In the region below the valve, the resolution in the radial coordinate was increased using a valve refinement parameter r_{ref} such that $\Delta r_{\mathrm{valve}} = \Delta r / r_{\mathrm{ref}}$.

Table 3.1: Mesh parameters for the discretization of the cylindrical vapour domain. Δr is the radial grid spacing, Δz the axial grid spacing, and r_{ref} the valve refinement parameter.

Scenario	Radius / m	Vapour height /m	Δr / m	Δz / m	$r_{\mathrm{v,ref}}$	N° cells
1	0.802	0.119	2×10^{-3}	4×10^{-3}	1	11571
2	0.802	2.771	1×10^{-2}	1×10^{-2}	4	22080
3	1.425	0.376	4×10^{-3}	5×10^{-3}	1	26196

A grid sensitivity analysis has been performed on the vertical vapour temperature profiles at the annulus located at $r = R_{\mathrm{T}}/2$ for the three scenarios studied. Three levels of refinement were considered based on the radial and vertical grid spacings defined in Table 3.1. The refinements were labelled as coarse ($\Delta r_{\mathrm{c}} = 2\Delta r$, $\Delta z_{\mathrm{c}} = 2\Delta z$), normal ($\Delta r_{\mathrm{n}} = \Delta r$, $\Delta z_{\mathrm{n}} = \Delta z$) and fine ($\Delta r_{\mathrm{f}} = \Delta r/2$, $\Delta z_{\mathrm{f}} = \Delta z/2$). For long-term storage of cryogens , the most relevant time period is the pseudo-steady state as it covers more than 99.9% of the evaporation time in typical applications [8], see section 5.2. The existence of the pseudo-steady state in the isobaric evaporation of cryogens will be thoroughly discussed in sections 5.1-5.3. The temperature difference at the onset of pseudo-steady state between the fine and normal spacings was less than 0.02%, 0.4% and 0.1% for Scenarios 1, 2 and 3, respectively. Hence, the meshes defined in Table 3.1, corresponding to the normal refinement, were selected to obtain mesh-independent solutions. The dimensionless vertical temperature profiles for each refinement at two representative simulation times and further details of grid sensitivity will be presented in Chapter 4.

3.2.5 Coupling the liquid bulk model with the vapour phase CFD model

The liquid bulk model has been implemented in OpenFOAM as a codedFixedValue dynamic boundary condition for velocity at the vapour-liquid interface. Dynamic boundary conditions are compiled at runtime and interact with the pre-compiled solvers. This approach has been selected to increase the reproducibility of the model, as it does not require the modification of the source code of overBuoyantPimpleDyMFoam. In the code of the dynamic boundary condition, Eqs.

(3.4), (3.6)-(3.10) are included in order to calculate the advective velocity at the interface using Eq. (3.15). The integrated vertical temperature gradient $\int_0^{R_\mathrm{T}} \frac{\partial T_\mathrm{V}}{\partial z}|_{z=0}\, rdr$ is read from the vapour database at each timestep to calculate $\dot{Q}_\mathrm{VL}$ using Eq. (4.9).

As a consequence of the evaporation of the liquid, the vapour domain will expand, and the vapour-liquid interface will slowly displace downwards. The velocity of the interface can be calculated directly from the advective velocity Eq. (3.15),

$$v_\mathrm{int} = -\frac{\dot{B}_\mathrm{L}}{\rho_\mathrm{L}\pi R_\mathrm{T}^2} = -\frac{\rho_\mathrm{V}(\mathrm{T_L})}{\rho_\mathrm{L}} v_z|_{z=0}. \tag{3.17}$$

The implementation of the dynamic mesh in overBuoyantPimpleDyMFoam [13] requires an artificial mesh diffusivity γ_m to improve the stability of the simulation [19]. The solver calculates the displacement of each point in the mesh solving the Laplace equation $\nabla \cdot (\gamma_m \nabla \mathbf{u}) = 0$, where $\mathbf{u}$ is the point displacement velocity field. The boundary conditions for $\mathbf{u}$ are no slip at the tank roof, slip at the tank axis and wall, and $\mathbf{u}|_{z=0,r} = (0, v_\mathrm{int})$ at the vapour-liquid interface, see Eq. (3.17). At each timestep, the location of each point of the mesh is updated through $\mathbf{x}_\mathrm{new} = \mathbf{x}_\mathrm{old} + \mathbf{u}\Delta t$. This results in a downwards expansion of the mesh elements with the progress of the evaporation. As all the meshes described in Table 3.1 are orthogonal and the interfacial velocity is radially homogeneous, the orthogonality is preserved across the whole simulation. The only impact of the interface displacement in mesh quality is an increase in vertical spacing of the hexahedra and prisms with the progress of the evaporation. However, in the studied scenarios the isobaric evaporation of a cryogen is extremely slow, and the final vapour volume is less than 0.1% higher than the initial vapor volume. This results in an average increase of vertical grid spacing of 0.1% across the simulation, which has a negligible effect in mesh quality.

The expansion of the vapour was implemented as a codedFixedValue dynamic boundary condition for the point displacement at the vapour-liquid interface. As this boundary condition automatically updates the vapour mesh at each time-step, the liquid volume in Eq. (3.8) can be evaluated directly through $V_\mathrm{L}(t) = V_\mathrm{T} - V_\mathrm{V}(t)$.

The implementation of the energy equation used the effective thermal conductivity $k_\mathrm{V,eff} = k_\mathrm{V} + k_\mathrm{t}$ to account for the enhancement of heat transfer by

turbulence. The turbulent thermal conductivity $k_t = c_{p,v}\mu_t/Pr_t$ is a function of the turbulent viscosity μ_t and the turbulent Prandtl number Pr_t. The turbulent viscosity is modelled differently in each turbulence model. In the k-ω-SST model [14], the turbulent viscosity is calculated as the ratio of the turbulent kinetic energy and a corrected turbulent dissipation rate. In the LES model, the turbulent viscosity arises to represent the sub-grid scale turbulence [15]. It is calculated as $\mu_t = \rho C_s \Delta^2 |\mathbf{S}|$, where $|\mathbf{S}| = \sqrt{2\bar{S}_{ij}\bar{S}_{ij}}$ is the magnitude of the resolved strain rate tensor and Δ is the filter width. The turbulent Prandtl number was set to 0.85 as this value provided a good agreement for experimental data on turbulent flow in a cylindrical pipe [20]. Finally, the convection-conduction boundary condition at the tank wall for the vapour temperature has been implemented through a codedMixed dynamic boundary condition.

3.2.6 Numerical schemes

Equations (3.12) - (3.14) and all boundary conditions have been discretised using the finite volume method to achieve high accuracy and stability. The finite volume method has been chosen over the finite element method because it is locally and globally conservative. While the finite element method allows for high orders of accuracy for unstructured and structured meshes, the discretised conservation equations obtained using the finite volume method are second-order accurate only if the mesh is structured. This requirement is satisfied by the structured orthogonal wedge meshes defined in Table 3.1. A grid independence study and visualisations of these meshes will be presented in section 4.5.

The time derivatives were discretised using second order backward time differences. This discretisation is implicit and uses the current and two previous time steps to improve the stability of the simulations. The temperature gradient and Laplacian operators were discretised using second-order accurate central differences. Similarly, the Laplacian of the mesh diffusivity in the numerical implementation of Eqs. (3.12) - (3.14) was discretised using second-order central differences.

The linear upwind stabilized transport (LUST) scheme [13] was applied to discretise the terms containing the divergence (div) of the fluxes of scalar fields. These

scalar fields were namely the enthalpy, turbulent kinetic energy, $\tilde{k}$, and turbulent dissipation rate, ω. To discretise the terms containing the div operator and the vapour velocity in Eqs. (3.12), (3.13), the linearUpwindV scheme [13] was applied. This scheme is a blend of linear and upwind schemes, where the weighting factors are a function of the velocity gradients. Both LUST and linearUpwindV schemes have an accuracy between first order, for regions with high velocity gradients, and second order, for regions with small velocity gradients. As the maximum vapour velocities observed in section 6.1 were small ($|\mathbf{v}| < 10$ cm s^{-1}), it is expected that only in regions of the highest velocities a discretisation error of order lower than two would occur.

The preconditioned bi-conjugate gradient (PBiCG) method [21] with a diagonal incomplete-LU preconditioner was selected to solve the linear systems associated with the discretised form of the pressure, velocity and energy equations. The PBiCG method provided enhanced robustness without a significant increase in computational time. A stringent convergence criterion for the residuals, $\epsilon < 10^{-9}$ was selected for these equations to prevent the divergence of PBiCG in the energy equation. The Gauss-Seidel method was applied to solve the discretised equations related to the turbulent scalar fields $\tilde{k}$ and ω. In OpenFOAM, this was implemented selecting the smoothSolver with the symGaussSeidel smoother. A more relaxed convergence criterion, $\epsilon < 10^{-6}$, was chosen for turbulent scalar fields to shorten simulation times.

To execute the transient simulation, the OpenFOAM PIMPLE algorithm [13] was selected. PIMPLE combines the Pressure-Implicit with Splitting Operators (PISO) method with the Semi-Implicit Method for Pressure-Linked Equations (SIMPLE). The implementation of PIMPLE in the overBuoyantPimpleDyMFoam solver also updates the mesh geometry at each timestep. The number of correctors and outer correctors was set to two. As the mesh is completely orthogonal, no non-orthogonal correctors were required. Although relaxation factors improved the stability of the simulation, they were not used because they produced an unphysical spurious transient behaviour at the beginning of the simulation. The maximum Courant number was set to 0.5 in order to achieve the convergence of the residuals.

The thermodynamic and thermophysical properties were evaluated using the COOLPROP open source thermophysical properties library [22]. All the code required

to generate the meshes, reproduce the results and implement the model in OpenFOAM v2006 is available in the Imperial College Data Repository [23]. A detailed documentation of the code is provided an Appendix B.

3.3 1-D non-equilibrium model

In this section, a realistic 1-D vapour phase heat transfer model relevant for the isobaric evaporation of pure cryogenic liquids is developed [8]. For this purpose, the same cylindrical storage tank used for the development of the vapour-CFD model is considered, see Figure 3.1. This model is coupled with the liquid phase bulk model, see Eqs. (3.1)-(3.11), to produce 1-D non equilibrium model [8]. In this thesis, the 1-D non equilibrium model for isobaric evaporation will be referred as the isobaric 1-D model. The new model [8] is based on Migliore et al. [1] non-equilibrium model, and it improves it in three aspects. First, it removes the assumption of semi-infinite space in the vapour phase. Second, the wall heat ingress is implemented as a source term dependent of the vertical coordinate. Finally, the advective heat transfer produced by the ascending evaporative flow is included. In subsection 3.3.1, the equations and assumptions that constitute the isobaric 1-D model are presented. In subsection 3.3.2, the computational implementation of the isobaric 1-D model is explained.

3.3.1 1-D vapour phase heat transfer model

The isobaric 1-D model is a reduction of the vapour-CFD model, see subsection 3.2.2, to only the heat transfer equation in the vertical dimension. The aim of the isobaric 1-D model is to accurately simulate the isobaric evaporation of pure cryogens without the need to perform CFD simulations. On one hand, the isobaric 1-D model constitutes a clear formulation that provides a better understanding of the dominant heat and mass transfer phenomena. On the other, it allows the simulation of time-scales unfeasible for CFD, such as months or years. To reduce the vapour-CFD model, the following assumptions were made. First, instead of solving the continuity and Navier-Stokes equation, a vertical vapour velocity is introduced. Second, the azimuthal velocity is neglected owing to axial symmetry. Finally, the effect of natural convection is included

as an enhancement of the vapour mixing in the radial direction only. The enhanced mixing in the radial direction supports the assumption of instantaneous heat transfer, which allows us to model the heating of the vapour through the walls as a source term.

The heating of the vapour through the walls will drive natural convection, even for low wall heat fluxes typical of cryogenic storage tanks with multi layered insulation (MLI). However, experimental studies on the evaporation of different cryogens have showed a stable, positive vertical temperature gradient in the vapour phase [3, 5, 6]. This suggests that the contribution of natural convection to heat transfer in the vertical direction is small. This argument is further supported by Migliore et al [1] sensitivity analysis of vapour temperature over a range of hypothetical convection heat transfer coefficients. They demonstrated that even a low convection coefficient of $h \approx 10$ W m^{-2} would predict a vapour temperature only up to 1 K hotter than the liquid. This low superheating is inconsistent with industrial evidence of vapour superheating of the order of 15 K [1] to 38 K [4] reported for large LNG storage tanks. Therefore, the contribution of natural convection to vertical heat transfer is small and will be neglected.

The magnitude of the contribution of natural convection on radial heat transfer in the vapour phase is less clear. A recent CFD study [10] suggests that the variation of temperature in the radial direction is negligible compared with its variation in the vertical direction. This suggests that natural convection significantly enhances radial heat transfer in the vapour phase. On the basis of this result, for the development of the isobaric 1-D model the vapour temperature has been assumed spatially homogeneous in the radial direction. This allows to reduce the energy equation of the vapour-CFD model to a one-dimensional model heat transfer model in the vertical direction.

The vapour phase has been modelled as a cylinder with variable height, to consider its expansion as the liquid level decreases during the evaporation. This approach is identical to the definition of the vertical dimension of the vapour domain in the vapour-CFD model, see 3.2.2. The domain $\Omega_{V,1D}$ is the closed, time-dependent interval $0 < z < l_V(t)$. The vapour height $l_V(t)$ is calculated by coupling the mass and energy balances, Eqs. (3.4), (3.6) -(3.9), (3.11) and (3.22), with the vapour-1-D model. The

vapour phase is heated through the walls and roof, and cooled by the vapour liquid interface, see Figure 3.1.

Under the assumption of instantaneous heat transfer in the radial direction, the vapour heating through the tank wall has been modelled as a source term $\dot{S}_{\mathrm{w,V}}$. The wall heating source $\dot{S}_{\mathrm{w,V}}$ has been defined using an energy shell balance in an infinitesimal vertical cylinder,

$$\dot{S}_{\mathrm{w,V}} = \frac{4U_{\mathrm{V}}d_o}{d_i^2}(T_{\mathrm{air}} - T_{\mathrm{V}}), \tag{3.18}$$

and it is a function of both time and height. As the vapour is being heated, its density will decrease, and its velocity will increase. Instead of solving the Navier-Stokes equation, it was assumed a spatially homogeneous vapour velocity evaluated at the density corresponding to the average vapour temperature. Furthermore, the velocity profile in the boundary layer has not been modelled explicitly. This choice is supported by the small width of the boundary layer compared to the tank radius in most practical applications. For low heat fluxes and typical storage tanks with $R_{\mathrm{T}} > 0.8$ m, the width of the boundary layer is between 20 to 1000 smaller than R_{T}. Under these assumptions, the average advective vapour velocity has been calculated by dividing the evaporation rate by the interface area and the average vapour density,

$$\bar{v}_z = \frac{4\dot{B}_{\mathrm{L}}}{\pi d_{\mathrm{i}}^2 \bar{\rho}_{\mathrm{V}}}. \tag{3.19}$$

The advective term $\bar{v}_z$ in (3.19) represents the overall upward movement of heat by the ascension of vapour. This ascension is caused by the vertical displacement in the vapour bulk by the denser vapour produced at the interface by evaporation. It is worth noting the similarity of Eq. (3.19) and the velocity boundary condition at the interface, $v_z|_{z=0,\mathrm{CFD}}$ in the vapour-CFD model, Eq. (3.15). However, the density in the average advective velocity, Eq. (3.19) is evaluated at $\bar{T}_{\mathrm{V}}$ while in Eq. (3.15) is evaluated at $T_{\mathrm{V}}(z = 0) = T_{\mathrm{L}}$. Therefore, in the vapour-1-D model $\bar{v}_z$ is spatially homogeneous and $\bar{v}_z \geq v_z|_{z=0,\mathrm{CFD}}$.

The increase of vapour temperature owing to wall heating will induce a temperature difference within the vapour phase, which will drive heat conduction. To

simplify heat conduction modelling, it has been assumed that the vapour density, heat capacity and thermal conductivity are weak linear functions of temperature [24]. Under these assumptions, the spatial-temporal evolution of the vapour temperature is governed by an advection diffusion equation with a linear source term,

$$\frac{\partial T_{\mathrm{V}}}{\partial t} = \bar{\alpha}_{\mathrm{V}} \frac{\partial^2 T_{\mathrm{V}}}{\partial z^2} - \bar{v}_z \frac{\partial T_{\mathrm{V}}}{\partial z} + \frac{\bar{\alpha}_{\mathrm{V}}}{\bar{k}_{\mathrm{V}}} \dot{S}_{\mathrm{w,V}}. \tag{3.20}$$

where $\bar{\alpha}_{\mathrm{V}} = \bar{k}_{\mathrm{V}}/\bar{\rho}_{\mathrm{V}}\bar{c}_{\mathrm{p}}$ and $\bar{k}_{\mathrm{V}}$ are the vapour thermal diffusivity and thermal conductivity, respectively, evaluated at the average vapour temperature, and $\bar{v}_z$ is the advective velocity. Eq. (3.20) is constrained by the following initial and boundary conditions,

$$\begin{aligned} &T_{\mathrm{V}}(t=0,z) = T_{\mathrm{L}} = T_{\mathrm{sat}}(P), \\ &T_{\mathrm{V}}(t,z=0) = T_{\mathrm{L}} = T_{\mathrm{sat}}(P)\,, \\ &\frac{\partial T_{\mathrm{V}}}{\partial z}(t,z=l_{\mathrm{V}}) = \frac{q_{\mathrm{roof}}}{k_{\mathrm{V}}(z=l_{\mathrm{V}})}. \end{aligned} \tag{3.21}$$

indicating that (i): at the beginning of the evaporation both vapour and liquid are in thermal equilibrium; (ii) continuity of temperature at the vapour-liquid interface and (iii) the roof is subject to a heat flux $q_{\mathrm{roof}} = \dot{Q}_{\mathrm{roof}}/A_{\mathrm{T}}$.

To summarize, although the PDE that constitutes the vapour phase heat transfer model, Eq. (3.20), includes an advective term, $\bar{v}_z(\partial T/\partial z)$, it only has a positive, vertical component. This advective term does not induce natural convection in the vapour bulk. Therefore, the heat ingress from the walls is transferred instantaneously across the tank radius, and it is transported by conduction and advection in the vertical direction.

The vapour to liquid heat transfer rate, $\dot{Q}_{\mathrm{VL}}$, is defined as the integrated heat flux transferred from the vapour to the vapour-liquid interface, see Eq. (3.10). For the 1-D model, the variations of vapour temperature with radius are neglected, and $\dot{Q}_{\mathrm{VL}}$ simplifies to:

$$\dot{Q}_{\mathrm{VL}} = \frac{\pi d_{\mathrm{i}}^2}{4} k_{\mathrm{V}}|_{z=0} \left.\frac{\partial T_{\mathrm{V}}}{\partial z}\right|_{z=0}. \tag{3.22}$$

3.3.2 Implementation of the isobaric 1-D model in MATLAB

The vapour phase heat transfer partial differential equation (PDE), Eq. (3.20), has been partially discretized using the method of lines [25]. This method consists in transforming the PDE into a system of ODEs by discretizing explicitly only the spatial dimension. The spatial discretization generates an ODE for each spatial node, and the resulting system has the flexibility to be coupled with other ODE systems. This flexibility is crucial in the isobaric 1-D model, because two subsystems are coupled and must be solved simultaneously. The moving boundary has been implemented using an adaptive moving mesh [26], using the velocity of the interface, Eq.(3.17), as the mesh velocity. A coordinate transformation of was performed to Eq. (3.20) to introduce the mesh velocity in the spatial gradients. The transformed version of Eq. (3.20) was discretized using the finite difference method. The diffusive and advective terms in Eq. (3.20) were discretized using second order central differences. The source term $\dot{S}_{w,V}$ was evaluated directly at the nodal temperature. The Neumann boundary conditions have been implemented using second order backward differences. The derivation of the coordinate transformation and the finite difference discretization of Eq. (3.20) is presented in Appendix C.

The mass and energy balances model, Eqs. (3.4), (3.6) -(3.9), (3.11) and (3.22), has been augmented by the spatial discretization of Eqs.(3.20)-(3.21). Therefore, the 1-D non-equilibrium model consists of $1 + n_z$ ODEs, where n_z is the number of nodes produced by the discretization of the vapour domain. The transport and thermodynamic properties have been evaluated using the REFPROP® 9.0 library [27]. The 1-D non-equilibrium model has been implemented in MATLAB 2018b®, and the ODE system has been integrated explicitly in time using the ode15s variable-step, variable-order routine [28]. For each equation, the convergence criterium has been determined by setting the absolute and relative tolerances at 10^{-6} and 10^{-4}, respectively. Reducing tolerances by a factor of 10 yields a negligible change in vapour temperatures or BOG rates (<0.01%), at the expense of simulation times one order of magnitude longer. A grid spacing of $\Delta z = 3$ cm was chosen as a result of a grid sensitivity analysis for the minimum and maximum liquid fillings. The numerical solution changed by less than 0.03% for BOG rates and by less than 0.01% for average vapour temperatures after

halving or doubling the grid spacing. A complete verification of all models for isobaric evaporation of cryogenic liquids is presented in Chapter 4. The simulations have been run in a 4-core Intel® Core ™ i7-7700 K CPU overclocked at 4300 MHz. The simulation time varied between 0.2 and 4 s depending on the liquid filling.

3.4 Analytical solutions

The 1-D model for isobaric evaporation of pure cryogens [8] developed in section 3.3 is a linear ODE system coupled with a linear PDE. Therefore, it is worth attempting to derive analytical solutions [29] for the isobaric 1-D model given by Eqs. (3.4), (3.6) - (3.9), (3.11) (3.22), (3.20)-(3.21). The aim of this section is to derive such analytical solutions [29] with three objectives in mind. First, the analytical solutions will provide a valuable tool for practitioners to estimate liquid volumes, BOG rate, and vapour temperature profiles. Second, the solutions can act as a limiting scenario that can be used to test and validate the numerical models. Finally, the solutions will provide a cleaner insight into the driving forces that govern the evaporation. In subsection 3.4.1, analytical solutions are developed for the limiting case of the vapour at thermal equilibrium with the liquid. In subsection 3.4.2, analytical solutions for the vapour-1-D model are developed under the assumption of pseudo-steady state in the vapour. Finally, in subsection 3.4.3 the computational implementation of the analytical solutions is described.

3.4.1 Analytical solutions for the equilibrium evaporation model

In the limit of infinitely efficient vapour to liquid heat transfer, the isobaric 1-D model developed in section 3.3 reduces to an equilibrium model. In the equilibrium evaporation model [9], the vapour is assumed to be spatially homogeneous and at thermal equilibrium with the liquid phase, $T_{\mathrm{L}} = T_{\mathrm{V}}$. This implies that all the heat entering the vapour contributes to evaporating the liquid, $\dot{Q}_{\mathrm{VL}} = \dot{Q}_{\mathrm{V,in}}$. Thus, the equilibrium model is then constituted by the liquid bulk phase model, Eqs. (3.2), (3.6)-(3.9) and (3.11), and the simplifying assumption of $\dot{Q}_{\mathrm{VL}} = \dot{Q}_{\mathrm{V,in}}$. Substituting the wall heat ingresses, Eq.(3.7), into Eq. (3.2), expresses the total liquid heat ingress as a linear

function of the volume. Incorporating the resulting expression into Eq. (3.6) yields a first-order, linear, ordinary differential equation (ODE) with constant coefficients for the liquid volume,

$$\frac{dV_{\mathrm{L}}}{dt} = CV_{\mathrm{L}} + D\,, \tag{3.23}$$

where the coefficients C and D are given by,

$$C = -\frac{4d_{\mathrm{o}}}{d_{\mathrm{i}}^2}\frac{(T_{\mathrm{air}} - T_{\mathrm{L}})}{\rho_{\mathrm{L}}\Delta H_{\mathrm{LV}}}(U_{\mathrm{L}} - U_{\mathrm{V}}), \tag{3.24}$$

$$D = -\frac{1}{\rho_{\mathrm{L}}\Delta H_{\mathrm{LV}}}\left(\frac{4d_{\mathrm{o}}}{d_{\mathrm{i}}^2}(T_{\mathrm{air}} - T_{\mathrm{L}})U_{\mathrm{V}}V_{\mathrm{T}} + \dot{Q}_{\mathrm{bot}}\right). \tag{3.25}$$

Considering the initial conditions, $V_{\mathrm{L}}(0) = V_{\mathrm{T}}LF$, the solution of Eq. (3.23) is given by,

$$V_{\mathrm{L}} = \frac{D}{C}(\exp(Ct) - 1) + V_{\mathrm{T}}LF\exp(Ct)\,, \qquad t \le \tau_{\mathrm{evap}}\,, \tag{3.26}$$

where τ_{evap} is defined as the time required for the complete evaporation of the liquid, obtained by setting Eq. (3.26) to zero, and it is given by,

$$\tau_{\mathrm{evap}} = \frac{1}{C}\ln\left(1 + V_{\mathrm{T}}LF\,\frac{C}{D}\right)^{-1} = -\frac{1}{C}\ln\left(1 + V_{\mathrm{T}}LF\frac{C}{D}\right)\,. \tag{3.27}$$

The solution for the evaporation rate, $\dot{B}_{\mathrm{L}}$, is obtained by simply multiplying Eq. (3.23) by the liquid density, while the BOG rate is given by,

$$\dot{B}(t) = (\bar{\rho}_{\mathrm{V}} - \rho_{\mathrm{L}})(CV_{\mathrm{L}}(t) + D). \tag{3.28}$$

It is worth noting that for the equilibrium model, the vapour average density is constant and evaluated at the liquid temperature, $\bar{\rho}_{\mathrm{V,eq}} = \rho_{\mathrm{V}}(T_{\mathrm{L}})$. If the heat flux through the liquid is higher than through the vapour, $U_{\mathrm{L}} > U_{\mathrm{V}} \rightarrow C < 0$. Hence the liquid volume and BOG rate will exhibit an exponential decrease, see Eqs. (3.26) and (3.28). Otherwise, $V_{\mathrm{L}}(t)$ will be concave and the BOG rate will increase with time. The analytical solutions simplify further when the heat transfer coefficients for both phases are the same, $U_{\mathrm{L}} = U_{\mathrm{V}} \rightarrow C = 0$. In this case, $D < 0$ and the liquid volume decreases linearly with time,

$$V_{\mathrm{L}}(t) = V_{\mathrm{T}}LF + Dt \tag{3.29}$$

while the BOG rate is constant and equal to $D(\bar{\rho}_{\mathrm{V,eq}} - \rho_{\mathrm{L}})$, as can be seen from Eq. (3.28).

3.4.2 Analytical solutions for the isobaric 1-D model

To derive analytical solutions for the isobaric 1-D model, a number of assumptions are made to simplify Eqs. (3.18)-(3.21). A plethora of experimental and industrial evidence [2, 3, 5-7] on cryogen isobaric evaporation shows that the vapour temperature reaches a pseudo-steady state. This pseudo-steady state is reached after a short transient period τ_{trans} after the beginning of the evaporation. The transient period is defined as the time before the average vapour temperature changed more slowly than 0.1 K h^{-1}. The pseudo-steady state vapour temperature profile produced by the isobaric-1-D model is similar to the steady-state solution of Eq. (3.20) subject to the boundary conditions (3.21) [8]. This similarity implies that the temporal variation of the vapour temperature is entirely a result of an increase of the amount of vapour owing to evaporation. Hence, the solutions are derived under the assumption that the vapour phase has already reached its pseudo-steady state.

The solutions for the non-equilibrium model are derived by neglecting the explicit dependence of the vapour temperature on time, setting $\partial T_{\text{V}}/\partial t = 0$ in Eq. (3.20). Hence, T_{V} is governed by a steady-state advection-diffusion equation with a linear source term for a given vapour volume. Furthermore, simulations [8] have confirmed that the vapour to liquid heat ingress is small and nearly constant during evaporation. Thus, the initial advective vapour velocity, Eq. (3.19), is estimated by neglecting $\dot{Q}_{\text{VL}}$ contribution to the total heat input. In this scenario, $\bar{v}_z$ is estimated from the initial evaporation rate, based on the initial liquid volume, as,

$$\bar{v}_z(t=0) \equiv \frac{4\left(\dot{Q}_{\text{L,in}} + \dot{Q}_{\text{bot}}\right)}{\rho_{\text{V}} \pi d_{\text{i}}^2 \Delta H_{\text{LV}}} = \text{Eq. (3.19)} = \frac{4\dot{B}_{\text{L}}}{\pi d_{\text{i}}^2 \bar{\rho}_{\text{V}}}, \tag{3.30}$$

Finally, the vapour thermophysical properties are evaluated at the average vapour temperature, as it was assumed in the derivation of the vapour-1-D model. By making these assumptions, Eq. (3.20) can be transformed into a second order, non-homogeneous, linear ODE with constant coefficients,

$$\bar{k}_{\text{V}} \frac{d^2 T_{\text{V}}}{dz^2} - H \frac{dT_{\text{V}}}{dz} - S T_{\text{V}} = -E, \tag{3.31}$$

where

$$H = \bar{\rho}_{\mathrm{V}}\bar{c}_{\mathrm{p,V}}\bar{v}_z, \quad S = \frac{4U_{\mathrm{V}}d_{\mathrm{o}}}{d_{\mathrm{i}}^2}, \quad E = ST_{\mathrm{air}}\,, \tag{3.32}$$

subject to the boundary conditions,

$$\begin{aligned} T_{\mathrm{V}}|_{z=0} &= T_{\mathrm{L}}\,, \\ \left.\frac{dT_{\mathrm{V}}}{dz}\right|_{z=l_{\mathrm{V}}} &= \frac{q_{\mathrm{roof}}}{k_{\mathrm{V}}(z=l_{\mathrm{V}})}. \end{aligned} \tag{3.33}$$

The discriminant of the characteristic polynomial associated with the homogeneous solution of Eq. (3.31), $\Delta = \sqrt{H^2 + 4\bar{k}_{\mathrm{V}}S}$, is always positive. Therefore, the vapour temperature profile is a linear combination of two exponential functions and the particular solution $T_{\mathrm{V}}(z) = T_{\mathrm{air}}$.

$$T_{\mathrm{V}}(z) = c_1\exp(z\chi_-) + c_2\exp(z\chi_+) + T_{\mathrm{air}}\,, \tag{3.34}$$

where $\chi_\pm$ is given by

$$\chi_\pm = \frac{H \pm \sqrt{H^2 + 4\bar{k}_{\mathrm{V}}S}}{2\bar{k}_{\mathrm{V}}}. \tag{3.35}$$

The average vapour temperature, $\bar{T}_{\mathrm{V}} = \frac{1}{l_{\mathrm{V}}}\int_0^{l_{\mathrm{V}}} T_{\mathrm{V}}(z)dz$, can be obtained by directly integrating Eq.(3.34),

$$\bar{T}_{\mathrm{V}}(l_{\mathrm{V}}) = T_{\mathrm{air}} + \frac{1}{l_{\mathrm{V}}}\left(\frac{c_1}{\chi_-}\left(\exp(l_{\mathrm{V}}\chi_-) - 1\right) + \frac{c_2}{\chi_+}\left(\exp(l_{\mathrm{V}}\chi_+) - 1\right)\right), \tag{3.36}$$

where c_1 and c_2 are arbitrary constants that can be evaluated by ensuring that the solution satisfies the boundary conditions. The boundary condition at the vapour liquid interface is of Dirichlet type, while at the tank roof, there are two possibilities which depend on the value of q_{roof}. If the heat ingress through the roof is a fixed value, the boundary conditions are of Dirichlet type at z = o and of Neumann type at $z = l_{\mathrm{V}}$. For this combination of boundary conditions, the constants c_1 and c_2 are given by,

$$c_1 = \frac{a_+(T_{\mathrm{L}} - T_{\mathrm{air}}) - \left.\frac{dT_{\mathrm{V}}}{dz}\right|_{z=l_{\mathrm{V}}}}{a_+ - a_-}, \quad c_2 = \frac{a_-(T_{\mathrm{air}} - T_{\mathrm{L}}) + \left.\frac{dT_{\mathrm{V}}}{dz}\right|_{z=l_{\mathrm{V}}}}{a_+ - a_-}, \tag{3.37}$$

where

$$a_{\pm} = \chi_{\pm} b_{\pm} \,, \tag{3.38}$$

$$b_{\pm} = \exp(l_{\mathrm{V}} \chi_{\pm}), \tag{3.39}$$

$$\left.\frac{dT_{\mathrm{V}}}{dz}\right|_{z=l_{\mathrm{V}}} = \frac{q_{\mathrm{roof,fixed}}}{k_{\mathrm{V}}|_{z=l_{\mathrm{V}}}} \,. \tag{3.40}$$

In the second case, a variable heat ingress through the roof is considered that depends on the roof temperature. In this case, the boundary conditions are of Dirichlet type at z = 0 and of Robin (mixed) type at $z = l_{\mathrm{V}}$. For this combination, the constants c_1 and c_2 are given by,

$$c_1 = \frac{(T_{\mathrm{L}} - T_{\mathrm{air}})(a_+ + \gamma b_+)}{(a_+ + \gamma b_+) - (a_- + \gamma b_-)}, \quad c_2 = \frac{(T_{\mathrm{air}} - T_{\mathrm{L}})(a_- + \gamma b_-)}{(a_+ + \gamma b_+) - (a_- + \gamma b_-)}, \tag{3.41}$$

Where γ is defined by,

$$\gamma = \frac{U_{\mathrm{roof}}}{k_{\mathrm{V}}|_{z=l_{\mathrm{V}}}}, \tag{3.42}$$

Eqs. (3.34)-(3.42), show that the temporal variation of the vapour temperature is primarily governed by the vapour phase height, l_{V}. The vapour height increases during evaporation, owing to the reduction of liquid volume. The vapour to liquid heat ingress is obtained directly by taking the derivative of Eq. (3.34), evaluating the expression at the vapour-liquid interface ($z = 0$) and replacing the derivative on Eq. (3.22) ,

$$\dot{Q}_{\mathrm{VL}} = \frac{\pi d_{\mathrm{i}}^2}{4} k_{\mathrm{V}}|_{z=0} (c_1 \chi_- + c_2 \chi_+) \,. \tag{3.43}$$

The vapour to liquid heat ingress, $\dot{Q}_{\mathrm{VL}}$, depends on the average thermophysical properties and the height of the vapour phase, see Eqs. (3.32), (3.35) and (3.36). These quantities change slowly during the evaporation, as they are a function of the vapour height. Consequently, $\dot{Q}_{\mathrm{VL}}$ changes slowly with time. If $\dot{Q}_{\mathrm{VL}}$ is assumed constant, the total liquid heat ingress becomes a linear function of the liquid volume, see Eqs. (3.2), (3.7) and (3.10). Therefore, the rate of change of liquid volume is also linear in V_{L}, see Eq. (3.6). The solution for V_{L} is obtained using Eq. (3.26) by substituting the coefficients C and D by the non-equilibrium coefficients C^{neq} and D^{neq}, defined as,

$$C^{\mathrm{neq}} = -\frac{4 d_{\mathrm{o}}}{d_{\mathrm{i}}^2} \frac{(T_{\mathrm{air}} - T_{\mathrm{L}})}{\rho_{\mathrm{L}} (h_{\mathrm{V}} - h_{\mathrm{L}})} U_{\mathrm{L}} \,, \tag{3.44}$$

$$D^{\mathrm{neq}} = -\frac{\dot{Q}_{\mathrm{bot}} + \dot{Q}_{\mathrm{VL}}}{\rho_{\mathrm{L}} \Delta H_{\mathrm{LV}}(P)}. \tag{3.45}$$

In a similar way, the time for complete evaporation and BOG rates for the non-equilibrium model are obtained by substituting the non-equilibrium coefficients in Eqs. (3.27) and(3.28), respectively.

It is worth noting that for both equilibrium and non-equilibrium models, the reduction of the liquid volume, Eq. (3.26), and the BOG rates, Eq. (3.28), have the same form. Considering that $\rho_{\mathrm{V}} \ll \rho_{\mathrm{L}}$ for operating conditions typical of isobaric cryogenic storage, the non-equilibrium model will predict lower BOG rates and higher liquid volumes compared to the equilibrium model. This is expected as in the equilibrium model, $\dot{Q}_{\mathrm{VL}} = \dot{Q}_{\mathrm{V,in}}$, while in the non-equilibrium model, $\dot{Q}_{\mathrm{VL}} < \dot{Q}_{\mathrm{V,in}}$. Furthermore, under conditions of no heat transfer into the vapour phase ($U_{\mathrm{V}} = \dot{Q}_{\mathrm{VL}} = 0$), the equilibrium constants C and D reduce to the non-equilibrium ones.

3.4.3 Implementation of the analytical solutions

The analytical solutions for the equilibrium case are implemented directly using the thermophysical properties of both phases evaluated at the saturation temperature. For the non-equilibrium case, the situation is more complicated as the analytical solutions for the vapour temperature are functions of the vapour height, see Eqs. (3.34) - (3.45). Hence, the vapour temperature profile, Eq. (3.34), and the vapour to liquid heat ingress, Eq. (3.45) can be only obtained sequentially. The sequential calculation starts at the initial conditions, see Eq. (3.21), where the initial vapour height , $l_{\mathrm{V0}} = V_{\mathrm{T}} \times (1 - LF)/A_{\mathrm{T}}$, is a known input. As the evaporation proceeds, the decrease in liquid volume will provide an appropriate value of l_{V} at the end of a prescribed time step.

The implementation of (3.34)-(3.45) also requires an evaluation of the thermophysical properties $\bar{c}_{p,\mathrm{V}}$ and $\bar{k}_{\mathrm{V}}$, and the advective velocity, $\bar{v}_z$, at the average vapour temperature. To calculate T_{V} and $\dot{Q}_{\mathrm{VL}}$ at a given l_{V}, two options are proposed. The first option is to assume that for the calculation of the vapour thermophysical properties, $\bar{T}_{\mathrm{V}} = T_{\mathrm{L}} = T_{\mathrm{sat}}(P)$ and that $\dot{Q}_{\mathrm{VL}}$ is negligible in the calculation of $\bar{v}_z$. This

option is straightforward to implement, but it introduces an error which will increase with the duration of the evaporation. The increase in the modelling error is a consequence of the increase in vapour temperature with vapour length, which makes $\bar{T}_{\mathrm{V}}$ considerably higher than T_{sat}. The second option is to adopt an iterative approach. In the first iteration, the vapour temperature profile is obtained evaluating the thermophysical properties at $\bar{T}_{\mathrm{V}} = T_{\mathrm{L}}$, and calculating $\bar{v}_z$ assuming that $\dot{Q}_{\mathrm{VL}} = 0$. With the obtained temperature profile and $\dot{Q}_{\mathrm{VL}}$; $\bar{c}_{p,\mathrm{V}}$, $\bar{k}_{\mathrm{V}}$ and $\bar{v}_z$ are updated and so are the values of H, c_1 and c_2. This allows for a new vapour temperature profile and $\dot{Q}_{\mathrm{VL}}$ to be calculated. The iteration is repeated until the average vapour temperature converges to within acceptable limits. In this thesis, the convergence criterium was set to $\bar{T}_V^{\mathrm{new}} - \bar{T}_V^{\mathrm{old}} < 0.01$ K, which was achieved in less than 10 iterations.

The calculation of the liquid volume and BOG is in principle straightforward, as Eqs. (3.26) and (3.28) can be used directly if $\dot{Q}_{\mathrm{VL}}$ is assumed negligible or constant in the total liquid heat ingress, see Eq. (3.2). However, a more accurate solution can be obtained if these two quantities are calculated sequentially using Eq. (3.43) to estimate $\dot{Q}_{\mathrm{VL}}$ at each iteration. First, the evaporation time τ_{evap} is partitioned in n_t intervals, based on a prescribed fixed time-step $\Delta t = \tau_{\mathrm{evap}}/n_t$. A time step between a week and a day is suggested, depending on the desired accuracy. To differentiate between the two calculation approaches, the former route has been named the direct route, while the latter the sequential route. In order to help with the implementation of the analytical solutions, the numerical methods are provided in a Jupyter Notebook hosted in Mendeley Data [30]. Additionally, a non-interactive version of the notebook with the code and a figure of a representative temperature profile can be found in Appendix D.

3.5 Non-equilibrium weathering model of LNG under isobaric conditions

Liquefied natural gas (LNG) is a cryogenic liquid with a boiling temperature of around -160 °C at standard pressure. Although the LNG mixtures are mainly composed by methane, they also contain nitrogen and small hydrocarbons such as ethane and propane. The large temperature difference between the stored LNG and the surrounding air drives a heat ingress through the vapour and liquid, as discussed in

sections 3.2-3.3. The heat ingress will produce the evaporation of the LNG and the heating of the vapour, as it was observed for pure cryogens. However, as methane and nitrogen would preferentially evaporate, the heat ingress will also lead to the weathering of the remaining LNG.

The change in the liquid composition during LNG storage will result in an increase of the LNG boiling temperature, as it becomes richer in heavier components. In this section, a non-equilibrium model for the weathering of LNG is proposed by extending the isobaric 1-D model developed in section 3.3 in four aspects. First, a thermodynamic model is included to calculate the phase equilibrium and the variation of liquid thermophysical properties with composition. Second, the mass and energy balances, Eqs.(3.1), (3.3) and (3.11), are rewritten for an expression valid to mixtures. Third, the LNG density is evaluated at each time-step using the Enhanced Revised Klosek and McKinley method (ERKM) [31, 32]. Finally, the temperature boundary condition at the vapour-liquid interface is a function dependent on time and the LNG composition $\boldsymbol{x}$, $T_{\mathrm{V}}|_{z=0}(t) = T_{\mathrm{L}}(P, \boldsymbol{x}, t)$.

The full weathering model is a combination of three sub-models: a mass and energy balances model, a thermodynamic model and a heat transfer model. The main novelty of the non-equilibrium model presented in this thesis is the coupling of the vapour phase heat transfer model, see section 3.3, to the other two sub-models. In subsections 3.5.1 - 3.5.3, incremental improvements are described to the first two sub-models, which were originally developed by Migliore et al [1, 9]. In subsection 3.5.4, the vapour phase heat transfer model is adapted for the isobaric evaporation of a multicomponent cryogenic liquid. Finally, in subsection 3.5.5 the implementation of the differential algebraic equations (DAE) system that constitutes the weathering model is presented. In particular, major improvements in the accuracy and efficiency for the first two sub-models were achieved with respect to the implementation of Migliore et al [1, 9].

3.5.1 Macroscopic mass and energy balances

The LNG composition and temperature were assumed spatially homogeneous, as the liquid is assumed to be stored at its boiling point under isobaric conditions. In 165,000 m³ storage tanks filled at 97% of its capacity used in industry, the saturation temperature of LNG can increase with depth up to 12.6 K owing to the hydrostatic head. However, this does not lead to a liquid bulk superheated with respect to the saturation temperature at the operating pressure evaluated at the interface. Saleem et al [10] CFD study demonstrated that for low heat transfer coefficients, $U_{\mathrm{L}} < 0.25$ W m^{-2}, T_{L} was nearly spatially homogeneous and less than 1 K superheated with respect to $T_{\mathrm{sat}}(P_{\mathrm{int}})$. This is a consequence of the onset of a buoyancy driven flow in the liquid. This buoyancy driven flow carries the heated liquid near the wall upwards until it reaches the interface. At the interface and slightly below, the liquid it evaporates at $T_{\mathrm{sat}} \approx T_{\mathrm{sat}}(P_{\mathrm{int}})$. Therefore, assuming a spatially homogeneous liquid temperature is an excellent assumption, and the dynamics of the liquid can be modelled as a bulk phase.

The evaporation rate, $\dot{B}_{\mathrm{L}}$, is defined by the global mass balance on the liquid subsystem, see Eq. (3.1). In contrast to the simplified equation for pure cryogens, Eq. (3.4), the density time derivative cannot be neglected for the weathering of LNG. The LNG density will change with time as the temperature increases and the liquid composition changes. In addition to the global mass balance in the liquid phase, a mass balance for each component of LNG is defined as,

$$-\dot{B}_{\mathrm{L}} x_i = \frac{d}{dt}(\rho_{\mathrm{L}} V_{\mathrm{L}} x_i) = \rho_{\mathrm{L}} V_{\mathrm{L}} \frac{dx_i}{dt} + \rho_{\mathrm{L}} x_i \frac{dV_{\mathrm{L}}}{dt} + V_{\mathrm{L}} x_i \frac{d\rho_{\mathrm{L}}}{dt} \quad \text{for } i = 1..n_{\mathrm{comp}}\,, \quad (3.46)$$

where x_i is the mole fraction of the i component of the LNG mixture in the liquid phase, and n_{comp} the number of components in the mixture. The BOG rate, $\dot{B}$, is defined by the same mass balance used in the evaporation model for pure cryogens, see Eq. (3.11). It should be noted that for LNG weathering, the average vapour density is also a function of the vapour composition. Performing an energy balance in the liquid phase, the evaporation rate is coupled with the liquid heat ingress and liquid enthalpy as defined in Eq. (3.3). In contrast to the evaporation of pure cryogenic liquids, both liquid density and enthalpy vary with time owing to weathering. Hence, Eq. (3.3) cannot be simplified

to Eq. (3.6). In this scenario, it is convenient to expand the derivative of the liquid enthalpy in Eq. (3.3),

$$\dot{Q}_{\mathrm{L,tot}} - \dot{B}_{\mathrm{L}} h_{\mathrm{V}}(T_{\mathrm{L}}) = h_{\mathrm{L}} \frac{d(\rho_{\mathrm{L}} V_{\mathrm{L}})}{dt} + \rho_{\mathrm{L}} V_{\mathrm{L}} \frac{dh_{\mathrm{L}}}{dt}, \tag{3.47}$$

Substituting Eq. (3.1) in (3.47) and rearranging terms, a clearer form of the energy balance in the liquid phase is obtained,

$$\dot{Q}_{\mathrm{L,tot}} = \dot{B}_{\mathrm{L}} \Delta H_{\mathrm{LV}}(P, \boldsymbol{x}, \boldsymbol{y}) + \rho_{\mathrm{L}} V_{\mathrm{L}} \frac{dh_{\mathrm{L}}}{dt}, \tag{3.48}$$

Eq. (3.48) shows that the total liquid heat ingress produces two different effects: evaporation at a rate $\dot{B}_{\mathrm{L}}$, and an increase in liquid enthalpy. For mixtures, the enthalpy of phase change, ΔH_{LV}, will not be constant but instead a function of the composition of the vapour and liquid phases. The increase in liquid enthalpy is a consequence of the increase in the liquid temperature, T_{L}, as the remaining LNG becomes richer in heavier components. It is worth noting that the term $\rho_{\mathrm{L}} V_{\mathrm{L}} \frac{dh_{\mathrm{L}}}{dt}$ is not present in the energy balance for the isobaric evaporation of pure cryogenic liquids, see Eq. (3.6). This is consistent, as the enthalpy of a pure liquid at its saturation point at constant pressure is constant. As the tank volume is fixed, $V_{\mathrm{T}} = V_{\mathrm{V}} + V_{\mathrm{L}}$ for both LNG and pure cryogenic liquids, see subsection 3.2.1. Taking advantage of the fixed tank volume, the mass and energy balances sub-model, Eqs. (3.1), (3.11), (3.46), (3.48), constitutes an implicit system of $3 + n_{\mathrm{comp}}$ ordinary differential equations.

3.5.2 Thermodynamic model

In the LNG weathering model, the liquid phase has been assumed to be at physicochemical equilibrium with the vapour interface. Additionally, it was assumed that the vapour composition was spatially homogeneous. This assumption is supported by the fact that the vapour phase of typical LNG mixtures is mostly methane [9]. The composition of the vapour and liquid phases are related by a phase equilibrium equation,

$$y_i = K_i x_i = \frac{\phi_i^{\mathrm{L}}}{\phi_i^{\mathrm{V}}} x_i \,. \tag{3.49}$$

where y_i is the mole fraction of each species in the vapour phase, and K_i is the equilibrium coefficient pertaining to the i^{th} species in the mixture. The quantities ϕ_i^{L}, ϕ_i^{V} are the fugacity coefficients of the i^{th} species in the liquid and vapour phases, respectively. The evolution of the composition during the weathering process was obtained by means of Eqs. (3.46) and (3.49). This approach was preferred over using the Rachford-Rice equation for vapour-liquid equilibrium [33], as proposed by Migliore et al. [1, 9], for two reasons. First, using Eqs. (3.46) and (3.49) resulted in a system which achieved convergence for a wider variety of LNG mixtures and parameters. Secondly, because the implementation of the Rachford-Rice equation in MATLAB to calculate K_i did not decrease simulation times.

In order to calculate the fugacity coefficients and all thermophysical properties, except the LNG liquid density, the Peng-Robinson equation of state (PR-EOS) was used. The standard Van der Waals mixing rules were used to calculate the mixture parameters a_m and b_m, using the binary interaction parameters quoted by Danesh [33]. As cubic equations of state underestimate the liquid density, the liquid LNG density was calculated using the ERKM method [31, 32]. This empirical correlation was specifically developed for LNG and it is recommended by the International Group of Liquefied Natural Gas Importers [34] owing to its high accuracy.

As part of this thesis, the accuracy of the PR-EOS was compared with the state-of-the-art GERG2008-EOS that was specifically developed for natural gas mixtures [35]. The differences were less than 1% in the BOG rates and in the prediction of the relevant thermophysical properties. Hence, PR-EOS was preferred because of its simplicity and better convergence in flash calculations. It is worth noting that the thermodynamic model, Eq. (3.49), comprises n_{comp} non-linear equations which must be solved simultaneously with the ODE system described in the previous section. Hence, the coupled systems of equations constitute a differential algebraic equations system.

3.5.3 Liquid phase heat transfer model

The heat transfer sub-model for the liquid bulk phase in the weathering model is similar to the sub-model used for pure cryogenic liquids. It is standard practice before

filling industrial LNG storage tank to precondition the internal wall until the wall temperature reaches a constant value [36]. During preconditioning, the external wall is in contact with the air and hence steady-state heat transfer in the tank wall is established. This assumption was also applied for the evaporation of pure cryogens, see subsection 3.2.1. However, in the case of LNG it requires further justification, as the liquid temperature raises during the evaporation. The increase in liquid temperature caused by weathering is small and slow, ranging from 0.1 K / year for nitrogen-free LNG to 4 K/year for LNG with 2% by volume of nitrogen [1]. Therefore, neglecting conjugate heat transfer will not affect the heat ingress into the liquid. On the other hand, as the vapour temperature increases appreciably during weathering, neglecting heat accumulation in the tank walls will slightly overestimate the heat ingress into the vapour.

Assuming a spatially homogeneous liquid temperature, the liquid heat ingress through the walls is governed by Eqs. (3.7)-(3.8). The bottom heat ingress can be a model input or calculated through an equation similar to Eq. (3.7), as discussed previously in subsection 3.2.1. Similarly, the overall heat transfer coefficient U_L can be either calculated using standard chemical engineering correlations or fitted to BOG data for a particular tank. In this thesis and for large LNG storage tanks, the coefficient was set to $U_L = 0.038$ $Wm^{-2}K$. This value of U_L was fitted to industrial data by Migliore et al., and then used to produce the simulations of their equilibrium [9] and non-equilibrium [1] weathering models. Therefore, setting the same overall heat transfer coefficient allows an easy comparison of between the new weathering model and their predecessors.

The only difference in the implementation of Eqs. (3.7)-(3.8) for LNG weathering is that the liquid saturation temperature will slowly vary with time. Therefore, the change in liquid heat ingress will also be a function of LNG composition. The vapour to liquid heat transfer during the weathering of LNG is defined by Eq. (3.22). This equation is applicable because the vapour phase has been considered a 1-D phase using the same assumptions described in subsection 3.3.1 for the evaporation of pure cryogens. Therefore, the total liquid heat ingress in the weathering of LNG is governed by Eq. (3.2).

3.5.4 Adaptation of vapour phase heat transfer model for vapour mixtures

For LNG stored in cylindrical tanks with multi-layered insulation, the assumption of negligible natural convection in the vertical direction owing to thermal stratification is still applicable. Hence, the vapour phare heat transfer model, Eqs. (3.18)-(3.21), can be applied considering the following modifications for vapour mixtures. First, the vapour thermophysical properties correspond to the mixture and not to the vapour of a pure cryogenic liquid. Second, the initial condition in Eq. (3.21) will be a function of the initial composition of the mixture, $T_{\mathrm{V}}(t=0,z) = T_{\mathrm{L}} = T_{\mathrm{sat}}(P, \boldsymbol{x}_0)$. Third, the non-homogeneous part of the Dirichlet boundary condition at the vapour liquid interface will vary with time owing to weathering, $T_{\mathrm{V}}(t, z=0) = T_{\mathrm{L}}(t) = T_{\mathrm{sat}}(P, \boldsymbol{x}(t))$.

It is worth noting that the vapour- phase heat transfer model applied for LNG will not lead to radically different temperature profiles compared to pure methane. The vapour phase of commercially available LNG mixtures is mainly composed of methane except at the last stages of weathering. Hence, the obtained temperature profiles in the vapour phase for LNG weathering are expected to be quantitatively similar to the ones obtained for the evaporation of pure methane. On the other hand, the saturation temperature for a range of typical LNG mixtures is not significantly different to T_{sat} for pure methane, $\Delta T_{\mathrm{sat}} < 5$ K [1] . This deviation is particularly small for LNG mixtures with low content of nitrogen. Finally, as the increase of T_{L} during weathering is very slow, $T_{\mathrm{V}}|_{z=0}$ changes very slowly with time compared with the thermal diffusion and advection time scales. Therefore, the time dependency of $T_{\mathrm{V}}|_{z=0}(t)$ is weak and will not significantly alter neither the onset of the pseudo-steady state nor vapour temperature profiles.

3.5.5 Numerical methods and implementation in MATLAB

The isobaric 1-D model adapted to mixtures was implemented using the method of lines, as previously described in subsection 3.3.2. In contrast to pure cryogens, the liquid temperature and vapour thermophysical properties now depend on time and composition. These quantities are inputs for the function that generates the ODE

system associated to Eqs. (3.20)-(3.21) using the method of lines. The resulting ODE system for the vapour phase is coupled with the mass and energy balances model. In contrast to the case for pure cryogenic liquids, see subsection 3.3.2, $n_{\text{comp}} - 1$ additional ODEs are included from the species mass balances, see Eq. (3.46). By analysing the degrees of freedom of the system, the subsystem composed by Eqs. (3.46) and (3.1) have one linearly dependent equation. In the implementation of the system, a specie j in Eq. (3.46) can be arbitrarily selected to be calculated as $x_j = 1 - \sum_{i \neq j} x_i$. This way, a linearly independent system of ODEs is obtained.

The main difference in implementation of the weathering model with respect to the non-equilibrium model for pure cryogens is the phase equilibrium equation for mixtures, Eq. (3.49). The phase equilibrium restricts the evolution of the ODE system through $n_{\text{comp}} - 1$ non-linear equations that must be satisfied at each time-step. By considering the degrees of freedom, the vapour phase mole fraction of one of the species can be calculated through $y_j = 1 - \sum_{i \neq j} y_i$, instead of solving the phase equilibrium equation for each species. The additional coupling of the thermodynamic model through the phase equilibrium equation to the previously described ODE subsystem constitute a DAE system. The weathering model has been implemented in MATLAB 2018b®, while the DAE system has been integrated implicitly in time using the ode15i variable-step, variable-order routine [37]. In contrast to the integrator ode15s used for pure cryogens, ode15i allows the solution of DAE systems of index 1. The system that constitutes the weathering model satisfies this condition, as Eq. (3.49) can be converted into an ODE for each specie by applying one differentiation step.

For each equation of the DAE system, the convergence criterium has been set by fixing absolute and relative tolerances at 10^{-6} and 10^{-4}, respectively. This criterion achieved the same robustness and accuracy compared to the implementation for pure cryogens. The simulations have been run in the same hardware as described in subsection 3.3.2. Although the system is larger and considerably more complex, the simulation time increased from 1-5 s for the evaporation of pure cryogens to 2-20 s for the weathering model. The longest simulation time was observed for the nitrogen rich LNG mixture, where the vapour-liquid equilibrium showed a slower convergence. This increase is a consequence of the non-linear nature of the phase equilibrium equation,

see Eq. (3.49). The equilibrium constant K_i depends in the temperature and composition of the mixture, which itself depend on the equilibrium constant. Thus, an iterative approach is required to K_i. This results in a higher number of iterations of the ode15i solver to satisfy the error tolerances at each time step, and hence longer simulation times. To facilitate the interpretation of the results, a summary of the working equations that constitute each model is given in Appendix E.

3.6 References

[1] C. Migliore, A. Salehi, and V. Vesovic, "A non-equilibrium approach to modelling the weathering of stored Liquefied Natural Gas (LNG)," *Energy,* vol. 124, pp. 684-692, 2017, doi: 10.1016/j.energy.2017.02.068.

[2] R. N. Krikkis, "A thermodynamic and heat transfer model for LNG ageing during ship transportation. Towards an efficient boil-off gas management," *Cryogenics,* vol. 92, pp. 76-83, 2018/06/01/ 2018, doi: https://doi.org/10.1016/j.cryogenics.2018.04.007.

[3] M. Seo and S. Jeong, "Analysis of self-pressurization phenomenon of cryogenic fluid storage tank with thermal diffusion model," *Cryogenics,* vol. 50, no. 9, pp. 549-555, Sep 2010, doi: 10.1016/j.cryogenics.2010.02.021.

[4] S. Effendy, M. S. Khan, S. Farooq, and I. A. Karimi, "Dynamic modelling and optimization of an LNG storage tank in a regasification terminal with semi-analytical solutions for N2-free LNG," *Comput. Chem. Eng.,* vol. 99, pp. 40-50, 2017, doi: 10.1016/j.compchemeng.2017.01.012.

[5] M. Kang, J. Kim, H. You, and D. Chang, "Experimental investigation of thermal stratification in cryogenic tanks," *Exp. Therm. Fluid Sci.,* vol. 96, pp. 371-382, 2018/09/01/ 2018, doi: https://doi.org/10.1016/j.expthermflusci.2017.12.017.

[6] Y. Lin, C. Ye, Y. Y. Yu, and S. W. Bi, "An approach to estimating the boil-off rate of LNG in type C independent tank for floating storage and regasification unit under different filling ratio," *Appl. Therm. Eng.,* vol. 135, pp. 463-471, May 2018, doi: 10.1016/j.applthermaleng.2018.02.066.

[7] F. Perez *et al.*, "Measurements of boil-off gas and stratification in cryogenic liquid nitrogen with implications for the storage and transport of liquefied natural gas," *Energy,* vol. 222, p. 119853, 2021/05/01/ 2021, doi: https://doi.org/10.1016/j.energy.2021.119853.

[8] F. Huerta and V. Vesovic, "A realistic vapour phase heat transfer model for the weathering of LNG stored in large tanks," *Energy,* vol. 174, pp. 280-291, 2019/05/01/ 2019, doi: https://doi.org/10.1016/j.energy.2019.02.174.

[9] C. Migliore, C. Tubilleja, and V. Vesovic, "Weathering prediction model for stored liquefied natural gas (LNG)," (in English), *J. Nat. Gas. Sci. Eng.,* vol. 26, pp. 570-580, Sep 2015, doi: 10.1016/j.jngse.2015.06.056.

[10] A. Saleem, S. Farooq, I. A. Karimi, and R. Banerjee, "A CFD simulation study of boiling mechanism and BOG generation in a full-scale LNG storage tank," *Comput. Chem. Eng.,* vol. 115, pp. 112-120, Jul 2018, doi: 10.1016/j.compchemeng.2018.04.003.

[11] Linde, "Cryogenic Standard Tanks LITS 2," Tacherting, Germany, 2019. [Online]. Available: https://www.linde-engineering.com/en/images/P_3_3_e_12_150dpi_tcm19-5774.pdf

[12] H. G. Weller, G. Tabor, H. Jasak, and C. Fureby, "A tensorial approach to computational continuum mechanics using object-oriented techniques," *Comput. Phys.,* vol. 12, no. 6, pp. 620-631, 1998/11/01 1998, doi: 10.1063/1.168744.

[13] OpenCFD Ltd. "OpenFOAM: API guide v2006." https://www.openfoam.com/documentation/guides/latest/api/index.html (accessed 25th of November, 2020).

[14] F. Menter, "Zonal two equation k-omega turbulence models for aerodynamic flows," presented at the 23rd Fluid Dynamics, Plasmadynamics, and Lasers Conference, Orlando, FL, U.S.A., 1993, 1993, 2906.

[15] J. Smagorinsky, "General circulation experiments with the primitive equations: I. The basic experiment," *Mon. Weather Rev.,* vol. 91, no. 3, pp. 99-164, 1963.

[16] T. M. Eidson, "Numerical simulation of the turbulent Rayleigh–Bénard problem using subgrid modelling," *J. Fluid Mech.,* vol. 158, pp. 245-268, 1985, doi: 10.1017/S0022112085002634.

[17] S.-H. Peng and L. Davidson, "Large eddy simulation for turbulent buoyant flow in a confined cavity," *Int. J. Heat Fluid Flow,* vol. 22, no. 3, pp. 323-331, 2001/06/01/ 2001, doi: https://doi.org/10.1016/S0142-727X(01)00095-9.

[18] C. Geuzaine and J.-F. Remacle, "Gmsh: A 3-D finite element mesh generator with built-in pre- and post-processing facilities," *Int. J. Numer. Meth. Eng.,* vol. 79, no. 11, pp. 1309-1331, 2009/09/10 2009, doi: 10.1002/nme.2579.

[19] H. Jasak, "Automatic mesh motion for the unstructured finite volume method," *T. FAMENA,* vol. 30, no. 2, pp. 1-20, 2006.

[20] V. Yakhot, S. A. Orszag, and A. Yakhot, "Heat transfer in turbulent fluids—I. Pipe flow," *Int. J. Heat Mass Transfer,* vol. 30, no. 1, pp. 15-22, 1987/01/01/ 1987, doi: https://doi.org/10.1016/0017-9310(87)90057-3.

[21] M. R. Hestenes and E. Stiefel, "Methods of conjugate gradients for solving linear systems," *J. Res. Natl. Bur. Stand.,* vol. 49, no. 6, pp. 409-436, 1952.

[22] I. H. Bell, J. Wronski, S. Quoilin, and V. Lemort, "Pure and Pseudo-pure Fluid Thermophysical Property Evaluation and the Open-Source Thermophysical Property Library CoolProp," *Ind. Eng. Chem. Res.,* vol. 53, no. 6, pp. 2498-2508, 2014/02/12 2014, doi: 10.1021/ie4033999.

[23] F. Huerta and V. Vesovic. *OpenFOAM Implementation of a model for the isobaric evaporation of pure cryogenic liquids*, Imperial College London Research Data Repository, 06/04/2021, doi: 10.14469/hpc/8072.

[24] R. B. Bird, W. E. Stewart, and E. N. Lightfoot, *Transport phenomena*, 2nd rev. ed. New York: John Wiley & Sons, 2007, pp. xii, 905 p.

[25] W. E. Schiesser and G. W. Griffiths, *A compendium of partial differential equation models: method of lines analysis with Matlab*, 1st ed. Cambridge ; New York: Cambridge University Press (in English), 2009.

[26] W. Huang and R. D. Russell, *Adaptive moving mesh methods*. Springer Science & Business Media, 2010.

[27] *NIST Standard Reference Database 23: Reference Fluid Thermodynamic and Transport Properties-REFPROP, Version 9.1, National Institute of Standards and Technology*. (2013).

[28] L. F. Shampine and M. W. Reichelt, "The matlab ode suite," *SIAM journal on scientific computing,* vol. 18, no. 1, pp. 1-22, 1997.

[29] F. Huerta and V. Vesovic, "Analytical solutions for the isobaric evaporation of pure cryogens in storage tanks," *Int. J. Heat Mass Transfer,* vol. 143, p. 118536, 2019/11/01/ 2019, doi: https://doi.org/10.1016/j.ijheatmasstransfer.2019.118536.

[30] F. Huerta and V. Vesovic. *Data for: Analytical solutions for the isobaric evaporation of pure cryogens in storage tanks*, Mendeley Data, doi: http://dx.doi.org/10.17632/9byrz62fjk.1.

[31] J. Klosek and C. McKinley, "Densities of liquefied natural gas and of low molecular weight hydrocarbons," in *First International Conference on LNG*, Chicago, 1968.

[32] C. Tietz, M. Richter, R. Kleinrahm, and R. Span, "Enhancement of the revised Klosek and McKinley method for density calculations of liquefied natural gas (LNG) over the temperature range from (100 to 135) K at pressures up to 10 MPa," *Fuel Process. Technol.,* vol. 165, pp. 19-26, 2017, doi: 10.1016/j.fuproc.2017.04.016.

[33] A. Danesh, *PVT and phase behaviour of petroleum reservoir fluids*, 1st ed. Elsevier, 1998.

[34] GIIGNL, "LNG custody transfer handbook," The International Group of Liquefied Natural Gas Importers (GIIGNL), Neuilly'sur'Seine, France, 2017. [Online]. Available: https://giignl.org/system/files/giignl_cthb_5.0.web_.pdf

[35] O. Kunz and W. Wagner, "The GERG-2008 wide-range equation of state for natural gases and other mixtures: an expansion of GERG-2004," *J. Chem. Eng. Data,* vol. 57, no. 11, pp. 3032-3091, 2012, doi: 10.1021/je300655b.

[36] GIIGNL, "LNG Information paper No. 2 the LNG process chain," The International Group of Liquefied Natural Gas Importers (GIIGNL), Neuilly'sur'Seine, France, 2009.

[37] L. F. Shampine, " Solving 0 = F(t, y(t), y′ (t)) in Matlab," *J. Num. Math.,* vol. 10, no. 4, p. 19, 2010, doi: 10.1515/JNMA.2002.291.

Chapter 4

Model verification I: isobaric evaporation of cryogens

4.1 Introduction

Three models for the isobaric evaporation of cryogenic liquids have been developed in Chapter 3. The aim of this chapter is to demonstrate the robustness of the computational implementation of the models against a set of verification tests. The tests were designed with an emphasis on the original contributions presented in this thesis. In section 4.2, the computational implementation of the isobaric 1-D model is verified through error estimation and order of accuracy analysis. The main contribution of the isobaric 1-D model is the vapour phase heat transfer modelling through a partial differential equation (PDE) [1]. In section 4.3, the accuracy of the temporal and spatial asymptotic convergence of the numerical solutions of Eq. (3.20) PDE is demonstrated using the analytical solutions derived in section 3.4.

In section 4.4, the weathering model is verified through an investigation of the discretisation error as a function of different liquid fillings and LNG compositions. The thermodynamic sub-models have already been validated in the BOG comparison for four different LNG mixtures against Migliore et al. non-equilibrium weathering model [1, 2]. As Migliore has already presented a comprehensive validation of the thermodynamic sub-models used in this work [3], that validation is considered sufficient. Finally, in section 4.5 verification tests specific to the vapour-CFD model are presented. An excellent agreement at the pseudo-steady state has been found between the vapour-CFD and isobaric 1-D models developed in Chapter 3 [4]. Hence, the verification is focused on testing the accuracy of the emerging phenomena that only the vapour-CFD model can predict. In particular, a grid-independence study is presented

not only for vapour temperatures, but also for the vertical velocity at the wall boundary layer.

4.2 Isobaric 1-D model verification

The method of lines applied to Eq. (3.20) using second order central finite differences for the advective and diffusive terms produces a system of ordinary differential equations defined by:

$$\frac{\partial T_{\mathrm{V},i}}{\partial t} = \bar{\alpha}_{\mathrm{V}} \frac{T_{\mathrm{V},i+1} - 2T_{\mathrm{V},i} + T_{\mathrm{V},i-1}}{(\Delta z)^2} - \bar{v}_z \frac{T_{\mathrm{V},i+1} - T_{\mathrm{V},i-1}}{(2\Delta z)} + \frac{\bar{\alpha}_{\mathrm{V}}}{\bar{k}_{\mathrm{V}}} \frac{4U_{\mathrm{V}} d_o}{d_i^2} \left(T_{\mathrm{air}} - T_{\mathrm{V},i}\right), \qquad (4.1)$$

which governs the temporal variation of the temperature in the node i of the discretized domain for $0 < i < n_{\mathrm{z}}$. The number of nodes in the vertical dimension is defined by $n_{\mathrm{z}} = l_{\mathrm{V}}/\Delta z$, where l_{V} is the vapour length. The grid spacing in a uniform mesh is defined by $\Delta z = z_i - z_{i-1}$. If the code is error-free, an order of accuracy around two in space is expected. The spatial discretisation of the differential operators in Eq. (3.20) is second order accurate. Similarly, the discretization of the source term is also second order accurate as the heat flux in a computational cell is evaluated at the temperature at the center of that cell. The discretization and integration of the temporal derivative in Eq. (4.1) has been performed using the ode15s [5] routine. This variable-step variable-order integration routine from MATLAB varies the discretization of $\partial T_{\mathrm{V},i}/\partial t$ depending on the stiffness of the system [5]. Hence, the formal order of accuracy of the method of lines discretization of Eq. (4.1) cannot be determined *a priori*.

Not only the accuracy of the numerical implementation of Eq. (4.1) is relevant, but also its stability. Although ode15s [5] is very efficient, its usage rules out any possibility to perform formal stability analysis because the code is not accessible. The issue of inaccessible or proprietary code or libraries is extremely frequent in scientific computing [6]. In consequence, most of the code verification theoretical developments have been focused on *a posteriori* analysis. For instance, the second order accurate central finite-difference discretisation of the first derivative is known to be unbounded. Fortunately, we observed that for a variety of storage scenarios [1, 7], advection was only two orders of magnitude higher than thermal diffusion. This produced a ratio between

advection and diffusion that resulted in a stable, non-oscillatory solutions for vapour temperature.

Nevertheless, the stability of the numerical implementation of Eq. (4.1) is not guaranteed for larger advective velocities than those observed in this work. Scaling analysis of Eqs. (3.5) and (3.19) provides a quick estimate that allows the early investigation of the range of stability in Eq. (4.1),

$$\bar{v}_z \sim \dot{Q}_{\mathrm{L,tot}} \Delta H_{\mathrm{LV}}^{-1} d_{\mathrm{i}}^{-2} \bar{\rho}_{\mathrm{V}}^{-1}. \tag{4.2}$$

Using Eq. (4.2), high advective velocities are expected for the storage of cryogens with low vapour density and low latent heat of vaporisation, stored in small tanks subject to high heat fluxes. In those scenarios, the discretization of the advective term in Eq. (4.1) may need to be modified to ensure stability. A more stable discretisation, such as upwind or a total variation diminishing (TVD) scheme is suggested. This would improve the stability of the numerical implementation at the expense of accuracy.

The remainder of this chapter is focused on error estimation rather than stability analysis. To determine the observed order of accuracy of the isobaric 1-D model, an extrapolation-based error estimation [6] is performed. As there is no analytical solution of Eq. (3.20), the Richardson extrapolation [8, 9] is performed as a way to estimate the exact solution of Eq. (3.22). This extrapolation is valid if the solutions are smooth, the high-order terms are small and if uniform computational grids are used. The discretisation error is defined as the difference between the numerical solution in a given mesh and the exact solution of a partial differential equation [6]:

$$DE_k = f_k - f_{\mathrm{exact}} = g_p h_k^p + HOT. \tag{4.3}$$

where f_k, f_{exact}, are the numerical solution in the mesh k and the exact solution of the partial differential equation, respectively. In Eq. (4.3), p is the order of accuracy of the numerical method, g_p is the coefficient of the leading order error term and h_k is the grid spacing. The term $g_p h_k^p$ and the higher order terms (HOT) arise from the estimation of the discretisation error estimate using a Taylor series expansion centered in a given node/cell centre.

Considering f_1 as the numerical solution of the PDE of interest in a fine mesh and f_2 its solution in a medium mesh, f_{exact} can be estimated using the generalized Richardson extrapolation [8, 9]:

$$f_{\text{exact}} \approx f_1 + \frac{f_1 - f_2}{r^p - 1}, \tag{4.4}$$

where $r = h_2/h_1$ is the grid refinement factor between the medium and fine meshes, respectively. To estimate the observed order of accuracy, three numerical solutions are required which share the same ratio of grid spacing. Considering f_3 a numerical solution of the PDE of interest in a coarse mesh such that $r = h_3/h_2 = h_2/h_1$, the observed order of accuracy can be estimated through [6]:

$$p = \frac{\ln\left(\frac{f_3 - f_2}{f_2 - f_1}\right)}{\ln(r)}. \tag{4.5}$$

Eqs. (4.4) and (4.5) provide a very simple and powerful method to estimate the observed order of accuracy of the numerical solution of PDEs after performing numerical simulations. It is worth noting that this method produces accurate estimates of p only for numerical solutions in the asymptotic range of the numerical discretization. The asymptotic range is defined as the grid spacings smaller than a critical value, $h_k < h_\infty$, which ensure that the high order terms in Eq. (4.3) vanish. If the method is applied to Eqs. (3.20) and (4.1), $f_k = T_{\text{V},k}$ and the error can be assessed as a function of both space and time. To obtain a global measure of the order of accuracy of the numerical solution, discrete norms for error measurements are frequently used [6]. The L_2 and L_∞ global error norms for two numerical solutions f_j, f_j are defined as $L_2(f_k, f_j) = \sqrt{\sum_i^n (f_{k,i} - f_{j,i})^2 / N}$ and $L_\infty = \max |f_{k,i} - f_{j,i}|$, respectively. Using the Richardson extrapolation [8, 9], the order of accuracy p using a particular norm can be estimated through:

$$p_{L_2} = \frac{\ln\left(\frac{L_2(f_3, f_2)}{L_2(f_2, f_1)}\right)}{\ln(r)}, \quad p_{L_\infty} = \frac{\ln\left(\frac{L_\infty(f_3, f_2)}{L_\infty(f_2, f_1)}\right)}{\ln(r)}. \tag{4.6}$$

In this chapter, both norms and the order of accuracy based on each norm are reported, as they indicate the average (L_2) and maximum (L_∞) discretisation errors.

4.2.1 Order of accuracy of vapour temperature spatial discretisation

The largest spatial and temporal gradients in the discretised ODE system given by Eq. (4.1) occur at the beginning of the evaporation. In other words, the stiffness of the ODE system decreases with time. As ode15i [10] has been used to discretise and integrate the temporal derivatives, the observed order of accuracy in the spatial discretisation of vapour temperatures is expected to change with time. This counterintuitive fact is a consequence of time integration errors also propagating through space. To measure the change in spatial order of accuracy with time, vapour temperature profiles at both the beginning ($t_s^* = 0.1$) and end ($t_s^* = 1$) of the storage period τ_s will be analysed, where $t_s^* = t/\tau_s$ is the dimensionless storage time. For consistency, the same scenarios that will be studied in Chapter 5 are considered. Namely, the discretisation error on vapour temperature is analysed for three different storage tanks: small, medium and large; and two different liquid fillings: low (LF = 0.3) and high (LF = 0.97). For simplicity, all the results in this section will be presented for liquid methane. The variation of spatial discretisation error as a function of the stored cryogen properties will be presented in section 4.3.

Figure 4.1 depicts the global error norms for vapour temperature as a function of the initial grid spacing using the isobaric 1-D model. The model was used to simulate the isobaric evaporation of methane in a large 165,000 m³ storage tank for high (a) and low (b) initial liquid fillings. In both subfigures, slopes representative of first and second order spatial accuracy, $\mathcal{O}(h)$ and $\mathcal{O}(h^2)$, are included in grey dashed and solid lines, respectively. This allows a quick visual assessment of the estimated order of accuracy. The L_∞ global error norms are depicted in blue, and the L_2 global error norm in cyan. Coloured dashed lines represent the norms at the beginning of the transient period, and coloured solid lines represent the norms at the end of the storage period.

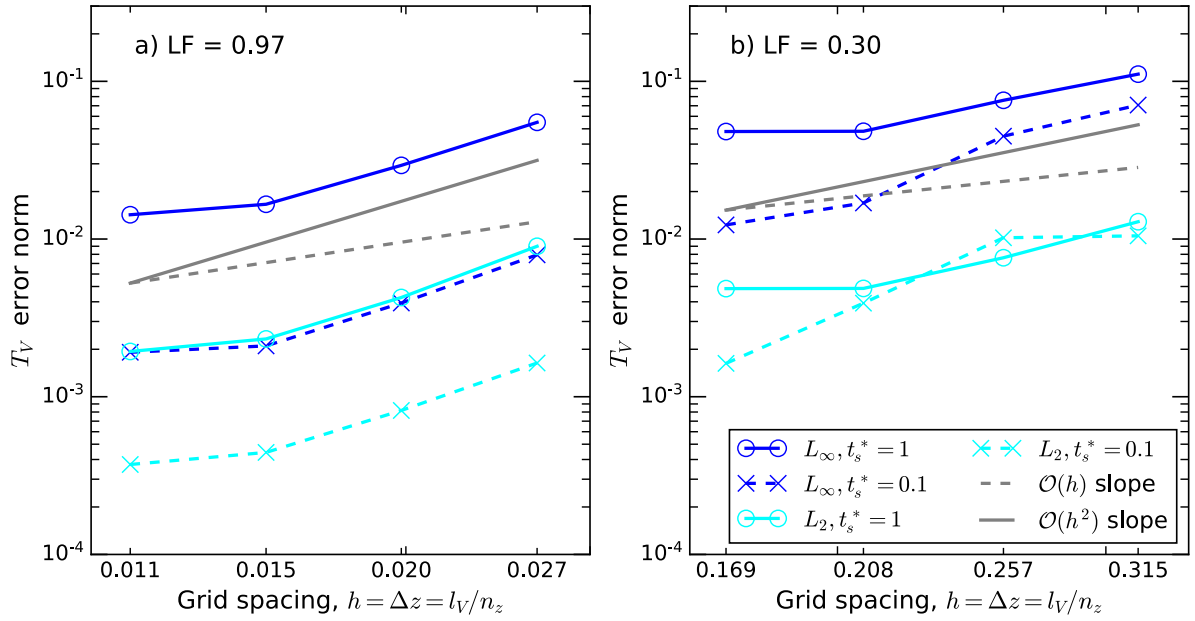

Figure 4.1: Global error norms for vapour temperature using the isobaric 1-D model to simulate the evaporation of liquid methane in a large 165,000 m³ storage tank. Subfigures (a) and (b) depict high and low initial liquid filling (LF), respectively.

Figure 4.1a shows that both L_∞ and L_2 error norms are lower at the beginning (t_s^* = 0.1) than at the end (t_s^* = 1) of the storage period for high liquid filling. The norms have been calculated using Eq. (4.3) and approximating the exact solution using the Richardson extrapolation, see Eq. (4.5). As expected, $L_\infty > L_2$ for all grid refinements. The grid refinement ratio was $r = 1.35$, and this value was used to estimate observed orders of accuracy using Eq. (4.6). A low grid refinement ratio was selected as MATLAB ode15i did not converge reliably over higher grid refinement ratios. The estimated order of accuracy on L_∞, p_{L_∞}, was 2 for t_s^* = 0.1 and 1.5 for t_s^* = 1. In contrast, no difference on the estimated order of accuracy between the beginning and end of the transient period was observed on L_2, p_{L_2}, resulting in a value of 2.2 for both timesteps. The different trend of the L_2 norms associated to the finest spacing, h = 0.011 m, can be attributed to uncertainty in the use of the Richardson extrapolation to estimate f_{exact}, see Eq. (4.4), and the low grid refinement ratio considered. Nevertheless, both L_∞ and L_2 norms show convergence with decreasing h and are low both at the beginning and at the end of the storage period. For all simulations, a grid spacing selection criterion was set by setting $L_\infty < 0.1$ K at pseudo-steady state. For high liquid filling in a large tank, this criterion was satisfied by the coarse mesh, demonstrating the robustness of the numerical implementation of the isobaric 1-D model.

Figure 4.1b shows that the error norms at the end of the storage period for low liquid fillings, t_s^* = 1, follow a similar trend to that observed for high liquid fillings, see Figure 4.1a. In contrast, at the beginning of the evaporation, t_s^* = 0.1, the change of error norms with grid spacing has a random component. This indicates that the selected grid spacings are not in the asymptotic range of convergence around t_s^* = 0.1. Thus, the error norms are affected by higher order terms, see Eq. (4.3). For $\Delta z = 0.257$ m, the error in the L_2 norm is higher at the beginning than at the end of the evaporation. The orders of accuracy for low liquid filling were estimated using a grid refinement ratio $r = 1.23$. For low liquid filling, the estimated orders of accuracy at $t_s^* = 0.1$ where $p_{L_\infty} = 2.2$ and $p_{L_2} = 4.5$. These high values are not representative of asymptotic convergence and further confirm the grid spacings outside the asymptotic range. On the other hand, at $t_s^* = 1$ the estimated orders of accuracy were $p_{L_\infty} = 2$ and $p_{L_2} = 2.2$. These orders of accuracy at the end of the storage period are very similar to the ones estimated for the high liquid filling case.

It is worth noting that for low liquid filling, the error norms are low even for grid spacings outside the asymptotic range of convergence, see Figure 4.1b. A grid spacing as coarse Δz = 0.315 m already satisfies the criterion $L_2(t_s^* = 1) < 0.1$ K. A close inspection of the L_2 global error norms at the steady state (cyan solid lines) in Figure 4.1 illustrates that for the same grid spacing, the error norm is lower for low liquid filling compared with high liquid filling scenarios. For high liquid filling, $L_2(t_s^* = 1, LF = 0.97) \approx 10^{-2}$ using Δz = 0.027 m. For low liquid filling, $L_2(t_s^* = 1, LF = 0.30) \approx 10^{-2}$ for Δz =0.257 m. A potential explanation for the lower error norms for lower liquid fillings is the smaller value of the advective term compared with the high liquid filling scenario. The advective term is 61% smaller in the low liquid filling scenario than in the high liquid filling scenario, owing to the reduction of wet area in contact with the tank walls. This hypothesis will be further investigated in section 4.3, taking advantage of the exactness of the analytical solutions developed in this thesis for vapour temperature [7].

The temporal dependence of the global error norms and orders of accuracy is evident for both liquid fillings, see Figure 4.1. For high liquid fillings, both error norms are roughly one order of magnitude larger at the end than at the beginning of the evaporation, see Figure 4.1a. As the evaporation progresses, the grid spacing increases

with time significantly. As $\Delta z = l_V(t)/n_z$ and $l_V(t_s^* = 1)/l_V(t_s^* = 0.1) = 4.2$, the grid spacing is up to 4 times higher than at the beginning of the evaporation. Considering the estimated order of accuracy for the global L_2 around 2, this effect alone would result in 21 times higher errors. However, the increase of error with time is smaller than this value. This suggests that MATLAB ode15i® [10] may automatically select time-integration of lower orders at the beginning of the evaporation. This allows for an improvement on stability, at the expense of an increase in discretisation error. The difference between the error norms at $t_s^* = 1$ and $t_s^* = 0.1$ for low liquid filling is smaller, see Figure 4.1b. This result is expected as a consequence of a lower ratio of final to initial grid spacing in the low liquid filling scenario compared to the high liquid filling scenario, $l_V(t_s^* = 1)/l_V(t_s^* = 0.1) = 1.1$.

After analysing the error norms in a large tank scenario, the error norms for methane evaporation in a medium-sized 80.4 m³ storage tank are investigated. Compared with the large tank, the medium tank has a lower diameter and a smaller height. This will induce higher advective velocities, see Eq. (4.2), and the discretisation of the vapour space will result in a smaller grid spacing for the same number of nodes because $\Delta z = l_V/n_z$. Figure 4.2 depicts the global error norms for vapour temperature as a function of initial grid spacing using the isobaric 1-D model for simulating the evaporation of methane in a medium 80.4 m³ storage tank. A grid refinement factor of $r = 2$ has been used for both high liquid filling (Figure 4.2a), and low liquid filling (Figure 4.2b).

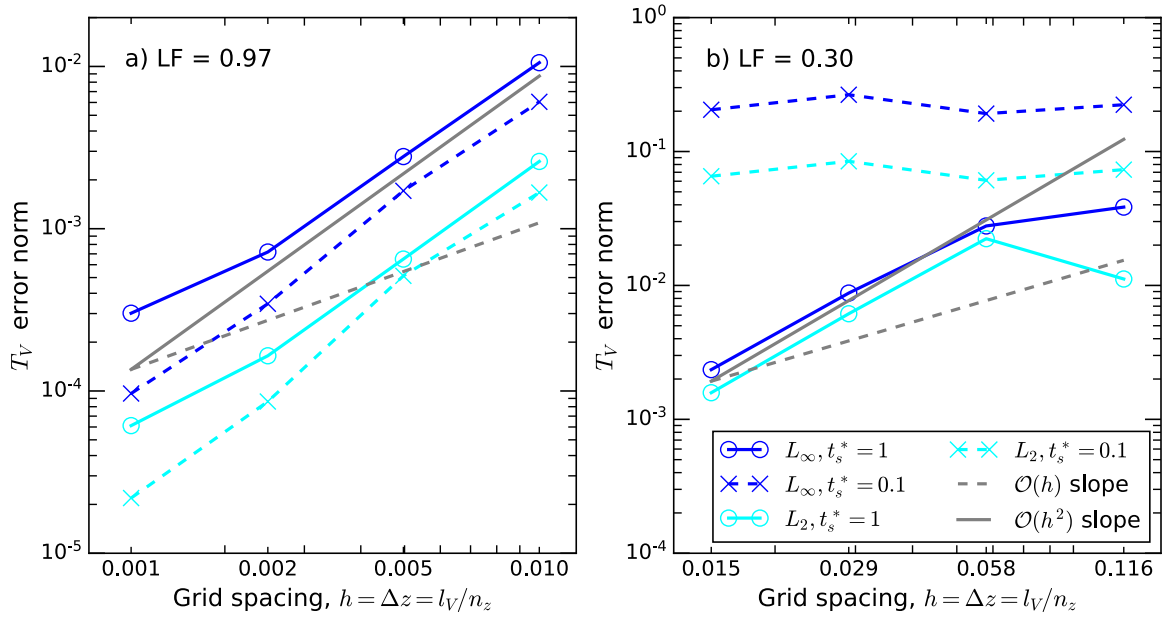

Figure 4.2: Global error norms for vapour temperature using the isobaric 1-D model to simulate the evaporation of liquid methane in a medium 80.4 m³ storage tank. Subfigures (a) and (b) depict high and low initial liquid filling (LF), respectively.

Figure 4.2a shows a decreasing trend for both L_∞ and L_2 global error norms which is very similar to what was observed for the large tank, see Figure 4.1a. The estimated order of accuracy of both norms at $t_s^* = 0.1$ and $t_s^* = 1$ was 2. This implies that for this scenario, the numerical implementation of the isobaric 1-D model achieved second order accuracy. Interestingly, second order accuracy matches the theoretical order of accuracy of the spatial discretisation scheme in Eq. (4.1). This implies that for this scenario, the temporal discretisation and integration performed by ode15i [10] did not reduce the order of accuracy of the spatial discretisation. Furthermore, it shows that grid spacings $\Delta z < 0.006$ m are within the asymptotic range. Compared with the large tank, the magnitude of the error norms, at all time-steps, are smaller.

The error norms on vapour temperature span over the range 10^{-5} to 10^{-2} for the medium tank, while for the large tank they span from 10^{-4} to 10^{-1}, see Figure 4.1a and Figure 4.2a. It is worth noting that the gap between the error norms at $t_s^* = 1$ and $t_s^* = 0.1$ is much narrower in the medium tank than in the large tank. This is a consequence of the smaller variation of grid spacing with time in the small tank, $l_V(t_s^* = 1)/l_V(t_s^* = 0.1) = 1.05$ compared with 4.2 for the large tank. The smaller variation in vapour length is a consequence of the shorter storage period considered for the medium-sized tank, $\tau_s = 231$ h, compared with $\tau_s = 8760$ h for the large tank. This

confirms the increase in spatial discretisation error with time, as a consequence of the increase of vapour length and hence grid spacing with the progress of evaporation.

Figure 4.2b shows the global error norms for vapour temperature on the medium tank filled at low liquid filling (LF = 0.30). These norms are substantially different from the norms observed in the large tank for the same liquid filling, see Figure 4.1b. At the beginning of the evaporation ($t_s^* = 0.1$), a completely random behaviour of both L_∞ and L_2 error norms as a function of grid spacing is observed. Furthermore, both norms are much larger for the medium sized tank, $\mathcal{O}(10^{-1})$, than for the large tank at the same liquid filling, $\mathcal{O}(10^{-2})$. For the medium-sized tank, the global error norms for $t_s^* = 0.1$ are between one and two orders of magnitude higher than the norms for $t_s^* = 1$. On the other hand, the error norms at the end of the transient period, $t_s^* = 1$, have a more consistent behaviour. The norms decrease monotonically with grid spacing except for the coarsest mesh with $\Delta z = 0.116$ m, which attained a lower L_2 global error norm than the mesh produced with $\Delta z = 0.058$ m. At the end of the storage period ($t_s^* = 1$) both L_∞ and L_2 error norms are lower in the medium tank at low liquid filling than the norms obtained for the large tank at the same liquid filling, see Figure 4.1 and Figure 4.2. This is a direct result of the smaller grid spacing used for the simulations in the medium tank.

The unexpectedly high error norms at $t_s^* = 0.1$ for low liquid fillings in the medium sized tank can be a consequence of unexpected behaviour of ode15i [10] integrator during the transient period. As the error tolerances seem to not be satisfied, the solver may have moved to the next time-step because the maximum number of iterations was achieved. Fortunately, for the convergence criteria set for the scenarios studied in this thesis, the larger errors at the transient period were not important. Nevertheless, Figure 4.2b justifies the importance of performing a posteriori error analysis of numerical simulations that rely on external libraries frequently used in research software development. This allows to assess the performance and identify unexpected behaviour of these libraries even if the code is not accessible.

Figure 4.3 depicts the error norms for vapour temperature obtained using the isobaric 1-D model for the simulation of methane evaporation in a small 8 m³ storage tank. Figure 4.3a and Figure 4.3b represent the results for high (LF = 0.97) and low (LF

= 0.30) initial liquid fillings, respectively. For high liquid fillings, the results are very similar to what has been observed for the medium tank, see Figure 4.2a and Figure 4.3a. The estimated order of accuracy of both norms at t_s^* = 0.1 and t_s^* = 1 was 2, the same value that the one obtained for the medium tank. The grid spacings in the small tank are roughly half of the spacings for the medium-sized tank. However, both global error norms are similar, spanning between 10^{-5} and 10^{-2}, see Figure 4.2a and Figure 4.3a. This suggest that the smaller diameter of the smaller tank, that drives an increase in the advective velocity, increases the error norms.

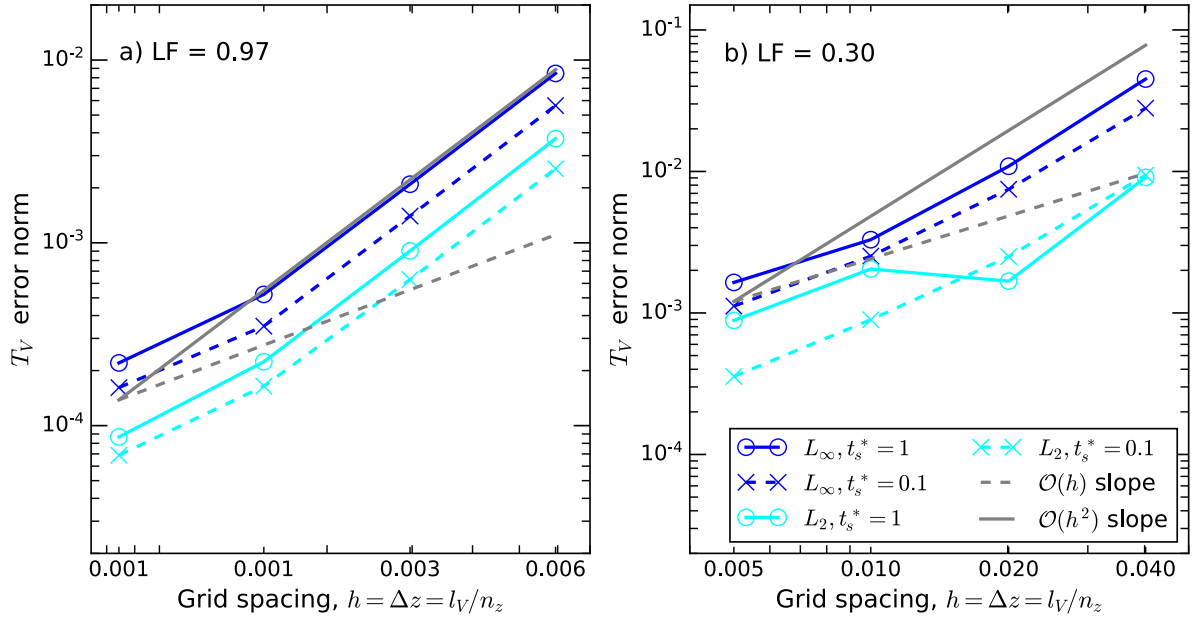

Figure 4.3: Global error norms for vapour temperature using the isobaric 1-D model to simulate the evaporation of liquid methane in a small 8 m³ storage tank. Subfigures (a) and (b) depict high and low initial liquid filling (*LF*), respectively.

Figure 4.3b shows that in the small tank under low liquid filling, both error norms are the lower than for the medium and large tanks. At t_s^* = 0.1, the norms are bounded between 3×10^{-4} and 2×10^{-2} for the small tank. For the medium tank, the norms span from 5×10^{-2} and 2×10^{-1}, while these figures for the large tank are 10^{-3} and 8×10^{-2}. At the end of the evaporation, $t_s^* = 1$, the range of global norms for the small tank, $9 \times 10^{-4} < L_{n,\text{small}} < 4 \times 10^{-2}$, and the medium tank, $10^{-3} < L_{n,\text{mid}} < 3 \times 10^{-2}$, are comparable. In contrast, the norms for the large tank at the same liquid filling and timestep, $9 \times 10^{-4} < L_{n,\text{large}} < 4 \times 10^{-2}$, are considerably larger. This suggests that for low liquid fillings, grid

spacing has a more dominant effect on error norms than the advective term. The convergence criterion, $L_2 < 0.1$ K, is satisfied for all tested grids.

At the beginning of the evaporation ($t_s^* = 0.1$), both L_∞ and L_2 decrease monotonically. The estimated order of accuracies for spatial discretisation of vapour temperature using the respective norms as an error measure are $p_{L_2} = 1.5$ and $p_{L_\infty} = 1.6$. Both norms are relatively close to 2, and the deviation are a potential result of the variation of the order of approximation of ode15i. On the other hand, near the end of the storage period ($t_s^* = 1$), the decreasing trend is clear for the L_∞ norm, while the L_2 does not decrease monotonically with grid spacing. The rapid larger drop of L_2 norm at Δz = 0.02 m, see Figure 4.3b, can be a consequence of ode15i using higher order formulas for that specific grid spacing.

In conclusion, For the isobaric evaporation of methane in all storage scenarios, the isobaric 1-D model predicts the vapour temperature with a global L_2 error norm lower than 0.1 K. The coarse grids used for low liquid filling in the large and medium tanks allowed to bound simulation times to less than 10 s, without violating the convergence criterion. Within the asymptotic region, a reduction of grid spacing produced the convergence of the numerical solutions with an order of accuracy $p_{L_2} \approx 2$. This demonstrates the correct computational implementation of Eq. (4.1) in MATLAB. Although ode15i MATLAB integrator [10] presented unpredictable behaviour in some scenarios, this did not affect the order of accuracy of spatial discretisation significantly. The results from this section confirm that the uncertainty introduced by ode15i variation of order of temporal integration is small. Therefore, the use of ode15i to efficiently solve the ODE system given by Eq. (4.1) has been verified.

4.2.2 BOG temporal discretisation error as a function of relative tolerances

In contrast to the explicit discretisation of temperature given by Eq. (4.1), which allowed for comparison of the temperature norms as a function of grid spacing, the time integration is fully implicit. For all solvers in the MATLAB® R2018b ODE suite [5], the time discretisation error is controlled by the absolute (ϵ_{abs}) and relative (ϵ_{rel}) tolerances. These tolerances can be set independently for each equation i of the ODE

system, hence $\epsilon_{\text{abs}}(i)$, $\epsilon_{\text{tol}}(i)$ are the absolute and relative tolerances associated with each equation. At each time-step, MATLAB estimates the error of the solution ϵ and performs fixed point iterations and varies the integration order and step-size until $\epsilon(i) < \max\left(\epsilon_{rel}(i), \epsilon_{abs}(i)\right)$. Then, it advances to the next step of the solution until the final time-step is reached. Unfortunately, the exact mechanism that ode15i estimates the error or adjust the integration order and step size is not accessible. It should be noted that the discretisation errors on the state variables are controlled only indirectly. MATLAB evaluates the error tolerances as the right-hand side of the system of equations $\mathbf{F}_{\text{exact}}(t, \mathbf{x}, d\mathbf{x}/dt) - \mathbf{F}_{\text{num}}(t, \mathbf{x}, d\mathbf{x}/dt) = \epsilon(i)$ [5]. In this formulation, $\mathbf{F}_{\text{exact}}$ is the exact solution vector of the ODE system, $\mathbf{F}_{\text{num}}$ the numerical solution and $\mathbf{x}$ the vector of state variables.

In order to provide a complete verification of the isobaric 1-D model, the L_2 and L_∞ global error norms for BOG predictions are investigated as a function of error tolerances. As a result of running a number of test simulations, it was observed that the relative tolerances controlled the error norm of the BOG. To calculate the norms, the exact solution has been approximated to a finely resolved simulation by setting the relative tolerance to 10^{-6} for all equations. For brevity, the analysis has only been performed for the evaporation of methane in the large tank. This choice supported by the fact that the storage period for the large tank, $\tau_{s,\text{large}} = 8760$ h, is the highest among all considered scenarios. Additionally, the spatial discretisation error for vapour temperatures for the large tank was also the maximum among the studied scenarios as discussed in subsection 4.2.1. Hence, the L_2 and L_∞ global error norms for the large tank will provide an upper bound for the error norms in the medium and small tanks.

Figure 4.4 depicts the L_2 and L_∞ global error norms for the numerical solution of boil-off gas (BOG) rate using the isobaric 1-D model. The norms are depicted as function of relative tolerances, and the scenario corresponds to the evaporation of methane in a large storage tank ($V_T = 165{,}000$ m^3). For simplicity, the same relative tolerance was considered for all the ODE's that constitute the isobaric 1-D model. One year of methane evaporation was considered, evaluating the norms on the BOG solutions at each week, which produced a total of 52 points. Two initial liquid fillings are considered, (a) high and (b) low liquid filling. In both figures, slopes that represent a decrease of the error

norms with the relative tolerances are depicted in grey. Grey dashed lines represent a first order scaling of the norms with relative tolerance, $L_n \sim \mathcal{O}(\epsilon_{rel})$, while grey pointed lines represent a 0.5 order scaling of the norms with relative tolerance, $L_n \sim \mathcal{O}(\epsilon_{rel}^{1/2})$. The criterion to choose the error tolerances for each simulation was $L_2(BOG) < 0.1$ kg h^{-1}.

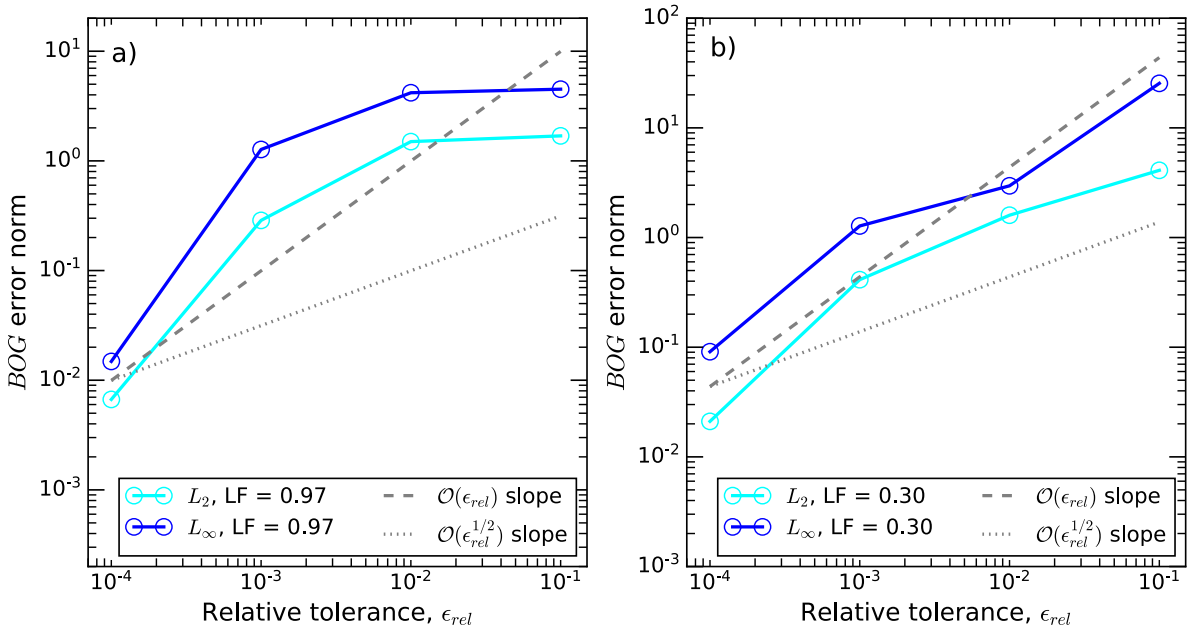

Figure 4.4: Global error norms for BOG using the isobaric 1-D model to simulate the evaporation of liquid methane in a large 165,000 m³ storage tank. Subfigures (a) and (b) depict high and low initial liquid filling (LF), respectively. The relative tolerance ϵ_{rel} is the accuracy control parameter for MATLAB® ode15i [10].

Figure 4.4a shows that for high liquid filling, both BOG global norms are large and do not satisfy the accuracy criterion until the relative tolerance is decreased to 10^{-4}. The L_∞ global norm is roughly four times higher than the L_2 global norm, and both norms decrease monotonically with relative tolerance. The scaling of the global norms with tolerance is not constant. Almost no decrease in the global norms is observed for a decrease in relative tolerances from 10^{-1} and 10^{-2}. In contrast, a sharp decrease is observed when the relative tolerance is decreased from 10^{-3} to 10^{-4}. A relative tolerance of 10^{-4} produced BOG global error norms of $L_2 = 7 \times 10^{-3}$ and $L_\infty = 1.5 \times 10^{-2}$.

Figure 4.4b shows that for low liquid filling, both global error norms are very large and do not satisfy the accuracy criterion until the relative tolerances decrease to 10^{-4}. The error norms decrease non-monotonically and their scaling with the relative

tolerance is not constant. This follows a similar behaviour to what has been observed for the BOG norms for high liquid filling, see Figure 4.4a. The gap between the L_∞ and L_2 varies significantly, in contrast to the relatively constant gap observed for high liquid filling. For the same values of relative tolerances, the norms are between 5 and 10 times higher than those for high liquid filling, see Figure 4.4a. For instance, a relative tolerance of 10^{-4} produced BOG global error norms of $L_2 = 2 \times 10^{-2}$ and $L_\infty = 9 \times 10^{-2}$.

The analysis of BOG error norms for implicit time discretisation as a function ode15i [10] evidences the benefits and limitations of this integration routine. On one hand, setting the relative tolerances to 10^{-4} allows to satisfy the BOG convergence criteria. On the other, the relationship between the relative tolerance and the error norms is complex, as it depends on each simulation, and it can only be found *a posteriori*. The BOG error norms for low liquid filling where higher than the norms for high liquid filling scenario using the same relative tolerances, see Figure 4.4 a-b. This can be a consequence of the spatial discretisation error propagating to the time integration, although a formal proof of this hypothesis cannot be given. In sum, in this the method of lines is an accurate and robust strategy to solve Eq. (3.20) for the studied scenarios. The numerical solution of the isobaric 1-D model obtained using the MATLAB® ode15i [10] satisfies all convergence criteria for relative tolerances lower than 10^{-4}.

4.3 Validation using analytical solutions

In this section, the analytical solutions for the isobaric evaporation of pure cryogens [7] are used to verify two sub-models of the isobaric 1-D model. One advantage of using the analytical solutions for verification is that they provide exact solutions for limiting scenarios. This allows an exact calculation of the global error norms, removing the uncertainty associated with error estimation methods such as the Richardson extrapolation [8, 9], Eq. (4.4). In subsection 4.3.1, the analytical solution for vapour temperature associated to the non-equilibrium model is used to verify a numerical solution of Eq. (3.20) at steady state ($\partial T_V/\partial t = 0$). In subsection 4.3.2, the analytical solutions for liquid volume in the limiting scenario of thermal equilibrium between

vapour and liquid are used to verify two integrators of the MATLAB® ODE suite. This aims to complement subsection 4.2.2 and provide further insight on the complex relationship between MATLAB® error tolerances and the global error norms.

4.3.1 Order of accuracy of steady-state vapour temperature

As an example of using the analytical solutions to verify the numerical solution of vapour temperature, the isobaric evaporation of liquid nitrogen (LN_2) in a small 8 m^3 has been considered. For simplicity, the thermophysical properties of nitrogen vapour have been evaluated at the saturation temperature. Although this assumption introduces a physical error, this does not affect the mathematical structure of the numerical and analytical solutions. Hence, the use of this assumption is appropriate of model verification. It has been further assumed that the vapour temperature has already achieved the steady state at the initial conditions. The tank roof is assumed thermally insulated and the vapour temperature at the interface is assumed equal to the liquid saturation temperature. This results in the boundary value problem (BVP) defined by Eqs. (3.31) – (3.33), which analytical solution is given by Eqs. (3.34) using the constants defined in Eqs. (3.35) and (3.37) – (3.40).

The numerical solution of Eqs. (3.31) – (3.33), was obtained using finite differences discretisation. The discretised form of Eq. (3.34) is given by the right-hand side of Eq. (4.1), where the discretisation of each term is second-order accurate in space. The Dirichlet and Neumann boundary conditions given by Eq. (3.33) were discretised using second order central differences by means of including a ghost node. The resulting linear system of equations was solved using the linalg.solve function of the Python 3 NumPy library.

Figure 4.5 shows the L_2 and L_∞ global error norms for steady state vapour temperature in the evaporation of LN_2 in a small 8 m^3 storage tank. Two liquid fillings (LF) are depicted, a) high liquid filling, LF = 0.97, and b) low liquid filling, LF = 0.30. As the decrease of both error norms with grid spacing is parallel to the $\mathcal{O}(\Delta z^2)$ slope for both liquid fillings, the numerical solution achieves second order accuracy. As the theoretical order of accuracy of the finite discretisation schemes of Eq. (4.1) is two,

Figure 4.5 verifies the computational implementation of Eq. (4.1). Figure 4.5a shows that for the high liquid filling, the asymptotic range of convergence is attained to grid spacings around $\Delta z \sim 10^{-2}$ m. For the smallest tested grid spacing, $\Delta z \sim 10^{-5}$ m, an increase in the L_2 norm is observed. The increase in L_2 norm with decreasing grid spacing shows that for $\Delta z \lesssim 10^{-5}$ m, the round-off errors become important.

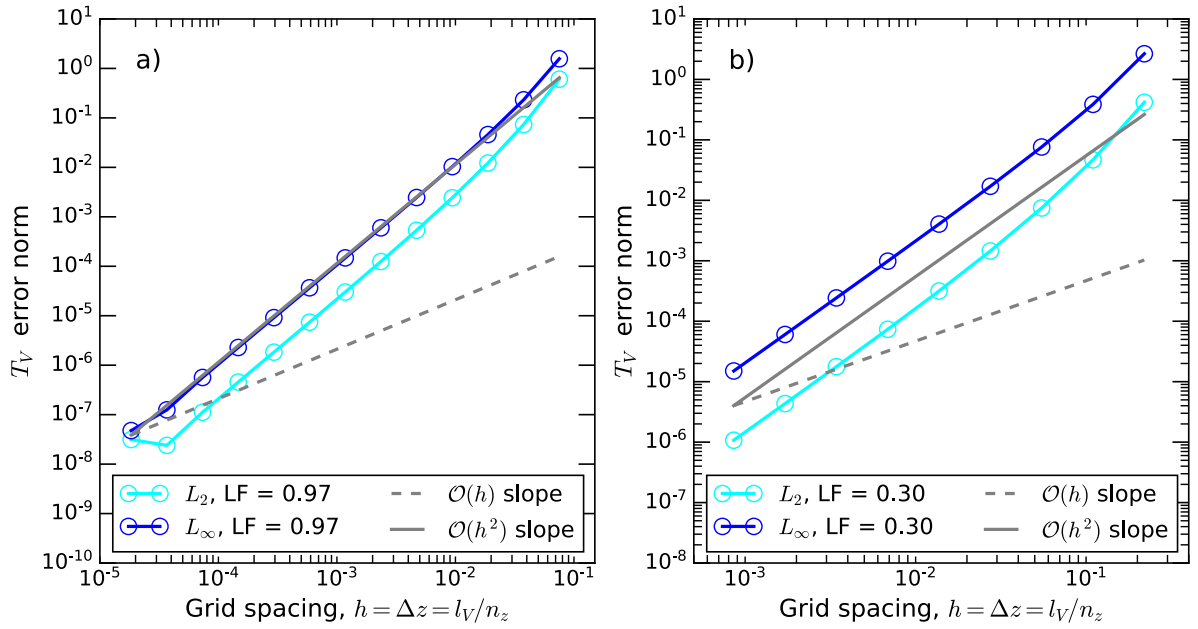

Figure 4.5: Global error norms for vapour temperature using the steady state isobaric 1-D model to simulate the isobaric evaporation of liquid nitrogen in a small 8 m³ storage tank. Subfigures (a) and (b) depict high and low initial liquid filling (LF), respectively. The error norms are calculated using the analytical solutions developed in section 3.3 [7] as the exact temperature profile.

Figure 4.5b shows that for low liquid fillings, the asymptotic range of convergence is attained at $\Delta z \sim 5 \times 10^{-2}$ m. This threshold is five times larger than what is observed for high liquid filling, see Figure 4.5a. Owing to the larger space of the vapour domain, the range of grid spacing depicted in Figure 4.5b is smaller than in Figure 4.5a. This justifies the absence of the influence of round-off errors in Figure 4.5b, as the smallest grid spacing, $\Delta z = 6 \times 10^{-3}$ m. This spacing is two orders of magnitude higher than the spacing at which round-off errors became important for high liquid filling, see Figure 4.5a. It is worth noting that the ratio between the global error norms, L_∞/L_2, is roughly 10 for both liquid fillings. Hence, both order of accuracies and the ratio of global error norms ratios are invariant to liquid filling. This is an important

result that demonstrates the robustness of the computational implementation of Eq. (4.1).

Figure 4.5 shows that for a fixed grid spacing, both L_2 and L_∞ global error norms are smaller for low liquid filling (b) than for high liquid filling (a). This result is consistent to what has been observed in the error norms for vapour temperatures using the isobaric 1-D model in subsection 4.2.1. As Figure 4.5 shows steady-state temperature profiles, the decrease of the global error norms with decreasing liquid filling is independent of time discretisation. Furthermore, as the global error norms are calculated using the exact analytical solution for vapour temperature, exact formulas for the discretisation error can be obtained. If Δz is within the asymptotic range, high order terms in the discretisation error can be neglected. Then, the coefficients g_2 for a second-order accurate discretisation can be estimated using Eq. (4.3) and Figure 4.5. For $LF = 0.97$, the global error norms formulas are $L_2(\Delta z) = 21.8\,\Delta z^2$ and $L_\infty(\Delta z) = 106.9\,\Delta z^2$, valid for 10^{-5} m $< \Delta z < 1 \times 10^{-2}$ m. For $LF = 0.3$, the global error norms formulas for vapour temperature are $L_2(\Delta z) = 1.5\,\Delta z^2$ and $L_\infty(\Delta z) = 20.5\,\Delta z^2$, valid for $\Delta z < 5 \times 10^{-2}$ m. Note that these formulas are only valid for the tested case of liquid nitrogen in an 8 m³ storage tank. Nevertheless, the procedure can be repeated for any scenario of interest to obtain a reliable estimation of the discretisation error for a given grid spacing Δz.

4.3.2 Error analysis for liquid volume using the equilibrium model

In this thesis, the routines ode15s and ode15i [10] of the MATLAB® ODE suite [5] have been used to integrate the ODE system associated with the isobaric 1-D model. These routines allow a very efficient integration of the ODE system. However, to keep their high efficiency, their accuracy can only be controlled through setting relative and absolute tolerances. Unfortunately, the relationship between global error norms as a function of these tolerances is not straightforward, as discussed in subsection 4.2.2. The aim of this subsection is to use the analytical solutions [7] developed in this thesis to verify the accuracy of time integration using two routines from the MATLAB® ODE suite [5]. In particular, the limiting case of thermal equilibrium between the vapour and the

liquid is considered. For this case, also defined as the equilibrium model for isobaric evaporation, Eq. (3.26) is the exact analytical solution. The discretisation and time integration of the numerical solution is performed automatically by MATLAB.

Figure 4.6 shows the global error norms for liquid volume on the evaporation of pure methane in a large 165,000 m³ using (a) ode45 and (b) ode15s routines. The same tank and storage period than the one presented in subsection 4.2.2 has been selected, as this case provides an upper bound to the error norms for smaller tanks. The absolute and relative tolerances for the numerical solution of Eq. (3.26) were set to the same value, $\epsilon = \epsilon_{\text{rel}} = \epsilon_{\text{abs}}$, and varied within the range $10^{-15} < \epsilon < 10^{-1}$. Figure 4.6a shows that if the ode45 routine is used, the error on liquid volume is small and invariant for a wide range of error tolerances, $10^{-9} < \epsilon < 10^{-1}$. If the error tolerances are further reduced, the error norms decrease at a non-constant rate. If the whole range of tolerances is considered, the error norm on liquid volume decreases very slowly with tolerances. For reference, slopes of error norms that scale $L_n \sim \epsilon^{0.2}$, $L_n \sim \epsilon^{0.3}$ are depicted in grey dashed and solid lines, respectively.

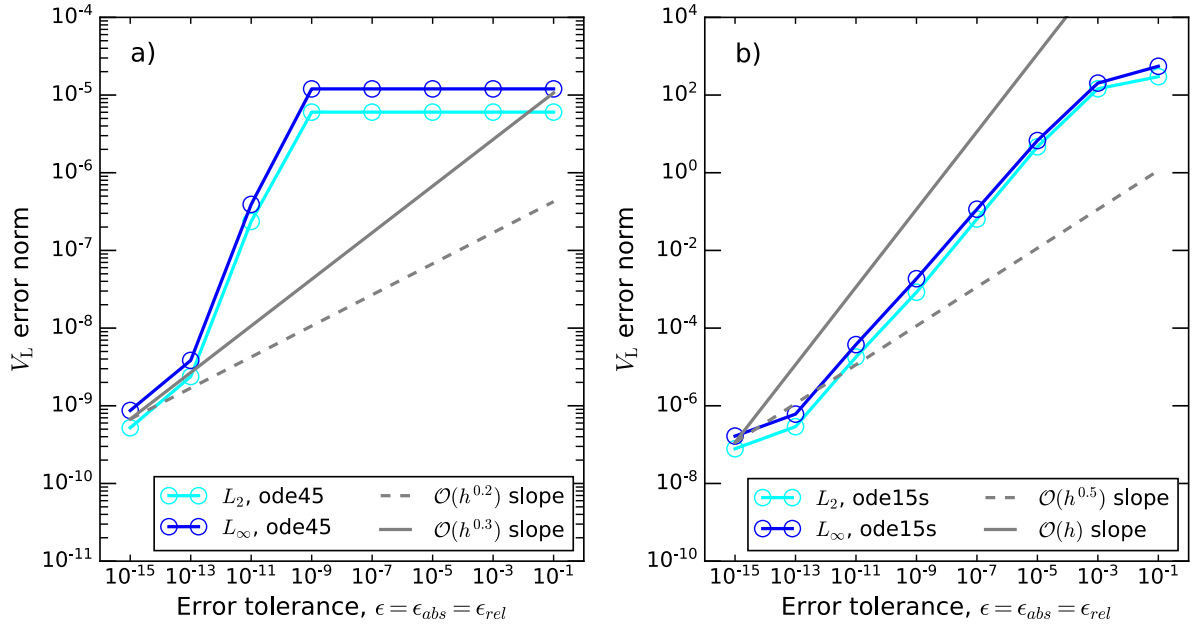

Figure 4.6: Global error norms for liquid volume (V_L) using the equilibrium model to simulate the evaporation of liquid methane in a large 165,000 m³ storage tank. The solutions obtained with two different MATLAB® numerical integration routines, (a) ode45 [5] and (b) ode15s [10], are depicted. The relative and absolute error tolerances were set at the same error tolerance value, $h = \epsilon = \epsilon_{\text{rel}} = \epsilon_{\text{abs}}$, which indirectly controls the accuracy of the solutions.

Figure 4.6b shows that if the ode15s routine is used, the global error norms on liquid volume are radically different to what was observed for ode45, see Figure 4.6a. For the same error tolerance range, the global error norms are significantly larger for ode15s. The norms range from 10^{-7} to 10^{2} for ode15s, while the same figures for ode45 are 10^{-7} to 2×10^{-5}. Another important difference is that for ode15s, the error norms decrease at a roughly constant scaling for a wide range of tolerances, $10^{-13} < \epsilon < 10^{-3}$. For reference, slopes of error norms that scale $L_n \sim \epsilon^{0.5}$, $L_n \sim \epsilon^{1}$ are depicted in grey dashed and solid lines, respectively. It can be observed that not only the error norms decrease with error tolerance, but they also decrease at a faster rate than the norms obtained using ode45, see Figure 4.6a. If an accuracy criterion is set to the $L_2(V_{\mathrm{L}}) < 0.1$ m^3, tolerances lower than 10^{-7} would be required for ode15s. In contrast, if ode45 is used, tolerances six order of magnitude larger ($\epsilon < 10^{-1}$) will suffice and provide a more accurate solution.

4.4 Weathering model verification

The aim of this section is to verify the LNG weathering model for three different LNG mixtures. As the vapour phase heat transfer sub-model is basically the same as the one for the isobaric 1-D model, only temporal discretisation is considered. The temporal discretisation and integration was performed automatically by MATLAB® ode15i [10]. As it has been thoroughly discussed in subsections 4.2.2 and 4.3.2, the behaviour of this integrator routine may be unexpected. Hence, error analysis for BOG and LNG temperatures are presented in this section for the weathering of three different LNG mixtures in a large tank under two liquid fillings. The error norms on BOG will be compared with the norms for the evaporation of pure methane in the same storage tank. On the other hand, the differences in LNG temperature are used as a representative measure of the accuracy on the evolution of LNG composition.

Figure 4.7 shows the L_2 and L_∞ global error norms as a function of relative tolerance for (a) BOG and (b) LNG temperature (T_{LNG}) for the weathering of light LNG in a large storage tank filled at 97% of its capacity. The weathering model has been used to simulate one year of storage. Following the same tolerance criteria to what has been used for pure methane, the exact solutions for BOG and T_{LNG} are estimated as the

numerical solutions setting a relative tolerance of 10^{-6}. Figure 4.7a depicts the L_∞ norm on BOG in solid blue lines and circles for light LNG, and in dashed blue lines and squares for pure methane. Similarly, the L_2 norms are depicted in cyan using the same line style and line marker conventions. It has been found that the same slopes for relative tolerances as the ones used in Figure 4.6b provide an adequate scaling estimate for $L_n \sim \epsilon^{p_\epsilon}$, $0.5 < p_\epsilon < 1$. Hence, in Figure 4.7a, $L_n \sim \epsilon^{0.5}, L_n \sim \epsilon^1$ slopes are depicted using grey dotted and dashed lines, respectively. It can be observed that the BOG error norms for light LNG and methane are comparable, and $\epsilon_{\text{rel}} < 10^{-3}$ satisfies the $L_2(BOG) < 0.1$ kg h^{-1} convergence criterion.

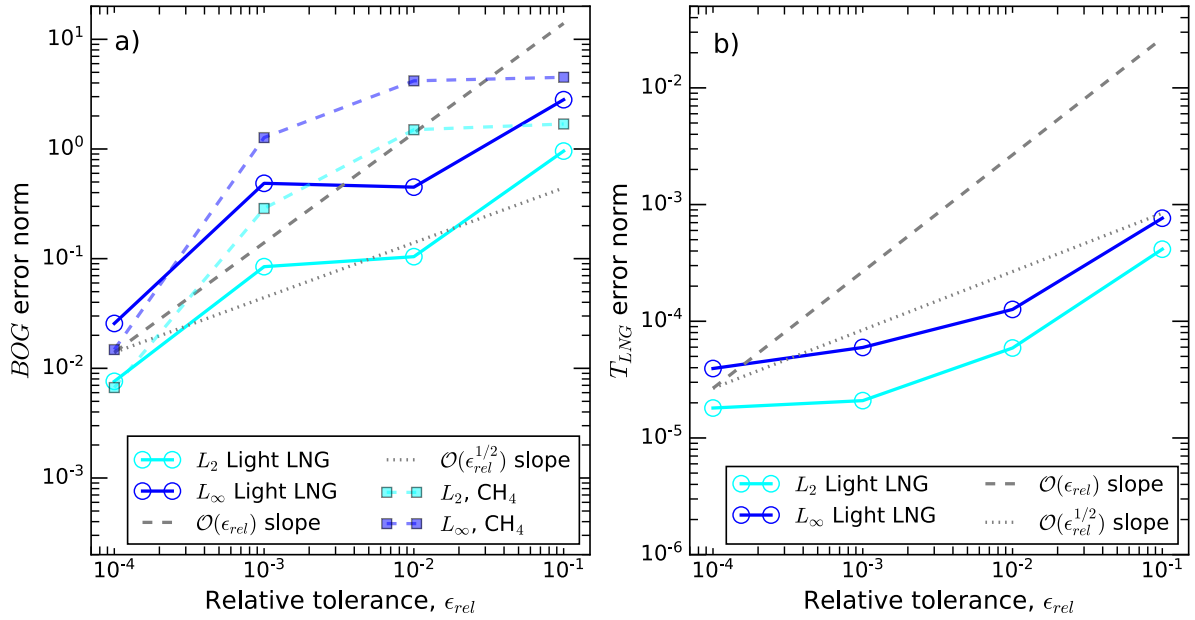

Figure 4.7: Global error norms for (a) BOG and (b) LNG temperature using the weathering model to simulate one year of evaporation of light LNG in a large 165,000 m^3 storage tank. The tank is initially filled at 97% of its capacity. The relative tolerance ϵ_{rel} is the accuracy control parameter for MATLAB® ode15i [10].

Figure 4.7b shows that the global error norms for T_{LNG} are small and decrease slowly with the relative tolerance. A convergence criterion of $L_2(T_{\text{LNG}}) < 10^{-4}$ has been selected. It can be observed that the convergence criterion is satisfied for $\epsilon_{\text{rel}} < 10^{-2}$. However, this value is not sufficient to satisfy the BOG error norm convergence criterion. To satisfy both convergence criteria, the relative tolerance has been set to $\epsilon_{\text{rel}} \leq \min(\epsilon_{\text{rel},T_{\text{LNG}}}, \epsilon_{\text{rel,BOG}})$. The subindices represent the quantities on which the relative tolerances are calculated to satisfy their respective accuracy criteria.

Figure 4.8 shows the BOG (a) and T_{LNG} (b) error norms for one year of weathering of light LNG in a large tank filled at 30% of its capacity. The differences of the BOG global error norms between the light LNG and pure methane are minimal, following the trend of what has been observed for high liquid filling, see Figure 4.7a. Similarly, the global error norms on T_{LNG} are small and follow the same trend to what was observed for high liquid filling. Consequently, $\epsilon_{rel} < 10^{-4}$ satisfies the accuracy criteria for both liquid fillings, verifying the computational implementation of the weathering model for light LNG.

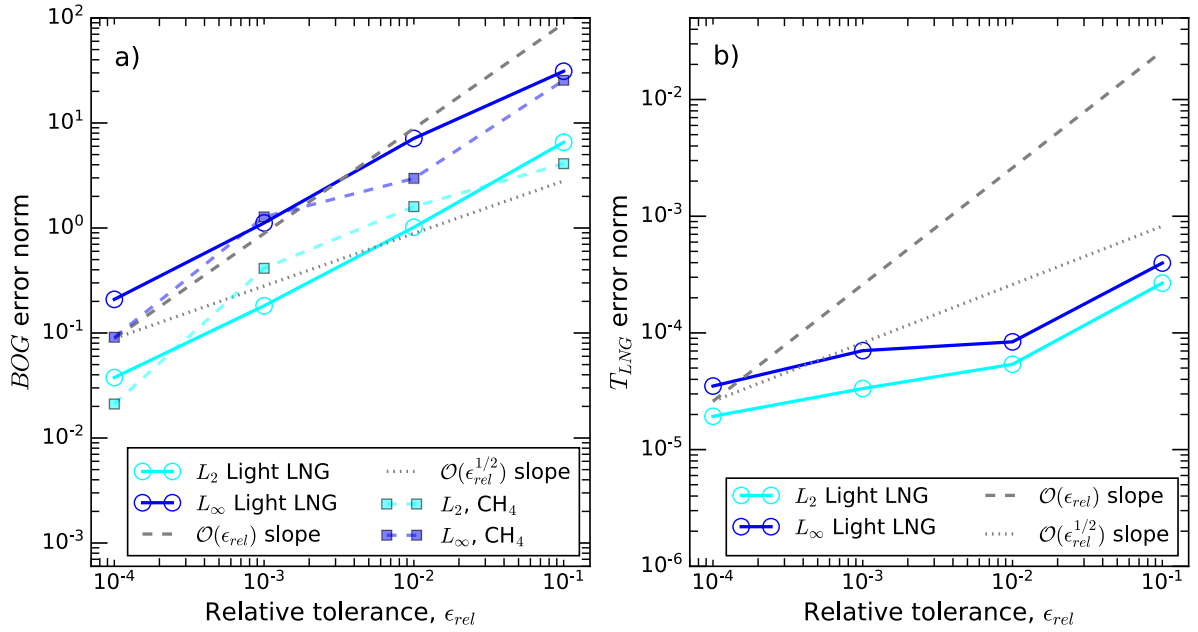

Figure 4.8: Global error norms for (a) BOG and (b) LNG temperature using the weathering model to simulate one year of evaporation of light LNG in a large 165,000 m³ storage tank. The tank is initially filled at 30% of its capacity. The relative tolerance ϵ_{rel} is the accuracy control parameter for MATLAB® ode15i [10].

Figure 4.9 and Figure 4.10 shows the error norms for BOG (a) and T_{LNG}(b) as a function of relative tolerance for the weathering of a heavy LNG mixture for high (LF = 0.97) and low (LF = 0.30) liquid fillings. The simulations considered the same storage tank and storage period than what was considered for pure methane and light LNG. A very small variation of the BOG global error norms respect to methane evaporation is observed in Figure 4.9a and Figure 4.10a. For the LNG temperatures, the global error norms for heavy LNG are slightly higher than those for light LNG, see Figure 4.9b and Figure 4.10b. Nevertheless, a relative tolerance of 10^{-4} sufficed to satisfy the accuracy criteria of BOG and T_{LNG}, verifying the numerical implementation of the weathering

model for heavy LNG. The threshold on relative tolerance is exactly the same than the one determined for light LNG.

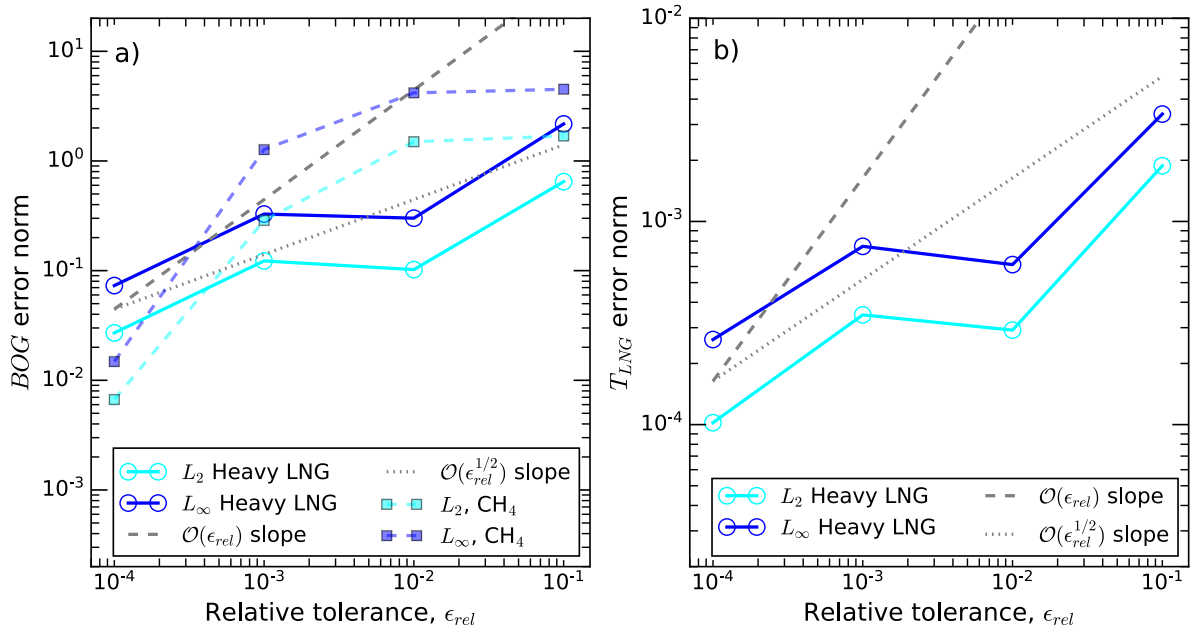

Figure 4.9: Global error norms for (a) BOG and (b) LNG temperature using the weathering model to simulate one year of evaporation of heavy LNG in a large 165,000 m³ storage tank. The tank is initially filled at 97% of its capacity. The relative tolerance ϵ_{rel} is the accuracy control parameter for MATLAB® ode15i [10].

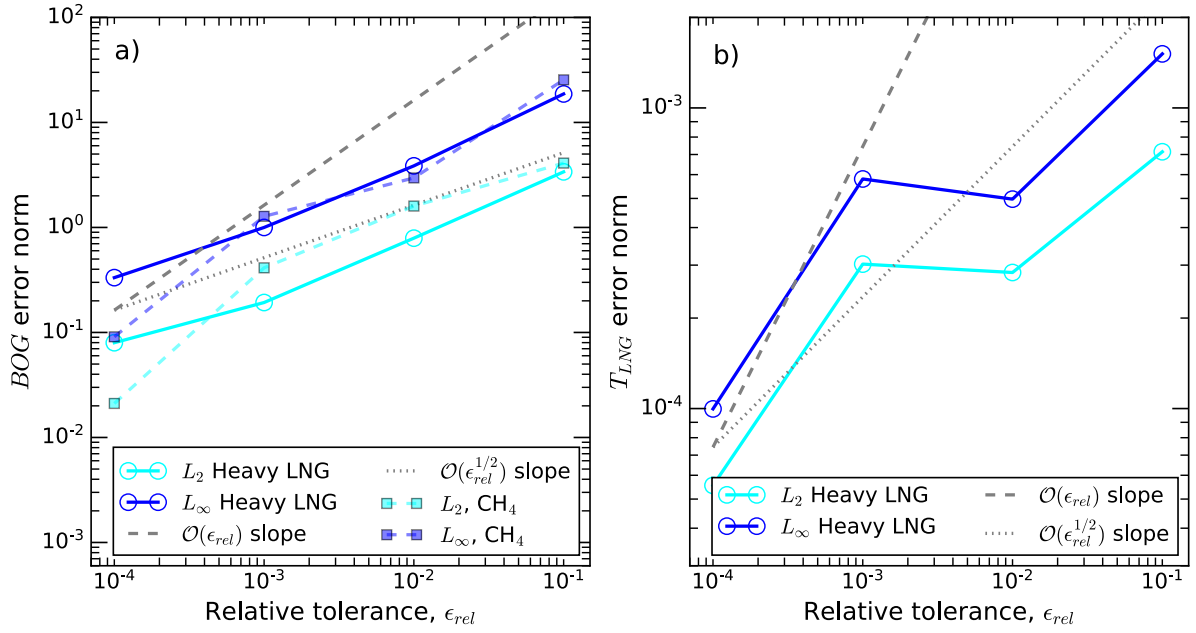

Figure 4.10: Global error norms for (a) BOG and (b) LNG temperature using the weathering model to simulate one year of evaporation of heavy LNG in a large 165,000 m³ storage tank. The tank is initially filled at 30% of its capacity. The relative tolerance ϵ_{rel} is the accuracy control parameter for MATLAB® ode15i [10].

Figure 4.11 and Figure 4.12 depict the error norms for BOG (a) and T_{LNG} (b) as a function of relative tolerances for the weathering of N_2-rich LNG. Figure 4.11 depicts the norms for high liquid filling (LF = 0.97), and Figure 4.12 depicts the norms for low liquid filling (LF = 0.30). The simulations considered the same storage tank and storage period than what was considered for pure methane, light LNG and heavy LNG mixtures. The BOG error norms for both liquid fillings behaved similarly to what was observed for light and heavy LNG. The global error norms of BOG for N_2-rich LNG show just small variations with the norms of pure methane, see Figure 4.11a and Figure 4.12a. The relative tolerance that satisfied the BOG accuracy criteria was also 10^{-4}, the same value as for pure methane, Light and heavy LNG.

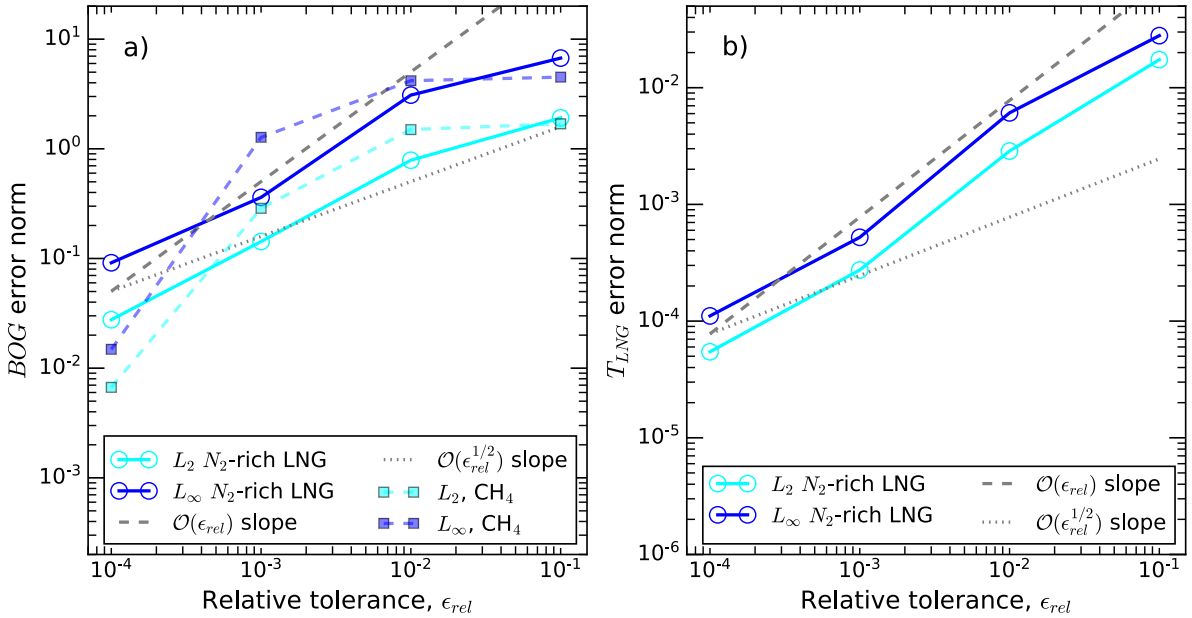

Figure 4.11: Global error norms for (a) BOG and (b) LNG temperature using the weathering model to simulate one year of evaporation of N_2-rich LNG in a large 165,000 m³ storage tank. The tank is initially filled at 97% of its capacity. The relative tolerance ϵ_{rel} is the accuracy control parameter for MATLAB® ode15i [10].

Figure 4.11b and Figure 4.12b show that the global error norms for T_{LNG} decrease considerably with relative tolerance. Furthermore, the error norms for T_{LNG} in the weathering N_2-rich LNG of are an order of magnitude larger than the ones for light and heavy LNG, see Figure 4.7(b)- Figure 4.10 (b). These higher errors are expected as the presence of nitrogen in the mixture produces a larger time derivative of LNG

composition. Nevertheless, a relative tolerance of 10^{-4} was sufficient to achieve the T_{LNG} accuracy criterion. Therefore, Figure 4.11 and Figure 4.12 verify the numerical implementation of the weathering model for N_2-rich LNG for $\epsilon_{rel} < 10^{-4}$.

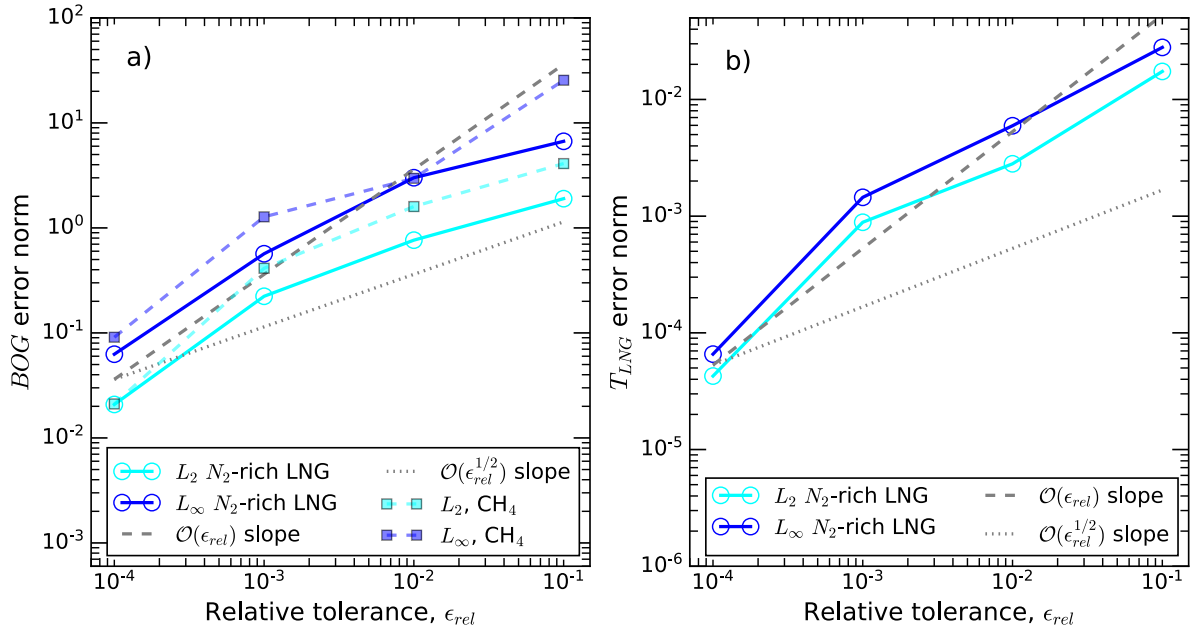

Figure 4.12: Global error norms for (a) BOG and (b) LNG temperature using the weathering model to simulate one year of evaporation of N_2-rich LNG in a large 165,000 m³ storage tank. The tank is initially filled at 30% of its capacity. The relative tolerance ϵ_{rel} is the accuracy control parameter for MATLAB® ode15i [10].

4.5 Vapour-CFD model verification

In contrast to the isobaric 1-D and weathering models that were implemented in MATLAB, the vapour-CFD model has been implemented using OpenFOAM v2006. This section aims to verify the OpenFOAM v2006 routines used for the temporal and spatial discretisation and integration of the vapour-CFD model given by Eqs. (3.1) – (3.16). In subsection 4.5.1, a grid sensitivity analysis of vapour temperature is performed for the three storage scenarios considered in Chapter 5.1. This grid independence study is based on the Supplementary Material 1 in Huerta and Vesovic CFD evaporation model [4]. In subsection 4.5.2, an additional grid sensitivity analysis is presented for the vertical vapour velocity in an infinitesimal annulus near the wall boundary layer for the evaporation of methane at low liquid filling. The aims of this additional analysis are to quantify the vapour velocity discretisation error and compare it with the vapour temperature discretisation error.

4.5.1 Grid-independence study on the vapour bulk

A detailed grid sensitivity analysis of the three scenarios presented in section 5.1 is presented to demonstrate the grid independence of the vapour temperature. To facilitate the visualisation of the temperature profiles, the vapour temperature and height have been scaled to the maximum vapour superheating and vapour height, respectively. The dimensionless temperature Θ has been defined as

$$\Theta = \frac{T_{\mathrm{V}} - T_{\mathrm{L}}}{T_{\mathrm{V,f}}(z = l_{\mathrm{V}}) - T_{\mathrm{L}}}, \tag{4.7}$$

where $T_{\mathrm{V,f}}(z = l_{\mathrm{V}})$ is the temperature of the vapour at the tank roof in the fine mesh. The dimensionless height ξ has been defined as $\xi = z/l_{\mathrm{V}}$, where l_{V} is the vapour height for each particular scenario. Similarly, two additional error measures are defined by normalizing the global error norms to the values of the variable of interest. The percentage average absolute deviation ($AAD\%$) between the functions obtained with two levels of refinement, k and j, is defined as $AAD(f_k, f_j) = \sum_i^n \left| f_{k,i} - f_{j,i} \right| / (N \times \bar{f_k})$. Similarly, the percentage maximum deviation associated to f_k and f_j is defined as $MD(x) = L_\infty(f_k, f_j)/\overline{f_k}$. These normalised error measures allow a quick percentage estimate of the deviation and will be thoroughly used in Chapters 5 and 8 to compare different models.

Figure 4.13 shows the dimensionless temperature profiles in an infinitesimal annulus located at the midpoint between the tank axis and wall as a function of dimensionless height, $\Theta(r = R_T/2, \xi)$. For each scenario, the simulations were run for three meshes based on the grid parameters provided in Table 4.1. Considering the meshes of Table 3.1 as the normal refinement, coarse and fine meshes were generated applying a fixed grid refinement ratio $r_{\mathrm{CFD}} = 2$. The dimensionless temperature profiles are depicted at the beginning of the transient period (t^*_{trans} = 0.1) and at the pseudo steady state (t^*_{trans} = 1). In all scenarios, the deviations between the results produced by the coarse and fine meshes are smaller at the pseudo-steady state than at the beginning of the transient period. This is expected as the magnitude of the temperature and velocity gradients, which govern the discretisation errors, are lower at the pseudo-steady state.

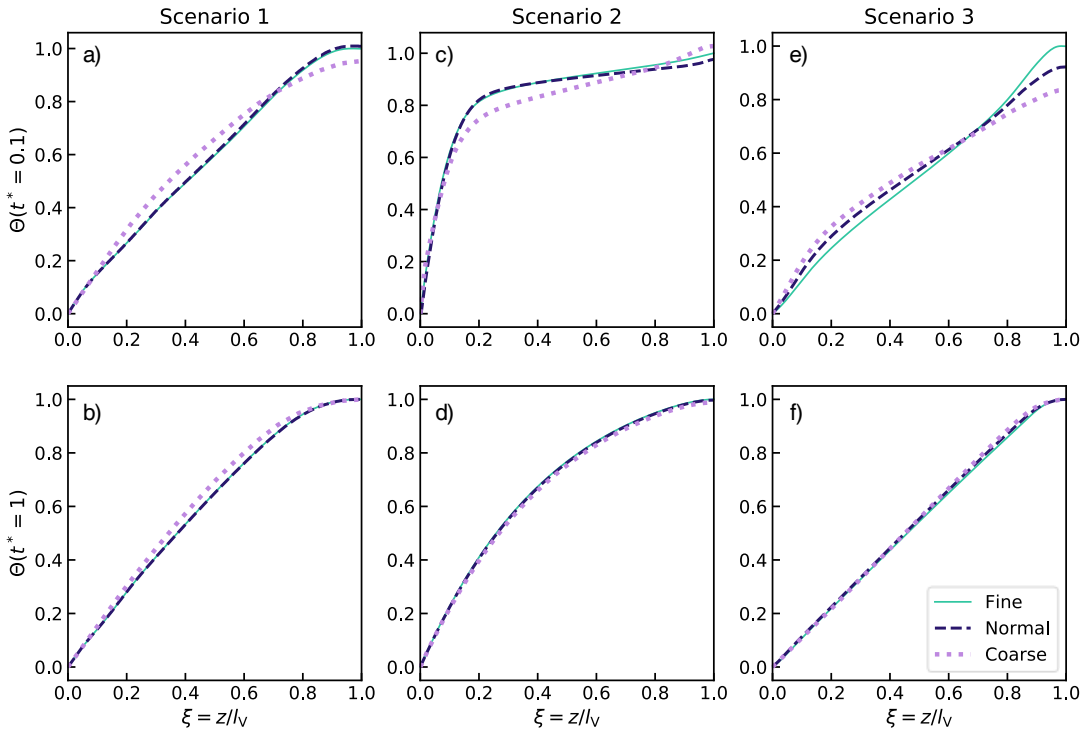

Figure 4.13: Grid sensitivity analysis of the CFD simulations for the isobaric evaporation of methane. Scenario 1 (V_T = 8m ³, LF = 0.97) is depicted in subfigures (a) and (b), Scenario 2 (V_T = 8m ³, LF = 0.30) is depicted in subfigures (c) and (d), and Scenario 3 (V_T = 80 m³, LF = 0.97) is depicted in subfigures (e) and (f), respectively. V_T is the volume of the storage tank and LF the initial liquid filling. For each scenario, the dimensionless temperature Θ is depicted as a function of the dimensionless height ξ for the beginning of the transient period, $t^*_{trans} = t_{trans}/\tau_{trans} = 0.1$, and at the pseudo-steady state, $t^*_{trans} = 1$.

For Scenario 1 (LF = 0.97, V_T = 8 m³), vapour temperatures for the normal and fine meshes are in excellent agreement at both timesteps, see Figure 4.13a-b. The maximum deviations on vapour temperature at the beginning of the transient period and at the pseudo-steady state were just 0.01% and 0.02%, respectively. For Scenario 2 (LF = 0.30, V_T = 8 m³), the agreement is good in both transient period (AAD = 0.26%, MD = 0.70%) and pseudo-steady state (AAD = 0.27%, MD = 0.39%), see Figure 4.13c-d. The slightly larger deviations in Scenario 2 with respect to Scenario 1 are a direct consequence of the larger grid spacing ($\Delta z, \Delta r$) used in Scenario 2, see Table 4.1. The larger grid spacing was selected to keep the CFD simulation time below 3 days, considering that the vapour domain is 33 times larger than in Scenario 1.

For Scenario 3, the agreement is again very good both at the transient period (AAD = 0.06%, MD = 0.16%) and at the pseudo-steady state (AAD = 0.07%, MD = 0.14%), see Figure 4.13e-f. The higher deviations observed in Scenario 3, compared with Scenario

1, are a consequence of slightly larger grid cells and higher velocities. Nevertheless, the maximum deviation at the pseudo-steady state, which is the most relevant period, is less than 0.4% for all scenarios studied. Therefore, using the fine mesh in all simulations would have provided a negligible improvement in the accuracy of the solutions at the expense of requiring a computational time eight times longer. The low deviations on vapour temperature and their reduction with grid spacing verifies the accuracy of the OpenFOAM numerical implementation of the vapour-CFD model.

4.5.2 Grid independence study on boundary layer at the tank wall

For the engineer, the vapour temperature and BOG rates are the most important quantities to predict during the storage of cryogenic liquids. Hence, the excellent agreement of vapour temperatures observed in subsection 4.5.1 constitutes the most important verification test for the vapour-CFD model. This is a consequence of the contribution of vapour phase heat transfer to evaporation and BOG rates through the vapour to liquid heat transfer rate, $\dot{Q}_{\mathrm{VL}}$. A good agreement in vapour temperature implies a good agreement in $\dot{Q}_{\mathrm{VL}}$, which results in a good agreement on evaporation and BOG rates. Thus, the results of subsection 4.5.1 can serve as the validation of the isobaric 1-D model assumptions from an engineering point of view.

From a scientific point of view, the vapour-CFD model provides the velocity and temperature profiles in the boundary layers, which are not explicitly modelled in the isobaric 1-D model. The most relevant boundary layer for the storage scenario is the boundary layer near the tank wall. As the velocity gradients in the tank wall boundary layer are large, their grid independence is not evident. To investigate the accuracy of the vapour-CFD model as a function of the grid resolution of the wall boundary layer, a grid sensitivity analysis of vapour velocity near the tank wall has been performed for Scenario 2. Scenario 2 has been chosen as it provides an error bound owing to the larger grid spacing selected, in comparison to the other scenarios.

Figure 4.14 depicts the vertical vapour velocity as a function of height in an infinitesimal annulus located at 4×10^{-3} m distance from the tank wall ($r = 0.995R_T$). Figure 4.14a depicts the beginning of the transient period, t^*_{trans} = 0.1, and Figure 4.14b

depicts pseudo-steady state, t^*_{trans} = 1. The velocity profile corresponds to Scenario 2, which comprises the evaporation of methane in an 8 m³ storage tank filled at 30% of its capacity. The coarse and normal meshes corresponds to the same meshes considered for subsection 4.5.1. To isolate the effect of the wall functions on the boundary layer, the fine mesh considered in this section was constructed using a non-uniform mesh with a radial refinement near the tank wall. This non-uniform mesh was constructed setting the centre of the cell nearest to the tank wall at 4 × 10⁻³ m distance. Far from the tank wall, the non-uniform mesh was equivalent to the fine uniform mesh considered in subsection 4.5.1. The difference in the vapour temperatures far from the wall for the non-uniform and uniform meshes was negligible (MD < 0.01%).

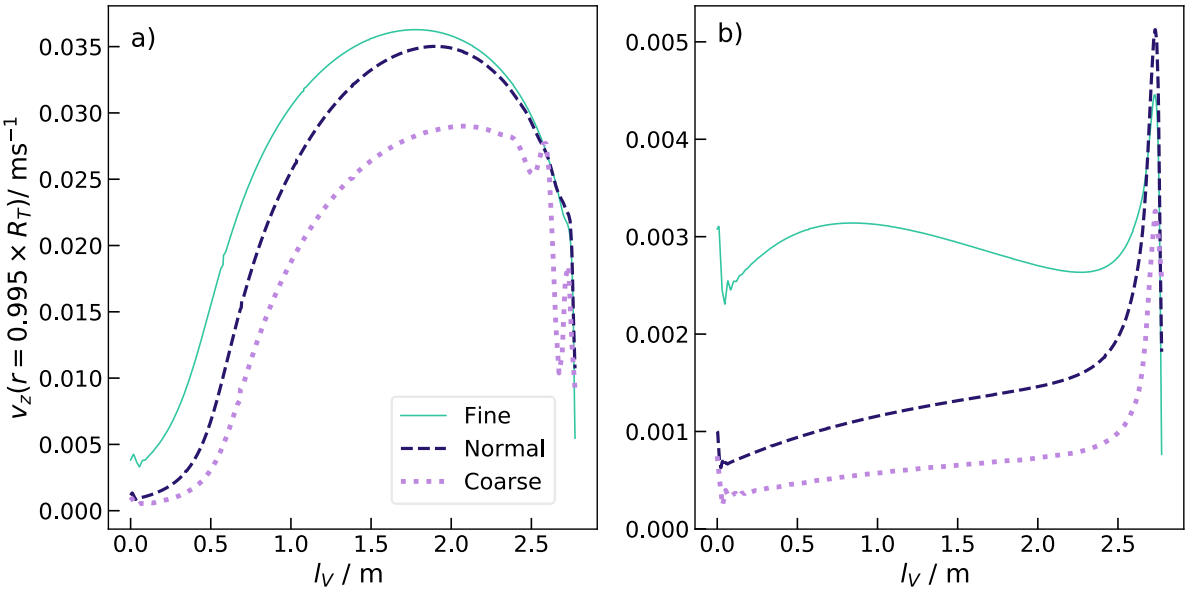

Figure 4.14: Grid independence study for vapour vertical velocity, v_z, in a vertical annulus located within the wall boundary layer, $r = 0.995\ R_T$. Subfigures (a) and(b) shows the velocity profile at the beginning ($t^*_{trans} = 0.1$) and at the end ($t^*_{trans} = 1$) of the transient period, respectively. The velocity profiles were obtained for Scenario 2, that comprises the evaporation of methane in an 8 m³ storage tank under low liquid filling (LF = 0.3).

Figure 4.14a shows that at the beginning of the transient period, a large deviation on vertical vapour velocity at the boundary layer is observed between the normal and fine meshes (AAD = 16%, MD = 34%). For the coarse mesh, the deviation with respect to the fine mesh is not only very large (AAD = 34%, MD = 54%), but the velocity presents large numerical oscillations near the tank roof. This suggest a significant effect of higher order terms for the grid spacing characteristic of the coarse mesh, Δz = 0.02 m. Figure 4.14b shows that at the pseudo-steady state, the deviations of velocity between normal

and fine meshes is even larger than for the transient period (AAD = 56%, MD = 76%). For the coarse mesh, the spurious oscillation near the tank wall is no longer observed, but the deviations are extremely large (AAD = 80%, MD = 89%). The larger deviation at the pseudo-steady state suggests that the discretisation on vertical vapour velocities error increases with the onset of thermal stratification.

The large deviations on vertical velocity are a consequence of the turbulent wall functions used in OpenFOAM. These wall functions can provide a reasonable calculation of the energy and momentum transport in the boundary layer taken as a whole. The resolutions of the coarse (Δz = 0.02 m) and normal (Δz = 0.01 m) meshes are insufficient to resolve the exact velocity profiles at the boundary layer. This forces the wall functions to estimate an average boundary layer velocity in the first cell near the wall of the coarse and normal meshes. Hence, the underprediction of vapour velocities in the coarse and normal meshes is expected, as far from the wall the vertical velocities decrease rapidly.

Although the wall functions fail to produce satisfactory velocity profiles inside the wall boundary layer, they do not produce a significant error on vapour temperatures in the vapour bulk, see subsection 4.5.1. Therefore, if the accurate resolution of the velocity profiles at the wall boundary layer is required, the mesh must be locally refined near the tank wall. To achieve this, non-uniform meshes with radial refinement are an excellent approach to ensure a balance between accuracy and computational efficiency. On the other hand, if the quantities of interest are unaffected by the variation of the velocity within the boundary layer, uniform meshes are sufficient. Furthermore, the uniform meshes can provide satisfactory solutions, as what has been observed subsection 4.5.1. for vapour temperature, while offering a speed up of 80-90% with respect to non-uniform meshes.

4.5.3 Mesh visualisation

Figure 4.15 shows the mesh associated with Scenario S1 in Table 3.1. It can be observed that the mesh is orthogonal, uniform, and the aspect ratio $\Delta z/\Delta r$ is 2. Figure 4.16 shows the mesh associated with Scenario S2 in Table 3.1. Below the roof, the mesh

is uniform and has an aspect ratio of 1. In the region below the tank valve, the mesh is radially refined and the aspect ratio $\Delta z/\Delta r_{\text{valve}}$ is 4. Finally, Figure 4.17 shows the mesh associated with Scenario S3 in Table 3.2, which is uniform and has an aspect ratio of 1.25 everywhere. Large aspect ratios significantly reduce the order of accuracy of the finite volume method. Therefore, higher discretisation errors are expected for Scenario S2.

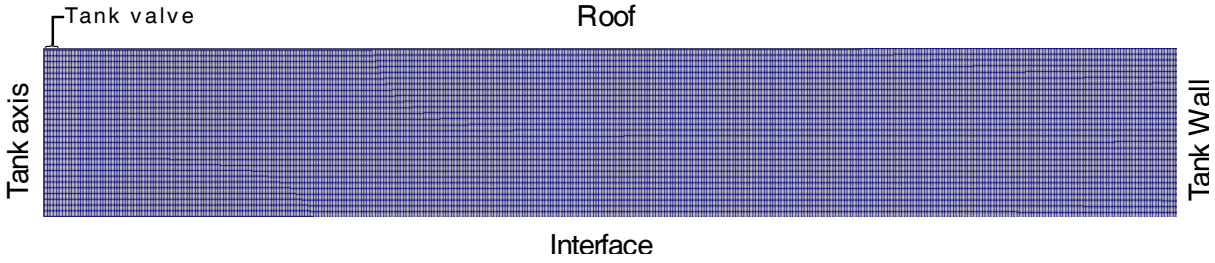

Figure 4.15: Vapour domain discretisation 2-D mesh for Scenario S1 (V_T = 8 m³, LF = 0.97).

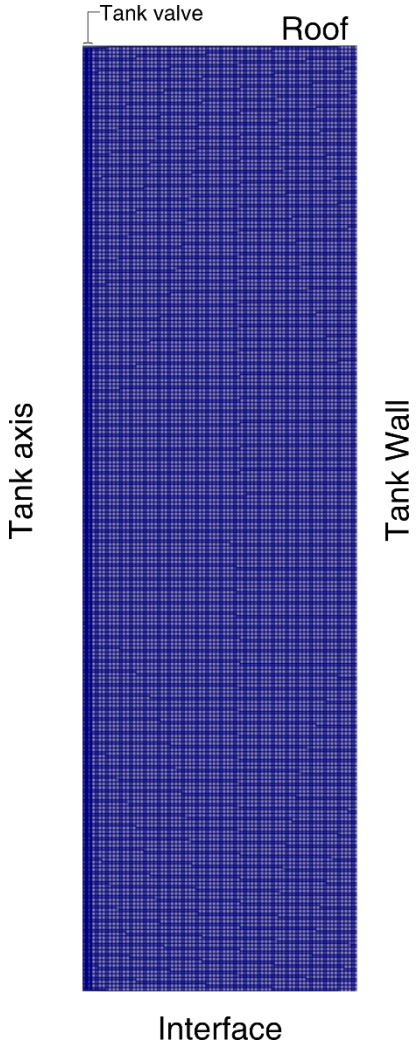

Figure 4.16: Vapour domain discretisation 2-D mesh for Scenario S2 (V_T = 8 m³, LF = 0.30).

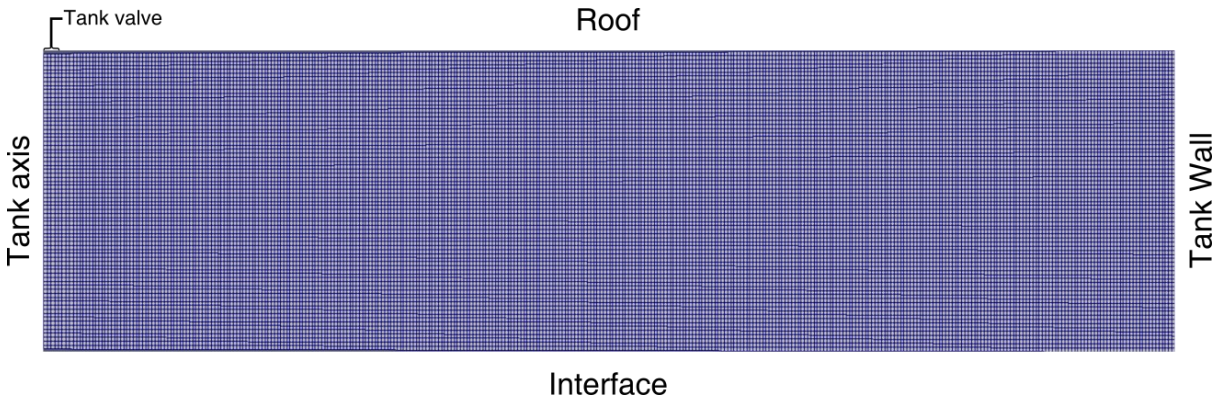

Figure 4.17: Vapour domain discretisation 2-D mesh for Scenario S3 (V_T = 80 m³, LF = 0.97).

4.6 References

[1] F. Huerta and V. Vesovic, "A realistic vapour phase heat transfer model for the weathering of LNG stored in large tanks," *Energy,* vol. 174, pp. 280-291, 2019/05/01/ 2019, doi: https://doi.org/10.1016/j.energy.2019.02.174.

[2] C. Migliore, A. Salehi, and V. Vesovic, "A non-equilibrium approach to modelling the weathering of stored Liquefied Natural Gas (LNG)," *Energy,* vol. 124, pp. 684-692, 2017, doi: 10.1016/j.energy.2017.02.068.

[3] C. Migliore Cappello, "Modelling the weathering process of stored liquefied natural gas (LNG)," 2015.

[4] F. Huerta and V. Vesovic, "CFD modelling of the isobaric evaporation of cryogenic liquids in storage tanks," *Int. J. Heat Mass Transfer,* vol. 176, p. 121419, 2021/09/01/ 2021, doi: https://doi.org/10.1016/j.ijheatmasstransfer.2021.121419.

[5] L. F. Shampine and M. W. Reichelt, "The matlab ode suite," *SIAM journal on scientific computing,* vol. 18, no. 1, pp. 1-22, 1997.

[6] C. J. Roy, "Review of code and solution verification procedures for computational simulation," *Journal of Computational Physics,* vol. 205, no. 1, pp. 131-156, 2005/05/01/ 2005, doi: https://doi.org/10.1016/j.jcp.2004.10.036.

[7] F. Huerta and V. Vesovic, "Analytical solutions for the isobaric evaporation of pure cryogens in storage tanks," *Int. J. Heat Mass Transfer,* vol. 143, p. 118536, 2019/11/01/ 2019, doi: https://doi.org/10.1016/j.ijheatmasstransfer.2019.118536.

[8] L. F. Richardson, "IX. The approximate arithmetical solution by finite differences of physical problems involving differential equations, with an application to the stresses in a masonry dam," *Philosophical Transactions of the Royal Society of London. Series A, Containing Papers of a Mathematical or Physical Character,* vol. 210, no. 459-470, pp. 307-357, 1911.

[9] L. F. Richardson and J. A. Gaunt, "VIII. The deferred approach to the limit," *Philosophical Transactions of the Royal Society of London. Series A, Containing Papers of a Mathematical or Physical Character,* vol. 226, no. 636-646, pp. 299-361, 1927/01/01 1927, doi: 10.1098/rsta.1927.0008.

[10] L. F. Shampine, " Solving 0 = F(t, y(t), y′(t)) in Matlab," *J. Num. Math.,* vol. 10, no. 4, p. 19, 2010, doi: 10.1515/JNMA.2002.291.

Chapter 5

Results of modelling isobaric evaporation of cryogenic liquids in storage tanks

5.1 Introduction

In this chapter, the models developed in Chapter 3 are used to simulate the isobaric evaporation of cryogenic liquids in several storage scenarios. In section 5.2, the vapour-CFD model [1] developed in section 3.1 is applied to simulate the storage of methane in small and medium-sized storage tanks. The generated profiles are compared with the isobaric 1-D model to establish its range of applicability. In section 5.3, the non-equilibrium weathering model [2] developed in section 3.4 is used to simulate the storage of four LNG mixtures in a large storage tank of 165,000 m^3 capacity. In these scenarios, the composition of the mixtures influences BOG rates, and the storage periods are longer than those for small and medium-sized storage tanks. Finally, in section 5.4 the performance of the analytical solutions developed in section 3.3 is evaluated. The analytical solutions are evaluated for all scenarios studied in section 5.2, and for pure methane stored in the large tank considered in section 5.3. The geometrical dimensions, initial liquid filling and operating pressure of all scenarios are summarised in Table 5.1.

Table 5.1: Vertically orientated cylindrical storage tanks considered for the isobaric evaporation of pure methane (S1-S3) and several LNG mixtures (S4).

Scenario	Height/ m	Internal diameter /m	External diameter / m	Pressure / kPa	LF
S1	3.959	1.604	1.630	100	0.97
S2	3.959	1.604	1.630	100	0.30
S3	12.540	2.850	2.900	100	0.97
S4	35.99	76.4	80	116.325	0.97*

* In subsections 5.3.1 and 5.3.2 scenario S4 is briefly investigated across a variety of liquid fillings (LF) between 0.30 and 0.97.

5.2 CFD simulations of the vapour phase

We start by considering the evaporation of liquid methane as it provides an excellent approximation to the heat transfer in the vapour phase during the weathering of LNG. There are a number of reasons for this. The vapour generated by the weathering of the LNG mixtures used in industry is mainly composed of methane [3], and hence its thermophysical and thermodynamic properties are approximately the same. Additionally, the saturation temperature of a typical LNG mixture changes by less than 1 K for a year of weathering [3]. Hence, not considering this slow change, as a consequence of using methane instead of LNG, would produce a negligible error in vapor phase heat transfer. This constitutes a trade-off between accuracy and complexity, as simulating the compositional change of LNG and its vapour would significantly increase the simulation time and hinder model convergence.

The vapour-CFD model [1] developed in section 3.2 was used to simulate the isobaric evaporation of methane in three scenarios, see S1-S3 in Table 5.1. Scenario 1 consists of an 8 m^3 small storage tank filled at 97% of its capacity (LF = 0.97). Scenario 2 consists of the same tank but filled only at 30% of its capacity (LF = 0.30). Finally, Scenario 3 consists of a medium-sized storage tank of 80 m^3 filled at 97% of its capacity (LF = 0.97). In all scenarios, the heat ingress was assumed to come only through the walls. The roof and bottom of the tanks were assumed thermally insulated. For all scenarios, the overall heat transfer coefficient for the vapour and liquid phases was taken as $U = U_L = U_V = 0.019$ W m^2 K^{-1}. This heat transfer coefficient was estimated from boil-off rate data of liquid nitrogen in cryogenic storage tanks at this scale [4], see Appendix A.

It has been established that the heating of a cryogenic vapour can be broadly divided into two stages [2, 5-8]. The first stage occurs at the beginning of the evaporation, where the vapour rapidly heats and expands as a consequence of heat ingress. The rapid heating occurs until the vapour heat ingress is balanced with the vapour to liquid heat transfer and the BOG removal. From that time, the cryogenic vapour follows a pseudo-steady state, during which its vapour temperature increases very slowly. The slow increase in vapour temperature is a consequence of the increase in the vapour height as the evaporation progresses. The onset of the pseudo-steady state

is demarcated by the transient period τ_{trans}. The transient period is defined as the earliest time at which the vapour temperature changes at a rate lower than 0.1 K h^{-1}.

The temperature profiles, evaporation rates and BOG rates obtained using the vapour-CFD model were compared with the isobaric 1-D model. At the pseudo-steady state, both models were validated using the analytical solutions for the isobaric evaporation of pure methane. After the transient period, $t > \tau_{\text{trans}}$, the stored cryogen slowly evaporates as a consequence of the low overall heat transfer coefficient of the storage tank. The total evaporation period, τ_{evap}, is defined as the time at which the stored cryogen has completely evaporated, $V_{\text{L}}(\tau_{\text{evap}}) = 0$. As $\tau_{\text{evap}}/\tau_{\text{trans}} \approx 10^3 - 10^4$ for all scenarios, simulating long-term storage with the vapour-CFD model was not feasible. This would have required between 3 and 37 years of simulation time. Long term storage is examined in section 5.4 using the isobaric 1-D model and its analytical solutions.

To facilitate the discussion of the results, two distinct dimensionless times are defined. The transient dimensionless time is defined as $t^*_{\text{trans}} = t/\tau_{\text{trans}}$, which provides an appropriate timescale to examine the transient period during short-term storage. The rapid transient stage of the evaporative process is defined by $t^*_{\text{trans}} < 1$, while the pseudo-steady state occurs when $t^*_{\text{trans}} > 1$. Similarly, the evaporation dimensionless time is defined by $t^*_{\text{evap}} = t/\tau_{\text{evap}}$ to examine long-term storage. In subsections 5.2.1-5.2.5, the results obtained with the vapour-CFD model are presented using large eddy simulation (LES) turbulence modelling. In subsection 5.2.6, the influence of turbulence modelling on vapour temperatures is quantified by comparing LES with the k-ω-SST turbulence model.

5.2.1 Temperature and velocity profiles in Scenario 1 (S1)

Figure 5.1 shows the temperature and velocity profiles obtained with the vapour-CFD model for methane evaporation in an 8 m^3 tank filled at 97% of its capacity at two different times. In Figure 5.1, the temperature profile is presented as the coloured background, while the velocity profile is depicted by arrow glyphs. The colour of the glyphs indicates the magnitude of the velocity. This style of presentation for the velocity

and temperature profiles will be followed consistently in subsections 5.2.2 and 5.2.3 for the remaining scenarios.

In Figure 5.1a, the temperature and velocity profiles are depicted after 480 s ($t^*_{\mathrm{trans}} = 0.1$) of evaporation. This timestamp was selected as a representative time of the rapid transient stage at the beginning of the evaporation [2]. Figure 5.1a shows that the vapour temperature increases with height, while the temperature variation in the radial direction is small. The arrow glyphs depict the circulation of the vertically thermally stratified vapour heated by the wall and cooled by the vapour-liquid interface. Firstly, the vapour circulates upwards close to the wall as a buoyancy driven flow. As the upward vapour flow is obstructed by the roof, the vapour recirculates radially towards the tank axis until it splits in two currents. The first current leaves the tank through the valve as BOG, while the second current recirculates back to the wall.

The maximum velocities are small and occur in two regions. The first region is located in a thin annulus adjacent to the wall, see Figure 5.1a, where the vapour velocity reaches approximately 2 cm s $^{-1}$. This maximum is expected as a consequence of the buoyancy driven flow provoked by wall heating. The second region is located at the tank axis and immediately below the tank valve, where the velocity reaches approximately 6 cm s $^{-1}$. Such relatively high velocity is a consequence of the tank outlet, where the vapour accelerates to satisfy the conservation of mass during the evaporation. The minimum velocities are observed at the vapour liquid interface and at the recirculating currents. At the interface, the small evaporative velocity $v_{z|r,z=0}$ = 0.04 cm s $^{-1}$ is a consequence of the high insulation of the tank. Low liquid heat ingress produces low evaporation rates, which define the evaporative velocity, see Eq. (3.15). Within the recirculating currents, the velocity decreases with distance from the roof from ~ 0.1 cm s $^{-1}$ after the flow splits to 0.01 cm s $^{-1}$ above the interface.

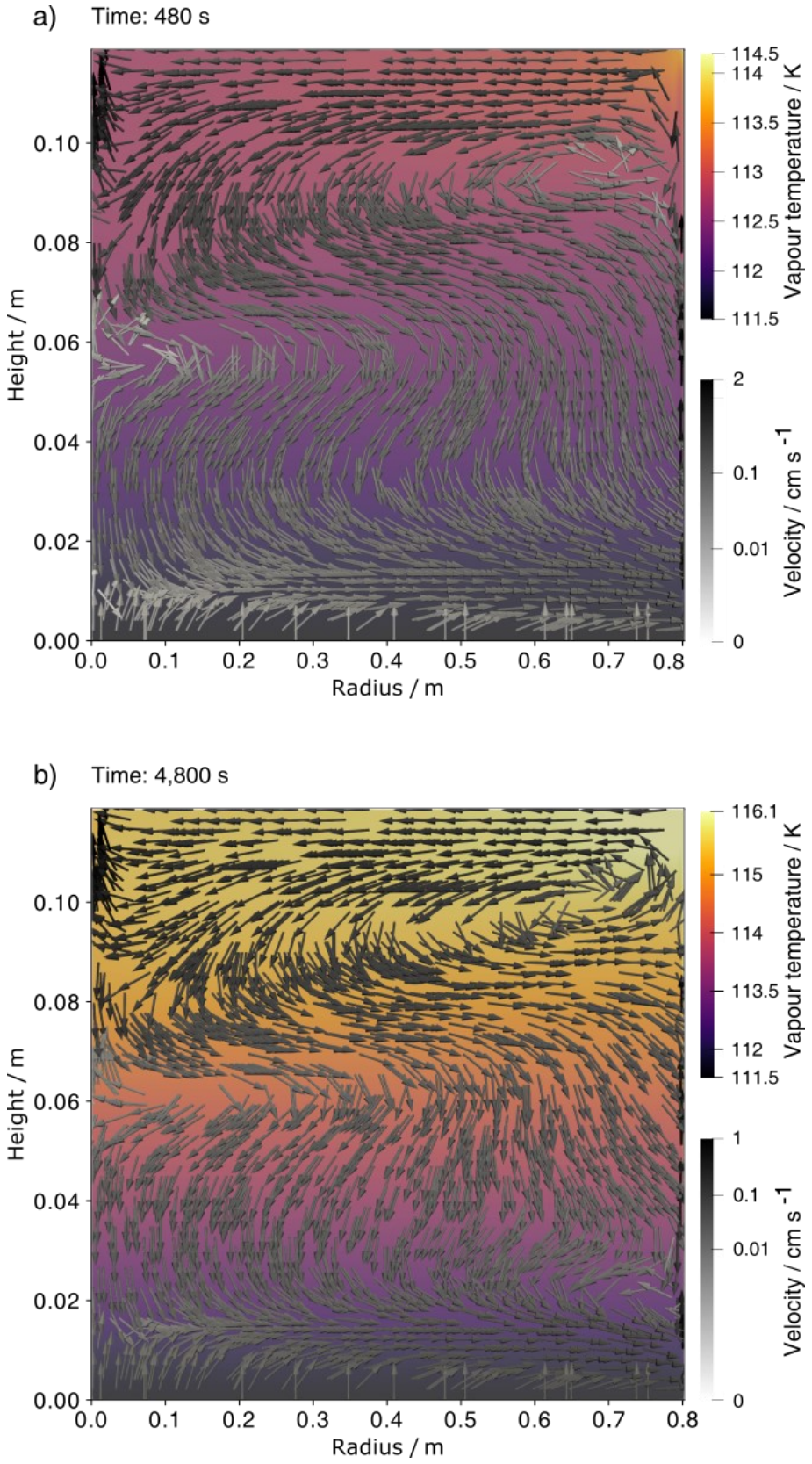

Figure 5.1: Velocity glyphs and temperature profiles in the vapour phase during the evaporation or pure methane in an 8 m³ storage tank filled to 97% of its capacity. The profiles correspond to (a) t = 480s ($t^*_{\text{trans}} = 0.1$), and (b) 4,800 s ($t^*_{\text{trans}} = 1$) from the beginning of the evaporation.

As time progresses, the vapour temperature increases until the vapour reaches its pseudo-steady state. Figure 5.1b shows the vapour velocity and vapour temperature profiles at the pseudo-steady state after 4,800 s ($t^*_{\text{trans}} = 1$) of evaporation in the same tank. The recirculation pattern and vertical thermal stratification have the same structure of the timestamp representative of the transient period, see Figure 5.1a. The vertical temperature gradient has increased from 11.7 K m^{-1} at 480 s to 26.7 K m^{-1} at 4800 s. At the pseudo-steady state, the increase in vertical thermal stratification dampened the buoyancy driven flow near the wall. As a consequence, the vertical velocity near the wall decreased to values lower than 1 cm s $^{-1}$.

Figure 5.2 shows the radial variation of vapour temperature produced by the vapour-CFD model in disks located at three different heights. These heights are located just above the interface ($z = 0.01 l_{\text{V}}$), at the maximum height at which the radial temperature gradient is negligible ($z = 0.75 l_{\text{V}}$) and at the roof. These locations were selected because they delimit regions with noticeably different velocity profiles, see Figure 5.1a, b. To aid the discussion, the cylindrical vapour domain is partitioned in three shells as a function of the tank geometry and boundary conditions. Shell 1 depicts the region below of the tank valve, $0 \leq r < 0.03 R_{\text{T}}$, Shell 2 depicts a free stream region, $0.03 R_{\text{T}} \leq r < 0.99 R_{\text{T}}$, and Shell 3 depicts a boundary layer close to the tank wall, $\delta_{\text{TW}} = 0.99 R_{\text{T}} \leq r < R_{\text{T}}$.

For the region far below the roof, $0 \leq z \leq 0.75 l_{\text{V}}$, the vapour temperature varies less than 0.2 K for $r < 0.99 R_{\text{T}}$ and less than 0.5 K within the boundary layer δ_{TW}. In this region, the maximum temperature is observed at the wall as a consequence of the heat ingress from the surrounding air, see Figure 5.2. The minimum temperature is achieved at the outer limit of the wall boundary layer, $r = 0.99 R_{\text{T}}$, before its sharp increase as $r \to R_{\text{T}}$. This minimum is expected, and it is denominated temperature defect. The temperature defect is characteristic of boundary layers near vertical walls driven by natural convection subject to a positive vertical thermal stratification, $\partial T_{\text{V}}/\partial z|_{r=R_{\text{T}}} > 0$ [9]. Considering all heat and momentum transfer, far from the wall and roof boundary layers the radial temperature variation is negligible (0.2%). This is a consequence of the highly effective advective heat transport in the radial direction induced by the recirculating currents, see Figure 5.1.

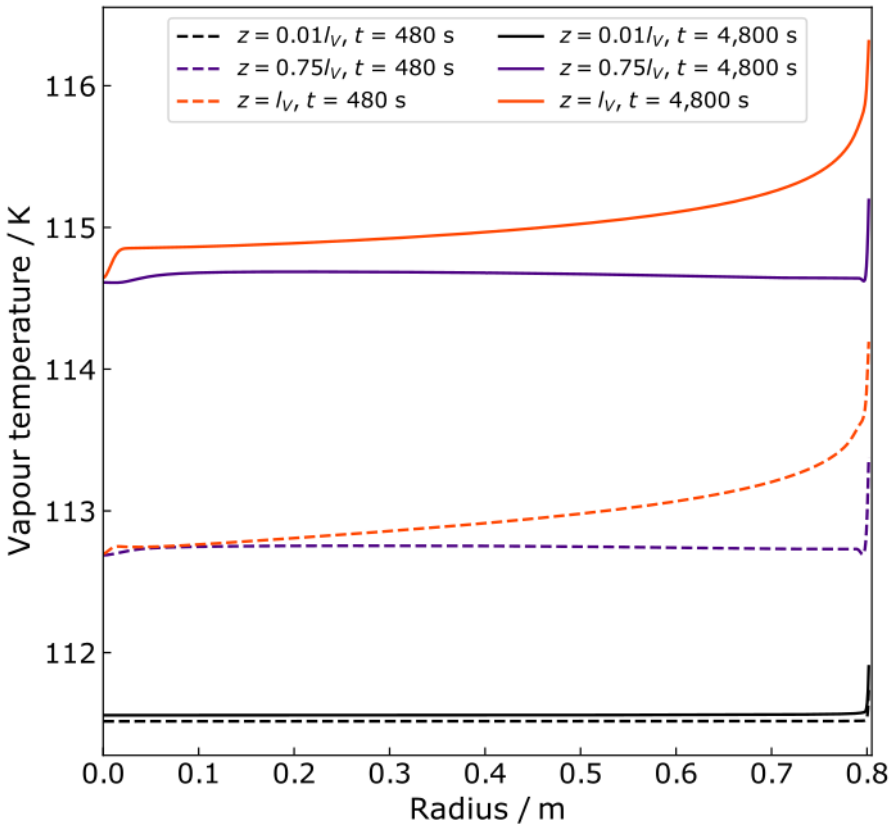

Figure 5.2: Vapour temperature profile as a function of radius. Three different vapour heights are depicted for the evaporation of pure methane in an 8 m³ storage tank filled at 97% of its capacity after 480 s ($t^*_{\text{trans}} = 0.1$) and 4,800 s ($t^*_{\text{trans}} = 1$).

Figure 5.2. shows that at the tank roof and in the region immediately below it, $\delta_{\text{TR}} = 0.75\, l_{\text{V}} \leq z \leq l_{\text{V}}$, the variation of vapour temperature with radius cannot be neglected. This region is denominated roof boundary layer, δ_{TR}, and the vapour temperature profile is completely different from the profile observed far from the roof. The maximum variation of vapour temperature with radius was observed at the roof, $z = l_{\text{V}}$. At the roof, the temperature increased with radius from 114.6 K to 116.3 K at $t^*_{\text{trans}} = 1$, see the orange lines in Figure 5.2. Additionally, at δ_{TW} the temperature defect is no longer observed. This is a consequence of the tank roof being insulated, which mitigates the positive vertical thermal gradient as $z \to l_{\text{V}}$ at δ_{TR}.

At the roof boundary layer, the removal of the vapour through the valve produces higher velocities than far from the roof, see Figure 5.1. These velocities enhanced advective heat transfer. The radial component of the velocity (up 0.7 cm s $^{-1}$) dominated everywhere in δ_{TR} except in the region below the valve. Below the valve, the vertical

component of the velocity (up to 6 cm s $^{-1}$) dominated as a consequence of the vapour removal. The enhanced advection at δ_{TR} led to more efficient heat transfer away from the wall. This enhancement is evidenced by the slow decrease in steepness of the vapour temperature profile with the increasing distance from the wall, $r \to 0$. This profile contrasts with the profile characteristic of the region far from the tank roof, $z \leq 0.75 l_V$. In that region, a sharp temperature decrease is observed near the tank wall, see the purple and black curves in Figure 5.2.

Figure 5.3 shows the vapour temperature profiles produced by the vapour-CFD model in an infinitesimal annulus located at the midpoint between the tank axis and wall. The vapour temperature profiles are compared with the profiles produced by the isobaric 1-D model for three different representative timestamps. At the beginning of the transient stage, $t^*_{trans} = 0.1$, both models predict a monotonic increase of vapour temperature with height. However, the shape of the temperature profiles is slightly different, see the black curves in Figure 5.3. In the isobaric 1-D model, a slightly larger temperature gradient is predicted at the interface, while far from the interface the vapour temperature is roughly constant. In contrast, the vapour-CFD model predicts a linear temperature profile in most of the vapour phase except in the region close to the roof, $z \geq 0.9 l_V$. The linear region of the temperature profile is a consequence of the more realistic velocity profiles predicted by the vapour-CFD model in the vapour bulk. Figure 5.1a shows spatial variation of effective advection. In contrast, the isobaric 1-D model assumes a spatially homogeneous, upwards average vertical velocity $\bar{v}_z \approx 3.6 \times 10^{-3}$ cm s $^{-1}$.

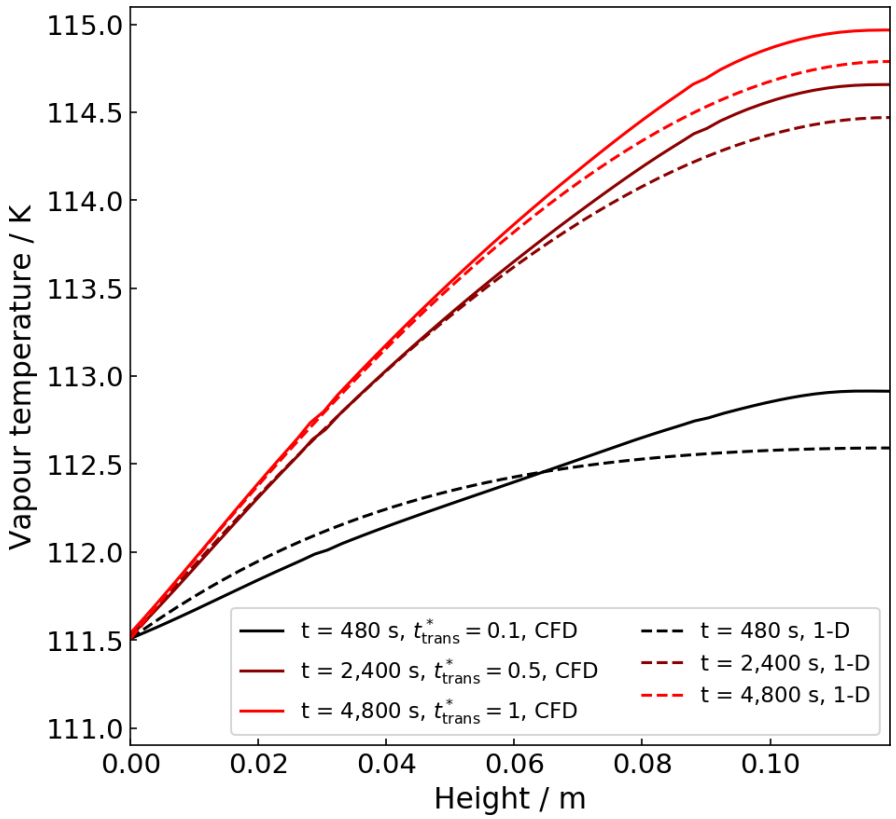

Figure 5.3: Vapour temperature profiles as a function of height for scenario S1. The profiles are sampled at the midpoint between the tank axis and the wall, $r = R_T/2$, for the evaporation of pure methane in an 8 m³ storage tank filled to 97% of its capacity, (---) vapour-CFD model, (- - -) isobaric 1-D model.

As time progresses, the agreement between the vapour temperature profiles improves, see the brown and red curves in Figure 5.3. The better agreement is a consequence of the establishment of vertical thermal stratification in the vapour bulk, which dampens the buoyancy driven flow. This validates the capacity of the isobaric 1-D models to predict vapour temperature profiles at the pseudo-steady state. Additionally, it demonstrates that $\partial T_V/\partial t = 0.1$ K h $^{-1}$ is an appropriate threshold to identify the pseudo-steady state for both 1-D and vapour-CFD models. At all times, the agreement between the vapour-CFD and isobaric 1-D models is excellent, with a maximum difference in temperature lower than 0.5 K.

Figure 5.4 shows the increase of average vapour temperature and BOG temperature predicted by the vapour-CFD and 1-D models as a function of time. The average vapour temperature predicted by both models are in excellent agreement and follow the same trend. The vapour-CFD model predicts an average vapour temperature slightly higher (0.1 K) than the 1-D model. This result is consistent with the higher

vapour temperature observed at the roof boundary layer, see Figure 5.3, as a consequence of reduced vertical advection. Similarly, the vapour-CFD model predicts a BOG temperature is slightly higher than the 1-D model (0.07 K). This difference decreases to 0.02K as the system approaches the pseudo-steady state. The differences are small and of the order of the discretisation error, that for this scenario were estimated to be 0.02 K, see subsection 4.4.1. It is worth noting that the vapour-CFD model predict a slightly longer (7.2%) transient period of 4,800 s compared with the 4,480 s for the 1-D model. The shorter transient time predicted by the 1-D model is a consequence of the assumption of instantaneous radial heat transfer.

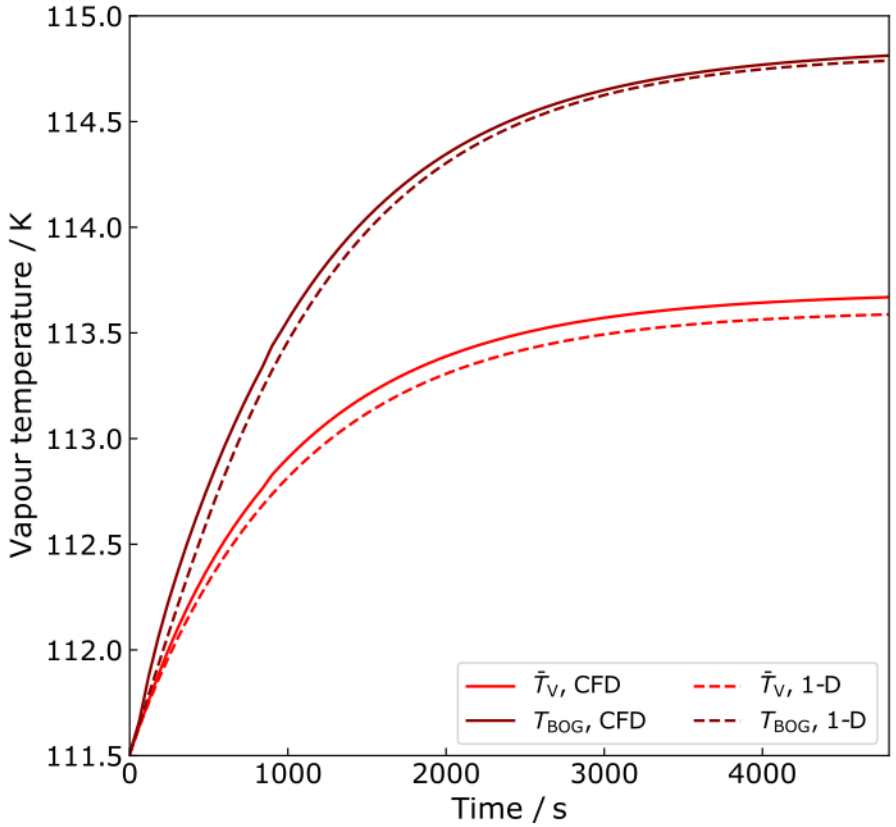

Figure 5.4: Comparison of average vapour temperature and boil-off gas (BOG) temperature for Scenario 1. The profiles correspond to the evaporation of pure methane in an 8 m³ storage tank filled to 97% of its capacity. (---) vapour-CFD model, (- - -) isobaric 1-D model.

5.2.2 Temperature and velocity profiles in Scenario 2 (S2)

The second scenario considers the isobaric evaporation of pure methane in an 8 m³ storage tank filled at 30% of its capacity. In Scenario 2, there are two important differences with respect to Scenario 1. First, the vapour phase occupies a space 23 times larger. Second, the wet area in contact with the tank walls decreases by 69%, which leads to initially 69% smaller liquid heat ingress, see Eqs. (3.7)-(3.8). Figure 5.5 shows the vapour temperature and velocity profiles produced by the vapour-CFD model for Scenario 2 at the beginning and at the end of the transient period. At both timestamps, the velocity profiles are significantly different to those observed in Scenario 1.

Figure 5.5a shows the profiles at the beginning of the transient period (t = 13,320 s, $t^*_{\text{trans}} = 0.1$). At this timestep, the vapour flows in an anticlockwise recirculation pattern. At the tank wall and roof, the vapour flow follows a similar buoyancy driven trajectory as in Scenario 1. In contrast, the recirculation pattern in Scenario 2 is less affected by the boundary layers below the tank roof and above the vapour-liquid interface. The maximum velocities near the wall are of the order of 3 cm s $^{-1}$, 50% larger than in Scenario 1. Although the evaporation rate in Scenario 2 is smaller, the buoyancy driven flow is stronger because of the larger vapour height. Additionally, Figure 5.5a shows that the vapour temperature at the roof is 33.2 K hotter than at the vapour-liquid interface. The difference between the maximum vapour temperature and the saturation temperature of the cryogen is defined as the maximum vapour superheating, $\Delta T_{\text{V,sh}} = \max\,(T_{\text{V}} - T_{\text{L}})$. In Scenario 2, the maximum vapour superheating is 13 times larger than the superheating of 2.6K observed in Scenario 1.

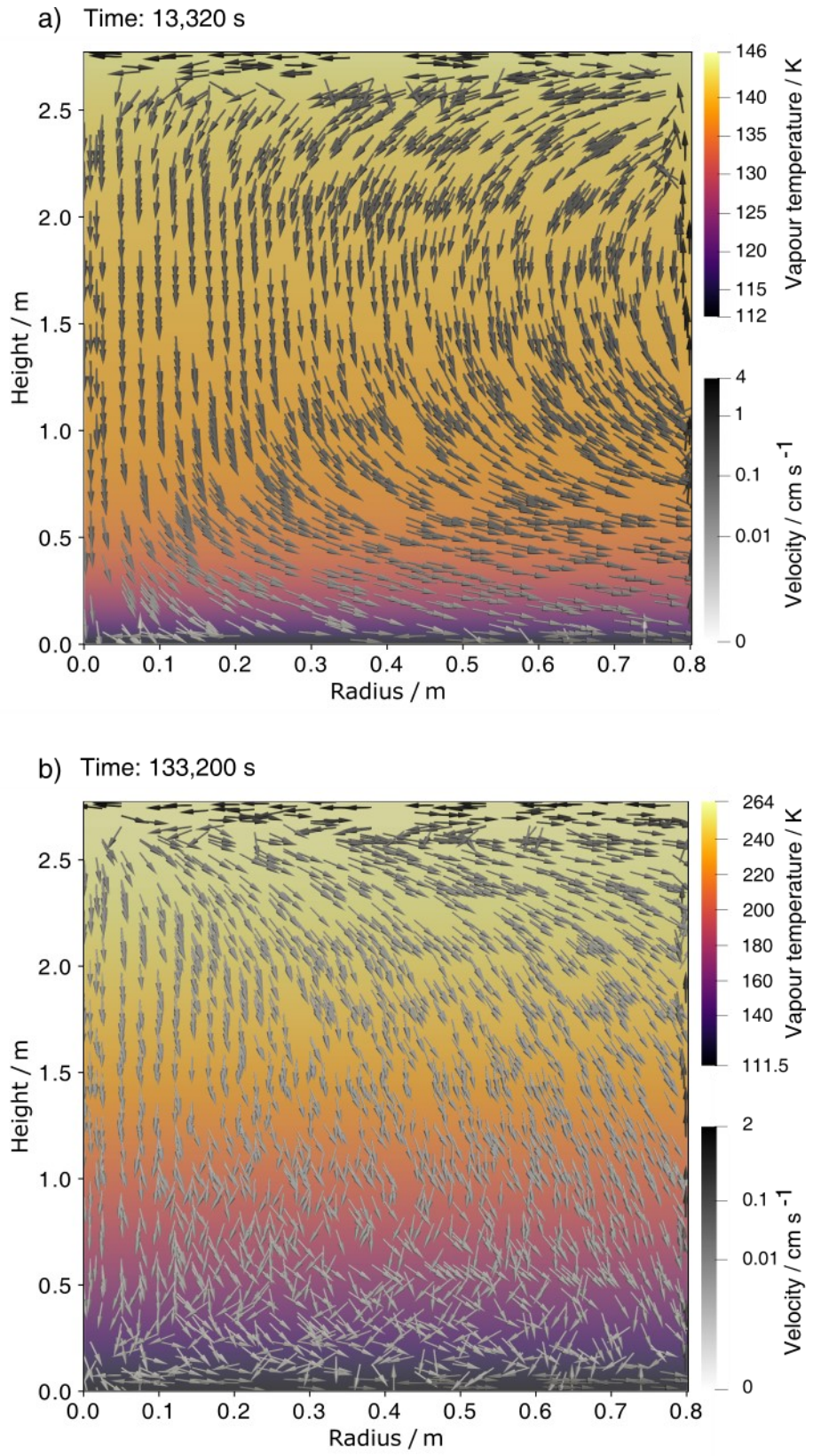

Figure 5.5: Velocity glyphs and temperature profiles in the vapour phase for Scenario S2. This scenario corresponds to the evaporation or pure methane in an 8 m³ storage tank filled to 30% of its capacity. The subfigures depict the profiles after: (a) t = 13,320 s (t^*_{trans} = 0.1) and (b) t = 133,200 s (t^*_{trans} = 1) the beginning of the evaporation. The log scale of the velocities hides the overall upward flow produced by continuous evaporation and vapour removal.

Figure 5.5b shows the vapour temperature and velocity profiles at the pseudo-steady state (t = 133,200 s, $t^*_{\text{trans}} = 1$) for Scenario 2. A very large temperature gradient is observed, as well as a recirculation pattern that is qualitatively different from the pattern observed at $t^*_{\text{trans}} = 0.1$. At the region near the wall, the heated vapour ascends and then flows radially inwards through the region below the roof. As the vapour flow approaches the valve, the flow is partitioned, and a downward flow becomes dominant in the vapour bulk. At the vapour bulk, the difference in recirculation patterns between the transient and pseudo-steady state time steps is driven by the increase in the vertical temperature gradient. The vertical temperature gradient increases from 12.7 K m^{-1} at the transient timestamp to 56.5 K m^{-1} at the pseudo-steady state. At the pseudo-steady state, the magnitude of the temperature gradient is 2.1 times larger than in Scenario 1, see subsection 5.2.1. In contrast to Scenario 1, the larger vertical temperature gradient in Scenario 2 dampens the natural convection buoyancy driven flow more strongly. As a consequence, the vapour bulk flow structure changes more noticeably between the transient and pseudo-steady state timestamps.

With the establishment of thermal stratification at the pseudo-steady state, the maximum velocities near the wall decrease to 0.3 cm s^{-1}, see Figure 5.5b. A thin boundary layer is observed in the near wall region. This boundary layer interacts strongly with the recirculating currents in the vapour bulk near the contact point between the wall and interface. The interaction between these two currents produces the emergence of a new recirculating current above the vapour-liquid interface, see the Figure 5.5b. This recirculating current above the interface was not observed in the high liquid filling case, see Figure 5.1b. The influence of the recirculating current on vapour to liquid heat transfer rates will be further explored in sections 5.2.4 and 5.2.5.

Figure 5.6 shows the vapour temperature predicted by the vapour-CFD and isobaric 1-D models as a function of height at three different times for Scenario 2. At the vapour liquid interface, both models show a good agreement with the vapour-CFD model predicting a slightly lower vertical temperature gradient. In contrast, in the region far above the interface, z > 1.5 m, the vapour-CFD model predicts a higher vapour temperature gradient. In this region, the vapour temperature is always higher in the CFD model as a consequence of the stronger recirculation driven by natural convection.

This leads to a more efficient heat transfer in the vertical direction than the results produced by the vapour- 1-D model. This deviation is expected as in the isobaric 1-D model, the influence of natural convection on vapour velocity is not explicitly modelled. Instead, the advective evaporative flow is assumed to be spatially homogeneous and a function of the evaporation rate only, see Eq. (3.19).

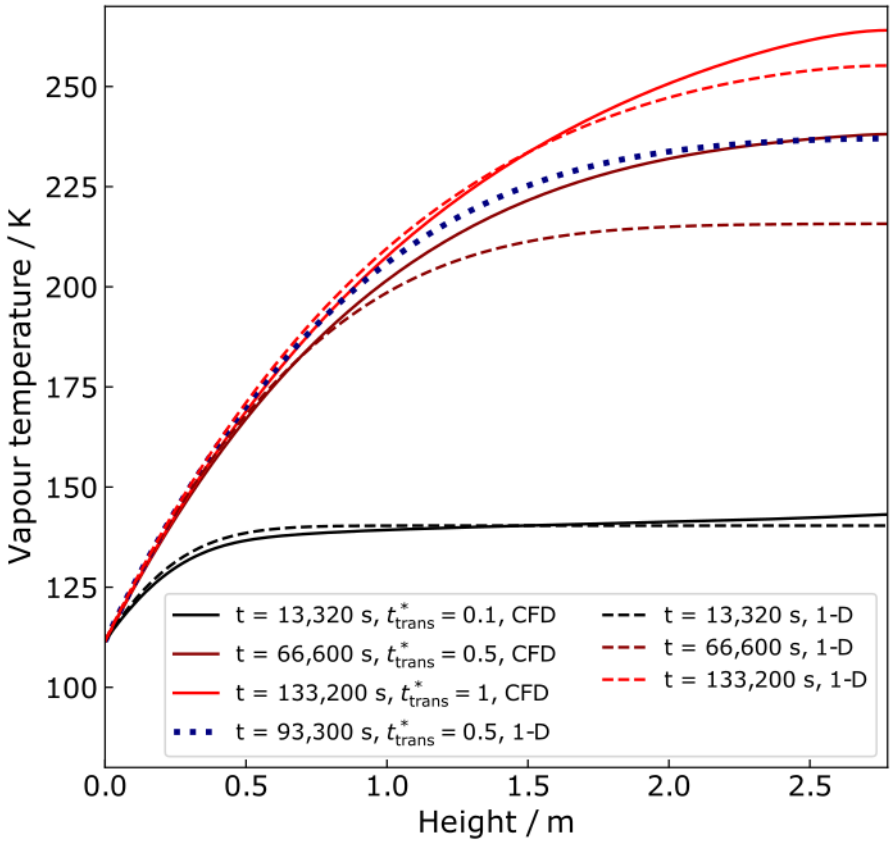

Figure 5.6: Vapour temperature profiles as a function of height for Scenario S2. The profiles are sampled at the midpoint between the tank axis and the wall, $r = R_T/2$, for the evaporation of pure methane in an 8 m³ storage tank filled to 30% of its capacity predicted by the vapour-CFD model and the isobaric 1-D model.

The maximum difference on vapour temperatures predicted by the vapour-CFD and isobaric 1-D models is observed at t = 66,600 s ($t^*_{trans} = 0.5$), see Figure 5.6. The agreement between the models improves when the CFD model reaches its pseudo-steady state. The temperature differences between the models are much larger than for Scenario 1, see Figure 5.3, as a consequence of the larger vapour space. As the height of the vapour phase increase, the enhancement of vertical heat transfer produced by natural convection significantly impacts the duration of the transient period. In the vapour-CFD model, the pseudo-steady state is attained within 133,200 s compared to

186,600 s for the isobaric 1-D model. Hence, for lower fillings the assumption of instantaneous radial heat transfer embodied in the isobaric 1-D model is less relevant for the onset of the pseudo-steady state. Instead, natural convection in the vapour bulk dominates the duration the transient period.

Figure 5.6 also displays the temperature profile predicted by the isobaric 1-D model at an additional timestamp, t = 93,300 s. This time corresponds to $t^*_{\text{trans}} = 0.5$ using the transient period of the vapour 1-D-model, $\tau_{1-\text{D}}$. The temperature profile is in very good agreement with the temperature profile predicted by the vapour-CFD model at the same transient dimensionless time. This good agreement demonstrates that the dynamics of vapour heating scale with the duration of the transient period. Figure 5.7 illustrates the average and BOG temperatures as a function of time, confirming that the vapour-CFD model predicts a faster vapour heating. The maximum temperature difference between the models is observed at approximately t = 66,660 s, in line with the results shown in Figure 5.6. As time progresses, the average vapour temperature and BOG temperature predicted by both models converge. The convergence confirm that the isobaric 1-D model accurately predicts vapour temperature profiles at the pseudo-steady state.

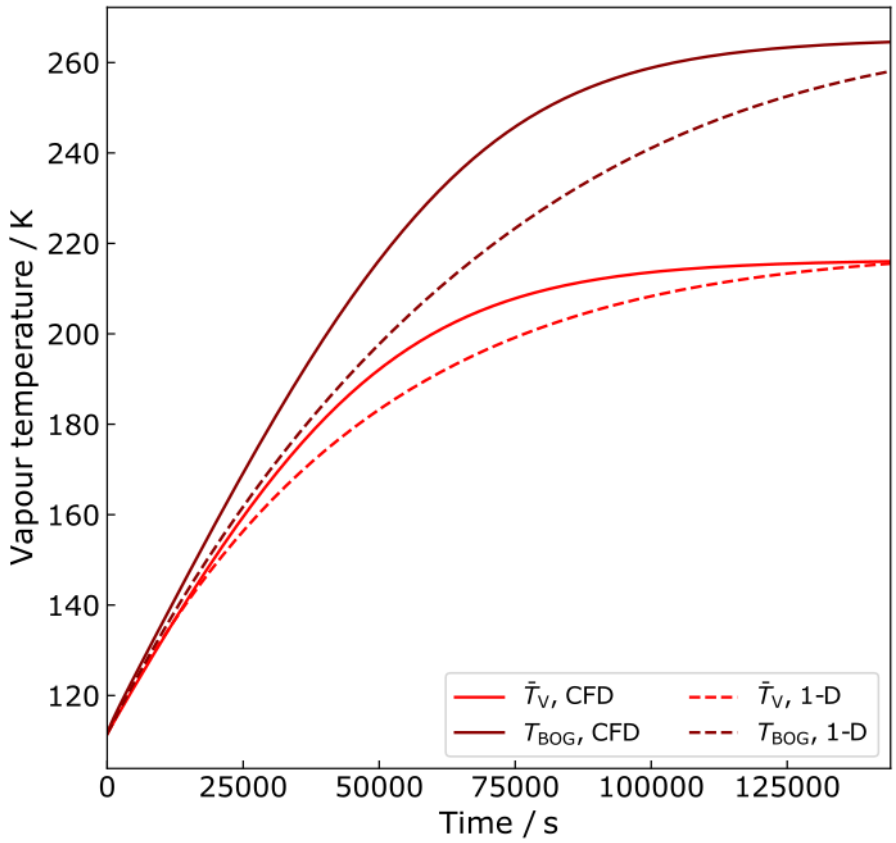

Figure 5.7: Comparison of average vapour temperature and BOG temperature for Scenario S2. This scenario consists of the evaporation of pure methane in an 8 m³ storage tank filled to 30% of its capacity. The trends show the profiles predicted by the vapour-CFD model and the isobaric 1-D model.

5.2.3 Temperature and velocity profiles in Scenario 3 (S3)

The third scenario considers the isobaric evaporation of pure methane in an 80 m³ medium-sized storage tank (L = 12.5 m, R_T = 1.425 m) filled to 97% of its capacity. Figure 5.8 illustrates the vapour velocity and temperature profiles produced by the vapour-CFD for this scenario. Figure 5.8a shows that at the beginning of the transient period (t = 1,080 s, t^*_{trans} = 0.1), the vertical temperature gradient is dominant. The structure of this temperature profile is similar to the profile observed in Scenario 1, see Figure 5.1a. In contrast, the velocity profile is slightly different. In Scenario 3, two stages of recirculation are observed below the roof, in addition to a stronger downward flow in the vapour bulk. The maximum vapour velocities close to the wall are of the order of 3 cm s $^{-1}$, 50% higher than those observed in Scenario 1. Higher near-wall velocities are expected as a consequence of a 3.2 times larger vapour height. A larger vapour height results in a higher buoyant force, as it was observed in Scenario 2, see subsection 5.2.2.

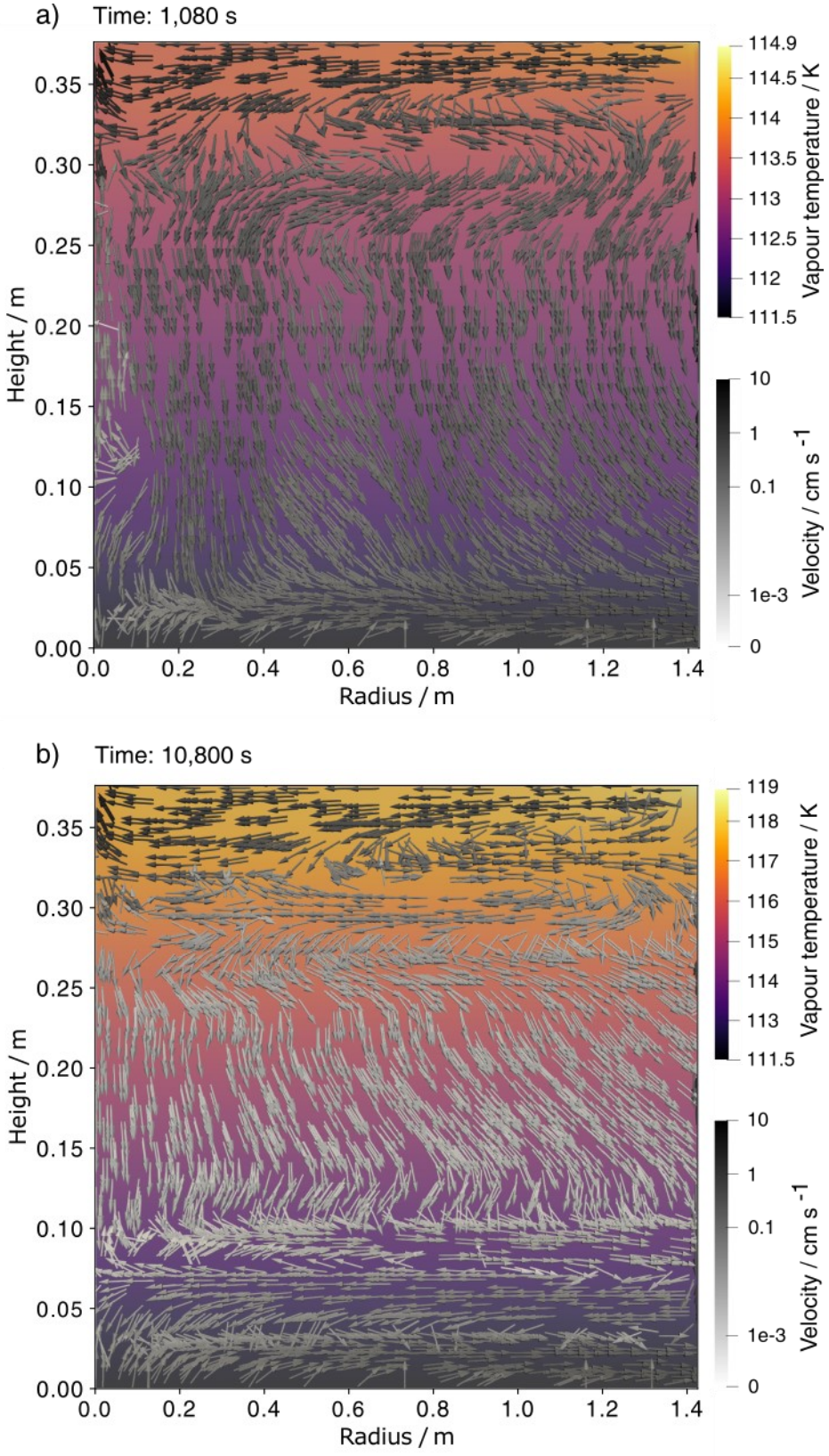

Figure 5.8: Velocity glyphs and temperature profiles in the vapour phase during the evaporation or pure methane in an 80 m³ storage tank filled to 97% of its capacity. Subfigures (a) and (b) represent the profiles after 1,080 s (t^*_{trans} = 0.1) and 10,800 s (t^*_{trans} = 1) the beginning of the evaporation, respectively.

Figure 5.8b shows that at the onset of the pseudo-steady state (t = 10,800 s, $t^*_{\text{trans}} = 0.1$) an additional recirculating flow structure emerges above the interface. This new structure, located at 0.03 m ≤ z ≤ 0.1 m, is not observed in Scenario 1, see Figure 5.1b. The maximum near wall velocity decreases from 3 to 1.5 cm s^{-1} with the onset of the pseudo-steady state. This decrease is a consequence of the establishment of the vertical temperature gradient, similarly to what was observed for Scenario 1, see Figure 5.1.

For the 80 m^3 tank of Scenario 3, both vapour-CFD and isobaric 1-D models predict temperature profiles of a similar shape as for Scenario 1. For the sake of brevity, only the main findings are highlighted. Both models predict an average vapour temperature and BOG temperature within 0.1 K of each other. The small difference is within the range of the numerical discretization error, which demonstrates that the agreement between the models for Scenario 3 is excellent. The transient period for the vapour-CFD model was 10,200 s, 11% longer than the transient period for the isobaric 1-D model, 9,200 s. The 1-D model underprediction of the transient period contrasts to what was observed for Scenario 2. In Scenario 3, the assumption of instantaneous radial heat transfer in the 1-D model is more relevant. This is a consequence of the larger radius of the 80 m^3 storage tank, that causes a longer heat dissipation in the radial direction. This longer heat dissipation dominates natural convection in predicting the onset of the pseudo-steady state. In Scenario 3, natural convection in the vapour bulk is significantly weaker than in Scenario 2 owing to a vapour height 7.4 times smaller.

In all scenarios, the effect of turbulence in the vapour bulk and close to the interface does not enhance heat transfer significantly ($k_{\text{V,t}}/k_{\text{V,eff}} \ll 1$). This is a consequence of low velocities and low velocity gradients in the vapour bulk. Although turbulence increases heat transfer within the wall and roof boundary layers (10 < $k_{\text{V,t}}/k_{\text{V,eff}}$ < 40), these regions constitute only small fraction of the vapour. The enhanced mixing below the roof produces a slightly higher BOG temperature in the vapour-CFD model than in the isobaric 1-D model. At the pseudo-steady state, the temperature difference is negligible (< 0.1 K) for high liquid fillings and very small (5 K) for low liquid fillings. This confirms that the use of an effective, advective velocity in the isobaric 1-D model allows a good prediction of vapour temperatures.

5.2.4 Vapour to liquid heat transfer rates

Based on the results presented in sections 5.2.1-5.2.3 one can conclude that below the roof boundary layer, the variation of vapour temperature with radius is small. This demonstrated the dominance of the vertical temperature gradient in the vapour. The vertical temperature gradient at the vapour-liquid interface determines the vapour to liquid heat transfer rate in both vapour-CFD and isobaric 1-D models. Figure 5.9 shows the interfacial heat flux $q_{\mathrm{VL}} = k_{\mathrm{V}} \partial T_{\mathrm{V}} / \partial z|_{z=0}$ as a function of dimensionless radius $\eta = r/R_{\mathrm{T}}$ predicted by the vapour-CFD model. The heat flux is sampled at the middle of the transient period for each scenario. In all scenarios, the heat flux increases with radius as a consequence of the buoyant boundary layer near the wall. The maximum heat flux occurs at the contact point between the interface and the tank wall, $r = R_{\mathrm{T}}$, This is expected as the maximum vertical temperature gradient is observed in the wall boundary layer.

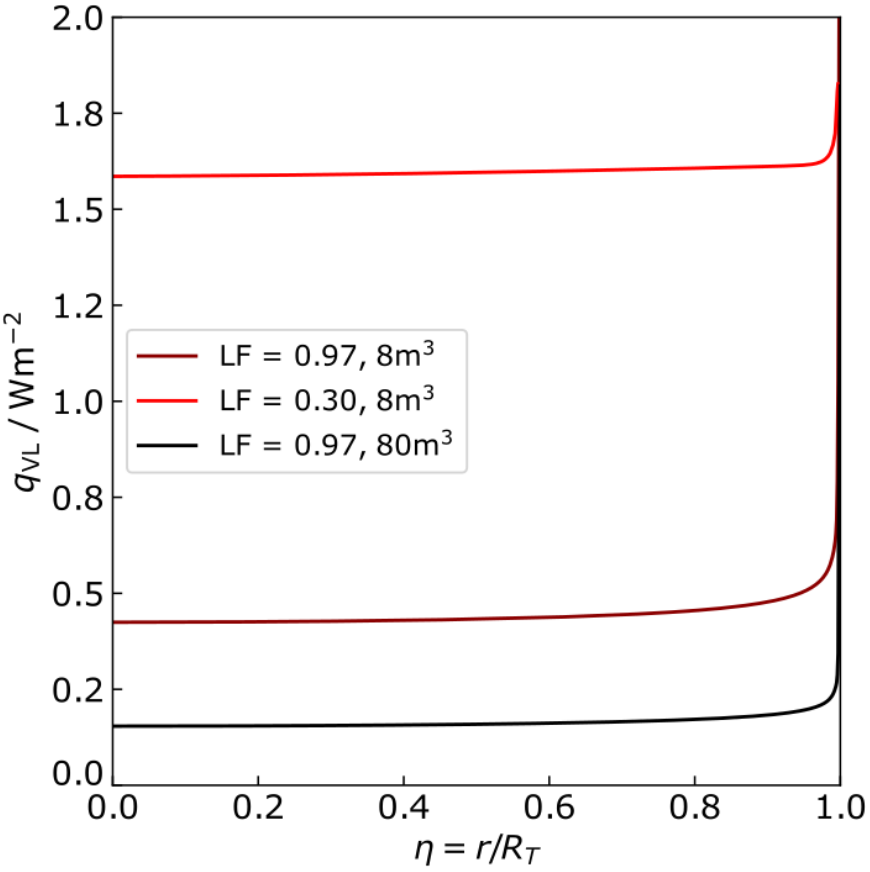

Figure 5.9: Vapour to liquid heat flux (q_{VL}) as a function of dimensionless radius. The fluxes are sampled at the midpoint of the dimensionless transient period, $t^*_{\mathrm{trans}} = 0.5$, for the evaporation of pure methane in three different scenarios: S1 (V_{T} = 8 m³, LF = 0.97), S2 (V_{T} = 8 m³, LF = 0.30) and S3 (V_{T} = 80 m³, LF = 0.97). V_{T} is the storage tank volume and LF the initial liquid filling.

For Scenarios 1 and 3, q_{VL} at the bottom of the wall boundary layer is up to four times higher than in the vapour bulk. In contrast, for Scenario 2 q_{VL} in the boundary layer is only at most 25% higher than in the vapour bulk. In Scenario 2, the vapour vigorously mixes above the interface, see Figure 5.5, while this is not observed in the high liquid filling scenarios, see Figure 5.1 and Figure 5.8. As a consequence, vapour temperature and its gradient above the interface are more radially homogeneous in Scenario 2 than in Scenarios 1 and 3. The lower variation of the vertical temperature gradient in Scenario 2 explains the lower radial variation of q_{VL}. Nevertheless, in all scenarios the radial variation of q_{VL} is confined to the boundary layer.

To further understand the dynamics of the vapour to liquid heat transfer rate, the spatially averaged vapour to liquid heat flux $\bar{q}_{\mathrm{VL}} = \dot{Q}_{\mathrm{VL}}/A_{\mathrm{T}}$ is examined. Figure 5.10 shows $\bar{q}_{\mathrm{VL}}$ as a function of dimensionless transient time using the vapour-CFD and isobaric 1-D models for all scenarios. Both models predict an increase of $\bar{q}_{\mathrm{VL}}$ with time as the system approaches the pseudo-steady state. The vapour-CFD model predicts a short period of slow increase in $\bar{q}_{\mathrm{VL}}$ at the beginning of the evaporation ($t^*_{\mathrm{trans}} \to 0$) for all scenarios. This period is also present in the first 360 s ($t^*_{\mathrm{trans}} = 0.003$) of the low liquid filling case. However, the period it is not visible in Figure 5.10, owing to the scale used. The period of slow increase in $\bar{q}_{\mathrm{VL}}$ is a consequence of time lag in energy distribution in the radial direction. This produces lower vertical temperature gradients in the beginning of the evaporation, until the vertical temperature gradient establishes in the vapour bulk.

In all scenarios, the isobaric 1-D model predicts slightly higher $\bar{q}_{\mathrm{VL}}$ than the vapour-CFD model, see Figure 5.10. The main differences are a consequence of the time lag in the radial direction at the beginning of the evaporation. As the system approaches to its pseudo-steady state, the agreement improves. At the pseudo-steady state, the differences in $\bar{q}_{\mathrm{VL}}$ predicted by both models are small for all scenarios (S1: 2.8%, S2:3.0%, S3: 7.7%): The overprediction of $\bar{q}_{\mathrm{VL}}$ by the isobaric 1-D model is a consequence of higher temperature gradients at the vapour-liquid interface. These overpredictions arise owing to a slightly less efficient heat transfer in the isobaric 1-D model, as discussed in sections 5.2.1-5.2.3.

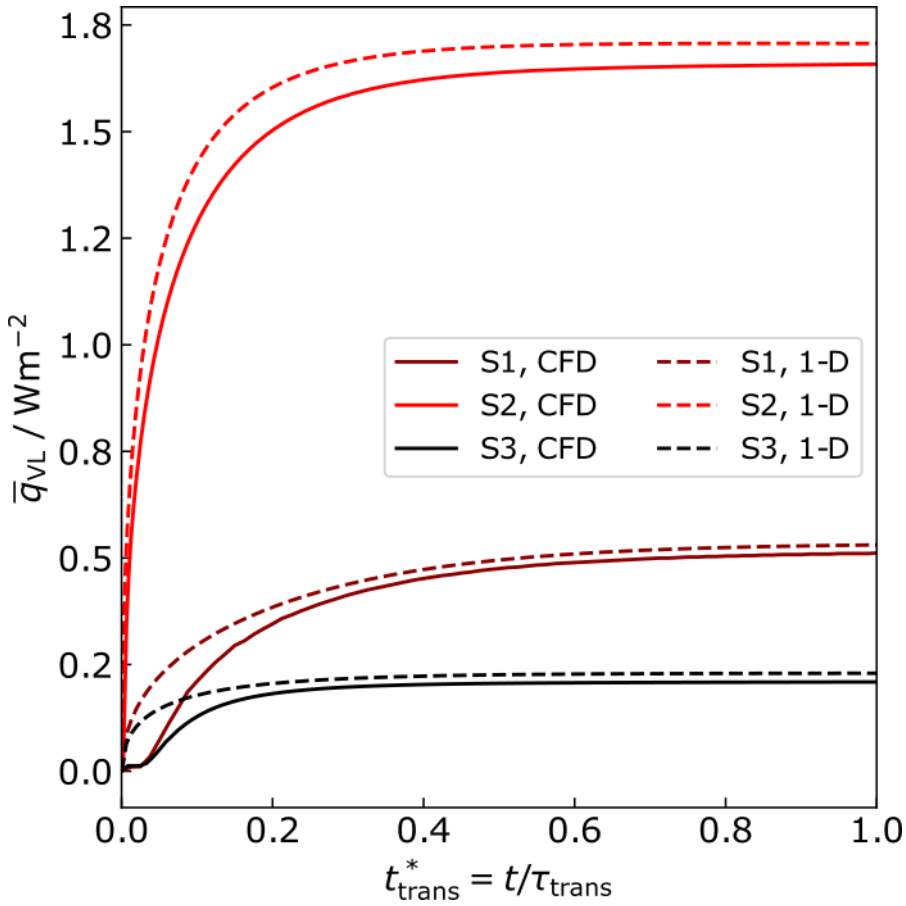

Figure 5.10: Spatially averaged vapour to liquid heat flux, $\bar{q}_{VL} = \dot{Q}_{VL}/A_T$, as a function of the transient dimensionless time for the evaporation of pure methane. Three different scenarios are displayed: S1 (V_T= 8 m³, LF = 0.97), S2 (V_T= 8 m³, LF = 0.30) and S3 (V_T= 80 m³, LF = 0.97), where V_T is the storage tank volume and LF the initial liquid filling. The vapour phase computational fluid dynamics model (CFD) and vapour phase one-dimensional model (1-D) are compared.

5.2.5 Evaporation and BOG rates

Figure 5.11 shows the evaporation rate as a function of transient dimensionless time predicted by both the vapour-CFD and isobaric 1-D models. For all scenarios, the agreement is excellent between the models with a maximum deviation (MD) lower than 0.2%. This good agreement is expected because evaporation rates are driven by the total heat ingress, see Eqs. (3.2) – (3.6). In all scenarios, more than 97% of the total heat ingress is liquid heat ingress. The liquid heat ingress is calculated by the same method in both vapour-CFD and isobaric 1-D models. In consequence, the differences in evaporation rates between both models are explained by the differences in $\dot{Q}_{VL}$ between both models. As the differences in $\dot{Q}_{VL}$ are lower than 10%, see Figure 5.10, they have a

minimal effect on the evaporation rates. Consequently, the isobaric 1-D model accurately predicts evaporation rates.

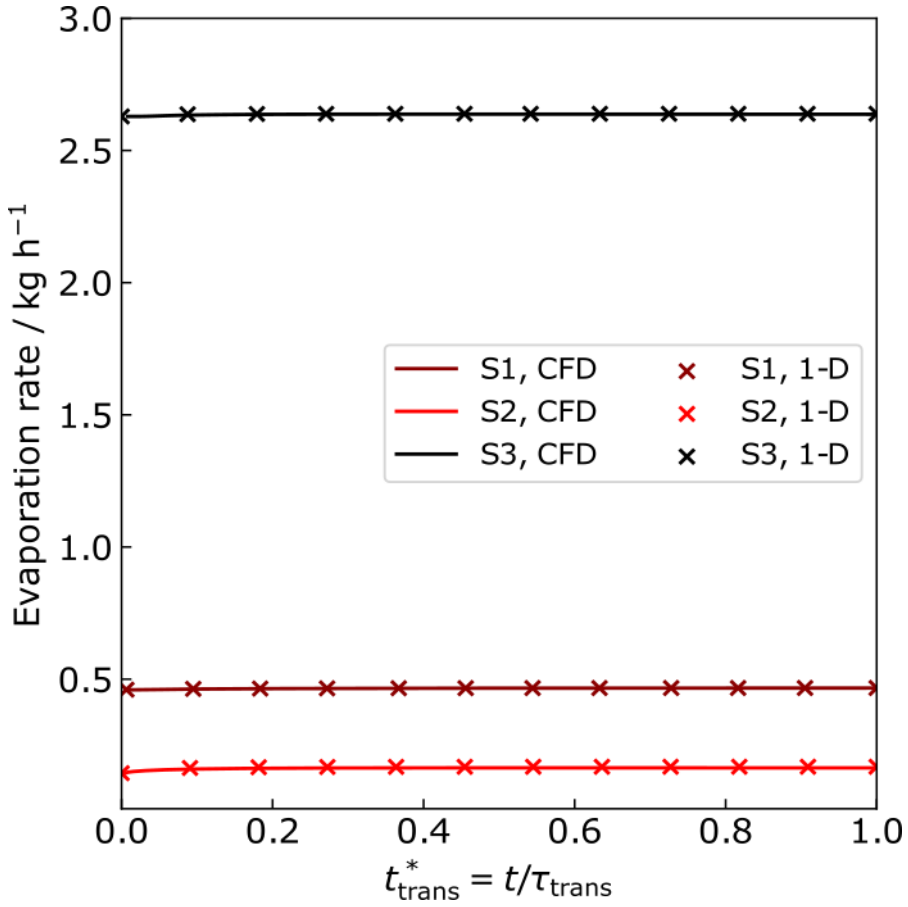

Figure 5.11: Evaporation rate as a function of transient dimensionless time during the isobaric evaporation of methane. Three different scenarios are depicted: S1 (V_T = 8 m^3, LF = 0.97), S2 (V_T = 8 m^3, LF = 0.30) and S3 (V_T = 80 m^3, LF = 0.97). V_T is the storage tank volume and LF the initial liquid filling. The vapour phase computational fluid dynamics model (CFD) and isobaric 1-D model (1-D) are compared.

Figure 5.12 shows the BOG rate as a function of transient dimensionless time predicted by both the vapour-CFD and isobaric 1-D models. An excellent agreement is observed between the two models. For the high liquid fillings, Scenarios 1 and 3, the isobaric 1-D model slightly overpredicts the vapour-CFD BOG rates by at most 0.7%. In contrast, for the low liquid filling Scenario 2, a more significant underprediction is observed during a finite time period. To understand the difference in BOG dynamics between low and high liquid fillings, the definition of BOG rate in Eq. (3.11) is examined.

The vapour-CFD model always predicts a slightly smaller evaporation rate, $\dot{B}_L$, and vapour accumulation, $\bar{\rho}_V dV_V/dt$, than the 1-D model. However, when it comes to vapour thermal expansion, $-V_V d\bar{\rho}_V/dt$, term, the vapour-CFD model produces both higher and lower predictions.

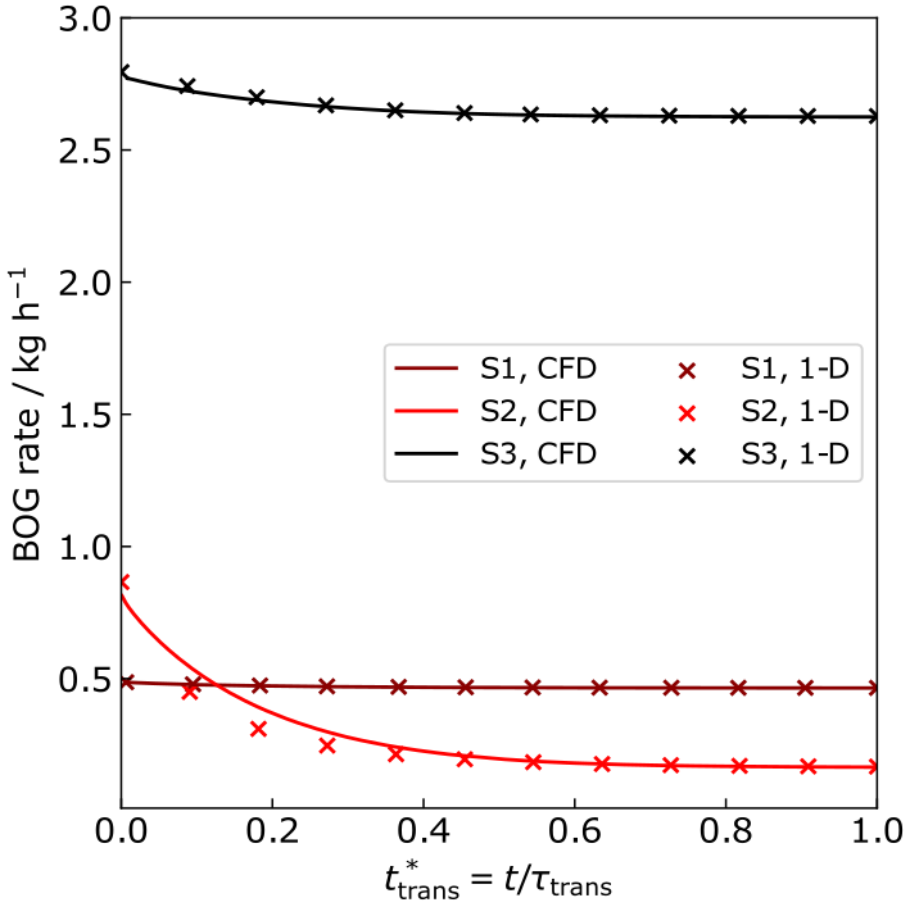

Figure 5.12: BOG rate as a function of transient dimensionless time during the isobaric evaporation of methane. Three different scenarios are depicted: S1 (V_T= 8 m³, LF = 0.97), S2(V_T= 8 m³, LF = 0.30) and S3 (V_T= 80 m³, LF = 0.97). V_T is the storage tank volume and LF the initial liquid filling. The vapour phase computational fluid dynamics model (CFD) and isobaric 1-D model (1-D) are compared.

For an ideal gas, the vapour thermal expansion is simplified to $-V_V\, d\bar{\rho}_V/dt = V_V R^{-1} \bar{T}_V^{-2} P\, d\bar{T}_V/dt$. In all scenarios, pressure (P) is constant and the vapour volume (V_V) varies less than 0.01% between the models. Hence, the vapour thermal expansion is governed by the quantity $\bar{T}_V^{-2}\, d\bar{T}_V/dt$. For the high liquid filling scenarios, the vapour-CFD model predicts up to 20% smaller $\bar{T}_V^{-2}\, d\bar{T}_V/dt$ than the 1-D model. This is expected as the vapour-CFD model predicts temperatures that increase more slowly and are

higher than the predictions of the isobaric 1-D model, see Figure 5.4. The lower $\bar{T}_V^{-2}\, d\bar{T}_V/dt$ predicted by the vapour-CFD model explains the lower BOG rates throughout the evaporation in the high liquid filling scenarios.

In contrast to Scenarios 1 and 3, in Scenario 2 there is a larger variation of $\bar{T}_V^{-2}\, d\bar{T}_V/dt$ with time. In particular, for $0.03 \leq t^*_{trans} < 0.4$, the vapour-CFD model predicts up to 20% larger $\bar{T}_V^{-2}\, d\bar{T}_V/dt$ term. This is a consequence of a more rapid vapour heating predicted by the CFD model for Scenario 2, see Figure 5.7. The higher $\bar{T}_V^{-2}\, d\bar{T}_V/dt$ predicted by the vapour-CFD model during this period explains the larger BOG predictions, compared with the isobaric 1-D model. Before and after this period, $\bar{T}_V^{-2}\, d\bar{T}_V/dt$ predicted by the vapour-CFD model is smaller than the isobaric 1-D-model, which produces smaller BOG rates. As the system approaches to its pseudo-steady state, the vapour thermal expansion tends to zero and both models show an excellent agreement (MD<0.1%).

5.2.6 Influence of turbulence modelling

The sensitivity of the vapour-CFD results to the choice of turbulence model is evaluated by its influence on the vapour temperature. Figure 5.13 shows the vertical temperature profiles obtained using LES and k-ω-SST turbulence models for Scenarios 1 and 2. The profiles are sampled at the beginning of the transient period , $t^*_{trans} = 0.1$, and at the pseudo-steady state, $t^*_{trans} = 1$. Figure 5.13a shows that for Scenario 1, the difference between vapour temperatures using two different turbulence sub models is negligible (MD < 0.2%). A similar agreement was observed for Scenario 3 (MD < 0.5%). In contrast, for Scenario 2 the difference between the calculated vapour temperatures using two different turbulence sub-models is larger, see Figure 5.13b. In particular, at the pseudo-steady state the differences are up to 26 K. Although the k-ω-SST turbulence sub model predicts a $\dot{Q}_{VL}$ up to 6% higher than LES, $\dot{Q}_{VL}/\dot{Q}_{L,tot} < 3\%$ for all scenarios. This led to evaporation rates which differ less than 0.2% between the two turbulence sub models. Therefore, while T_{BOG} is sensitive to the choice of the turbulence sub-model in low liquid filling scenarios, BOG and evaporation rates are not.

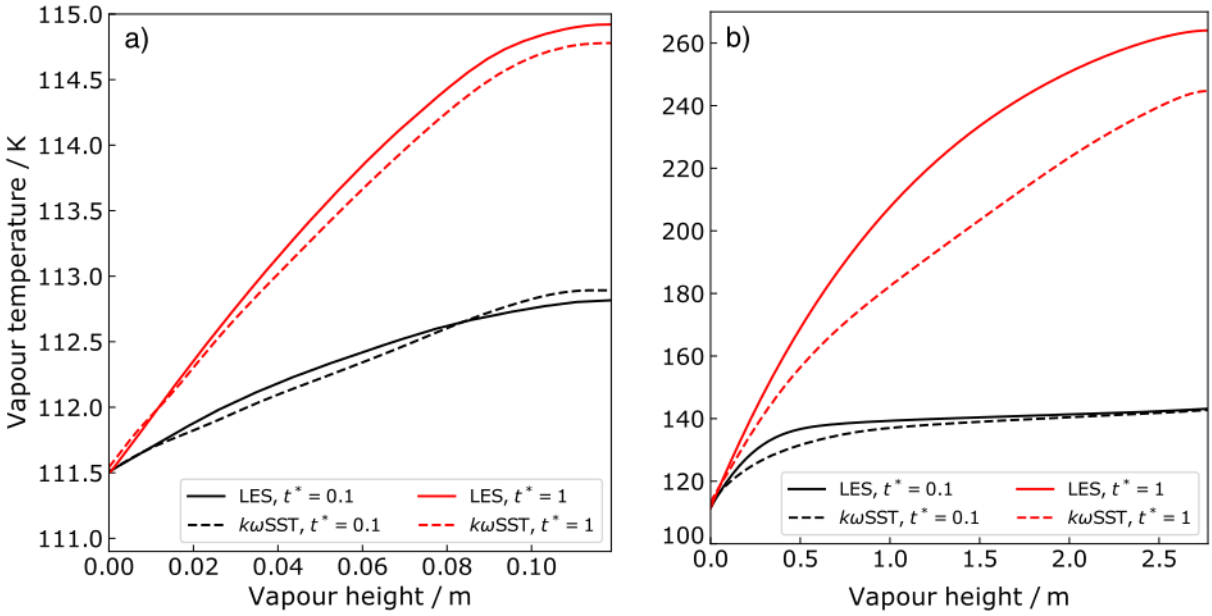

Figure 5.13: Comparison of vapour temperature profiles using large eddy simulation (LES) and k-ω-SST turbulence models. For the LES model, the Smagorinsky sub-grid scale modelling with $C_S = 0.21$ has been selected. Vapour temperatures are sampled at the midpoint between the tank axis and the wall, $r = R_T/2$, at two different transient dimensionless times for the evaporation of pure methane. Two scenarios are displayed for an 8 m³ storage tank initially filled to (a) 97% and (b) 30% of its capacity.

5.2.7 Summary of findings

- Although a complex flow pattern emerges in the vapour, the temperature profile at the pseudo-steady state can be predicted by assuming 1-D advective flow.
- A short transient period is observed at the beginning of the evaporation.
- For low liquid fillings, the isobaric 1-D model overestimates the duration of the transient period.
- Vertical thermal stratification in the vapour dampens buoyant forces, reducing the magnitude of natural convection.
- Vapour temperature increases monotonically with vapour height
- Vapour temperature is nearly spatially homogeneous in the radial direction except near the tank wall, which increases rapidly within the thermal boundary layer.
- Turbulence does not significantly enhance heat transfer in the vapour bulk.
- The choice of turbulence sub-models has a small effect on vapour temperatures and a negligible effect on evaporation and BOG rates.

5.3 Simulations of LNG weathering using the non-equilibrium model

In section 5.2, it was demonstrated that the isobaric 1-D model accurately predicts vapour phase heat transfer during the storage of methane in small and medium storage tanks. For large storage tanks and storage periods typical of industrial applications, performing CFD simulations of is not feasible. In this section, the isobaric 1-D and weathering models developed in sections 3.3 and 3.5, respectively, are used to simulate the weathering of LNG in a 165,000 m^3 cylindrical storage tank. A constant air temperature was assumed (T_{air} = 298.15 K), which yields the overall heat transfer coefficients $U_L = U_V$ = 0.038 Wm^{2}K^{-1}. The same tank was employed as in the weathering models of Migliore et al [3, 10]. This allows an easy comparison between the results produced by the isobaric 1-D model developed in this thesis its predecessor. A storage period of only 52 weeks will be considered, as this is a limit of industrial use. The full evaporation will be investigated in section 5.4 for small, medium and large tanks.

In large tanks, the transient period is expected to be longer than for small and medium tanks owing to larger vapour volumes. Additionally, owing to the larger diameter of the large tank, the wall heating source term and advective velocity are expected to be smaller, see and Eqs. (3.18) and (4.2). In subsections 5.3.1 and 5.3.2, the temperature profiles and heat transfer rates in the vapour phase are presented for the evaporation of pure methane. In subsection 5.3.3, an in-depth analysis of the transient period is presented at the beginning of the evaporation is presented. In this section, emphasis is given to the evolution of heat transfer rates, thermodynamic properties and process variables. In subsection 5.3.4, the non-equilibrium weathering model [2] developed in section 3.4 is used to simulate the weathering of four different LNG and compare BOG rates. The industrial significance of the weathering and isobaric 1-D models is given in subsection 5.3.5. Finally, a summary of findings is provided in subsection 5.3.6.

5.3.1 Vapour temperature profiles in Scenario 4 (S4)

Firstly, the temperature profiles in the vapour phase for the evaporation of methane in a 165,000 storage tank filled at 97% of its capacity. This scenario will be

defined as Scenario 4 in the remaining of this subsection. As discussed in subsection 5.2, modelling LNG as pure methane is an excellent approximation for non-nitrogen containing LNG. For non-nitrogen containing LNG, the vapour phase primarily consists of methane until the last stages of the evaporation period [11]. Figure 5.14 depicts the temperature profiles as a function of the vapour height for five evaporation periods representative of common industrial scenarios, see Table 5.2.

Table 5.2: Evaporation periods and dimensionless times for the evaporation of methane in a 165,000 storage tank filled at 97% of its capacity.

Evaporation period	Dimensionless time t^*_{evap}
30 h	9×10^{-5}
13 w	0.008
26 w	0.016
39 w	0.024
52 w	0.032

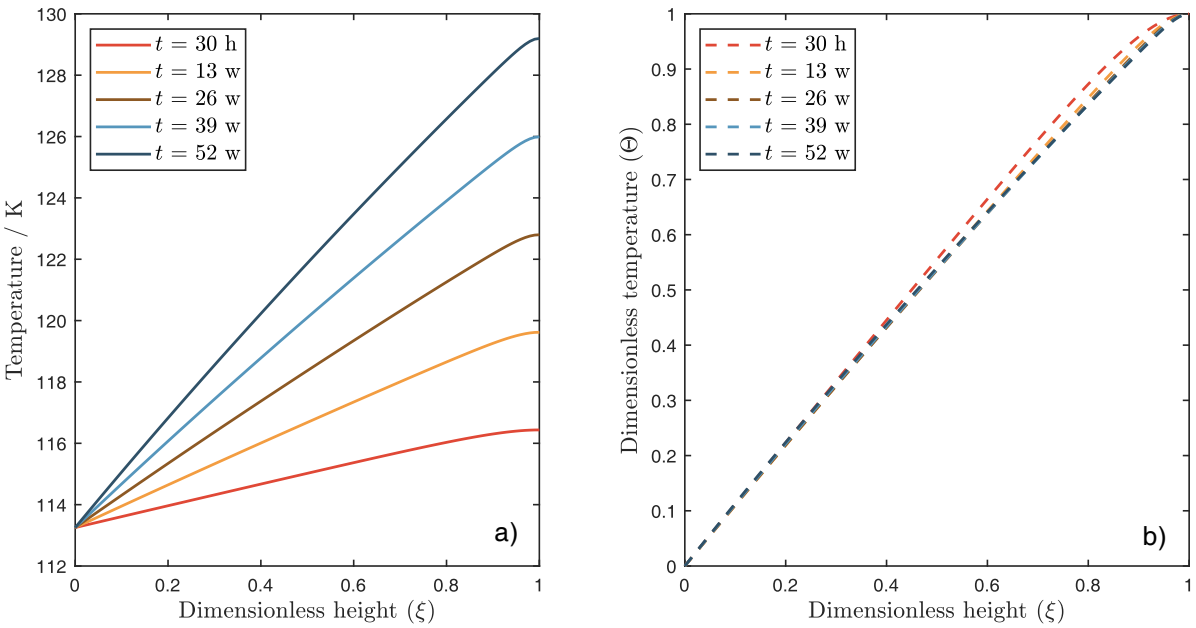

Figure 5.14: Vapour temperature profiles predicted by the non-equilibrium weathering model for the evaporation of methane in a 165,000 m³ storage tank initially filled at 97% of its capacity. Temperature is plotted against dimensionless height, $\xi = z/l_V$, where l_V represents the vapour height and z is the vertical coordinate. The profiles are displayed in dimensional form (a) and dimensionless form (b) at five different times from the beginning of the evaporation.

The temperature profiles predicted by the 1-D-weathering model show a nearly linear temperature profile in the whole vapour domain, see Figure 5.14a. As the evaporation progresses, the vapour temperature increases as a consequence of the

increase in heat transfer area owing to increasing vapour height. As the liquid level decreases, the vapour height increases from 1.1 m in the first week to 4.9 m in the last week of evaporation. It is worth noting that at timescales of the order of weeks, the liquid volume decreases noticeably for methane evaporation in a large tank. This contrasts with the short evaporation periods simulated for small and medium-scale tank in section 5.2, where the liquid volume decreased less than 0.1%.

To study the characteristics of the vapour temperature profiles independent of the scale, the following scaling was used to obtain the dimensionless height (ξ) and dimensionless temperature (Θ):

$$\xi = \frac{z}{l_V}, \tag{5.1}$$

$$\Theta = \frac{T_V(z) - T_L}{T_V(l_V) - T_L}. \tag{5.2}$$

Figure 5.14b illustrates the temperature profiles at the same time steps, but now in dimensionless space. As previously discussed in section 5.2, the new non-equilibrium weathering model shows that the vapour temperature profiles undergo a brief transient period. For the large storage tank considered for Scenario 4, the transient period lasted 12 h. This period is longer than the transient periods for the small (1.3 h) and medium-sized (3 h) tanks considered for Scenarios 1 and 3. These scenarios constitute a good base of comparison, as they comprise methane evaporation in tanks initially filled at 97% of their capacity, see subsections 5.2.1 - 5.2.3. Following the transient period, the vapour temperature profiles become quasi-linear for the whole evaporation period typical of industrial storage, $t^*_{evap} \approx 0.032$. This profile represents a pseudo-steady state similar to the steady state solution of the advection diffusion equation in the vapour phase, see Eq. (3.31). It is also observed that the dimensionless vertical temperature gradient, $\partial\Theta/\partial\xi$, is nearly constant for the duration of the evaporation.

Figure 5.15 illustrates the average vapour temperature, $\bar{T}_V$, and BOG temperature, T_{BOG}, as a function of evaporation time for Scenario 4. In the transient period at the beginning of the evaporation, both average and BOG temperature increase rapidly, relative to the 52 weeks of the full storage period. Following the transient period, $\bar{T}_V$, and BOG temperatures increases monotonically with following a nearly linear profile.

As the transient period is more relevant for large tanks, an in-depth analysis will be provided in subsection 5.3.4.

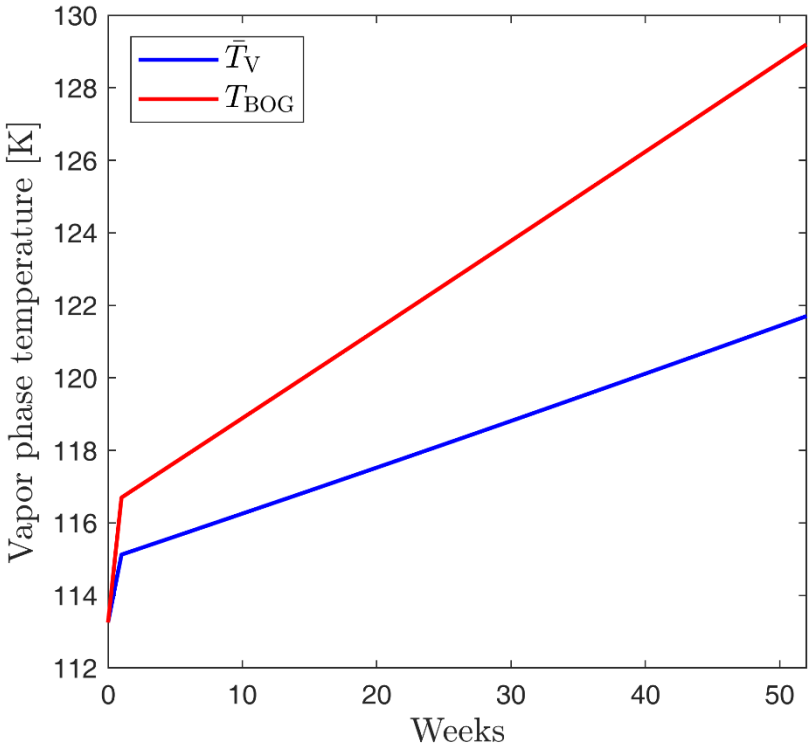

Figure 5.15: Average vapour temperature, $\bar{T}_V$, and boil-off gas temperature, T_{BOG}, during the evaporation of pure methane in a large 165,000 m³ storage tank. The trends correspond to the predictions obtained using the isobaric 1-D model for the storage tank initially filled at 97% of its capacity.

The CFD simulations in section 5.2 showed that the volume of methane in the storage tank had a pronounced effect on the evolution of temperature in vapour space. In what follows, the effect of initial liquid filling for methane evaporation in the large tank considered in Scenario 4 will be explored.

Figure 5.16a illustrates the vapour temperature profiles for four different initial liquid fillings (LF) after 1 and 52 weeks of evaporation. For the lowest liquid filling (LF = 30%), much higher average vapour and BOG temperatures were observed, the latter reaching 210 K after 52 weeks. For this scenario, the transient period was significantly longer ($\tau_{trans,30\%}$ = 11.5 days). This is mainly a consequence of two effects. First, the higher average vapour temperature decreases the heat flux through the vapour, represented as a source term in Eq. (3.18). Secondly, the average advective velocity is lower owing to a 69% lower liquid heat ingress, similarly to what has been observed in

subsection 5.2.2. For low liquid filling (LF = 0.30), the curvature of the temperature profiles for the large tank in smaller than for the small tank considered in Scenario 2, see subsection 5.2.2. This effect can be observed comparing the red dashed line in Figure 5.6 with the orange dashed line in Figure 5.16a.

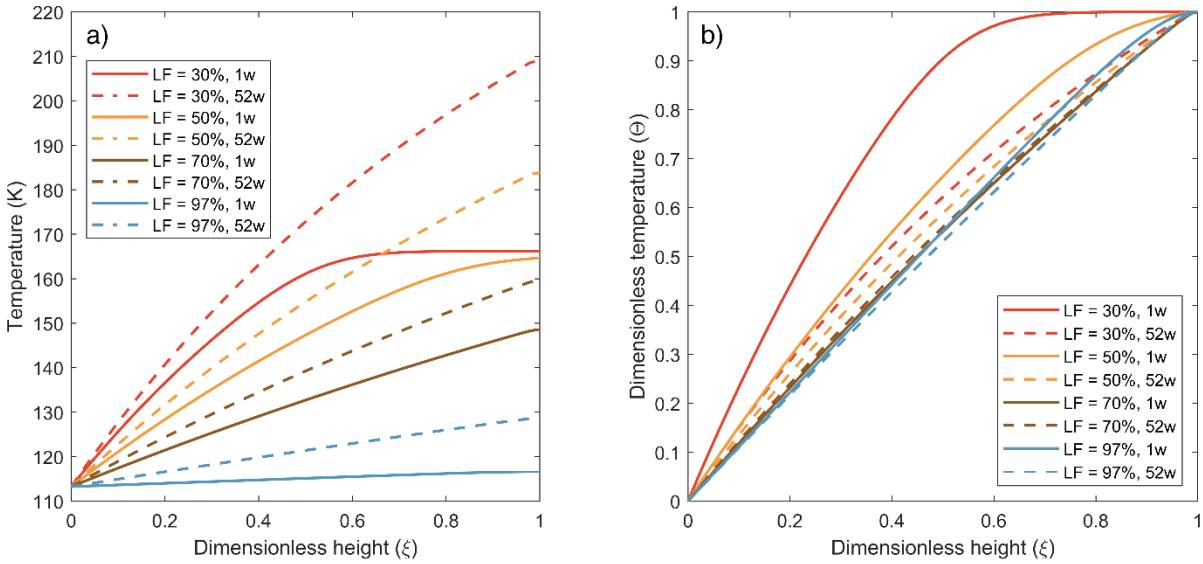

Figure 5.16: Vapour temperature profiles as a function of dimensionless height, $\xi = z/l_V$, for the evaporation of methane in a 165,000 m³ storage tank for different liquid fillings (LF). The profiles are displayed in dimensional form (a) and dimensionless form (b) after 1 and 52 weeks of evaporation.

There is very limited experimental data in open literature on the vapour temperature profile in industrially sized storage tanks. The available data [5],[12] is insufficient to perform a rigorous validation of the isobaric 1-D model for large storage tanks. Nevertheless, the existence of thermal stratification has been observed in a number of experiments across different scales, as discussed in subsection 2.1.1. Thus, owing to the lack of experimental data, the computational validation of the isobaric 1-D model [1] performed in section 5.2 constitutes the most rigorous validation up to date. For lab scale, experimental data of vapour temperature profiles is available [6, 7]. Thus, a comprehensive validation of the isobaric 1-D model against experiments will be presented in Chapter 8 for lab-scale storage tanks.

5.3.2 Heat transfer in the vapour phase in Scenario 4 (S4)

Figure 5.17 illustrates the evolution of the vapour heat ingress, $\dot{Q}_{V,in}$, and the vapour to liquid heat transfer rate, $\dot{Q}_{VL}$, for the evaporation of pure methane in a storage tank filled at 97% of its capacity. The vapour heat ingress increases with time because of an increase in the vapour area in contact with the wall as the evaporation progresses, see Eq. (3.7). On the other hand, $\dot{Q}_{VL}$ slowly increases from 175 W to 220 W (26%) after one year of evaporation, see Figure 5.17. The nearly constant $\dot{Q}_{VL}$ during the evaporation is a consequence of the rapid onset of a pseudo-steady state, as demonstrated in section 5.2. It is worth noting that the duration of the transient period is very short compared with respect to the total evaporation period, $\tau_{trans} \ll \tau_{evap}$. An analysis of the variation of $\dot{Q}_{VL}$ during the transient period will be discussed in subsection 5.3.3.

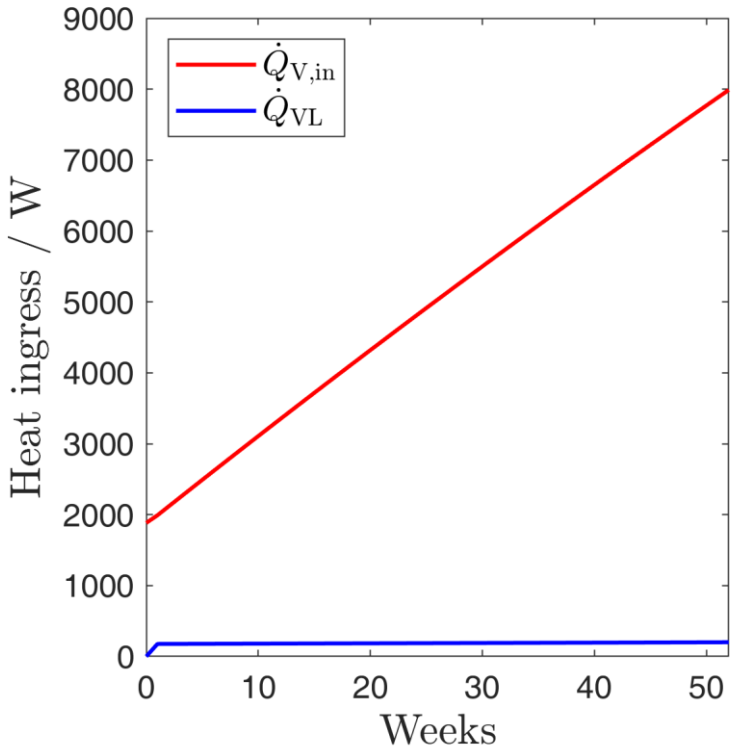

Figure 5.17: Heat ingress to the vapour, $\dot{Q}_{V,in}$, and vapour to liquid heat transfer rate, $\dot{Q}_{VL}$, predicted by the non-equilibrium weathering model. The model has been used to simulate the evaporation of pure methane in a large 165,000 m³ storage tank filled at 97% of its capacity.

The influence of the initial liquid filling (LF) on weathering has been assessed by the variation of $\dot{Q}_{V,in}$ and $\dot{Q}_{VL}$ with liquid filling. As expected, the heat ingress into the vapour, $\dot{Q}_{V,in}$, increases with decreasing LF because the vapour area in Eq. (3.7)

increases. However, as illustrated in Figure 5.17, the heat flux associated with the vapour heat ingress, $q_{V,in} = \dot{Q}_{V,in}$, decreases with LF. This is a direct consequence of the increase in average vapour temperatures with decreasing LF, see

Figure 5.16. The initial vapour to liquid heat transfer rate $\dot{Q}_{VL}$ increases with decreasing LF, from 0.175 kW at LF = 97% to 0.275 kW at LF 30%. This is direct consequence of the larger temperature gradients observed above the vapour-liquid interface for low liquid fillings, see Figure 5.16a. However, the observed 0.1 kW increase in $\dot{Q}_{VL}$ is negligible compared to the 41.7 kW decrease in the liquid heat ingress, $\dot{Q}_{L,in}$, as the evaporation progresses. The decrease $\dot{Q}_{L,in}$ is a consequence of the decrease in liquid area in contact with the walls with decreasing liquid filling, see Eqs. (3.7) – (3.8). Overall, a lower liquid filling results in a lower total heat ingress to the liquid. see Eq. (3.2).

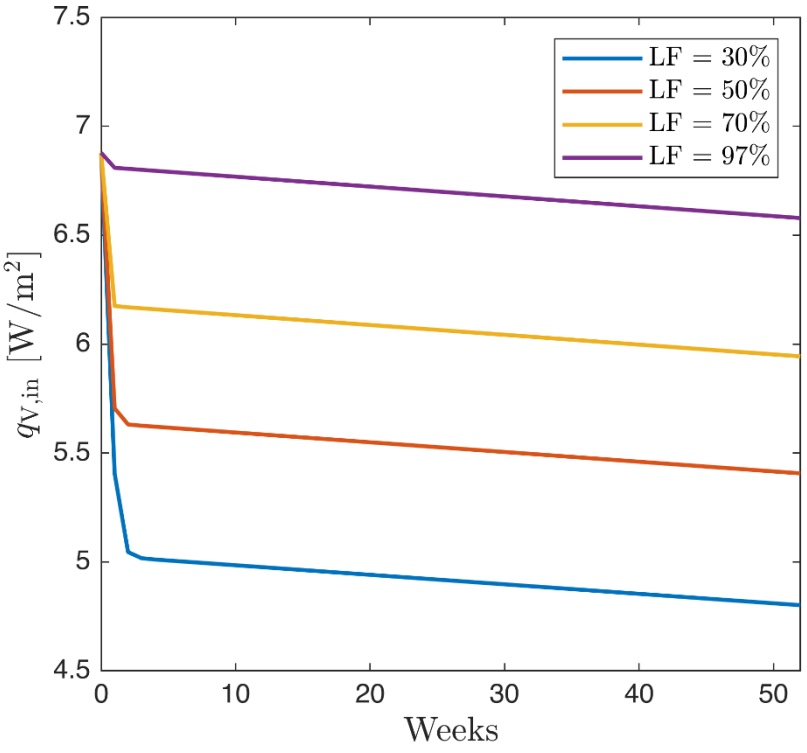

Figure 5.18: Heat flux into the vapour phase from the surroundings, $q_{V,in} = \dot{Q}_{V,in}/A_V$, as a function of time during the evaporation of pure methane in a large 165,000 m³ storage tank. The heat fluxes are depicted for four different initial liquid fillings (LF).

5.3.3 Analysis of the transient period in Scenario 4 (S4)

At early times of evaporation ($t \leq \tau_{\text{trans}}$), strong transient dynamics can be observed as illustrated in Figure 5.19. Figure 5.19a shows the variation of the dimensionless vapour temperature profile with time within the transient period. It can be observed that the dimensionless temperature profiles quickly converge, and the variations after 12 h are negligible. The convergence of dimensionless temperature profiles indicate that the vapour phase achieves a pseudo-steady state after 30 h. This result is confirmed by the slow variation of average vapour temperature and BOG temperatures in Figure 5.19b. Figure 5.19c shows the evolution of the vapour heat ingress, $\dot{Q}_{\text{V,in}}$, during the transient period. It can be observed that in the first 8 hours of evaporation, $\dot{Q}_{\text{V,in}}$ initially decreases until it reaches a minimum, and thereafter increases monotonically with time. The initial decrease in $\dot{Q}_{\text{V,in}}$ can be attributed to a rapid vapour heating. As the vapour is heated, a decrease is observed in the difference between the average vapour temperature and the temperature of the surrounding air that drives the heat ingress. The local minimum of $\dot{Q}_{\text{V,in}}$ is achieved when the decrease in temperature driving force is balanced by the increase in vapour area. Thereafter, $\dot{Q}_{\text{V,in}}$ increases monotonically as the increase in vapour area dominates the decrease in heat flux produced by the increase of average vapour temperature.

Figure 5.19d shows that the vapour to liquid heat transfer rate, $\dot{Q}_{\text{VL}}$, increases rapidly at early times as the temperature gradient at the interface increases. Once the pseudo-steady state vapour temperature profile develops, see Figure 5.19 a-b, $\dot{Q}_{\text{VL}}$ reaches a nearly constant value. Figure 5.19e illustrates that during the transient period, the average vapour density decreases rapidly because of vapour heating. As a consequence of the rapid vapour thermal expansion, the BOG rate at $t \to 0$ is maximum, see Figure 5.19f. Thereafter, the BOG rate decreases progressively as the vapour density tends to a pseudo-steady state. After the pseudo steady state ($t > \tau_{\text{trans}}$) the BOG rate is always lower than the evaporation rate. This is expected as a fraction of the evaporated liquid accumulates in the tank to maintain the pressure constant while the thermal expansion vanishes. The dynamics of $\dot{Q}_{\text{VL}}$ for the large tank considered in Scenario 4 are in good qualitative agreement with the results obtained with the vapour-CFD simulations for small and medium tanks, see Figure 5.10.

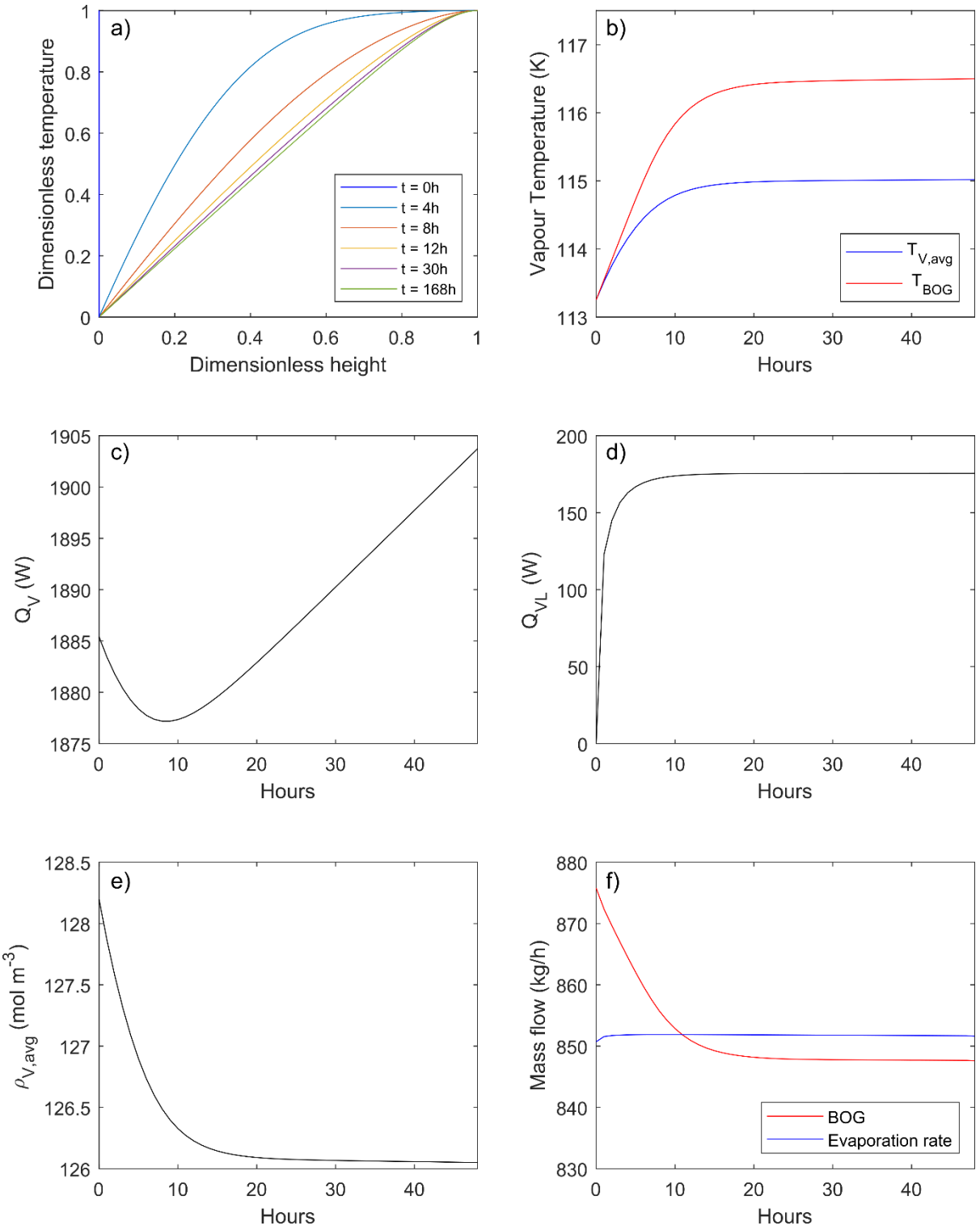

Figure 5.19: Evolution of process variables during the first 48 h of evaporation of pure methane in a large 165,000 m³ LNG storage tank initially filled at 97% of its capacity. The subfigures depict (a) dimensionless vapour temperature, (b) vapour temperature, (c) vapour heat ingress, (d) vapour to liquid heat transfer rate, (e) average vapour density, (f) BOG and evaporation rates.

Several recent works [13, 14] attributed the pseudo steady state only to the balance between the vapour heat ingress and the vapour to liquid heat transfer rate. Those approaches assumes that natural convection is the predominant heat transfer mechanism in the vapour phase bulk. The results of the current work indicate that this is not the case. Furthermore, the results obtained with the vapour-CFD model demonstrate that although natural convection is present, it does not significantly increase neither vertical heat transfer in the vapour bulk nor $\dot{Q}_{\mathrm{VL}}$, see subsection 5.2.4. If natural convection is considered dominant, it is not possible to reproduce the vapour superheating observed in industrial set-ups and in experiments. This was demonstrated by Migliore et al [10], who also argued that the large negative density gradient in the vapour would limit natural convection. The dampening of natural convection with the density gradient has been validated using the vapour-CFD model in sections 5.2.1 - 5.2.3.

As discussed in subsection 5.2.3, natural convection correlations will overestimate the vapour to liquid heat transfer rate $\dot{Q}_{\mathrm{VL}}$ [15, 16]. Additionally, by neglecting the accumulation and BOG removal terms on Eq. (3.20), previous works [13, 14] have overestimated the vapour enthalpy. The vapour to liquid interfacial heat fluxes, $q_{\mathrm{VL}} = \dot{Q}_{\mathrm{VL}}/A_{\mathrm{T}}$, calculated with our model are lower than 0.1 W m^{-2}. In contrast, non-equilibrium weathering models which assume a predominant effect of natural convection predict heat fluxes of 6.9 Wm^{-2} [14] and 7.6 Wm^{-2} [13]. These values overestimate the interfacial heat flux by almost two orders of magnitude [5-7, 17, 18], see subsection 5.2.4.

The transient period τ_{trans} was 12 hours for the evaporation of methane in our specific tank at 97% initial liquid filling. Scaling analysis of Eq. (3.20) shows that the transient period depends on a number of parameters. To further elucidate the interplay between conduction and advection, the isobaric 1-D model was executed for different average advective velocities ($\bar{v}_z$) and initial liquid fillings. For each simulation, the transient period τ_{trans} was determined as the earliest time from which $d\bar{T}_{\mathrm{V}}/dt < 0.1$ K h^{-1}, as defined previously. Figure 5.20 shows the variation of the transient period with the advective velocity (a) and vapour height (b). It is observed that τ_{trans} is a linear function of l_{V} and it is inversely proportional to $\bar{v}_z$. Hence, the transient period scales as $\tau_{trans} \sim l_{\mathrm{V}}/\bar{v}_z$, which indicates that advection is the heat transfer mechanism that

dominates the onset of the pseudo-steady state. This scaling is accurate for small vapour lengths. For large vapour lengths, the scaling will overestimate the transient period as natural convection would dominate the onset of the pseudo-steady state, as demonstrated in subsection 5.2.2.

The dominant heat transfer mechanism was determined by calculating the Péclet number, which represents the ratio between advection and conduction, for different liquid fillings. The Péclet number varied with initial liquid filling between 10 at LF = 97% to 120 at LF = 30%, indicating the predominance of advection. However, these values of the Péclet number are not high enough to neglect heat conduction, particularly in the case of high liquid fillings. For better insulated tanks with overall heat transfer coefficients lower than what was assumed in this work, conduction will become more dominant. In better insulated tanks, $\bar{v}_z$ will decrease owing to lower evaporation rates. Additionally, in the small and medium-sized tanks, the Péclet numbers are considerably lower, indicating a more predominant role of conduction at smaller scales. This phenomenon will be further investigated in section 5.4.

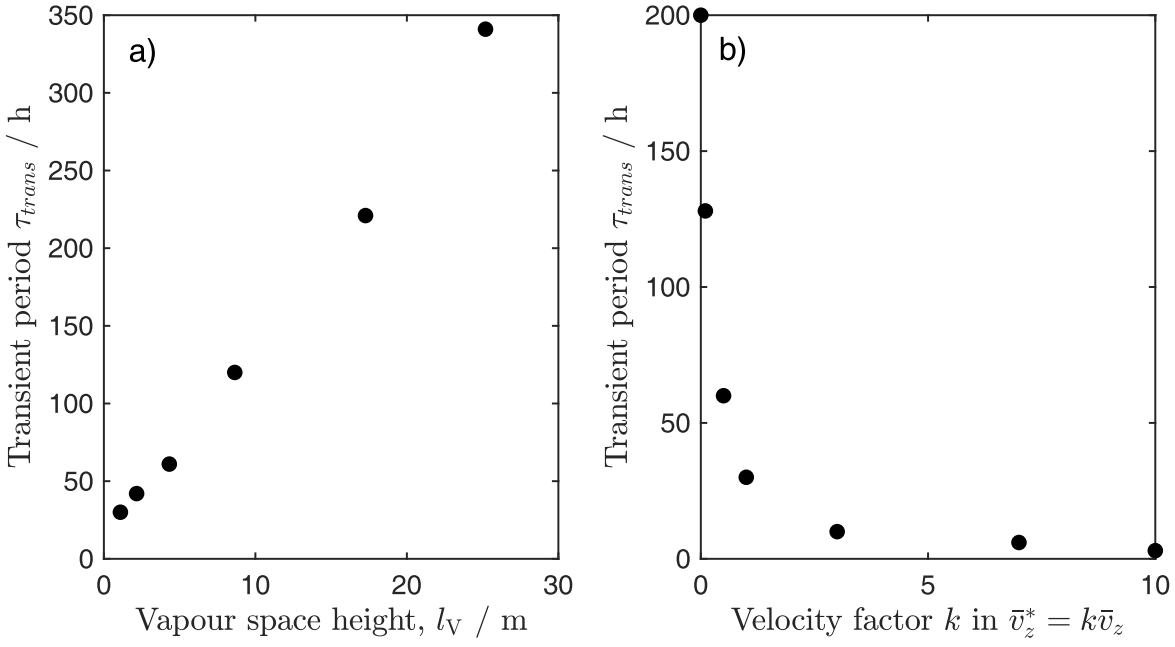

Figure 5.20: Transient period τ_{trans} as a function of (a) the vapour height l_V; and (b) the average advective velocity $\bar{v}_z^* = k\bar{v}_z$ for the evaporation of pure methane in a 165,000 m³ storage tank.

The effect of the source term $\dot{S}_{w,V}$ on the relaxation time was also investigated. For a particular tank, the source term increases with the increasing air temperature and decreases with lower overall heat transfer coefficients for the vapour, see Eq. (3.18). As

a consequence, any increase in the source term will also increase $\bar{v}_z$ because of two reasons. Firstly, higher source terms will imply higher evaporation rates, as $U_L \approx U_V$ for industrial scale tanks [3]. Secondly, as the average vapour temperatures will increase with the source term, lower average vapour densities will be observed, see Eq. (3.19). To assess the interplay between the source term and advective term, the model was executed for different overall heat transfer coefficients and air temperatures. Simulations were executed for the parametric domains $U_V^* \in [0.1U_V,\ 10U_V]$ and $T_{air}^* \in [T_{air} - 100\ K,\ T_{air} + 100\ K]$. An overall decrease in the transient period was observed with the increase of either the overall heat transfer coefficient or the air temperature. Conversely, decreasing the source term will decrease the advective term, increase the transient period and reduce the Péclet number making conduction more predominant.

5.3.4 Influence of composition in BOG rates for typical LNG mixtures

The non-equilibrium weathering model developed in section 3.5 is expected to accurately predict vapour temperatures, as it uses the same vapour phase heat transfer sub-model used than the isobaric 1-D model. During the isobaric evaporation of pure cryogens, the thermophysical and thermodynamic properties of the liquid cryogen are constant, see sections 3.2-3.3. In contrast, the storage of LNG is more complex because it is a mixture that undergoes weathering. To include the change in composition and thermophysical properties of the stored LNG and its vapour, the isobaric 1-D model was extended with two features. First, mass balances were written for each specie in each phase, see Eqs. (3.46). Second, a thermodynamic model was included to predict the composition of each phase during the evaporation period, see (3.49). Hence, the non-equilibrium weathering model was defined as the extension of the isobaric 1-D model for mixtures.

To assess the effect of composition on BOG rates, the non-equilibrium weathering model was used to simulate the weathering of typical LNG mixtures encountered in industry. For this purpose, the same three LNG mixtures studied by Migliore et al [3, 10]. were considered, which cover a range of commercially available LNG. For convenience, Table 5.3 summarizes the composition of these mixtures. For all mixtures, namely light LNG, heavy LNG and N_2-rich LNG, similar temperature profiles

and $\dot{Q}_{VL}$ were observed as for pure methane evaporation. This is expected as the vapour phase of both light and heavy LNG is made up primarily (> 0.997 mole fraction) by methane during the 52 weeks of weathering. The vapour phase of the N_2-rich LNG mixture is initially nitrogen rich, as nitrogen preferentially evaporates [3]. This has a very small effect on temperature profiles and $\dot{Q}_{VL}$, as the thermophysical properties of nitrogen vapour are similar to those of methane.

Table 5.3: Composition of three different LNG mixtures considered for weathering simulation using the non-equilibrium weathering model.

Component	Formula	Light	Heavy	N_2-rich
Methane	CH_4	0.9613	0.9164	0.9307
Ethane	C_2H_6	0.034	0.0576	0.0661
Propane	C_3H_8	0.0039	0.0204	0.0006
Butane	n – C_4H_{10}	0.0003	0.0022	0
Isobutane	i – C_4H_{10}	0.0004	0.0029	0
Isopentane	i – C_5H_{12}	0	0.0002	0
Nitrogen	N_2	0.0001	0.0003	0.0026

Figure 5.21 illustrates compares the BOG rates predicted by the non-equilibrium weathering model and Migliore et al.[10] model. The three LNG mixtures defined in Table 5.3 and pure methane have been considered, for the large tank used in Scenario 4 filled at 97% of its capacity, see subsection 5.3.1. The non-equilibrium weathering model [2] developed in section 3.4 predicts lower BOG rates for all mixtures compared with the Migliore et al. model [10]. As Figure 5.21 considers the period after the pseudo-steady state is achieved, lower BOG rates are a direct consequence of lower $\dot{Q}_{VL}$, which induce lower evaporation rates. The difference in the predicted BOG rates between the two models increases with the duration of weathering. For light LNG, the difference in the BOG rate increases from -6.8 kg h^{-1} (-0.8%) in the first week to -30.2 kg h^{-1} (-3.8%) in the last week. On the other hand, for heavy LNG these figures are -0.9% and -3.8%, respectively.

For the light and heavy LNG mixtures, both models predict a decreasing BOG rate, see Figure 5.21. In contrast, for the N_2-rich LNG mixture both models predict a local maximum. The appearance of the maximum in the BOG rate is a consequence of the interplay between the decreasing heat ingress into the liquid and decreasing enthalpy

of vaporization, as discussed by Migliore et al. [10]. The non-equilibrium weathering model predicts the maximum in BOG fifteen weeks earlier than Migliore et al. model [10]. This is expected as in the new non-equilibrium weathering model the decrease in liquid heat ingress during weathering is more rapid. The rapid decrease is a consequence of $\dot{Q}_{VL}$ being an order of magnitude lower in the new model, as illustrated in Figure 5.21.

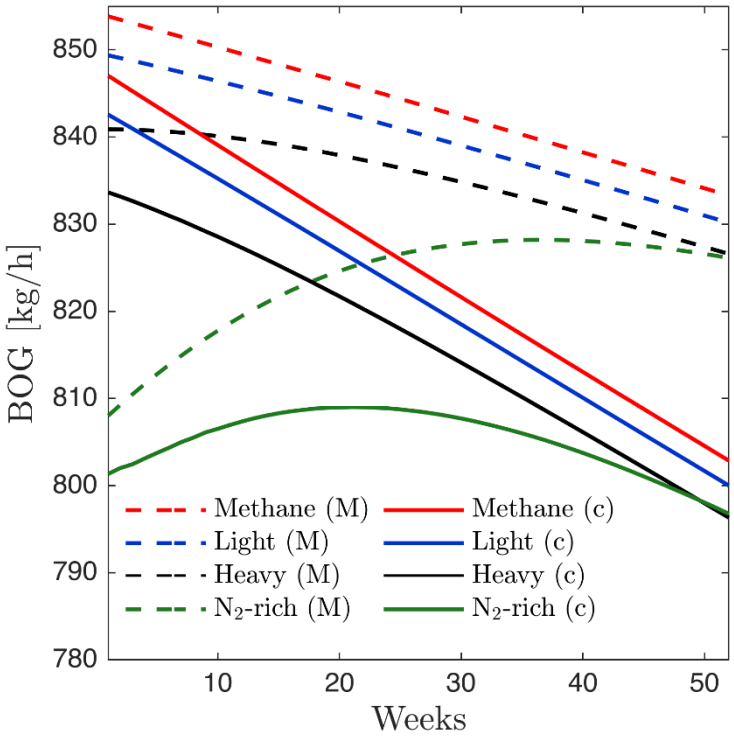

Figure 5.21: Boil-off gas (BOG) rate as a function of time for four different LNG mixtures during their weathering in a 165,000 m³ storage tank initially filled at 97% of its capacity. The predictions are depicted as solid lines for the current 1-D-weathering model (c), and as dashed lines for the Migliore et al [10] model.

5.3.5 Industrial significance

In this subsection, some applications of the results obtained with the non-equilibrium weathering model are explored for the design and operation of real LNG storage tanks. For the design and operation of these tanks, determining the BOG temperature is important. In subsection 5.3.3 it was established that the transient period τ_{trans} decreases with increasing amount of LNG present in the tank. Once the pseudo-steady state has been reached, the dimensionless temperature profile is roughly constant, see

Figure 5.19b. Additionally, for high initial liquid fillings the vapour temperature profile is nearly linear, see

Figure 5.16a. This would indicate that for high initial liquid fillings, the ratio of temperature difference between T_{BOG} and T_{LNG} and vapour height remains constant during the evaporation. Typical storage times, τ_s, are around two orders of magnitude longer than the transient period τ_{trans}. For this scenario, one can propose a rule of thumb to predict the BOG temperature,

$$\frac{T_{\mathrm{BOG}} - T_{\mathrm{L}}}{l_{\mathrm{V}}} \approx \text{constant for } \tau_s \gg \tau_{\mathrm{trans}} \;\&\; LF \to 1, \tag{5.3}$$

For large liquid fillings, the vapour height l_{V} increases approximately linearly with time at a constant rate. This rate is expressed in terms of the tank characteristics:

$$l_{\mathrm{V}}(t) = l_{\mathrm{V}}^0 + \frac{\dot{Q}_{\mathrm{L}}^0 + \dot{Q}_{\mathrm{slab}}}{\pi d_{\mathrm{i}}^2 \rho_{\mathrm{L}}^0 (h_{\mathrm{V}}^0 - h_{\mathrm{L}}^0)} t, \tag{5.4}$$

where t is the time in seconds and the superscript 0 indicates that the quantities are evaluated at the initial LNG composition, temperature and vapour height. Eq. (5.3) gives accurate estimates of BOG temperature for LNG storage tanks that are initially filled to 70% of more of their capacity. The good agreement is irrespective of the LNG composition. The agreement can be assessed taking the worst-case scenario that considers the 165,000 m³ cylindrical storage tank initially filled with 70% of N_2-rich LNG.

For the worst-case scenario, Eq. (5.3) was applied to calculate the constant using T_{BOG} and l_{V} at the end of the first week. Then, Eq. (5.4) was used to predict the BOG temperature in the 12$^{\mathrm{th}}$ and 52$^{\mathrm{nd}}$ week. Using this rule of thumb, the errors were just 0.7 K (0.4%) and 1.8 K (1.2%), respectively. For lower initial liquid fillings, the deviations are higher as a result of the non-linearity of the pseudo-steady state temperature profile, see

Figure 5.16a. To estimate T_{BOG} and l_{V} for low liquid fillings, it is advised to apply the analytical solutions developed in section 3.3. In section 5.4, the performance of the

analytical solutions for the evaporation of methane in the tank considered for Scenario 4 will be verified.

The developed non-equilibrium weathering model allows for a better characterization of the transient period of rapid vapour heating at the beginning of the evaporation. This provides new insight relevant for the design and operation of cryogenic control valves, BOG compressors and the gas receiving network. From the beginning of the evaporation until the transient period, $t \leq \tau_{\mathrm{trans}}$, a rapid increase in the vapour temperature and decrease in BOG rate was observed, see Figure 5.19b and f. This variation was rapid compared to the variation in both parameters once the pseudo-steady state has been reached, see Figure 5.15 and the red line in Figure 5.21. The changes are more pronounced for low initial liquid fillings, $LF \to 0$, corresponding to a larger vapour height in a given storage tank. As an example, one can consider a storage tank initially filled with light LNG at 30% of its capacity. For this scenario, T_{BOG} will be 100 K higher than the liquid temperature after one week of weathering. Additionally, the initial BOG rate, $\dot{B}(t = 0)$, will be 158% higher than after one week of weathering. The knowledge of the rapid variation in both quantities during $t \leq \tau_{\mathrm{trans}}$ can aid the development of optimal operations in the gas receiving facilities.

In subsection 5.3.4 it was concluded that the new non-equilibrium weathering model predicts smaller BOG rates than previous equilibrium and non-equilibrium models [3, 10]. This result is of special interest for ballast voyages, where the initial amount of LNG is small. As an example, the weathering of light LNG was simulated in the same 165,000 m³ storage tank used in Scenario 4, see subsection 5.3.1. In this case, using the equilibrium and non-equilibrium models developed by Migliore et al. [3, 10] would overestimate the BOG rates in 100% and 26%, respectively.

5.3.6 Summary of findings

- Advection is the dominant heat transfer mechanism in the vapour phase.
- The transient period at the beginning of the evaporation is small when compared with the duration of the evaporation.
- The transient period follows the scaling $\tau_{\mathrm{trans}} \sim \bar{v}_z / l_{\mathrm{V}}$.

- Following the transient period, a pseudo-steady state arises characterised by a slow variation of vapour temperatures, BOG rates and vapour and liquid thermodynamic properties.
- The vapour to liquid heat transfer rate is very small for large scale storage.
- For N_2-rich LNG, BOG rates attain a global maximum after a period that is highly sensitive to vapour to liquid heat transfer modelling.

5.4 Analytical solutions

In section 5.3, it was concluded that the isobaric 1-D model provides an excellent physical description of the isobaric evaporation of pure cryogens. This demonstrated that the complex interplay between thermal stratification, buoyancy driven flows and boundary layers in the vapour can be modelled using effective advection. The agreement between the more complex vapour-CFD model and the isobaric 1-D model improved in all scenarios as the system approached its pseudo-steady state, $t \to \tau_{\text{trans}}$. In this section, the attention is focused on the long-term storage of cryogenic liquids in tanks, $t = \tau_{\text{evap}} \gg \tau_{\text{trans}}$. For this timescale, of the order of months and years, computational fluid dynamics models are not applicable in the foreseeable future, as discussed in section 5.3. For instance, the isobaric 1-D model and its analytical solutions require less than 4 seconds to simulate a year of evaporation. This constitutes a speed up of $10^8 - 10^9$ with respect to the vapour-CFD model [1].

The analytical solutions derived in section 3.4 were applied to predict the evaporation of pure cryogens in small, medium-sized and large storage tanks. The small and medium-sized tanks correspond to the tanks considered in Scenarios 1 and 3, see sections 5.2.1 and 5.2.3, respectively. The large tank corresponds to Scenario 4, investigated in section 5.3. An in-depth analysis is provided for Scenario 4, as for the large tank the transient period is longer and of major industrial relevance [2]. In contrast to short term storage, in long term storage the liquid volume changes significantly. Two different initial liquid fillings, low (LF = 0.30) and high (LF = 0.97) were studied for the evaporation of the cryogens in each storage tank.

For the limiting case of thermal equilibrium between the vapour and the liquid, the analytical solutions are exact. The deviation between the analytical and numerical

solution of the equilibrium evaporation model, see Appendix E, was lower than 0.001% for all the process variables and all scenarios. The process variables are, namely: heat ingresses, liquid volume, evaporation rate, BOG rate and total evaporation period. Therefore, in subsections 5.3.1-5.3.3 only analytical solutions of the isobaric 1-D model, where the vapour is assumed superheated with respect to the liquid, are evaluated.

5.4.1 Small scale storage in Scenario 1 (S1)

To establish the range of applicability of the analytical solutions, simulations were executed for the evaporation of LN_2 in a small tank. This tank was previously considered for the evaporation of pure methane in Scenarios 1 and 2, see subsections 5.2.1 - 5.2.2. The simulations were executed for high (LF = 0.97) and low (LF = 0.30) initial liquid fillings until the stored cryogen was completely evaporated. The time until the complete evaporation of the stored cryogen is defined as the total evaporation period, τ_{evap}. This period was calculated using the numerical solution of the isobaric 1-D model. To facilitate the visualization of the results, the evaporation dimensionless time $t^*_{\text{evap}} = t/\tau_{\text{evap}}$ was used as an appropriate timescale for long-term storage. At $t^*_{\text{evap}} = 0$, the tank is filled with the cryogen at its initial liquid filling, and at $t^*_{\text{evap}} = 1$, the cryogen is completely evaporated.

Table 5.4 summarizes the deviations between the analytical and numerical solutions for liquid volume, BOG rates and BOG temperature for both the direct and sequential routes. Although the direct route resulted in larger deviations than in the medium tank, the sequential calculation produced a very good agreement for all quantities. For liquid methane, it was found that the agreement between the numerical and analytical solutions for this tank was very similar to LN_2.

Table 5.4: Deviations of the analytical solutions from the numerical solution of the isobaric 1-D model, for LN_2 evaporation in an 8 m^3 small tank. The deviations for two different initial liquid fillings (LF) using direct (D) and sequential (S) route are presented.

	LF = 0.97				LF = 0.30			
	AAD		MD		AAD		MD	
	D	S	D	S	D	S	D	S
V_L	1.3%	0.8%	4.3%	1.0%	1.7%	0.8%	5.4%	1.0%
BOG	2.0%	0.4%	3.1%	1.8%	2.6%	0.2%	4.3%	0.7%
T_{BOG}	3.0%	2.4%	4.5%	4.4%	0.8%	0.1%	1.0%	0.1%

5.4.2 Medium-sized storage with bottom heating in Scenario 3-bot (S3-b)

The analytical solutions were tested for LN_2 stored in the same 80,4 m^3 medium-sized cylindrical storage tank used in Scenario 3, see subsection 5.2.3. This tank was selected as a representative of LN_2 storage in industrial applications [4]. In contrast to Scenario 3, in Scenario 3-bot the tank is also heated through the bottom at a constant bottom heat ingress $\dot{Q}_b = U_L A_T (T_{air} - T_L)$. At the tank roof, it has been assumed that the overall heat transfer coefficient was $U_{roof} = U_V$. Hence, the heat ingress through the roof depends on the temperature just below the tank roof, $q_{roof} = U_{roof}(T_{air} - T_V(l_v))$ in Eq. (3.33).

Figure 5.22 depicts the analytical solution and numerical solutions for vapour temperature profiles for the isobaric evaporation of LN_2 using the isobaric 1-D model. A set of profiles is depicted for two initial liquid fillings, high (Figure 5.22a) and low (Figure 5.22b), sampled at six different evaporation dimensionless times. The dimensionless times range from the mid-point of the transient period, t^*_{trans} = 0.5, until the cryogen is depleted, t^*_{evap} = 1.

The transient periods for the medium-sized tank were $\tau_{trans,97\%} = 1 \times 10^{-4}$, $\tau_{evap,97\%}$ (4 h) and $\tau_{trans,30\%} = 8 \times 10^{-3}$, $\tau_{evap,30\%}$ (5.1 days) for high and low initial liquid fillings, respectively. To establish the range of applicability of the solutions, a representative timestep during the transient period has been considered. At the mid-

point of the transient period, the agreement was poor for both high *LF* ($t^*_{evap,97\%} = 5 \times 10^{-5}$) and low *LF* ($t^*_{evap,30\%} = 4 \times 10^{-3}$). At this timestep, the percentage average absolute deviation (AAD%) and percentage maximum deviations (MD%) of the analytical solutions were moderate for both liquid fillings. For high liquid filling, the deviations were small (AAD = 2%, MD = 4%), see Figure 5.22a. For low liquid filling, the deviations were higher (AAD = 7%, MD = 12%), see Figure 5.22b. Although this agreement is good, it is outside the theoretical range of applicability of the analytical solutions. After the pseudo-steady state is achieved, the agreement improves considerably. For the pseudo-steady state, the analytical solutions show a very good agreement for high *LF* (AAD =1.1%, MD = 4.5%) and low *LF* (AAD = 0.8%, MD = 2.2%).

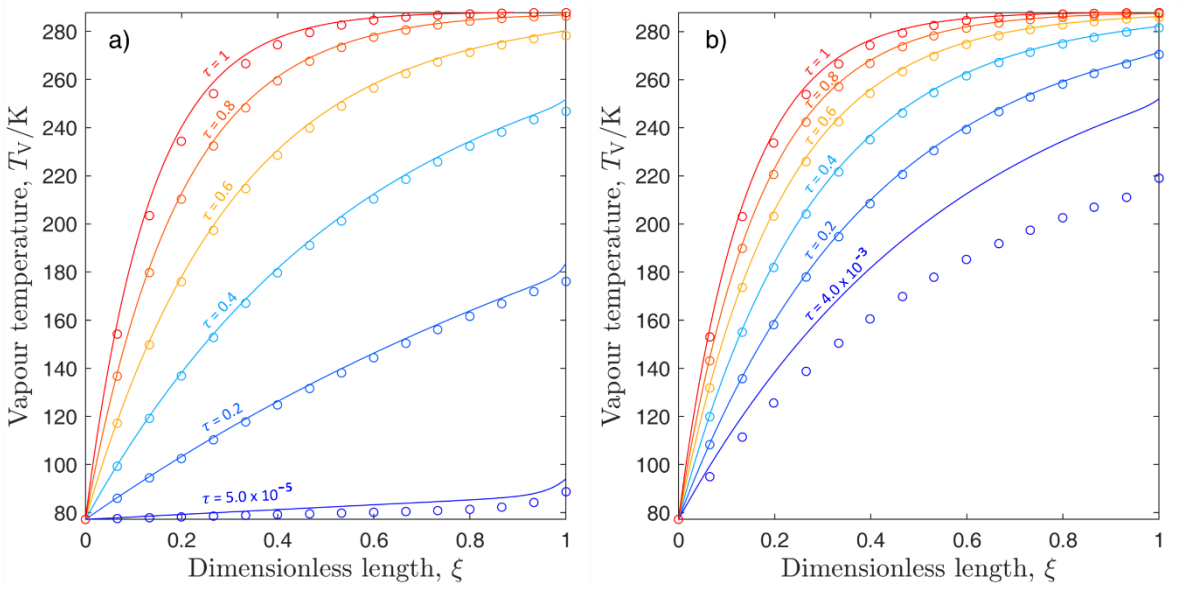

Figure 5.22: Vapour temperature profiles as a function of the dimensionless length, $\xi = z/l_V$, and the evaporation dimensionless time, $t^*_{evap} = t/\tau_{evap}$. The trends correspond to the evaporation of liquid nitrogen stored in a medium cylindrical storage tank (V_T = 80.4 m^3) filled at 97% (a) and 30% (b) of its capacity. The lowest dimensionless time in each sub-plot corresponds to the mid-point of the transient period, which is a function of the initial liquid filling. The analytical solutions are plotted in solid lines, and the numerical solution of the isobaric 1-D model are plotted in empty circles.

The failure of the analytical solutions for vapour temperature at the beginning of the evaporation is a consequence of the steady state assumption [19], see Figure 5.22. This assumption makes the solutions valid for long term storage $t > \tau_{trans}$. As a consequence, at $t < \tau_{trans}$, the solutions fail to capture the transient dynamic of rapid vapour heating [2] , see subsections 5.2.1-5.2.3. During the transient period, the

temperature profile is governed by an unsteady partial differential equation, Eq. (3.20). In contrast, in the analytical solution the transient term is neglected, $\partial T_V/\partial t = 0$, which produces a temperature profile governed by an ODE, Eq. (3.31). The large deviation observed for low liquid fillings is as a consequence of the large vapour volume. This larger vapour volume requires a longer transient period to achieve the pseudo-steady state, see subsections 5.2.1 and 5.2.2.

It is worth noting that the analytical temperature profile near the vapour-liquid interface, $0 \leq \xi \leq 0.1$, agrees exceptionally well with the isobaric 1-D model, see Figure 5.22. This good agreement is observed even for low liquid fillings during the transient period (AAD = 0.9%; MD = 1.9% for $t^*_{evap,30\%} = 4 \times 10^{-3}$). The good agreement on vapour temperature and its gradient at the vapour-liquid interface ($\xi = 0$) is a crucial feature of the analytical solutions. This gradient governs the vapour to liquid heat transfer rate $\dot{Q}_{VL}$, see Eq. (3.10). The quantification of $\dot{Q}_{VL}$ is a key advantage of non-equilibrium evaporation models over equilibrium models [2, 10, 13, 18].

Figure 5.23 shows the vapour to liquid heat transfer rate (a) and the BOG rate (b) predicted by the analytical and numerical solutions of the isobaric 1-D model. The analytical solutions accurately predict $\dot{Q}_{VL}$ for both high (AAD = 0.1%, MD = 0.5%) and low (AAD = 0.1%, MD = 0.4%) liquid fillings. This excellent agreement is a consequence of the good agreement of the vapour temperature profiles at the vapour-liquid interface, see Figure 5.22a-b. The analytical BOG rates obtained by the direct route also showed a good agreement with the numerical results following the transient period. The deviations were small for both LF = 0.97 (AAD = 1.8%, MD = 2.4%) and LF = 0.30 (AAD = 2.5%, MD = 3.9%). These deviations were reduced substantially using the sequential route for both LF = 0.97 (AAD = 0.3%, MD = 1.1%) and LF = 0.30 (AAD = 0.1%, MD = 0.5%). This improvement is a consequence of updating $\dot{Q}_{VL}$ at each step following the method described in subsection 3.4.3.

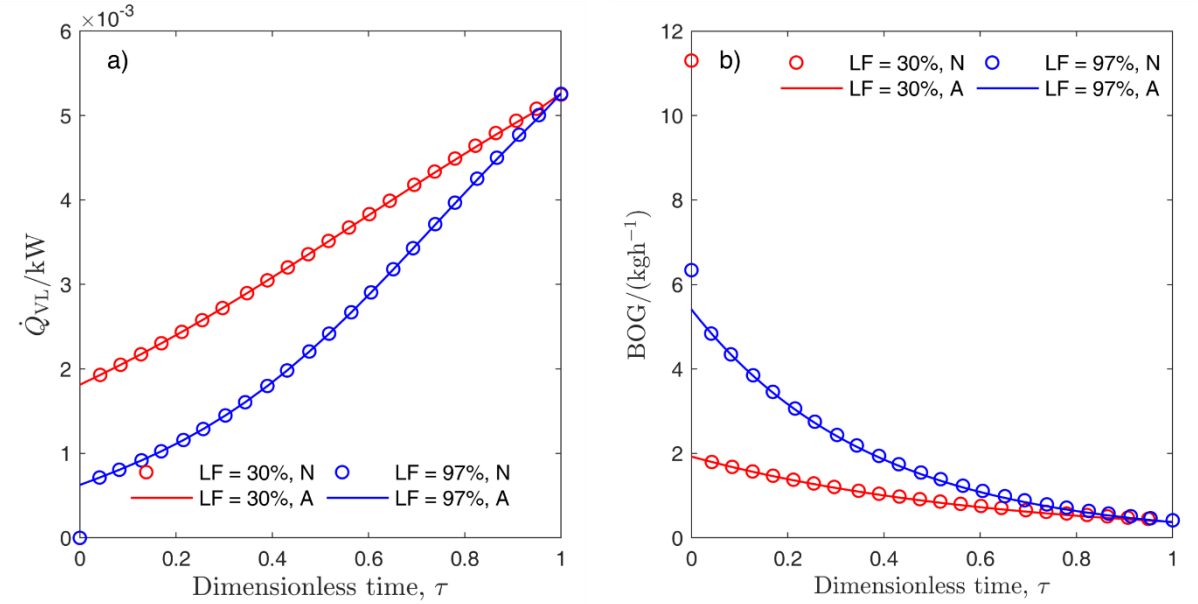

Figure 5.23: Vapour to liquid heat transfer rate, $\dot{Q}_{VL}$, (a) and evaporation rate, $\dot{B}_L$, (b) as a function of the evaporation dimensionless time $t^*_{evap} = t/\tau_{evap}$. The trends correspond to the evaporation of liquid nitrogen stored in a medium cylindrical storage tank (V_T = 80.4 m³) filled at two different initial liquid fillings (LF). The analytical solutions are plotted in solid lines, and the numerical solutions of the isobaric 1-D model are plotted in empty circles.

Table 5.5 shows a comparison between direct and sequential routes of calculating the liquid volume and BOG temperature using the analytical solutions for Scenario 3-bot. The results indicate that the sequential calculation significantly improves the estimation of all the quantities of interest for the practising engineer.

Table 5.5: Deviations of the analytical solutions from the numerical solution of the isobaric 1-D model, for LN_2 evaporation in an 80.4 m³ medium-sized tank. The deviations for two different initial liquid fillings (LF) using direct (D) and sequential (S) route are presented.

	LF = 0.97				LF = 0.30			
	AAD		MD		AAD		MD	
	D	S	D	S	D	S	D	S
V_L	0.9%	0.5%	3.0%	0.6%	1.5%	0.6%	4.7%	0.7%
BOG	1.2%	0.3%	2.0%	1.1%	2.0%	0.1%	3.4%	0.5%
T_{BOG}	1.2%	1.0%	2.4%	2.4%	0.2%	0.0%	0.4%	0.0%

5.4.3 Large scale storage in Scenario 4 (S4)

Many cryogens are stored in large storage tanks. As the size of the storage tank increases, the transient times increase which reduces the range of applicability of the analytical solutions ($t > \tau_{\text{trans}}$). On the other hand, in large tanks the vapour to liquid heat transfer rate, $\dot{Q}_{\text{VL}}$, is proportionally smaller [2], see subsection 5.3.2. A lower $\dot{Q}_{\text{VL}}$ reduces the error introduced by the assumption of constant $\dot{Q}_{\text{VL}}$ used to estimate the advective velocity in the analytical solutions, see Eq. (3.30). This section examines the accuracy of the analytical solution for the large tank considered in Scenario 4. The large tank is representative of above-ground LNG storage tanks used in industry [3, 10]. It was assumed that the heat ingress through the tank bottom was constant, $\dot{Q}_{\text{b}} = 60$ kW, and that the roof was insulated, $\dot{Q}_{\text{roof}} = 0$. The overall heat transfer coefficients for the vapour and liquid phases in this scenario were taken as $U_{\text{L}} = U_{\text{V}} = 0.037$ W m^{-2} K^{-1}. Simulations for low (LF = 0.3) and high (LF = 0.97) initial liquid fillings were executed for the total evaporation period τ_{evap}.

Figure 5.24 depicts the vapour temperature profiles predicted by the isobaric 1-D model and the analytical solutions for liquid methane evaporation for six different timesteps. For the high liquid filling case, the analytical temperature profiles show an excellent agreement during the whole process of evaporation, see Figure 5.24a. The absolute average percentage deviation and maximum percentage deviations between the analytical solutions and the isobaric 1-D model decrease with time. The deviations decrease from 0.5% and 1.2% at $t^*_{\text{evap}} = 5.5 \times 10^{-5}$ to 0.2% and 0.3% at $t^*_{\text{evap}} = 1$. The first plotted line at $t^*_{\text{evap}} = 5.5 \times 10^{-5}$ was selected as a representative temperature profile of the transient period, $t^*_{\text{trans}} = 0.5$. In contrast, for the low liquid filling case the agreement on temperature profiles is poor at the beginning of the evaporation, see Figure 5.24b. At $t^*_{\text{trans}} = 0.5$, $t^*_{\text{evap}} = 3.25 \times 10^{-3}$, AAD = 12.0% and MD = 32.5%. After the pseudo-steady state is achieved ($t \geq \tau_{\text{trans}}$, $t^*_{\text{evap}} \geq 6.5 \times 10^{-3}$) the agreement improves considerably (AAD < 0.2%; MD < 0.3%). In this large tank, the deviations at the pseudo-steady state were 5 times smaller than in the medium tank, see subsection 5.4.2.

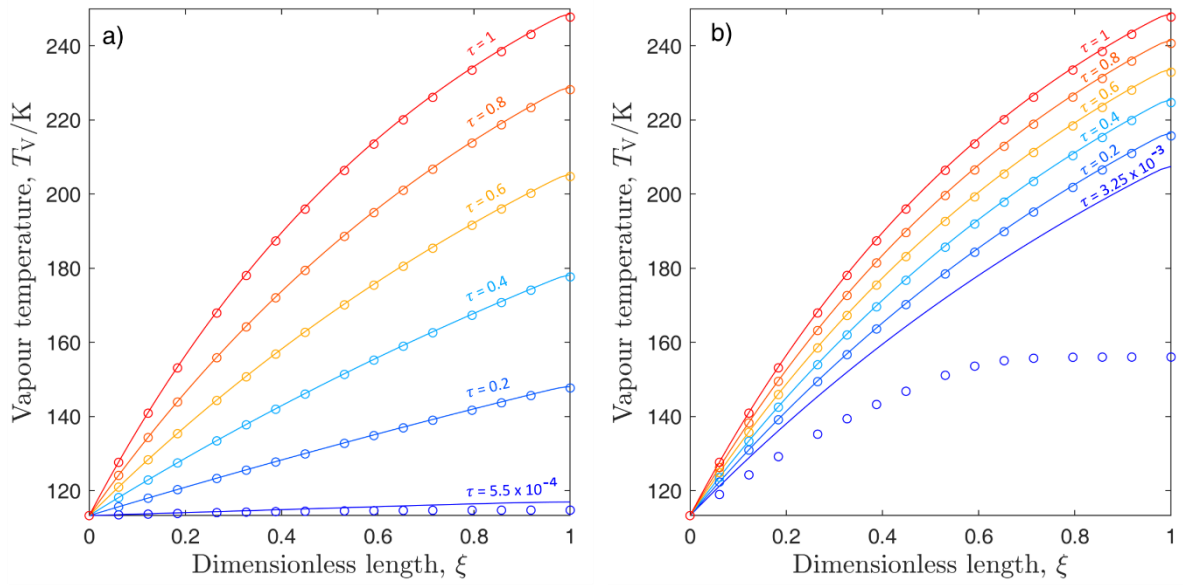

Figure 5.24: Vapour temperature profiles as a function of the dimensionless length, $\xi = z/l_V$, and the evaporation dimensionless time $\tau = t^*_{evap} = t/\tau_{evap}$. The trends correspond to the evaporation of methane stored in a large cylindrical storage tank (V_T= 165,000 m³) filled at 97% (a) and 30% (b) of its capacity. The analytical solutions are plotted in solid lines, and the numerical solution of the isobaric 1-D model are plotted in empty circles.

The vapour temperature profiles show a significantly lower curvature than the profiles for the medium-sized tank, see Figure 5.22. The lower curvature can be primarily attributed to the decrease of the contribution of the source term, $\dot{S}_{w,V}$, with increasing tank diameter, see Eq. (3.18). It is also worth noting the excellent estimate of the vapour temperature near the tank roof $0.9 \leq \xi \leq 1$ after the transient period. As the BOG is removed from the top of the tank, $T_{BOG} = T_V(\xi = 1)$. For both liquid fillings and $t > \tau_{trans}$, the agreement on T_{BOG} is excellent (AAD = 0.1%, MD = 0.2%).

Based on the isobaric 1-D model, the duration of the transient period scales as the ratio of the vapour height to the average advective velocity, $\tau_{trans} \sim l_V/\bar{v}_z$ [2]. For low liquid fillings, not only l_V is larger but also $\bar{v}_z$ is smaller than for high liquid fillings, as discussed in subsections 5.2.2 and 5.3.3. For Scenario 4, the transient periods are $\tau_{trans,97\%} = 1.1 \times 10^{-4}$ (12 h) and $\tau_{trans,30\%} = 6.5 \times 10^{-3}$ (11.5 days) for high and low liquid fillings, respectively. This suggests that the range of applicability of the analytical solutions decreases with decreasing liquid filling. However, in section 5.2 it was concluded that the isobaric 1-D model overpredicted the transient period for low liquid fillings, $\tau_{trans,CFD} < \tau_{trans,1-D} \sim l_V/\bar{v}_z$. This was a consequence of the isobaric 1-D model assumption of average advective velocity, which neglects natural convection in the

vapour. As natural convection increases with vapour height, the range of applicability of the analytical solutions is wider for large tanks and low liquid fillings, $t \geq \tau_{\text{trans,CFD}}$.

Figure 5.25 shows the vapour to liquid heat transfer rate (a) and the evaporation rate (b) predicted by the isobaric 1-D model and the analytical solutions for methane evaporation. The analytical solutions reproduce extremely accurately $\dot{Q}_{\text{VL}}$ for both low (MD = 0.2%) and high (MD = 0.1%) liquid fillings after the transient period. This is a consequence of the excellent agreement on vapour temperatures at the vapour-liquid interface, see Figure 5.24a-b, which determines $\dot{Q}_{\text{VL}}$, see Eq. (3.22). The analytical solutions accuracy is excellent on evaporation rates (MD < 0.2%) for both liquid fillings and throughout the whole evaporation, see Figure 5.25b.

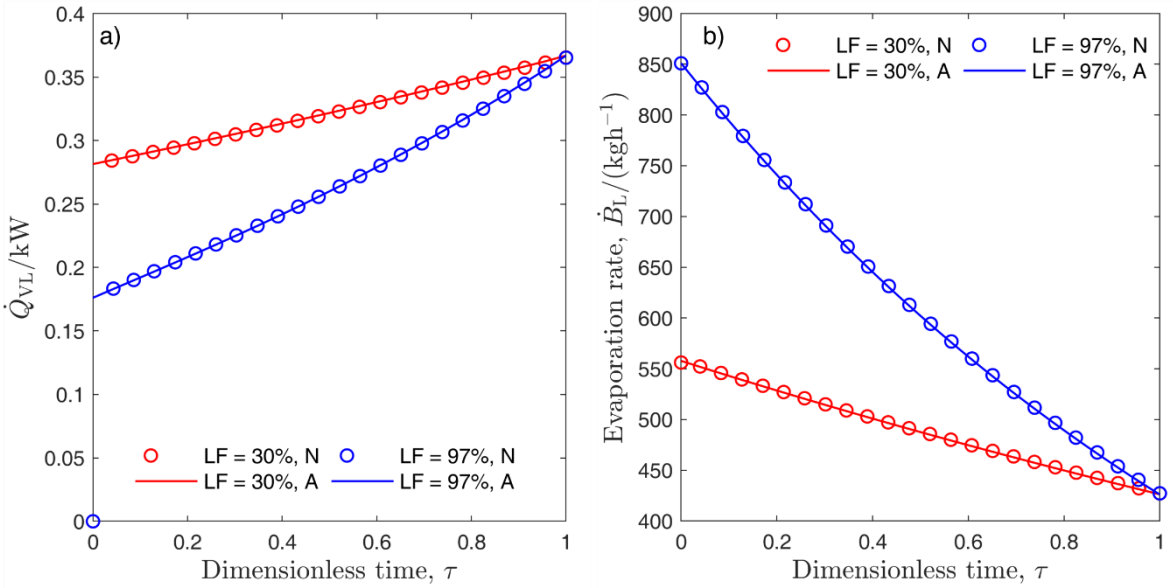

Figure 5.25: Vapour to liquid heat transfer rate, $\dot{Q}_{\text{VL}}$, (a) and evaporation rate, $\dot{B}_{\text{L}}$, (b) as a function of the evaporation dimensionless time $\tau = t^*_{\text{evap}} = t/\tau_{\text{evap}}$. The trends correspond to the evaporation of methane stored in a large cylindrical storage tank (V_{T} = 165,000 m³) filled at two different initial liquid fillings (LF). The analytical solutions are plotted in solid lines, and the numerical results produced by the isobaric 1-D model are plotted in empty circles.

Figure 5.26a-c shows the BOG rates produced by the isobaric 1-D model and the analytical solutions by direct route for methane evaporation. At the beginning of the evaporation, $t < \tau_{\text{trans}}$, the analytical solutions underestimate the BOG rates, see Figure 5.26b-c. This underestimation is observed for both high liquid filling (AAD = 1.0%; MD = 8.9%) and low liquid filling (AAD = 16.7%; MD = 55.2%). After the pseudo-steady state is achieved, $t > \tau_{\text{trans}}$, the agreement between the analytical solutions and the isobaric

1-D model is excellent. Low deviations in BOG rates are observed for both high (AAD = 0.4%, MD = 0.5%) and low (AAD = 0.3%, MD = 0.4%) liquid fillings. Similarly, the agreement for liquid volumes was excellent for both high (AAD < 0.1%, MD = 0.1%) and low (AAD = 0.3%, MD = 0.5%) liquid fillings.

The influence of the cryogen in the accuracy of the analytical solutions was evaluated repeating the simulations for liquid nitrogen in the same tank. The deviations obtained were similar except for BOG rates during the transient period, see Figure 5.26d. The larger deviations in BOG rates for nitrogen evaporation are a result of the lower boiling point of nitrogen compared with methane, which produces a faster change of vapour density with temperature. For the pseudo-steady state period, $t \geq \tau_{\text{trans}}$, the agreement on BOG rates was similar to that observed for liquid methane (AAD = 0.55%, MD = 0.6%).

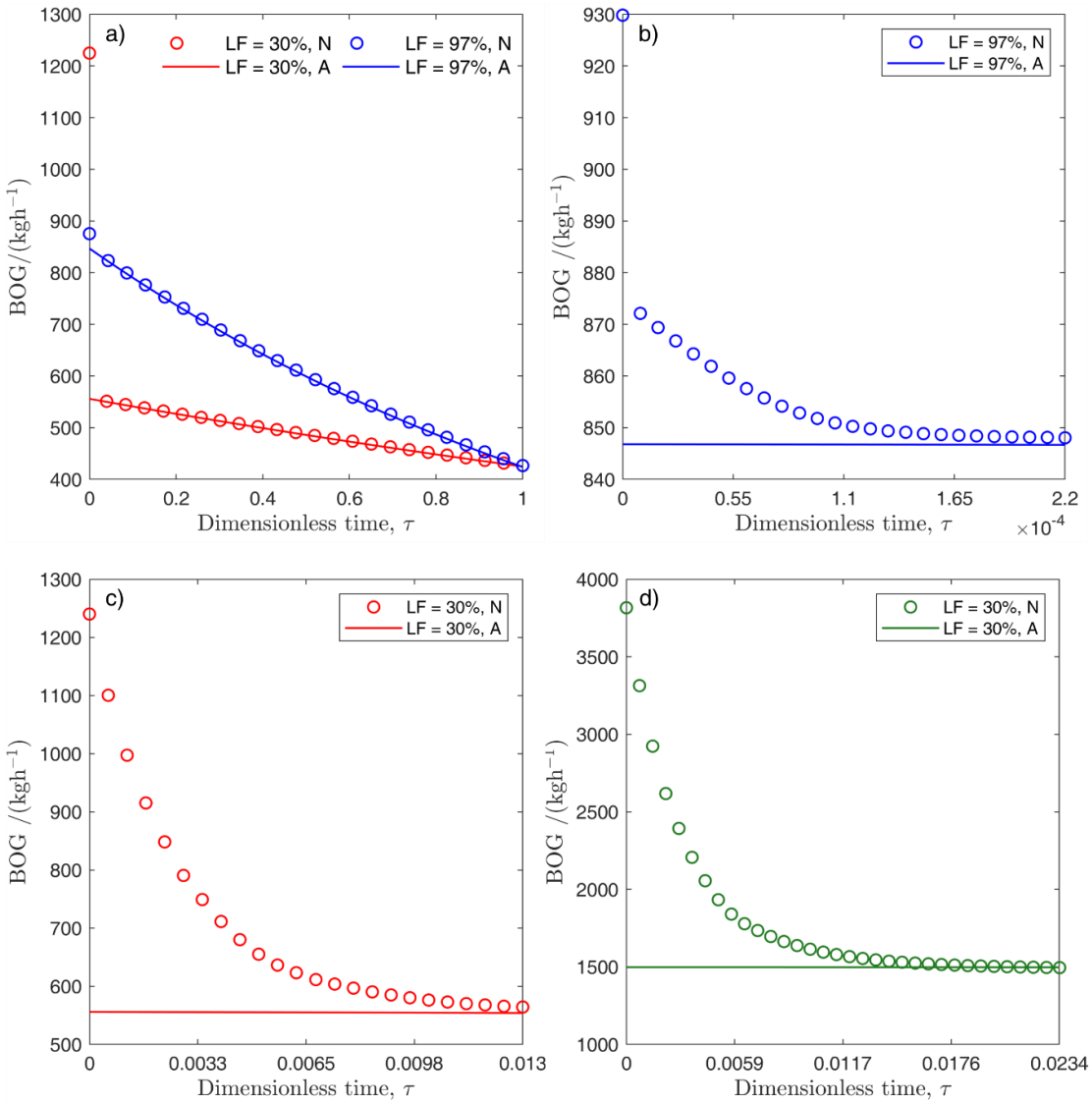

Figure 5.26: BOG rates during the storage of pure cryogens in a large tank as a function of evaporation dimensionless time $\tau = t^*_{evap} = t/\tau_{evap}$. The evaporation of liquid methane in the tank filled at 97% of its capacity is depicted in (a) for long term storage, and (b) for the transient period at the beginning of the evaporation. The transient period of evaporation for the tank filled at 30% of its capacity is displayed in (c) for methane and (d) for nitrogen. The analytical solutions are plotted in solid lines, and the numerical results produced by the isobaric 1-D model are plotted in empty circles.

The difference between the direct and sequential route on the implementation of the analytical solutions was evaluated for methane evaporation in Scenario 4. On the direct route, the vapour thermophysical properties are evaluated at the average vapour temperature, avoiding the iterative procedure required by the sequential route. The change was negligible for liquid volumes (ΔAAD < 0.1%), small for BOG rates (ΔAAD ~ 0.4%) and for vapour and BOG temperatures (ΔAAD ~ 1%). The increase in maximum deviation, ΔMD, was negligible in all cases. This is to be expected for the liquid volume

and BOG temperature as they are independent of the vapour temperature for $t > \tau_{\text{trans}}$. The small change in MD is also expected for evaporation rates and BOG rates, as $\dot{Q}_{\text{VL}}$ in large tanks is small [2], see subsection 5.3.2. More generally, the vapour density is negligible compared with the liquid density during typical conditions for cryogenic liquids storage, see Eq. (3.28). In contrast, the increase in deviations for $\dot{Q}_{\text{VL}}$ was moderate (ΔAAD ~ 4%) with ΔMD = 6% for low LF and ΔMD = 18% for high LF. Finally, the performance of the analytical solutions on estimating the evaporation time τ_{evap} was evaluated. The analytical solution, Eqs. (3.27) using Eqs. (3.44)-(3.45) for *C* and *D*, underestimates the evaporation period by on average 0.5% irrespective of the initial liquid filling.

5.4.4 Error analysis

For the small storage tank, the sequential route achieved a good agreement in spite of a larger contribution of $\dot{Q}_{\text{VL}}$ to evaporation rates. The agreement for $\dot{Q}_{\text{VL}}$ was also good for both high LF (AAD = 0.4%, MD = 4.4%) and low LF (AAD = 1.4%, MD = 2.3%). This is a consequence of the good agreement of vapour temperature at the vapour-liquid interface, which was also observed for medium tanks, see Figure 5.22. Evaluating vapour properties at the saturation temperature instead of the average vapour temperature resulted only in a small increase in deviations for the quantities displayed in Table 5.4. The change in AAD (ΔAAD) was small for BOG rates (ΔAAD ~ 0.4%) and liquid volume (ΔAAD ~ 0.6%), and moderate for BOG temperature (ΔAAD ~ 1.5%). Hence, accurate estimates of BOG rates, liquid volume and BOG temperature can be obtained without using the iterative temperature loop. In contrast, using the saturation temperature to calculate the vapour temperature profile and especially $\dot{Q}_{\text{VL}}$ resulted in large deviations. To accurately estimate these two quantities using the analytical solutions, the iterative temperature loop is required.

The decrease in deviations, as the tank size increases, can be attributed to the increase in magnitude of the vapour to liquid heat transfer rate $\dot{Q}_{\text{VL}}$. To understand the of impact $\dot{Q}_{\text{VL}}$, the average ratio of $\dot{Q}_{\text{VL}}$to the total liquid heat ingress, $\dot{Q}_{\text{L,tot}}$, is defined as $r_q = \int_0^{\tau_{\text{evap}}} \dot{Q}_{\text{VL}}/\dot{Q}_{\text{L,tot}}$. In small tanks, this quantity is 4 to 6 times higher than for the

medium-sized tank and 26 to 56 times higher than for the large tank, see Table 5.6. For the large tanks, the contribution of $\dot{Q}_{\mathrm{VL}}$ to the total liquid heat ingress $\dot{Q}_{\mathrm{L,tot}}$ that drives the evaporation, see Eq. (3.6), is very small. The accuracy of the analytical solutions increases with decreasing r_q, as the solutions for $\dot{Q}_{\mathrm{L,in}}$ and $\dot{Q}_{\mathrm{b}}$, that contribute (1-r_q)% $\dot{Q}_{\mathrm{L,tot}}$, are exact.

Table 5.6: Time-averaged ratio of vapour to liquid heat transfer rate to the total liquid heat ingress. This ratio is defined as $r_q = \int_0^{\tau_{\mathrm{evap}}} \dot{Q}_{\mathrm{VL}}/\dot{Q}_{\mathrm{L,tot}}$ where $\dot{Q}_{\mathrm{VL}}$ is the vapour to liquid heat ingress and $\dot{Q}_{\mathrm{L,tot}}$ the liquid heat ingress. The ratios have been calculated for the three storage tanks filled at low and high initial liquid filling (*LF*) considered in subsections 5.4.1-5.4.3.

Tank size	Liquid filling (LF)	Capacity / m³	r_q
Small	30%	8	18.6%
Medium	30%	80.4	3.3%
Large	30%	165,000	0.60%
Small	97%	8	6.0%
Medium	97%	80.4	1.6%
Large	97%	165,000	0.23%

For large tanks, the assumption of a small, constant $\dot{Q}_{\mathrm{VL}}$ used to derive the analytical solutions is more appropriate than for small and medium-sized tanks. In small tanks, higher values of r_q do not corroborate the assumption of either small or constant $\dot{Q}_{\mathrm{VL}}$ made in deriving the analytical solution. An inaccurate estimation of $\dot{Q}_{\mathrm{VL}}$ would introduce an error to the estimate of $\dot{Q}_{\mathrm{L,tot}}$, that governs the liquid volume and the advective velocity $\bar{v}_z$, see Eqs. (3.2), (3.4), (3.6) and (3.19). The vapour temperature profile is very sensitive to the estimation of the advective velocity, as advection dominates the heat transfer in the vapour phase [2]. Hence, higher errors in $\dot{Q}_{\mathrm{VL}}$ in small tanks will also produce higher deviations on T_{BOG} and BOG rates, see Table 5.4. and Table 5.5.

5.4.5 Summary of findings

- For superheated vapour, the solutions are accurate for industrial applications.
- The solutions are exact if the vapour is at saturation temperature.
- The pseudo-steady state assumption used to derive the analytical solutions is well justified.

- The initial amount of cryogen has a pronounced effect on evaporation rate across all storage tank sizes
- The vapour to liquid heat transfer rates decreases with increasing tank diameter.
- At pseudo-steady state, the vapour temperature profile is mainly governed by the liquid level in the storage tank.

5.5 References

[1] F. Huerta and V. Vesovic, "CFD modelling of the isobaric evaporation of cryogenic liquids in storage tanks," *Int. J. Heat Mass Transfer,* vol. 176, p. 121419, 2021/09/01/ 2021, doi: https://doi.org/10.1016/j.ijheatmasstransfer.2021.121419.

[2] F. Huerta and V. Vesovic, "A realistic vapour phase heat transfer model for the weathering of LNG stored in large tanks," *Energy,* vol. 174, pp. 280-291, 2019/05/01/ 2019, doi: https://doi.org/10.1016/j.energy.2019.02.174.

[3] C. Migliore, C. Tubilleja, and V. Vesovic, "Weathering prediction model for stored liquefied natural gas (LNG)," (in English), *J. Nat. Gas. Sci. Eng.,* vol. 26, pp. 570-580, Sep 2015, doi: 10.1016/j.jngse.2015.06.056.

[4] Linde, "Cryogenic Standard Tanks LITS 2," Tacherting, Germany, 2019. [Online]. Available: https://www.linde-engineering.com/en/images/P_3_3_e_12_150dpi_tcm19-5774.pdf

[5] R. N. Krikkis, "A thermodynamic and heat transfer model for LNG ageing during ship transportation. Towards an efficient boil-off gas management," *Cryogenics,* vol. 92, pp. 76-83, 2018/06/01/ 2018, doi: https://doi.org/10.1016/j.cryogenics.2018.04.007.

[6] M. Seo and S. Jeong, "Analysis of self-pressurization phenomenon of cryogenic fluid storage tank with thermal diffusion model," *Cryogenics,* vol. 50, no. 9, pp. 549-555, Sep 2010, doi: 10.1016/j.cryogenics.2010.02.021.

[7] M. Kang, J. Kim, H. You, and D. Chang, "Experimental investigation of thermal stratification in cryogenic tanks," *Exp. Therm. Fluid Sci.,* vol. 96, pp. 371-382, 2018/09/01/ 2018, doi: https://doi.org/10.1016/j.expthermflusci.2017.12.017.

[8] S. Wu, Y. Ju, J. Lin, and Y. Fu, "Numerical simulation and experiment verification of the static boil-off rate and temperature field for a new independent type B liquefied natural gas ship mock up tank," *Appl. Therm. Eng.,* vol. 173, p. 115265, 2020/06/05/ 2020, doi: https://doi.org/10.1016/j.applthermaleng.2020.115265.

[9] K. T. Yang, J. L. Novotny, and Y. S. Cheng, "Laminar free convection from a nonisothermal plate immersed in a temperature stratified medium," *Int. J. Heat Mass Transfer,* vol. 15, no. 5, pp. 1097-1109, 1972/05/01/ 1972, doi: https://doi.org/10.1016/0017-9310(72)90242-6.

[10] C. Migliore, A. Salehi, and V. Vesovic, "A non-equilibrium approach to modelling the weathering of stored Liquefied Natural Gas (LNG)," *Energy,* vol. 124, pp. 684-692, 2017, doi: 10.1016/j.energy.2017.02.068.

[11] C. Conrado and V. Vesovic, "The influence of chemical composition on vaporisation of LNG and LPG on unconfined water surfaces," *Chem. Eng. Sci.,* vol. 55, no. 20, pp. 4549-4562, Oct 2000, doi: 10.1016/s0009-2509(00)00110-x.

[12] R. N. Krikkis, B. Wang, and S. Niotis, "An analysis of the ballast voyage of an LNG Carrier. The significance of the loading and discharging cycle," *Appl. Therm. Eng.,* vol. 194, p. 117092, 2021/07/25/ 2021, doi: https://doi.org/10.1016/j.applthermaleng.2021.117092.

[13] S. Effendy, M. S. Khan, S. Farooq, and I. A. Karimi, "Dynamic modelling and optimization of an LNG storage tank in a regasification terminal with semi-analytical solutions for N2-free LNG," *Comput. Chem. Eng.,* vol. 99, pp. 40-50, 2017, doi: 10.1016/j.compchemeng.2017.01.012.

[14] A. Saleem, S. Farooq, I. A. Karimi, and R. Banerjee, "A CFD simulation study of boiling mechanism and BOG generation in a full-scale LNG storage tank," *Comput. Chem. Eng.,* vol. 115, pp. 112-120, Jul 2018, doi: 10.1016/j.compchemeng.2018.04.003.

[15] S. Roh and G. Son, "Numerical study of natural convection in a liquefied natural gas tank," *J. Mech. Sci. Technol.,* vol. 26, no. 10, pp. 3133-3140, 2012, doi: 10.1007/s12206-012-0820-x.

[16] S. Roh, G. Son, G. Song, and J. Bae, "Numerical study of transient natural convection in a pressurized LNG storage tank," *Appl. Therm. Eng.,* vol. 52, no. 1, pp. 209-220, 2013/04/05/ 2013, doi: https://doi.org/10.1016/j.applthermaleng.2012.11.021.

[17] Y. Lin, C. Ye, Y. Y. Yu, and S. W. Bi, "An approach to estimating the boil-off rate of LNG in type C independent tank for floating storage and regasification unit under different filling ratio," *Appl. Therm. Eng.,* vol. 135, pp. 463-471, May 2018, doi: 10.1016/j.applthermaleng.2018.02.066.

[18] F. Perez *et al.*, "Measurements of boil-off gas and stratification in cryogenic liquid nitrogen with implications for the storage and transport of liquefied natural gas," *Energy,* vol. 222, p. 119853, 2021/05/01/ 2021, doi: https://doi.org/10.1016/j.energy.2021.119853.

[19] F. Huerta and V. Vesovic, "Analytical solutions for the isobaric evaporation of pure cryogens in storage tanks," *Int. J. Heat Mass Transfer,* vol. 143, p. 118536, 2019/11/01/ 2019, doi: https://doi.org/10.1016/j.ijheatmasstransfer.2019.118536.

Chapter 6

Model development for the non-isobaric evaporation of cryogenic liquids in storage tanks

6.1 Introduction

Under non-isobaric conditions, the heat ingress not only drives the evaporation of the stored cryogenic liquid but also the pressure build-up. As the pressure builds up, the saturation temperature of the cryogen increases more quickly than the rate at which the heat is transferred from the interface to the liquid bulk. This produces a vertical temperature gradient in the liquid, in addition to the vapour vertical thermal stratification observed during isobaric evaporation. Although the liquid temperature in the liquid bulk will be lower than the saturation temperature, this is not the case at the tank wall. At the tank wall, nucleate boiling will occur, and the wall heat flux will be partitioned in evaporation, natural convection and quenching. Hence, a fraction of the heat ingress will evaporate the liquid near the wall, while the remainder will heat the liquid.

In section 6.2, simplified equilibrium and 1-D non equilibrium models are developed to present a base for comparison against more complex models. In section 6.3, a vapour-bulk – CFD-SP model is developed taking the Panzarella et al. evaporation model [1] as a starting point. The model is extended to allow the superheating of the vapour with respect to the saturation temperature, and to include the contribution of wall evaporation to evaporation rates. Finally, in section 6.4 the multiphase two-fluid Euler-Euler CFD solver reactingTwoPhaseEulerFoam [2] is presented for the non-isobaric evaporation of cryogens. The solver is extended through the inclusion of convection-conduction boundary conditions at the tank bottom, wall and roof.

6.2 Equilibrium and 1-D models for non-isobaric evaporation

The cryogenic storage tank has been modelled as a vertical cylinder with multi layered insulation. The physical model of the tank is the same as the one considered for isobaric evaporation in section 4. The vapour and liquid have been initially assumed to be separated by a smooth horizontal interface orthogonal to the acceleration of gravity. This is the same assumption applied for isobaric evaporation in section 4, valid for low wall heat fluxes ($q_L < 0.5$ kW m^{-2}) and large tank volumes ($V_T \sim 200.000$ m^3) [3]. However, the threshold for q_L is not necessarily the same for a smaller tank and non-isobaric evaporation, as wall boiling may occur [4].

Ferrin and Pérez-Pérez [5] performed multiphase CFD simulations for the non-isobaric evaporation of methane in a 0.5 m^3 cylindrical storage tank. They reported a smooth vapour-liquid interface for a heat flux range typical of industrial applications, $q_L \sim 10$-54 Wm^{-2}. However, several numerical studies for isobaric [3] and non-isobaric [5] evaporation used the Volume of Fluid (VoF) method with the Lee sub-model to characterise phase change [6]. This introduces a modelling uncertainty, as the evaporation and condensation rates are highly sensitive to the choice of empirical parameters [7]. These empirical parameters are typically not available for the evaporation of cryogenic liquids. Consequently, extrapolation or estimation of the empirical parameters is required. Another limitation of VoF is that wall boiling cannot be explicitly modelled. In section 6.4, a Euler-Euler multiphase model that includes more accurate wall boiling and phase change sub-models is developed. One of the objectives of this multiphase model is to test the smooth interface assumption removing the uncertainty introduced by the simpler VoF simulations. Nevertheless, for heat fluxes typical for cryogenic storage it is hardly likely that the interface would be greatly disrupted, particularly far from the tank wall.

Figure 6.1 depicts a schematic of the cryogenic storage tank under non-isobaric conditions. At the beginning of the storage period, the liquid cryogen and its vapour are at temperatures far below the surrounding air temperature. This temperature gradient drives a heat ingress to both vapour and liquid phases through the tank walls, through the same mechanisms discussed in Chapter 3. In this chapter, the applicability of the assumptions in deriving this heat transfer model will be revised with a focus on the

emerging phenomena during non-isobaric evaporation. In summary, heat flows from the air to the outer wall of the multi-layered insulation (MLI) system through natural convection. Then, heat flows by conduction from the outer layer of the MLI cylindrical wall to the innermost layer in contact with the cryogen. Finally, heat it is transferred by natural convection from the solid wall in contact with the cryogen to the liquid and vapour phases. A detailed explanation of mixed convection and conduction for isobaric evaporation is provided in sections 3.2-3.3 and in Migliore et al. equilibrium model [8].

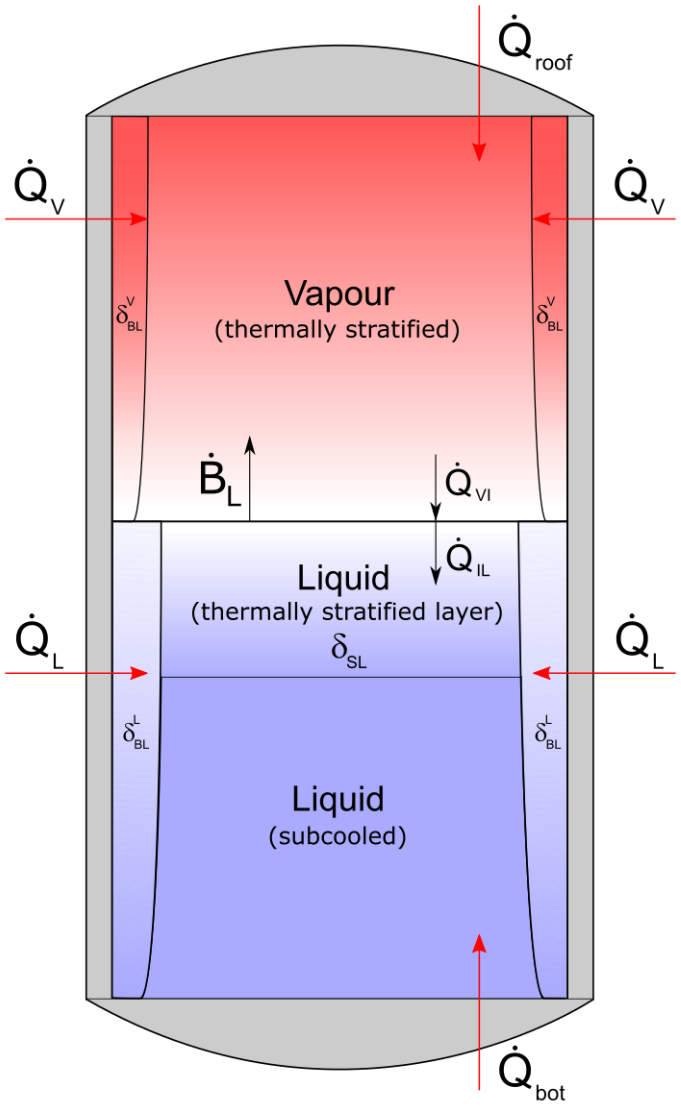

Figure 6.1: Schematic of the modelled closed cryogenic storage tank. The red and black arrows represent heat and mass flows, respectively. δ_{BL} depict the wall boundary layers in the vapour and liquid phase, respectively, indicated with the superscripts V and L. δ_{SL} depicts the thermally stratified layer in the liquid side of the vapour-liquid interface. δ_{BL} and δ_{SL} have been amplified for illustrative purposes, and do not correspond to their physical scale.

The vapour phase is heated through the roof at a rate $\dot{Q}_{\mathrm{roof,in}}$ and through the tank walls at a rate $\dot{Q}_{\mathrm{V,in}}$. At the vapour-liquid interface, the vapour will heat the vapour-liquid interface by conduction at a vapour to interface heat transfer rate, $\dot{Q}_{\mathrm{VI}}$. Similarly, the liquid phase is heated through the walls at a rate $\dot{Q}_{\mathrm{L,in}}$ and through the bottom at a rate $\dot{Q}_{\mathrm{bot}}$. At the interface, the liquid phase will cool the vapour-liquid interface by conduction at an interface to liquid heat transfer rate $\dot{Q}_{\mathrm{IL}}$. The interfacial heat transfer rates have been defined considering a positive vertical direction with a normal vector pointing from the interface towards the vapour. Therefore, the net heat transfer rate to the interface is defined by $\dot{Q}_{\mathrm{int}} = \dot{Q}_{\mathrm{VI}} - \dot{Q}_{\mathrm{IL}}$. If wall boiling is neglected, the evaporation rate $\dot{B}_{\mathrm{L}}$ is determined by the energy balance at the vapour-liquid interface. The evaporation rate has been defined positive for evaporation and negative for condensation.

As the evaporation progresses, the pressure of the vapour will increase as a consequence of vapour heating and liquid evaporation. As a consequence, the saturation temperature of the stored cryogen will increase. For heat fluxes typical of cryogenic storage, the increase in saturation temperature, dT_{sat}/dt, is much slower than the speed of thermal diffusion in the vapour [9]. Hence, the vapour is expected to be superheated with respect to the vapour-liquid interface which implies that $\dot{Q}_{\mathrm{VI}}$ will be positive. In this scenario, the vapour heat ingress through the walls, $\dot{Q}_{\mathrm{V,in}}$, will drive natural convection in the vapour phase. As time progresses, the natural convection will be dampened by the onset of thermal stratification [10], see section 5.1. In contrast to the isobaric case, in non-isobaric storage the evaporated cryogen is not removed as it is generated. Therefore, there will be no advection in the vapour phase, and a larger vertical temperature gradient will be established in comparison with isobaric storage. The larger temperature gradient during non-isobaric evaporation will dampen natural convection faster and more strongly than during isobaric evaporation.

In contrast to the rapid vapour heating, the heating of the liquid phase will occur at a slower rate than the increase of saturation temperature. Hence, the liquid will be subcooled with respect to the interface. The liquid heat ingress through the walls, $\dot{Q}_{\mathrm{L,in}}$, will heat a thin layer of liquid next to the wall. The decrease in density owing to liquid heating will produce a buoyancy driven flow. The liquid will ascend from the near wall

region to the region below the interface, where it will be efficiently mixed in the radial direction. With the increase of saturation temperature, the interface will heat the liquid immediately below by conduction at a rate $\dot{Q}_{\mathrm{IL}}$. As the liquid temperature below the interface increases, a transient layer of thermal stratification, δ_{TS}, will be produced. The thermally stratified layer will propagate downwards from the interface to the liquid bulk as the evaporation progresses [11-16]. The onset of thermal stratification in the liquid phase will dampen the buoyancy driven flow by the establishment of a stable negative density gradient [11-14, 16, 17].

Although both vapour and liquid phases will undergo vertical thermal stratification, the thermally stratified layer in the vapour will propagate faster than in the liquid. For instance, the ratio of thermal diffusivities between the vapour and liquid phases, $\gamma_\alpha = \alpha_{\mathrm{V}}/\alpha_{\mathrm{L}}$, is of liquid nitrogen at P = 100 kPa is 16.7. Not only will vertical heat conduction occur at a different time scale for each phase, but the structure and magnitude of natural convection is also expected to be different in each phase. The ratio between the Rayleigh numbers of each phase, $\gamma_{Ra} = Ra_{\mathrm{V}}/Ra_{\mathrm{L}}$, will be a strong function of liquid filling at thermal stratification. For instance, the value of γ_{Ra} is 0.09 in a cylindrical tank filled with LN_2 at 50% of its capacity, operating at P = 100kPa, at the beginning of the evaporation. Therefore, below the thermally stratified layer natural convection will last longer and will more efficiently mix the liquid phase than the vapour phase.

In summary, the evaporation rate and pressure build-up during the non-isobaric storage tank of a cryogenic liquid depend on the net heat transfer rate at the interface. Simultaneously, the net heat transfer rate depends on the temperature profiles in the vapour and liquid phases. As the saturation temperature is a time varying boundary condition for both liquid and vapour phases, the evolution of the state variables is coupled. As it was discussed previously, the velocity and temperature profiles in each phase are also coupled owing to natural convection and thermal stratification. This highly coupled system makes non-isobaric evaporation considerably more challenging to model than isobaric evaporation. As discussed in Chapters 2 and 5, there is still a lack of agreement on modelling approaches for the simpler isobaric evaporation, particularly on how to model the heat transfer in the vapour phase. In this section, the knowledge

developed in Chapters 3 and 5 is used as a foundation to develop non-isobaric models under the assumption of no wall boiling.

6.2.1 Equilibrium model

The simplest modelling approach is to assume that the liquid and vapour phases are at thermal equilibrium at a spatially homogeneous, common temperature $T_{\mathrm{L}} = T_{\mathrm{V}} = T$. This approach is realistic only for few applications, such as the forced mixing of vapour and liquid to remove thermal stratification during cryogenic storage [1]. Nevertheless, it is worth modelling for two reasons. First, it provides a baseline to analyse the departure from equilibrium in more realistic storage conditions. Second, because it gives light on the thermodynamic relationships between densities, temperatures and pressure which are intricate even if thermal equilibrium is assumed.

The relationship between the evaporation rate, $\dot{B}_{\mathrm{L}}$, and the liquid mass is obtained through a mass balance in the liquid subsystem,

$$-\dot{B}_{\mathrm{L}} = \frac{d}{dt}(\bar{\rho}_{\mathrm{L}} V_{\mathrm{L}}) = \bar{\rho}_{\mathrm{L}} \frac{dV_{\mathrm{L}}}{dt} + V_{\mathrm{L}} \frac{d\bar{\rho}_{\mathrm{L}}}{dt}. \tag{6.1}$$

Eq. (6.1) is valid for the general case of non-isothermal, non-spatially homogeneous liquid. For the equilibrium model, the liquid density is spatially homogeneous, $\bar{\rho}_{\mathrm{L}} = \rho_{\mathrm{L}}(t)$, as a consequence of the spatially homogeneous liquid temperature assumption. Eq. (6.1) is similar equivalent to the mass balance for isobaric evaporation for pure cryogens, Eq. (3.4), plus a thermal expansion term $V_{\mathrm{L}} d\rho_{\mathrm{L}}/dt$. For the isobaric evaporation, the liquid temperature is constant during the evaporation and the thermal expansion term vanishes, see Eq. (3.4). However, this is not true for non-isobaric storage. Assuming that the liquid is spatially homogeneous, its temperature will be equal to the saturation temperature at the interface, $T_{\mathrm{L}} = T_{\mathrm{sat}}(P)$. As the pressure of the system will increase with the progress of evaporation, the saturation temperature will increase producing liquid thermal expansion. Although the increase in pressure will compress the liquid, the magnitude of the isothermal compressibility is negligible compared with isobaric expansivity, $|\partial\rho_{\mathrm{L}}/\partial P| < |\partial\rho_{\mathrm{L}}/\partial T|$, for the operational ranges of non-isobaric storage, $P \sim$ 0.1 – 1 MPa. It has been observed experimentally that for typical storage conditions, particularly at high liquid fillings, the liquid thermal

expansion can be significant [11, 12]. Therefore, the liquid thermal expansion term will not be neglected.

Under non-isobaric conditions, there is no removal of the evaporated liquid as BOG, $\dot{B} = 0$. In this scenario, the global mass balance in the storage tank is,

$$\frac{d}{dt}(\bar{\rho}_{\mathrm{L}} V_{\mathrm{L}} + \bar{\rho}_{\mathrm{V}} V_{\mathrm{V}}) = -\dot{B}_{\mathrm{L}} + \bar{\rho}_{\mathrm{V}} \frac{dV_{\mathrm{V}}}{dt} + V_{\mathrm{V}} \frac{d\bar{\rho}_{\mathrm{V}}}{dt} = 0 \tag{6.2}$$

which indicates that the evaporated cryogen will accumulate in the vapour phase at a rate $\dot{B}_{\mathrm{L}}$. Eq. (6.2) is valid for a non-isothermal vapour phase. Assuming a spatially homogeneous vapour temperature equal to the saturation temperature of the cryogen in the tank, $T_{\mathrm{V}} = T_{\mathrm{sat}}(P)$ and $\bar{\rho}_{\mathrm{V}} = \rho_{\mathrm{V}}$. In consequence, for the equilibrium model all thermodynamic properties for liquid and vapour are assumed spatially homogeneous. In contrast to isobaric evaporation of a pure cryogen, the liquid heat ingress will not only drive evaporation but also the heating of the liquid. The liquid phase energy balance that considers liquid heating has already been derived in section 3.5 for the weathering model, see Eqs. (3.47)-(3.48). However, in this chapter a different approach will be considered to be consistent with Figure 6.1 and to include interface to liquid heat transfer. The interface is modelled as a separate subsystem from the vapour and liquid phases. In the equilibrium model, wall boiling has been neglected, and it has been assumed that all the evaporation occurs at the vapour-liquid interface. Therefore, the evaporation rate is defined by an energy balance at the interface,

$$\dot{Q}_{\mathrm{VI}} - \dot{Q}_{\mathrm{IL}} = \dot{B}_{\mathrm{L}} \Delta H_{\mathrm{LV}}(P_{\mathrm{sat}}), \tag{6.3}$$

By the usage of an interfacial heat balance, it is assumed that the energy jump characteristic of phase change occurs at the interface. The energy balance in the liquid subsystem is given by,

$$\dot{Q}_{\mathrm{bot}} + \dot{Q}_{\mathrm{L,in}} + \dot{Q}_{\mathrm{IL}} - \dot{B}_{\mathrm{L}} h_{\mathrm{L}}(T_{\mathrm{sat}}) = \frac{d}{dt}(\bar{\rho}_{\mathrm{L}} V_{\mathrm{L}}) \bar{h}_{\mathrm{L}} + \bar{\rho}_{\mathrm{L}} V_{\mathrm{L}} \frac{d\bar{h}_{\mathrm{L}}}{dt}. \tag{6.4}$$

Under the assumption of spatially homogeneous liquid temperature, the average liquid density and enthalpy are also spatially homogeneous, $\bar{\rho}_{\mathrm{L}} = \rho_{\mathrm{L}}$, $\bar{h}_{\mathrm{L}} = h_{\mathrm{L}}$. Eq. (6.4) is notably distinct than the liquid energy balance stated in the weathering model, see Eq. (3.47). In Eq. (6.4), the energy leaves the liquid subsystem, through evaporation at the

interface, at a rate $\dot{B}_{\mathrm{L}} h_{\mathrm{L}}$. In contrast, In Eq. (3.47) the energy leaves the liquid subsystem at a rate $\dot{B}_{\mathrm{L}} h_{\mathrm{V}}$ because the interface was included in the liquid subsystem. By substituting Eq. (6.1) in Eq. (6.3) and rearranging terms, the energy balance in the liquid phase is simplified to,

$$\dot{Q}_{\mathrm{bot}} + \dot{Q}_{\mathrm{L,in}} + \dot{Q}_{\mathrm{IL}} = \bar{\rho}_{\mathrm{L}} V_{\mathrm{L}} \frac{d\bar{h}_{\mathrm{L}}}{dt}, \tag{6.5}$$

which is explicit in the rate of change of liquid sensible heat. Assuming a spatially homogeneous liquid temperature, $\bar{\rho}_{\mathrm{L}} = \rho_{\mathrm{L}}$ and $\bar{h}_{\mathrm{L}} = h_{\mathrm{L}}$, as discussed previously. If a constant specific heat capacity at constant volume, $c_{\mathrm{v,L}}$, is assumed for the liquid, its internal energy can be calculated as $u = c_{\mathrm{V}} T$. Thus, the derivative of the liquid enthalpy can be written as,

$$\frac{dh_{\mathrm{L}}}{dt} = \frac{d}{dt}\left(c_{\mathrm{v,L}} T_{\mathrm{L}} + P v_{\mathrm{L}}\right) = c_{\mathrm{v,L}} \frac{dT_{\mathrm{L}}}{dt} + v_{\mathrm{L}} \frac{dP}{dt} + P \frac{dv_{\mathrm{L}}}{dt}, \tag{6.6}$$

Where $v_{\mathrm{L}} = 1/\rho_{\mathrm{L}}$ is the specific volume of the liquid. As the specific volume of a cryogenic liquid is small, and its change over time during typical non-isobaric storage scenarios is slow, the last two terms in Eq. (6.6) have been neglected. By substituting this expression for the enthalpy in Eq. (6.5), $\dot{Q}_{\mathrm{IL}}$ can be expressed as a function of dT_{sat}/dt and the heat ingresses through the bottom and tank walls,

$$\dot{Q}_{\mathrm{IL}} = \rho_{\mathrm{L}} V_{\mathrm{L}} c_{\mathrm{v,L}} \frac{dT_{\mathrm{L}}}{dt} - \dot{Q}_{\mathrm{bot}} - \dot{Q}_{\mathrm{L,in}}, \tag{6.7}$$

Eq. (6.7) provides an important insight regarding the direction of heat transfer between the interface and liquid bulk during non-isobaric evaporation. Under the assumption of spatially homogeneous liquid temperature, $T_L = T_{\mathrm{sat}}$ on Eq. (6.7). If the interface is superheated with respect to the liquid, the interface to liquid heat transfer rate must be positive, $\dot{Q}_{\mathrm{IL}} > 0$. Eq. (6.7) provides a condition that allows the interface to be at thermal equilibrium or superheated with respect to the liquid,

$$\frac{dT_{\mathrm{sat}}}{dt} \geq \frac{\dot{Q}_{\mathrm{bot}} + \dot{Q}_{\mathrm{L,in}}}{\bar{\rho}_{\mathrm{L}} V_{\mathrm{L}} c_{\mathrm{v,L}}}. \tag{6.8}$$

On the contrary, if Eq. (6.8) is not satisfied, then liquid bulk will be superheated with respect to the interface. In other words, $\dot{Q}_{\mathrm{IL}} \leq 0$ will imply that the heating of the liquid bulk will contribute to evaporation rates, see Eq. (6.3).

The vapor to interface heat ingress, $\dot{Q}_{\mathrm{VI}}$, is defined by an energy balance in the vapour phase,

$$\dot{Q}_{\mathrm{V,in}} + \dot{Q}_{\mathrm{roof}} - \dot{Q}_{\mathrm{VI}} + \dot{B}_{\mathrm{L}} h_{\mathrm{V}}(T_{\mathrm{sat}}) = \frac{d}{dt}\left(\bar{\rho}_{\mathrm{V}} V_{\mathrm{V}} \bar{h}_{\mathrm{V}}\right). \tag{6.9}$$

Expanding the derivative at the right-hand side of Eq. (6.9), and substituting Eq. (6.2), results in the following expression,

$$\dot{Q}_{\mathrm{V,in}} + \dot{Q}_{\mathrm{roof}} - \dot{Q}_{\mathrm{VI}} = \bar{\rho}_{\mathrm{V}} V_{\mathrm{V}} \frac{d\bar{h}_{\mathrm{V}}}{dt}, \tag{6.10}$$

which is explicit in the rate of change of sensible heat in the vapour phase. If a spatially homogeneous vapour temperature is assumed, $\bar{\rho}_{\mathrm{V}} = \rho_{\mathrm{V}}$ and $\bar{h}_{\mathrm{V}} = h_{\mathrm{V}} = u_{\mathrm{V}} + P v_{\mathrm{V}}$ in Eqs. (6.9) -(6.10). By assuming a constant specific heat capacity at constant volume in the vapour, $c_{\mathrm{v,V}}$, and rearranging terms in Eq. (6.10), $\dot{Q}_{\mathrm{VI}}$ is simplified to,

$$\dot{Q}_{\mathrm{VI}} = \dot{Q}_{\mathrm{V,in}} + \dot{Q}_{\mathrm{roof}} - \bar{\rho}_{\mathrm{V}} V_{\mathrm{V}} \left(c_{\mathrm{v,V}} \frac{d\bar{T}_{\mathrm{V}}}{dt} + v_{\mathrm{V}} \frac{dP}{dt} + P \frac{dv_{\mathrm{V}}}{dt} \right). \tag{6.11}$$

Where $v_{\mathrm{V}} = 1/\rho_{\mathrm{V}}$ is the specific volume of the vapour. The specific volume of the vapour phase of a stored cryogen and its time derivative are more than three orders of magnitude higher than those of the liquid phase. Thus, the second and third terms at the right hand side of Eq. (6.11) cannot be neglected. Under the assumption of spatially homogeneous vapour temperature, $\bar{T}_{\mathrm{V}} = T_{\mathrm{sat}}$. Thus, Eq. (6.11) provides a maximum threshold of dT_{sat}/dt for the vapour bulk to be superheated with respect to the interface,

$$\frac{dT_{\mathrm{sat}}}{dt} < \frac{1}{c_{\mathrm{v,V}}} \left(\frac{\dot{Q}_{\mathrm{V,in}} + \dot{Q}_{\mathrm{roof}}}{\rho_{\mathrm{V}} V_{\mathrm{V}} c_{\mathrm{v,V}}} - v_{\mathrm{V}} \frac{dP}{dt} - P \frac{dv_{\mathrm{V}}}{dt} \right) \rightarrow \dot{Q}_{\mathrm{VI}} > 0\,. \tag{6.12}$$

During the non-isobaric evaporation of a cryogen, $dP/dt > 0$ and $dv_{\mathrm{V}}/dt < 0$. Thus, Eq. (6.12) shows that it is more intricate to determine the sign of the vapour to interface heat transfer rate than the sign of the interface to liquid heat transfer rate, see Eq. (6.8). The consistency of the energy balances can be easily checked by adding Eqs. (6.3), (6.5) and (6.10) to obtain the global energy balance for the storage tank,

$$\dot{Q}_{\mathrm{bot}} + \dot{Q}_{\mathrm{L,in}} + \dot{Q}_{\mathrm{V,in}} + \dot{Q}_{\mathrm{V,roof}} = \dot{B}_{\mathrm{L}} \Delta H_{\mathrm{LV}}(P_{\mathrm{sat}}) + \bar{\rho}_{\mathrm{L}} V_{\mathrm{L}} \frac{d\bar{h}_{\mathrm{L}}}{dt} + \bar{\rho}_{\mathrm{V}} V_{\mathrm{V}} \frac{d\bar{h}_{\mathrm{V}}}{dt}\,. \tag{6.13}$$

The liquid and vapour heat ingresses have been defined assuming pseudo-steady state heat conduction in the solid walls. This assumption was derived using the same arguments for isobaric storage and a complete justification can be found in sections 3.2 - 3.3. In the most general case of non-isobaric evaporation, the temperature of the liquid is not necessarily homogeneous. Hence, the liquid and vapour heat ingresses are defined by $\dot{Q}_{\mathrm{L,in}} = U_{\mathrm{L}} A_{\mathrm{L}} (T_{\mathrm{air}} - \bar{T}_{\mathrm{L}})$ and $\dot{Q}_{\mathrm{V,in}} = U_{\mathrm{V}} A_{\mathrm{V}} (T_{\mathrm{air}} - \bar{T}_{\mathrm{V}})$, respectively. For equilibrium evaporation, $\bar{T}_{\mathrm{L}} = T_{\mathrm{L}} = \bar{T}_{\mathrm{V}} = T_{\mathrm{V}} = T_{\mathrm{sat}}$. The liquid and vapour areas in contact with the tank walls are $A_{\mathrm{L}} = 4(V_{\mathrm{T}} - V_{\mathrm{V}}) d_o / d_i^2$ and $A_{\mathrm{V}} = \frac{4 V_{\mathrm{V}} d_o}{d_i^2}$, respectively, which are equivalent to the areas defined for isobaric evaporation, see Eqs. (3.8)-(3.9). Similarly, the heat ingress through the tank bottom and the roof are defined by $\dot{Q}_{\mathrm{bot}} = U_{\mathrm{bot}} A_{\mathrm{T}} (T_{\mathrm{air}} - T_{\mathrm{L}}|_{z=0})$ and $\dot{Q}_{\mathrm{roof}} = U_{\mathrm{roof}} A_{\mathrm{T}} (T_{\mathrm{air}} - T_{\mathrm{V}}|_{z=l_{\mathrm{L}}+l_{\mathrm{V}}})$, respectively. For the equilibrium model, $T_{\mathrm{L}}|_{z=0} = T_{\mathrm{V}}|_{z=l_{\mathrm{L}}+l_{\mathrm{V}}} = T_{\mathrm{sat}}$. For non-isobaric storage, U_{bot} is introduced as the overall heat transfer coefficient to the liquid through the bottom. Additionally, the vertical coordinate is assumed to start in the bottom of the tank. Hence, $z = l_{\mathrm{L}} + l_{\mathrm{V}}$ represents the position of the roof, and $z = l_{\mathrm{L}}$ is the liquid height that coincides with the location of the vapour-liquid interface.

The total heat ingress to the storage tank, $\dot{Q}_{\mathrm{tot}}$, is defined by the sum of all heat ingresses through the solid boundaries,

$$\dot{Q}_{\mathrm{tot}} = \dot{Q}_{\mathrm{bot}} + \dot{Q}_{\mathrm{L,in}} + \dot{Q}_{\mathrm{V,in}} + \dot{Q}_{\mathrm{roof}}, \tag{6.14}$$

If thermal equilibrium between the vapour and the liquid phases is assumed, $T_{\mathrm{L}} = T_{\mathrm{V}} = T_{\mathrm{sat}}(P)$, the driving force for all terms in Eq. (6.14) is $T_{\mathrm{air}} - T_{\mathrm{sat}}(P)$. Furthermore, $\dot{Q}_{\mathrm{tot}}$ can be expressed as a function of the thermodynamic properties of the cryogen and the overall heat transfer coefficients of the tank MLI,

$$\dot{Q}_{\mathrm{tot}} = \left((U_{\mathrm{bot}} + U_{\mathrm{roof}}) A_{\mathrm{T}} + \frac{4 d_o}{d_i} \left(V_{\mathrm{T}} U_{\mathrm{L}} + V_{\mathrm{V}} (U_{\mathrm{V}} - U_{\mathrm{L}}) \right) \right) (T_{\mathrm{air}} - T_{\mathrm{sat}}). \tag{6.15}$$

Under the assumption of constant specific heat capacity at constant pressure for both phases, using Eq. (6.15) in Eq. (6.13) and rearranging the resulting expression, one obtains

$$\frac{dT_{\text{sat}}}{dt} = \frac{\dot{Q}_{\text{tot}} - \dot{B}_{\text{L}}\Delta H_{\text{LV}}(P_{\text{sat}}) - \rho_{\text{V}}V_{\text{V}}\left(P\frac{dv_{\text{V}}}{dt} + v_{\text{V}}\frac{dP}{dt}\right)}{\left(\rho_{\text{L}}c_{\text{v,L}}(V_{\text{T}} - V_{\text{V}}) + \rho_{\text{V}}c_{\text{v,V}}V_{\text{V}}\right)}, \tag{6.16}$$

that is an explicit ODE for the saturation temperature. To provide closure to this non-isobaric equilibrium model, any suitable equation of state can be used by solving the phase equilibrium condition. This condition implies that the fugacity coefficient calculated with the selected EOS must be equal in both phases,

$$\phi_{\text{L}} = \phi_{\text{V}}\,. \tag{6.17}$$

In this thesis, two equations of states were tested. For the most accurate numerical implementation, the Peng-Robinson EOS was used for both phases. Additionally, a simplified model has been derived by neglecting liquid thermal expansion and using the ideal gas equation of state with the Clausius-Clapeyron relationship. The simplified model constitutes an easy to implement explicit ODE system with fast convergence, useful to verify more complex models. The derivation of the simplified model is presented in Appendix F.

6.2.2 Non-isobaric 1-D model

In this subsection, the equilibrium model developed in subsection 6.2.1 is taken as the starting point to develop a 1-D non-equilibrium model. This model will be denominated non-isobaric 1-D model, to differentiate it from the isobaric 1-D evaporation model developed in section 3.3. In the non-isobaric 1-D model, the thermal equilibrium assumption between vapour and liquid is removed. For each phase, a 1-D heat transfer model is developed that allows the prediction of thermal stratification. For the vapour, the 1-D vapour phase heat transfer model developed in section 3.3 for isobaric evaporation is taken as the starting point. For the heat transfer in the liquid phase, an unsteady heat conduction with a source term equation is used. This approach constitutes an improvement to the thermal diffusion model proposed by Seo et al. [11] in four areas: (i) the change of liquid level due to evaporation and liquid thermal expansion are considered, (ii) the vapour and liquid are heated by a non-uniform source term, (iii) the resulting displacement of the vapour-liquid interface is implemented

through a moving mesh and (iv) the variation of vapour thermal diffusivity with density is not neglected.

In the 1-D non-equilibrium model, the temperature in the vapour and liquid phases are not spatially homogeneous. Excluding the assumptions of thermal equilibrium, spatial homogeneity and surface evaporation, all the assumptions used to derive the equilibrium model will be maintained. Eqs. (6.1) and (6.2) constitute the mass balances in the liquid phase and in the whole tank. In contrast to the equilibrium model, the average density of each phase ψ is not spatially homogeneous nor equal to the density at the saturation point, $\bar{\rho}_\psi \neq \rho_\psi(z) \neq \rho_\psi(T_{\text{sat}})$. Instead, the average densities are calculated from a volume average of the density in each phase, $\bar{\rho}_\psi = 1/l_\psi \int_{l_\psi} \rho_\psi\big(T_\psi(z)\big)dz$, where l_ψ is the height of the phase ψ. Eqs. (6.5) and (6.10) constitute the energy balances for the liquid and vapour phases. The average enthalpy of the phase ψ is calculated by the same volume averaging process as for the density, $\bar{h}_\psi = 1/l_\psi \int_{l_\psi} h_\psi\big(T_\psi(z)\big)dz$.

Owing to wall boiling, a fraction η_{e} of the wall heat flux to the liquid will directly evaporate the liquid adjacent to the tank wall. Therefore, the liquid heat ingress that produces wall boiling, $\dot{Q}_{\text{w,b}}$, is defined by,

$$\dot{Q}_{\text{w,b}} = \eta_{\text{e,w}}\dot{Q}_{\text{L,in}} + \eta_{\text{e,b}}\dot{Q}_{\text{bot}}. \tag{6.18}$$

where $\eta_{\text{e,w}}, \eta_{\text{e,b}} \in [0,1]$ are the evaporative fractions, defined as the fractions of the heat ingress that produce liquid evaporation at the tank wall and bottom, respectively. As a first approximation, $\eta_{\text{e,w}}, \eta_{\text{e,b}}$ assumed to be inputs that can be either fixed or fitted to pressure build-up experimental data. In subsections 6.3.3 and 6.4.4 a detailed procedure to calculate the evaporative fractions using more complex models will be given. The onset of wall boiling acts as an additional energy source to the interfacial energy balance that defines the evaporation rate. Therefore, considering surface evaporation and wall boiling, the evaporation rate for the non-isobaric 1-D model is given by,

$$\dot{B}_{\text{L}} = \frac{\left(\dot{Q}_{\text{VI}} - \dot{Q}_{\text{IL}} + \dot{Q}_{\text{w,b}}\right)}{\Delta H_{\text{LV}}} = \dot{B}_{\text{L,s}} + \dot{B}_{\text{L,w}}. \tag{6.19}$$

where $\dot{B}_{\mathrm{L,s}} = (\dot{Q}_{\mathrm{VI}} - \dot{Q}_{\mathrm{IL}})/\Delta H_{\mathrm{LV}}$ and $\dot{B}_{\mathrm{L,w}} = \dot{Q}_{\mathrm{w,b}}/\Delta H_{\mathrm{LV}}$ are the surface evaporation and wall boiling contributions to the evaporation rate, respectively. An important difference between the non-equilibrium and equilibrium model is how the interfacial heat flows $\dot{Q}_{\mathrm{VI}}$ and $\dot{Q}_{\mathrm{IL}}$ are calculated. In the equilibrium model, they were defined implicitly as a function of the heat ingress in each phase and the change in saturation temperature of the cryogen, see Eqs. (6.7) and (6.10). In the non-equilibrium model, they are calculated using the Fourier's law of heat conduction,

$$\dot{Q}_{\mathrm{VI}} = \pi R_{\mathrm{T}}^2 \left(k_{\mathrm{V}} \frac{\partial T_{\mathrm{V}}}{\partial z} \right) \Big|_{z=l_{\mathrm{L}}} \tag{6.20}$$

$$\dot{Q}_{\mathrm{IL}} = \pi R_{\mathrm{T}}^2 \left(k_{\mathrm{L}} \frac{\partial T_{\mathrm{L}}}{\partial z} \right) \Big|_{z=l_{\mathrm{L}}}. \tag{6.21}$$

The temperature gradients at the vapour and liquid sides of the vapour liquid interface are required to calculate the interfacial heat ingresses. This requires the temperature profiles at each phase, which are the solution of full continuum model of each phase. Using a similar approach to that used for the isobaric 1-D model, a 1-D heat transfer model for each phase is developed to simplify the full continuum model.

As discussed in section 6.2, the heat transfer in the vapour phase during non-isobaric storage is remarkably similar to the isobaric evaporation. One important difference is the absence of BOG removal during non-isobaric storage, which removes advection from the system. The absence of advection and the smaller volume scales of non-isobaric storage will make vertical heat transfer due to natural convection even less significant. Another important difference is the change of vapour density. For isobaric evaporation, the density decreased monotonically owing to vapour heating, while for non-isobaric evaporation, the situation is more complicated. If the net heat flow at the vapour-liquid interface is positive, the vapour density will increase with the accumulation of evaporated moles in the vapour phase. In contrast, if the net heat flow at the interface is negative, the vapour density with the decrease of number of moles in the vapour space by condensation. Although the two cases represent important physical phenomena, they do not alter the dominance of heat transfer in the vertical direction.

The continuous vapour heating will increase the pressure of the vapour bulk with time. This increase in pressure will be observed for both evaporation and condensation.

The increase in the pressure of the vapour will itself increase the saturation temperature of the cryogenic liquid. If the increase in saturation temperature is faster than heat diffusion in the vapour bulk, the vapour temperature may be lower than the saturation temperature at a particular position. This will drive the condensation of some of the vapour, removing the local subcooling with respect to the saturation temperature. To consider this effect, a condensation source term is defined as,

$$\dot{S}_c = \begin{cases} f_c(T_{\text{sat}} - T_{\text{V}}) & \text{if } T_{\text{V}} < T_{\text{sat}} \\ 0 & \text{otherwise} \end{cases} \tag{6.22}$$

where f_c is a condensation coefficient that represents the physical time of bulk condensation as a function of the degree of vapour subcooling. Using the Tanasawa [18] simplification of the Schrage kinetic gas theory evaporation model [19], the condensation and evaporation coefficients can be written as,

$$f_c = \frac{\Delta H_{\text{LV}}^2}{c_{p,V} T_{\text{sat}}^{3/2}} \sqrt{\frac{MW}{2\pi R}} \frac{2\gamma}{2-\gamma}, \tag{6.23}$$

Where MW is the molar weight of the cryogen and γ is the accommodation coefficient that takes values from 0.01 to 1. For cryogen evaporation, Kassemi and Kartuzova [20] observed that a value of γ = 0.01 presented the best fit against experimental results. Nevertheless, the same authors observed that evaporation rates where insensitive to the accommodation coefficients in the range of γ = 0.01 – 1. This yields to condensation coefficients between 17.6 to 3503 s^{-1} for liquid methane and between 17.7 and 3514 for liquid nitrogen. After performing a sensitivity analysis on f_c, it has been found that the vapour temperature profiles are invariant to the values of f_c in the range $10 < f_c < 3600$. Thus, f_c can be tuned within that range to improve model convergence.

We now consider an enthalpy balance in the vapour phase which is given by the partial differential equation that governs the heat transfer in the vapour,

$$\frac{\partial}{\partial t}(\rho_{\text{V}} c_{\text{V}} T_{\text{V}}) = \frac{\partial}{\partial z}\left(k_{\text{V}} \frac{\partial T}{\partial z}\right) + \dot{S}_{\text{w,V}} + \rho_{\text{V}} c_{\text{V}} \dot{S}_c, \tag{6.24}$$

where $\dot{S}_{\text{w,V}} = 4U_{\text{V}} d_{\text{o}}/d_{\text{i}}^2 (T_{\text{air}} - T_{\text{V}})$ is the heating of the vapour through the walls assuming instantaneous heat transfer in the radial direction, see Eq. (3.20). By assuming

constant heat capacity in the vapour phase and expanding the derivatives in the right hand of Eq. (6.24), one obtains

$$c_{\mathrm{V}}\left(\frac{\partial \rho_{\mathrm{V}}}{\partial t}T_{\mathrm{V}}+\rho_{\mathrm{V}}\frac{\partial T_{V}}{\partial t}\right)=\frac{\partial k_{\mathrm{V}}}{\partial z}\frac{\partial T_{\mathrm{V}}}{\partial z}+k_{\mathrm{V}}\frac{\partial^{2}T_{\mathrm{V}}}{\partial z^{2}}+\dot{S}_{\mathrm{w,V}}+\rho_{\mathrm{V}}c_{\mathrm{V}}\dot{S}_{c}. \tag{6.25}$$

Eq. (6.25) can be simplified with two additional assumptions. First, assuming a spatially homogeneous vapour thermal conductivity evaluated at the average vapour temperature, $\bar{k}_{\mathrm{V}}=k_{\mathrm{V}}(\bar{T}_{\mathrm{V}})$, the first term at the right hind side of Eq. (6.25) vanishes. Second, the transient term $\frac{\partial \rho_{\mathrm{V}}}{\partial t}T_{\mathrm{V}}$ is neglected on the basis of experimental results for the evaporation of pure cryogens. Experimental vapour temperature profiles for the non-isobaric evaporation of LH_2 [17], LN_2 [11-13] and liquid methane [14] for a variety of heat ingresses and liquid fillings indicate a rapid onset of a pseudo-steady state. Furthermore, Kang et al. and Pérez-Pérez et al. [12, 13] observed independently that the evaporation rate was small, and in certain scenarios it alternated between evaporation and condensation [12, 13]. Thus, $\partial\rho_{\mathrm{V}}/\partial t$ is expected to be very small compared with $\rho_{\mathrm{V}}\,\partial T_{\mathrm{V}}/\partial t$. Even if $\partial\rho_{\mathrm{V}}/\partial t$ is large, by neglecting this term only the transient temperature profile will be affected. In that less frequent scenario, neglecting $\partial\rho_{\mathrm{V}}/\partial t$ would underestimate the transient period for evaporation and would overestimate it for condensation. Applying these assumptions to Eq. (6.25) yields a vapour temperature profile governed by an unsteady heat conduction equation with a source term,

$$\frac{\partial T_{\mathrm{V}}}{\partial t}=\bar{\alpha}_{\mathrm{V}}\frac{\partial^{2}T_{\mathrm{V}}}{\partial z^{2}}+\frac{\bar{\alpha}_{\mathrm{V}}}{\bar{k}_{V}}\left(\dot{S}_{\mathrm{w,V}}+\dot{S}_{c}\right). \tag{6.26}$$

Eq. (6.26) is constrained by the following initial and boundary conditions,

$$\begin{gathered}T_{\mathrm{V}}(t=0,\ l_{\mathrm{L}}<z<l_{\mathrm{V}})=T_{\mathrm{sat}}(P_{0}),\\ T_{\mathrm{V}}(t,z=l_{\mathrm{L}})=T_{\mathrm{sat}}(P_{\mathrm{I}}),\\ \frac{\partial T_{\mathrm{V}}}{\partial z}(t,z=l_{\mathrm{L}}+l_{\mathrm{V}})=\frac{q_{\mathrm{roof}}}{k_{\mathrm{V}}(z=l_{\mathrm{L}}+l_{\mathrm{V}})},\end{gathered} \tag{6.27}$$

indicating that (i) at the beginning of the evaporation the totality of the vapour space is at the saturation temperature evaluated at the initial pressure, P_0, (ii) at the vapour-liquid interface the vapour is at thermal equilibrium with the interface and (iii) the roof is subject to a heat flux $q_{\mathrm{roof}}=\dot{Q}_{\mathrm{roof}}/A_{\mathrm{T}}$. The calculation of the pressure in the vapour

phase is performed considering the average properties and a suitable equation of state, $P = P(\bar{\rho}_V, \bar{T}_V)$. In contrast to the equilibrium model, phase equilibrium only occurs at the vapour liquid interface, $f_V(z = l_L) = f_L(z = l_V)$.

The heat transfer in the liquid phase has important similarities with the heat transfer in the vapour, as discussed in section 6.2. Therefore, the liquid temperature is assumed radially homogeneous, and advection is neglected. Hence, the enthalpy balance in the liquid phase will produce an equation analogous to Eq. (6.24), but with liquid thermodynamic and thermophysical properties instead of vapour ones. The heat source term for the liquid phase representing wall heating, $\dot{S}_{w,L}$, is defined through an infinitesimal cylindrical section,

$$\dot{S}_{w,L} = \frac{4U_L d_o}{d_i^2}(T_{air} - T_L). \tag{6.28}$$

As a consequence of liquid heating through the walls and from interface, the liquid temperature may exceed the saturation temperature in a particular position. This phenomenon will drive the boiling of some liquid in that position, removing the local superheating with respect to the saturation temperature. To consider this effect, an evaporation sink term is defined as,

$$\dot{S}_e = \begin{cases} f_b(T_L - T_{sat}) & \text{if } T_L > T_{sat} \\ 0 & \text{otherwise} \end{cases} \tag{6.29}$$

where f_b is the evaporation coefficient that represents the physical time of bulk evaporation. The Tanasawa [18] simplification of the Schrage kinetic gas theory evaporation model [19] also assumes that the evaporation and condensation coefficients are equal, $f_b = f_c$. After performing a sensitivity analysis in the same parametric range as for the condensation coefficient, $10 < f_b < 3600$, it was observed that evaporation rates and liquid temperatures were insensitive to f_b. Thus, f_b can be tuned within that parametric range to improve model convergence, analogously to what has been discussed for f_c.

The change of liquid density with time is expected to be considerably smaller than the change of vapour density. Additionally, the maximum liquid subcooling, $\Delta T_{sc} = T_{sat} - T_L|_{z=0}$, is expected to be lower than the maximum vapour superheating, $\Delta T_{sh} = T_V|_{z=l_L+l_V} - T_{sat}$. This will produce a lower variation of liquid thermal

conductivity with height. Therefore, neglecting the terms $\partial\rho_{\mathrm{L}}/\partial t\, T_{\mathrm{L}}$ and $\partial k_{\mathrm{L}}/\partial z\ \partial T_{\mathrm{L}}/\partial z$ will produce a smaller error than that obtained in the vapour phase by neglecting these terms. Hence, by substituting the vapour thermophysical properties for the liquid ones in Eq. (6.26), substituting $\dot{S}_{\mathrm{w,V}}$ by $\dot{S}_{\mathrm{w,L}}$ and including the evaporation sink term $\dot{S}_{\mathrm{e}}$, the liquid temperature is governed by,

$$\frac{\partial T_{\mathrm{L}}}{\partial t} = \bar{\alpha}_{\mathrm{L}} \frac{\partial^2 T_{\mathrm{L}}}{\partial z^2} + \frac{\bar{\alpha}_{\mathrm{L}}}{\bar{k}_{\mathrm{L}}} (\dot{S}_{\mathrm{w,L}} - \dot{S}_{\mathrm{e}}). \tag{6.30}$$

Eq. (6.30) is constrained by the following initial and boundary conditions,

$$\begin{gathered} T_{\mathrm{L}}(t = 0, 0 < z < l_{\mathrm{L}}) = T_{\mathrm{sat}}(P_0), \\ T_{\mathrm{L}}(t, z = l_{\mathrm{L}}) = T_{\mathrm{sat}}(P_{\mathrm{I}}), \\ \frac{\partial T_{\mathrm{L}}}{\partial z}(t, z = 0) = \frac{q_{\mathrm{bot}}}{k_{\mathrm{L}}(z = 0)}, \end{gathered} \tag{6.31}$$

indicating that (i) at the beginning of the evaporation the whole of the liquid phase is at the saturation temperature of the cryogen evaluated at the initial pressure (ii) at the vapour-liquid interface the liquid temperature is the saturation temperature of the cryogen at the pressure at the interface, P_{I}, and (iii) the tank bottom is subject to a heat flux $q_{\mathrm{bot}} = \dot{Q}_{\mathrm{bot}}/A_{\mathrm{T}}$.

As the vapour density is small, the variation of the pressure of the vapour with height owing to the hydrostatic head has been neglected. This assumption allows to calculate the pressure of the vapour phase using a suitable equation of state and the average density and temperature. In contrast, the liquid density is 200 to 600 times higher than the vapour for typical cryogenic liquids. This will produce an increase in pressure with liquid depth 200 to 600 times higher than in the vapour. The negative vertical pressure gradient in the liquid, $\partial P/\partial z < 0$, will induce a negative gradient in saturation temperature in the liquid from the bottom to the interface. This effect has been considered in the calculation of the evaporative sink term in Eq. (6.29), but otherwise neglected in the global mass and energy balances. Thus, the pressure of the vapour-liquid interface is assumed to be equal to the pressure of the vapour, that can be calculated using a suitable equation of state,

$$P_{\mathrm{int}} = P_{\mathrm{V}}(\bar{\rho}_{\mathrm{V}}, \bar{T}_{\mathrm{V}}) \ , \tag{6.32}$$

Finally, the saturation temperature can then be obtained implicitly using the selected equation of state and considering phase equilibrium at the vapour liquid interface for a pure cryogen,

$$\phi_{\mathrm{L}}(z = l_{\mathrm{L}}, P_{\mathrm{int}}, T_{\mathrm{sat}}) = \phi_{\mathrm{V}}(z = l_{\mathrm{L}}, P, T_{\mathrm{sat}}). \tag{6.33}$$

In the derivation of the non-equilibrium model, natural convection has been neglected in both phases. However, natural convection is expected to be more significant in the liquid than in the vapour for the following reasons. First, the Rayleigh number is estimated to be at least an order of magnitude higher than in the vapour phase for liquid fillings higher than 50%. Second, the vertical thermal stratification will develop more slowly in the liquid phase than in the liquid. If thermal diffusion is assumed to dominate onset of the pseudo steady state, the penetration length of the thermally stratified layer for the phase ψ scales as,

$$\delta_{\psi}^{\mathrm{SL}} \sim \sqrt{\alpha_{\psi} t} \ , \tag{6.34}$$

where α_{ψ} is the thermal diffusivity of the phase ψ. Consequently, the transient period for each phase scales as,

$$\tau_{\mathrm{trans},\Psi} \sim \frac{l_{\psi}^2}{\alpha_{\psi}} . \tag{6.35}$$

Taking liquid nitrogen as a representative cryogenic liquid, $\alpha_{\mathrm{V}}/\alpha_{\mathrm{L}} = 16.7$. For a liquid filling of 50%, this will imply that $\tau_{\mathrm{trans,L}}/\tau_{\mathrm{trans,V}} = 16.7$. The longer the transient period, the higher the influence of natural convection in the bulk of the phase ψ. Thus, the non-equilibrium model is expected to be a better representation of the physical reality for low liquid fillings. For low liquid fillings, both the Rayleigh number and the transient period in the liquid are expected to be smaller than for high liquid fillings. This will mitigate the modelling error introduced by neglecting the enhancement of the vertical heat transfer by natural convection in the liquid bulk.

6.2.3 Computational implementation

The equilibrium and non-equilibrium models for non-isobaric evaporation of pure cryogens have been implemented in MATLAB R2018b®. The equilibrium model is described by Eqs. (6.1)-(6.2)-(6.4)-(6.9) coupled with a non-linear Equation of State for the vapour. This coupling constitutes an index-1 differential algebraic equations system (DAE), which has been integrated using the ode15i variable-step, variable-order routine [21]. The non-isobaric evaporation model is much more complex than the isobaric model developed in section 3.3, even for the simplest equilibrium models for pure cryogens. For the isobaric equilibrium model, developing analytical solutions was straightforward, while for the non-isobaric model equilibrium model, obtaining a DAE was unavoidable. For each equation, the convergence criterion has been established by setting the absolute and relative tolerances to 10^{-9} and $10^{-4,}$ respectively, for all equations. In contrast to the isobaric evaporation model, much stricter absolute tolerances were required to achieve a smooth evolution of the thermodynamic variables. Although the convergence criteria were strict, the convergence was very quick. The simulation of 10 hours of non-isobaric evaporation took less than 5 s in a single core of an Intel® Core™ i5-7300HQ CPU processor.

In the non-equilibrium model, the partial differential equations (PDE) that govern heat transfer in the liquid and vapour phases, Eqs. (6.26)-(6.30), have been discretised using the method of lines [22]. This method has already been described in section 4.2.4, and it discretises the spatial dimension of the domain and the differential operators to obtain an ODE system for each computational node. In contrast to the vapour-1-D model, an additional ODE system is generated as a consequence of the spatial discretization of the liquid phase. The vapour and liquid phases were discretized in the vertical direction into a uniform meshes composed by $n_{z,\mathrm{V}} = l_\mathrm{V}/\Delta z_\mathrm{V}$ and $n_{z,\mathrm{L}} = l_\mathrm{L}/\Delta z_\mathrm{L}$ nodes. The vapour grid spacing was set to $\Delta z_\mathrm{V} = 1.5 \times 10^{-3}$ m, while a finer spacing was required for the liquid to achieve grid-independent results, $\Delta z_\mathrm{L} = 7 \times 10^{-4}$ m. This is a consequence of the larger gradients in the liquid, produced by its smaller thermal diffusivity, that induce higher discretisation errors in coarse grids.

The displacement of the interface that modifies the size of both vapour and liquid domains, $l_\mathrm{L}(t), \mathrm{l_V}(t) = H_\mathrm{T} - l_\mathrm{L}(t)$, has been implemented using an adaptive moving

mesh [23]. This method was also used for the vapour-1-D model. The coordinate transformation of Eqs. (6.26)-(6.30) required to implement the moving mesh is presented in Appendix C. The Laplacian operators ∂/∂^2 in the transformed version of Eqs. (6.26)-(6.30) have been discretised using second-order central finite differences. The source terms $\dot{S}_{w,V}$, $\dot{S}_{w,L}$ have been evaluated at the node temperatures. The Neumann boundary conditions for the vapour subsystem at the tank node has been implemented using second-order backward differences. Similarly, the Neumann boundary condition for the liquid subsystem at the tank bottom has been implemented using second-order forward differences.

The boundary condition at the vapour-liquid interface for both subsystems is implemented directly and is obtained at each time-step from the solution of the non-isobaric non-equilibrium model, Eqs. (6.1)-(6.3), (6.20)-(6.33). The numerical implementation of the model constitutes a DAE system of $n_{z,L} + n_{z,V}$ ODEs with a non-linear equation of state. The absolute and relative tolerances were set to 10^{-9} and 10^{-3}, the same values as for the equilibrium model, as the ODE systems produced associated with each PDE did not require stricter tolerances. The model was solved with the ode15i MATLAB routine [21]. The simulations took around a minute to solve 10 hours of non-isobaric evaporation in a single core of an Intel® Core™ i5-7300HQ CPU processor.

It is worth noting that Eqs. (6.26)-(6.30) are parabolic PDE's owing to the absence of advection, in contrast to the hyperbolic PDE that governs vapour phase heat transfer during isobaric evaporation, see Eq. (3.20). Hence, Eqs. (6.26)-(6.30) for the non-isobaric evaporation may be considered easier to solve than Eq. (3.20) owing to their lack of advection. However, the simulations for the non-isobaric model required around an order of magnitude higher simulation time. This is a consequence of the larger number of nodes produced as a consequence of the discretization of the vapour and liquid sub-domains. Additionally, thermal equilibrium at the vapour-liquid interface produces a time dependent boundary condition much more complex than constant saturation temperature used in the isobaric model. This induces a rapid variation of vertical temperature gradients in both phases, which further justify the requirement of a higher number of nodes in the discretization of the vapour and liquid subdomains.

6.3 Single phase CFD model (CFD-SP)

In this section, a CFD model for the non-isobaric evaporation of cryogenic liquids that has been developed as part of this research is described. We start, in subsection 6.3.2, by first considering the experimental evidence that that led us to need to develop the CFD model. In comparison to non-equilibrium 1-D model developed in subsection 6.2.2, two key improvements are considered in the development of the CFD model. Firstly, in subsection 6.3.2 a continuum formulation for the liquid phase is provided using the incompressible Navier-Stokes, continuity and energy equations with the Boussinesq approximation. This will allow to accurately resolve natural convection in the liquid phase to obtain a realistic temperature gradient at the liquid side of the interface. Secondly, in subsection 6.3.3 a wall boiling sub-model is included to consider the contribution of wall boiling to evaporation rates.

Most experimental vapour temperature profiles confirm that the heating of the vapour is slow [11-14, 17]. These profiles also depict that the average vapour temperature slowly increases with time, in a similar magnitude to the saturation temperature. Therefore, the experimental evidence suggests the onset of a pseudo-steady state for the vapour temperature. The absence of BOG removal in non-isobaric evaporation implies that, at the pseudo-steady state, most of the vapour heat ingress would be transferred to the liquid. Considering the slow vapour heating and assuming the onset of a pseudo-steady state, in subsection 6.3.4 a vapour bulk-model is developed assuming that the vapour is at thermal equilibrium with the interface. Although this model cannot reproduce vapour temperature profiles, it will not introduce a significant error neither in evaporation nor pressurization rates. In subsection 6.3.5, a 1-D simplified superheated vapour sub-model is presented using the pseudo-steady state solution of Eqs (6.26) and (6.27). Finally, in subsections 6.3.6-6.3.8 the computational implementation of the CFD-SP model in OpenFOAM is presented.

6.3.1 Experimental evidence

Among the complex array of transport phenomena that arise during the non-isobaric storage of cryogenic liquids, liquid thermal stratification is of paramount

importance. This phenomena has been observed by Seo et al. [11] and Kang et al. [12] in their experiments on the evaporation of liquid nitrogen. Although those studies provided valuable self-pressurization data, the temperature profiles reported for the liquid were either scarcely sampled or only available over a short evaporation period. Recent experimental data for liquid nitrogen evaporation [13] and methane-ethane mixtures [14] have measured more accurately the temperature profile in the liquid phase. Using these advanced methods, Pérez et al. [13] and Al Ghafri et al. [14] have measured temperature profiles during the totality of the evaporation period for liquid nitrogen and a liquid methane-ethane mixture, respectively.

For most experimental temperature profiles, for the non-isobaric evaporation of cryogens [11-14, 17], the magnitude of the temperature gradient in the liquid side of the interface is comparable to the temperature gradient in the vapour side of the interface. These results enable further testing of the assumptions of the non-isobaric 1-D model developed in section 6.2. In order to do so, the ratio of the liquid and vapour temperature gradients at their respective side of the interface is defined by,

$$\gamma_{\partial_z T} = \frac{\frac{\partial T_\mathrm{L}}{\partial z}\Big|_{z=\mathrm{int}=l_\mathrm{L}}}{\frac{\partial T_\mathrm{V}}{\partial z}\Big|_{z=\mathrm{int}=l_\mathrm{L}}}. \tag{6.36}$$

Similarly, the ratio of thermal conductivities between the liquid and vapour of a cryogen at the vapour liquid interface is defined by,

$$\gamma_k = \left(\frac{k_\mathrm{L}}{k_\mathrm{V}}\right)\Big|_{z=\mathrm{int}=l_\mathrm{L}}. \tag{6.37}$$

If the vapour-liquid interface is assumed unperturbed, substituting Eqs. (6.36) and (6.37) in Eqs. (6.3) and (6.5), one obtains,

$$\gamma_k \gamma_{\partial_z T} < 1 \rightarrow \dot{B}_\mathrm{L} > 0, \tag{6.38}$$

which is a straightforward rule of thumb that allows to determine whether evaporation or condensation occurs at the vapour-liquid interface. For instance, γ_k is 20 for LN_2 and 16 for liquid methane, and $\gamma_{\partial_z T}$ is approximately between 0.2 and 1 during self-pressurization experiments [11-14, 17]. Therefore, $3.2 < \gamma_k \gamma_{\partial_z T} < 20$, which implies that condensation is the dominant phase change at the vapour-liquid interface.

The identification of the dominant phase change mechanism during the non-isobaric storage of cryogenic liquids through experiments has been proven highly challenging. Only Kang et al. [12] have reported data for evaporation rates during non-isobaric storage of LN_2 being heated through the walls and bottom. They found a mixed phase change regime, on which evaporation was observed at early stages of self-pressurization, followed by condensation. In particular, condensation occurred earlier for the case with largest liquid filling and heat ingress, at t = 55 min and LF = 0.8. Kang et al. [12] justified this result as a consequence of a more rapid pressurization. If only interface evaporation is assumed, this explanation would be reasonable. As the saturation temperature increases with pressure, the temperature gradient below the liquid interface will produce a faster cooling of the interface by the liquid. The problem with this justification is that for the same high liquid filling scenario, $\gamma_k \gamma_{\partial_z T} > 5$ for $t \leq$ 20 min. Hence, based on the fast pressurization argument only, condensation should have been observed even earlier.

Kang et al. [12] experimental temperature profiles and evaporation rates indicate that phase change does not only occur at the vapour-liquid interface. As the liquid cryogen is being heated through the walls, a temperature difference will be established between the inner tank wall and the liquid bulk. The liquid bulk will then be heated by natural convection with a heat flux through the liquid bulk defined by $q_{\mathrm{L}} = h_{\mathrm{i,L}}(T_{w,\mathrm{L}} - T_{\mathrm{L}\infty})$, where the wall temperature is defined by $T_{w,\mathrm{L}} = T_{\mathrm{L}}(R_{\mathrm{T}})$, $T_{\mathrm{L}\infty}$ is the liquid temperature outside the boundary layer, and $h_{\mathrm{i,L}}$ is the convection coefficient of the liquid. This implies that at least a fraction of the wall will be superheated with respect to the saturation temperature of the cryogen, $T_{\mathrm{w,L}} > T_{\mathrm{sat}}$. If this is the case, subcooled and saturated nucleate boiling will occur at the tank wall [24]. Consequently, the liquid heat ingress through the wall will be divided between heating the liquid bulk and evaporating some liquid near the wall.

The presence of wall boiling is likely to be observed during cryogenic liquid storage for two reasons. First, these liquids have low thermal conductivity. Second, the thermally stratified layer below the interface [11-14, 17] will dampen natural convection, reducing the convection coefficient of the liquid. Both effects will increase the superheating of the wall with respect to the liquid bulk, driving wall boiling even for

low wall heat fluxes [25, 26]. Acknowledging the presence of wall boiling allows to better explain evaporation rates and temperature profiles observed by Kang et al [12]. The measured change from evaporation and condensation can be explained by an interplay between boiling at the wall and condensation at the interface.

6.3.2 CFD model

In the cylindrical cryogenic storage tank, the heating of the liquid through the walls is homogeneous in the azimuthal direction. The additional heating of the liquid through the bottom wall and the interface will not induce significant transport phenomena in the azimuthal direction. Under these assumptions, axis-symmetry has been assumed to simplify the system. This allows to model the liquid phase as a 2-D domain extending in the radial and vertical (r, z) directions. The domain has been defined as the rectangle $\Omega_{\mathrm{L}} = (0,\ 0) \times (R_{\mathrm{T}}, l_{\mathrm{L}}(t = 0))$, where $l_{\mathrm{L}}(t = 0)$ is the liquid height corresponding to the initial liquid filling.

In contrast to the vapour-CFD model developed in section 3.2, the displacement of the vapour-liquid interface has been neglected in the liquid domain. This simplification is supported by the small change (<5%) in liquid volume during typical non-isobaric storage periods. Typical storage periods are short compared to isobaric storage, as they are restricted by the tank maximum allowable working pressure (MAWP). For instance, the leading international tank standard for the storage of a variety of cryogens in stationary tanks between 3 and 80 m³ specifies a MAWP that ranges from 1.8 to 3.6 MPa [27]. For smaller vehicle sized tanks of 0.42 m³ capacity used in LNG trucks, the MAWP is 1 MPa [28]. These small values of MAWP, the high liquid to vapour density ratio in cryogenic liquids and the compensating effect of liquid thermal expansion will yield to a small variation in liquid volume. Therefore, the small change in liquid height during evaporation will not significantly affect transport phenomena in the liquid. It is worth noting that dV_{L}/dt has only been neglected in the continuum model for the liquid domain. In the vapour phase sub-models, dV_{L}/dt is considered in the calculation of thermodynamic properties, see subsections 6.3.4 - 6.3.5.

In contrast to the vapour of cryogenic liquids, see section 3.1, the isothermal compressibility of liquid cryogens is negligible. Hence, the incompressible Navier-

Stokes equations govern the liquid pressure and velocity profiles. The continuity equation for an incompressible fluid is given by,

$$\nabla \cdot \mathbf{v}_{\mathrm{L}} = 0 \tag{6.39}$$

where $\mathbf{v}_{\mathrm{L}} = (v_{\mathrm{L},r}, v_{\mathrm{L},z})$ is the liquid velocity. The buoyant forces produced by natural convection in the liquid have been implemented using the Boussinesq approximation. This approximation includes the effect of buoyancy as a source term only in the momentum conservation equation, which enables to keep Eq. (6.39) unaltered. Thus, the momentum conservation equation for an incompressible fluid including buoyancy through the Boussinesq approximation is given by,

$$\frac{\partial \mathbf{v}_{\mathrm{L}}}{\partial t} + \mathbf{v}_{\mathrm{L}} \cdot \nabla \mathbf{v}_{\mathrm{L}} = -\nabla P_{\mathrm{rgh}} + \nabla \cdot \left(\nu_{\mathrm{L}} (\nabla \mathbf{v}_{\mathrm{L}} + (\nabla \mathbf{v}_{\mathrm{L}})^{\mathrm{T}}) \right) - \frac{2}{3} \nu_{\mathrm{L}} (\nabla \cdot \mathbf{v}_{\mathrm{L}}) \mathbf{I} + \rho_{\mathrm{k}} \mathbf{g} \tag{6.40}$$

where $P_{\mathrm{rgh}} = (P - \rho_{\mathrm{L}} g_z z)/\rho_{\mathrm{L}}$ is the modified kinematic pressure, $\nu_{\mathrm{L}} = \mu_{\mathrm{L}}/\rho_{\mathrm{L}}$ is the kinematic viscosity of the liquid, μ_{L} is the dynamic viscosity of the liquid and $\mathbf{I}$ is the unit tensor. The buoyant effects are incorporated in the last term of Eq. (6.40), where $\rho_{\mathrm{k}} = 1 - \beta_{\mathrm{L}}(T_{\mathrm{L}} - T_{\mathrm{L,ref}})$ is defined as the kinematic density, $\beta_{\mathrm{L}} = \partial \rho_{\mathrm{L}}/\partial T_{\mathrm{L}}$ is the liquid thermal expansion coefficient and $T_{\mathrm{L,ref}}$ a reference temperature. The reference temperature has been assumed to correspond to the saturation temperature of the cryogen at the initial pressure, $T_{\mathrm{L,ref}} = T_{\mathrm{sat}}\big(P(t=0)\big)$. Using the Boussinesq approximation, the energy conservation equation can be written explicitly for the liquid temperature as an unsteady advection diffusion equation given by,

$$\frac{\partial T_{\mathrm{L}}}{\partial t} = \nabla \cdot (\alpha_{\mathrm{L}} \nabla T_{\mathrm{L}}) - \nabla \cdot (\mathbf{v}_{\mathrm{L}} T_{\mathrm{L}}). \tag{6.41}$$

The velocity boundary conditions were defined as no-slip at the tank bottom, tank wall in contact with the liquid and at the vapour-liquid interface. At the tank axis ($r = 0$), a symmetry boundary condition was imposed for velocity, $\partial v_r/\partial r(r=0) = 0$. As all velocity boundary conditions were prescribed, the boundary conditions for the modified kinematic pressure were calculated. The temperature initial boundary and boundary conditions were defined as,

$$T_{\mathrm{L}}|_{t=0} = T_{\mathrm{sat}}(P_{\mathrm{V}}|_{t=0}), \tag{6.42}$$

$$\left.\frac{\partial T_{\mathrm{L}}}{\partial z}\right|_{r=0,z} = 0,$$

$$T_{\mathrm{L}}|_{r,z=l_L} = T_{\mathrm{sat}}(P_{\mathrm{V}}),$$

$$k_{\mathrm{L}}\left.\frac{\partial T_{\mathrm{L}}}{\partial z}\right|_{r,z=0} = \dot{q}_b = (1-\eta_{\mathrm{e,b}})U_{\mathrm{L},b}\left(T_{\mathrm{air}} - T_{\mathrm{L}}|_{r,z=0}\right),$$

$$k_{\mathrm{L}}\left.\frac{\partial T_{\mathrm{L}}}{\partial r}\right|_{r=R_{\mathrm{T}},z} = (1-\eta_{\mathrm{e,w}})\dot{q}_{\mathrm{L,w}} = (1-\eta_{\mathrm{e,w}})U_{\mathrm{L}}\left(T_{air} - T_L|_{r=R_{\mathrm{T}},z}\right),$$

indicating that (i) the liquid temperature is initially spatially homogeneous and equal to the saturation temperature at the initial pressure of the vapour, $P_{\mathrm{V}}|_{t=0}$, (ii) the temperature profile is symmetrical with respect to the vertical axis, (iii) the temperature of the liquid at the vapour-liquid interface is equal to the saturation temperature evaluated at the vapour pressure, (iv) the liquid is heated through the bottom by a $(1-\eta_{\mathrm{e,b}})$ fraction of the heat flux through the bottom $\dot{q}_b$ and (v) the liquid is heated through the tank wall by a $(1-\eta_{\mathrm{e,w}})$ fraction of the total liquid wall heat flux $\dot{q}_{\mathrm{L,w}}$. The calculation of $\eta_{\mathrm{e,b}}$, $\eta_{\mathrm{e,w}}$ requires a suitable wall boiling model, which is detailed in subsection 6.3.3.

6.3.3 Wall boiling model

The mechanistic model of wall heat flux partitioning [29, 30] has been used to determine evaporation rates and liquid bulk heating during subcooled boiling. The mechanistic model, also known as the Rensselaer Polytechnic Institute (RPI) model, consists of splitting the heat flux through the walls in three components. These components describe the heat transfer between a wall that is superheated with respect to the saturation temperature of the liquid, the liquid bulk and the generated bubbles. The total wall heat flux to the liquid wall, q_{w}, is partitioned in an evaporative flux, q_{e}, a natural convection heat flux, q_{c}, and transient conduction or quenching between the wall and the liquid that replaces the position of the nucleating bubbles, q_q, through:

$$q_{\mathrm{w}} = q_{\mathrm{e}} + q_{\mathrm{c}} + q_{\mathrm{q}}. \tag{6.43}$$

In the RPI model, the evaporative heat flux is defined by,

$$q_{\mathrm{e}} = \left(\frac{\pi d_B^3}{6}\right) N_{\mathrm{A}} f \rho_{\mathrm{V}}(T_{\mathrm{w}}) \Delta H_{\mathrm{LV}} \tag{6.44}$$

where N_{A} is the active nucleation site density, f is the nucleation frequency and d_B is the diameter of the departing bubbles. The convective heat flux is defined by,

$$q_c = h_{\mathrm{i,L}}(1 - A_{\mathrm{b}})(T_{\mathrm{w}} - T_{\mathrm{L},\infty}) \tag{6.45}$$

where A_{b} is the bubble area that denotes the fraction of the wall area which is in contact with the liquid. Finally, the transient heat conduction heat flux is defined by

$$q_{\mathrm{q}} = \left(\frac{2}{\sqrt{\pi t_w}} \sqrt{k_{\mathrm{L}} \rho_{\mathrm{L}} c_{p,\mathrm{L}}}\right) A_b (T_{\mathrm{w}} - T_{\mathrm{L},\infty}) \tag{6.46}$$

where t_w is the bubble waiting time, defined as the period required to re-establish the conditions for the initiation of a nucleus after a bubble has departed from a cavity [31].

In order to determine the contribution of the heat fluxes defined by Eqs. (6.44) - (6.46), closure sub-models are required to model the bubble parameters. Among these sub-models, the active nucleation site density and bubble departure diameter are the sub-models that affect more strongly the heat flux partitioning during the evaporation of cryogenic liquids [24]. In this thesis, two models for the active nucleation site density will be tested to understand the sensitivity of the pressure build-up with respect to the active nucleation site density sub-model. The first model has been proposed by Lemmert and Chawla [32] for pool boiling of saturated water, and it is given by,

$$N_{\mathrm{A}} = [n \times (T_{\mathrm{w}} - T_{\mathrm{sat}})]^m, \tag{6.47}$$

where n =185 and m = 1.805. It is worth noting that it is extremely difficult to predict a priori the values of n and m for different experiments. This is a consequence of the influence of the processes that were used to finish the surface where boiling occurs on the active nucleation site density [33]. In most experiments, these processes are not controlled.

For liquid nitrogen, Zhang et al. [34] have found that the active nucleation site density follows a power law with an exponent much lower than for water. This implies that the onset of nucleate boiling (ONB) for liquid nitrogen requires a much lower wall superheating, $T_{\mathrm{w}} - T_{\mathrm{sat}}$, than for water. In concrete, Zhang et al. [34] fitted the active

nucleation site density with the departure cavity radius based on three experimental points, and obtained $n = 2.5 \times 10^4$ and m = 0.925. In this thesis, m = 0.925 has been selected as they provide a much better modelling representation of heat flux partitioning for cryogenic liquids. On the other hand, the value of n has been fitted to experimental data from [11, 12]. This fitting procedure is the standard approach for wall boiling modelling [33], as it has been demonstrated that the constant is highly dependent on the experimental setup and fluid flow conditions [24, 34].

The second model has been proposed by Kirichenko et al. for the subcooled boiling of different cryogenic liquids [35],

$$N_A = n\left[\frac{\rho_{\mathrm{V}}(T_{\mathrm{sat}})\Delta H_{\mathrm{LV}}(T_{\mathrm{w}} - T_{\mathrm{sat}})}{\sigma T_{\mathrm{sat}}}\right]^m \tag{6.48}$$

where $n = 10^{-7}$ and m = 2 if $P/P_{\mathrm{cr}} \geq 0.04$, and $n = 6.25 \times 10^{-6}$ and m = 3 otherwise, considering P_{cr} the critical pressure of the cryogenic liquid. The bubble departure diameter, d_{B}, has been calculated using the correlation developed by Kim and Kim [36],

$$d_{\mathrm{B}} = 0.1649\sqrt{\frac{\sigma}{|\mathbf{g}|(\rho_L - \rho_V)}}\, Ja^{0.7}, \tag{6.49}$$

where $Ja = \rho_{\mathrm{L}} c_{\mathrm{p,L}}(T_{\mathrm{w}} - T_{\mathrm{sat}})/(\rho_V \Delta H_{\mathrm{LV}})$ is the Jakob number. This empirical correlation has shown the best fit to experimental data of bubble departure diameter during pool boiling of liquid nitrogen [34]. The fraction of the wall area in contact with the liquid subject to cooling by transient conduction cooling, A_b, is defined by,

$$A_{\mathrm{b}} = N_{\mathrm{A}}\left(K_{\mathrm{ac}}\frac{\pi d_B^2}{4}\right) \tag{6.50}$$

where K_{ac} is a proportional constant for the diameter of influence of the bubble. The value of K_{ac} has been determined through Del Valle and Kenning fitting [37],

$$K_{\mathrm{ac}} = 4.8\exp\left(-\frac{Ja}{80}\right). \tag{6.51}$$

As part of this research, the Kirichenko et al. [35] active nucleation site density sub-model and the Kim and Kim [36] bubble departure diameter sub-model have been added to OpenFOAM-v2006.

A mechanistic relationship between the nucleation frequency and the bubble wait time is given by,

$$f = \frac{1}{t_w + t_g}, \tag{6.52}$$

where t_g is the bubble growth time. In this thesis, the bubble growth time has not been explicitly modelled. Instead, waiting time has been assumed to be $t_w = 0.8/f$, following the Tolubinsky and Kostanchuk [38] assumption. The nucleation frequency has been calculated using the model of McFadden and Grassmann [39], which has been developed to characterise the bubble departure frequency of liquid nitrogen during pool boiling,

$$f = 0.56\sqrt{\frac{|\mathbf{g}|(\rho_L - \rho_V)}{d_B \rho_L}}. \tag{6.53}$$

The McFadden and Grassmann [39] model is similar to the Cole [40] model, $f = \sqrt{\frac{4}{3}\frac{|\mathbf{g}|(\rho_L - \rho_V)}{d_B \rho_L}}$, which has been fitted for water evaporation and it is a default choice when scarce experimental data for a particular fluid is available. After running preliminary simulations, it has been observed that the nucleation frequency obtained with Cole [40] model was unrealistically high. This produced a higher quenching heat transfer and lower wall evaporation rates than McFadden and Grassmann [39] model. In consequence, a poor fit with the pressure build-up experimental data from Seo et al. [11] and Kang et al [12]. Furthermore, experimental data of pool boiling of liquid nitrogen [34] confirms that the McFadden and Grassmann [39] model is able to accurately capture the bubble departure frequency. As part of this research, the McFadden and Grassmann [39] has been added to OpenFOAM-v2006 as a bubble departure frequency sub-model.

The convection coefficient $h_{i,L}$ can be calculated directly using the temperature field at the tank wall provided by CFD,

$$h_{i,L} = \frac{k_L \frac{\partial T_L}{\partial \mathbf{n}}}{(T_w - T_{L,\infty})}, \tag{6.54}$$

where $\partial T_{\mathrm{L}}/\partial \mathbf{n}$ is the directional derivative of the liquid temperature in the direction of the solid boundary surface normal vector.

A simpler but potentially less accurate alternative is to use empirical correlations to estimate the Nusselt number, $Nu = hL_{\mathrm{c}}/k$, in the liquid boundary layer near the wall. The characteristic length for the boundary layer flow, L_{c} has been assumed to be equal to the initial liquid height $l_L(t = 0)$. As it is expected to observe turbulent natural convection, the Nusselt number is calculated through a combination of the laminar and turbulent Nusselt numbers [41] by,

$$Nu_{\mathrm{i,L}} = \left[Nu_{\mathrm{i,L}}^{\mathrm{comb}} + Nu_{\mathrm{i,L}}^{\mathrm{turb}}\right]^{\frac{1}{m_c}}, \tag{6.55}$$

where m_c was set to 6, assuming that the value for isothermal vertical plates is a good approximation for a vertical cylinder. For low convective heat fluxes from the wall to the liquid, natural convection is expected to be small. In this scenario, the combined Nusselt number, $Nu_{\mathrm{i,L}}^{\mathrm{comb}}$, allows to correct the laminar Nusselt number for very low velocities at the wall boundary layer [41],

$$Nu_{\mathrm{i,L}}^{\mathrm{comb}} = \left[\left(Nu_{\mathrm{i,L}}^{\mathrm{lam}}\right)^{n_{\mathrm{c}}} + \left(Nu_{\mathrm{i,L}}^{\mathrm{cond}}\right)^{n_{\mathrm{c}}}\right]^{\frac{1}{n_c}}, \tag{6.56}$$

where $n_{\mathrm{c}} = 1.07$ as this is a good approximation for a variety of geometrical shapes [42]. Assuming an aspect ratio $l_{\mathrm{L}}/d_i = 0.5$ as a representative for different storage scenarios, the conduction Nusselt number for internal flow in a vertical cylinder was set to $Nu_{\mathrm{i,L}}^{\mathrm{cond}} = 1.93$ [41]. This choice is supported as it is expected that $Nu_{\mathrm{i,L}}^{\mathrm{cond}}$ will not contribute significantly to heat transfer in turbulent regimes. Furthermore, $Nu_{\mathrm{i,L}}^{\mathrm{cond}}$ varies slightly for a long range of aspect ratios, from 2.55 for an infinitely thin cylinder to 0.99 for $l_L/d_i = 4$.

If a CFD model is not available, determining the temperature difference between the tank wall and the liquid bulk, $\Delta T_w = T_{\mathrm{w}} - T_{L,\infty}$, is not straightforward. This is a problem as typically the Nusselt number is a function of the Grashof number, $Gr_{\mathrm{L}} = g\beta_L \Delta T_{\mathrm{w}} L_c^3/\nu_{\mathrm{L}}^2$, which is itself a function of ΔT_{w} and an iterative procedure will be required to determine ΔT_{w} and Gr_{L}. A more direct approach is to use the modified Grashof number [43],

$$Gr_{\mathrm{L}}^{*} = \frac{g\beta_{\mathrm{L}} q_{\mathrm{c}} L_c^4}{k_{\mathrm{L}} \nu_{\mathrm{L}}^2}, \tag{6.57}$$

for which the value of the convective heat flux q_{c} is more readily available. In the limiting case of no evaporation, $q_{\mathrm{c}} = q_{\mathrm{w}}$. Using the modified Grashof number, the Nusselt number for buoyancy driven flow in the internal surface of a vertical cylinder heated at a constant heat flux can be estimated using Guha et al. [43] correlation,

$$Nu_{\mathrm{vert,L}}^{\mathrm{lam}} = 0.616 \left(\frac{Gr_{\mathrm{L}}^{*} Pr^2}{\frac{4}{5} + Pr} \right)^{\frac{1}{5}}. \tag{6.58}$$

Finally, if it is assumed that the totality of the wall boundary layer is turbulent and that the boundary layer inside a cylinder is similar to the one in a vertical plate, the turbulent Nusselt number is approximated by [41],

$$Nu_{\mathrm{vert,L}}^{\mathrm{turb}} = \frac{C_3 \left(Gr_{\mathrm{L}}^{*} Nu_{\mathrm{vert,L}}^{\mathrm{turb}} Pr_{\mathrm{L}} \right)^{\frac{1}{3}}}{1 + \left(1.4 \times 10^9 Gr_{\mathrm{L}}^{*} Nu_{\mathrm{vert,L}}^{\mathrm{turb}} \right)}, \tag{6.59}$$

which is implicit and should be solved by any suitable numerical iterative procedure. The constant C_3 for a vertical isothermal flat plate is given by [41],

$$C_3 = \frac{0.13 Pr_{\mathrm{L}}^{0.22}}{(1 + 0.61 Pr_{\mathrm{L}}^{0.84})^{0.42}}. \tag{6.60}$$

A similar procedure can be followed to determine the natural convection heat transfer coefficient at the tank bottom. The characteristic length for the buoyancy driven flow at the tank bottom is the tank internal diameter, $L_c = 2R_{\mathrm{T}}$. For a constant-heat-flux horizontal surface, the Nusselt number is given by [44],

$$Nu_{\mathrm{hor,L}}^{\mathrm{lam}} = 0.595 \left(\frac{Gr_{\mathrm{L}}^{*} Pr^2}{\frac{4}{7} + Pr} \right)^{\frac{1}{6}}. \tag{6.61}$$

Under the assumption that the totality of the boundary layer formed at the tank bottom is turbulent, the turbulent Nusselt number above the tank bottom is given by [41] ,

$$Nu_{\mathrm{hor}}^{\mathrm{turb}} = \left(0.479 \times (Gr_L^{*} Pr)^{\frac{1}{4}} \right)^{\frac{4}{5}}. \tag{6.62}$$

The fraction of the wall heat flux that is used to evaporate the liquid cryogen in the vicinity of a solid boundary is defined by the boundary evaporation fraction,

$$\eta_{\mathrm{e},\partial\Omega} = \frac{q_{\mathrm{e},\partial\Omega}}{q_{\mathrm{w},\partial\Omega}}, \tag{6.63}$$

which is a function of both time and position. In Eq. (6.63), the subscript $\partial\Omega$ denotes a particular solid boundary in contact with the liquid subdomain. Similarly, the fraction of the heat flux across a solid boundary that is used to heat the liquid phase by convection and transient conduction is defined by $1 - \eta_{\mathrm{e},\partial\Omega}$.

The wall boiling model can be implemented through two different approaches. The first approach consists of coupling the wall boiling sub-model, Eqs. (6.43) - (6.54), as a boundary condition in the liquid phase assuming. Implementing wall boiling as a boundary condition allows a calculation of $\eta_{\mathrm{e},\partial\Omega}$ as a function of the position and time and space. This allows resolution of the time dependence of the heat flux partitioning on the unsteady boundary layer near the tank wall and bottom. Furthermore, it also allows resolution of the spatial dependence as a consequence of thermal stratification in the vertical wall of the tank. It is worth noting that the wall boiling sub-model constitutes a separate subsystem from the single- phase CFD model for the liquid. Therefore, the bubble generation is only considered for the calculation of the heat flux partitioning, see Eq. (6.43), and the momentum transfer between the bubbles and the liquid are not modelled.

The second approach consists of using a number of additional assumptions to estimate the spatial-temporal average value of the boundary evaporation fraction η_{e},

$$\bar{\eta}_{\mathrm{e},\partial\Omega} = \frac{1}{\tau_s}\int_0^{\tau_\mathrm{s}} \frac{1}{A_{\partial\Omega}}\left[\int_{\partial\Omega} \eta_\mathrm{e} d\mathbf{S}\right] dt, \tag{6.64}$$

where $d\boldsymbol{S}$ is the differential area element associated to the solid boundary $\partial\Omega$ and τ_s is the storage period. The storage period is defined as the time to reach the maximum allowable working pressure, as a consequence of the evaporation and heating of the cryogenic liquid and its vapour under non-isobaric conditions. In typical storage scenarios, the occurrence of wall boiling is expected to happen mainly at the tank wall. If the heat fluxes through the bottom and wall are small and of a similar magnitude, the liquid at the bottom will be significantly subcooled with respect to the vapour liquid

interface [11-14, 17]. Thus, for all times except at the beginning of the evaporation, the totality of the bottom heat ingress will heat the liquid bulk. Therefore, it is assumed that no evaporation will occur at the tank bottom, $\bar{\eta}_{\mathrm{e,b}} = 0$. This assumption also simplifies the temperature boundary condition at the tank bottom, see Eq. (6.42).

At the tank wall and mainly below the vapour liquid interface, the wall temperature will be higher than the saturation temperature of the cryogen. This will drive the evaporation of the cryogenic liquid in a finite evaporative region that extends downwards from the interface to the tank bottom. As the vertical distance below the interface increases, the temperature of the liquid will decrease, and the saturation temperature will increase owing to the increase in pressure with the hydrostatic head. The exact width of the evaporative region at the wall is difficult to evaluate *a priori*, as it depends on the local distribution of the wall heat flux and the velocity profile at the boundary layer.

The situation is even more complex if the heat transfer within the wall thermal boundary layer is closely inspected. The fraction of the wall heat ingress used to heat the liquid in the boundary layer, $(1 - \eta_{\mathrm{e,w}})$, will heat the liquid as it ascends to the interface. Below the vapour liquid-interface, a thin layer of superheated liquid with width $\delta_{\mathrm{z,se}}$ will circulate inwards to the tank axis. Along the interface, some of this superheated liquid will evaporate at a rate proportional to the degree of superheating, $\dot{m}_{\mathrm{se}}\ \alpha\ (T_{\mathrm{L}}|_{l_L} - T_{\mathrm{sat}})$. This is a consequence of the finite superheating of the liquid at the vapour-liquid interface, $T_{\mathrm{L}}|_{l_L} - T_{\mathrm{sat}}$, that is required to drive the evaporation as a consequence of non-equilibrium thermodynamics [19]. This mechanism is denominated surface evaporation, and it has not been included explicitly in the single-phase liquid - CFD model. Instead, it is included inside the wall boiling methodology that will be described below. Surface evaporation is included by means of an interfacial heat transfer sub-model in the multiphase model that is described in section 6.4. At the same time that the superheated layer evaporates, it will be cooled by the liquid bulk through conduction. In reality, the interplay of wall evaporation, surface evaporation and heat conduction determine the evaporation and pressurization rates.

Instead of modelling the evaporative fraction and surface evaporation, the following equivalent system is proposed. Saleem et al. [3] found that the effect of

hydrostatic pressure on evaporation rates during isobaric storage did not affect the pseudo-steady state evaporation rates. This implies that to determine pseudo-steady state evaporation rates, the width of the evaporative region can be assumed equal to the liquid length if the increase in saturation temperature with pressure is also neglected. The presence of vertical thermal stratification during non-isobaric storage is not expected to alter the independence of hydrostatic pressure observed by Saleem et al. [3]. This assumption is supported by the fact that the main effect of vertical thermal stratification is cooling the interface through conduction. Therefore, only for the estimation of the evaporative fraction, the liquid saturation temperature is assumed constant and equal to the saturation temperature at the initial conditions. This assumption also allows to include the effect of surface evaporation within the wall evaporation. With the removal of the vertical gradient of saturation temperature in the equivalent system, the liquid that leaves the wall boundary layer below the interface will not be superheated with respect to its saturation temperature.

Although the presence of vertical thermal stratification will produce the dampening of buoyancy driven flow in the liquid bulk, this effect is partially mitigated at the wall boundary layer [10]. Furthermore, the temperature difference between the tank wall and the liquid bulk is expected not be a strong function of time. This assumption is supported by the fact that the wall heat flux to the liquid is expected to show a small variation with time if the tank is already preconditioned [45]. In contrast to the vapour phase, where the maximum temperature difference in the vapour could be larger than 100 K [46, 47], in the liquid phase the maximum subcooling, $\Delta T_{\mathrm{L,sc}} = T_{\mathrm{sat}} - \min(T_{\mathrm{L}})$, is expected to be moderate. This is a consequence of the low maximum allowable working pressures, which will limit $\Delta T_{\mathrm{L,sc}}$ to less than 20 K. Therefore, as a first approximation, a constant wall superheating, $T_{\mathrm{w}} - T_{\mathrm{L},\infty}$, has been assumed.

Considering the initial conditions as representative for the whole evaporation period, by assuming small variation in heat flux partitioning, the fraction of the wall heat flux that will evaporate the liquid can be approximated by,

$$\bar{\eta}_{\mathrm{e,w}} \approx \int_{\mathrm{w}} \eta_{\mathrm{e}}(t=0)\, d\mathbf{S} = \eta_{\mathrm{e,w}}(t=0) \tag{6.65}$$

which is not a function of the vertical coordinate because the initial temperature of the liquid is spatially homogeneous, see Eq. (6.42). Using Eq. (6.65) alongside with Eqs. (6.43)-(6.52), (6.55)-(6.63), yields a non-linear system for equations for T_{w}. The solution of this system will provide the heat flux partitioning at the pseudo-steady state, and hence, $\bar{\eta}_{\mathrm{e,w}}$.

6.3.4 Vapour bulk equilibrium model

The vapour bulk equilibrium model is based on the equilibrium model presented in subsection 6.2.1 augmented with wall boiling. The mass and energy balances for the vapour phase are given by Eqs. (6.2) and (6.9), respectively. The interfacial energy balance is given by Eq. (6.19), using Eq. (6.18) to calculate the fraction of liquid heat ingress that produce wall boiling. For the vapour bulk model, the vapour to interface heat transfer rate in Eq. (6.19) is obtained using Eq. (6.11). As the liquid temperature is allowed to vary with radius, $\dot{Q}_{\mathrm{IL}}$ is given by the Fourier's law at the liquid side of the interface:

$$\dot{Q}_{\mathrm{IL}} = 2\pi k_{\mathrm{L}}(T_{\mathrm{sat}}) \int_0^{R_{\mathrm{T}}} \frac{\partial T_{\mathrm{L}}}{\partial z}|_{z=l_{\mathrm{L}}}\, r dr\,. \tag{6.66}$$

The evaporative fractions $\eta_{\mathrm{e,w}}$ and $\eta_{\mathrm{e,b}}$ in Eq. (6.19) can be either fixed as model inputs or calculated using procedure subsection 6.3.3. The vapour phase has been assumed to be an ideal gas. Using the Clausius-Clapeyron relationship, neglecting liquid thermal expansion, and using Panzarella et al. [1] simplified model, the pressurization rate can be calculated explicitly by,

$$\frac{dP_{\mathrm{V}}}{dt} = F(\dot{Q}_{\mathrm{VI}} - \dot{Q}_{\mathrm{IL}} + \dot{Q}_{\mathrm{w,b}}), \tag{6.67}$$

where the factor F is given by [1],

$$F = \frac{\Delta H_{\mathrm{LV}}}{V_{\mathrm{V}}}\left(c_{\mathrm{V,V}}T_{\mathrm{sat}} + \left(\frac{\Delta H_{\mathrm{LV}}}{RT_{\mathrm{sat}}} - 1\right)\frac{\bar{\rho}_{\mathrm{L}}}{\bar{\rho}_{\mathrm{L}} - \rho_{\mathrm{V}}}\left[\Delta H_{\mathrm{LV}} - P_{\mathrm{V}}\left(\frac{1}{\rho_{\mathrm{V}}} - \frac{1}{\bar{\rho}_{\mathrm{L}}}\right)\right]\right)^{-1}. \tag{6.68}$$

6.3.5 Non-equilibrium 1-D vapour phase model using analytical solutions

As a first approximation, the analytical solutions for vapour temperature developed in section 3.4 have been used to calculate the vapour temperature during non-isobaric evaporation. This approach is supported by the slow change in average vapour temperature evidenced by a plethora of experimental results for the non-isobaric evaporation of cryogens [11-14, 17]. The slow variation of the vapour temperature, 1 K h^{-1} $< d\bar{T}_V/dt \sim dT_{sat}/dt \leq 17$ Kh^{-1}, demonstrates the onset of a pseudo-steady state in the vapour. However, the transient period during non-isobaric evaporation is expected to be longer than for isobaric evaporation, owing to the absence of boil-off gas removal. Therefore, the use of the analytical solutions is expected to produce physically valid temperature profiles only for high liquid fillings.

The pseudo-steady state is characterised by the balance of the wall and roof heat ingress to the vapour with its cooling at the interface. The analytical solutions for the vapour temperature developed in section 3.4 are applicable for the pseudo-steady state solution of Eqs. (6.26) and (6.27) assuming that the vapour condensation source, $\dot{S}_c$, is negligible. To apply them, the advective term has been set to zero, and the Dirichlet-Neumann combination of boundary conditions at the interface and roof has been selected. Only the solutions for average vapour temperature and vapour to liquid heat transfer, Eqs. (3.36) and (3.43), have been noting that $\dot{Q}_{VL} = \dot{Q}_{VI}$. The solutions were evaluated at each time-step, which allowed to update the thermophysical properties with the progress of the evaporation. The quantity that is expected to show the largest change is the vapour density, owing to the vapour accumulation as a consequence of evaporation.

The mass and energy balances for the vapour phase are defined by Eqs. (6.2) and (6.9). The average vapour density in Eq. (6.2) has been approximated evaluating the vapour density at average vapour temperature. As the vapour is superheated with respect to the liquid, Eq. (6.10) derived for the equilibrium model is not applicable. Instead, Eqs. (6.18)-(6.21) are used to calculate the evaporation rate. The vapour to interface heat transfer rate, $\dot{Q}_{VI}$ on Eq. (6.20), is calculated from the analytical solution, Eq. (3.43), setting $\bar{v}_z$ = 0. The interface to liquid heat transfer rate, $\dot{Q}_{IL}$, is calculated using the same approach as for the vapour bulk equilibrium model, see Eq. (6.66). The

pressure of the vapour has been assumed spatially homogeneous using the same arguments exposed for the equilibrium and 1-D models, see section 6.2. Eqs. (6.2), and (6.9) constitute a system of two ODEs for vapour volume and average vapour temperature, implicitly coupled by Eq. (3.36). The closure of this ODE system obtained by using a suitable equation of state. To facilitate the implementation of the model, an equation of state explicit in the pressure has been selected, see Eq. (6.32). The coupling of the ODE system with the non-linear equation of state produces a differential algebraic equations (DAE) system.

For the limiting case of short storage periods and low heat fluxes, the liquid thermal expansion can be neglected to calculate vapour pressure. If it is further assumed that the vapour is an ideal gas, a simplified version of the non-equilibrium model can be derived. For an ideal gas, the pressure, temperature and density derivatives are related by,

$$\frac{dP_{\mathrm{V}}}{dt} = R\left(\bar{T}_{\mathrm{V}}\frac{\partial\bar{\rho}_V}{\partial t} + \bar{\rho}_{\mathrm{V}}\frac{\partial\bar{T}_{\mathrm{V}}}{\partial t}\right), \tag{6.69}$$

Using Eqs. (6.1) and (6.2), neglecting $d\rho_L/dt$ and using the volume balance $dV_L/dt = -dV_V/dt$, the time derivative of the vapour density can be expressed by,

$$\frac{\partial\bar{\rho}_{\mathrm{V}}}{\partial t} = \frac{\dot{B}_{\mathrm{L}}}{V_{\mathrm{V}}}\left(1 - \frac{\rho_{\mathrm{V}}}{\rho_{\mathrm{L}}}\right). \tag{6.70}$$

Rearranging Eq. (6.10) and grouping terms, the rate of change of the average vapour temperature can be expressed explicitly through,

$$\frac{d\bar{T}_{\mathrm{V}}}{dt} = \frac{\dot{Q}_{\mathrm{roof}} + \dot{Q}_{\mathrm{V,in}} - \dot{Q}_{\mathrm{VI}} - \dot{B}_{\mathrm{L}}c_{\mathrm{p,V}}(\bar{T}_{\mathrm{V}} - T_{\mathrm{sat}})}{\bar{\rho}_{\mathrm{V}}V_{\mathrm{V}}c_{\mathrm{p,V}}}. \tag{6.71}$$

Substituting Eqs. (6.72) and (6.70) on (6.69) allows to express the pressurization rate as an explicit ODE,

$$\frac{dP_{\mathrm{V}}}{dt} = \frac{R}{V_{\mathrm{V}}}\left(\dot{B}_{\mathrm{L}}\left[T_{\mathrm{sat}} - \bar{T}_{\mathrm{V}}\frac{\bar{\rho}_{\mathrm{V}}}{\bar{\rho}_{\mathrm{L}}}\right] + \frac{\dot{Q}_{\mathrm{roof}} + \dot{Q}_{\mathrm{V,in}} - \dot{Q}_{\mathrm{VI}}}{c_{p,\mathrm{V}}}\right). \tag{6.72}$$

Using Eq. (6.72) instead of the algebraic equation (6.32) allows to simplify the vapour-1-D sub-model from a DAE system to a system of ODEs. It is worth noting that although

Eq. (6.72) is a reasonable approximation for the pressurization rate, it should not be used to predict liquid or vapour volumes. The liquid thermal expansion term in Eq. (6.1), $V_{\mathrm{L}} \frac{d\bar{\rho}_{\mathrm{L}}}{dt}$, is expected to be higher than the evaporative term, $\bar{\rho}_{\mathrm{L}} \frac{dV_{\mathrm{L}}}{dt}$. It is expected that liquid thermal expansion will be large particularly at the beginning of the evaporation, as the liquid thermally stratified layer will heat rapidly.

6.3.6 CFD implementation in OpenFOAM

A customised solver, buoyantBoussinesqPvapFoam, was created to couple the liquid continuum model with the vapour phase bulk models. This solver is based on the OpenFOAM solver buoyantBoussinesqPimpleFoam [2], which is a transient solver for turbulent flow of incompressible fluids. BuoyantBoussinesqPimpleFoam includes buoyancy effects as a source term only in the momentum equation using the Boussinesq approximation. This choice is supported by the small superheating ($\Delta T_{\mathrm{L,sc}}$, < 4K) that is expected for reasonably small changes in pressure (($P(t_{\mathrm{f}}) - P(t_0)$ < 1 bar). For this conditions, the Boussinesq approximation is valid [48]. Furthermore, as liquid thermal stratification develops, it is expected that buoyancy will be dampened, and it will not contribute to vertical heat transfer [10]. Hence, it is expected that the range of applicability of the Boussinesq approximation will be even higher ($\Delta T_{\mathrm{L,sc}}$ > 4K) than what has been obtained analytically [48] for non-thermally stratified fluids.

The vapour-bulk models were included in the customised solver using the OpenFOAM ODE class for ordinary differential equations. This allows a consistent integration of the ODE system with the discretised linear systems obtained for the partial differential equations of the liquid bulk, Eqs. (6.39) - (6.41). The equilibrium and non-equilibrium vapour bulk models are selectable at runtime. All vapour-bulk models are integrated using the 4^{th}-5^{th} order Runge-Kutta-Fehlberg (RKF) [49] method. The solver computes all the quantities required by the vapour-bulk model sequentially, while the resulting ODE is coupled with the liquid phase PDE and solved simultaneously.

In the vapour bulk calculations, the first step consists in the spatial integration of the temperature gradient at the liquid side of the interface to compute $\dot{Q}_{\mathrm{LI}}$ using Eq.

(6.66). Secondly, the liquid density field is integrated to obtain the average liquid density. If the equilibrium vapour bulk model is used, the thermodynamic variables of the vapour are updated, the factor F in Eq. (6.68) can be computed directly and the ODE system is ready to be solved. If the non-equilibrium model is used, the evaporation rate $\dot{B}_{\mathrm{L}}$ can be calculated using Eq. (6.19). Then, Eqs. (6.1)-(6.2) can be combined to obtain an explicit equation for the vapour volume that includes liquid thermal expansion,

$$V_{\mathrm{V}} = \frac{\dot{B}_{\mathrm{L}}\left(1-\frac{\bar{\rho}_{\mathrm{V}}}{\bar{\rho}_{\mathrm{L}}}\right)+\frac{\bar{\rho}_{\mathrm{V}}}{\bar{\rho}_{\mathrm{L}}}\left(\frac{d\rho_{\mathrm{L}}}{dt}V_{\mathrm{T}}\right)}{\frac{d\rho_{\mathrm{V}}}{dt}+\frac{\bar{\rho}_{\mathrm{V}}}{\bar{\rho}_{\mathrm{L}}}\frac{d\rho_{\mathrm{L}}}{dt}}. \tag{6.73}$$

The temporal derivatives of the average vapour and liquid densities in Eq. (6.73) can be calculated using backward differences. This requires storing the average vapour and liquid densities for the current and previous time-step. With these values, the derivatives can be computed through $d\bar{\rho}_{\mathrm{V}}/dt = (\bar{\rho}_{\mathrm{V}}^{t} - \bar{\rho}_{\mathrm{V}}^{t-1})/\Delta t$, $d\rho_{\mathrm{V}}/dt = (\bar{\rho}_{\mathrm{L}}^{t} - \bar{\rho}_{\mathrm{L}}^{t-1})/\Delta t$, where the superscripts $t, t-1$ represent the current and previous time-steps, respectively. After updating the vapour volume, the remaining vapour thermodynamic properties are updated and the ODE system for the non-equilibrium model is ready to be solved.

The boundary condition for liquid temperature at the vapour liquid interface, $T_{\mathrm{L}}|_{r,z=l_L}$ in Eq. (6.42), was implemented in OpenFOAM using a codedFixedValue dynamic boundary condition. At each time-step, the boundary condition reads the pressure of the vapour bulk and calculates the saturation temperature. Then, it sets the temperature of all the faces in the interface boundary to be equal to the calculated saturation temperature. The convection-conduction boundary conditions at the wall and bottom boundaries, see Eq. (6.42), have been implemented using a codedMixed boundary condition. The parameters $\bar{\eta}_{\mathrm{w}}$, $\bar{\eta}_{\mathrm{b}}$, are received as input values in the dictionary transportProperties. To evaluate the heat transfer in the solid walls, the effective thermal conductivity $k_{\mathrm{L,eff}} = k_{\mathrm{L}} + k_{\mathrm{L,t}}$ is used, where $k_{\mathrm{L,t}} = \rho_{\mathrm{L}} c_{\mathrm{p,L}} \nu_{\mathrm{t,L}}/Pr_{\mathrm{t,L}}$ is the turbulent thermal conductivity. The quantity $\nu_{\mathrm{t,L}}$ is the kinematic eddy viscosity, which represents the enhancement of molecular momentum diffusion owing to turbulence at the Kolmogorov scale. The turbulent Prandtl number, $Pr_{\mathrm{t,L}}$, was set to

0.85 [50]. As the Kolmogorov scale is three orders of magnitude lower than the mesh size, $\nu_{t,L}$ is a quantity that is modelled by each turbulence sub-model and calculated at each time-step.

6.3.7 Liquid domain discretization

The 2-D domain corresponding to the liquid phase has been discretised into a uniform structured wedge mesh composed by hexahedra and prisms using the blockMesh utility of OpenFOAM. A non-uniform mesh has been generated with the higher refinement concentrated near the vapour-liquid interface and domain boundaries. This is required to ensure an appropriate resolution of the high temperature and vapour gradients expected in these regions. The mesh non-uniformity is given by the grid expansion factors in the vertical ($\gamma_z = \Delta z_{max}/\Delta z_{min}$) and radial ($\gamma_r = \Delta r_{max}/\Delta r_{min}$) directions. For the radial coordinate, the cells with minimum radial width are located near the tank wall and near the vertical axis. In this arrangement, the cells with maximum radial width are located at the mid-point between the tank wall and the vertical axis. For the vertical coordinate, the cells with minimum width are located below and above the interface and above the tank bottom.

In order to obtain a fully resolved boundary layer near the tank wall, the grid spacing in the radial direction has been obtained setting $\Delta r_{min} = y$ corresponding to $y_L^+|_{r=R_T} = 1$. The quantity y^+ is the dimensionless wall coordinate, $y^+ = u_\tau y/\nu_L$, and y is the distance from the wall. This implies that the first cell near to the wall lies within the viscous sublayer of the boundary layer. The value of $y_L^+|_{r=R_T}$has been estimated using the k-ω-SST [51] turbulence model. Similarly, the grid spacing in the vertical direction has been obtained using the value of y_L^+ corresponding to the boundary layer below the tank roof. Hence, $\Delta z = y_L^+|_{z=l_L}$. For the purpose of this calculation and to restrict the grid spacing to reasonable values, y_L^+ has been evaluated after 180 s of evaporation. This choice will not induce a significant modelling error, as the onset of liquid thermal stratification will produce the increase of y_L^+ with time. Table 6.1. summarizes the 8 scenarios studied, the tank radius and height of the liquid phase for each scenario and the mesh parameters.

Table 6.1: Mesh parameters of the cylindrical liquid domain for the CFD-SP model. LF represents the initial liquid filling, R_T the tank radius, l_L the length of the liquid phase, n_r and n_z the number of cells in the radial and vertical directions, respectively. The grid expansion factors for the axial and radial coordinated are defined as $\gamma_z = \Delta z_{max}/\Delta z_{min}$ and $\gamma_r = \Delta r_{max}/\Delta r_{min}$ respectively. Scenarios S1, S2 and S3 correspond to Seo and Jeong experimental data for LN2 evaporation in a 6.75 L storage tank [11]. Scenarios K1, K2 and K3 correspond to Kang et al. experimental data for LN2 evaporation in a 12 L storage tank [12]. Scenarios N1 and N2 correspond to simulations for the non-isobaric storage of LN2 in an 8 m3 storage tank.

Scenario	LF	R_T / m	l_L / m	n_r	n_z	γ_z	γ_r	N° cells
S1	0.70	0.100	0.149	50	100	4	4	5000
S2	0.50	0.100	0.107	50	100	4	4	5000
S3	0.30	0.100	0.063	50	100	4	4	5000
K1	0.80	0.065	0.640	80	120	4	5	9600
K2	0.50	0.065	0.400	80	120	4	5	9600
K3	0.30	0.065	0.240	80	80	4	5	6400
N1	0.97	0.802	3.579	120	324	4	4	38,880
N2	0.30	0.802	1.107	120	100	4	4	33,400

6.3.8 Numerical schemes

The continuum model for the liquid phase given by Eqs. (6.39) - (6.41) and their boundary conditions have been discretised using the finite volume method. The time derivatives were discretised using a second order backward differencing scheme. This scheme has been selected because of its good accuracy and stability for the compressible vapour model [10], see section 6.1. The Laplacian and gradient terms associated with the molecular transport of momentum and energy in Eqs. (6.40) and (6.41) were discretised using second-order accurate central differencing scheme. The divergence of advective fluxes in Eqs. (6.39) - (6.41), as well as the advective fluxes of the turbulent kinetic energy, $\tilde{k}_L$, and turbulent dissipation rate, $\tilde{\omega}_L$, were discretised using the second order accurate upwind scheme developed by Warming and Beam [52]. In OpenFOAM this scheme is available under the name linearUpwind. It receives the velocity gradient as a parameter to improve the stability of the simulation in regions with high velocity gradients.

The preconditioned bi-conjugate gradient (PBiCG) method [53] with a Diagonal-based Incomplete Cholesky (DIC) preconditioner was selected to solve the linear system associated with the kinematic pressure equation. Similarly, the PBiCG method with a diagonal incomplete-LU preconditioner was selected to solve the momentum, energy

and turbulent equations. For all these linear systems, the absolute and relative tolerances for the residuals were set to 10^{-9} and 10^{-3}, respectively. As the solver buoyantBoussinesqPvapFoam assumes that the liquid is incompressible, the choice of PBiCG did not significantly increase simulation times. Furthermore, the speed of the simulations of the CFD-SP model were much faster than the vapour-CFD model for isobaric evaporation and that the multiphase model that will be presented in section 6.4. For instance, simulating an hour of evaporation in a single processor using a coarse mesh of 8000 cells took 30 minutes for the CFD-SP model, 24 h for the vapour-CFD model and 120 h for the multiphase model.

To execute the transient simulation, the OpenFOAM PIMPLE algorithm has been selected, which has already been described in subsection 3.2.6. The number of correctors was set to 2, which implies that the discretised kinematic pressure equation is solved two additional times for each solution time-step. The number of outer correctors was set to 1, which implies that the whole system of discretized equations is solved one additional time for each solution time-step. No relaxation factors have been used as the solver did not show any convergence issue. The maximum Courant number was set to 0.75 as this value was sufficient to achieve stability and keep the cumulative time-step continuity negligible ($< 10^{-9}$).

The thermodynamic and thermophysical properties other than the saturation temperature were evaluated using COOLPROP [54]. The saturation temperature is calculated using the Antoine's equation $T_{\mathrm{sat}} = B/(\ln P_{\mathrm{sat}} - A) - C$. For nitrogen ($N_2$), the coefficients were obtained from Edejer and Thodos [55] experimental data valid for the temperature range 63.14 K - 126.15 K: $A_{N_2} = 20.116$, $B_{N_2} = -609.381$ and $C_{N_2} = -6.788$. For methane (CH_4), the coefficients were obtained from Prydz and Goodwin [56] experimental data valid for the temperature range 90.99-189.99 K: $A_{N_2} = 20.699$, $B_{N_2} = -1020.110$ and $C_{N_2} = -0.49$.

6.4 Multiphase CFD model (CFD-MP)

In the previous sections, a number of simplifying assumptions have been made to derive reduced order models for non-isobaric evaporation of cryogens in storage

tanks. In section 6.2, bulk-phase and 1-D models are constructed by neglecting the velocity field in both phases, and assuming that the evaporation occurs only at the vapour-liquid interface. In section 6.3, the CFD-SP model allows for a removal of the strongest assumptions by explicitly modelling the velocity field in the liquid and wall boiling. This allows to precisely calculate the velocity and temperature fields in the wall boundary layer and below the vapour-liquid interface. However, the vapour velocity field and interfacial heat and mass transfer between the bubbles and the liquid bulk have not been considered by the previous models.

Although the experimental temperature profiles suggest the dominance of vertical heat conduction in the vapour bulk, they do not provide information about the boundary layers. This limitation restricts considerably the conclusions that can be drawn from the experiments, as the transport phenomena in the vapour boundary layers are crucial to determine evaporation rates and the vapour pressure. At the vapour wall, a buoyancy driven boundary layer, $\delta_{\mathrm{w}}^{\mathrm{V}}$ is expected, see Chapter 6.1. However, for small tanks it is not possible to determine *a priori* the effect of the boundary layer on the vapour bulk. The situation is considerably more complicated for the boundary layer at the vapour-liquid interface, $\delta_{\mathrm{i}}^{\mathrm{V}}$. As the evaporation will occur at the wall and at the vapour-liquid interface, high spatial variation is expected for the vapour velocity field just above the interface. The structure of this boundary layer will depend on its interaction with the vapour bulk and the vapour boundary layer. Furthermore, the temperature gradient at $\delta_{\mathrm{i}}^{\mathrm{V}}$ will determine the vapour to interface heat transfer rate, $\dot{Q}_{\mathrm{VI}}$, see Eq. (6.20), which contribute to evaporation.

In this section, a multiphase two-fluid model using the Eulerian-Eulerian framework is implemented to resolve the transport phenomena during the non-isobaric evaporation of a pure cryogen. The two-fluid framework allows to model the interfacial exchange of heat, mass and momentum between the vapour and liquid phases, as well as the transport phenomena in the bulk of each phase. This model constitutes the most complex modelling approach presented in this thesis. Although the two-fluid model has been widely used to model nucleate boiling [24, 33, 57], significant uncertainties remain in the modelling of interfacial heat transfer [58] and wall boiling [24]. The situation becomes even more complex taking in consideration the total absence of experimental

data for the boiling of cryogenic liquids under low wall heat fluxes, $q_w < 500 \mathrm{Wm^{-2}}$. Nevertheless, the two-fluid model allows for potentially ground-breaking results if all sub-models are chosen carefully. In this section, a special emphasis is given on the strong justification of the choice of each sub-model to ensure that the multiphase model will produce physically reasonable results.

6.4.1 Two-fluid Euler-Euler model

The two-fluid approach considers the liquid and vapour phases as two interpenetrating continua. The averaged phase continuity equations [59, 60] for the liquid and vapour phases are given by ,

$$\frac{\partial(\rho_L \alpha_L)}{\partial t} + \nabla \cdot (\rho_L \alpha_L \mathbf{v}_L) = -\Gamma_{LV} \,, \tag{6.74}$$

$$\frac{\partial(\rho_V \alpha_V)}{\partial t} + \nabla \cdot (\rho_V \alpha_V \mathbf{v}_V) = \Gamma_{LV} \,, \tag{6.75}$$

where α_L and α_V are the volume fraction of the liquid and vapour phases, respectively. The volume fraction of the phase is dependent of the size of each finite volume, and it is defined as,

$$\alpha_\psi = \frac{V_{\psi,\mathrm{cell}}}{V_{\mathrm{cell}}} \quad \text{for } \psi = \mathrm{L}, \mathrm{V}, \tag{6.76}$$

where V_{cell} is the volume of each cell produced by the finite volume discretization of the computational domain, and $\alpha_L + \alpha_V = 1$ for all cells and for every subdomain of the computational domain.

The source term Γ_{LV} at the right-hand side of Eqs. (6.74) and (6.75) is the volumetric evaporation rate, defined as,

$$\Gamma_{LV} = \frac{h_{i,L} a_{if} (T_L - T_{sat}) + h_{i,V} a_{if} (T_V - T_{sat})}{\Delta H_{LV}}, \tag{6.77}$$

where $h_{i,L}$, $h_{i,V}$ are the interfacial heat transfer coefficients of the liquid and vapour side of the interface, respectively. In Eq. (6.77), a_{if} is the interfacial area concentration of the dispersed phase in the continuous phase. The dispersed phase is defined as the phase with the lowest volume fraction in a particular computational cell. For instance, if $\alpha_V <$

0.5 in a cell, the vapour phase is assumed to be dispersed as bubbles surrounded by liquid. Similarly, if $\alpha_{\mathrm{L}} < 0.5$, the liquid is assumed to be dispersed as droplets surrounded by vapour. For simplicity, a mono-dispersed particle size [61] has been assumed, which considers that bubbles and droplets are spherical and characterised by their Sauter mean diameter. This allows to define the interfacial area concentration as,

$$a_{\mathrm{if}} = \begin{cases} \dfrac{6\alpha_{\mathrm{V}}}{d_{\mathrm{s,d}}}, & \alpha_{\mathrm{V}} < 0.5, \ \text{vapour bubbles dispersed in liquid} \\ \dfrac{6\alpha_{\mathrm{L}}}{d_{\mathrm{s,b}}}, & \alpha_{\mathrm{V}} \geq 0.5, \ \text{liquid droplets dispersed in vapour} \end{cases} \tag{6.78}$$

where $d_{\mathrm{s,b}}$, $d_{\mathrm{s,d}}$ are the Sauter mean diameters of a bubble and a droplet, respectively.

The heat transfer coefficients for the liquid and vapour phases were calculated using the heuristic correlation for mixed conduction and convection proposed by Wolfert [62],

$$Nu_{\mathrm{i,L}} = \left(\frac{12}{\pi} Ja + \frac{2}{\sqrt{\pi}} \cdot k_{\mathrm{L}} Pe_{\mathrm{LV}}^{1/2}\right) \tag{6.79}$$

$$Nu_{\mathrm{i,V}} = \left(\frac{12}{\pi} Ja + \frac{2}{\sqrt{\pi}} \cdot k_{\mathrm{V}} Pe_{\mathrm{VL}}^{1/2}\right) \tag{6.80}$$

where $Pe_{\mathrm{LV}} = Re_{\mathrm{b}} Pr_{\mathrm{L}}$ is the particle Péclet number for vapour bubbles dispersed in a continuous liquid. Similarly, $Pe_{\mathrm{VL}} = Re_{\mathrm{d}} Pr_{\mathrm{V}}$ is the particle Péclet number for liquid droplets dispersed in a continuous vapour. The Reynolds number for vapour bubbles and liquid droplets are defined by,

$$Re_{\mathrm{b}} = \frac{\rho_{\mathrm{L}} |\mathbf{v}_{\mathrm{V}} - \mathbf{v}_{\mathrm{L}}| d_{\mathrm{s,b}}}{\mu_{\mathrm{L}}}. \tag{6.81}$$

$$Re_{\mathrm{d}} = \frac{\rho_{\mathrm{V}} |\mathbf{v}_{\mathrm{L}} - \mathbf{v}_{\mathrm{V}}| d_{\mathrm{s,d}}}{\mu_{\mathrm{V}}}. \tag{6.82}$$

where $\mathbf{v}_{\mathrm{rel,b}} = \mathbf{v}_{\mathrm{V}} - \mathbf{v}_{\mathrm{L}}$ is the relative or "slip" velocity of the vapour bubbles with respect to the continuous liquid. Similarly, the relative velocity between a liquid droplet with respect to a continuous vapour phase is defined as $\mathbf{v}_{\mathrm{rel,d}} = \mathbf{v}_{\mathrm{L}} - \mathbf{v}_{\mathrm{V}}$.

The Wolfert [62] heuristic correlation for interfacial heat transfer has been preferred over the frequently used Ranz-Marshall [63] correlation. This choice is

supported by the ability of the former to capture conduction dominated heat transfer under low or zero slip velocities, while the latter is only applicable for convection-dominated flow. Although the liquid flow is expected to be dominated by convection near the wall, below the vapour-liquid interface it is not the case. The thermally stratified layer that will developed shortly after the beginning of the evaporation, as a consequence of the rapid increase in saturation temperature [11, 12], will mitigate convective currents below the vapour liquid interface. For low liquid heat fluxes typical of cryogenic storage, the Jakob number is expected to be between 0.1 and 1. In this range, Liao and Lucas [58] found that the Wolfert [62] correlation was the most accurate interfacial heat transfer correlation to predict bubble growth in convective-turbulent dominated regimes. Therefore, the use of Wolfert [62] correlation enables to accurately represent the heat transfer between the dispersed bubbles and the liquid bulk in both high and low velocity regions. As part of this research, the Wolfert [62] correlation has been implemented in OpenFOAM-v2006.

The averaged momentum conservation equations for the liquid and vapour phases are governed by the averaged compressible Navier-Stokes equations [59, 60],

$$\frac{\partial(\rho_{\mathrm{L}}\alpha_{\mathrm{L}}\mathbf{v}_{\mathrm{L}})}{\partial t} = -\alpha_{\mathrm{L}}\nabla P + \nabla\cdot\left[\alpha_{\mathrm{L}}\mu_{\mathrm{L}}(\nabla\mathbf{v}_{\mathrm{L}} + (\nabla\mathbf{v}_{\mathrm{L}})^{\mathrm{T}}) - \frac{2}{3}\alpha_{\mathrm{L}}\mu_{\mathrm{L}}(\nabla\cdot\mathbf{v}_{\mathrm{L}})\mathbf{I}\right] - \nabla\cdot[\rho_{\mathrm{L}}\alpha_{\mathrm{L}}\mathbf{v}_{\mathrm{L}}\mathbf{v}_{\mathrm{L}}] + \alpha_{\mathrm{L}}\rho_{\mathrm{L}}\mathbf{g} + \Gamma_{\mathrm{LV}}(\mathbf{v}_{\mathrm{V}} - \mathbf{v}_{\mathrm{L}}) + \mathbf{M}_{\mathrm{LV}}, \tag{6.83}$$

$$\frac{\partial(\rho_{\mathrm{V}}\alpha_{\mathrm{V}}\mathbf{v}_{\mathrm{V}})}{\partial t} = -\alpha_{\mathrm{L}}\nabla P + \nabla\cdot\left[\alpha_{\mathrm{L}}\mu_{\mathrm{V}}(\nabla\mathbf{v}_{\mathrm{V}} + (\nabla\mathbf{v}_{\mathrm{V}})^{\mathrm{T}}) - \frac{2}{3}\alpha_{\mathrm{V}}\mu_{\mathrm{V}}(\nabla\cdot\mathbf{v}_{\mathrm{V}})\mathbf{I}\right] - \nabla\cdot[\rho_{\mathrm{V}}\alpha_{\mathrm{V}}\mathbf{v}_{\mathrm{V}}\mathbf{v}_{\mathrm{V}}] + \alpha_{\mathrm{V}}\rho_{\mathrm{V}}\mathbf{g} + \Gamma_{\mathrm{LV}}(\mathbf{v}_{\mathrm{L}} - \mathbf{v}_{\mathrm{V}}) + \mathbf{M}_{\mathrm{VL}}, \tag{6.84}$$

where $\mathbf{M}_{\mathrm{LV}}$ is the volumetric momentum source for the liquid phase generated by different interfacial sub-forces between the vapour and the liquid. It should be noted that the momentum transferred from one phase to the other by interfacial forces must be conserved. Hence, $\mathbf{M}_{\mathrm{VL}} = -\mathbf{M}_{\mathrm{LV}}$. In the description of the interfacial forces, it will be assumed that the vapour is the dispersed phase on the liquid. This is expected as at the wall the volume fraction of vapour is expected to be of the order of 10^{-3} – 10^{-4} [57] owing to the low wall heat fluxes typical of the non-isobaric storage of a cryogen in a static tank [20, 64]. Thus, the volumetric momentum source in the liquid owing to interfacial

momentum transfer between the liquid bulk and the dispersed bubbles is constituted by five contributions,

$$\mathbf{M}_{\mathrm{LV}} = F_{\mathrm{D,LV}} + F_{\mathrm{L,LV}} + F_{\mathrm{W,LV}} + F_{\mathrm{VM,LV}} + F_{\mathrm{TD,LV}}, \tag{6.85}$$

where F_{D} is the drag force, F_{L} is the lift force, F_{W} is the lift force, F_{VM} the virtual mass and F_{TD} the turbulent dispersion.

The drag force that the liquid exerts on the gas is given by,

$$F_{\mathrm{D,LV}} = \frac{1}{8} C_{\mathrm{D}} a_{\mathrm{if}} \rho_{\mathrm{L}} |\mathbf{v}_{\mathrm{V}} - \mathbf{v}_{\mathrm{L}}| (\mathbf{v}_{\mathrm{V}} - \mathbf{v}_{\mathrm{L}}), \tag{6.86}$$

where C_{D} is the drag coefficient of bubbles in the liquid. The drag coefficient has been modelled using the Schiller and Naumann [65] correlation,

$$C_{\mathrm{D}} = \begin{cases} \dfrac{24\left(1 + 0.15\, Re_{\mathrm{p}}^{0.687}\right)}{Re_{\mathrm{p}}}, & Re_{\mathrm{p}} \leq 1000 \\ 0.44\,, & Re_{\mathrm{p}} > 1000 \end{cases} \tag{6.87}$$

where Re_{p} is the particle Reynolds Number. In this case, as the vapour is dispersed in the liquid as bubbles, the particle Reynolds number is given by,

$$Re_{\mathrm{p}} = \frac{\rho_{\mathrm{L}} |\mathbf{v}_{\mathrm{v}} - \mathbf{v}_{\mathrm{L}}| d_{\mathrm{b}}}{\mu_{\mathrm{L}}}. \tag{6.88}$$

As a consequence of the bubble raising through the liquid, the bubble is subject to a lift force. The lift force acts in the direction perpendicular to the relative motion between the bubble and the liquid bulk, and it is given by:

$$F_{\mathrm{L,LV}} = \frac{1}{8} C_{\mathrm{L}} \alpha_{\mathrm{V}} \rho_{\mathrm{L}} (\nabla \times \mathbf{v}_{\mathrm{L}}) \times (\mathbf{v}_{\mathrm{V}} - \mathbf{v}_{\mathrm{L}}), \tag{6.89}$$

Where C_{L} is the lift coefficient. For typical storage scenarios, nucleate boiling will onset at the tank wall in a thin region below the vapour-liquid interface. This is a consequence of a quicker increase of liquid saturation temperature when compared against the increase of average liquid temperature. Consequently, the bubbles are expected to be contained in a thin region within the wall boundary layer. Additionally, for wall heat fluxes typical of cryogenic liquid storage, vapour volume fractions are expected to be lower than 0.01. Although the lift force is maximum near the wall and will tend to spread the bubbles outside the boundary layer, the low volume fraction inside the thin boiling

region below the interface will limit the contribution of lift to interfacial momentum transfer. In this thesis, the lift force has been neglected. This assumption is reasonable for non-isobaric evaporation and low wall heat fluxes only, which limits the range of applicability of the CFD-MP model.

The wall lubrication is an additional lateral force owing to surface tension, which prevents the attachment of the bubbles to the solid wall. The wall lubrication has been modelled using the Antal et al. [66] model,

$$F_{\mathrm{LV,WL}} = \frac{\alpha_{\mathrm{V}}\rho_{\mathrm{L}}|(\mathbf{v}_{\mathrm{V}} - \mathbf{v}_{\mathrm{L}}) - [\mathbf{n}_{\mathrm{w}} \cdot (\mathbf{v}_{\mathrm{V}} - \mathbf{v}_{\mathrm{L}})]\mathbf{n}_{\mathrm{w}}|^2}{d_{\mathrm{b}}} \left(C_{w1} + C_{w2}\frac{d_{\mathrm{b}}}{x_{\mathrm{w}}}\right)\mathbf{n}_{\mathrm{w}}, \qquad (6.90)$$

where $\mathbf{n}_{\mathrm{w}}$ is the unit outward normal vector on the surface of the wall and x_{w} the distance between the bubble and the wall. The constants C_{w1} = -0.01, C_{w2} = 0.05 were fitted by Antal et al. [66] against a three-dimensional direct numerical simulation of flow past a bubble near a wall.

The virtual mass interfacial force is defined as the resistance force that an accelerating bubble dispersed in a continuum fluid [67] experiences, which is proportional to the bubble acceleration. The virtual mass force has been included using the Drew and Lahey [67] model,

$$F_{\mathrm{LV,VM}} = C_{\mathrm{VM}}\alpha_{\mathrm{V}}\rho_{\mathrm{L}}\left(\frac{\mathrm{D}\mathbf{v}_{\mathrm{V}}}{\mathrm{D}t} - \frac{\mathrm{D}\mathbf{v}_{\mathrm{L}}}{\mathrm{D}t}\right), \qquad (6.91)$$

where the operator $D(\mathbf{v})/Dt = \partial\mathbf{v}/\partial t + \mathbf{v}\cdot\nabla\mathbf{v}$ is the material derivative of the vector field $\mathbf{v}$ and C_{VM} the virtual mass coefficient. The virtual mass coefficient has been assumed equal to 0.5, as this value provides the exact solution of the virtual mass force for an ascending sphere in inviscid flow [67].

The turbulent dispersion force represents the time-averaged drag forces at the bubble – liquid interface. The turbulent dispersion force has been included in the multiphase model using the Favre-averaged drag model developed by Burns et al. [68],

$$F_{\mathrm{LV,TD}} = -C_{\mathrm{TD}}\left[\frac{1}{8}C_{\mathrm{D}}a_{\mathrm{if}}\rho_{\mathrm{L}}|\mathbf{v}_{\mathrm{V}} - \mathbf{v}_{\mathrm{L}}|\right]\frac{\mu_{\mathrm{V,t}}}{\rho_{\mathrm{V}}Pr_{\mathrm{t,b}}}\left(\frac{\nabla\alpha_{\mathrm{V}}}{\alpha_{\mathrm{V}}} - \frac{\nabla\alpha_{\mathrm{L}}}{\alpha_{\mathrm{L}}}\right), \qquad (6.92)$$

where C_{TD} is the turbulent dispersion coefficient and it has been set to a value of 1, and $\mu_{\mathrm{V,t}}$ is the turbulent dynamic viscosity of the vapour phase. The turbulent bubble

Prandtl number, $Pr_{t,b} = \nu_{t,L}/\hat{\alpha}_{turb,b}$, represents the ratio of the turbulent kinematic viscosity to the turbulent thermal diffusivity of the bubbles in the liquid. The turbulent bubble Prandtl number has been set to a value of 0.9 as recommended by Burns et al. [68]. Finally, the averaged energy equations for the liquid and vapour phases are given by,

$$\frac{\partial(\rho_L \alpha_L h_L)}{\partial t} = -\nabla \cdot (\rho_L \alpha_L \mathbf{v}_L h_L) + \nabla \cdot [\alpha_L k_L (\nabla T_L)] + \alpha_L \rho_L (\mathbf{v}_L \cdot \mathbf{g}) + \Gamma_{LV}(h_L - h_V) + \alpha_L \frac{dP}{dt}, \tag{6.93}$$

$$\frac{\partial(\rho_V \alpha_V h_V)}{\partial t} = -\nabla \cdot (\rho_V \alpha_V \mathbf{v}_V h_V) + \nabla \cdot [\alpha_V k_V (\nabla T_V)] + \alpha_V \rho_V (\mathbf{v}_V \cdot \mathbf{g}) + \Gamma_{LV}(h_V - h_L) + \alpha_V \frac{dP}{dt}. \tag{6.94}$$

The liquid density has been modelled using a linear fit as a function of the temperature , $\rho_L(T) = \beta_0 + \beta_1 T_L$, using the data provided by the open-source thermodynamic library COOLPROP [54]. For liquid nitrogen, β_0 = 1161.58 and β_1 = -4.595. This allows the model to include liquid thermal expansion during non-isobaric storage. The vapour has been assumed an ideal gas, $\rho_V = P/RT_V$, as nitrogen and methane are simple gases that can be reasonably approximated to an ideal gas. Equations (6.74)-(6.75), (6.83)-(6.84) and (6.93)-(6.94) constitute a system of 6 partial differential equations that govern non-isothermal, compressible multiphase fluid flow. In order solve this system, suitable initial and boundary conditions for each variable that represent the physical phenomena during non-isobaric storage are required. In what follows, the computational domain that has been used to model the cylindrical cryogenic storage tank will be described with the boundary conditions associated to each domain boundary.

6.4.2 Computational domain and boundary conditions

The computational domain has been modelled as a 2-D domain extending in the radial and vertical (r, z) directions. This choice is supported by the symmetry of the heating through the tank walls. A recent review [64] on two-phase CFD models for cryogen self-pressurization has shown that 2-D models predict liquid temperatures and

pressure build-up accurately. Although the 2-D assumption neglects an oscillatory, three-dimensional flow near the vapour-liquid interface and near the tank centreline [64]. In Panzarella et al. [64] validation study, this effect slightly underpredicted vapour temperatures by less than 0.5 K. Consequently, the differences on pressure and temperature profiles between 2-D and 3-D models are expected to be very small, supporting the axis-symmetrical assumption.

The domain has been defined as the rectangle $\Omega = (0,0) \times (R_T, H_T)$ where $H_T = V_T/A_T$ is the tank height. The domain is enclosed by three solid boundaries representing the tank bottom ($z = 0, r$), tank walls (z, R_T) and tank roof ($z = H_T, r$), and one open boundary represent the tank vertical axis ($z, r = 0$). The initial amount of liquid and vapour inside the domain is demarked by the initial conditions for the volume fraction of each phase. For a particular initial liquid filling, the initial liquid height can be calculated through $l_L|_{t=0} = V_T LF_0$. Therefore, all the cells below the initial liquid height will have a liquid volume fraction of 1 and a vapour volume fraction of 0. This condition implies that at the beginning of the evaporation there is no dispersed bubbles in the liquid. Similarly, all the cells above the initial liquid length will have a vapour volume fraction of 1 and a liquid volume fraction of 0. Figure 6.2 depicts the computational domain and its boundaries for a storage tank initially filled at 70% of its capacity.

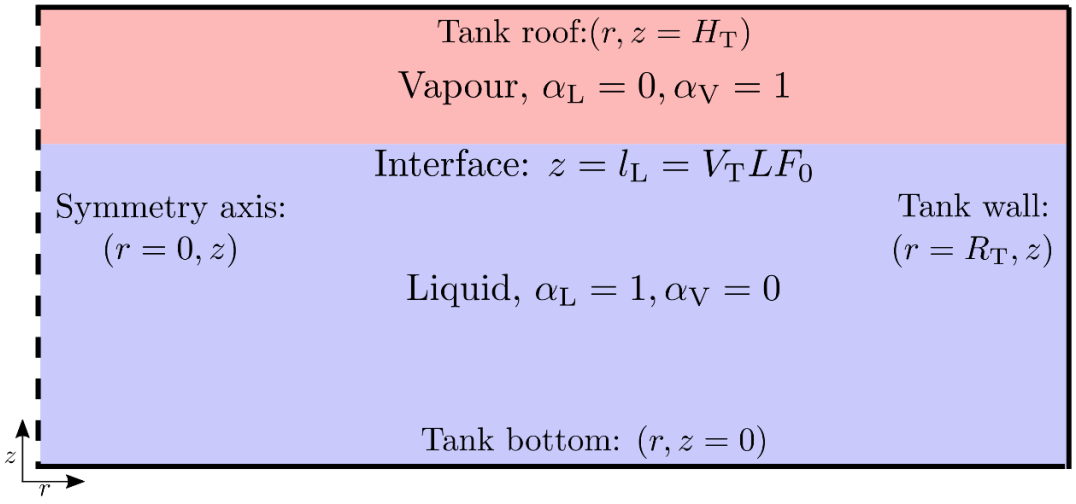

Figure 6.2: Schematic of the storage tank modelled as a 2-D cylindrical domain. The liquid phase is represented in blue colour and the vapour phase is represented in red colour. Solid black lines represent the solid boundaries, while dashed lines represent open boundaries. R_T, H_T are the radius and height of the storage tank, respectively, while α_L, α_V are the volume fractions of the liquid and vapour phases. The interface is set at a liquid height corresponding to an initial liquid filling $LF_0 = 0.7$ to illustrate a common storage scenario.

Table 6.2 summarizes the boundary conditions for the velocity, temperature and volume fraction of each phase, and for the shared pressure between the phases, respectively. Similarly,

Table 6.3 summarizes the initial conditions for the above-mentioned quantities. The liquid and vapour phases are assumed to be stagnant at the beginning of the evaporation, $\mathbf{v_V}|_{t=0} = \mathbf{v_L}|_{t=0} = \mathbf{0}$. At the tank axis, a zero gradient boundary condition for vapour and liquid velocities been used to enforce the azimuthal symmetry. In contrast to the isobaric evaporation scenarios, there is no valve to vent the BOG during non-isobaric storage. Hence, at all solid boundaries, zero-velocity boundary conditions have been imposed for the liquid and vapour velocity.

Table 6.2: Boundary conditions for the multiphase model. U_{bot} and U_{L} are the overall heat transfer coefficients of the storage tank at the tank bottom at the tank wall in contact with liquid. U_{roof} and U_{V} are the overall heat transfer coefficients of the storage tank at the tank roof and at the tank wall in contact with vapour.

Field	Axis	Bottom	Wall	Roof
P	$\frac{\partial P}{\partial r} = 0$	Calculated	Calculated	Calculated
$\mathbf{v}_{\mathrm{L}}$	$\frac{\partial v_{r,\mathrm{L}}}{\partial r} = 0$	(o o)	(o o)	(o o)
$\mathbf{v}_{\mathrm{V}}$	$\frac{\partial v_{r,\mathrm{V}}}{\partial r} = 0$	(o o)	(o o)	(o o)
T_{L}	$\frac{\partial T_{\mathrm{L}}}{\partial r} = 0$	$\frac{\partial T_{\mathrm{L}}}{\partial z} = \frac{U_{\mathrm{bot}}}{k_{\mathrm{L}}}(T_{\mathrm{air}} - T_{\mathrm{L}})$	$\frac{\partial T_{\mathrm{L}}}{\partial r} = \frac{U_{\mathrm{L}}}{k_{\mathrm{L}}}(T_{\mathrm{air}} - T_{\mathrm{L}})$	$\frac{\partial T_{\mathrm{L}}}{\partial z} = 0$
T_{V}	$\frac{\partial T_{\mathrm{V}}}{\partial r} = 0$	$\frac{\partial T_{\mathrm{V}}}{\partial z} = 0$	$\frac{\partial T_{\mathrm{V}}}{\partial r} = \frac{U_{\mathrm{V}}}{k_{\mathrm{V}}}(T_{\mathrm{air}} - T_{\mathrm{V}})$	$\frac{\partial T_{\mathrm{V}}}{\partial z} = \frac{U_{\mathrm{roof}}}{k_{\mathrm{V}}}(T_{air} - T_{\mathrm{V}})$
α_{L}	$\frac{\partial \alpha_{\mathrm{L}}}{\partial r} = 0$	$\frac{\partial \alpha_{\mathrm{L}}}{\partial z} = 0$	$\frac{\partial \alpha_{\mathrm{L}}}{\partial r} = 0$	$\frac{\partial \alpha_{\mathrm{L}}}{\partial z} = 0$
α_{V}	$\frac{\partial \alpha_{\mathrm{V}}}{\partial r} = 0$	$\frac{\partial \alpha_{\mathrm{V}}}{\partial z} = 0$	$\frac{\partial \alpha_{\mathrm{V}}}{\partial r} = 0$	$\frac{\partial \alpha_{\mathrm{V}}}{\partial z} = 0$

Table 6.3: Initial conditions for the multiphase model. l_{L} is the liquid height, l_{V} is the vapour height and $H_{\mathrm{T}} = l_{\mathrm{L}} + l_{\mathrm{V}}$ is the tank height.

Field	Initial condition
P	$\rho_{\mathrm{V}} g \max(H_T - z, l_{\mathrm{V}}) + \rho_{\mathrm{L}} g \max(l_L - z, 0) + 10^5$
$\mathbf{v}_{\mathrm{L}}$	(o o)
$\mathbf{v}_{\mathrm{V}}$	(o o)
T_{L}	$T_{\mathrm{L}} = T_{\mathrm{sat}}(P_0)$
T_{V}	$T_{\mathrm{V}} = T_{\mathrm{sat}}(P_0)$
α_{L}	$\alpha_{\mathrm{L}} = 1$ if $z \leq l_{\mathrm{L}}$, $\alpha_{\mathrm{L}} = 0$ otherwise

α_V	$\alpha_V = 1$ if $z > l_L$, $\alpha_V = 0$ otherwise

At the beginning of the evaporation, the pressure minus the hydrostatic pressure is assumed to be 1 bar. At the tank axis, the axial symmetry is forced by setting a zero-gradient in the direction normal to the axis, $\partial P/\partial r|_{z,0} = 0$. The pressure at all solid boundaries is calculated from the velocity profiles for each phase. As it is depicted in Figure 6.2, the initial conditions for the volume fraction are a function of the liquid filling. For the liquid and vapour volume fraction, a zero gradient boundary condition in the direction normal to the boundary has been used. This choice is supported by the assumption that the meniscus formed between the vapour and liquid interface and the tank wall has a negligible effect in temperature profiles and evaporation rates.

As the non-isobaric evaporation is driven by the heat ingress from the surroundings, the temperature boundary conditions drive the mass, momentum and heat fluxes. At the beginning of the evaporation, the vapour and liquid are assumed to be at the saturation temperature of the cryogenic liquid at the initial pressure. At the tank axis, the temperature profiles are forced to be axis-symmetrical by setting their radial derivative to zero, $\partial T_L/\partial r|_{z,0} = \partial T_V/\partial r|_{z,0} = 0$. At the tank bottom, tank wall and tank roof a convection conduction boundary condition adapted for the averaged energy equation has been implemented. This boundary condition takes the form of $\partial T_\psi/\partial \mathbf{n} = U_\psi/k_\psi(T_{air} - T_\psi)$, where U_ψ and k_ψ are the overall heat transfer coefficient and thermal conductivities of the phase ψ, respectively.

It is worth noting that wall boiling has not been included explicitly in the temperature boundary condition at the tank wall and bottom. From a physical point of view, wall boiling can be understood as a non-uniform source term in the evaporation rate in the region close to the tank wall. The implementation of wall boiling is dependent of each particular CFD package. In OpenFOAM, wall boiling is implemented as a customized boundary condition for the turbulent thermal diffusivity. This implementation, which is dependent of the choice of the turbulence model, will be described in subsection 6.4.3.

6.4.3 CFD implementation in OpenFOAM.

The multiphase model has been implemented using the OpenFOAM v2006 CFD library [2], which makes use of the finite volume method [69] to discretize the domain and partial differential equations. The solver reactingTwoPhaseEulerFoam [2] has been selected because it is a solver for the two-fluid Euler-Euler model presented in Eqs. (6.74)-(6.75), (6.83)-(6.84) and (6.93)-(6.94). This solver treats both liquid and vapour phases as interpenetrating continua. At each time-step, the solver classifies at runtime the disperse phase as the phase with lowest volume fraction in a given computational cell. Furthermore, the solver allows each phase to be modelled as a compressible, turbulent fluid. This feature allows to predict with high accuracy the pressure build-up in the vapour owing to evaporation, and the liquid thermal expansion.

In all the tested scenarios, the Rayleigh number for the liquid phase was higher than 10^9. This implies that turbulence modelling is required for the liquid in order to solve the multiphase model in a reasonable mesh. For the vapour phase, the Rayleigh number ranged from 10^7 to 10^9. Given that it is not clear the threshold for turbulence for natural convective flow in a cylinder with vertical thermal stratification, turbulence in the vapour phase has also been considered. Two recent reviews have demonstrated that using the mixture k-ε turbulence model for the vapour phase inside a cryogenic storage tank under non-isobaric conditions under predicts vapour temperature [20, 64]. This is a consequence of the overestimation of vapour turbulent thermal diffusivity by the k-ε model near stagnant regions [70]. Additionally, the same reviews highlight the limitations of the Volume of Fluid method in the calculation of the slip velocities between liquid and vapour phases. To model more accurately slip velocities and to prevent the spurious underprediction of vapour temperatures, Large Eddy Simulation (LES) turbulence models have been used in both phases. This choice has the cost of reduced reliability of LES in 2-D simulations owing to neglecting 3-D turbulence. Additionally, LES modelling of sub-grid scale turbulence is simpler than that of k-ε. Nevertheless, in test simulations, it was observed that the limitations of LES introduced a much smaller modelling error than the gross underprediction of vapour temperature using k-ε.

Vapour phase turbulence has been modelled using the same LES model that the one used for isobaric storage. This choice is supported by the robustness of the LES model in providing a physically consistent characterization for cryogenic methane vapour, see section 3.2.3. This LES sub-grid scale model corresponds to the Smagorinsky model [71] with a Smagorinsky coefficient $C_S = 0.21$ as suggested by Eidson [72] for turbulent buoyancy driven flow. It is worth noting that this model has been designed for single-phase flow. This is not expected to induce a modelling error anywhere except at the vapour liquid interface, where the droplet induced turbulence may modify the eddy viscosity predicted by the Smagorinsky [71] model. Nevertheless, this effect is expected to be small in the pseudo-steady state, as the onset of thermal stratification will dampen vapour velocity at the vapour-liquid interface [10].

In contrast to the vapour phase, the amount of induced turbulence by the bubbles that are expected to be generated at the wall may be significant. To consider this additional turbulence source, the one equation sub-grid scale model developed by Niceno [73] has been used. This model has been developed for bubbly flows. The turbulent dispersion induced by the bubbles is physically reasonable as long as the LES filter size is larger than the bubble diameter [73]. In the OpenFOAM implementation of the LES turbulence model that, the filter size is equal to the grid spacing. This condition is expected to be satisfied as very low volume fractions of bubbles near the tank wall are expected during the slow boiling of cryogenic liquids. Furthermore, the bubble size is expected to be lower than 0.3 mm [34], specially far from the interface where the wall superheating is expected to be small.

6.4.4 Wall boiling implementation

Wall boiling has been implemented using the OpenFOAM alphatWallBoilingWallFunction [2] wall function. This is a wall function for the liquid turbulent thermal diffusivity, $\hat{\alpha}_{\text{turb,L}}$. The wall function sets $\hat{\alpha}_{\text{turb,L}}$ in the cells adjacent to the boiling boundary to a value that enforces the wall temperature to satisfy the wall heat flux partitioning described in subsection 6.3.3. As a result, the boundary condition is expressed in an implicit form,

$$\frac{q_w}{\rho_{\mathrm{L}} c_{\mathrm{p,L}}} = \left(\hat{\alpha}_{\mathrm{lam,L}} + \hat{\alpha}_{\mathrm{turb,L}}\right) \frac{T_w - T_{\mathrm{c}}}{y_{\mathrm{c}}} \tag{6.95}$$

where T_{c} is the temperature at the center of the cell adjacent to the solid boundary where wall boiling is occurring. Similarly, y_{c} is the distance between the solid boundary and the center of the cell adjacent to the boundary. Because of the onset of boiling at the wall, the turbulent thermal diffusivity in Eq. (6.95) requires special treatment to be calculated. In OpenFOAM, $\hat{\alpha}_{\mathrm{turb,L}}$ is calculated using the Koncar and Borut approach for boiling two phase flows [74].

In addition to modifying the liquid temperature and liquid turbulent thermal diffusivity, the alphatWallBoilingWallFunction [2] adds the evaporation rate owing to the evaporative heat flux at the wall, see Eq. (6.44), to the volumetric evaporation rate, Γ_{LV}, in Eq. (6.77). Hence, the volumetric evaporation rate in the cell neighbouring a boundary where wall boiling is updated by the following expression,

$$\Gamma_{\mathrm{LV}}|_{\partial\Omega,\mathrm{wb}} = \Gamma_{\mathrm{LV}} + \frac{q_e}{\Delta H_{\mathrm{LV}}} = \Gamma_{\mathrm{LV}} + \left(\frac{\pi d_B^3}{6}\right) N_{\mathrm{A}} f \rho_{\mathrm{V}}(T_{\mathrm{w}}), \tag{6.96}$$

where $\Gamma_{\mathrm{LV}}|_{\partial\Omega,\mathrm{wb}}$ represents the volumetric evaporation rate in the computational cell neighbouring the boundary undergoing wall boiling denoted by $\partial\Omega_{\mathrm{wb}}$.

Eqs. (6.95) - (6.96) require the specification of the wall heat flux closure sub-models to calculate the evaporative heat flux q_{e} using Eq. (6.44). The closure sub-models are the same as the ones described in subsection 6.3.3. In summary, Eqs. (6.47)-(6.48) have been used to model the active nucleation site density N_A, while Eq. (6.49) was used to model the bubble departure diameter d_{B} and Eq. (6.53) for the bubble departure frequency. The constant m in Eq. (6.47) will be fitted for the multiphase model against Seo et al. [11] and Kang et al. [12] experimental data on liquid nitrogen evaporation. The fitted value of the constant m using the multiphase model is expected to be different to the one fitted using the single-phase model. developed in section 6.3.

The modelling of vapour turbulence in conjunction with the liquid turbulence is a characteristic feature of the presented multiphase model. Traditional Euler-Euler simulations normally assume the vapour phase as laminar, as this is a good hypothesis when the bubbles are dispersed along the whole liquid domain. Two examples of

situation where this assumption is applicable are bubble columns [34] and water wall in a nuclear reactor [57]. Unfortunately, the vapour and liquid phases during the non-isobaric storage of cryogenic liquids are segregated everywhere in the domain except in the region close to the tank wall. Including the turbulence in the vapour phase bulk is crucial for an accurate description of the transient period of vapour heating, and buoyancy driven flow, see section 5.2.6 and [10]. Therefore, the methodology that has been presented in subsections 6.4.1 - 6.4.4 aims to propose a foundation for the Euler-Euler large-eddy simulation (EELES) for the evaporation of cryogenic liquids.

6.4.5 Domain discretization

The 2-D domain representing the storage tank has been discretised into non-uniform structured wedge meshes composed by hexahedra and prisms using the blockMesh utility of OpenFOAM. In contrast to the vapour domain discretisation performed for the isobaric evaporation of cryogens in subsection 3.2.4, the absence of an outlet simplifies considerably the mesh generation. Nevertheless, Euler-Euler simulations require much finer meshes than single-phase simulations, particularly if LES turbulence models are used. The grid spacing in the radial and vertical direction has been set to ensure that the cell centre of the cell neighbouring the wall and interface lie in the viscous sublayer of both phases. To determine grid spacing, it has been assumed that wall-boiling and interfacial phase change do not decrease the width of the viscous sublayers near the wall and interface, respectively. Furthermore, as the liquid laminar sub-layer is expected to be thinner than the laminar vapour sublayer, the grid size is assumed to be controlled by the width of the liquid sublayer. This allows the usage of the CFD-SP model with the k-ω-SST [51] turbulence model and the procedure described in subsection 6.3.7 to determine the radial and vertical grid spacings. Table 6.4 summarizes the 4 scenarios studied, the tank radius and height of the cylindrical storage tanks and the mesh parameters.

Table 6.4: Mesh parameters of the cylindrical domain for the multiphase CFD model. *LF* represents the initial liquid filling, R_T the tank radius, H_T the tank height, Δr the radial spacing and Δz the vertical spacing. The grid expansion factors for the axial and radial coordinated are defined as $\gamma_z = \Delta z_{\max}/\Delta z_{\min}$ and $\gamma_r = \Delta r_{\max}/\Delta r_{\min}$. Scenarios S1 and S2 correspond to Seo and Jeong experimental data for LN2 evaporation in a 6.75 L storage tank [11]. Scenarios N1 and N2 correspond to simulations for the non-isobaric storage of LN2 in an 8 m3 storage tank.

Scenario	LF	R_T / m	H_T / m	n_r	n_z	γ_z	γ_r	N° cells
S1	0.70	0.100	0.213	100	167	5	3.7	12,000
S2	0.50	0.100	0.213	100	167	5	3.7	12,000
N1	0.97	0.802	3.959	150	501	4	4	38,880
N2	0.30	0.802	3.959	150	501	4	4	33,400

6.4.6 Numerical schemes

The equations of the multiphase model and all boundary conditions presented in subsections 6.4.1 - 6.4.4 have been discretised using the finite volume method. Achieving high accuracy in the Euler-Euler multiphase model is much more difficult than for the single-phase models presented in sections 3.2 and 6.3. In the multiphase model, there are six partial differential equations to be solved instead of three. Not only the dimensionality of the system of equations is larger, but also the continuity, momentum and energy equations for each phase are inherently more complex to solve than the single-phase equations. This is a consequence of the additional non-linear source terms that are included to model the interfacial heat, mass and momentum transfer. Additionally, most quantities in the equations of the multiphase model are multiplied by a volume fraction corresponding to the phase that the equation is modelling. As the volume fraction of vapour and liquid are restricted by $\alpha_L + \alpha_V = 1$, this adds an additional constraint to the numerical solution of the multiphase model. In this subsection, the discretization scheme chosen for of each differential operator in the continuum model and its numerical implementation in OpenFOAM will be described.

For the divergence operator that operates on the mass of each phase in the continuity equations, Eqs. (6.74)-(6.75), a flux corrected transport (FCT) scheme has been used. The flux corrected transport scheme facilitates the discretization of hyperbolic partial differential equations by means of blending higher and lower order discretization schemes. The face flux limiter proposed by Van Leer [75] is used in the FCT scheme to enforce that the volume fractions of each phase ψ remain within their physical bounds, $0 \leq \alpha_\psi < 1$.

The remaining discretization schemes for the time derivative, gradient, Laplacian and divergence operators are the same as the ones chosen for the vapour-CFD

model. This choice is supported by the good stability that these schemes provided for isobaric evaporation. In what follows, the numerical schemes will only be listed, while full details and a justification for each scheme can be found in subsection 4.1.6. The time derivatives in Eqs. (6.74)-(6.75), (6.83)-(6.84) and (6.93)-(6.94) were discretised using second order backward differences. The temperature gradients in Eqs. (6.93)-(6.94) and the Laplacian operators in Eqs. (6.83)-(6.84) and (6.93)-(6.94) were discretised using second-order accurate central differences. The divergence of the advective terms in Eqs. (6.83)-(6.84) were discretised using the linearUpwindV scheme [2]. The divergence of the advective terms associated with liquid and vapour enthalpies in Eqs. (6.93)-(6.94) were discretized using the linear upwind stabilized transport (LUST) [2] scheme. Both linearUpwindV and LUST schemes are a blend of upwind central linear differences. The discretization is closer to upwind differences for regions with large velocity gradients and linear everywhere else, which aims to achieve a balance between accuracy and stability.

In OpenFOAM, the numerical solution of the discretized version of the continuity equations, Eqs. (6.74)-(6.75), is obtained through the multidimensional universal limiter for explicit solution (MULES) algorithm [2]. The MULES algorithm has been developed by Weller [76] in a private report, while its code is readily available [2] and the algorithm has been explained thoroughly by Lin et al [77]. It basically consists in a number of fixed-point iterations to provide a stable implementation of the flux corrected transport scheme to ensure that the volume fractions remain bounded. To improve the stability of the simulation, 3 temporal sub-cycles were selected as the nAlphaSubCycles parameter in the fvSolution dictionary of the OpenFOAM simulation case. This implies that for each temporal iteration of reactingTwoPhaseEulerFoam at a timestep Δt, the continuity equations are solved three times using a $\Delta t/3$ time-step. A single corrector of the volume fraction, nAlphaCorr = 1, was selected for both continuity equation. This implies that for each temporal iteration, an additional fixed-point iteration is performed on the continuity equation to decrease the residuals.

The OpenFOAM geometric agglomerated algebraic multigrid (GAMG) [2] solver was selected to solve the linear system associated with the discretised form of the pressure equations. The coarsest level matrix is being solved by the preconditioned bi-

conjugate gradient (PBiCG) method [53]. The Gauss-Seidel Diagonal-based Incomplete Cholesky (DIC) preconditioner has been selected to solve the finer matrix level. The choice of GAMG for the multiphase model has been motivated to achieve a balance between accuracy and efficiency. The high cell count of the discretised domain in the multiphase model, see Table 6.4, makes the use of pure PBiCG impractical. In contrast to the vapour-CFD model developed in section 3.2, the lack of outlet enabled a more stable convergence of the pressure equation, further justifying the use of the GAMG solver over pure PBiCG. An absolute tolerance for the residuals, ϵ, of 10^{-8} in conjunction with a relative tolerance of 10^{-3} where sufficient to provide accuracy and stability.

In the multiphase model, the linear systems associated with the discretised energy equations were more difficult to solve than in the single-phase models. This is a consequence of the presence of phase change at the vapour-liquid interface and at the tank walls. The preconditioned bi-conjugate gradient (PBiCG) method [53] with a diagonal incomplete-LU preconditioner was selected to solve the linear systems associated with the discretised form of the energy equations for each phase. This method is more stable than the GAMG method, at the expense a higher computational cost. A very strict absolute tolerance for the residuals of the energy equations, $\epsilon \leq 10^{-11}$, in conjunction with a relative tolerance of 10^{-3} have been selected. The strict tolerances were required to prevent unphysical negative temperatures during intermediate iterations that produced the failure of the solver.

For the discretized momentum equations for the vapour and liquid phases, the Gauss-Seidel method was applied using a symmetric pre-conditioner. In OpenFOAM, this corresponds to the smoothSolver solver with the symGaussSeidel smoother. An absolute tolerance for the residuals of $\epsilon \leq 10^{-9}$ and a relative tolerance of 0.001 was sufficient to accuracy and stability. The velocity equations showed a quick and stable convergence. To execute the transient simulation, the OpenFOAM PIMPLE [2] algorithm was selected, which has already been described in subsection 3.2.6. To ensure the stability of the solver, two energy correctors were required. This implies that two additional iterations of the energy equations are performed at each time-step. As the temperature may change quickly owing to phase change and it is coupled with the pressure, velocity and density fields, two outer correctors were required. This implies

that for each time-step the linear system of the continuity, energy and momentum equations are solved with two additional fixed-point iterations. No relaxation factors were included as this produced spurious transient behaviours in a similar way as they did for the computational implementation of the vapour-CFD model [10].

The maximum Courant number was set to 0.25 in order to keep the cumulative time-step continuity error bounded. The thermodynamic and thermophysical properties were evaluated using COOLPROP [54], which has been used for the implementation of the single-phase models. All the code required to generate the meshes, implement the model in OpenFOAM v2006 and reproduce the results will be made available in the Imperial College Research Data Repository once the relevant papers are submitted to journals and published.

6.5 References

[1] C. H. Panzarella and M. Kassemi, "On the validity of purely thermodynamic descriptions of two-phase cryogenic fluid storage," *J. Fluid Mech.,* vol. 484, pp. 41-68, 2003, doi: 10.1017/s0022112003004002.

[2] OpenCFD Ltd. "OpenFOAM: API guide v2006." https://www.openfoam.com/documentation/guides/latest/api/index.html (accessed 25th of November, 2020).

[3] A. Saleem, S. Farooq, I. A. Karimi, and R. Banerjee, "A CFD simulation study of boiling mechanism and BOG generation in a full-scale LNG storage tank," *Comput. Chem. Eng.,* vol. 115, pp. 112-120, Jul 2018, doi: 10.1016/j.compchemeng.2018.04.003.

[4] J. Ren, H. Zhang, J. Yu, M. Bi, and S. Sun, "Experimental research of heat-mass coupling response of liquid storage tanks," *J Hazard Mater,* vol. 338, pp. 502-507, Sep 15 2017, doi: 10.1016/j.jhazmat.2017.05.060.

[5] J. L. Ferrín and L. J. Pérez-Pérez, "Numerical simulation of natural convection and boil-off in a small size pressurized LNG storage tank," *Comput. Chem. Eng.,* vol. 138, p. 106840, 2020/07/12/ 2020, doi: https://doi.org/10.1016/j.compchemeng.2020.106840.

[6] W. H. Lee, "Pressure iteration scheme for two-phase flow modeling," *IN" MULTIPHASE TRANSPORT: FUNDAMENTALS, REACTOR SAFETY, APPLICATIONS"*. pp. 407-432, 1980.

[7] C. R. Kharangate and I. Mudawar, "Review of computational studies on boiling and condensation," *Int. J. Heat Mass Transfer,* vol. 108, pp. 1164-1196, 2017-05-01 2017, doi: 10.1016/j.ijheatmasstransfer.2016.12.065.

[8] C. Migliore, C. Tubilleja, and V. Vesovic, "Weathering prediction model for stored liquefied natural gas (LNG)," (in English), *J. Nat. Gas. Sci. Eng.,* vol. 26, pp. 570-580, Sep 2015, doi: 10.1016/j.jngse.2015.06.056.

[9] C. Panzarella and M. Kassemi, "One-dimensional model of evaporation and condensation in the presence of a noncondensable gas with applications to cryogenic fluid storage," *Int. J. Heat Mass Transfer,* vol. 52, no. 15-16, pp. 3767-3777, Jul 2009, doi: 10.1016/j.ijheatmasstransfer.2009.02.027.

[10] F. Huerta and V. Vesovic, "CFD modelling of the isobaric evaporation of cryogenic liquids in storage tanks," *International Journal of Heat and Mass Transfer,* vol. 176, p. 121419, 2021/09/01/ 2021, doi: https://doi.org/10.1016/j.ijheatmasstransfer.2021.121419.

[11] M. Seo and S. Jeong, "Analysis of self-pressurization phenomenon of cryogenic fluid storage tank with thermal diffusion model," *Cryogenics,* vol. 50, no. 9, pp. 549-555, Sep 2010, doi: 10.1016/j.cryogenics.2010.02.021.

[12] M. Kang, J. Kim, H. You, and D. Chang, "Experimental investigation of thermal stratification in cryogenic tanks," *Exp. Therm. Fluid Sci.,* vol. 96, pp. 371-382, 2018/09/01/ 2018, doi: https://doi.org/10.1016/j.expthermflusci.2017.12.017.

[13] F. Perez *et al.*, "Measurements of boil-off gas and stratification in cryogenic liquid nitrogen with implications for the storage and transport of liquefied natural gas," *Energy,* vol. 222, p. 119853, 2021/05/01/ 2021, doi: https://doi.org/10.1016/j.energy.2021.119853.

[14] S. Z. S. Al Ghafri *et al.*, "Advanced boil-off gas studies for liquefied natural gas," *Appl. Therm. Eng.,* vol. 189, p. 116735, 2021/05/05/ 2021, doi: https://doi.org/10.1016/j.applthermaleng.2021.116735.

[15] S. Gursu, S. A. Sherif, T. N. Veziroglu, and J. W. Sheffield, "Analysis and optimization of thermal stratification and self-pressurization effects in liquid-hydrogen storage-systems - Part 2: Model results and conclusions," *J Energ. Resour. ASME,* vol. 115, no. 3, pp. 228-231, Sep 1993, doi: 10.1115/1.2905998.

[16] R. W. Arnett and R. O. Voth, "A computer program for the calculation of thermal stratification and self-pressurization in a liquid hydrogen tank," National Aeronautics and Space Administration, 1972. [Online]. Available: <Go to WoS>://WOS:000345232900026

[17] J. W. Tatom, W. H. Brown, L. H. Knight, and E. F. Coxe, "Analysis of thermal stratification of liquid hydrogen in rocket propellant tanks," in *Advances in Cryogenic Engineering*: Springer, 1964, pp. 265-272.

[18] I. Tanasawa, "Advances in condensation heat transfer," in *Advances in heat transfer*, vol. 21: Elsevier, 1991, pp. 55-139.

[19] R. W. Schrage, *A theoretical study of interphase mass transfer*. Columbia University Press, 1953.

[20] M. Kassemi and O. Kartuzova, "Effect of interfacial turbulence and accommodation coefficient on CFD predictions of pressurization and pressure control in cryogenic storage tank," *Cryogenics,* vol. 74, pp. 138-153, 2016/03/01/ 2016, doi: https://doi.org/10.1016/j.cryogenics.2015.10.018.

[21] L. F. Shampine, " Solving 0 = F(t, y(t), y′ (t)) in Matlab," *J. Num. Math.,* vol. 10, no. 4, p. 19, 2010, doi: 10.1515/JNMA.2002.291.

[22] W. E. Schiesser and G. W. Griffiths, *A compendium of partial differential equation models: method of lines analysis with Matlab*, 1st ed. Cambridge ; New York: Cambridge University Press (in English), 2009.

[23] W. Huang and R. D. Russell, *Adaptive moving mesh methods*. Springer Science & Business Media, 2010.

[24] G. H. Yeoh and X. Zhang, "Computational fluid dynamics and population balance modelling of nucleate boiling of cryogenic liquids: Theoretical developments," *The Journal of Computational Multiphase Flows,* vol. 8, no. 4, pp. 178-200, 2016/12/01 2016, doi: 10.1177/1757482X16674217.

[25] R. Zhou, W. Zhu, Z. Hu, S. Wang, H. Xie, and X. Zhang, "Simulations on effects of rated ullage pressure on the evaporation rate of liquid hydrogen tank," *Int. J. Heat Mass Transfer,* vol. 134, pp. 842-851, 2019/05/01/ 2019, doi: https://doi.org/10.1016/j.ijheatmasstransfer.2019.01.091.

[26] J. Ren, H. Zhang, M. Bi, J. Yu, and S. Sun, "Numerical investigation of the coupled heat transfer of liquefied gas storage tanks," *Int. J. Hydrogen Energy,* vol. 42, no. 38, pp. 24222-24228, 2017, doi: 10.1016/j.ijhydene.2017.07.155.

[27] Linde, "Cryogenic Standard Tanks LITS 2," Tacherting, Germany, 2019. [Online]. Available: https://www.linde-engineering.com/en/images/P_3_3_e_12_150dpi_tcm19-5774.pdf

[28] Volvo Truck Corporation, "Fact sheet gas tank LGAS205," 2018. [Online]. Available: https://stpi.it.volvo.com/STPIFiles/Volvo/FactSheet/LGAS155,%20LGAS205_Eng_02_3120592228.pdf

[29] N. Kurul and M. Z. Podowski, "Multidimensional effects in forced convection subcooled boiling," 1990: Begel House Inc.

[30] M. Z. Podowski, "Toward mechanistic modeling of boiling heat transfer," *Nuclear engineering and technology,* vol. 44, no. 8, pp. 889-896, 2012.

[31] R. L. Judd, "The Role of Bubble Waiting Time in Steady Nucleate Boiling," *Journal of Heat Transfer,* vol. 121, no. 4, pp. 852-855, 1999, doi: 10.1115/1.2826075.

[32] M. Lemmert and L. M. Chawla, "Influence of flow velocity on surface boiling heat transfer coefficient," in *Heat Transfer in Boiling*. New York, NY, USA.: Academic Press and Hemisphere, 1977.

[33] E. Krepper and R. Rzehak, "CFD for subcooled flow boiling: Simulation of DEBORA experiments," *Nucl. Eng. Des.,* vol. 241, no. 9, pp. 3851-3866, 2011/09/01/ 2011, doi: https://doi.org/10.1016/j.nucengdes.2011.07.003.

[34] X. Zhang, J. Chen, W. Xiong, and T. Jin, "Visualization study of nucleate pool boiling of liquid nitrogen with quasi-steady heat input," *Cryogenics,* vol. 72, pp. 14-21, 2015/12/01/ 2015, doi: https://doi.org/10.1016/j.cryogenics.2015.07.002.

[35] Y. A. Kirichenko, M. L. Dolgoj, N. M. Levchenko, V. V. Tsybiul'skij, L. A. Slobozhanin, and N. S. Scherbakova, "Study on cryogenic liquid boiling," presented at the All-union conference on heat and mass transfer, Minsk, Belarus, 1976.

[36] J. Kim and M. H. Kim, "On the departure behaviors of bubble at nucleate pool boiling," *International Journal of Multiphase Flow,* vol. 32, no. 10, pp. 1269-1286, 2006/10/01/ 2006, doi: https://doi.org/10.1016/j.ijmultiphaseflow.2006.06.010.

[37] V. H. Del Valle and D. B. R. Kenning, "Subcooled flow boiling at high heat flux," *Int. J. Heat Mass Transfer,* vol. 28, no. 10, pp. 1907-1920, 1985/10/01/ 1985, doi: https://doi.org/10.1016/0017-9310(85)90213-3.

[38] V. I. Tolubinsky and D. M. Kostanchuk, "Vapour bubbles growth rate and heat transfer intensity at subcooled water boiling," 1970, vol. 23: Begel House Inc.

[39] P. W. McFadden and P. Grassmann, "The relation between bubble frequency and diameter during nucleate pool boiling," *Int. J. Heat Mass Transfer,* vol. 5, no. 3, pp. 169-173, 1962/03/01/ 1962, doi: https://doi.org/10.1016/0017-9310(62)90009-1.

[40] R. Cole, "A photographic study of pool boiling in the region of the critical heat flux," *AlChE J.,* https://doi.org/10.1002/aic.690060405 vol. 6, no. 4, pp. 533-538, 1960/12/01 1960, doi: https://doi.org/10.1002/aic.690060405.

[41] W. M. Rohsenow, J. P. Hartnett, and Y. I. Cho, *Handbook of heat transfer*. McGraw-Hill New York, 1998.

[42] R. B. Bird, W. E. Stewart, and E. N. Lightfoot, *Transport phenomena*, 2nd rev. ed. New York: John Wiley & Sons, 2007, pp. xii, 905 p.

[43] A. Guha and K. Pradhan, "A unified integral theory of laminar natural convection over surfaces at arbitrary inclination from horizontal to vertical," *International Journal of Thermal Sciences,* vol. 111, pp. 475-490, 2017/01/01/ 2017, doi: https://doi.org/10.1016/j.ijthermalsci.2016.08.011.

[44] A. Guha and S. Samanta, "Closed-form analytical solutions for laminar natural convection on horizontal plates," *Journal of heat transfer,* vol. 135, no. 10, 2013.

[45] J.-J. Ren, J.-Y. Shi, P. Liu, M.-S. Bi, and K. Jia, "Simulation on thermal stratification and de-stratification in liquefied gas tanks," *Int. J. Hydrogen Energy,* vol. 38, no. 10, pp. 4017-4023, 2013/04/01/ 2013, doi: https://doi.org/10.1016/j.ijhydene.2013.01.116.

[46] F. Huerta and V. Vesovic, "A realistic vapour phase heat transfer model for the weathering of LNG stored in large tanks," *Energy,* vol. 174, pp. 280-291, 2019/05/01/ 2019, doi: https://doi.org/10.1016/j.energy.2019.02.174.

[47] F. Huerta and V. Vesovic, "Analytical solutions for the isobaric evaporation of pure cryogens in storage tanks," *Int. J. Heat Mass Transfer,* vol. 143, p. 118536, 2019/11/01/ 2019, doi: https://doi.org/10.1016/j.ijheatmasstransfer.2019.118536.

[48] D. D. Gray and A. Giorgini, "The validity of the boussinesq approximation for liquids and gases," *Int. J. Heat Mass Transfer,* vol. 19, no. 5, pp. 545-551, 1976/05/01/ 1976, doi: https://doi.org/10.1016/0017-9310(76)90168-X.

[49] E. Fehlberg, *Low-order classical Runge-Kutta formulas with stepsize control and their application to some heat transfer problems*. National Aeronautics and Space Administration, 1969.

[50] V. Yakhot, S. A. Orszag, and A. Yakhot, "Heat transfer in turbulent fluids—I. Pipe flow," *Int. J. Heat Mass Transfer,* vol. 30, no. 1, pp. 15-22, 1987/01/01/ 1987, doi: https://doi.org/10.1016/0017-9310(87)90057-3.

[51] F. Menter, "Zonal two equation k-omega turbulence models for aerodynamic flows," presented at the 23rd Fluid Dynamics, Plasmadynamics, and Lasers Conference, Orlando, FL, U.S.A., 1993, 1993, 2906.

[52] R. F. Warming and R. M. Beam, "Upwind Second-Order Difference Schemes and Applications in Aerodynamic Flows," *AIAA J.,* vol. 14, no. 9, pp. 1241-1249, 1976/09/01 1976, doi: 10.2514/3.61457.

[53] M. R. Hestenes and E. Stiefel, "Methods of conjugate gradients for solving linear systems," *J. Res. Natl. Bur. Stand.,* vol. 49, no. 6, pp. 409-436, 1952.

[54] I. H. Bell, J. Wronski, S. Quoilin, and V. Lemort, "Pure and Pseudo-pure Fluid Thermophysical Property Evaluation and the Open-Source Thermophysical Property Library CoolProp," *Ind. Eng. Chem. Res.,* vol. 53, no. 6, pp. 2498-2508, 2014/02/12 2014, doi: 10.1021/ie4033999.

[55] M. P. Edejer and G. Thodos, "Vapor pressures of liquid nitrogen between the triple and critical points," *J. Chem. Eng. Data,* vol. 12, no. 2, pp. 206-209, 1967/04/01 1967, doi: 10.1021/je60033a014.

[56] R. Prydz and R. D. Goodwin, "Experimental melting and vapor pressures of methane," *The Journal of Chemical Thermodynamics,* vol. 4, no. 1, pp. 127-133, 1972/01/01/ 1972, doi: https://doi.org/10.1016/S0021-9614(72)80016-8.

[57] E. Krepper, R. Rzehak, C. Lifante, and T. Frank, "CFD for subcooled flow boiling: Coupling wall boiling and population balance models," *Nucl. Eng. Des.,* vol. 255, pp. 330-346, 2013/02/01/ 2013, doi: https://doi.org/10.1016/j.nucengdes.2012.11.010.

[58] Y. Liao and D. Lucas, "Evaluation of interfacial heat transfer models for flashing flow with two-fluid CFD," *Fluids,* vol. 3, no. 2, p. 38, 2018.

[59] D. P. Hill, "The computer simulation of dispersed two-phase flow," 1998.

[60] A. Behzadi, R. I. Issa, and H. Rusche, "Modelling of dispersed bubble and droplet flow at high phase fractions," *Chem. Eng. Sci.,* vol. 59, no. 4, pp. 759-770, 2004/02/01/ 2004, doi: https://doi.org/10.1016/j.ces.2003.11.018.

[61] R. Krishna, J. M. van Baten, and M. I. Urseanu, "Three-phase Eulerian simulations of bubble column reactors operating in the churn-turbulent regime: a scale up strategy," *Chem. Eng. Sci.,* vol. 55, no. 16, pp. 3275-3286, 2000/08/01/ 2000, doi: https://doi.org/10.1016/S0009-2509(99)00582-5.

[62] K. Wolfert, " The simulation of blowdown processes with consideration of thermodynamic nonequilibrium phenomena," in *Proceedings of the Specialists Meeting of Transient Two-Phase Flow*, Toronto, ON, Canada, 3–4 August, 1976 1976: OECD/Nuclear Energy Agency.

[63] W. E. Ranz and W. R. Marshall, "Evaporation from drops, Part I," *Chem. Eng. Prog,* vol. 48, no. 3, pp. 141-146, 1952.

[64] M. Kassemi, O. Kartuzova, and S. Hylton, "Validation of two-phase CFD models for propellant tank self-pressurization: Crossing fluid types, scales, and gravity levels," *Cryogenics,* vol. 89, pp. 1-15, 2018/01/01/ 2018, doi: https://doi.org/10.1016/j.cryogenics.2017.10.019.

[65] L. Schiller, "A drag coefficient correlation," *Zeit. Ver. Deutsch. Ing.,* vol. 77, pp. 318-320, 1933.

[66] S. P. Antal, R. T. Lahey, and J. E. Flaherty, "Analysis of phase distribution in fully developed laminar bubbly two-phase flow," *International Journal of Multiphase Flow,* vol. 17, no. 5, pp. 635-652, 1991/09/01/ 1991, doi: https://doi.org/10.1016/0301-9322(91)90029-3.

[67] D. A. Drew and R. T. Lahey, "The virtual mass and lift force on a sphere in rotating and straining inviscid flow," *International Journal of Multiphase Flow,* vol. 13, no. 1, pp. 113-121, 1987/01/01/ 1987, doi: https://doi.org/10.1016/0301-9322(87)90011-5.

[68] A. D. Burns, T. Frank, I. Hamill, and J.-M. Shi, "The Favre averaged drag model for turbulent dispersion in Eulerian multi-phase flows," 2004, 2004.

[69] H. G. Weller, G. Tabor, H. Jasak, and C. Fureby, "A tensorial approach to computational continuum mechanics using object-oriented techniques," *Comput. Phys.,* vol. 12, no. 6, pp. 620-631, 1998/11/01 1998, doi: 10.1063/1.168744.

[70] T. J. Craft, L. J. W. Graham, and B. E. Launder, "Impinging jet studies for turbulence model assessment—II. An examination of the performance of four turbulence models," *Int. J. Heat Mass Transfer,* vol. 36, no. 10, pp. 2685-2697, 1993-07-01 1993, doi: 10.1016/s0017-9310(05)80205-4.

[71] J. Smagorinsky, "General circulation experiments with the primitive equations: I. The basic experiment," *Mon. Weather Rev.,* vol. 91, no. 3, pp. 99-164, 1963.

[72] T. M. Eidson, "Numerical simulation of the turbulent Rayleigh–Bénard problem using subgrid modelling," *J. Fluid Mech.,* vol. 158, pp. 245-268, 1985, doi: 10.1017/S0022112085002634.

[73] B. Ničeno, M. T. Dhotre, and N. G. Deen, "One-equation sub-grid scale (SGS) modelling for Euler–Euler large eddy simulation (EELES) of dispersed bubbly flow," *Chem. Eng. Sci.,* vol. 63, no. 15, pp. 3923-3931, 2008, doi: 10.1016/j.ces.2008.04.050.

[74] B. Končar and M. Borut, "Wall function approach for boiling two-phase flows," *Nucl. Eng. Des.,* vol. 240, no. 11, pp. 3910-3918, 2010/11/01/ 2010, doi: https://doi.org/10.1016/j.nucengdes.2010.08.004.

[75] B. van Leer, "Towards the ultimate conservative difference scheme. II. Monotonicity and conservation combined in a second-order scheme," *Journal of Computational Physics,* vol. 14, no. 4, pp. 361-370, 1974/03/01/ 1974, doi: https://doi.org/10.1016/0021-9991(74)90019-9.

[76] H. G. Weller, "A new approach to VOF-based interface capturing methods for incompressible and compressible flow," *OpenCFD Ltd., Report TR/HGW,* vol. 4, p. 35, 2008.

[77] Z. Lin *et al.*, "Communication optimization for multiphase flow solver in the library of OpenFOAM," *Water,* vol. 10, no. 10, p. 1461, 2018.

Chapter 7

Model verification II: non-isobaric evaporation of cryogens

7.1 Introduction

In Chapter 8, it will be shown that the CFD-MP and non-isobaric 1-D models are in excellent agreement with experimental data. These models were validated against Seo and Jeong [1] and Kang et al. [2] experiments on LN_2 evaporation in 6.75 L and 10 L storage tanks, respectively. However, a successful validation does not guarantee the correct computational implementation of the non-isobaric evaporation models. In contrast to the isobaric evaporation models that have already been completed [3-5], non-isobaric evaporation models are still in their final stages of development. This implies that model assumptions and physics can change before the models are ready to be used in academic and industrial environments.

In this chapter, the models developed in Chapter 6 are verified by being tested for grid independence for scenarios N1 and N2 in Table 6.1. These scenarios comprise the evaporation of LN_2 in an 8 m^3 storage tank filled at 30% and 97% of its capacity. Scenarios N1 and N2 constitute the most exacting verification tests, because of the large scale of the domain and high non-uniformity of the mesh. Consequently, performing model verification for scenarios N1 and N2 is sufficient to demonstrate the correct implementation of the models for all scenarios [6]. In section 7.2, the non-isobaric 1-D model will be verified through a grid independence study on temperature and pressure. In section 7.3, the single phase model (CFD-SP) will be verified on pressure, liquid temperature and boundary layer velocities. Finally, in section 7.4 the multiphase model (CFD-MP) will be verified on pressure, temperatures and boundary layer velocities for both phases.

Table 7.1 summarizes the grid parameters corresponding to the normal refinement for each model and scenario. For all models and for the spatial and vertical coordinate, a refinement factor of 1.5 has been selected, see Eqs (4.4)-(4.5). This allows to generate the coarse and fine meshes in a straightforward way: $n_x^{\text{fine}} = 1.5 \times n_x^{\text{normal}} = 1.5^2 \times n_x^{\text{coarse}}$ for $x = r, z$. For the CFD-SP and CFD-MP models, the fine and coarse meshes maintain the non-uniformity of the normal mesh in the axial ($\gamma_z = \Delta r_z/\Delta r_z$) and radial ($\gamma_r = \Delta r_{\max}/\Delta r_{\min}$) directions. For the radial coordinate, the cells with minimum radial width are located near the tank wall and near the vertical axis. In this arrangement, the cells with maximum radial width are located at the mid-point between the tank wall and the vertical axis. For the vertical coordinate, the cells with minimum width are located below and above the interface, above the tank bottom and below the tank roof. Consequently, the cells with the maximum vertical width are located at the middle of the length of each phase.

Table 7.1: Mesh parameters of the normal refinement for the grid independence study of non-isobaric evaporation models for pure cryogens. Namely, 1-D non equilibrium (1-D), singlephase (CFD-SP) and multiphase (CFD-MP) models. n_r and n_z are the number of cells in the radial and vertical directions, respectively. The grid expansion factors for the axial and radial coordinated are defined as $\gamma_z = \Delta z_{\max}/\Delta z_{\min}$ and $\gamma_r = \Delta r_{\max}/\Delta r_{\min}$ respectively, where $\gamma_z = \gamma_r = 1$ represents a uniform mesh.

Model	Scenario	n_r	n_z	γ_z	γ_r	Cell count
1-D	N1	1	300	1	1	300
1-D	N2	1	300	1	1	300
CFD-SP	N1	120	324	4	4	38,880
CFD-SP	N2	120	100	4	4	12,000
CFD-MP	N1	100	334	4	4	33,400
CFD-MP	N2	100	334	4	4	33,400

7.2 Non-isobaric 1-D model

Figure 7.1 shows the pressure build-up predicted by the isobaric 1-D model with no wall boiling ($\eta_e = 0$) for scenarios N1 (a) and N2 (b), see Table 6.1. Neglecting wall boiling is justified by the very small evaporative coefficient observed in the CFD-MP simulations, $\eta_e < 0.001$, for both scenarios. The results produced using the coarse, normal and fine meshes are depicted in lilac dots, purple triangles and a cyan line, respectively. Figure 7.1a shows that the coarse mesh slightly overpredicts the pressure, while the difference between the normal and fine refinements is less than 0.1 kPa. The

grid independence criteria will be established by comparing the absolute percentage error on pressure, $\epsilon_{\Delta P} = |(\Delta P - \Delta P_{\text{fine}})|/\ P_{\text{fine}}$, to a certain threshold. In this thesis, a percentage error of $|\epsilon_{\Delta P}| < 1\%$ will be considered as an appropriate threshold for engineering applications. Figure 7.1b shows that for low liquid filling, an excellent convergence is quickly achieved for the normal ($\epsilon_{\Delta P} < 0.01\%$) and coarse ($\epsilon_{\Delta P} = 0.02\%$) meshes. Hence, the grid independence is achieved at the mid and coarse refinements for high and low liquid fillings, respectively.

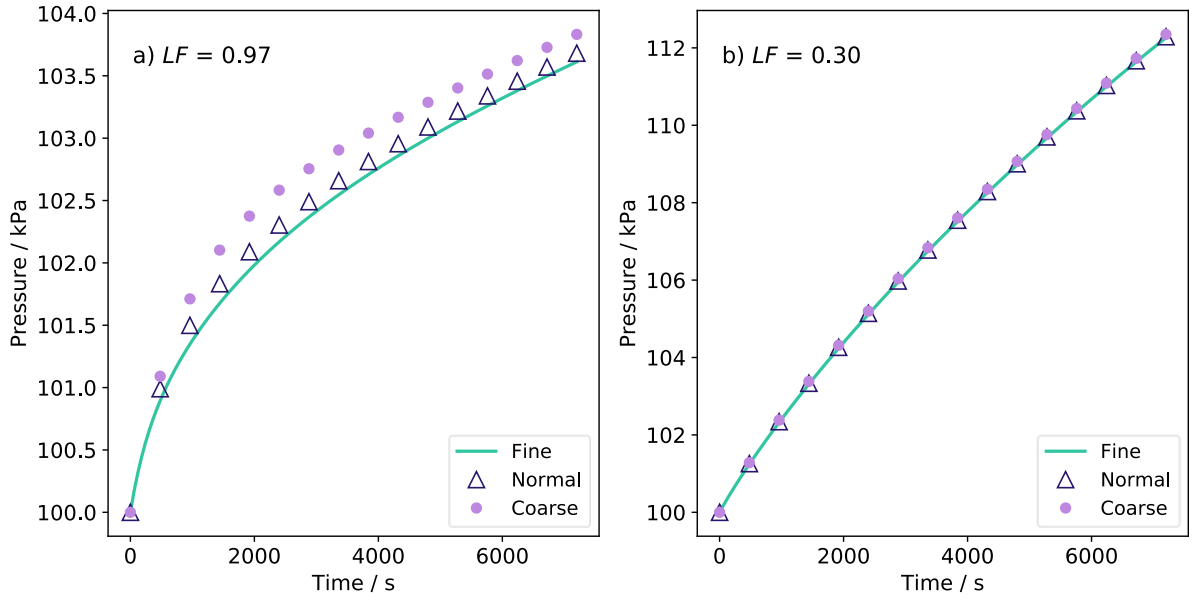

Figure 7.1: Grid independence study of the pressure build-up predicted by the non-isobaric 1-D model for LN_2 evaporation in an 8 m^3 storage tank. Subfigures (a) and (b) depict high (LF = 0.97) and low (LF = 0.30) initial liquid fillings.

Pressure grid independence is achieved at coarser meshes for low liquid fillings than for high liquid fillings, see Figure 7.1, because of the dominance of vapour heating over evaporation/condensation on pressure build-up, $\partial P/\partial T_V \gg \partial P/\partial \rho_V$. Bulk vapour heating is less affected by discretisation errors than the heat flux at the vapour-liquid interface, that governs evaporation and condensation rates. In contrast, for high liquid fillings, the vapour heating is smaller, and the contributions of vapour heating and evaporation/condensation to pressure build-up are of a similar magnitude, $\partial P/\partial T_V \sim \partial P/\partial \rho_V$.

Figure 7.2 shows the temperature profiles predicted by the 1-D non equilibrium model with no wall boiling ($\eta_e = 0$) for scenarios N1 (a-b) and N2 (c-d), see Table 6.1. three different time-steps at depicted, 720 s in cyan, 3,600 s in purple and 7,200s in lilac. The results produced by coarse, normal and fine meshes are depicted in dots, triangles and solid lines, respectively.

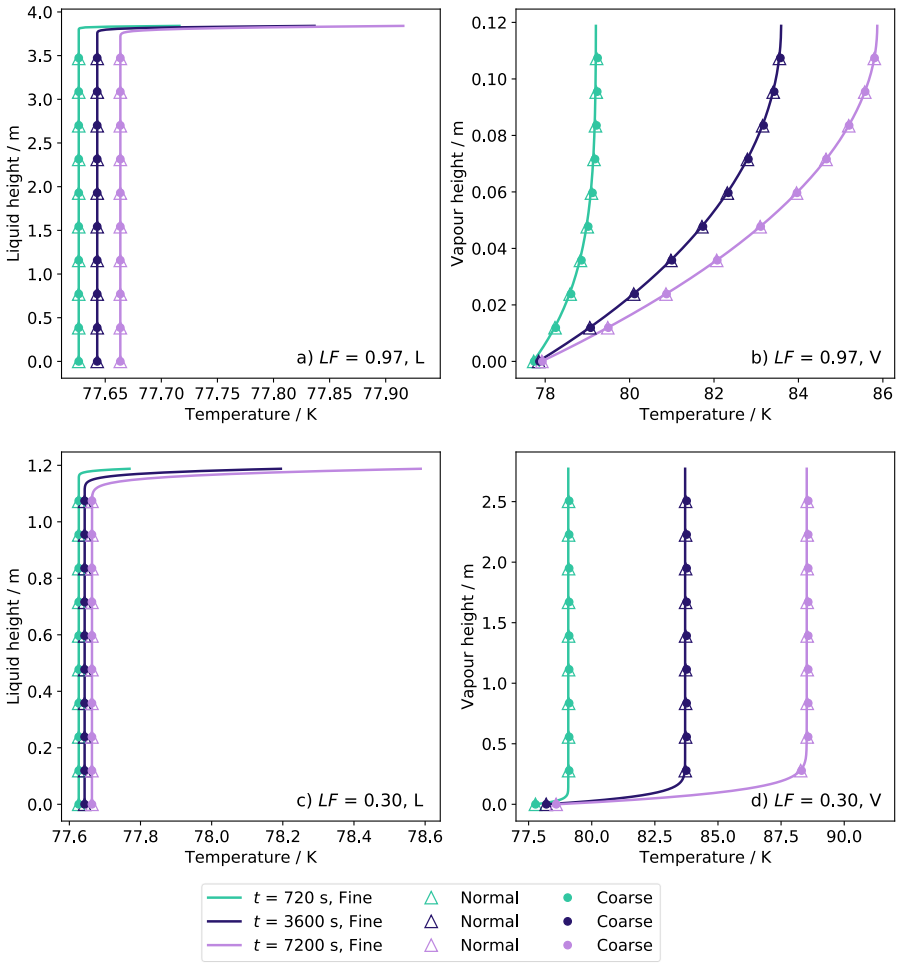

Figure 7.2: Grid independence study of the temperature profiles predicted by the 1-D non equilibrium model during the evaporation of LN_2 in an 8 m^3 storage tank. Subfigures (a) and (b) show the liquid and vapour temperature profiles for the tank initially filled at 97% of its capacity. Similarly, subfigures (c) and (d) show the liquid and temperature profiles for the tank initially filled at 30% of its capacity.

A negligible error on bulk temperatures between the different refinements can be observed for liquid and vapour phases in both high (Figure 7.2 a-b) and low (Figure 7.2 c-d) liquid fillings. However, in the thermally stratified layer at the liquid side of the interface the normal and coarse meshes slightly overpredicted the liquid temperature. The magnitude of these variations was lower than 0.05K and are not depicted in Figure 7.2 for convenience. To assess temperature grid independence, a temperature threshold

is defined by limiting average absolute deviation (AAD) and maximum deviation (MD) to values lower than 0.5% and 1%, respectively. Therefore, the coarse mesh (AAD = 0.1%, MD = 0.2%) achieves grid independence for both low and high liquid fillings.

7.3 Single phase model (CFD-SP)

Figure 7.3 shows the pressure build-up predicted by the CFD-SP model with no wall boiling ($\eta_e = 0$) for scenarios N1 (a) and N2 (b), see Table 6.1. Figure 7.3a shows that for high liquid fillings, pressure shows a rapid convergence with grid refinement, but more slowly than for the isobaric 1-D model, see Figure 7.1a. The percentage error on pressure build-up for the coarse and normal meshes were 0.9% and 0.4%, respectively. Thus, grid independence is quickly achieved using the coarse mesh. Figure 7.3b that for low liquid fillings, grid independence is achieved even more quickly by using the coarse mesh ($\epsilon_{\Delta P} = 0.09\%$). This trend is similar to what has been observed for the non-isobaric 1-D model, see Figure 7.1b. Thus, the explicit solution of the liquid velocity profile by the CFD-SP model does not hinder grid convergence for low liquid fillings.

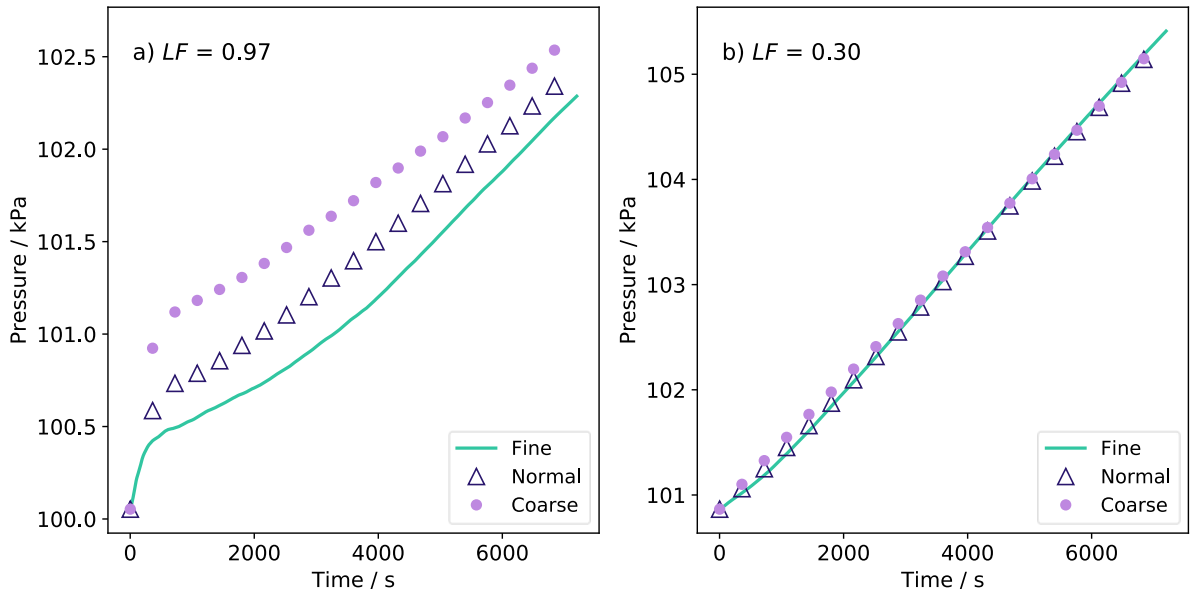

Figure 7.3: Grid independence study of the pressure build-up predicted by the liquid-CFD model during the non-isobaric evaporation of LN_2 in an 8 m^3 storage tank. Two scenarios for high and low liquid fillings (*LF*) are depicted: (a) *LF* = 0.97 and (b) *LF* = 0.30.

Figure 7.4 shows the liquid temperature profiles predicted by the CFD-SP model with no wall boiling ($\eta_e = 0$) for scenarios N1 (a) and N2 (b). Figure 7.4a shows that for

the high liquid filling scenario, the coarse and normal meshes slightly overpredict the liquid bulk temperature. The magnitude of the overprediction is more noticeable than what has been observed for the non-isobaric 1-D model, see Figure 7.2a. This explains the slightly larger variation on pressure build-up with grid refinement for the liquid-CFD model when compared against the non-isobaric 1-D model. Therefore, small discretisation errors on liquid temperature (~ 0.05K), particularly below the vapour-liquid interface, have a larger impact on pressure build-up. Furthermore, for high liquid fillings scenarios, the resolution of liquid velocity in the CFD-MP model slightly hinders grid convergence when compared with the non-isobaric 1-D model. Figure 7.4b shows that for low liquid fillings, the variation of liquid temperature between the three different refinements is negligible. This explains the very small deviation on pressure build-up at low liquid fillings, see Figure 7.3b.

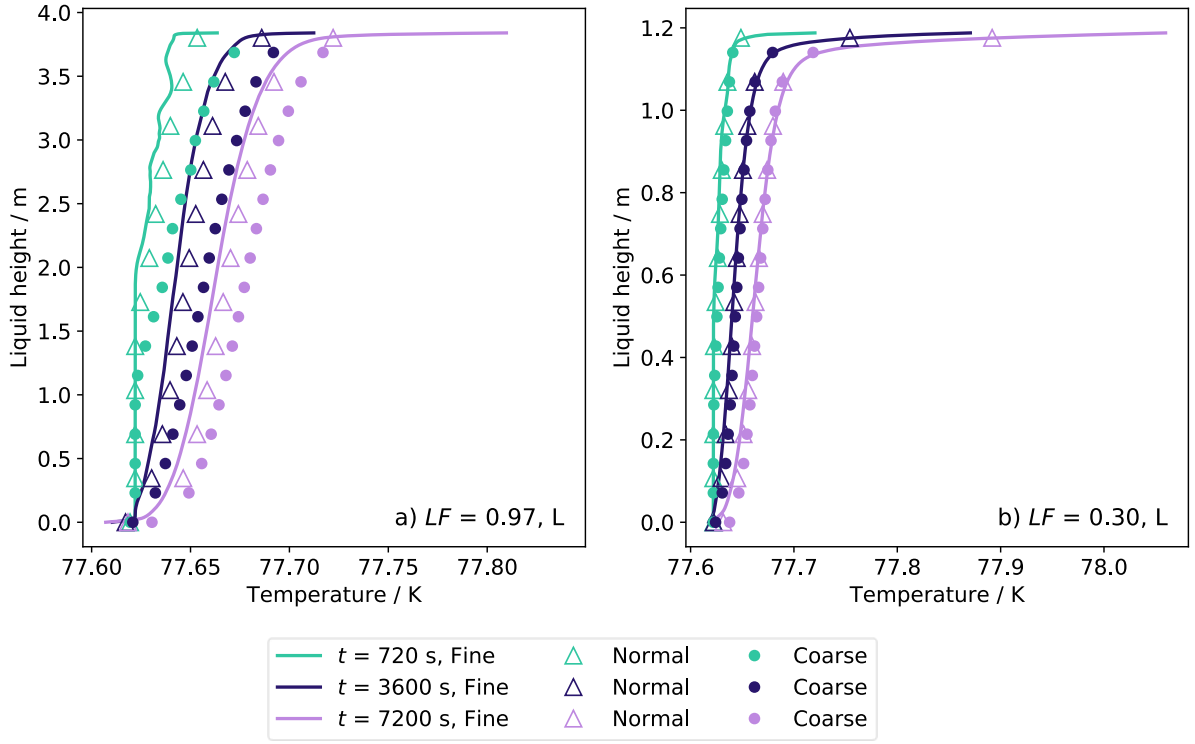

Figure 7.4: Grid independence study of the liquid temperature profiles predicted by the CFD-SP model during the non-isobaric evaporation of LN_2 in an 8 m^3 storage tank. Two scenarios for high and low liquid fillings (*LF*) are depicted: (a) *LF* = 0.97 and (b) *LF* = 0.30.

Figure 7.5 shows the liquid vertical velocity at 2.4 mm from the tank wall, representative of the viscous boundary layer driven by natural convection. Figure 7.5a-b depict the velocity profiles for Scenario N1 of high liquid filling at the middle (t = 3,600

s) and the end (t = 7,200 s) of the evaporation. Similarly, Figure 7.5c-d depict the velocity profiles for Scenario N2 of low liquid filling at t = 3,600 s and at t = 7,200 s, respectively. Figure 7.5a shows that the velocity profiles have the same trend for all refinements, while the coarse and normal meshes underpredict the boundary layer velocity. Figure 7.5b shows that the underprediction decreases with time, which is expected as a consequence of decreasing velocity gradients with the onset of thermal stratification. Figure 7.5c shows a good agreement on vertical velocity between the normal and fine meshes, while the coarse mesh slightly underpredicts liquid velocity. In a similar trend to what was observed for high liquid fillings, Figure 7.5d shows that the variations on liquid velocity for low liquid filling decrease with time.

The maximum deviation, $MD = |(v_z^{\text{normal}} - v_z^{\text{fine}})|/|v_z^{\text{fine}}|$ on liquid velocity at the end of the evaporation in the high liquid filling scenario between the normal and fine meshes is 9.6%. This maximum deviation on vertical velocities is one order of magnitude higher than the percentage error on pressure build-up for high liquid filling. This result suggests that discretisation errors in boundary layer velocity have a very small influence on pressure build-up and liquid temperature. Therefore, for non-isobaric evaporation it is necessary a coarse convergence threshold for the boundary layer velocity in the liquid phase is sufficient. A threshold of $MD(v_{\text{L}z}) < 50\%$ at the end of the evaporation is used to test the grid independence of velocity. Hence, the normal mesh achieves the convergence requirements for liquid velocity at the boundary layer near the tank wall.

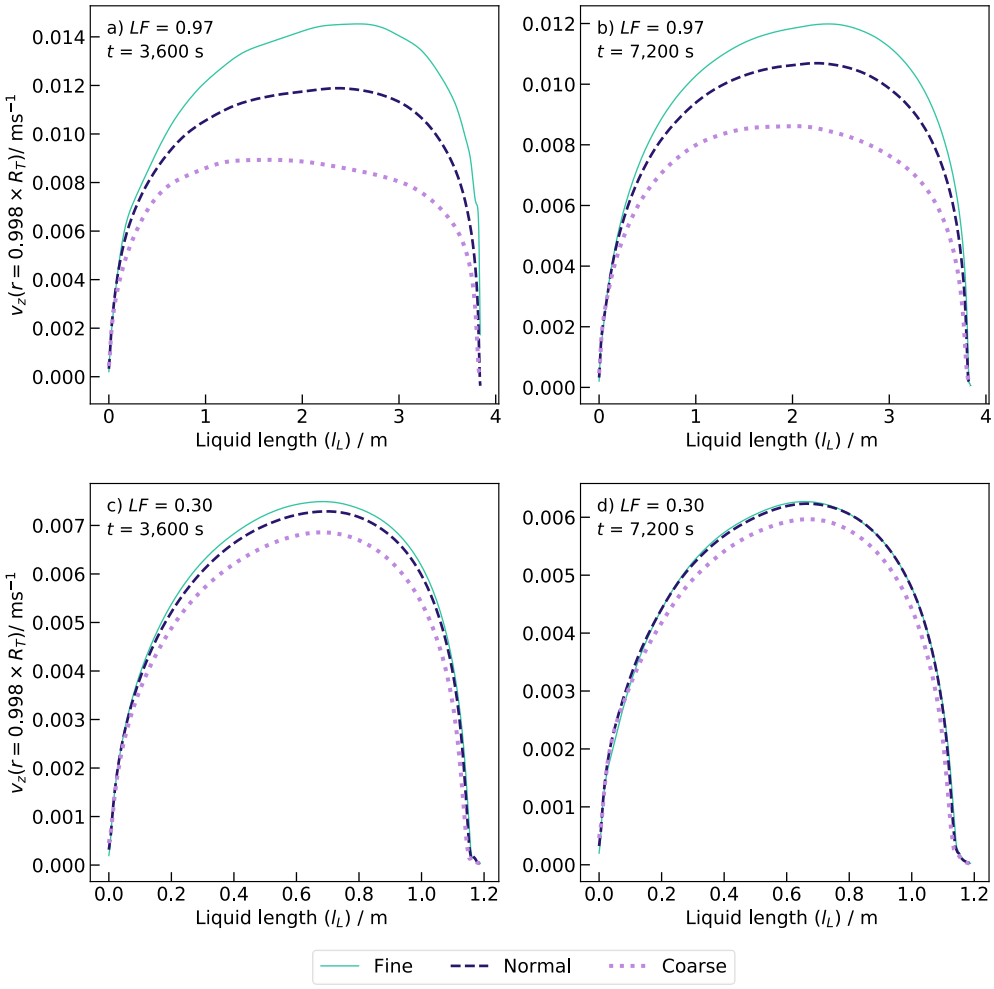

Figure 7.5: Grid independence study of the liquid vertical velocity in the wall boundary layer predicted by the CFD-SP model. The velocity v_{Lz} has been sampled in a vertical annulus located within the wall boundary layer at $r = 0.995\ R_T$. Subfigures (a) and (b) depict the velocity profile after 3,600 s and 7,200 s the beginning of the evaporation of LN_2 stored in an 8 m^3 storage tank filled at 97% of its capacity. Subfigures (c) and (d) depict the vertical velocity profile after 3,600 s and 7,200 s the beginning of the evaporation of for an 8 m^3 storage tank filled at 30% of its capacity.

7.4 Multiphase model (CFD-MP)

Figure 7.6 shows the pressure build-up predicted by the multiphase model for scenarios N1 (a) and N2 (b), see Table 6.1. Figure 7.6a shows that for the high liquid filling scenario, the pressure build-up predicted by the normal and coarse meshes are very different to the pressure obtained using the fine mesh. Quantitatively, both models slightly underpredict the pressure ($\epsilon_{\Delta P} > 1.4\%$). Qualitatively, the normal and coarse meshes are not able to predict the transition of the pressure build-up from convex to concave at $t \sim 3{,}600$ s. This indicates that the normal and coarse meshes produce under-

resolved simulations which do not represent the solution of the multiphase model. Hence, although the coarse mesh satisfies the convergence criteria for $\epsilon_{\Delta P}$, the results obtained with the fine mesh will be analysed in subsection 8.4.1. In future work, finer meshes will be considered for the high liquid filling scenario taking the fine mesh as the starting point. On the other hand, Figure 7.6b shows that the coarse and normal meshes are monotonically converging to the pressure predicted by the fine mesh. The percentage error on pressure build-up for the coarse and fine meshes are 1% and 0.5%, respectively. This shows that the coarse mesh achieves the pressure convergence criteria. However, another simulation with an ultrafine mesh $N_x^{\text{ultrafine}} = 1.5 \times N_x^{\text{fine}}$ will be required to verify grid independence.

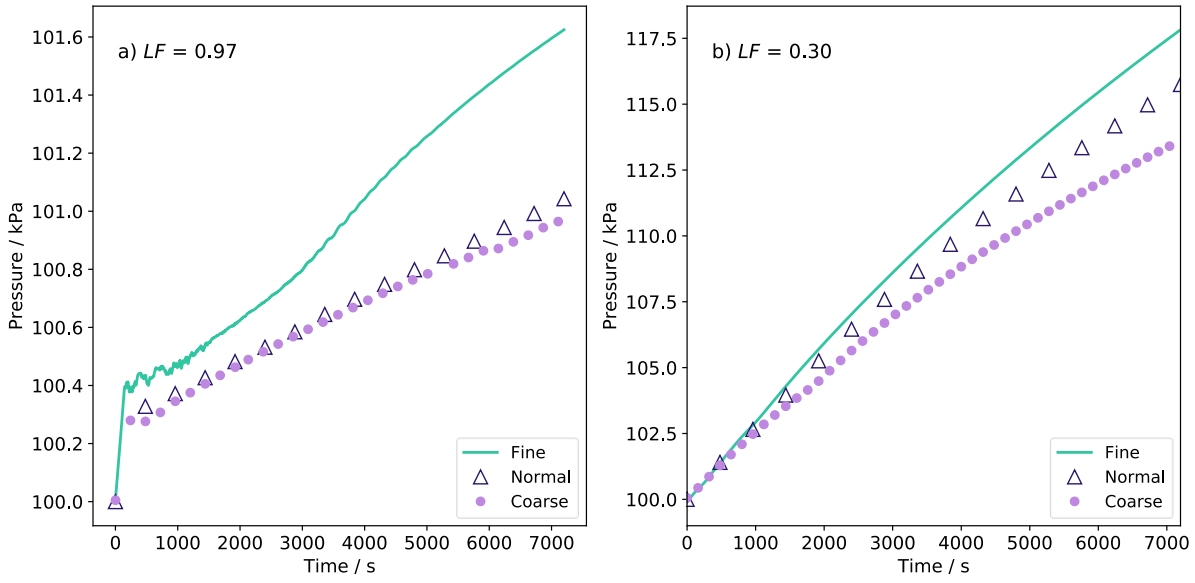

Figure 7.6: Grid independence study of the pressure build-up predicted by the multiphase (CFD-MP) model during the non-isobaric evaporation of LN_2 in an 8 m^3 storage tank. Two initial liquid fillings are depicted, (a) *LF* = 0.97 and (b) *LF* = 0.30.

Figure 7.7 shows liquid and vapour temperature profiles predicted by the multiphase model for scenarios N1 (a-b) and N2 (c-d), see Table 6.1. Three different refinement levels and two time-steps are depicted, using the same presentation style of Figure 7.2. Figure 7.7a shows that for high liquid fillings, the differences on liquid temperature between the three levels of refinement are negligible in the liquid bulk. However, this is not the case for the region below the vapour-liquid interface. This difference is driven mainly by the underprediction of pressure by the coarse and normal meshes, see Figure 7.6a.

To further understand the under-resolution of the coarse and fine meshes, the vapour vertical temperature profiles are explored in Figure 7.7b. This figure shows that the normal and coarse meshes fail to predict the vapour superheating. This is a consequence of spurious currents that emerge at the vapour domain which induce unrealistically high velocity gradients in the whole vapour phase. In the model, these spurious velocity gradients increase the effective thermal diffusivity of the vapour, $\alpha_{V,eff} = \alpha_V + \nu_t/Pr_t$, by 300%. This unrealistically enhances vapour phase heat transfer. Therefore, the under-resolution problem can be solved by refining the mesh region corresponding to the vapour phase, particularly above the vapour-liquid interface. This approach will be taken in future work, as it will demand lower cell count and lower simulation times than refining the whole mesh.

Figure 7.7c-d show a good convergence of the liquid and vapour temperature profiles with grind refinement for the low liquid filling scenario. This shows that for low liquid fillings, the number of cells that are included in the vapour phase provide sufficient resolution. Namely, for low liquid fillings the grid spacing obtained with all refinements is within the asymptotic range of convergence. Figure 7.7c shows that the coarse and normal meshes slightly overpredict the liquid temperature, and the difference increases with time. On the other hand, at the vapour side of the vapour-liquid interface, all refinements produce almost the same temperature gradient (AAD < 0.1%), see Figure 7.7d. Far from the interface, the coarse and normal meshes slightly underpredict the vapour temperature by 2 K and 1 K, respectively, see Figure 7.7d. Nevertheless, for scenario N2 the AAD of liquid and vapour temperatures between the normal and fine meshes are smaller 1%. This implies that for low liquid filling, the normal mesh achieves grid independence on temperatures.

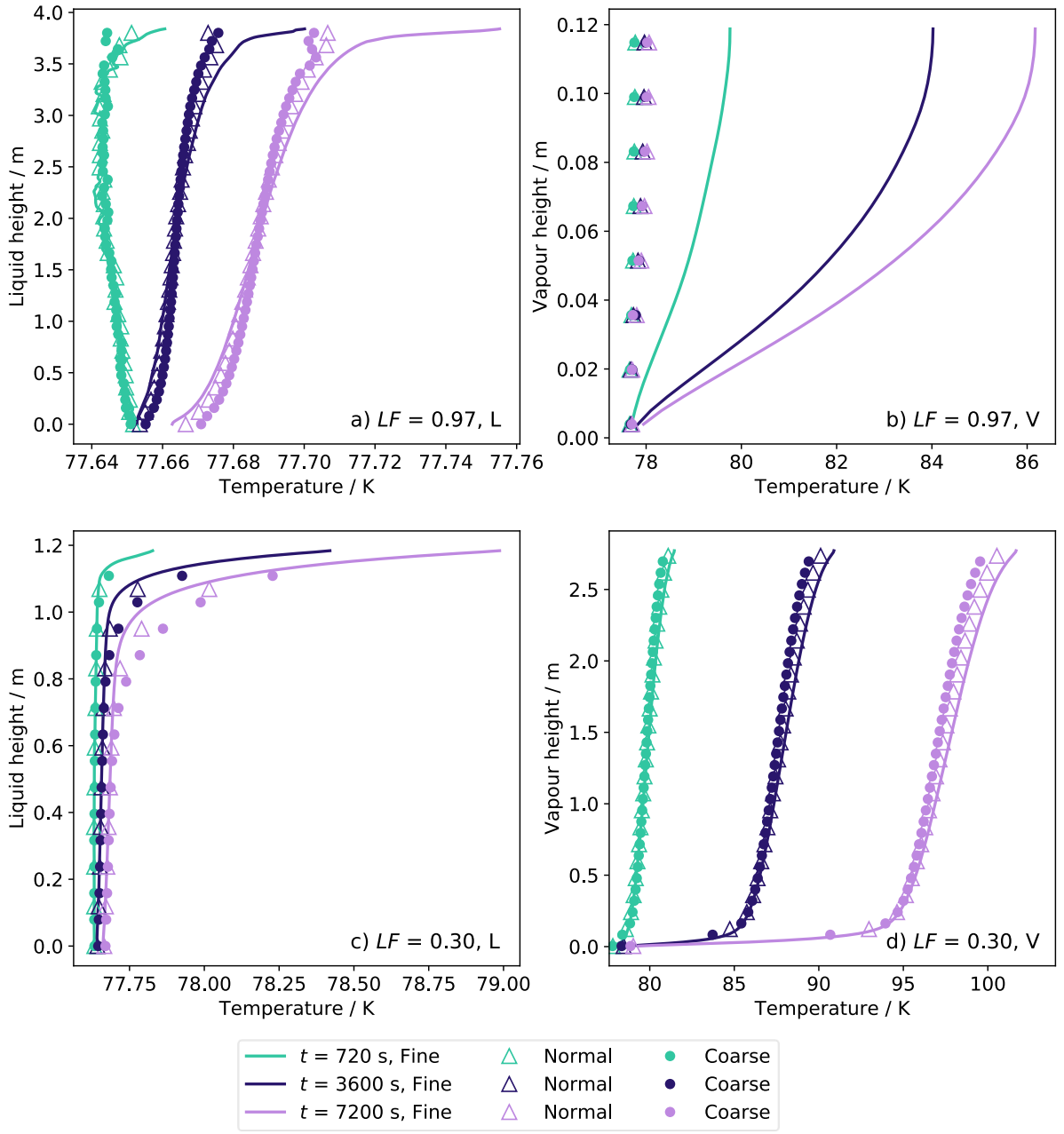

Figure 7.7: Grid independence study of the temperature profiles predicted by the multiphase model (CFD-MP) during the non-isobaric evaporation of LN_2 in an 8 m^3 storage tank. The profiles correspond to an infinitesimal annulus located at the mid-point between the tank wall and the vertical axis, $r = R_T/2$. Subfigures (a) and (b) show the liquid and vapour temperature profiles for the tank initially filled at 97% of its capacity. Similarly, subfigures (c) and (d) show the liquid and temperature profiles for the tank initially filled at 30% of its capacity.

Figure 7.8 shows the liquid vertical velocity at 2.4 mm from the tank wall, representative of the viscous boundary layer driven by natural convection. Figure 7.8 a-b depict the velocity profiles for Scenario N1 of high liquid filling at the middle (t = 3,600 s) and the end (t = 7,200 s) of the evaporation. Figure 7.8 c-d depict the velocity profiles for Scenario N2 of low liquid filling at t = 3,600 s and at t = 7,200 s, respectively. For

both liquid fillings and time-steps, the velocity profiles converge to the results obtained by the fine mesh, albeit rather slowly. Figure 7.8a-b shows that for high liquid filling, the normal mesh satisfies the convergence criteria except in the region just below the vapour-liquid interface. In this region, oscillations on liquid vertical velocity are observed for the coarse and normal meshes, see Figure 7.8a-b. This is a consequence of the disruption of the boundary layer owing to the spurious currents generated in the vapour phase owing to under-resolution. Thus, these figures further confirm the need of using a high mesh resolution near the vapour liquid interface.

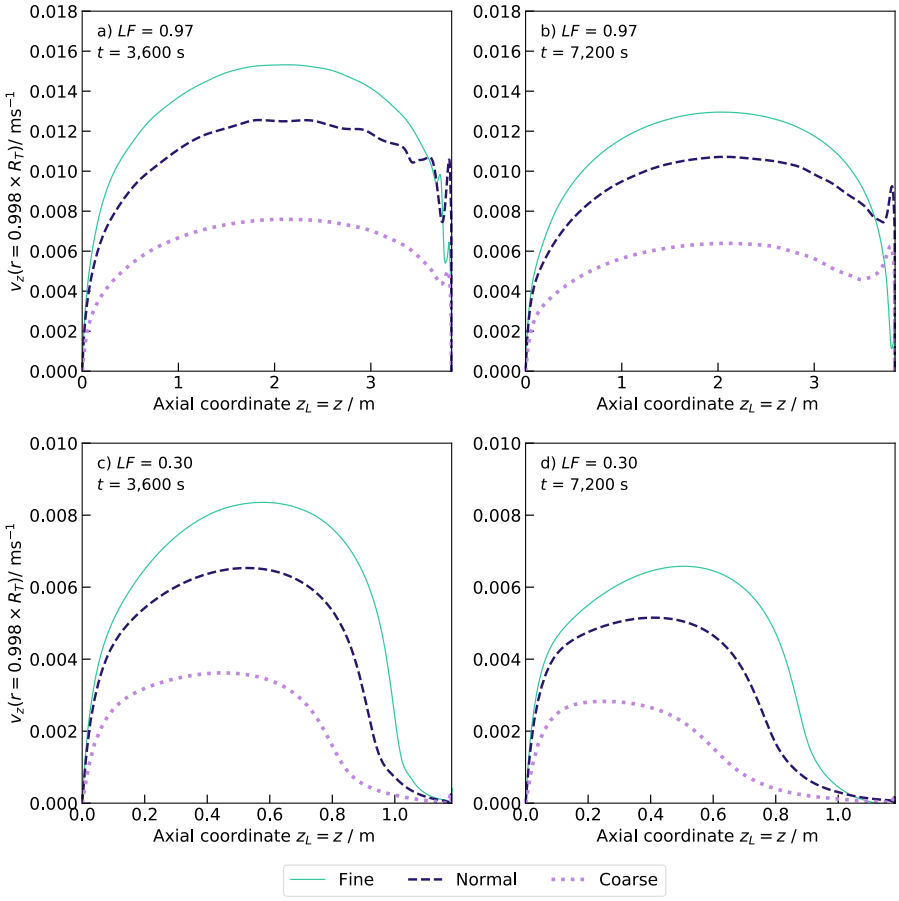

Figure 7.8: Grid independence study of the liquid vertical velocity in the wall boundary layer predicted by the CFD-MP model. The liquid velocity, v_{Lz}, has been sampled in a vertical annulus located within the wall boundary layer at 2.4 mm from the wall ($r = 0.998\ R_T$). Subfigures (a) and (b) depict the velocity profile after 3,600 s and 7,200 s the beginning of the evaporation of LN_2 stored in an 8 m^3 storage tank filled at 97% of its capacity. Subfigures (c) and (d) depict the vertical velocity profile after 3,600 s and 7,200 s the beginning of the evaporation of for an 8 m^3 storage tank filled at 30% of its capacity.

Figure 7.8c-d show that for low liquid filling, the coarse mesh significantly underpredicts the boundary layer vertical velocity. However, the normal mesh satisfies

the convergence criteria, $MD(v_{\mathrm{L}z})$ = 30% < 50%. Figure 7.9 shows the vapour vertical velocity at 2.4 mm from the tank wall, representative of the viscous boundary layer driven by natural convection. In Figure 7.9, the x axis $z_V = z - l_{\mathrm{L}}$ represents the vertical distance from the vapour-liquid interface located at $z = l_L$. Thus, $z_V = 0$ represents the vapour liquid interface and $z_V = l_{\mathrm{V}} - l_{\mathrm{L}}$ the tank roof.

Figure 7.9 a-b depict the velocity profiles for Scenario N1 of high liquid filling at the middle (t = 3,600 s) and the end (t = 7,200 s) of the evaporation. Figure 7.9 c-d depict the velocity profiles for Scenario N2 of low liquid filling at t = 3,600 s and at t = 7,200 s, respectively. Figure 7.9 a-b show that for high liquid fillings, the normal and coarse meshes produce completely different velocity profiles in the vapour phase when compared against the fine mesh. This confirms the vapour phase momentum transfer is under-resolved in the normal and coarse meshes. Figure 7.9 c-d show that for low liquid fillings, the vapour velocity shows slow convergence with progressive grid refinements. For the sake of consistency with the liquid boundary layer threshold, the threshold for vapour boundary layer velocity is set to $MD(v_{\mathrm{V}z} < 50\%)$, evaluated at the end of the evaporation. The maximum deviation on the vapour vertical velocity between the normal and fine meshes at t = 7,200 s is 16%, see Figure 7.9d. Hence, the normal mesh satisfies the convergence criteria.

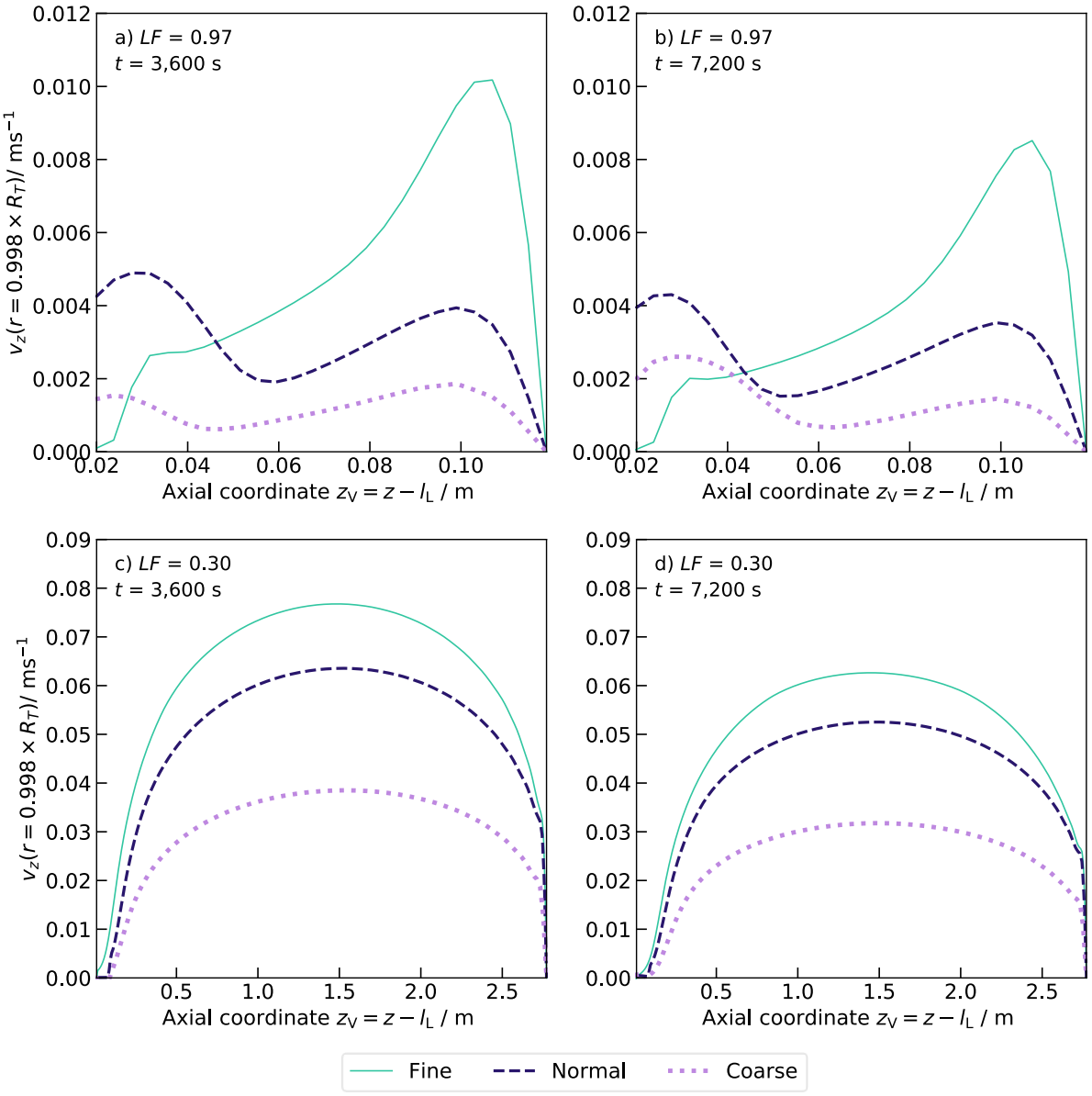

Figure 7.9: Grid independence study of the vapour vertical velocity in the wall boundary layer predicted by the CFD-MP model. The vapour velocity, v_{vz}, has been sampled in a vertical annulus located within the wall boundary layer at $r = 0.998\,R_T$. The x-axis, $z_V = z - l_L$, re represents the vertical distance from the vapour-liquid interface located at $z = l_L$ Subfigures (a) and (b) depict the velocity profile after 3,600 s and 7,200 s the beginning of the evaporation of LN_2 stored in an 8 m^3 storage tank filled at 97% of its capacity. Subfigures (c) and (d) depict the vertical velocity profile after 3,600 s and 7,200 s the beginning of the evaporation of for an 8 m^3 storage tank filled at 30% of its capacity.

7.5 Mesh visualisation

Figure 7.10 shows the mesh associated with the liquid domain discretisation corresponding to Scenario N1 in Table 7.1 for the CFD-SP model. It can be observed that the mesh is highly refined radially near the tank axis and tank wall, and vertically near

the bottom and roof. A maximum aspect ratio $\Delta z/\Delta r$ of 8 is observed at half of the liquid height and near the tank axis and wall. Figure 7.11 shows the mesh associated with the liquid domain discretisation corresponding to Scenario N2 in in Table 7.1 for the CFD-SP model. The local refinement near domain boundaries is much more subtle than for the mesh in Scenario N1 owing to the smallest dimension of the vertical domain, as a consequence of a lower liquid filling. This results in a maximum aspect ratio of 4. As discussed in subsection 4.5.3, high aspect ratios are associated with large discretisation errors. This potential discretisation error will be taken into consideration when analysing the results obtained with the CFD-SP model.

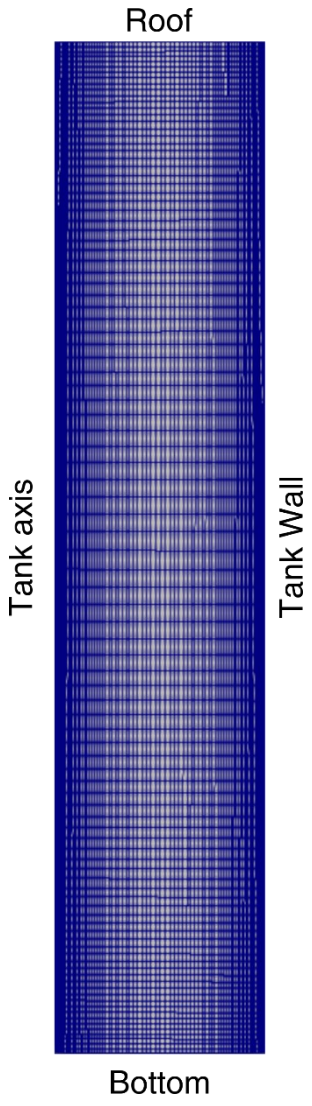

Figure 7.10: Liquid domain discretisation 2-D mesh corresponding to the CFD-SP model for Scenario N1 (V_T = 8 m³, LF = 0.97) in Table 7.1.

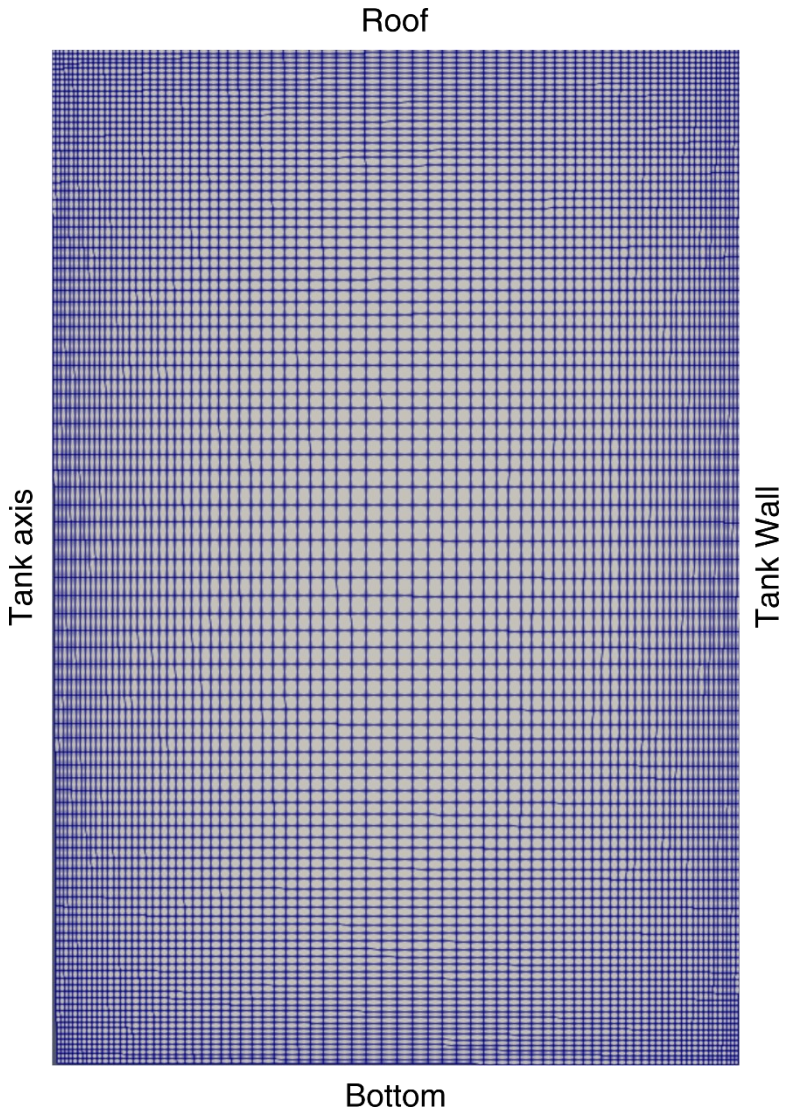

Figure 7.11: Liquid domain discretisation 2-D mesh corresponding to the CFD-SP model for Scenario N2 (V_T = 8 m^3, LF = 0.30) in Table 7.1.

Figure 7.12 shows the mesh associated with the domain discretisation corresponding to Scenario N1 in Table 7.1 for the CFD-MP model. The vapour-liquid interface is depicted by a horizontal red line near the tank roof, as the initial liquid filling for this scenario is LF = 0.97. The mesh is locally refined near the tank wall and near the vapour liquid interface. To better observe this effect, Figure 7.13 shows a zoom-in of the region near the vapour-liquid interface for Scenario N1. Similarly, Figure 7.14 and Figure 7.15 shows the mesh and a zoom-in near the vapour liquid interface corresponding to Scenario N2 in Table 7.1. For both meshes, the range of aspect ratios vary considerably, from 0.125 at $r = R_T/2$ and near the vapour liquid interface to 8 far from the interface and near the tank wall. The large range of aspect ratios will increase the discretisation

errors. In future work, the mesh quality will be improved by increasing the number of finite volumes to decrease the maximum aspect ratio.

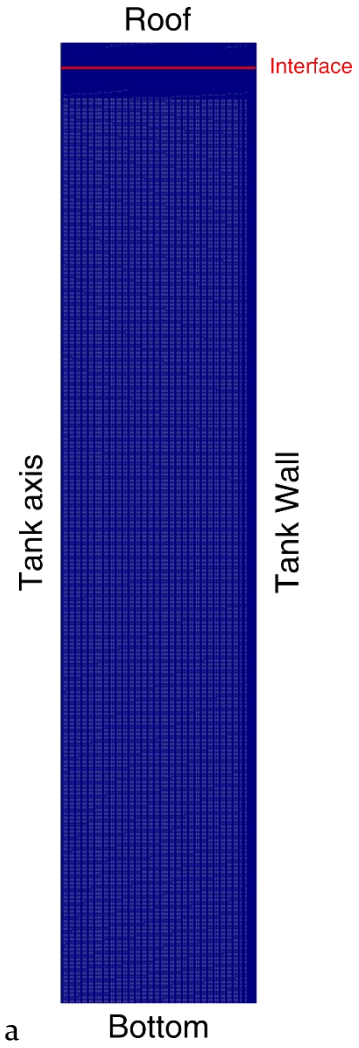

Figure 7.12: Domain discretisation 2-D mesh associated with the multiphase model (CFD-MP) for Scenario N1 (V_T = 8 m³, LF = 0.97) in Table 7.1.

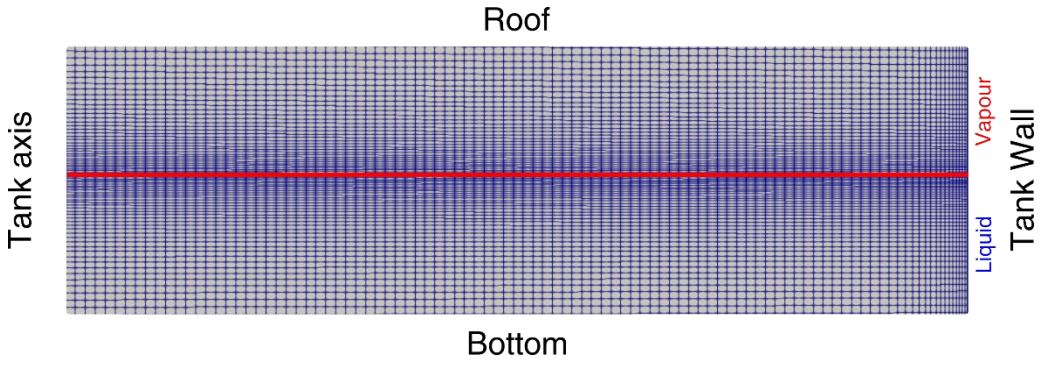

Figure 7.13: Near-interface zoom-in of the mesh associated with the multiphase model (CFD-MP) for Scenario N1 (V_T = 8 m³, LF = 0.97) in Table 7.1.

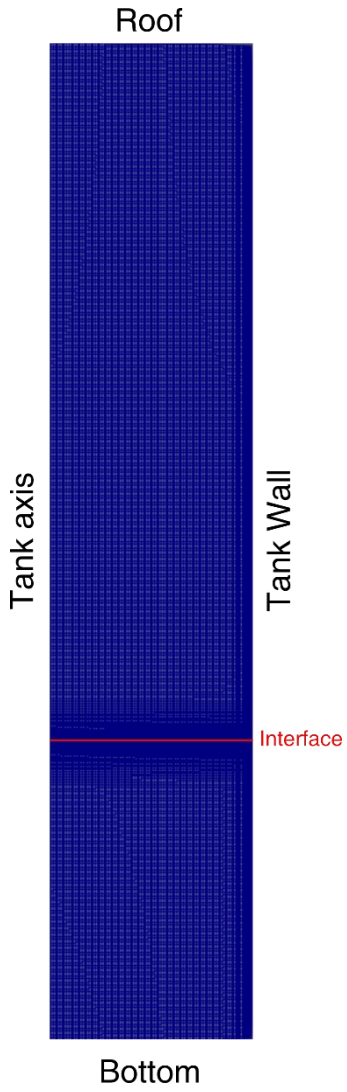

Figure 7.14: Domain discretisation 2-D mesh associated with the multiphase model (CFD-MP) for Scenario N2 (V_T = 8 m³, LF = 0.30) in Table 7.1.

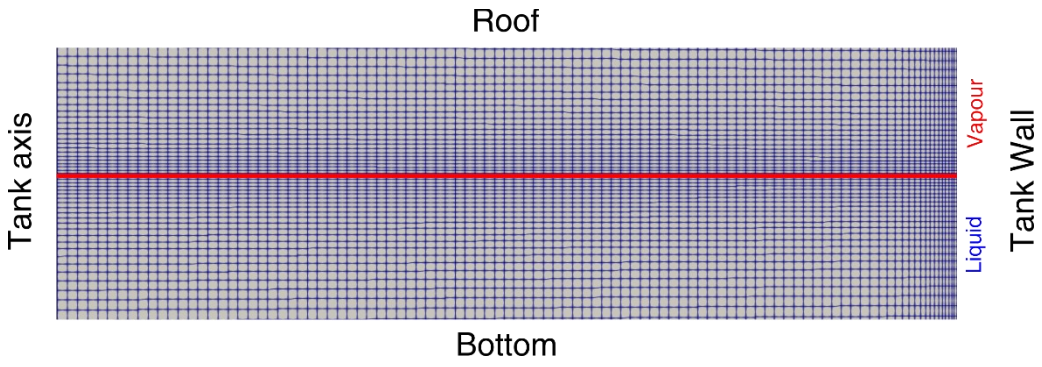

Figure 7.15: Near-interface zoom-in of the mesh associated with the multiphase model (CFD-MP) for Scenario N2 (V_T = 8 m³, LF = 0.30) in Table 7.1.

7.6 Chapter summary

- The non-isobaric 1-D model achieved grid independence using the coarse mesh for both low and high liquid fillings.
- The single phase CFD-SP model achieved grid independence on liquid temperature using the coarse mesh for both low and high liquid fillings.
- In the multiphase CFD-MP model for high liquid fillings, the normal and coarse meshes produced under-resolved vapour temperature and vapour velocity profiles.
- The multiphase CFD-MP model for low liquid fillings, grid independence
- A finer mesh is required in the multiphase CFD-MP model for high liquid fillings to provide an accurate estimate of the discretisation errors.

7.7 References

[1] M. Seo and S. Jeong, "Analysis of self-pressurization phenomenon of cryogenic fluid storage tank with thermal diffusion model," *Cryogenics,* vol. 50, no. 9, pp. 549-555, Sep 2010, doi: 10.1016/j.cryogenics.2010.02.021.

[2] M. Kang, J. Kim, H. You, and D. Chang, "Experimental investigation of thermal stratification in cryogenic tanks," *Exp. Therm. Fluid Sci.,* vol. 96, pp. 371-382, 2018/09/01/ 2018, doi: https://doi.org/10.1016/j.expthermflusci.2017.12.017.

[3] F. Huerta and V. Vesovic, "A realistic vapour phase heat transfer model for the weathering of LNG stored in large tanks," *Energy,* vol. 174, pp. 280-291, 2019/05/01/ 2019, doi: https://doi.org/10.1016/j.energy.2019.02.174.

[4] F. Huerta and V. Vesovic, "Analytical solutions for the isobaric evaporation of pure cryogens in storage tanks," *Int. J. Heat Mass Transfer,* vol. 143, p. 118536, 2019/11/01/ 2019, doi: https://doi.org/10.1016/j.ijheatmasstransfer.2019.118536.

[5] F. Huerta and V. Vesovic, "CFD modelling of the isobaric evaporation of cryogenic liquids in storage tanks," *Int. J. Heat Mass Transfer,* vol. 176, p. 121419, 2021/09/01/ 2021, doi: https://doi.org/10.1016/j.ijheatmasstransfer.2021.121419.

[6] C. J. Roy and W. L. Oberkampf, "A comprehensive framework for verification, validation, and uncertainty quantification in scientific computing," *Computer Methods in Applied Mechanics and Engineering,* vol. 200, no. 25, pp. 2131-2144, 2011/06/15/ 2011, doi: https://doi.org/10.1016/j.cma.2011.03.016.

Chapter 8

Results of modelling non-isobaric evaporation of cryogenic liquids in storage tanks

8.1 Introduction

One of the main objectives of this chapter is to fill the experimental validation gap of this thesis. The main limitation for the validation of the isobaric evaporation models in Chapters 3-5 was the lack of accurate, openly available experimental data. Thus, only a qualitative validation of these models have been performed by Huerta and Vesovic [1] for large scale storage tanks. Fortunately, for the non-isobaric evaporation of cryogens in lab-scale storage tanks, there is a growing number of experimental data for pressure build-up and temperature profiles [2-5]. In sections 8.2 and 8.3, a comprehensive validation of the non-isobaric evaporation models developed in Chapter 6 are presented. Additionally, the initial conditions of the cryogen evaporation experiments [2-5] correspond to the pseudo-steady state isobaric evaporation. The initial conditions of the experiments [2-5] will be also used to validate, albeit at the lab-scale, the isobaric 1-D model [1, 6] developed in section 3.3.

In section 8.2, the models are validated against experimental results of Seo and Jeong [2]. Seo and Jeong [2]. experiments are representative of cryogen evaporation under low wall heat fluxes (18.1 – 24.8 W $m^{-2}K^{-1}$) and narrow pressure ranges (0.1 - 0.14 MPa). In section 8.3, the range of applicability of the developed models are investigated through validation against Kang et al. experiments [3]. Kang et al [3]. experiments are representative of cryogen evaporation under moderate heat fluxes (24 - 700 W $m^{-2}K^{-1}$) and a broad pressure range (0.1 - 1 MPa). The evolution of the pressure and temperature profiles predicted by the models is compared against experimental measurements for a variety of initial liquid fillings. In particular, the four models for the non-isobaric evaporation of pure cryogenic liquids in storage tanks developed in Chapter 6 are

considered. Namely, (i) equilibrium model, see subsection 6.2.1 (ii) non-isobaric 1-D model, see subsection 6.2.2, (iii) single phase (CFD-SP) model with non-equilibrium vapour, see section 6.3 and subsection 6.3.5, and (iv) multiphase (CFD-MP) model, see section 6.4.

For the non-isobaric evaporation of cryogens in industrially sized storage tanks, there is very few experimental or industrial data for pressure or temperature profiles. To overcome this limitation, in section 8.4 the models developed in Chapter 6 are used to simulate the evaporation of LN_2 in an 8 m^3 storage tank under low and high liquid fillings. The tank selected correspond to the same tank used for Scenarios 1 and 3 on Chapter 5, but with no vent. One of the key strengths of the CFD models is the detailed velocity profiles in the liquid (CFD-SP) and liquid and vapour (CFD-MP). This will allow us to investigate natural convection and interfacial phenomena at scale where experimental measurements are unfeasible for cryogenic liquids.

8.2 LN_2 evaporation under narrow pressure ranges

In this section, the models developed in Chapter 6 are validated against Seo and Jeong [2] experimental data for the evaporation of liquid nitrogen in a 6.75 L cylindrical vessel. A subset of three experiments representative of different liquid fillings (*LF*) and heat fluxes (q) was selected to cover a wide range of operational conditions. Seo and Jeong [2] experiments were executed in a vacuum vessel with heating from the surroundings. They reported an average total heat ingress into the liquid using boil-off gas calorimetry at the beginning and at the end of the evaporation [2]. Unfortunately, no temperature measurements within the solid walls or void space in the multi-layered insulation (MLI) of the vacuum vessel were provided. Therefore, it is not possible to determine the spatial-temporal dependency of the heat flux between the inner tank wall and the stored cryogen. Figure 8.1 depicts a diagram of Seo and Jeong [2] experimental setup, where the thermocouples are located in the midpoint between the tank axis and sidewall, $r = R_T/2$. Recent experimental and numerical evidence on cryogenic nitrogen [3], hydrogen [7] and methane [8] lab-scale storage suggests that most of the heat ingress from the surroundings is transferred directly into the liquid. This phenomenon

was observed for a variety of initial liquid fillings [3, 7, 8], suggesting a non-homogeneity in the wall heat flux to both liquid and vapour. Based on these results [3, 7, 8], a sequential methodology has been developed to estimate the heat transfer coefficients in each phase.

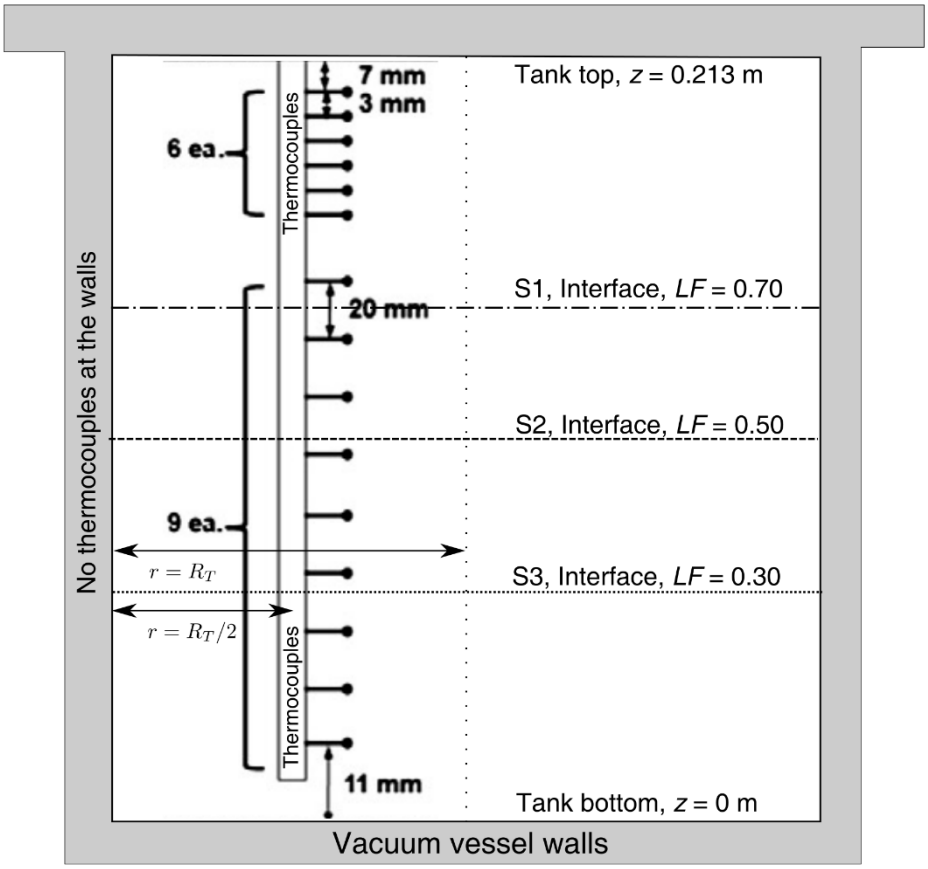

Figure 8.1: Schematic of Seo and Jeong [2] experimental setup for their experiments of LN2 evaporation in a 6.75 L vertically oriented cylindrical tank. The thermocouples were located at the midpoint between the tank sidewall and the axis, $r = R_T/2$. No temperature measurements were performed in the inner, inside or outer walls of the vacuum vessel.

The vapour phase heat transfer coefficients, U_V and U_{roof}, were estimated using Huerta and Vesovic [6] analytical solutions for vapour temperature. The heat transfer coefficients were obtained by least-squares fitting of the vapour temperature between the experimental profile at the beginning of the evaporation and the analytical solutions for each experiment. It was found that setting the advective term to zero produced the best fit. This suggests that the initial temperature profiles reported by Seo and Jeong [2]

correspond to a timestep shortly after the valve is closed. With the fitted vapour phase heat transfer coefficients, the total vapour heat ingress was determined, and the liquid heat ingress was calculated through $\dot{Q}_{\mathrm{L,in}} = \dot{Q}_{\mathrm{tot}} - \dot{Q}_{\mathrm{V,in}}$. From the reported experimental temperature profiles, it was assumed that the bottom of the tank was perfectly insulated (U_{bot} = 0). Consequently, the liquid phase heat transfer coefficient at the tank walls was estimated by $U_{\mathrm{L}} = \dot{Q}_{\mathrm{L,in}}/(\pi d_{\mathrm{o}} l_{\mathrm{L}}(T_{\mathrm{air}} - T_{\mathrm{sat}}))$.

The CFD-SP and non-isobaric 1-D models for non-isobaric evaporation require an evaporative fraction coefficient, η_e, to determine the fraction of wall heat flux used for wall boiling compared to the total wall heat flux. The models were ran using two values of η_e . The first value, $\eta_{\mathrm{e,calc}}$, was obtained using the a priori calculation methodology presented in subsection 6.3.3. To assess the a priori methodology, a second value $\eta_{\mathrm{e,fit}}$ was estimated through least squares fitting on pressure between the CFD-SP model predictions and experimental results for each experiment. Table 8.1 summarizes all known and fitted parameters required to simulate Seo and Jeong [2] using the non-isobaric models developed in this work.

Table 8.1: Simulation parameters for Seo and Jeong [2] experiments of LN2 evaporation in a 6.75 LN_2 storage tank using the CFD-SP and non-isobaric 1-D models.

Scenario	LF	P_0 / kPa	U_{V} / $\mathrm{Wm^{-2}K^{-1}}$	U_{L} / $\mathrm{Wm^{-2}K^{-1}}$	$\eta_{\mathrm{e,calc}}$	$\eta_{\mathrm{e,fit}}$
S1	0.7	100	0.003	0.12	0.32	0.24
S2	0.5	100	0.001	0.0762	0.17	0.34
S3	0.3	100	0.001	0.117	0.18	0.36

The most important result of Table 8.1 is that the estimated heat transfer coefficients of the vapour are two orders of magnitude lower than the ones for the liquid. As the material of the tank multi-insulation layers is homogeneous and there is no special insulation of the vapour, the fitting demonstrates that the wall heat flux is not spatially homogeneous. The lower heat transfer coefficient in the vapour implies that $q_{\mathrm{V}} \ll q_{\mathrm{L}}$, thus, most of the heat ends up flowing to the liquid. This suggests that for Seo and Jeong [2] experiments, the heat ingress from the surroundings drives a 2-D temperature profile within the vacuum vessel walls, see Figure 8.1. Non-spatially homogeneous wall heat flux during non-isobaric storage of cryogens has been recently investigated by a number of experimental [3, 9] and computational [8, 10, 11] studies.

These studies have concluded that although wall heat flux can be a complicated function of the inner surface position, it quickly reaches a pseudo-steady state for several storage scenarios. In this work, conjugate heat transfer between the vacuum vessel walls and the stored cryogen has not been explicitly modelled. Instead, the non-homogeneous wall heat fluxes have been implemented through the previously described fitting procedure of heat transfer coefficients. This approximation is reasonable as long as pseudo-steady state heat transfer is established within the walls.

8.2.1 Scenario S1: 6.75 L cryogenic storage vessel filled to 70% of its capacity

We start analysing the pressure build-up during the evaporation of liquid nitrogen in a 6.75 L storage filled at 70% of its capacity. Figure 8.2 shows a comparison between the experimental pressure build-up reported by Seo and Jeong. [2], and the models developed in Chapter 6. For this scenario, the equilibrium model predicted a much lower pressure build-up than the experiments, see Figure 8.2. A similar underprediction of pressure build-up was observed for the 1-D model with no wall boiling, see the light blue dashed lines in Figure 8.2. As expected, the 1-D model predicts a slightly higher-pressure build-up than the equilibrium model owing to the inclusion of vapour and liquid thermal stratification. However, the pressure predicted by the 1-D model is significantly below the experimental pressure.

Figure 8.2 also shows the pressure build-up predicted by the 1-D model using the and fitted evaporative fraction coefficient, $\eta_{e,fit}$, see the light blue line. The pressure obtained using the isobaric 1-D model with wall boiling was in good agreement with the experimental results. This contrasts to the underestimation of pressure build-up by the equilibrium and 1-D models with no wall boiling. These results show that it is not possible to reproduce the experimental pressure build-up without considering wall boiling.

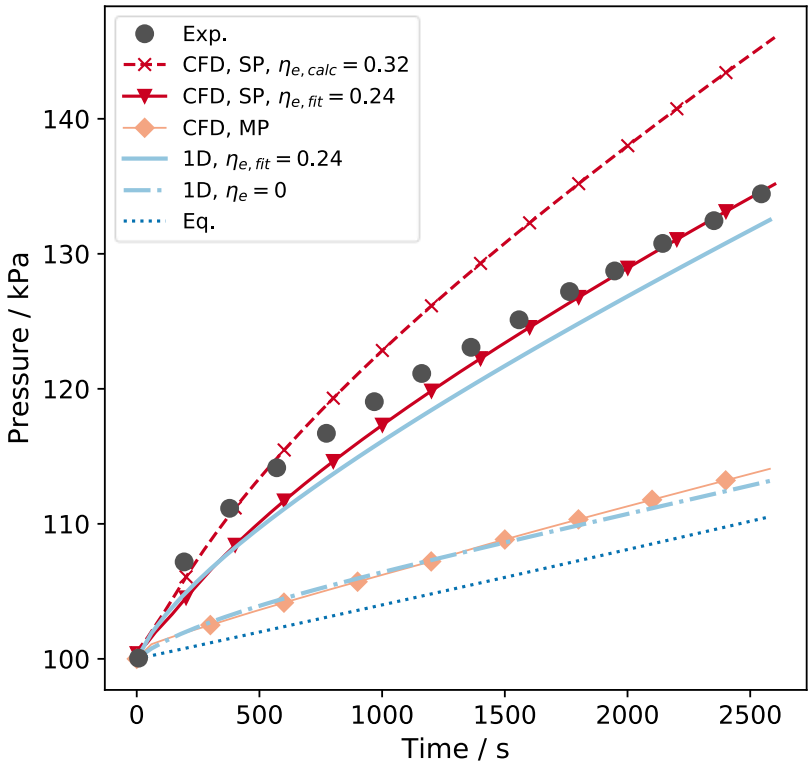

Figure 8.2: Pressure evolution during the non-isobaric evaporation of liquid nitrogen in a 6.75 L storage tank filled at 70% of its capacity. The experimental results of Seo et al [2] are depicted in grey circles. Light-blue lines depict the pressure obtained with the equilibrium model (dotted), 1-D model without wall boiling (dot and lines) and 1-D model with wall boiling (solid line). Red lines depict the results obtained with the single-phase CFD-SP model (CFD, SP) using the calculated (dashed lines) and fitted (solid lines) evaporative fraction coefficient η_e. The pressure obtained with the multiphase (MP) model is depicted in yellow lines with diamond markers.

Figure 8.2 also shows the pressure build-up predicted by the CFD-SP model using the calculated ($\eta_{e,calc}$, in dashed red lines) and fitted ($\eta_{e,fit}$, in solid red lines) evaporative fraction coefficients. Using the calculated evaporative coefficient provided an accurate prediction of the pressure build-up during the first 600 s of evaporation. After this period, the CFD-SP model using $\eta_{e,calc}$ overestimated the pressure build-up, and the overestimation increased with time. In contrast, using the fitted evaporative coefficient slightly underestimated the pressure build-up during the first 1,200 s of evaporation. After t = 1,200 s, the CFD-SP model produced an excellent agreement in both pressure and pressurization rates. The experimental pressure is closest to the pressure predicted by the CFD-SP model at (i) early times using the higher $\eta_{e,calc}$ and (ii) late times using the lower $\eta_{e,fit}$, see Figure 8.2.

The last trend in Figure 8.2 corresponds to the pressure build-up predicted by the CFD-MP model. In contrast to the 1-D and CFD-SP models, the evaporative fraction is neither calculated *a priori* nor fitted. Instead, the spatial profile of the evaporative coefficient is calculated for each timestep by solving the heat-flux partitioning sub-model, see subsection 6.2.3. The CFD-MP predicted a pressure similar to that predicted by the 1-D model with no wall evaporation, see yellow and light blue dashed lines in Figure 8.2.

The good agreement between the CFD-MP model and 1-D model with no wall boiling (η_e = 0) is a consequence of the low evaporative fraction coefficient calculated by the multiphase model. The average evaporative fraction for the CFD-MP model, $\bar{\eta}_{\mathrm{e,MP}}$ was just 0.03, implying that only 3% of the liquid heat ingress produces wall boiling. This average evaporative coefficient is much lower than the best-fit coefficient for the CFD-SP model, $0.03 = \bar{\eta}_{\mathrm{e,MP}} \ll \eta_{\mathrm{e,fit}} = 0.36$. Consequently, the pressure predicted by the CFD-MP model showed a poor fit against the experimental pressure build-up, see Figure 8.2. To further investigate the lack of fit on experimental pressure predicted by the multiphase model, the parameters on the wall boiling sub-models were varied up to 2 orders of magnitude. It was observed that the pressure evolution varied less than 1% across the parametric range. Hence, the pressure evolution is not sensitive to the parameters of the wall boiling sub-models for this scale.

Experimental evidence on water evaporation in a cylindrical storage external heating of the walls suggest that significant thermal stratification develops in the solid walls [12]. In Ren et al. experiments [12], thermal stratification in the wall developed as a consequence of the low thermal conductivity of the vapour. The stratification in the walls drove vertical heat transfer from the wall in contact with the vapour to the wall in contact with the liquid. This non-uniform heat flux at the wall drove wall boiling, as Ren et al. concluded that both surface evaporation and wall boiling were present in this storage scenario [12]. In a subsequent numerical study based on the abovementioned experiments [12], Ren et al. demonstrated that the heat transfer from the solid wall to the vapour was much smaller than to the liquid [7]. The numerical results [7] show that under the thermal stratification of the solid wall, most wall boiling happens in a small region below the vapour-liquid interface. This suggests that the underestimation of wall

boiling by the multiphase model, see Figure 8.2, is a consequence of the spatially homogeneous heat flux assumption for each phase.

Although the wall boundary conditions on Seo and Jeong experiments [2] are uncertain, the CFD-SP and 1-D models accurately predicted the pressure build-up for Scenario 1. This was possible by fitting both the evaporative fraction, η_e, and overall heat transfer coefficient for the vapour phase, U_V, to pressure and temperature data. This result suggests that the evaporative fraction captures uncertainties in both wall heat flux and wall boiling. On the other hand, the low evaporative fraction predicted by the multiphase model suggests that the *a priori* calculation procedure does not estimate accurately the evaporative fraction. Nevertheless, the usage of an evaporative fraction coefficient is a convenient approach when the temperature boundary conditions are uncertain. In this context, the CFD-SP and 1-D models are more flexible than the multiphase model.

In what follows, the temperature profiles in the liquid and vapour phases will be investigated. In both phases, the temperature profiles are strongly dependent on the temperature at the vapour-liquid interface, which is a function of the saturation pressure. Hence, only the 1-D model and the CFD-SP model with $\eta_{e,fit}$ = 0.24 will be considered further, as they provided the best agreement on the experimental pressure build-up, see Figure 8.2. Figure 8.3 shows the temperature in the x-axis and the liquid height in the y-axis for the evaporation of LN_2 in a 6.75 L storage tank filled at 70% of its capacity. The temperature measurements of Seo and Jeong [2] are compared with the profiles obtained using the 1-D model and the CFD-SP model, see Figure 8.3. Two representative time-steps at depicted, at 20 and 40 minutes after the beginning of the evaporation. To aid the discussion, two regions in the liquid are defined as a function of the interface location and time. Below the vapor-liquid interface, a time-dependent thermally stratified layer, δ_{TS}, develops because of the rapid increase of saturation pressure with time, see Figure 8.3. The region affected by thermal stratification, $l_L - \delta_{TS} < z < l_L$, is labelled as thermally stratified region. The region below the thermally stratified region, $z \leq l_L - \delta_{TS}$, is identified as liquid bulk. In the liquid bulk, the temperature is expected to be a weak function of height because of natural convection driven by wall heating [2-5, 11, 13-15].

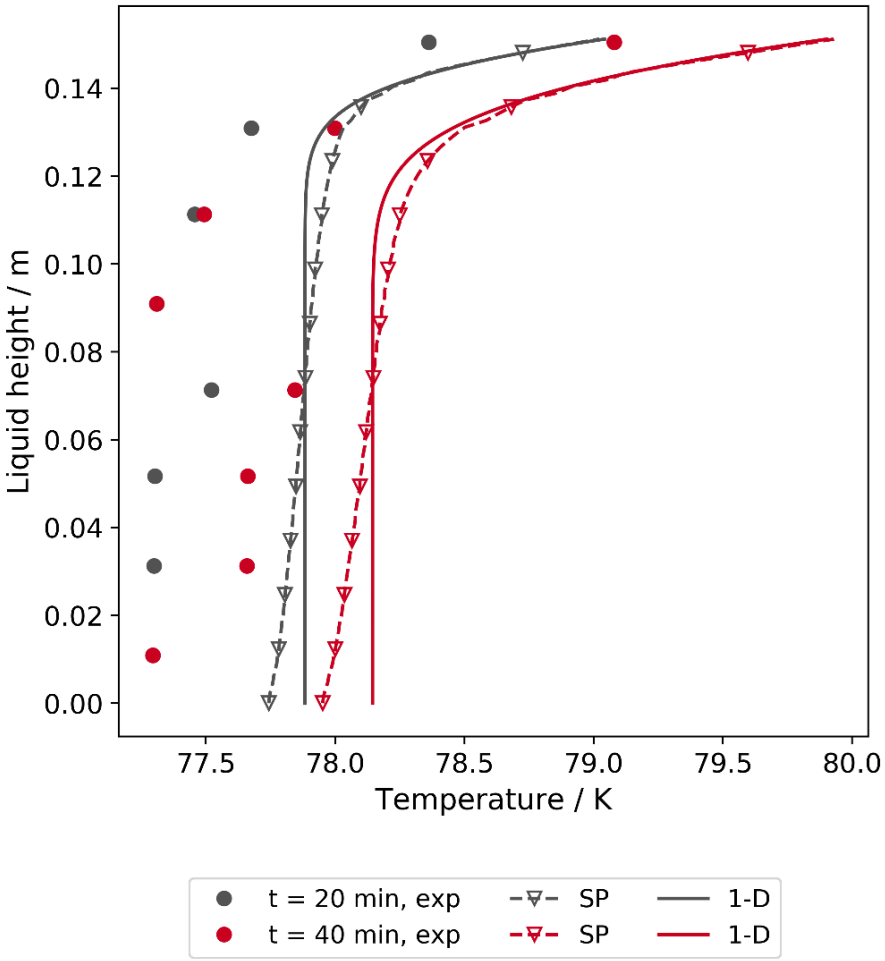

Figure 8.3: Liquid temperature profiles during the non-isobaric evaporation of liquid nitrogen in a 6.75 L storage tank filled at 70% of its capacity. The experimental results of Seo and Jeong [2] are depicted in solid circles, where grey and red colours represent the profiles after 20 and 40 minutes of evaporation, respectively. The liquid temperature profiles obtained using the CFD-SP (SP) model and 1-D models are depicted in dashed lines with empty triangle markers and solid lines, respectively.

Figure 8.3 shows that both models predicted an increase on liquid bulk temperature and thermal stratification as the time progresses, in agreement with the experimental measurements. However, the model predictions are around 1 K higher than the experimental measurements at all time-steps, compare solid and dashed lines with the filled circles in Figure 8.3. The slight overestimation of the saturation temperature is inconsistent with the good agreement with the experimental pressure build-up of the CFD-SP and 1-D models, see Figure 8.2. Therefore, either the experimental pressure or the temperature measurements present a small bias. Unfortunately, the accuracy of the temperature and pressure has not been reported by Seo and Jeong [2]. Given that the temperature variation is smaller than the pressure

variation, it will be assumed that the uncertainty is on the temperature measurements. This approach is supported by the scatter on experimental liquid temperature, see Figure 8.3, which shows that there is at least 0.5 K experimental uncertainty.

In both models, the temperature in the bulk ($z < 0.11$ m) and in the thermally stratified region ($z \geq 0.11$ m) increases with time, see Figure 8.3. The thermally stratified region propagates downwards with time, from $\delta_{SL,1}$ = 26 mm at t = 20 min to $\delta_{SL,2}$ = 35.6 mm at t = 40 min. The width of the thermally stratified layer is proportional to $t^{1/2}$, showing that thermal conduction dominates the growth of this layer. Both CFD-SP and 1-D models are in excellent agreement in the thermally stratified region, while at the liquid bulk the temperature profiles are slightly different. The good agreement on the thermally stratified region suggests that in that region, conduction is the dominant mechanism of heat transfer. Furthermore, it suggests that the effect of natural convection in the thermally stratified layer can be effectively modelled as a volumetric source term.

In the liquid bulk, the 1-D model predicts a spatially homogeneous temperature profile, see Figure 8.3. In contrast, the CFD-SP model predicts a small monotonic increase of temperature with height from 77.7 to 77.9 K at t = 20 min and 77.9 to 78.3 K at t = 40 min. The temperature profile at the bulk predicted by the CFD-SP model is in better agreement to the experimental results than that of the 1-D model. This is expected as in the 1-D model, natural convection is included in a simplified manner as a volumetric source term. On the other hand, the CFD-SP model fully resolves the velocity profile driven by natural convection, which allows a more accurate prediction of the liquid bulk temperature.

Figure 8.4 shows the temperature as a function of vapour height for the evaporation of LN_2 in a 6.75 L storage filled at 70% of its capacity. The experimental results are compared against the CFD-SP and 1-D models after 20 and 40 minutes from the beginning of the evaporation. Owing to time limitations, the vapour temperature profile in the CFD-SP has been obtained by using the analytical solutions for isobaric evaporation, see subsection 6.3.5. Although this approach is accurate only for high liquid fillings, it has been observed that it provided a better agreement on pressure

build-up and liquid temperature when compared against the vapour bulk equilibrium model developed in subsection 6.3.4.

Both CFD-SP and 1-D models predict a monotonic increase on temperature with height and time, in line with experimental temperature profiles, see Figure 8.4. However, both models slightly overpredict the vapour temperature. The overprediction is a consequence of experimental uncertainties in the spatial distribution of the wall heat flux. These uncertainties are also compounded with the assumptions made in the fitting procedure of the vapour phase heat transfer coefficient. Nevertheless, both models predict the vapour temperature with a reasonable accuracy. The maximum deviation (MD) on vapour temperature was just 1.3% for the CFD-SP model and 2.6% for the CFD-SP model.

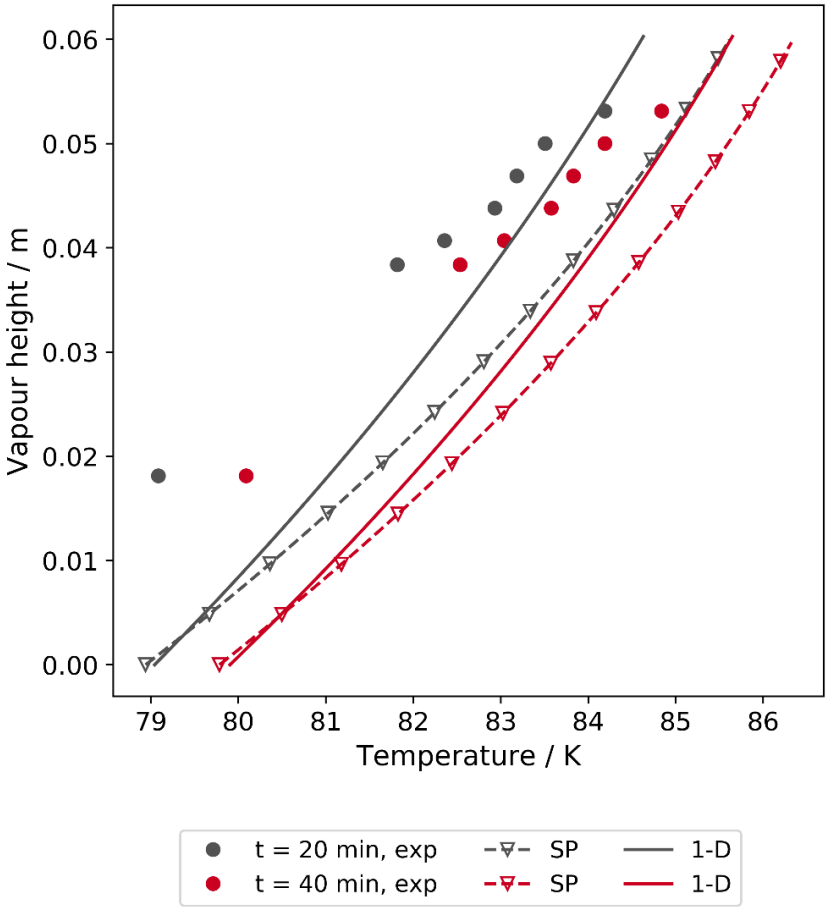

Figure 8.4: Vapour temperature profiles during the non-isobaric evaporation of liquid nitrogen in a 6.75 L storage tank filled at 70% of its capacity. The experimental results of Seo and Jeong [2] are depicted in solid circles, where grey and red colours represent the profiles after 20 and 40 minutes of evaporation, respectively. The vapour temperature profiles obtained using the CFD-SP model and non-isobaric 1-D models are depicted in dashed lines with empty triangle markers and solid lines, respectively.

It is not clear from Figure 8.4 whether the CFD-SP or the 1-D models produces the best agreement on vapour temperature. Although the 1-D model has a lower absolute average deviation, the CFD-SP model seems to better predict the slope of the temperature profile. In the CFD-SP model, the vapour temperature is assumed to be at a pseudo-steady state. This assumption neglects the transient dynamics of vapour heating in the vapour, and hence it is expected to overestimate vapour temperature. In contrast, in the 1-D model the transient evolution of vapour temperature is fully resolved, and a source term regarding vapour accumulation is included. The good agreement of the CFD-SP model suggests that for high liquid fillings and low heat fluxes, the pseudo-steady approximation for vapour phase heat transfer is reasonable. Consequently, assuming pseudo-steady vapour phase heat transfer in this scenario has a small influence on vapour to interface heat transfer rates, see Eqs. (6.21) and (3.43) considering $\dot{Q}_{\mathrm{VI}} = \dot{Q}_{\mathrm{VL}}$.

The inclusion of more realistic physics for the vapour phase heat transfer modelling in the 1-D model explains its slightly better agreement with the experimental vapour temperature measurements than that one of the CFD-SP model. It is worth noting that at the vapour-liquid interface, both models predict a very similar vertical temperature gradient.

8.2.2 Scenario S2: 6.75 L cryogenic storage vessel filled to 50% of its capacity

The second validation scenario, S2, comprises the evaporation of liquid nitrogen in the same 6.75 L storage vessel as for Scenario S1 under an intermediate liquid filling (LF = 0.50). Figure 8.5 depicts the pressure predicted by the non-isobaric evaporation models and the experimental results of Seo and Jeong [2]. The equilibrium model and non-equilibrium model without wall boiling significantly underpredict the experimental results, similarly to what has been observed for the high liquid filling scenario, see Figure 8.2. This is a consequence of neglecting wall boiling, as discussed in the previous scenario of high liquid filling (LF = 0.7). The best fit to experimental pressure was achieved by the CFD-SP and 1-D model with a fitted evaporative fraction of $\eta_{\mathrm{e,fit}}$ = 0.34, see Figure 8.5. This confirms that wall boiling is significant for

intermediate liquid filling (LF = 0.5), in a similar way to what was concluded for the high liquid filling (LF = 0.7) scenario. Both CFD-SP and 1-D models using $\eta_{e,fit}$ = 0.34 are in excellent agreement with each other, as it was also observed for Scenario S1, see Figure 8.2. and Figure 8.5.

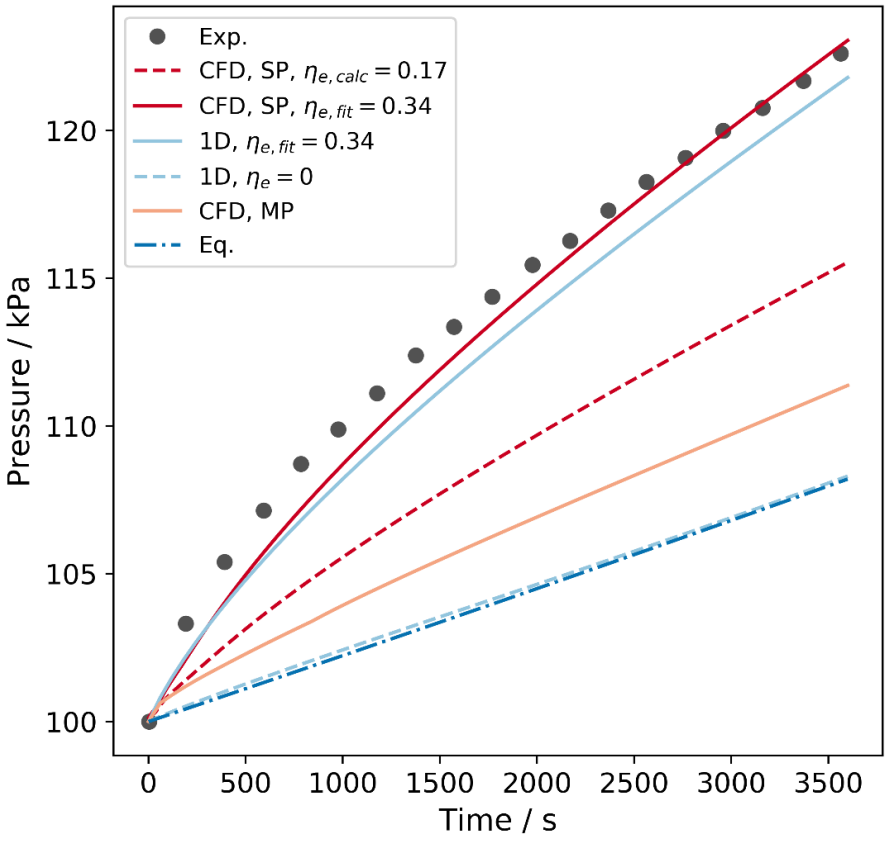

Figure 8.5: Pressure evolution during the non-isobaric evaporation of liquid nitrogen in a 6.75 L storage tank filled at 50% of its capacity. The experimental results of Seo et al [2] are depicted in grey circles. Light-blue lines depict the pressure obtained with the equilibrium model (dotted), 1-D model without wall boiling (dot and lines) and 1-D model with wall boiling (solid line). Red lines depict the results obtained with the single-phase CFD-SP model (CFD, SP) using the calculated (dashed lines) and fitted (solid lines) evaporative fraction coefficient η_e. The pressure obtained with the multiphase (MP) model is depicted in yellow lines with diamond markers.

In contrast to the high liquid filling scenario, the *a priori* calculation procedure underestimated the fitted value of the evaporative fraction coefficient, η_e, see Figure 8.2 and Figure 8.5. The lack of predictive power of the *a priori* calculation method implies that the method does not provide an accurate heat flux partitioning for non-isobaric evaporation. For Scenario S2, the multiphase model underpredicted the pressure build-up, in a similar way to what was observed for the high liquid filling Scenario S1, see

Figure 8.2 and Figure 8.5. As a consequence of $\eta_{e,fit} > \eta_{e,calc.} > \bar{\eta}_{MP}$, a non-homogeneous wall heat flux is also present for the LF = 0.50 scenario.

Figure 8.6 shows liquid temperature profiles during the evaporation of LN_2 in a 6.75 L storage filled at 50% of its capacity. The experimental temperature profiles obtained by Seo and Jeong [2] are compared with the profiles obtained with the CFD-SP and 1-D models for three representative time-steps. Both models show an agreement with the experimental trends, although they slightly overpredict the liquid temperature, see Figure 8.6. These results are analogous to what was observed for the high liquid filling scenario, see Figure 8.3. As the liquid filling in this Scenario 2 is smaller than in Scenario 1, the thermally stratified layer covers a higher proportion of the liquid domain, see Figure 8.3 and Figure 8.6.

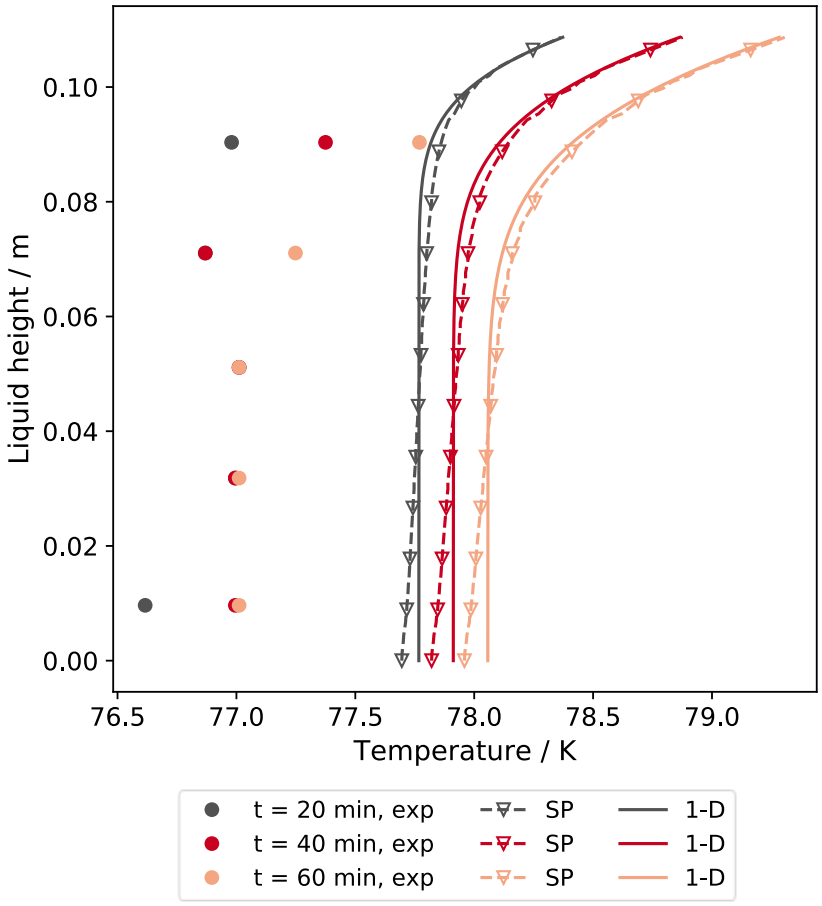

Figure 8.6: Liquid temperature profiles during the non-isobaric evaporation of liquid nitrogen in a 6.75 L storage tank filled at 50% of its capacity. The experimental results of Seo and Jeong [2] are depicted in solid circles, where grey and red colours represent the profiles after 20 and 40 minutes of evaporation, respectively. The liquid temperature profiles obtained using the CFD-SP (SP) model and 1-D models are depicted in dashed lines with empty triangle markers and solid lines, respectively.

The smaller liquid height and wall heat flux in Scenario S2 (LF = 0.5, q_L = X) explains the better agreement between the 1-D and CFD-SP models when compared with Scenario S1 (LF = 0.5, q_L = X). see Figure 8.3 and Figure 8.6. Smaller liquid height and heat flux drive a weaker natural convection in Scenario S2, compared with Scenario S1. This suggest that liquid natural convection can be effectively modelled as a volumetric source term in the 1-D model for scenarios where natural convection is weak, see Eq. (6.28). Both CFD-SP and 1-D models show a good agreement on the liquid temperature gradient below the vapour-liquid interface, as it was also observed for Scenario 1, see Figure 8.3 and Figure 8.6.

Figure 8.7 shows the vapour temperature (x-axis) as a function of vapour height (y-axis) for the evaporation of LN_2 in a 6.75 L storage filled at 50% of its capacity. The predictions obtained using the CFD-SP and 1-D model (using $\eta_{e,\mathrm{fit}}$ = 0.34) are compared against experimental results from Seo and Jeong [2] for three different time-steps. The agreement with the experimental vapour temperature using both models is very good. The 1-D model depicts a lower absolute average deviation on vapour temperature than the CFD-SP model. However, it is not completely clear which of these two models better the vapour temperature for the same reasons discussed in Scenario 1, see subsection 8.2.1. The agreement on vapour temperature for *LF* = 0.50 is slightly better than what has been observed for Scenario S1, see Figure 8.4 and Figure 8.7. Overall, the validation of both CFD-SP and non-isobaric 1-D models for LF = 0.50 results in satisfactory results similar to what has been concluded for Scenario S1.

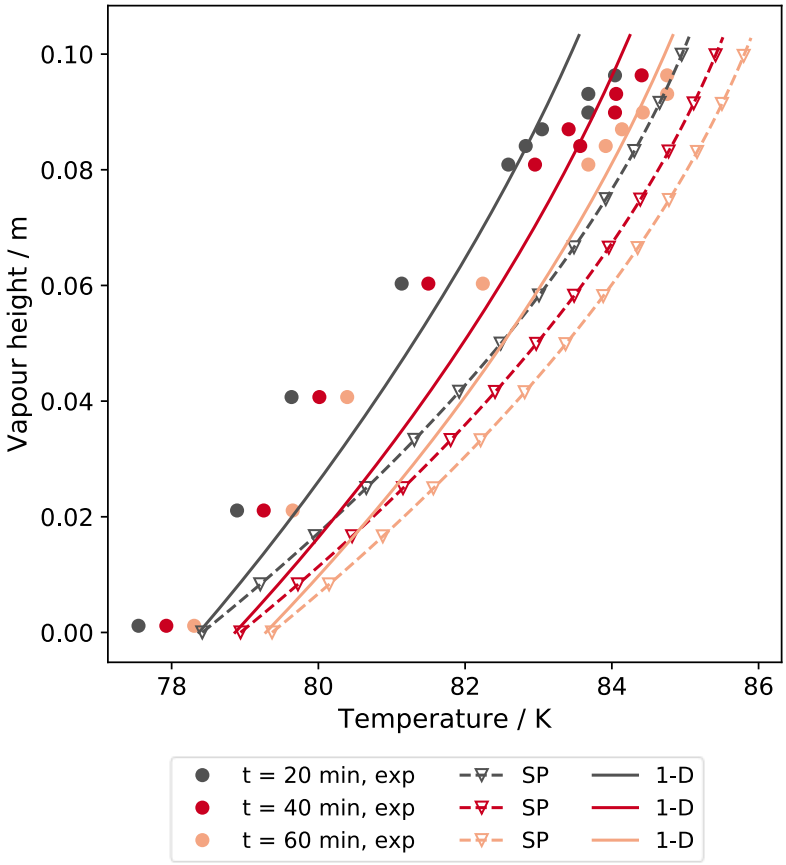

Figure 8.7: Vapour temperature profiles during the non-isobaric evaporation of liquid nitrogen in a 6.75 L storage tank filled at 50% of its capacity. The experimental results of Seo and Jeong [2] are depicted in solid circles, where grey and red colours represent the profiles after 20 and 40 minutes of evaporation, respectively. The vapour temperature profiles obtained using the CFD-SP (SP) model and 1-D models are depicted in dashed lines with empty triangle markers and solid lines, respectively.

8.2.3 Scenario S3: 6.75 L cryogenic storage vessel filled to 30% of its capacity

The last validation scenario, S3, comprises the evaporation of liquid nitrogen in the same 6.75 L storage vessel, initially filled at 30% of its capacity. Figure 8.8 depicts the pressure predicted by non-isobaric evaporation models and the experimental results of Seo and Jeong [2]. The results are analogous to the previous two scenarios. The best fit for pressure was obtained by the CFD-SP and 1-D models using $\eta_{e,fit}$ = 0.36. This demonstrates that wall boiling is also significant for the low liquid filling scenario, see Figure 8.8. The underestimation of the pressure build-up predicted by the equilibrium and non-equilibrium models is smaller than for intermediate and high liquid filling, see Figure 8.2, Figure 8.5 and Figure 8.8. This is a consequence of the lower thermal

stratification under low liquid fillings [2]. For lower degrees of liquid thermal stratification, pressure predictions using equilibrium models are expected to provide a better fit with the experimental results [2, 3]. A scenario of low liquid thermal stratification implies that a higher fraction of the heat ingress is used to evaporate the liquid bulk. Hence, the experimental pressure rise has a higher contribution from bulk evaporation of the liquid. Hence, even though the fitted evaporative fraction coefficient for S3 is higher than for previous scenarios, the effect of wall boiling on the pressure rise less significant.

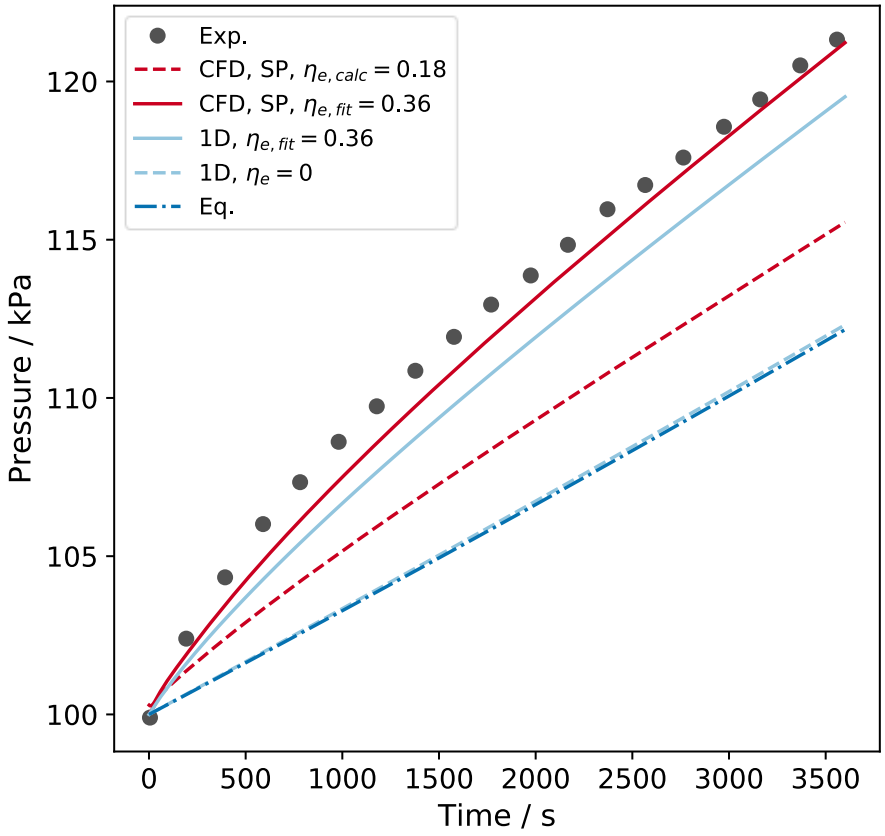

Figure 8.8: Pressure evolution during the non-isobaric evaporation of liquid nitrogen in a 6.75 L storage tank filled at 30% of its capacity. The experimental results of Seo et al [2] are depicted in grey circles. Light-blue lines depict the pressure obtained with the equilibrium model (dotted), 1-D model without wall boiling (dot and lines) and 1-D model with wall boiling (solid line). Red lines depict the results obtained with the single-phase CFD-SP model (CFD, SP) using the calculated (dashed lines) and fitted (solid lines) evaporative fraction coefficient η_e. The pressure obtained with the multiphase (MP) model is depicted in yellow lines with diamond markers.

Figure 8.9 depicts the liquid temperature (x-axis) as a function of height (y-axis) during the evaporation of liquid nitrogen stored in a 6.75 L storage tank filled at 30% of its capacity. In terms of model performance, results are analogous to what has been

observed for Scenarios S1 and S2, see Figure 8.3 and Figure 8.6. For the low liquid filling scenario, the liquid bulk heating is larger than for the intermediate and high liquid filling scenarios, see Figure 8.9. Additionally, the difference between the saturation temperature and the liquid bulk temperature is smaller for the low liquid filling scenario, see Figure 8.3, 8.5, 8.8. Although the thermal stratification is smaller in magnitude, the thermally stratified layer predicted by both CFD-SP and non-isobaric 1-D models seems to permeate more than 50% of the liquid domain.

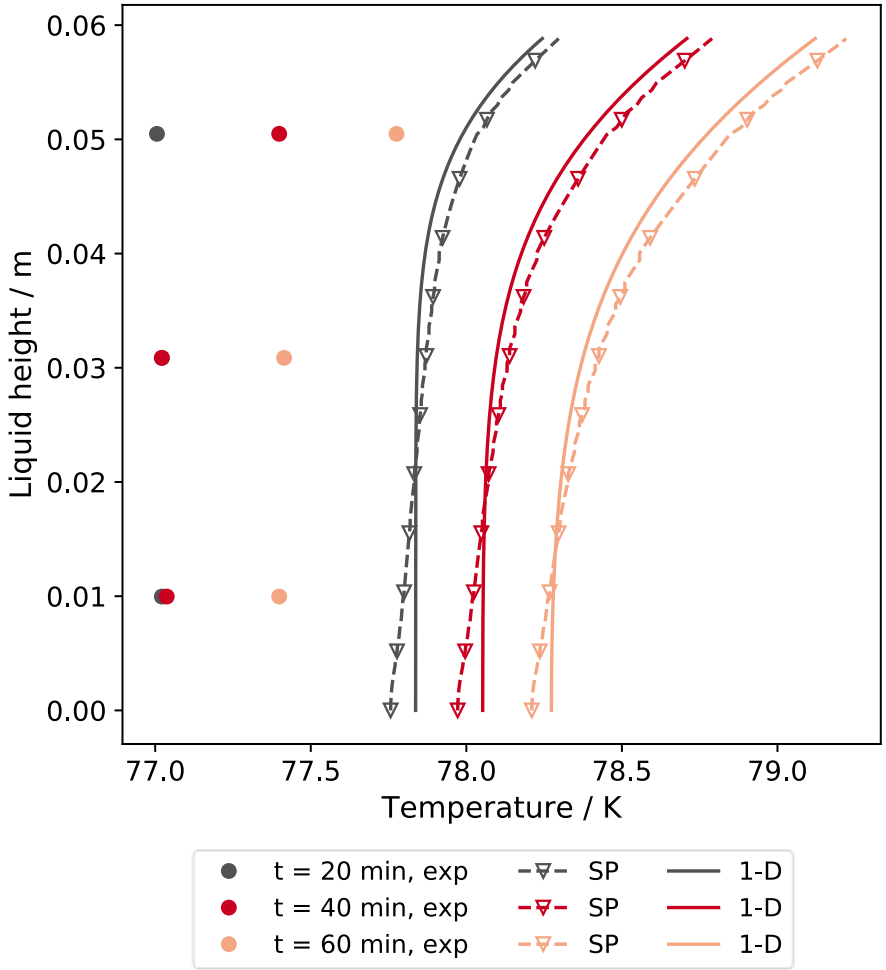

Figure 8.9: Liquid temperature profiles during the non-isobaric evaporation of liquid nitrogen in a 6.75 L storage tank filled at 50% of its capacity. The experimental results of Seo and Jeong [2] are depicted in solid circles, where grey and red colours represent the profiles after 20 and 40 minutes of evaporation, respectively. The liquid temperature profiles obtained using the CFD-SP (SP) model and 1-D models are depicted in dashed lines with empty triangle markers and solid lines, respectively.

Figure 8.10 depicts the vapour temperature (x-axis) as a function of vapour height (y-axis) for the evaporation of LN_2 in a 6.75 L storage vessel filled at 30% of its capacity. The 1-D model provides an excellent agreement on the vapour temperature, while the

CFD-SP model overestimates the vapour temperature, see Figure 8.10. As discussed previously, the overestimation of the CFD-SP model is a consequence of the pseudo-steady state assumption on vapour heat transfer. For this low liquid filling scenario, the overestimation of vapour temperature is larger than for the intermediate and high liquid filling scenarios, see Figure 8.4 Figure 8.7. This is a direct consequence of the larger vapour space for smaller liquid fillings. As the transient period scales with the vapour length, the pseudo-steady state assumption is less accurate for low liquid fillings. For this scenario, the small difference on vapour temperature between CFD-SP and 1-D models did not significantly affect the pressure rise, see Figure 8.8.

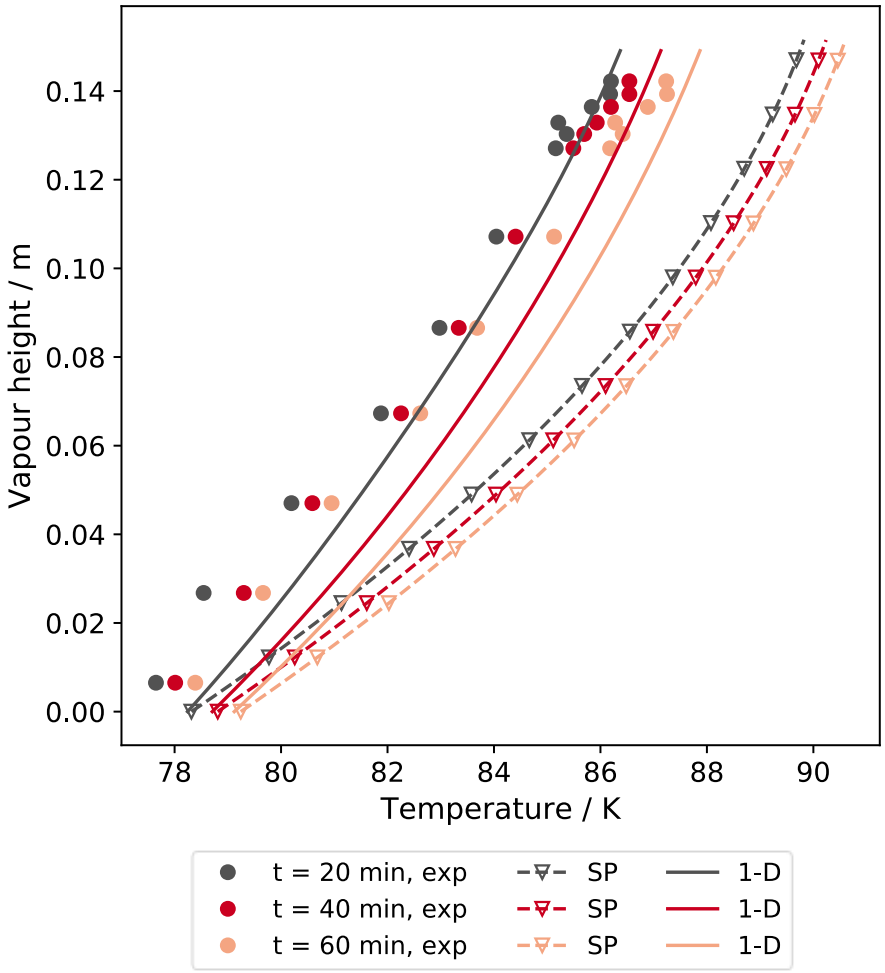

Figure 8.10: Vapour temperature profiles during the non-isobaric evaporation of liquid nitrogen in a 6.75 L storage tank filled at 30% of its capacity. The experimental results of Seo and Jeong [2] are depicted in solid circles, where grey and red colours represent the profiles after 20 and 40 minutes of evaporation, respectively. The vapour temperature profiles obtained using the CFD-SP (SP) model and 1-D models are depicted in dashed lines with empty triangle markers and solid lines, respectively.

8.2.4 Summary of findings

- The CFD-SP and 1-D non-isobaric models were validated against Seo and Jeong [2] experiments for evaporation of liquid nitrogen in a 6.75 L storage tank.
- An excellent agreement on experimental pressure build-up and temperature profiles for all scenarios was observed for the CFD-SP and 1-D models.
- The equilibrium and 1-D models without wall boiling underestimated the experimental pressure, showing that wall boiling cannot be neglected.
- The CFD-MP model underpredicted experimental pressure, suggesting that the experimental temperature within the tank wall is not spatially homogeneous.
- Fitting an evaporative fraction coefficient for the 1-D and CFD-SP models is able to capture both wall boiling and non-homogeneous temperature boundary conditions.
- A constant evaporative fraction provided good predictions of pressure build-up, suggesting that both wall boiling and non-homogeneous wall heat flux reach a pseudo-steady state.
- The pseudo-steady state approximation for the vapour temperature profile is accurate for low vapour lengths, when the transient period is smaller than the storage period.

8.3 LN_2 evaporation under broad pressure ranges

In section 8.2, the non-isobaric evaporation models have been successfully validated for small pressure ranges and low heat fluxes. In this section, the models are validated against Kang et al. [3] experiments on the evaporation of liquid nitrogen in a 10 L storage tank, which cover a broader range of pressures and heat fluxes than Seo and Jeong [2] experiments. Additionally, in Kang et al. [3] experiments the stored LN_2 was heated both from the walls and tank bottom to explore the effect of the thermal aspect ratio. Therefore, these experiments allow for the validation of the non-isobaric models under more complex temperature boundary conditions. Table 8.2 shows the three storage scenarios investigated: low liquid filling (K1), intermediate liquid filling (K2) and high liquid filling (K3).

Table 8.2: Simulation parameters for Kang et al. [3] experiments of LN_2 evaporation in a 10 L storage tank using the CFD-SP and non-isobaric 1-D model.

Scenario	*LF*	P_0 / kPa	U_V / $Wm^{-2}K^{-1}$	U_L / $Wm^{-2}K^{-1}$	U_{bot} / $Wm^{-2}K^{-1}$	$\eta_{e,fit}$
K1	0.8	100	0.0165	0.35	3.12	0.20
K2	0.5	100	0.0083	0.39	2.73	0.30
K3	0.3	100	0.0072	0.38	2.75	0.65

In Table 8.2, the overall heat transfer coefficients for the vapour wall (U_V), liquid wall (U_L) and tank bottom (U_{bot}) in have been estimated using the methodology described in section 8.2 for Seo and Jeong [2] experiments. In contrast to Seo and Jeong [2] experiments, Kang et al. [3] gave more detail on the experimental boundary conditions. Kang et al. [3] fitted a finite element numerical heat transfer model of the storage tank to the boundary conditions of their experiments. With these, they estimated not only the heat flow into each phase through each boundary, but also shown that a stable vertical temperature profile was established. In such a storage scenario, it is expected that most of the heat ingress goes directly to the liquid [7], as discussed previously. Vertical thermal stratification in the solid tank explains the large difference between the vapour and liquid overall heat transfer coefficients for Kang et al. experiments, see Table 8.2.

For each scenario, the evaporative fraction coefficient for the CFD-SP and 1-D models, $\eta_{e,fit}$ Table 8.2, was fitted using the methodology described in section 8.2. In section 8.2, it was demonstrated that the assumptions of the *a priori* calculation method are not valid for non-isobaric evaporation. Hence, for Kang et al. experiments [3], only fitted evaporative fractions have been explored. Similarly, in section 8.2 it was concluded that the CFD-MP model did not reproduce the experimental pressure build-up owing to the non-homogeneity of experimental boundary conditions. Non-homogeneous boundary conditions are expected as a consequence of the thermal stratification in the solid walls for Kang et al [3] experiments. Hence, in this section the multiphase model has been excluded. A closer examination of the multiphase model is provided in section 8.4, where homogeneous temperature boundary conditions at the tank wall and bottom are imposed.

8.3.1 Scenario K1: 10 L cryogenic storage vessel filled to 80% of its capacity

Figure 8.11 shows the pressure build-up during the evaporation of liquid nitrogen in a 10 L storage tank corresponding to scenario K1 in Table 8.2. The experimental results of Kang et al. [3] are compared against the equilibrium, 1-D and CFD-SP models. Both equilibrium and non-equilibrium models underpredicted the pressure build-up. This result is in agreement to what has been observed in the validation against Seo and Jeong [2] experiments, see subsection 8.2.1. However, in contrast to the low liquid filling scenario, the equilibrium model predicted a slightly higher pressure than the non-equilibrium model without wall boiling, see Figure 8.2 and Figure 8.11. This is a consequence of the larger evaporation rate predicted by the equilibrium model, which in this scenario is dominates over the increase in pressure owing to vapour heating in the 1-D model.

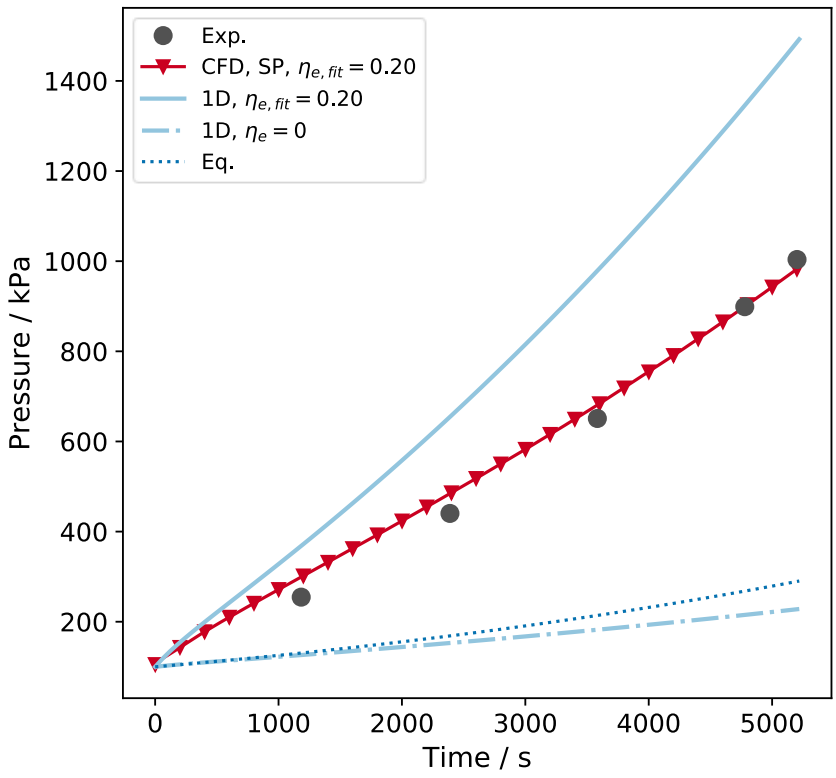

Figure 8.11: Pressure evolution during the non-isobaric evaporation of liquid nitrogen in a 10 L storage tank filled at 80% of its capacity. The experimental results of Kang et al. [3] are depicted in grey circles. Light-blue lines depict the pressure obtained with the equilibrium model (dotted), 1-D model without wall boiling (dot and lines) and 1-D model with wall boiling (solid line). Red lines depict the results obtained with the single-phase CFD-SP model (CFD, SP) using the fitted evaporative fraction coefficient η_e.

Figure 8.11 shows that the CFD-SP model with an evaporative fraction coefficient $\eta_{e,fit}$ = 0.2 achieved an excellent fit with the experimental pressure build-up. On the other hand, the non-isobaric 1-D using the same evaporative fraction coefficient model significantly overpredicted the pressure build-up. The disagreement between both models sharply contrasts the excellent agreement observed for Seo and Jeong [2] high liquid filling experiment, see Figure 8.2. The overprediction in the pressure by the 1-D model is a consequence of two effects. First, liquid natural convection is higher in Scenario K1 than in Scenario S1 owing to the larger wall heat flux. Secondly, the effect of bottom heating in Scenario K1 drive more complex convective currents than in Scenario S1.

To further understand the overprediction of pressure by the non-isobaric 1-D model for Scenario K1, the temperature profiles in the liquid are examined. Figure 8.12 depicts the liquid temperature (x-axis) as a function of liquid height (y-axis) for Scenario K1. The temperature profiles obtained with the 1-D and CFD-SP models are compared against Kang et al. [3] experimental results. In contrast to Seo and Jeong [2] experiments, no bias is observed on the measured liquid temperature, and the profiles were sampled at a higher resolution. Additionally, five different timesteps are reported in Figure 8.12, which allows a more reliable validation of the non-isobaric models. Figure 8.12 shows that the liquid temperature profile predicted by the CFD-SP model is in excellent agreement with Kang et al. [3] experimental results. The agreement is very good near the vapour-liquid interface and in most of the liquid bulk. In an intermediate region of the liquid bulk, $0.2 \leq z \leq 0.4$m, the model slightly overpredicts the liquid temperature. The small differences in the temperature profile are likely a consequence of currents induced by wall boiling near the tank wall [7]. The CFD-SP model cannot capture these currents, as the effect of wall boiling is only included in the energy balance and not in the momentum conservation equations.

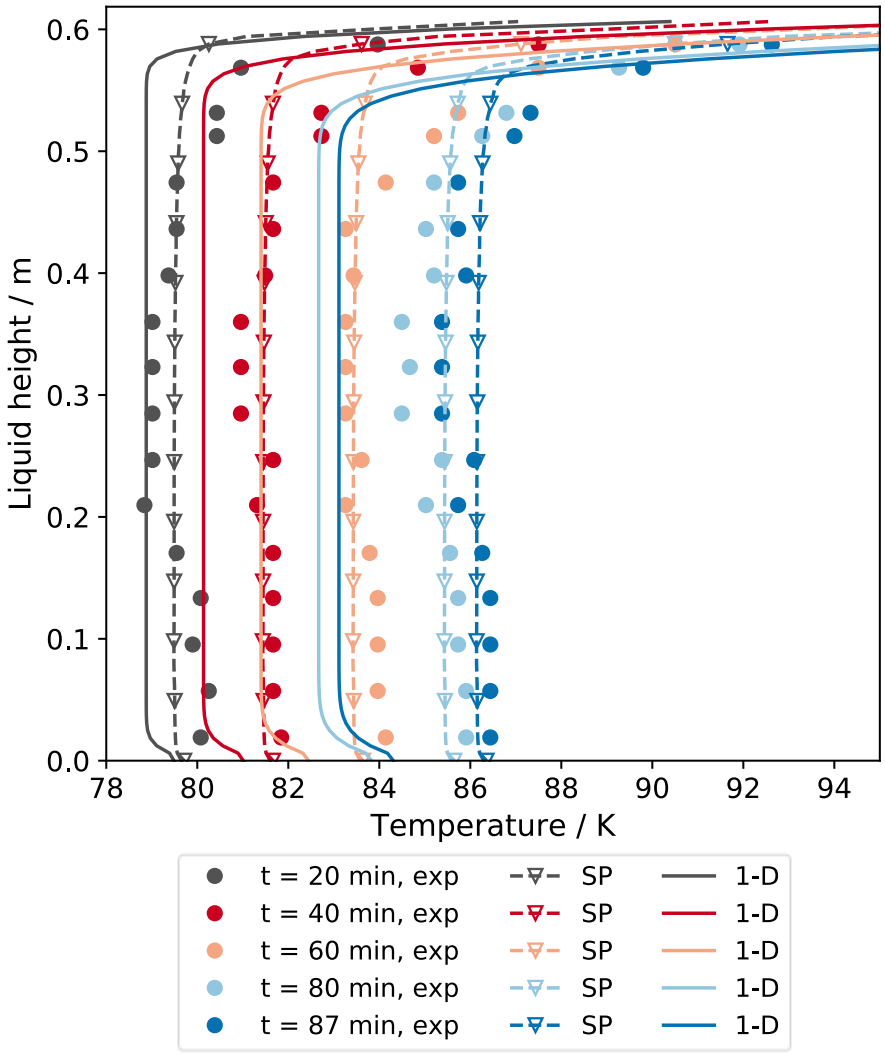

Figure 8.12: Liquid temperature profiles during the non-isobaric evaporation of liquid nitrogen in a 10 L storage tank filled at 80% of its capacity. The experimental results of Kang et al. [3] are depicted in solid circles, where different colours represent different time-steps from 20 to 87 minutes after the beginning of the evaporation. The liquid temperature profiles obtained using the CFD-SP (SP) model and 1-D models are depicted in dashed lines with empty triangle markers and solid lines, respectively.

Figure 8.12 shows that the 1-D model underpredicts liquid bulk heating and overpredicts the extent of thermal stratification. Additionally, in the 1-D model an unphysical temperature gradient is observed. This is a consequence of the heat conduction boundary condition at the tank bottom. As the velocity profile in the 1-D model is not solved, the modelling of natural convection in this scenario using a volumetric source term yields an inaccurate temperature profile. The lower average liquid temperature predicted by the 1-D model produces a higher liquid heat ingress, $\dot{Q}_{\mathrm{L,in}} = U_{\mathrm{L}} A_{\mathrm{L}} (T_{\mathrm{a}} - \bar{T}_{\mathrm{L}})$. This contributes to the overestimation of the evaporation rate by

the 1-D model, and hence the pressure build-up, when compared against Kang et al. [3] experimental results.

Figure 8.13 depicts the vapour temperature (x-axis) as a function of vapour height (y-axis) during evaporation of LN_2 corresponding to Scenario K1 in Table 8.2. This Scenario comprises the evaporation of liquid nitrogen in a 10 L storage tank filled at 80% of its capacity. The temperature profiles obtained with the 1-D and CFD-SP models are compared against Kang et al. [3] experimental results for the high liquid filling (LF = 0.80) scenario. The CFD-SP model overpredicts the average vapour temperature in more thanks 30 K, and the overestimation increases with time. This is a consequence of the pseudo-steady state approximation taken for the vapour phase in the CFD-SP model. This overestimation is much larger than the overestimation observed for Seo and Jeong [2] validation, see section 8.2. This is a consequence of the longer storage period, higher heat fluxes and higher pressure build-up. In contrast, the 1-D model predicts the vapour temperature profiles more accurately than the CFD-SP model, see Figure 8.12. The inclusion of more realistic physics for the vapour in the 1-D model explains its better agreement with the experimental temperature profiles.

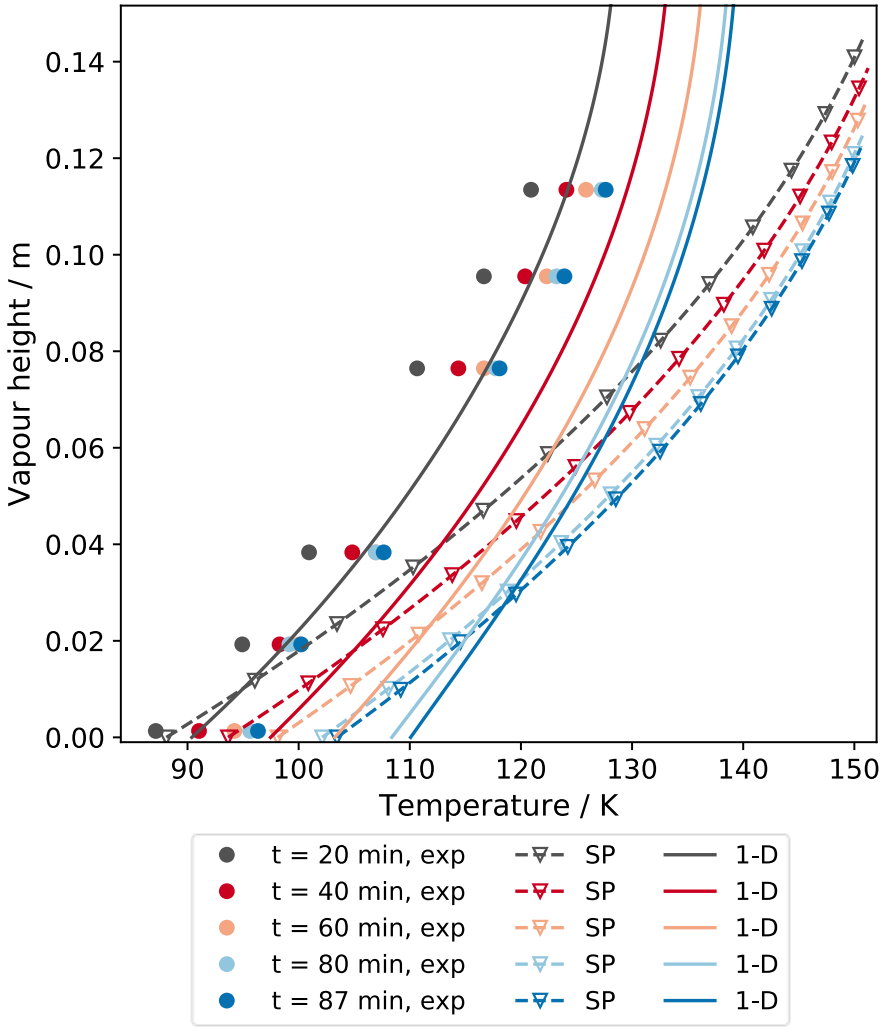

Figure 8.13: Vapour temperature profiles during the non-isobaric evaporation of liquid nitrogen in a 10 L storage tank filled at 80% of its capacity. The experimental results of Kang et al. [3] are depicted in solid circles, where different colours represent different time-steps from 20 to 87 minutes after the beginning of the evaporation. The vapour temperature profiles obtained using the CFD-SP (SP) model and 1-D models are depicted in dashed lines with empty triangle markers and solid lines, respectively.

As the 1-D model accurately predicts the experimental vapour temperature, see Figure 8.13, the overprediction of pressure build-up by this model is a consequence of inaccuracies in the liquid heat transfer sub-model. Figure 8.12 shows that the temperature gradient below the vapour-liquid interface is similar between the CFD-SP and 1-D models. Therefore, the 1-D model seems not to introduce a significant error on the modelling of the interface to liquid heat transfer. On the other hand, the 1-D model produces an unrealistically hot liquid just below the interface, see Figure 8.12. This is a consequence of the neglecting of natural convection in that region. As the simulation progresses, this region will be spuriously superheated with respect to the saturation

temperature. The superheating of this region will drive an instantaneous evaporation of some of the liquid, see Eq. (6.28), rapidly rising the pressure of the vapour. Therefore, the 1-D model overpredicts the evaporation and pressurization rates for Scenario K1 because of not resolving natural convection in the liquid phase.

8.3.2 Scenario K2: 10 L cryogenic storage vessel filled to 50% of its capacity

Figure 8.14 shows the pressure build-up during the evaporation of LN_2 in a 10 L storage tank filled at 50% of its capacity, corresponding to Scenario K2 in Table 8.2. Both equilibrium and non-equilibrium models without wall boiling underpredict the experimental pressure, see Figure 8.14. The equilibrium model predicts a final pressure rise 100% higher than the 1-D model. This phenomenon was also observed for the high liquid filling scenario K1, see Figure 8.11, but in a smaller magnitude. For intermediate liquid filling (LF = 0.50) the vapour space is larger, and the difference on average vapour temperature predicted by the equilibrium and non-equilibrium models increases. This explains the higher pressure difference for intermediate liquid filling.

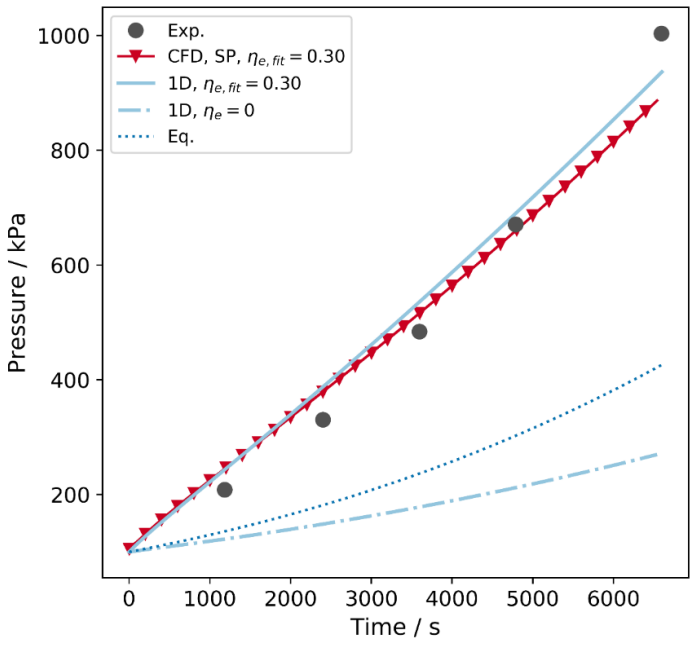

Figure 8.14: Pressure evolution during the non-isobaric evaporation of liquid nitrogen in a 10 L storage tank filled at 50% of its capacity. The experimental results of Kang et al. [3] are depicted in grey circles. Light-blue lines depict the pressure obtained with the equilibrium model (dotted), 1-D model without wall boiling (dot and lines) and 1-D model with wall boiling (solid line). Red lines depict the results obtained with the single-phase model (CFD-SP) using the calculated (dashed lines) and fitted (solid lines) evaporative fraction coefficient η_e.

Both CFD-SP and 1-D models with an evaporative fraction coefficient of $\eta_{e,fit}$ = 0.30 provided a reasonable prediction of the experimental pressure for Scenario K2, see Figure 8.14. The CFD-SP and 1-D models also showed an excellent agreement on pressure evolution, which contrasts to the disagreement observed for high liquid filling see Figure 8.11. For intermediate liquid filling, both models underestimate the non-linearity on the pressure rise, Figure 8.14. This contrasts to what was observed for the same liquid filling on Seo and Jeong experiments, [2] see Figure 8.5. The worse qualitative agreement on pressure rise in Scenario K2 suggests that for broader pressure ranges, some assumptions of both models are less valid. For instance, the latent heat of vaporisation will decrease with pressure, from 199 kJ kg^{-1} at 0.1 MPa to 152 kJ kg^{-} at 1 MPa. In the development of both models, the latent heat of vaporisation has been assumed constant, which will underestimate the pressure rise. Secondly, the evaporative fraction coefficient and the spatial profile of vapour wall heat flux will vary with time more significantly than for Scenario S2. This is a consequence of a larger vapour superheating and liquid thermal expansion in Scenario K2 and will be further explored in the subsequent paragraphs.

Figure 8.15 depicts the liquid temperature profile (x-axis) as a function of liquid height (y-axis) for Scenario K2. In Figure 8.15, the profiles predicted by the CFD-SP and 1-D models are compared against the experimental profiles obtained by Kang et al. [3] for five different representative timesteps. The 1-D model underpredicted the temperature of the liquid bulk and overpredicted the temperature gradients at the vapour-liquid interface and tank roof, see Figure 8.12. For intermediate liquid filling, the underprediction increases with time, and it is larger than for the high liquid filling Scenario K1, see Figure 8.12.

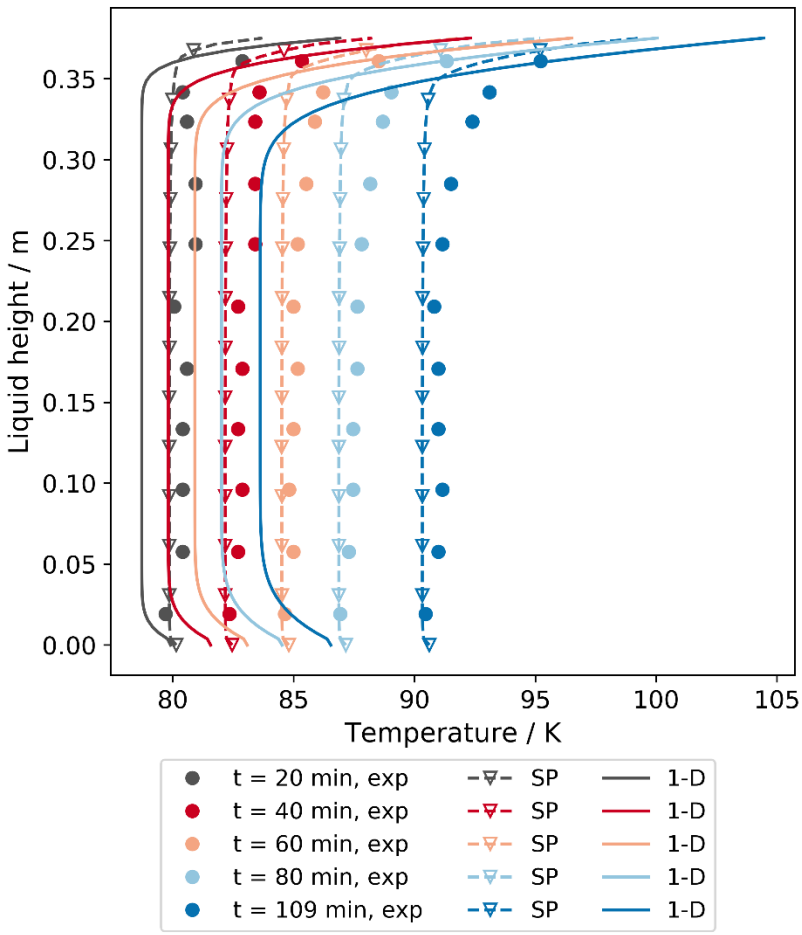

Figure 8.15: Liquid temperature profiles during the non-isobaric evaporation of liquid nitrogen in a 10 L storage tank filled at 50% of its capacity. The experimental results of Kang et al. [3] are depicted in solid circles, where different colours represent different time-steps from 20 to 87 minutes after the beginning of the evaporation. The liquid temperature profiles obtained using the CFD-SP (SP) model and 1-D models are depicted in dashed lines with empty triangle markers and solid lines, respectively.

This underestimation of liquid bulk temperature by the 1-D model for intermediate liquid filling, see Figure 8.15, seems to contradict the hypothesis of smaller impact of convection for smaller liquid fillings. To further understand the phenomenon, the temperature profiles predicted by the CFD-SP model for this Scenario are examined. Figure 8.15 shows that the CFD-SP model also underpredicted the liquid bulk temperature for intermediate liquid fillings. This contrasts with the good predictions of liquid temperature observed for LF = 0.80, see Figure 8.12. Additionally, the experimental results for Scenario K2 show a smaller thermal stratification below the liquid interface, see Figure 8.15. This suggests that both wall boiling and evaporation drive convective currents in the liquid that mix the liquid more efficiently than what is predicted by the CFD-SP model.

Figure 8.16 depicts the vapour temperature (x-axis) as a function of vapour height (y-axis) during the evaporation of LN_2 corresponding Scenario K2 on Table 8.2. The 1-D model provided a good agreement on the experimental temperature profiles, and the agreement improved with vapour height, see Figure 8.16. On the other hand, the CFD-SP model overestimated the vapour temperature up to 40 K for $z = 0.25\ l_V$, and the overestimation increased with height. The remainder of the temperature profile predicted by the CFD-SP model has not been displayed because of its lack of fit. Surprisingly, the poor estimation of vapour temperature using the CFD-SP model has negligible effects on the good estimation of the experimental pressure. As the pressure rises with the increase in average vapour temperature, the CFD-SP model predicts an increase on average vapour temperature of roughly 15 K. This increase is roughly the same increase in the experimental average vapour temperature. The different vapour heat ingresses predicted by both CFD-SP and 1-D is models does not significantly affect the agreement in pressure rise, see Figure 8.14. This shows that for Scenario K2, the pressure rise is mainly a consequence of the accumulation of evaporated liquid in the vapour phase.

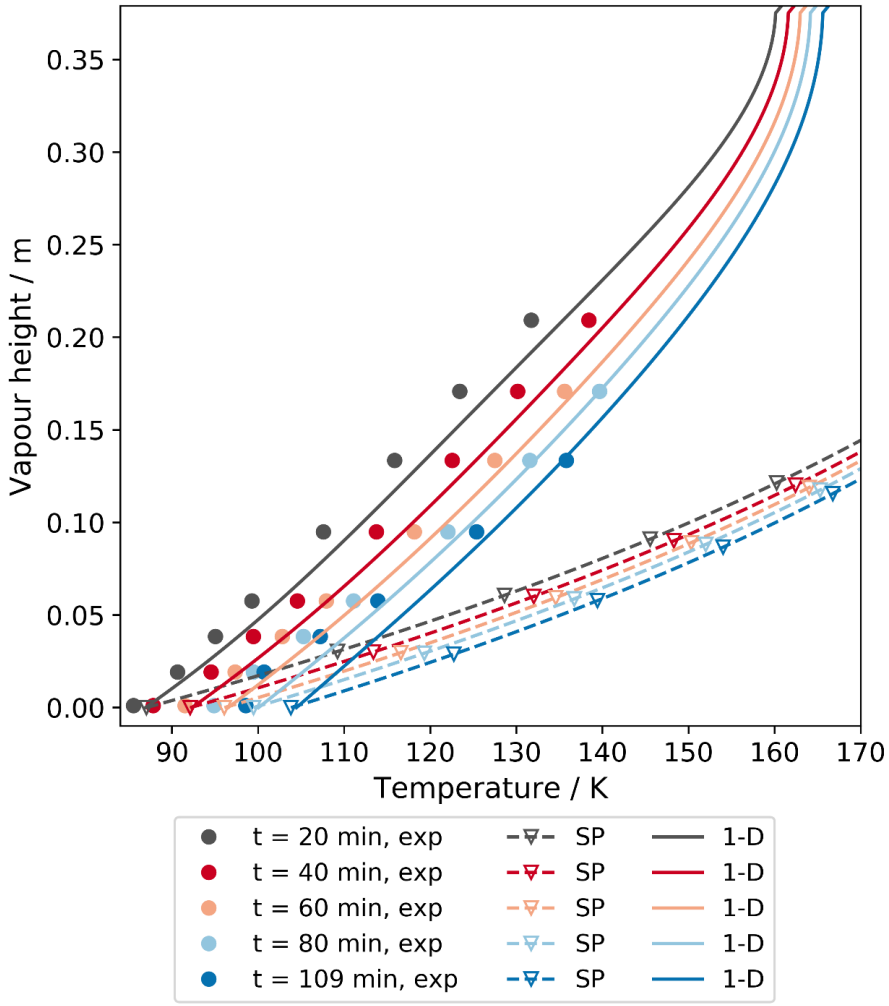

Figure 8.16: Vapour temperature profiles during the non-isobaric evaporation of liquid nitrogen in a 10 L storage tank filled at 50% of its capacity. The experimental results of Kang et al. [3] are depicted in solid circles, where different colours represent different time-steps from 20 to 87 minutes after the beginning of the evaporation. The vapour temperature profiles obtained using the CFD-SP (SP) model and 1-D models are depicted in dashed lines with empty triangle markers and solid lines, respectively.

8.3.3 Scenario K3: 10 L cryogenic storage vessel filled to 30% of its capacity

Figure 8.17 depicts the pressure build-up during the evaporation of liquid nitrogen in a 10 L storage tank filled at 30% of its capacity, see Scenario K3 on Table 8.2. Both equilibrium and 1-D models with no wall boiling underpredicted the experimental pressure rise, see Figure 8.17 . This phenomenon is similar to what has been observed for Scenarios K1 and K2, see Figure 8.11 and Figure 8.15 . However, for this scenario of low liquid filling the pressure predicted by the equilibrium model is much higher than the one predicted by the 1-D model with no wall boiling, see Figure 8.17. This confirms that for lower liquid fillings, the liquid is better mixed, and its pressurization behaviour

approaches the predictions of the equilibrium model. The improving agreement on experimental pressure obtained by the equilibrium model with decreasing liquid filling was also observed for the validation against Seo and Jeong [2] experiments, see section 8.2.

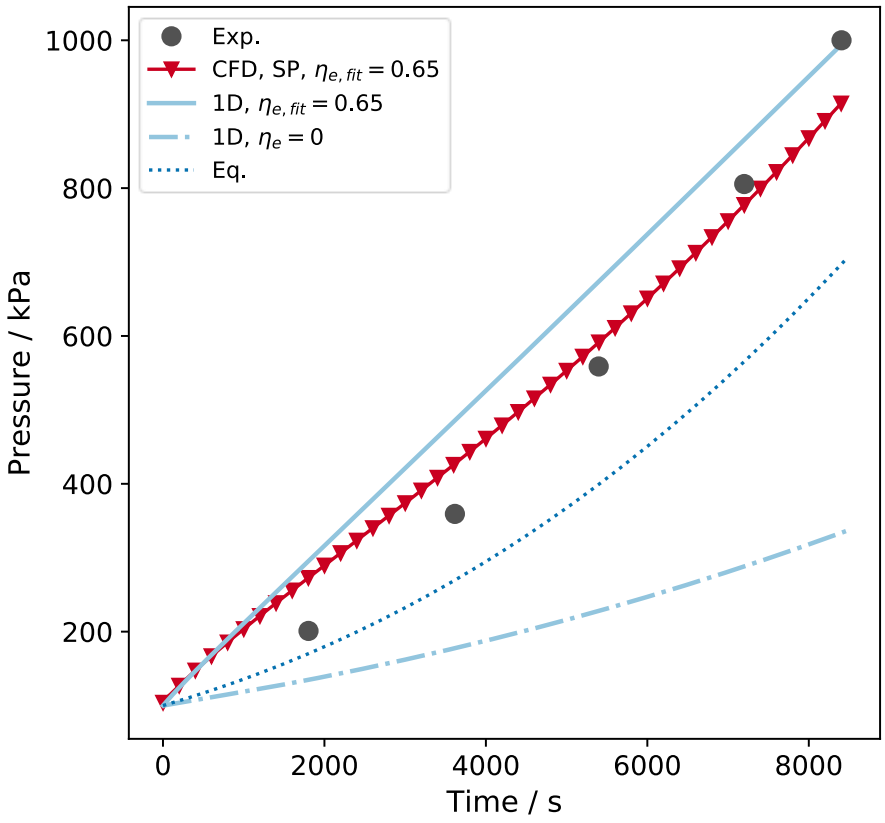

Figure 8.17: Pressure evolution during the non-isobaric evaporation of liquid nitrogen in a 10 L storage tank filled at 30% of its capacity. The experimental results of Kang et al. [3] are depicted in grey circles. Light-blue lines depict the pressure obtained with the equilibrium model (dotted), 1-D model without wall boiling (dot and lines) and 1-D model with wall boiling (solid line). Red lines depict the results obtained with the single-phase CFD-SP model (CFD, SP) using the calculated (dashed lines) and fitted (solid lines) evaporative fraction coefficient η_e.

Figure 8.17 shows that both the CFD-SP and 1-D models predict the experimental pressure with a reasonable accuracy by using a fitted value of the evaporative fraction of $\eta_{e,fit}$ = 0.65. However, both models fail to predict the non-linearity of the pressurization rate. This phenomenon was also observed for intermediate liquid fillings, see Figure 8.14 and Figure 8.17, and it is mainly a consequence of the time dependence of the evaporative fraction in the experiments. Figure 8.18 depicts the liquid temperature (x-axis) as a function of liquid height (y-axis) for Scenario K3. For low liquid fillings, the 1-D model predicted a reasonable temperature profile near the vapour liquid

interface. In contrast, the 1-D model significantly underpredicted the liquid bulk temperature and provided an unrealistic temperature profile near the bottom of the tank. As discussed previously, the lack of fit on liquid temperature by the 1-D model is a consequence of neglecting the mixing driven by wall boiling and phase change. Figure 8.18 also shows that although the CFD-SP model was able to predict the well mixing of the liquid bulk, it underpredicted the magnitude of the liquid bulk heating.

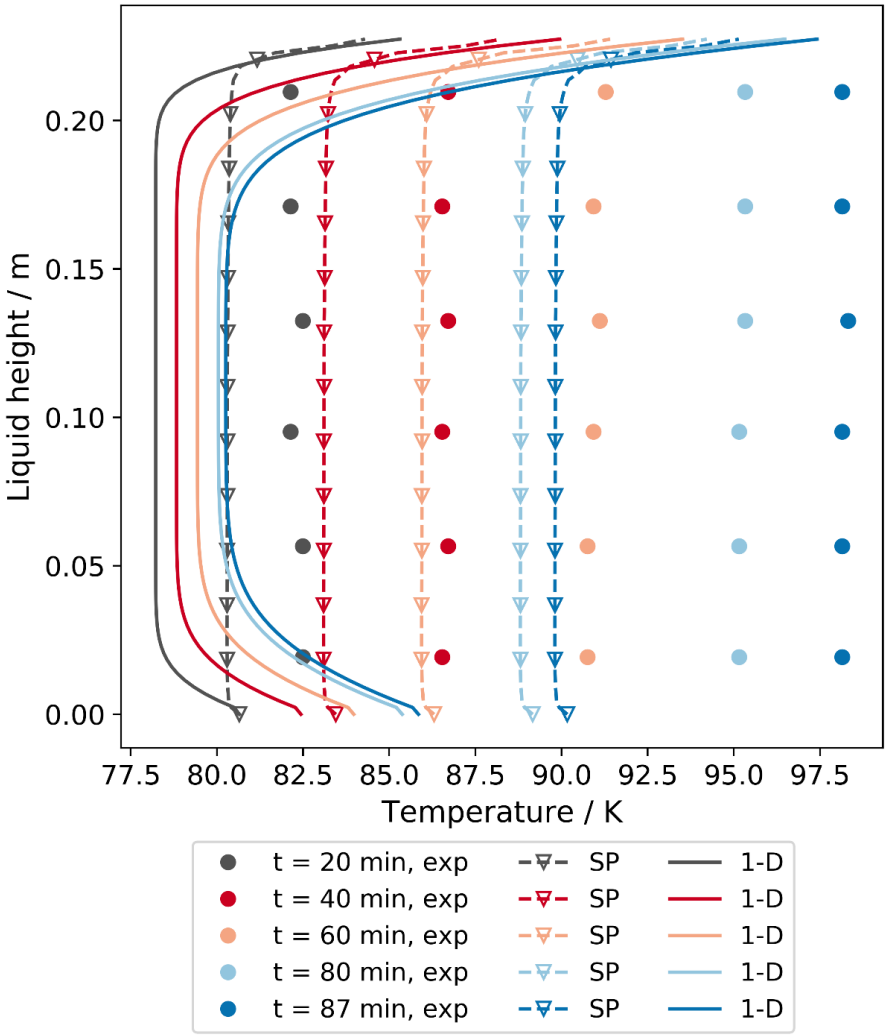

Figure 8.18: Liquid temperature profiles during the non-isobaric evaporation of liquid nitrogen in a 10 L storage tank filled at 30% of its capacity. The experimental results of Kang et al. [3] are depicted in solid circles, where different colours represent different time-steps from 20 to 87 minutes after the beginning of the evaporation. The liquid temperature profiles obtained using the CFD-SP (SP) model and non-isobaric 1-D models are depicted in dashed lines with empty triangle markers and solid lines, respectively.

Figure 8.19 depicts the vapour temperature (x–axis) as a function of vapour height (y-axis) for Scenario K3. The 1-D model accurately captured Kang et al. [3] experimental temperature profile after t = 20 min of evaporation, see Figure 8.19. As

time progressed, the 1-D model underpredicted the vapour temperature, particularly far from the interface. This suggests a larger influence of convection in the vapour phase far from the vapour-liquid interface. The enhanced mixing owing to convection was observed for isobaric evaporation under low liquid fillings in Chapter 5 and by Huerta and Vesovic [16]. It is worth noting that near the vapour liquid interface, the 1-D model predicted accurately the temperature gradient at all timesteps. This allows the accurate estimation of the vapour to interface heat transfer rate, see Eq. (6.20). The CFD-SP model overestimated the experimental vapour temperature by more than 100 K, and it is not displayed in Figure 8.19. This is a consequence of the pseudo-steady state assumption, as discussed in 8.3.2.

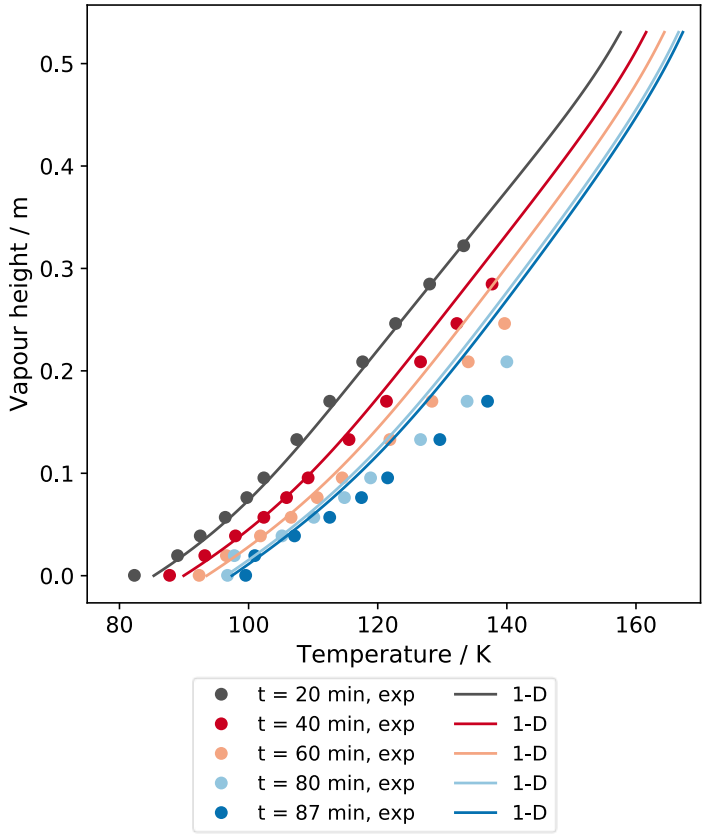

Figure 8.19: Vapour temperature profiles during the non-isobaric evaporation of liquid nitrogen in a 10 L storage tank filled at 30% of its capacity. The experimental results of Kang et al. [3] are depicted in solid circles, where different colours represent different time-steps from 20 to 87 minutes after the beginning of the evaporation. The vapour temperature profiles obtained using the non-isobaric 1-D model are depicted solid lines.

8.3.4 Summary of findings

- The developed non-isobaric evaporation models have been partially validated against Kang et al. [3] experimental results for LN_2 evaporation in 10 L storage tank, by fitting the evaporative fraction parameter.
- The CFD-SP and 1-D models predicted pressurization rates with an AAD < 15% error in a pressure range of 0.1 to 1.0 MPa and heat fluxes spanning from 24 to 700 $Wm^{-2}K^{-1}$.
- The CFD-SP and non-isobaric 1-D models accurately predicted the liquid temperature gradient below the vapour liquid interface.
- The pseudo-steady state assumption for vapour phase heat transfer in the CFD-SP model significantly overestimates the vapour temperature, particularly for low liquid fillings.
- For moderate heat fluxes and broad pressure ranges, natural convection and wall boiling become more relevant.

8.4 LN_2 non-isobaric evaporation in an 8 m^3 storage tank

In sections 8.2 and 8.3, the non-isobaric evaporation models were validated for the evaporation of liquid nitrogen in small storage tanks. The validation against Kang et al. [3] experiments suggests that multiphase momentum transfer enhances liquid heat transfer in the vertical direction. In particular, the mixing induced by wall boiling and interfacial phase change was more pronounced for low liquid fillings, see subsection 8.3.3. Therefore, the accuracy of the models on predicting vapour and liquid temperature profiles rapidly decreased with the increase in heat flux and vapour length, even for a 10 L lab-scale storage tank. Nevertheless, 1-D and CFD-SP models provided a reasonable fit for the pressure evolution for lab-scale storage tanks. The good agreement achieved by the simpler 1-D and CFD-SP models opens the possibility of enormous efficiency gains. For instance, the simulations for Seo and Jeong [2] experiments required between 24 and 144 h for the multiphase model, 0.5 h for the single-phase model and 15 s for the 1-D model. Thus, for the prediction of pressure, the CFD-SP and

1-D models provide a reduction in simulation time between 2 and 4 orders of magnitude compared against the multiphase model across their range of applicability.

For larger storage tanks, convection and multiphase momentum transfer is expected to be even more significant than for lab-scale tanks. Consequently, it is not clear whether the non-isobaric models are accurate for the storage of cryogen in large tanks. In contrast to the lab-scale tanks, there is very limited experimental data for the non-isobaric evaporation of cryogenic liquids for industrially sized storage tanks ($V_T >$ 0.1 m^3). Furthermore, there is a total absence of experimental data for vapour and liquid velocity profiles inside the tank. This is crucial to understand the influence of convection and multiphase momentum transfer. The objective of this section is to validate the assumptions used in the CFD-SP and 1-D models against the multiphase (CFD-MP) model for large scale storage. In particular, the effect of multiphase flow during the non-isobaric evaporation of liquid nitrogen in an 8 m^3 cylindrical storage tank will be investigated. This will allow us to determine the range of applicability of the simpler non-isobaric evaporation models.

In sections 8.2 and 8.3, it was not possible to fully validate the multiphase model because of the presence of vertical thermal stratification in the solid wall. In this section, the heat transfer coefficient will be set to be a homogeneous value for all the domain boundaries, $U_L = U_V$. Through this simplification, the evaporative fraction coefficient in the CFD-SP and 1-D models, η_e, will no longer be confounded with non-homogeneous wall heat flux and will effectively represent wall boiling. Additionally, setting $U_L = U_V$ provided a simple and efficient basis to compare different isobaric evaporation models [16], as it was demonstrated in section 5.2 and Chapter 5. In this section, the same storage tanks and liquid fillings that were investigated for isobaric storage in subsections 5.2.1 and 5.2.2 will be considered. This will allow to contrast the transport phenomena during non-isobaric evaporation against the isobaric storage scenario. In subsection 8.4.1, the non-isobaric evaporation of liquid nitrogen in an 8 m^3 storage tank filled at 97% of its capacity is investigated. In subsection 8.4.2, the non-isobaric evaporation of liquid nitrogen in the same tank is considered filled only at 30% of its capacity. Finally, in subsection 8.4.3 a summary of findings is presented.

8.4.1 Scenario N1: High initial liquid filling

Scenario N1 consists of the non-isobaric evaporation of liquid nitrogen in an 8 m^3 storage tank filled at 97% of its capacity. The mid-scale tank (V_T = 8 m, d_o = 1.63 m, d_i = 1.605 m, $U_L = U_V$ = 0.019 Wm^2K^{-1}) corresponds to the same tank considered for Scenario 1 in Chapter 5 of isobaric evaporation. The storage tank has been assumed to be perfectly insulated at the tank roof and tank bottom, $q_{roof} = q_{bot} = 0$. Therefore, it is assumed that the heat ingress from the surroundings heats and evaporates the cryogens only through the walls. For this non-isobaric evaporation scenario, the tank valve is closed allowing the pressure to build-up during the storage period. This contrasts with Scenario 1, where a fixed pressure was set in the opened valve allowing the evaporated cryogen to be continuously removed as BOG. Figure 8.20 shows the temperature and velocity profiles for the liquid phase obtained with the multiphase model for scenario N1 after (a) 720 s and (b) 7,200 s the beginning of the evaporation. These two time-steps are representative of early and intermediate stages of non-isobaric storage.

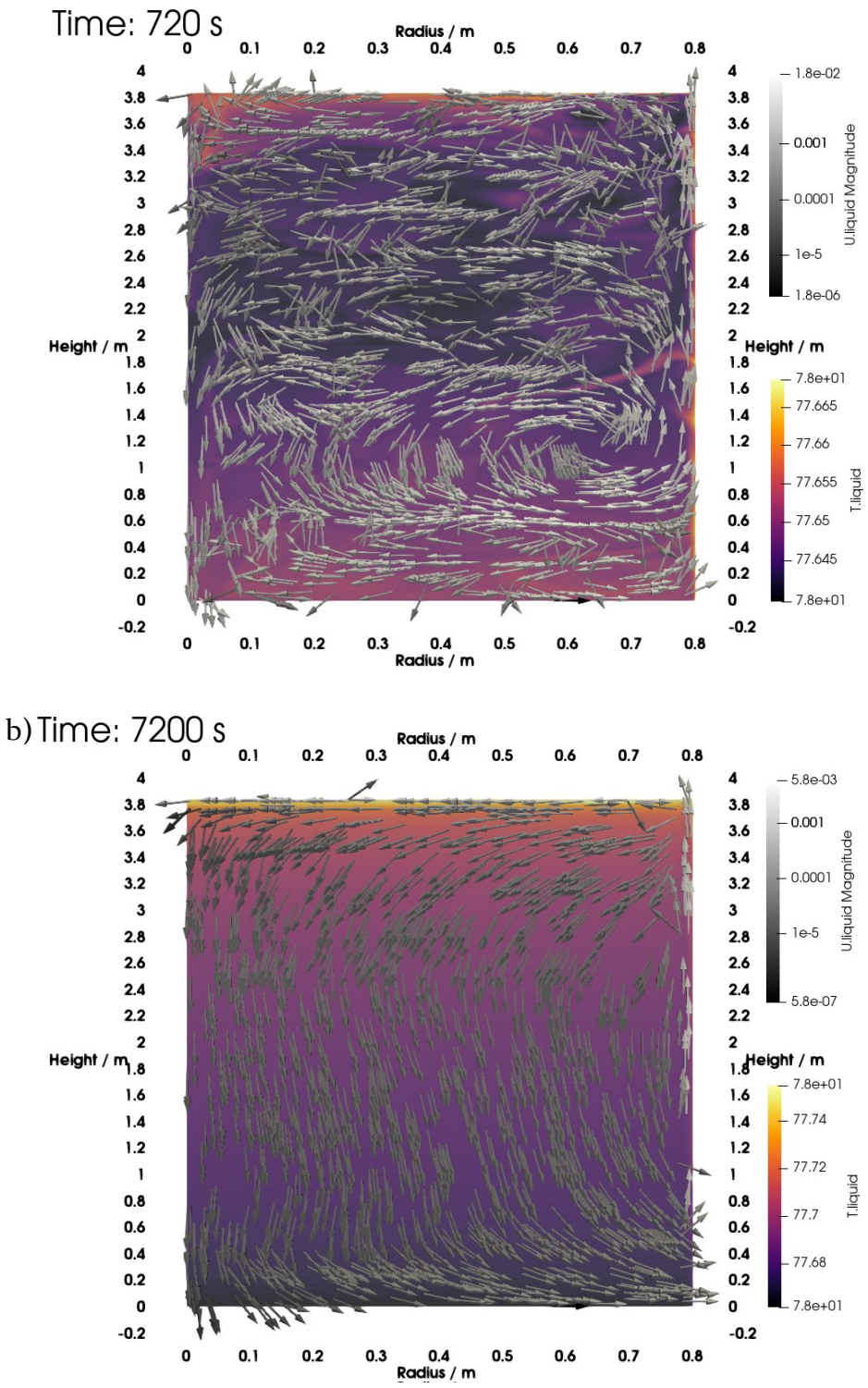

Figure 8.20: Velocity glyphs and temperature profiles in the liquid phase predicted by the CFD-MP model during the non-isobaric evaporation of LN_2 in an 8 m^3 storage tank. The simulations were run considering the tank initially filled to 97% of its capacity. Each subfigure depicts a timestep after (a) 720 s and (b) 7,200 s the beginning of the evaporation.

In Figure 8.20, the temperature profile is presented as the coloured background, while the velocity profile is depicted by arrow glyphs. This presentation style is consistent with the CFD results presented in subsections 5.2.1-5.2.3 for isobaric evaporation, and it will be followed for scenario N2 in subsection 8.4.2. Figure 8.20a depicts that after 720 s of evaporation, the velocity and temperature fields have a strong spatial dependence. However, the maximum velocity was small (~ 2 cm s^{-1}) as well as the temperature difference (~ 0.03 K). Vortical and recirculating structures emerge in the totality of the liquid domain, efficiently mixing the liquid, see Figure 8.20a. At this early stage of evaporation, regions of low temperature appear in the centre of the domain. In contrast, high temperatures are found at the tank bottom, tank wall and near the vapour liquid interface.

Figure 8.20a shows that after 720 s from the beginning of the evaporation, a buoyancy driven flow begins to establish in the liquid phase in the region near the tank wall ($r = R_T$ = 0.8 m). The flow circulates upwards from the bottom to the top of the tank, as consequence of wall heating. At this time-step, a boundary layer near the tank wall emerges, which is the only clear flow structure in Figure 8.20a. As vertical thermal stratification has not been developed yet in Figure 8.20a, it is difficult to assess whether the flow structures will disappear with time. The maximum liquid velocities are not found in the boundary layer but inside the vortical structures within the liquid domain, see Figure 8.20a. This suggests that the timestep t = 720 s is representative of a strong transient period.

Figure 8.20b shows that after 7,200 s of evaporation, a small vertical temperature gradient is established in the liquid domain. The velocity profiles are simpler than the strong transient profiles at t = 720 s, see Figure 8.20a. In the thermally stratified region just below the interface, a thin anticlockwise loop is observed. Below this region, an anti-clockwise circulation typical of pure buoyancy driven flows in cylindrical enclosures is observed [17]. The maximum velocities are small are observed near the tank wall (|v| ~ 0.6 cm s^{-1}) and below the vapour-liquid interface (|v| ~ 0.1 cm s^{-1}), see Figure 8.20b. In the tank wall boundary layer ($\delta_{BL} = 0.98R_T < r < R_T$), the maximum velocities are observed around z = 2.4 m, while near the interface the velocity decreases as natural convection dampens the buoyancy driven flow. Below the vapour-liquid

interface, the flow does not simply circulate inwards. At r = 0.3 m and r = 0.7 m, the r-velocity sign changes near the vapour-liquid interface. This phenomenon is attributed to the drag force exerted by the vapour on the liquid. This drag force is a consequence of the vapour velocity profile just above the vapour-liquid interface. We will examine vapour phase temperature and velocity profiles in the second half of this subsection.

To further understand multiphase flow effects on heat and momentum transfer in the liquid, the simpler CFD-SP model is considered as base of comparison. In the CFD-SP model, multiphase momentum transfer is neglected, while multiphase heat transfer is simplified. Wall evaporation and interface condensation were modelled as source and sink energy terms at the wall and below the interface, respectively. Therefore, the CFD-SP model allows to examine how the liquid temperature profile would be when only natural convection and vertical stratification drive fluid flow. The multiphase velocity and temperature profiles presented in Figure 8.20 correspond to the superposition of the solutions provided by the CFD-SP model and the interfacial heat and momentum transfer sources calculated by the CFD-MP model.

Figure 8.21 shows the temperature and velocity profiles for the liquid phase obtained with the CFD-SP model for scenario N1 after (a) 720 s and (b) 7,200 s the beginning of the evaporation. Figure 8.21a shows the emergence of a boundary layer flow near the tank wall. The liquid flow ascends through the boundary layer until it reaches the vapour-liquid interface. Then, it circulates inwards below the interface until it reaches the tank axis, and then circulates back to the tank wall. This pattern is repeated three times, constituting three stages of circulation. These three stages of circulation are a consequence of buoyancy driven flow coupled with thermal stratification. This flow pattern is in qualitative agreement with Das et al. [17] experiments of natural convection in the cubical enclosure filled with liquid.

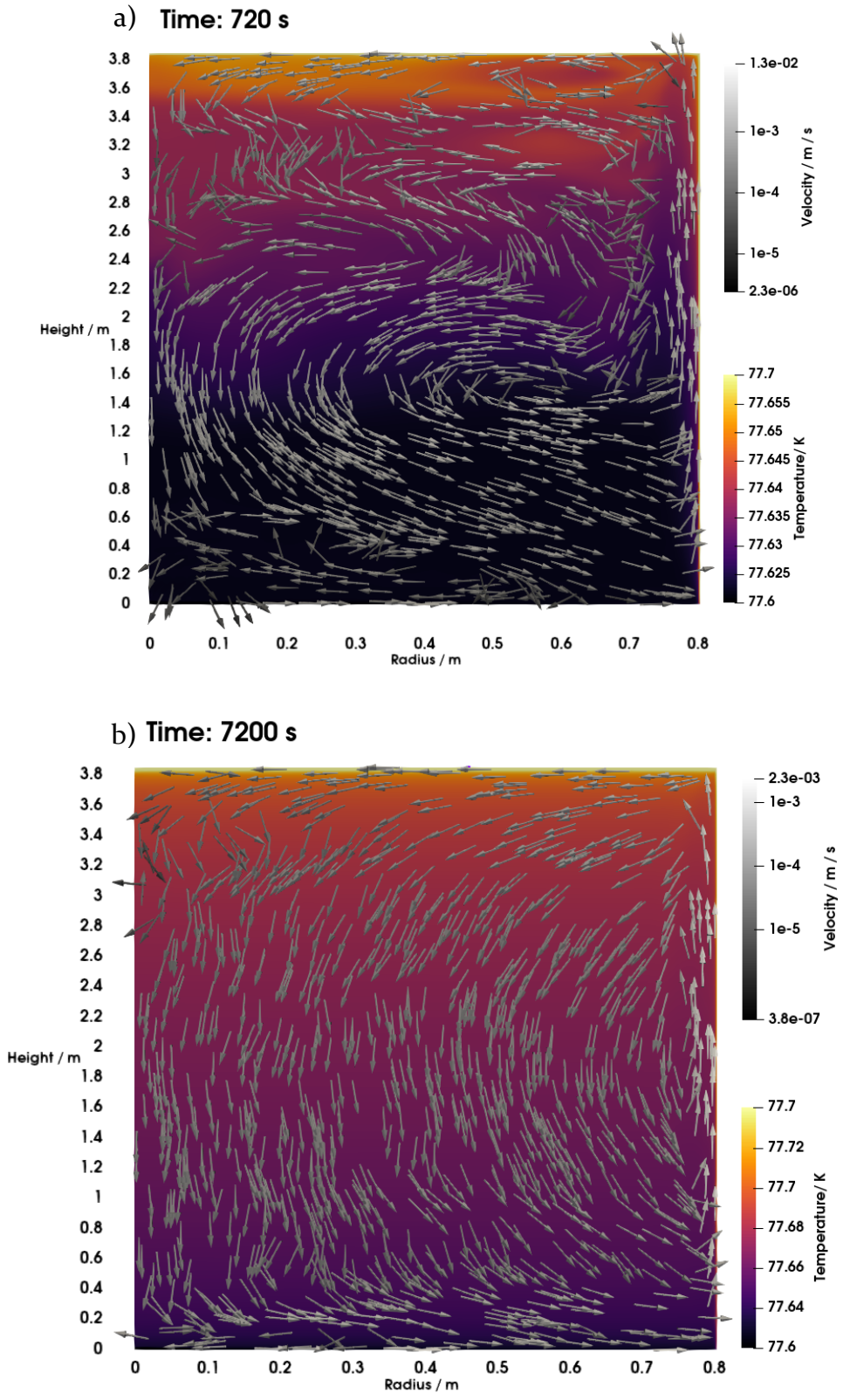

Figure 8.21: Velocity glyphs and temperature profiles in the liquid phase predicted by the CFD-SP model during the non-isobaric evaporation of LN_2 in an 8 m^3 storage tank. The simulations were run considering the tank initially filled to 97% of its capacity. Each subfigure depicts a timestep after (a) 720 s and (b) 7,200 s the beginning of the evaporation.

Figure 8.21a shows that at t = 720 s the maximum velocities predicted by the CFD-SP model are slightly smaller than the ones predicted by the multiphase model ($\max|\mathbf{v}_L^{SP}| \sim 1.3$ cm s^{-1} < $\max|\mathbf{v}_L^{MP}| \sim 1.8$ cm s^{-1}). The temperature gradient develops downwards as a consequence of natural convection and the increase of saturation temperature, see Figure 8.21a. This contrasts with the slightly more efficient mixing observed in the velocity and temperature profiles predicted by the multiphase model, see Figure 8.20a. Finally, the zero-velocity boundary condition at the vapour-liquid interface in the CFD-SP model produces a negative radial velocity for all radial positions immediately below the interface, see Figure 8.20a. This is not the case for the profiles predicted by the multiphase model, where a flow complex pattern is observed below the interface, see Figure 8.20b.

Figure 8.21b shows that the velocity and temperature profiles produced by the CFD-SP model at t = 7,200 s are very similar to the ones produced by the multiphase model, see Figure 8.20b. The velocity profiles in the CFD-SP model show that the circulating loops below the interface observed at t = 720 s disappear with the onset of thermal stratification. This is expected as in the CFD-SP model, thermal stratification dampens the buoyancy driven flow, which is the main driver of fluid flow. In contrast, the multiphase model predicts a stable recirculation just below the vapour-liquid interface, see Figure 8.20. As thermal stratification is present in both simulations, the flow structure below the interface in the CFD-MP model is driven by the vapour drag. The maximum velocities predicted by the CFD-SP model are very small (~ 0.23 cm s^{-1}) and occur at the wall boundary layer. The maximum velocities predicted by the CFD-MP model are larger (~ 0.58 cm s^{-1}) but of the same order of magnitude. These velocities occur near the tank wall and below the vapour-liquid interface. In the CFD-MP model, the slightly larger velocities produce a slightly better mixed liquid with a less steep temperature gradient than in the CFD-SP model, see Figure 8.20b, Figure 8.21b. This demonstrates that the multiphase effect of vapour drag at the vapour-liquid interface slightly enhances vertical heat transfer in the liquid.

Figure 8.22 depicts the liquid temperature (x-axis) as a function of the liquid height (y-axis) during the non-isobaric evaporation of liquid nitrogen in an 8 m^3 storage tank filled at 97% of its capacity. It was found that the radial variation of the temperature

is minimal in both CFD-SP and multiphase models. Hence, the vertical temperature profiles are representative of the whole liquid domain and have been evaluated at an infinitesimal annulus located at $r = R_T/2$. In scenario N1, the wall evaporation rate was extremely small, and the evaporative fraction constituted just 0.1% of the liquid heat ingress. To simplify the comparison between evaporation models, no wall boiling (η_e = 0) has been assumed for the 1-D and CFD-SP models.

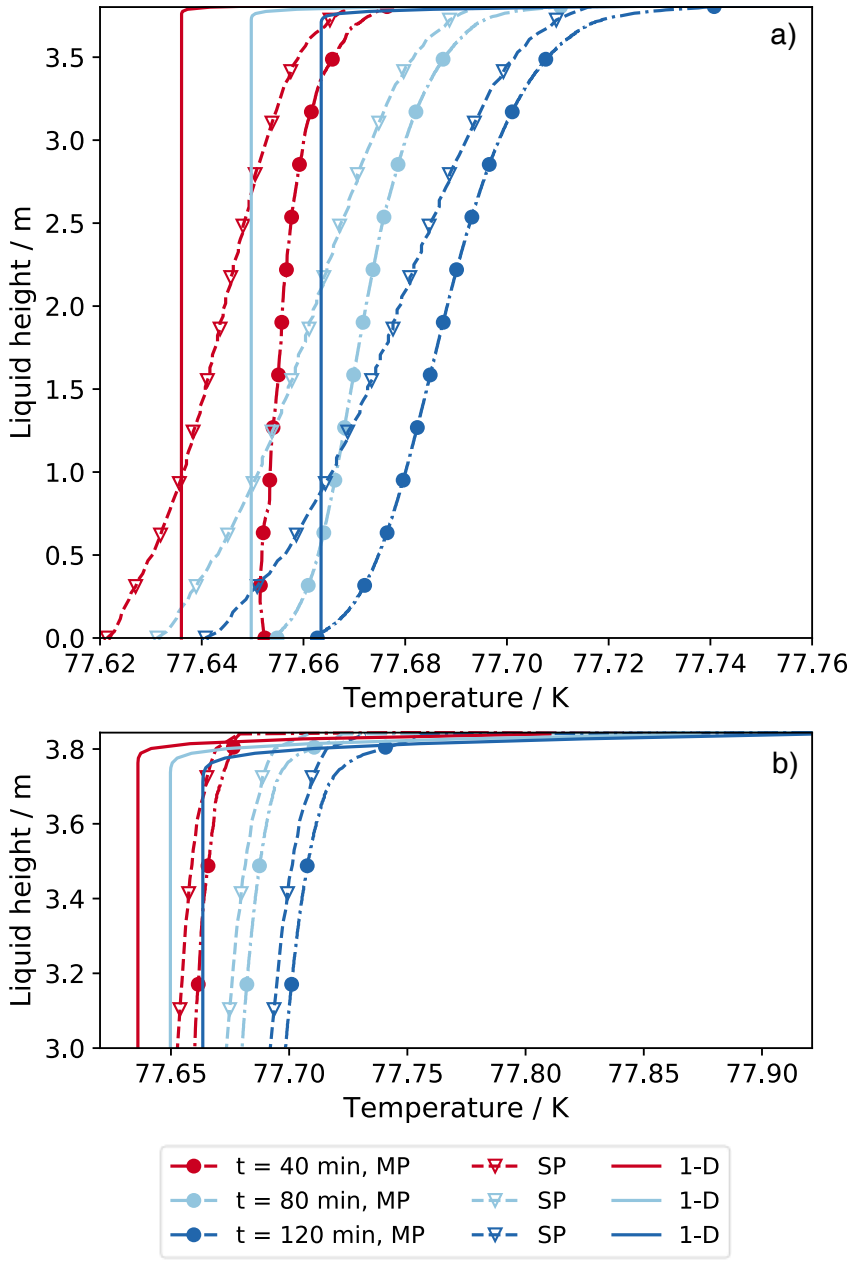

Figure 8.22: Liquid temperature as a function of liquid height during the non-isobaric evaporation of LN_2 in an 8 m^3 storage tank filled at 97% of its capacity. The profiles obtained with three models are depicted: CFD-SP (SP) and multiphase (MP) model at $r = R_T/2$, and by the 1-D model. Sub-figure (a) depicts the temperature at the liquid bulk, while sub-figure (b) depicts a zoom in of the thermally stratified layer below the vapour-liquid interface.

Figure 8.22a shows that in the liquid bulk, the CFD-MP predicts the highest liquid temperature at all timesteps. The CFD-SP model predicts lower liquid temperatures, although the vertical gradients are slightly larger. Hence, the CFD-SP model slightly underestimate the magnitude of convection in the liquid because of neglecting the vapour drag at the vapour-liquid interface. Figure 8.22a also shows that the 1-D model predicts a homogeneous temperature in the liquid bulk. The liquid temperature predicted by the 1-D model is lower than the temperatures predicted by the CFD-MP and CFD-SP models. Figure 8.22b shows a zoom-in of the region just below the vapour liquid interface for scenario N1. This figure depicts that the 1-D model predicts a temperature at the interface, $T_{\mathrm{L}}(z = 3.85\ \mathrm{m})$, slightly higher than the CFD-SP and CFD-MP models. Additionally, Figure 8.22b shows that just below the interface, the differences between the CFD-SP and CFD-MP models slightly increase. This is explained by the enhancement of liquid mixing just below the interface owing to vapour drag. Only the CFD-MP model is able to predict this effect, see z ~ 3.8 m in Figure 8.20a and Figure 8.21a.

Figure 8.23 shows the temperature and velocity profiles for the vapour phase obtained with the multiphase model for scenario N1 after (a) 720 s and (b) 7,200 s the beginning of the evaporation. Figure 8.23a shows complex velocity and temperature profiles, suggesting a strong transient period at 720 s. In contrast to what was observed for the liquid phase of scenario N1 in Figure 8.20a, vertical thermal stratification in the vapour is already noticeable. This is a consequence of the larger thermal diffusivity of the vapour compared with the liquid. The maximum velocities are of a similar magnitude to liquid phase velocities, $\max|\mathbf{v}_{\mathrm{V}}| \sim 1.4\ \mathrm{cm\ s^{-1}}$, and are observed in the region just above the interface. In the boundary layer adjacent to the tank wall and above the interface, the vapour velocities are of the order of 1 cm $\mathrm{s^{-1}}$. In the rest of the vapour domain, the velocities are lower than 0.1 cm $\mathrm{s^{-1}}$.

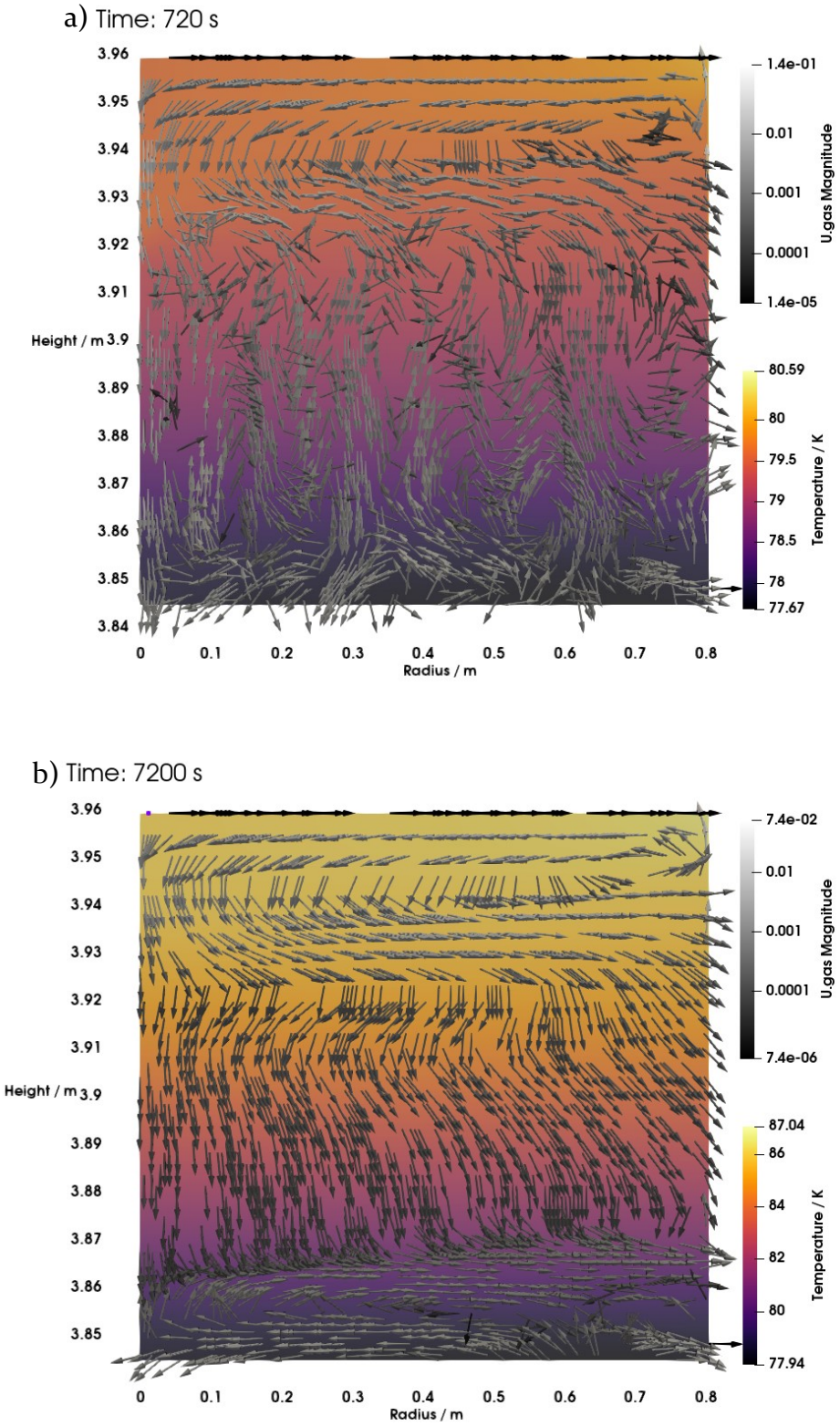

Figure 8.23: Vapour velocity glyphs and temperature profiles predicted by the CFD-MP model during the non-isobaric evaporation of LN_2 in an 8 m^3 storage tank filled to 97% of its capacity. Each subfigure depicts a timestep after (a) 720 s and (b) 7,200 s the beginning of the evaporation.

Figure 8.23b shows that after 7,200 s of the evaporation, the velocity profile in the vapour is different than at 720 s, Figure 8.23a. To facilitate the analysis, the vapour phase can be separated in two regions: a well-mixed layer above the interface (3.84 m < z < 3.87 m) and the vapour bulk (z > 3.87 m). Most vortical structures observed in the vapour bulk at 720 s disappear at t = 7,200 s, see Figure 8.23 a-b. This is a consequence of the development of the vertical temperature gradient, which increases from 1.6 K at t = 720 s to 4.8 K m^{-1} at t = 7,200 s. In contrast, the in the well-mixed layer, a stable clockwise circulation remains that efficiently enhances vapour heat transfer, see Figure 8.23 b. Above the circulation in the well mixed layer, the vapour circulates towards the tank wall. The maximum velocities emerge in the well-mixed layer (~ 0.7 cm s^{-1}) and near the tank wall boundary layer (0.3 cm s^{-1}).

The clockwise circulation above the vapour-liquid interface (z < 3.78 m) observed in Figure 8.23b is caused by the interplay of the wall boiling and interface condensation. The wall heat flux to the liquid phase drives wall boiling at an average evaporation rate of 1.4 g h^{-1}. Simultaneously, the increase in vapour temperature produced an in pressure, which led to condensation at the vapour-liquid interface at a rate 27.6 g h^{-1}. As the condensation rate at the interface is higher than the evaporation rate at the wall, the overall evaporation rate is -26.2 g h^{-1}. Hence, condensation is the dominant mechanism for scenario N1. In the region near the wall, the evaporated gas circulates towards the tank axis just below the interface until r = 0.1 m, see Figure 8.23b. At that point, the vapour flow is partitioned between a condensing flow near the axis centre line, and a flow that recirculates back to the walls. The condensation rate is maximum in the region near the tank axis, where the temperature is minimum. The circulation in the vapour side of the interface drags the liquid immediately below the interface. Thus, the vapour drag constitutes an interfacial momentum transfer source to the liquid phase, see Figure 8.20b.

Figure 8.24 shows the vapour temperature (x-axis) as a function of vapour height (y-axis) for scenario N1 at three different timesteps. The vapour temperature varied with radius less than 0.01 K. Hence, the infinitesimal annulus was located at $r = R_T/2$ to provide profiles consistent with the liquid temperature profiles depicted in Figure 8.22. Only the profiles obtained with the CFD-MP and 1-D models are depicted, as the CFD-

SP overpredicted the vapour temperature. This shows that the pseudo-steady state assumption is not appropriate for large tanks, even for high initial liquid fillings (LF = 0.97). Figure 8.24 shows that both CFD-MP and 1-D models predict a monotonic increase of vapour temperature with height and time. Both models are in excellent agreement between themselves, particularly far from the vapour-liquid interface.

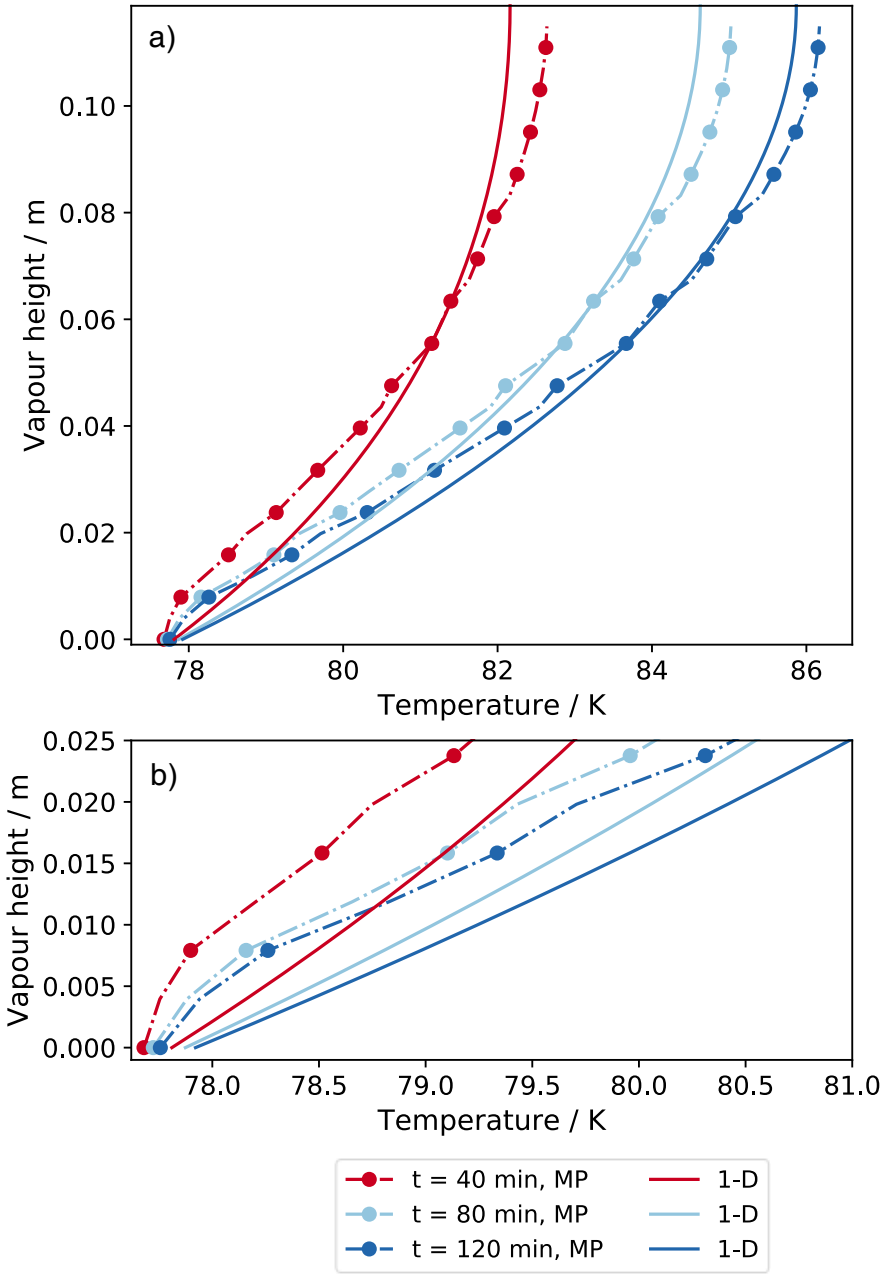

Figure 8.24: Vapour temperature as a function of vapour height during the non-isobaric evaporation of LN_2 in a storage tank filled at 97% of its capacity. The profiles obtained with two models are depicted: CFD-MP model at $r = R_T/2$, and by the non-isobaric 1-D model. Sub-figure (a) depicts the temperature at the vapour bulk, while sub-figure (b) depicts a zoom in of the region just above the vapour liquid interface.

The smaller temperature gradient predicted by the CFD-MP model just above the interface, see Figure 8.24b, can be attributed to interfacial phenomena. The interplay between evaporation, condensation and the recirculation just above the interface produce a vapour velocity with a positive vertical component, see Figure 8.23b. This component will induce heat advection in a direction opposite to heat conduction, thus, decreasing the temperature gradient at the vapour-liquid interface. The very good agreement between the CFD-MP and 1-D models far from the interface shows that this region is not significantly influenced by the interface. Thus, for high liquid fillings, the 1-D model developed in subsection 6.2.2 accurately predicts vapour temperature profiles during the non-isobaric evaporation of pure cryogens.

We finalise this subsection examining the pressure build-up predicted by the non-isobaric evaporation models for the scenario N1. Figure 8.25 shows the pressure build-up during the evaporation of liquid nitrogen in an 8 m^3 storage tank initially filled at 97% of its capacity. All models predicted a small pressure build-up. The highest pressure build-up was predicted by the 1-D model, reaching just 103.5 kPa after 2 hours of evaporation, see Figure 8.25. The minimum pressure build-up was predicted by the equilibrium model, where the pressure increased just 0.4 kPa during 2 hours of evaporation, see Figure 8.25. All models except the equilibrium model predict a rapid pressure build-up in the first 200 s of simulation. This rapid increase in pressure at the beginning of the evaporation is a consequence of the rapid vapour heating.

Following the rapid vapour heating period, the CFD-MP model predicted non-linear increase in pressure, monotonically transitioning from a convex to concave trend, until it reached 102.1 kPa after 2 hours of evaporation. The CFD-SP model predicted a higher pressure build-up than the CFD-MP model for t = 200 s to t = 6000s. Near the end of the storage period (t > 6000 s), the pressurization rate dP/dt predicted by the CFD-SP is in excellent agreement with the CFD-MP model.

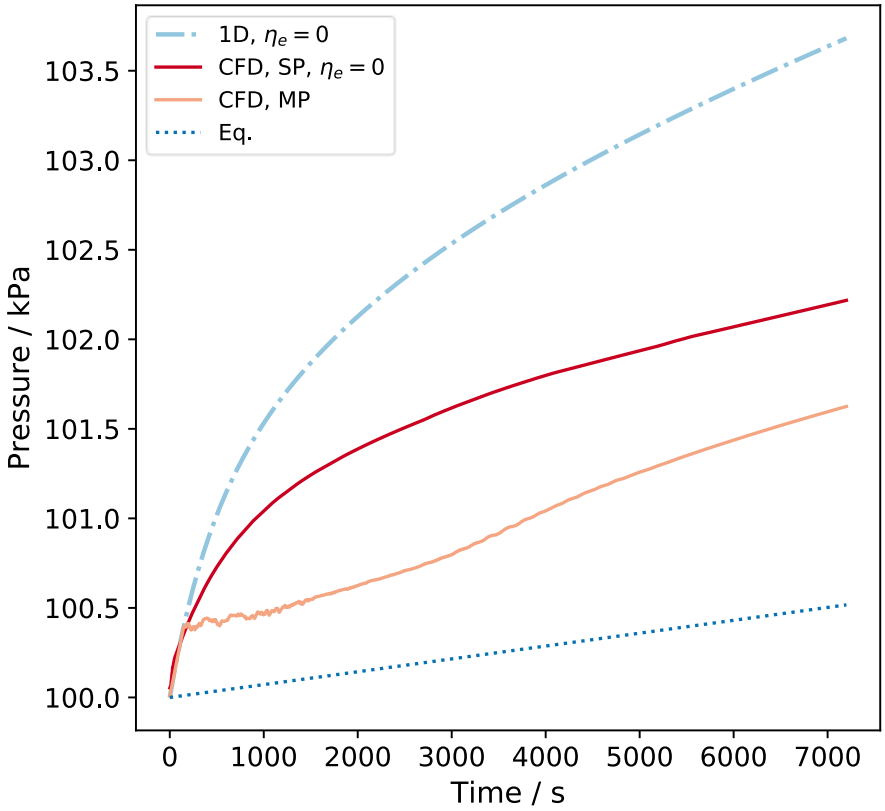

Figure 8.25: Pressure build-up during the non-isobaric evaporation of liquid nitrogen in an 8 m³ storage tank filled at 97% of its capacity. Light-blue lines depict the pressure obtained using the equilibrium model (dotted) and the 1-D model with no wall boiling (dot and lines). Red and yellow lines depict the pressure predicted by the CFD-SP model with no wall boiling and the CFD-MP model.

8.4.2 Scenario N2: Low initial liquid filling

Scenario N2 consists of the non-isobaric evaporation of liquid nitrogen in the same 8 m³ storage tank considered for scenario N1. All boundary conditions are the same, but now the tank is filled just at 30% of its capacity. As it was discussed in subsection 5.2.2, the lower liquid filling implies a 66% lower liquid heat ingress owing to the reduction of wet area. In scenario N2, the vapour length is 33 times larger, which is expected to drive stronger natural convection in the vapour phase [16]. For scenario N2, the condensation rate obtained with the multiphase model was 3 orders of magnitude higher than the wall evaporation. Hence, for simulating scenario N1 using the CFD-SP and 1-D models no wall evaporation ($\eta_e = 0$) has been assumed. Figure 8.26 shows the temperature and velocity profiles for the liquid phase obtained with the multiphase model for scenario N2 after (a) 720 s and (b) 7,200 s the beginning of the

evaporation. At both time-steps, the temperature and velocity profiles are substantially different to the ones observed for the high liquid filling scenario N1, see Figure 8.20.

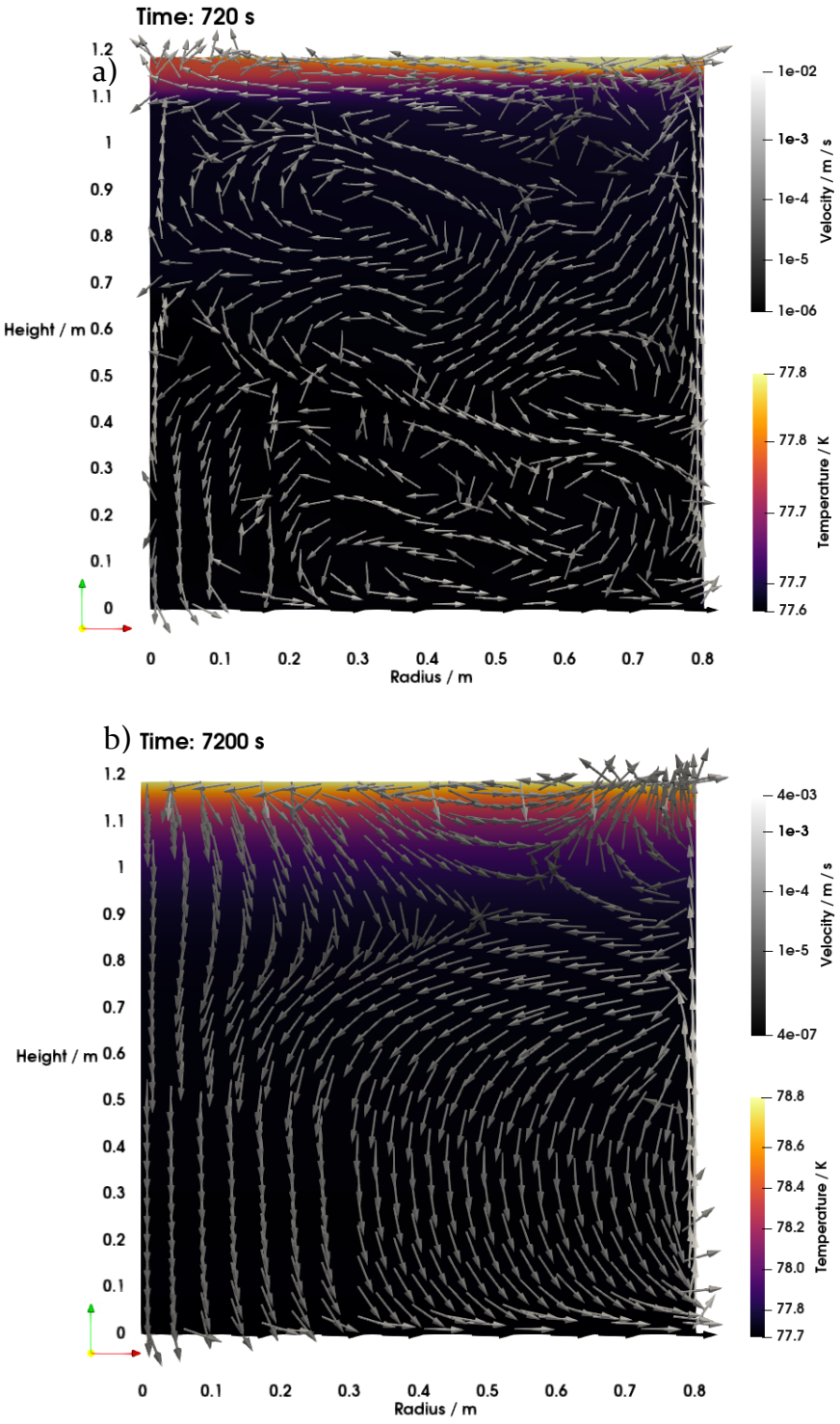

Figure 8.26: Liquid velocity glyphs and temperature profiles predicted by the CFD-MP model during the non-isobaric evaporation of LN_2 in an 8 m^3 storage tank filled to 30% of its capacity. Each subfigure depicts a timestep after (a) 720 s and (b) 7,200 s the beginning of the evaporation.

Figure 8.26a shows that after 720 s of evaporation, the maximum velocities in the liquid for scenario N2 are of the order of 1 cm s^{-1}. This maximum velocity is lower to the 1.8 cm s^{-1} observed for the high liquid filling scenario N1, see Figure 8.20. The maximum velocity is achieved at the tank wall. Figure 8.26a also shows that even at the transient timestep at 720 s, a sharp vertical temperature gradient develops just below the interface. In the liquid bulk far below the interface, the temperature is nearly spatially homogeneous. This strong stratification and poor mixing contrast to what was observed for scenario N1, see Figure 8.20, where the liquid currents effectively mixed the liquid. This is a consequence of the 69% smaller liquid length in scenario N2, which reduces the magnitude of natural convection in the liquid. In contrast to scenario N1, no recirculating structures driven by vapour drag are observed below the vapour-liquid interface for scenario N2, see Figure 8.26a and Figure 8.20a.

Figure 8.26b shows that after 7,200 s of evaporation for scenario N2, natural convection drives an anti-clockwise recirculation in the liquid bulk ($0 < z < 1$ m). Just below the vapour-liquid interface, a large vertical temperature gradient is observed, driven by the rapid increase of saturation temperature. The rapid increase of saturation temperature, driven by the increase in vapour pressure, drives the condensation of the vapour just above the interface. The condensation rate in scenario N2 is 889 g h^{-1}, 200 times the condensation rate in scenario N1 -0.4 g h^{-1}. The large condensation rate drives the descending flow observed just below the vapour-liquid interface, see Figure 8.26b.

In scenario N1, the evaporation rate was 20 times smaller than the interfacial condensation rate, see section 8.4.1, In contrast, in scenario N2 the wall boiling rate is just 0.2 g h^{-1}, which is 400 times smaller than the condensation rate. This explains the disruption of the recirculating structure below the interface in the low liquid filling scenario (N2), see Figure 8.20b, Figure 8.26b. In scenario N2, the velocities just below the interface are of the order of 0.4 cm s^{-1}. These velocities are similar in magnitude to the ones observed in scenario N1 (~0.6 cm s^{-1}) but have a larger vertical component. This is a consequence of the larger influence of the condensing vapour on liquid velocity and temperature profiles just below the interface.

The interaction between natural convection and interface condensation produces a complex flow pattern. Below the interface and in the region near the tank

axis (0 m < r < 0.3 m), the condensed liquid circulates downwards and feeds the circulation driven by natural convection, see Figure 8.26-b. In an intermediate region below the interface (0.3 m < r < 0.65 m), the condensed liquid divides in two currents. The first current joins the natural convection that governs the flow in the liquid bulk. The second current circulates near the interface towards the tank wall, producing a small narrow vortical structure. In the region below the interface and just next to the tank wall (0.65 m < r < 0.8 m), the condensed liquid flow does not affect the flow patterns, see Figure 8.26-b. Instead, in that region the liquid circulates upwards; a small amount is evaporated at the interface, and the remainder recirculates back towards the tank axis.

Figure 8.27 shows the temperature profiles and velocity glyphs for scenario N2 predicted by the CFD-SP model. Figure 8.27a shows that for t = 720 s, in the region below the vapour-liquid interface the CFD-SP model predicts different profiles than the multiphase model. In the region below the interface (1.05 m < z < 1.2 m), the multiphase model predicts a slightly larger temperature difference (~0.2K) than the CFD-SP model (~0.05K). This is a result of a faster increase in saturation temperature predicted by the multiphase model when compared with the CFD-SP model for scenario N2. For scenario N2, the multiphase model predicted a faster pressurization rate than the CFD-SP model. This contrasts to what was observed for scenario N1, see Figure 8.25, where the multiphase model predicted a smaller pressure build-up than the CFD-SP model. At the end of this subsection, the physics that explains the faster pressure build-up predicted by the multiphase model for low liquid fillings will be revisited.

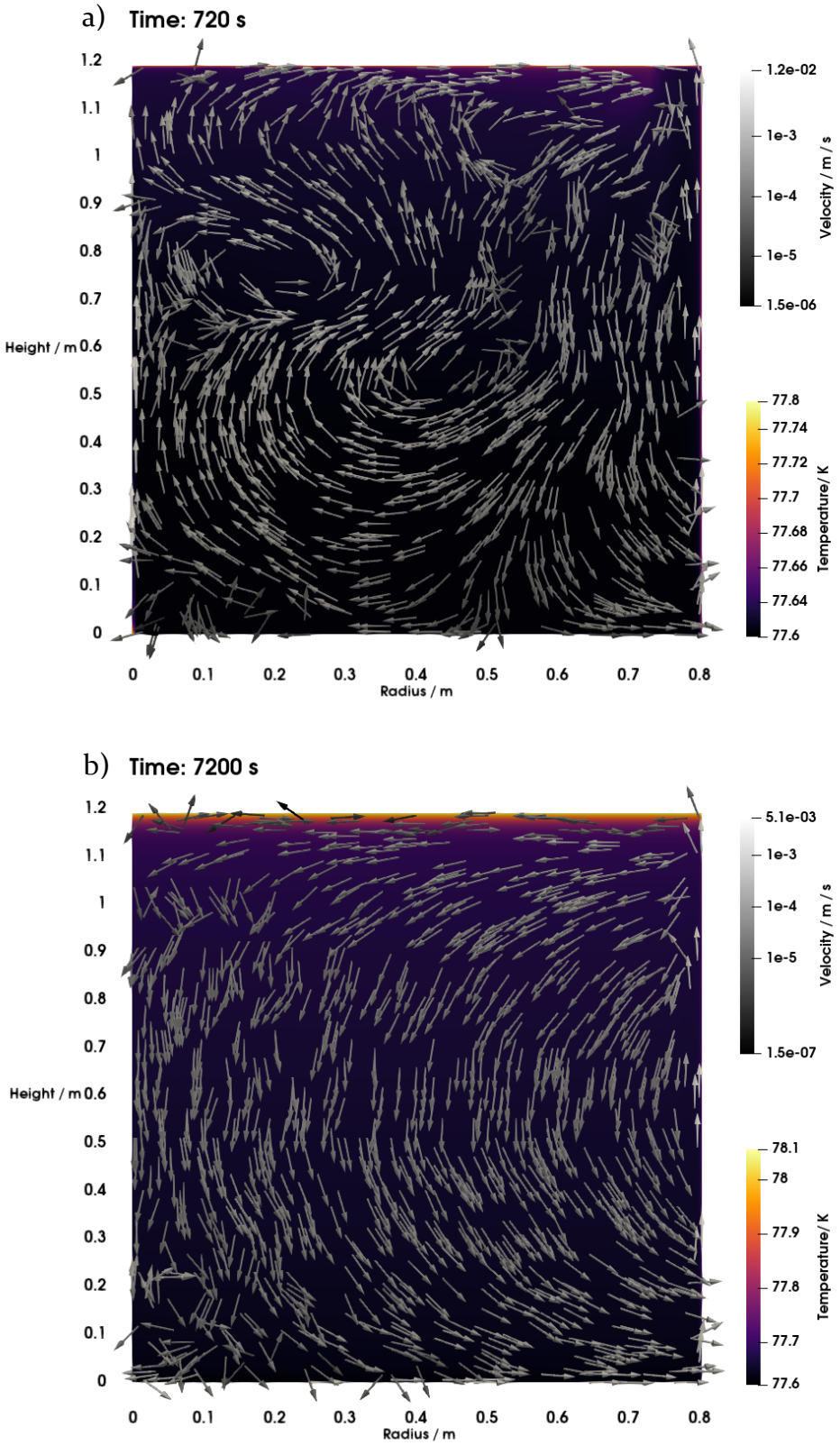

Figure 8.27: Liquid velocity glyphs and temperature profiles predicted by the CFD-SP model during the non-isobaric evaporation of LN_2 in an 8 m^3 storage tank filled to 30% of its capacity. Each subfigure depicts a timestep after (a) 720 s and (b) 7,200 s the beginning of the evaporation.

In the CFD-SP model, a vortical structure drives a clockwise circulation of the liquid near the vapour-liquid interface, see Figure 8.27a. The vortical structure arises from the interaction between the buoyancy-driven flow near the wall and the vapour-liquid interface. This structure is not observed in the multiphase-CFD model, see Figure 8.26a, as thermal stratification dampens the buoyancy driven flow. The maximum velocity predicted by the CFD-SP model (~ 1.2 cm s^{-1}) is of a similar magnitude to that predicted by the CFD-MP model. In contrast to the low liquid filling scenario, in scenario N2 convection drives stronger flows than interfacial momentum transfer at t = 720 s, see Figure 8.26a, Figure 8.27a.

Figure 8.27b shows that at t = 7,200 s the CFD-SP model predicts an anticlockwise recirculation pattern. The maximum velocities are observed at the tank wall and are of the order of 0.5 cm s^{-1}. On the other hand, just below the vapour-liquid interface the velocities are small (< 0.01 cm s^{-1}), suggesting a strong dampening of natural convection in that region. The maximum liquid subcooling, $\Delta T_{\mathrm{sc}} = T_{\mathrm{sat}} - T_{\mathrm{L}}(z = 0)$, at t = 7,200 s, is 0.5 K for scenario N2 compared with 0.1 K for scenario N1. This explains the much smaller velocity below the interface predicted by the CFD-SP model for scenario N2 when compared against scenario N1, see Figure 8.21b, Figure 8.27b. Far from the vapour-liquid interface, both the CFD-SP and CFD-MP models predict a recirculating pattern, see Figure 8.26a, Figure 8.27b. In contrast, below the vapour-liquid interface the CFD-SP model predicts a completely different velocity and temperature profile to those predicted by the CFD-MP model. The CFD-SP model predicts a larger temperature gradient below the interface and a lower temperature in the region (1.05 m < z < 1.2 m). This is a consequence of the neglect of the condensing flow and vapour drag at the interface by the CFD-SP model, as discussed previously.

Figure 8.28 depicts the liquid temperature (x-axis) as a function of the liquid height (y-axis) predicted by the non-isobaric evaporation models for scenario N2. As the radial variation of liquid temperature after 40 minutes of storage was negligible, the vertical temperature profiles were taken at an infinitesimal annulus $r = R_{\mathrm{T}}/2$. Figure 8.28a shows that the 1-D model predicted a spatially homogeneous temperature in the liquid bulk. Figure 8.28b depicts a zoom-in of the thermally stratified region and shows that the 1-D model predicts the smallest thermally stratified layer below the interface.

This is a consequence of the neglect of natural convection and multiphase momentum transfer by the 1-D model.

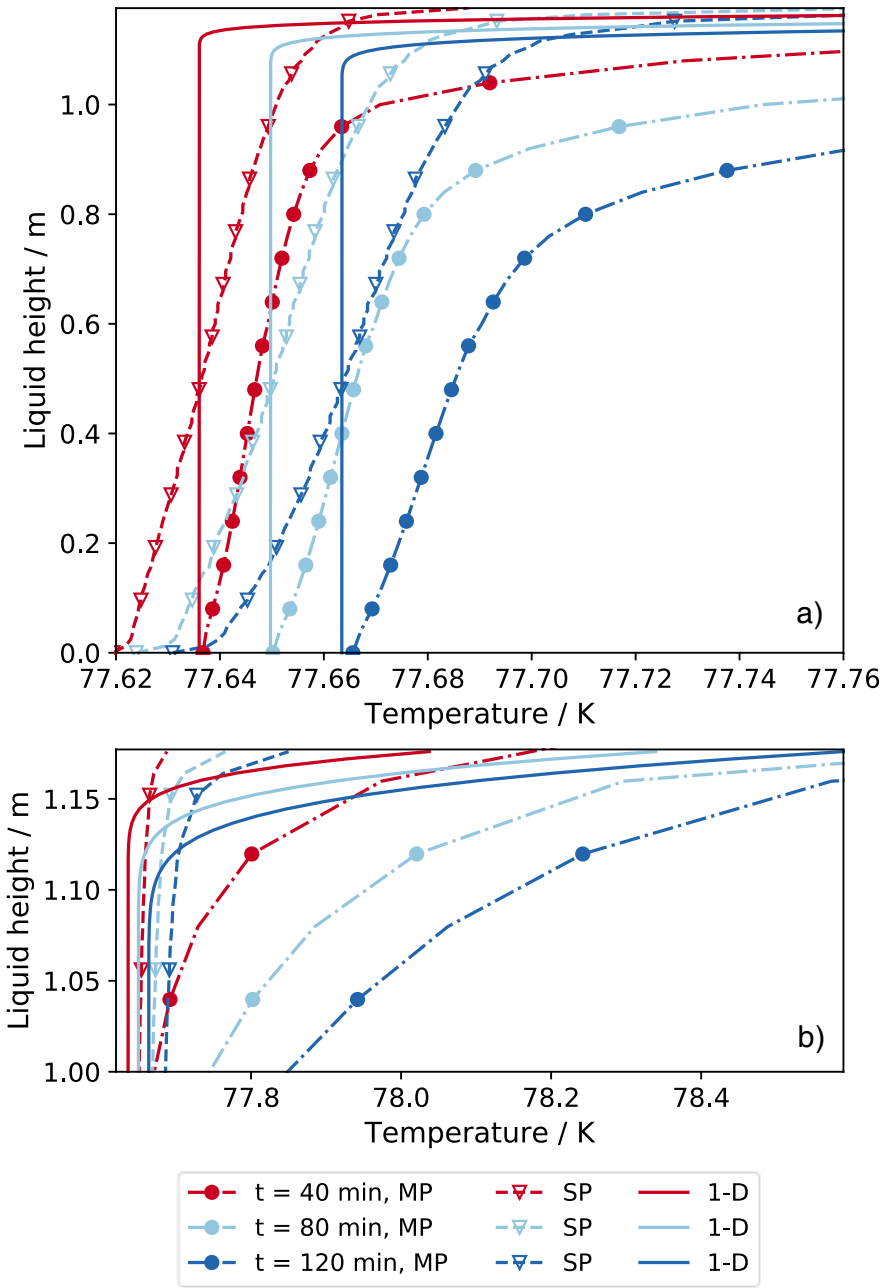

Figure 8.28: Liquid temperature as a function of liquid height during the non-isobaric evaporation of LN_2 in a storage tank filled at 30% of its capacity. The profiles obtained with three models are depicted: CFD-SP and CFD-MP model at $r = R_T/2$, and 1-D model, Sub-figure (a) depicts the temperature at the liquid bulk, while sub-figure (b) depicts a zoom in of the thermally stratified layer below the vapour-liquid interface.

Figure 8.28 shows that the CFD-SP model predicts lower liquid bulk temperatures and a thinner thermally stratified layer than the CFD-MP model for scenario N2. This is a consequence of the CFD-SP model neglect of the condensing flow

at the vapour-liquid interface. It is worth noting that for both high and low liquid filling scenarios (N1, N2), interfacial momentum transfer enhanced liquid mixing. In scenario N1, the condensation rate was moderate, and mixing was enhanced mainly by the shear stress produced by the vapour drag above the interface. In contrast, in scenario N2 the condensation rate was high, and mixing was enhanced by the momentum carried by the condensing liquid. The effect of interfacial momentum transfer was similar or higher than natural convection in the liquid, see Figure 8.20, Figure 8.26. Interfacial momentum transfer enhanced the mixing not only below the interface but in the whole liquid bulk. Importantly, below the vapour-liquid interface interfacial momentum transfer produced a less steep temperature gradient below the interface, decreasing the interface to liquid heat transfer by thermal conduction.

Figure 8.29 shows the temperature and velocity profiles for the vapour phase obtained with the multiphase model for scenario N2 after (a) 720 s and (b) 7,200 s of the beginning of the evaporation. The vapour temperature profiles at both time-steps are significantly different to the ones for the high liquid filling scenario N1, see Figure 8.23. Figure 8.29a shows that after 720 s of the beginning of the evaporation, a strong buoyancy driven flow near the tank wall is established. The maximum velocity is observed near the wall boundary layer (~ 3 cm s^{-1}), and an anticlockwise recirculation emerges. This contrasts with the complex vortical structures and slightly larger velocities (~ 7 cm s^{-1}) observed in scenario N1, see Figure 8.23a. The vortical structures above the interface observed for scenario N1 are no longer observed for scenario N2 at t = 720 s, see Figure 8.29. The maximum vapour superheating, $\Delta T_{\mathrm{sh}} = T_{\mathrm{V}}(z = l_{\mathrm{V}}) - T_{\mathrm{sat}}$, is 3 K for the high liquid filling scenario and 4K for the low liquid filling scenario after 720 s of evaporation, see Figure 8.29a, Figure 8.23a.

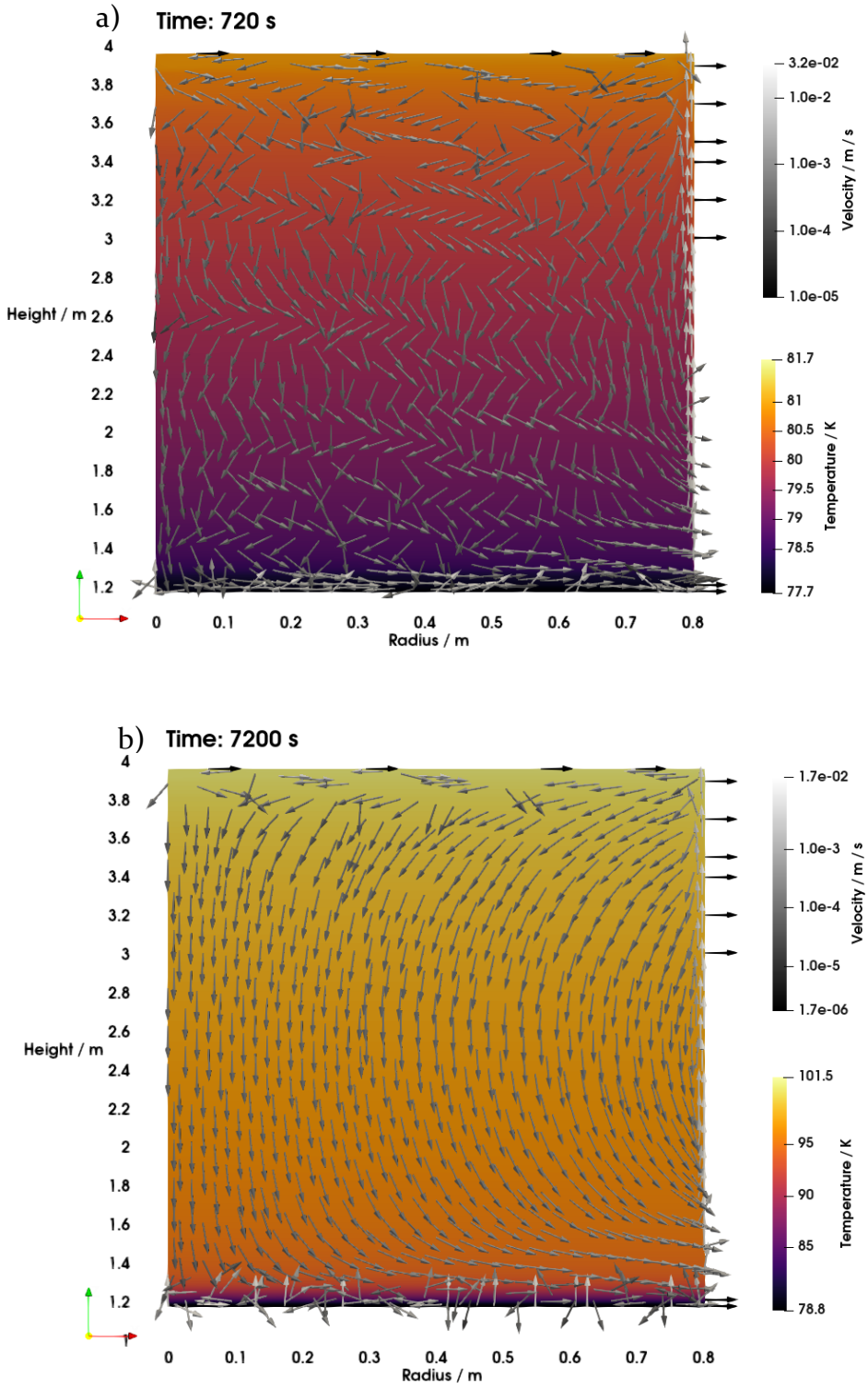

Figure 8.29: Vapour velocity glyphs and temperature profiles predicted by the CFD-MP model during the non-isobaric evaporation of LN_2 in an 8 m^3 storage tank filled to 97% of its capacity. Each subfigure depicts a timestep after (a) 720 s and (b) 7,200 s of the beginning of the evaporation.

Figure 8.29 shows that as time progresses from t = 720 s (a) to t = 7,200 s (b) in scenario N2, the vertical temperature gradient increases from 1.4 Km^{-1} to 8 Km^{-1}. Figure

8.29b shows that after 7,200 s of evaporation, the anticlockwise recirculation in the vapour becomes more evident. In the low liquid filling scenario, two different regions can be identified. Far from the interface (z > 1.3 m) natural convection efficiently mixes the vapour bulk and a weak vertical temperature gradient is established, see Figure 8.29b. Just above the vapour-liquid interface (1.19 m < z < 1.3 m), a very steep vertical temperature gradient is observed, and the vapour velocities are high, see Figure 8.29b.

The larger dominance of natural convection on vapour mixing was also observed for scenario S2 of isobaric storage, see section 5.1.2. However, the large temperature gradient just above the vapour-liquid is an emerging feature of non-isobaric storage. This gradient is explained by the absence of an effective advection through the vapour domain, and the condensing vapour flow in scenario N2. In contrast, in scenario S2 of 5.2.2, evaporation was modelled as a spatially homogeneous velocity boundary condition at the interface [16]. This velocity boundary condition at the interface in the vapour-CFD model prevents the formation of the boundary layer above observed in scenario N2, see Figure 8.29b. In the region just above the interface, vapour condensation owing to self-pressurization acts as an additional energy sink that cools the vapour.

Figure 8.30 shows the vapour temperature (x-axis) as a function of vapour height (y-axis) for scenario N2 at three different time-steps. In Figure 8.30, the vertical vapour temperature profiles were evaluated at the infinitesimal annulus located at $r = R_T/2$. This location is representative of an arbitrary radial location because the radial variation of temperature is negligible ($\partial T_V/\partial r << \partial T_V/\partial z$), see Figure 8.29. The CFD-SP model overpredicted vapour temperatures by more than 100 K owing to the pseudo-steady state assumption. As expected from the discussion in subsection 8.4.1 and in section 8.3, this assumption is not less valid for low liquid fillings. Hence, the vapour temperature profiles predicted by the CFD-SP model are not displayed in Figure 8.30.

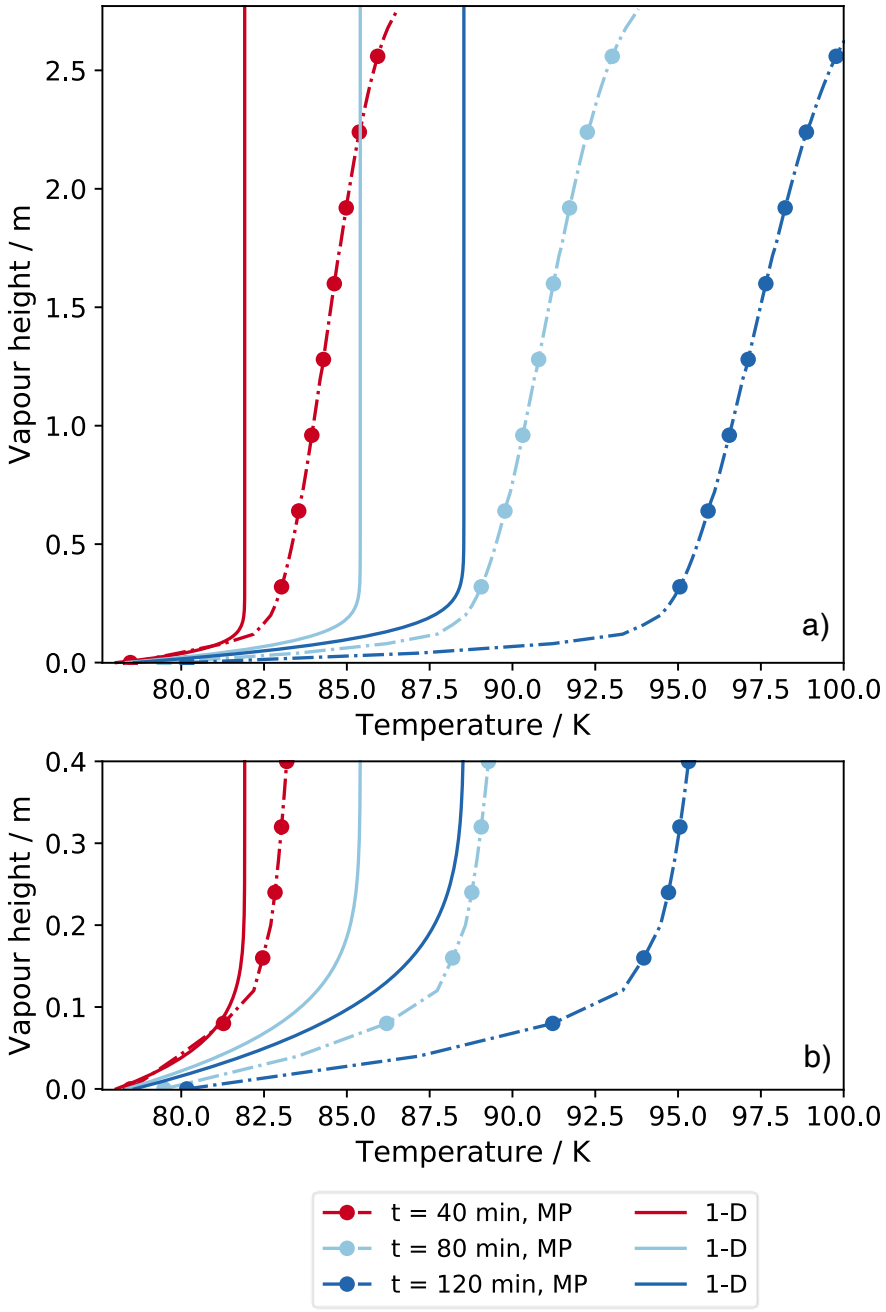

Figure 8.30: Vapour temperature as a function of liquid height during the non-isobaric evaporation of LN_2 in an 8 m^3 storage tank filled at 30% of its capacity. The profiles obtained with two different models are depicted: CFD-MP model at $r = R_T/2$, and by the non-isobaric 1-D model, Sub-figure (a) depicts the temperature at the vapour bulk, while sub-figure (b) depicts a zoom in of the region just above the vapour-liquid interface.

The temperature profiles for the low liquid filling scenario N2 show a subtle difference from the ones for the high liquid filling scenario N1, see Figure 8.24, Figure 8.30. Figure 8.30 shows that the multiphase model predicted the highest vapour temperature for scenario N2. Although the 1-D model predicted a lower temperature than the CFD-MP model, both models predicted a similar shape of the vapour

temperature profile far from the vapour-liquid interface. In contrast, just above the interface the CFD-MP model predicts a slightly larger vertical temperature gradient than the 1-D model, see Figure 8.30b. Although the difference in temperature gradients is small at t = 40 min, the difference increases with time. Nevertheless, just above the interface both models predict the presence of a boundary layer where conduction dominates heat transfer in the vapour. In the region far above the interface, the 1-D model predicts a roughly spatially homogeneous profile which displaces horizontally with time. This shape is a consequence of modelling natural convection as a volumetric source term. In contrast, the CFD-MP model predicts a gradual vertical temperature gradient as it fully resolves natural convection far from the vapour-liquid interface, see Figure 8.30.

In summary, for low liquid fillings, a boundary layer above the interface emerges which constitutes an efficient resistance to vapour phase heat transfer, see Figure 8.29-b. Far from the interface, the vapour temperature increases quickly owing to natural convection in a thermally stratified fluid, see Figure 8.29-b. The resistance to heat transfer at the interfacial boundary layer combined with natural convection explain the higher temperature predicted by the multiphase model for low liquid fillings, see Figure 8.30. The effect of natural convection, interfacial heat and interfacial momentum transfer on vapour temperatures are different for low and high liquid filling scenarios. For the high liquid filling scenario (N1), a narrow high-velocity, well mixed layer emerges because of the interplay between wall evaporation and interfacial condensation.

Figure 8.31 shows the pressure build-up during the non-isobaric evaporation of liquid nitrogen in an 8 m³ storage tank initially filled at 30% of its capacity. The maximum pressure build-up is significantly higher for scenario N2 ($\Delta P_{\mathrm{N2}} = 16$ kPa) than that for scenario N1 ($\Delta P_{\mathrm{N2}} = 3.5$ kPa), see Figure 8.25. The equilibrium model predicted the same pressure build-up as for low liquid filling, see Figure 8.25. This is expected as in the equilibrium model, if $U_{\mathrm{L}} = U_{\mathrm{V}}$, the pressure build-up is only a function of the total heat ingress $\dot{Q}_{\mathrm{tot}} = \dot{Q}_{\mathrm{V,in}} + \dot{Q}_{\mathrm{L,in}}$, which is the same for scenarios N1 and N2. In contrast to scenario N1, the multiphase model predicted the maximum pressure build-up when compared against the CFD-SP and 1-D models, see Figure 8.31. This is a direct

consequence of the highest vapour temperature predicted by the multiphase model, see Figure 8.30.

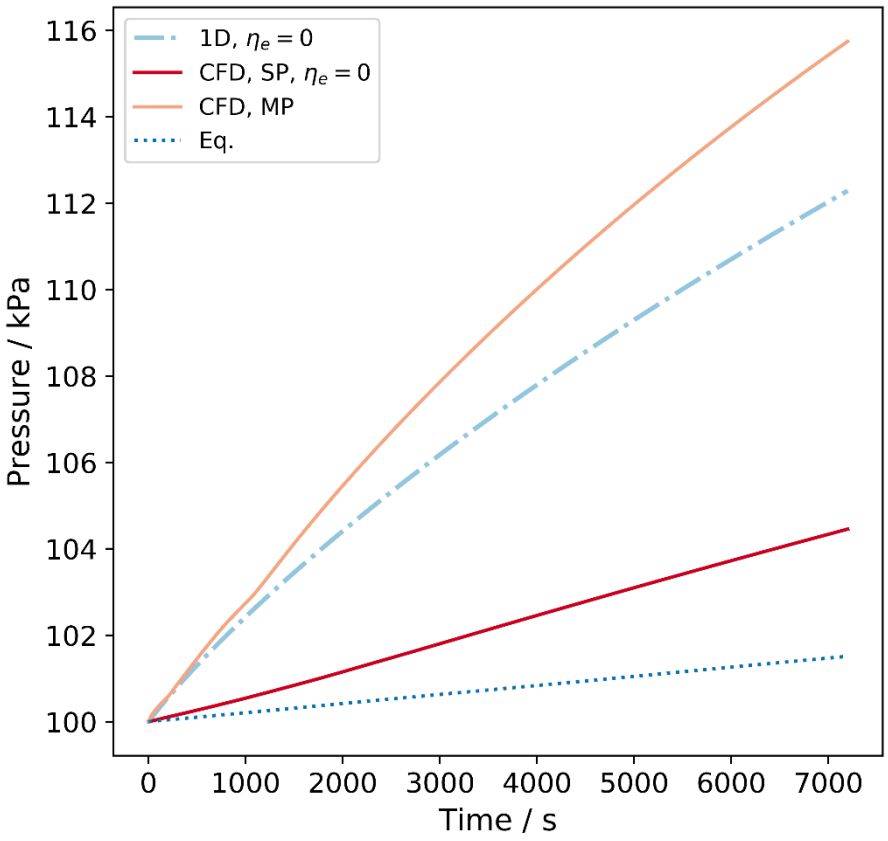

Figure 8.31: Pressure build-up during the non-isobaric evaporation of liquid nitrogen in an 8 m³ storage tank filled at 30% of its capacity. Light-blue lines depict the pressure obtained using the equilibrium model (dotted) and the 1-D model with no wall boiling (dot and lines). Solid red and yellow lines depict the pressure predicted by the CFD-SP model with no wall boiling, and the CFD-MP model.

Figure 8.31 shows that the pressure predicted by the 1-D model is in reasonable agreement with the pressure predicted by the multiphase model for scenario N2. On the other hand, the CFD-SP model underpredicts the pressure build-up owing to the pseudo-steady state approximation for vapour phase heat transfer. Thus, for low liquid fillings and at the beginning of the storage period, the pressurization rate is mainly determined by vapour heating. As the increase of average liquid temperature for scenario N2 is small, the pressurization rates are influenced more strongly by the cooling of the interface by the liquid than by liquid thermal expansion, see Figure 8.28. For scenario N2, the 1-D model predicted a temperature gradient below the interface in good agreement with the multiphase model, see Figure 8.28.

8.4.3 Summary of findings

- The non-isobaric evaporation of liquid nitrogen in an 8 m^3 vertically orientated, cylindrical tank has been simulated using 3 different models.
- Vapour heating has the highest influence on pressure build-up, particularly at the beginning of the evaporation and at low liquid fillings.
- Wall evaporation and interfacial condensation can occur simultaneously, driving complex flow structures below and above the vapour-liquid interface. **However, this is a result of a 2-D simulation, and a 3-D model would be required to confirm the main features of the observed flow structures.**
- Condensation was the dominant phase change mechanism for the scenarios investigated.
- Interfacial momentum transfer slightly enhances heat transfer in the liquid phase.
- The non-isobaric 1-D model provides a pressure build-up in good agreement with the multiphase (CFD-MP) model.

8.5 References

[1] F. Huerta and V. Vesovic, "A realistic vapour phase heat transfer model for the weathering of LNG stored in large tanks," *Energy,* vol. 174, pp. 280-291, 2019/05/01/ 2019, doi: https://doi.org/10.1016/j.energy.2019.02.174.

[2] M. Seo and S. Jeong, "Analysis of self-pressurization phenomenon of cryogenic fluid storage tank with thermal diffusion model," *Cryogenics,* vol. 50, no. 9, pp. 549-555, Sep 2010, doi: 10.1016/j.cryogenics.2010.02.021.

[3] M. Kang, J. Kim, H. You, and D. Chang, "Experimental investigation of thermal stratification in cryogenic tanks," *Exp. Therm. Fluid Sci.,* vol. 96, pp. 371-382, 2018/09/01/ 2018, doi: https://doi.org/10.1016/j.expthermflusci.2017.12.017.

[4] F. Perez *et al.*, "Measurements of boil-off gas and stratification in cryogenic liquid nitrogen with implications for the storage and transport of liquefied natural gas," *Energy,* vol. 222, p. 119853, 2021/05/01/ 2021, doi: https://doi.org/10.1016/j.energy.2021.119853.

[5] S. Z. S. Al Ghafri *et al.*, "Advanced boil-off gas studies for liquefied natural gas," *Appl. Therm. Eng.,* vol. 189, p. 116735, 2021/05/05/ 2021, doi: https://doi.org/10.1016/j.applthermaleng.2021.116735.

[6] F. Huerta and V. Vesovic, "Analytical solutions for the isobaric evaporation of pure cryogens in storage tanks," *Int. J. Heat Mass Transfer,* vol. 143, p. 118536, 2019/11/01/ 2019, doi: https://doi.org/10.1016/j.ijheatmasstransfer.2019.118536.

[7] J. Ren, H. Zhang, M. Bi, J. Yu, and S. Sun, "Numerical investigation of the coupled heat transfer of liquefied gas storage tanks," *Int. J. Hydrogen Energy,* vol. 42, no. 38, pp. 24222-24228, 2017, doi: 10.1016/j.ijhydene.2017.07.155.

[8] J. L. Ferrín and L. J. Pérez-Pérez, "Numerical simulation of natural convection and boil-off in a small size pressurized LNG storage tank," *Comput. Chem. Eng.,* vol. 138, p. 106840, 2020/07/12/ 2020, doi: https://doi.org/10.1016/j.compchemeng.2020.106840.

[9] R. Zhou, W. Zhu, Z. Hu, S. Wang, H. Xie, and X. Zhang, "Simulations on effects of rated ullage pressure on the evaporation rate of liquid hydrogen tank," *Int. J. Heat Mass Transfer,* vol. 134, pp. 842-851, 2019/05/01/ 2019, doi: https://doi.org/10.1016/j.ijheatmasstransfer.2019.01.091.

[10] M. Kassemi and O. Kartuzova, "Effect of interfacial turbulence and accommodation coefficient on CFD predictions of pressurization and pressure control in cryogenic storage tank," *Cryogenics,* vol. 74, pp. 138-153, 2016/03/01/ 2016, doi: https://doi.org/10.1016/j.cryogenics.2015.10.018.

[11] M. Kassemi, O. Kartuzova, and S. Hylton, "Validation of two-phase CFD models for propellant tank self-pressurization: Crossing fluid types, scales, and gravity levels," *Cryogenics,* vol. 89, pp. 1-15, 2018/01/01/ 2018, doi: https://doi.org/10.1016/j.cryogenics.2017.10.019.

[12] J. Ren, H. Zhang, J. Yu, M. Bi, and S. Sun, "Experimental research of heat-mass coupling response of liquid storage tanks," *J Hazard Mater,* vol. 338, pp. 502-507, Sep 15 2017, doi: 10.1016/j.jhazmat.2017.05.060.

[13] S. Gursu, S. A. Sherif, T. N. Veziroglu, and J. W. Sheffield, "Analysis and optimization of thermal stratification and self-pressurization effects in liquid-hydrogen storage-systems - Part 1: Model development.," *J Energ. Resour. ASME,* vol. 115, no. 3, pp. 221-227, Sep 1993, doi: 10.1115/1.2905997.

[14] S. Gursu, S. A. Sherif, T. N. Veziroglu, and J. W. Sheffield, "Analysis and optimization of thermal stratification and self-pressurization effects in liquid-hydrogen storage-systems - Part 2: Model results and conclusions," *J Energ. Resour. ASME,* vol. 115, no. 3, pp. 228-231, Sep 1993, doi: 10.1115/1.2905998.

[15] C. H. Panzarella and M. Kassemi, "On the validity of purely thermodynamic descriptions of two-phase cryogenic fluid storage," *J. Fluid Mech.,* vol. 484, pp. 41-68, 2003, doi: 10.1017/s0022112003004002.

[16] F. Huerta and V. Vesovic, "CFD modelling of the isobaric evaporation of cryogenic liquids in storage tanks," *Int. J. Heat Mass Transfer,* vol. 176, p. 121419, 2021/09/01/ 2021, doi: https://doi.org/10.1016/j.ijheatmasstransfer.2021.121419.

[17] S. P. Das, S. Chakraborty, and P. Dutta, "Studies on thermal stratification phenomenon in LH2 storage vessel," *Heat Transfer Engineering,* vol. 25, no. 4, pp. 54-66, Jun 2010, doi: 10.1080/01457630490443767.

Chapter 9

Conclusions and future work

9.1 Conclusions

New realistic models for the evaporation of cryogenic liquids in storage tanks under isobaric and non-isobaric conditions have been developed. The models accurately include a complex array of transport phenomena that determine BOG rates, pressurization rates, liquid and vapour temperatures. For isobaric evaporation, the liquid phase can be reliably modelled as an isothermal bulk phase, while the vapour is superheated with respect to the liquid. Consequently, transport phenomena in the vapour phase such as vertical thermal stratification, advection and heat conduction play an important role in determining BOG rates. For non-isobaric evaporation, the scenario is much more complex as a consequence of the pressure rise, which drives liquid thermal stratification. For non-isobaric evaporation, thermal stratification, natural convection, conduction, wall boiling and interfacial momentum transfer in the liquid are relevant in addition to vapour phase transport phenomena.

9.1.1 Isobaric evaporation

A non-equilibrium model for the isobaric evaporation of cryogenic liquids has been developed. The model includes a detailed 1-D heat transfer model for the vapour phase. In this model, the heat ingress from the outside is modelled as a source term, assuming efficient radial mixing owing to natural convection. Within the vapour bulk, conduction and advection dominate heat transfer in the vertical direction. Advection is modelled using an effective, advective velocity that results from the upward flow of the evaporated stored cryogen. The non-equilibrium model has been numerically solved using a moving mesh in the vapour sub-domain and adaptive time-steps for temporal integration. The former allows to represent interface displacement as the evaporation progresses, while the latter captures the initial transient behaviour with high

computational efficiency. For instance, the model can simulate one year of evaporation in 5 s of computational time in one core of a 3.1 GHz processor.

After an initial transient period at the beginning of the evaporation, the vapour temperature achieves a pseudo-steady state profile. The transient period at the beginning of the evaporation is a consequence of the rapid vapour heating. Within the transient period, steep changes in vapour temperature and density, vapour to liquid heat transfer and BOG rates were observed. At all times, vapour temperature monotonically increases with height, in agreement with recently published experimental and industrial results for several cryogenic liquids. The transient time increases with decreasing liquid filling as a consequence of two effects. Firstly, as the initial liquid filling decreases, the height of the vapour phase increases, which is the physical length scale for heat transfer. Secondly, the heat ingress to the liquid decreases with initial liquid filling. This results in lower evaporation rates, and therefore, lower advective velocities. Consequently, for low liquid fillings, the pseudo-steady state in vapour temperature takes longer than for high liquid fillings.

In all the simulations performed with the 1-D isobaric evaporation model, the vapour to liquid heat transfer was small. For large storage tanks (165,000 m^3), it was estimated that the vapour to liquid heat transfer rate contributed less than 0.3% to BOG rates. In general, less than 10% of the heat that enters the vapour is transferred to the liquid, and that ratio decreases with the progress of evaporation. The low vapour to liquid heat transfer rate is explained by the advective upward flow, which dominates heat exchange in the vapour. This conclusion is supported by the good qualitative agreement between experimental results and industrial observations of vapour temperature during cryogenic storage in isobaric conditions. Although heat conduction in the vapour is important and cannot be neglected, it alone would overestimate vapour to liquid heat transfer, and consequently BOG rates. The results obtained with the non-equilibrium model support the assumption that natural convection has a negligible effect on heat transfer in the vapour phase.

An important application of the isobaric evaporation model is the weathering of LNG stored in large tanks. A new non-equilibrium weathering model has been developed by extending the isobaric evaporation model for pure cryogenic liquids with

a mixture thermodynamic sub-model. The new weathering model represents LNG weathering as a transient evaporation of a liquid mixture with continuous BOG removal. It has been observed that the BOG rate decreases as a function of weathering duration for non-nitrogen containing LNG. The presence of nitrogen leads to a maximum in BOG, as a result of the interplay between decreasing liquid heat ingress and decreasing enthalpy of vaporisation. The BOG temperature increases with the progress of weathering and is a strong function of the initial liquid filling. The new weathering model allows for the optimization of LNG storage and different scenario planning, considering the initial liquid filling and nitrogen content.

The developed heat transfer model for the vapour phase consists primarily of a 1-D, unsteady advection-diffusion partial differential equation (PDE) with a linear source term. Therefore, the non-equilibrium model constitutes an ordinary differential equations system coupled with a PDE. As it was discussed previously, a pseudo-steady state for the heat transfer in the vapour phase is rapidly achieved for large scale storage scenarios. For long term storage applications, the pseudo-steady state constitutes more than 99% of the storage period. By invoking the pseudo-steady state assumption, the heat transfer model for the vapour phase can be simplified to an ordinary differential equation. Using this approach, analytical solutions for the non-equilibrium model have been derived for the liquid volume, BOG rate, vapour temperature and vapour to liquid heat transfer rate. Additionally, analytical solutions for a simpler equilibrium model, that considers the vapour and liquid at thermal equilibrium, were also derived.

For the equilibrium model, the analytical solutions are exact, regardless of the tank size or stored cryogenic liquid. The only assumptions made in the derivation are constant air temperature and constant heat ingress through the bottom of the tank. For the non-equilibrium model, the analytical solutions are valid for the whole evaporation, except for a short transient period at the beginning of the evaporation. The analytical solutions provide quick and accurate estimate of liquid volume, BOG rate and BOG temperatures. These three quantities are of particular interest to practising engineers. Although the accuracy decreases with the size of the storage tank, the maximum deviations with respect to the numerical solution of the non-equilibrium model were small. The deviations did not exceed 1% for liquid volumes, 2% for BOG rates and 4.5%

for BOG temperatures, for the three different tank sizes explored in this work. The analytical solutions also provide accurate estimates of the vapour temperature profiles and vapour to liquid heat transfer rates.

One of the rationales in deriving the analytical solutions was to obtain further insight in the evaporation process. The analytical solutions for the vapour temperature indicate that following the transient period, the temporal evolution of the profiles is primarily governed by the increase in the vapour height. This demonstrates that the system reaches a pseudo-steady state with respect to heat ingress. The increase in vapour temperature with the progress of evaporation is a result of a lower volume of liquid being present. It is also observed that the contribution of the source term, that represents wall heating, increases with decreasing tank diameter. For smaller tanks, the evolution of the vapour temperature exhibits large curvatures and is driven primarily by heat ingress from the outside. In contrast, for larger tanks the evolution of temperature is driven more by advection and conduction and less by wall heating. Finally, the analytical solution for the vapour to liquid heat transfer, $\dot{Q}_{\mathrm{VL}}$, is in very good agreement with the numerical results. Even for the smallest tank, where the contribution of $\dot{Q}_{\mathrm{VL}}$ is large, the maximum deviation is below 5%. This indicates that the analytical solution for $\dot{Q}_{\mathrm{VL}}$ can be used as a building block in more complex evaporation models.

The analytical solutions of the non-equilibrium model show that after the transient period, the BOG rate is mainly governed by the evolution of liquid volume. This is a consequence of the vapour density term being negligible in comparison to the liquid density. The temporal variation in BOG rates is greatest for small tanks with poor insulation (small d_i and large $U_{\mathrm{V}}, U_{\mathrm{L}}$). The solutions show an interesting behaviour when the heat ingress to the liquid through the walls is larger than the vapour to liquid heat transfer rate and the heat ingress through the tank bottom. Under these circumstances, BOG rates will decrease exponentially through evaporation, leading to longer evaporation times.

To further investigate the transport phenomena in the vapour phase during the isobaric storage of cryogenic liquids, a new CFD model has been developed. The CFD model was limited to the vapour phase only, as its focus was to accurately predict velocity and temperature profiles in the vapour phase. The liquid phase was assumed as

a bulk phase, using an identical approach to the one used for the 1-D non-equilibrium model. Thus, the newly developed CFD model can also be used to verify the assumptions of the 1-D non-equilibrium model. Furthermore, it gives well-resolved velocity and temperature profiles, as well as evaporation and BOG rates. For all the tested scenarios, the main flow pattern is that the vapour circulates upwards close to the tank wall, then radially along the roof towards the tank axis. Thereafter, the flow is partitioned between a fluid that leaves the tank, and a fluid that recirculates towards the vapour bulk.

The CFD simulations confirm the existence of a transient period for vapour flow and heat transfer at the beginning of the evaporation. After this period, a pseudo-steady state is reached. The velocity magnitude of the vapour decreases with time, owing to the formation of a vertical temperature gradient that dampens the buoyancy driven flow. The vapour temperature is mainly one dimensional, it increases with height, and it displays a small radial variation (< 2 K) only below the insulated roof. The heating of the vapour through the walls drives natural convection that efficiently mixes the vapour in the radial direction. In the vertical direction, a stable vertical temperature gradient is established as the system reaches it pseudo-steady state. The simulations indicate that the effect of turbulence on vapour heat transfer is small, and that natural convection does not produce a thermally homogeneous vapour bulk. Hence, the vapour to liquid heat transfer rate should not be estimated using correlations for natural convection in semi-infinite domains.

The CFD simulations indicate that the vapour to liquid heat transfer is small, and mostly radially independent. It varies only near the tank wall, where it increases rapidly with radius as a consequence of the large vertical temperature gradient inside the natural convection boundary layer. At the beginning of the evaporation, the vapour to liquid heat transfer slowly increases with time. This is a consequence of the time lag in energy distribution in the radial direction. After that time lag, the vapour to liquid heat transfer rate increases rapidly until it reaches a slowly varying, pseudo-steady state value.

The evaporation rate exhibits minimal variation during the transient period, while the BOG rate decreases rapidly. These effects are in excellent agreement with the transient profiles predicted by the 1-D model. The CFD model confirms that the BOG

rate initially decreases before stabilizing. This is a consequence of the interplay between increasing vapour temperature, that decreases the vapour density, and liquid evaporation, that increases the vapour space.

The results of the CFD simulations were compared to the 1-D isobaric evaporation model. An excellent agreement was observed in vapour temperature profiles for all scenarios. The observed differences can be attributed to two simplifying assumptions of the 1-D model, namely: (i) radially homogeneous temperature and (ii) modelling vapour flow as an advective, spatially homogeneous upwards velocity. The former is broadly confirmed by the CFD simulation, while the latter is only valid at the level of effective heat transfer. Nevertheless, the temperature profiles predicted by the CFD and 1-D non-equilibrium models are very similar when plotted against dimensionless time. This indicates that for predicting vapour heating, the observed flow complexity can be simplified by replacing it with an effective, advective, spatially homogeneous flow. Once the pseudo-steady state is achieved, an excellent agreement between the CFD and 1-D non-equilibrium models is observed in vapour temperatures, BOG and evaporation rates. The excellent agreement validates, albeit at the computational level, the 1-D isobaric evaporation model developed in this thesis [1].

9.1.2 Non-isobaric evaporation

A 1-D non equilibrium model for the non-isobaric evaporation of pure cryogenic liquids stored in cylindrical tanks has been developed. The model considers the vapour and liquid as continuum phases separated by a smooth horizontal interface, allowing the prediction of thermal stratification in both phases. The heating of the liquid through the tank wall and bottom has been modelled as a volumetric source term. The vapour-liquid interface acts as an additional heat ingress to the liquid, while within the liquid heat is transferred by conduction. The heating of the vapour has been implemented using a 1-D model based on the model developed in this work for isobaric evaporation. The heat ingress through the walls is partitioned between heat used for wall boiling and for liquid heating. A new interfacial boundary condition has been developed to accurately represent the interplay between heat conduction, wall boiling, pressure build-up and phase change.

The non-isobaric 1-D model was validated against Seo and Jeong [2] and Kang et al. [3] experimental data for the evaporation of liquid nitrogen. An excellent agreement between the model predictions and experimental data on pressure build-up was observed for all tested scenarios. For liquid temperature, an excellent agreement was observed with Seo and Jeong [2] experiments that comprised low heat fluxes and small pressure ranges. For Kang et al. [3] experiments, that comprised moderate heat fluxes and a large pressure range, a very good agreement with the measured liquid temperature, below the vapour-liquid interface, was observed. The scenarios comprised a variety of liquid fillings and heat fluxes, suggesting a wide range of applicability for the developed non-isobaric 1-D model. The model was used to simulate the limiting scenario of no wall boiling, which resulted in an underprediction of experimental pressure build-up in all scenarios. These results show that wall boiling is important even for low heat ingresses from the surroundings and cannot be neglected.

The non-isobaric 1-D model was used to simulate the evaporation of liquid nitrogen in an 8 m^3 vertically oriented, cylindrical storage tank, under two different liquid fillings. For both high and low liquid fillings, vapour heating has the highest influence on pressure build-up. Furthermore, for both high and liquid fillings, condensation is the dominant phase change mechanism. After 7,200 s of storage, neither liquid nor vapour phases achieved a pseudo-steady state on heat transfer. This contrasts with what has been observed for the same storage tank undergoing isobaric evaporation, that reaches its pseudo-steady state approximately after 4,800 s. As a consequence of the lack of BOG removal, the duration of the transient period during non-isobaric evaporation is governed by the wall heating source term and heat conduction. These terms are typically much smaller than the advective term, which dominates heat transfer in the vapour during isobaric evaporation, resulting in longer transient periods. Therefore, the pseudo-steady state approximation is not suitable for neither vapour nor liquid phases for modelling the non-isobaric evaporation of cryogenic liquids.

To further investigate the transport phenomena in the liquid phase during the non-isobaric evaporation of cryogens, a new single phase CFD model (CFD-SP) has been developed. The CFD modelling is restricted to the liquid phase, while the vapour phase

is allowed to be modelled as a bulk or 1-D phase. Wall boiling is implemented as a boundary condition in the liquid, and as an additional evaporation source in the mass and energy balances for the vapour phase.

The CFD-SP model was used to simulate the evaporation of LN_2 in the same $8m^3$ storage tank and liquid fillings considered for the non-isobaric 1-D model. The liquid heating through the walls produces a natural convection boundary layer at the wall, where the warm liquid ascends from the bottom to the interface. Thereafter, the liquid circulates towards the tank axis and downwards towards the liquid bulk, producing an anti-clockwise recirculation pattern. The liquid temperature is one dimensional everywhere except at in the boundary layer at the tank wall. Within this boundary layer driven by natural convection, the radial temperature variation was lower than 0.1 K. The onset of thermal stratification in the liquid dampens the buoyancy driven flow, similarly to what was observed in the vapour phase for isobaric evaporation. It is worth noting that liquid thermal stratification is driven by the combination of two effects. First, the pressure build-up in the vapour increases the temperature of the vapour-liquid interface. Second, the liquid heating through the walls warms a thin layer of liquid, which ascends to the top of the liquid phase. As liquid velocities and their gradients were small everywhere, particularly in the liquid bulk, turbulence did not significantly enhance heat transfer in the liquid.

The CFD-SP model was validated against the experimental data of Seo and Jeong [2] and Kang et al. [3] and excellent agreement with experimental liquid temperature and pressurization rates was observed. The temperature profiles and pressurization rates were also compared with the non-isobaric 1-D model. For small pressurization ranges and heat fluxes, the agreement with non-isobaric 1-D model was also excellent. In these scenarios, the 1-D model slightly underpredicted the liquid temperature by no more than 2 K. The underestimation of liquid temperature by the 1-D model increases with time and with decreasing liquid filling. For large pressurization rates and heat fluxes, the CFD-SP model outperforms the 1-D model in the prediction of liquid bulk temperatures. In these scenarios, the 1-D model underpredicted the liquid temperature up to 18 K for low liquid fillings. These results confirm that the 1-D model underestimates the liquid bulk temperature as a consequence of not modelling

explicitly natural convection in the liquid phase. Owing to time limitations, it was not possible to implement a transient 1-D heat transfer model for the vapour phase as a sub-model for the CFD-SP model. This results in the CFD-SP model spuriously overpredicting vapour temperatures and slightly underpredicting pressurization rates. Nevertheless, the CFD-SP model allows us to find the range of applicability of the liquid phase sub-model in the 1-D model.

Overall, the non-isobaric 1-D model provides an excellent estimation of pressure rise, and a reasonable estimation of the liquid thermal stratification. The 1-D model requires just 20 seconds to simulate two hours of evaporation, while the CFD-SP model requires 2 hours. Care must be taken to apply the 1-D model for liquid fillings close to 1. In that scenario, the liquid thermal expansion will dominate the pressure build-up, and the systematic underestimation of liquid bulk temperature by the 1-D model will underpredict the pressurization rate. Nevertheless, for most scenarios of industrial interest, the 1-D model is an excellent tool for the practising engineer to estimate pressure build-up and thermal stratification.

The 1-D and CFD-SP model assume a smooth, horizontal vapour-liquid interface in which the interfacial momentum transfer is neglected. Furthermore, the models also neglect the spatial distribution of evaporation and condensation rates. To investigate the influence of the interfacial transport phenomena and multiphase effects during the non-isobaric evaporation of pure cryogens, a new multiphase CFD model (CFD-MP) has been developed. It incorporates a two-fluid, Euler-Euler approach in order to accurately resolve the velocity profiles at the vapour and liquid side of the interface. Wall boiling has been modelled using the heat flux partitioning approach, where the heat ingress is divided in evaporation, transient conduction and natural convection.

The CFD-MP model was validated against the experimental results of Seo and Jeong [2] and Kang et al. [3] experiments. In all experiments, a lack of fit in temperatures and pressures was observed despite the detailed wall boiling modelling. These results suggest that the uniform heat flux for the vapour phase, considered for the multiphase model, does not represent the experimental setup. Therefore, conjugate heat transfer in Seo and Jeong [2] and Kang et al. [3] experiments is significant and cannot be neglected. The good fit of the CFD-SP or 1-D non-equilibrium models is a consequence of implicitly

including conjugate heat transfer in the evaporative coefficient. This result suggests that the heat flux between the tank wall and the vapour is spatially non-uniform, it does not vary significantly with time.

The CFD-MP model was used to simulate the evaporation of LN_2 in the same 8 m^3 storage tank and liquid fillings considered for the 1-D and CFD-SP models. The results show that the wall evaporation and interfacial condensation can occur simultaneously, driving complex flow structures above and below the vapour-liquid interface. This generates an evaporative vapour flow that starts at the tank wall, recirculates towards the tank axis, and then back to the wall. Just above the vapour liquid interface, an anticlockwise recirculating structure emerges. The vapour flow structure slightly enhances the heat transfer from the vapour to the interface and also drags the liquid through the interface. The drag of the vapour is an interfacial momentum transfer source that slightly enhances the heat transfer within the liquid phase.

The results obtained with the CFD-MP confirm that condensation is the dominant phase change mechanism for both low and high liquid fillings. The liquid temperature profiles obtained with the CFD-MP model were compared to the profiles obtained with the CFD-SP model. The CFD-MP model predicted slightly higher temperatures in the liquid phase, as a consequence of the higher velocities driven by interfacial momentum transfer. Nevertheless, the maximum differences were below than 0.05 K and for all engineering purposes can be neglected. Similarly, the vapour temperature profiles obtained with the CFD-MP model were compared to the profiles obtained with the 1-D non-equilibrium model. Although a good agreement is observed at the vapour-liquid interface, the CFD-MP model predicts higher vapour temperatures as a consequence of natural convection. The difference increases with decreasing liquid filling, time and height, and it reaches 12.5 K at the end of the evaporation for low liquid fillings. Although this results in the 1-D non-isobaric model underpredicting the pressure when compared against the CFD-MP model, the maximum difference is just 5 kPa after two hours of evaporation.

The results obtained with the CFD-MP model confirm that vapour heating is the phenomenon that dominates pressure build-up. The increase of pressure owing to

vapour heating was highest at the beginning of the storage period, where the vapour temperature increases rapidly. For all scenarios studied, liquid thermal expansion and phase change had a smaller effect on pressure build-up than vapour heating. Interfacial momentum transfer is relevant at the level of fluid recirculation for both vapour and liquid phases. Nevertheless, its impact on liquid temperatures, pressure build-up and average vapour temperature is small for the scenarios studied in this thesis. Considering the experimental results for vapour temperature, the CFD-MP model allows to complete the validation of the assumptions of the 1-D non-equilibrium model. Overall, if the fraction of heat ingress that undergoes directly to evaporation is known, the 1-D model provides an excellent first estimate of vapour temperatures, liquid temperatures and pressure build-up. For large tanks and low liquid fillings, the 1-D model should be used with care, as it will slightly underestimate both vapour temperature and pressure.

9.2 Future work

To improve the accuracy, reliability and range of applicability of the evaporation models for cryogenic liquids in storage tanks, the following research objectives are suggested:

9.2.1 Include conjugate heat transfer between tank walls and fluid phases

The main challenge for the validation of the models developed in this work was the uncertainty for experimental temperature boundary conditions. The modelling uncertainty can be reduced by including a heat transfer sub-model for the storage tank and their multi layered insulation (MLI) system. This will allow us to predict the spatially non-uniform heat flux from the walls to the liquid and vapour phases. Importantly, a conjugate heat transfer model will also allow the experimental validation of the CFD-MP model for non-isobaric evaporation. In particular, it will verify whether the lack of fit of the CFD-MP model is a consequence of neglecting the heat flux non-uniformity or a modelling error. If the validation is successful, the CFD-MP model could be used to predict the evaporative fraction in the non-isobaric 1-D model. This will allow the application of the non-isobaric 1-D model to novel scenarios of industrial interest.

9.2.2 Improve the modelling of the vapour phase advective velocity

The advective flow in the vapour phase, in the isobaric evaporation model, has been modelled by using a spatially homogeneous, upwards, advection velocity. In reality, the vapour velocity would increase with height as the density of the vapour decreases with temperature. Simultaneously, depending on the location and size of the tank valve, the velocity may decrease as it approaches to the tank roof. By including these effects, which can be effectively modelled as one-dimensional, $v_z(z)$, a more realistic velocity and temperature profile in the vapour phase will be obtained. For the non-isobaric evaporation model, the advective velocity is expected to change strongly with height. In this scenario, a more accurate advective velocity should be formulated separately for evaporation and condensation. Additionally, it should consider the no-slip boundary condition for velocity at the tank roof.

9.2.3 Further investigate the influence of interfacial momentum transfer

The CFD-MP model developed in this thesis shows that interfacial momentum transfer significantly influences the vapour and liquid velocity profiles, enhancing heat transfer. Although this effect was small for the scenarios investigated in this thesis, it may not be the case for different tank sizes and geometries. We propose to improve the CFD-MP model using a 3-D, fine uniform mesh with an aspect ratio very close to 1. This will result in a more realistic simulation of turbulence and buoyancy driven flow, and it will increase the theoretical order of accuracy of the finite volume discretisation of the governing transport equations. These two improvements will allow to verify the preliminary results obtained in this thesis regarding interfacial heat and mass transfer.

With the improved CFD-MP model, we propose investigate a wider variety of storage scenarios and operating conditions. The model can also be used to simulate isobaric evaporation by modifying the domain physical boundaries and boundary conditions. A comprehensive investigation of the effect of interfacial momentum transfer on temperatures, evaporation rates and BOG will allow to further verify the 1-D models developed in this thesis. If interfacial momentum transfer is significant for several scenarios of industrial interest, the following approach is proposed. Each vapour and liquid phases should be partitioned in a sublayer near the interface, and a bulk layer.

This will allow to retain the simplicity of the 1-D model, while considering the enhancement of heat transfer owing to interfacial momentum transfer.

9.2.4 Implement variable thermophysical properties for the vapour

The models developed in this research demonstrate that the vapour can be more than 100 K superheated with respect to the vapour-liquid interface during the storage of cryogenic liquids. In this broad temperature range, the thermophysical properties, and in particular the vapour thermal conductivity, are expected to vary. For the non-isobaric evaporation models, the latent heat of vaporisation is also expected to change noticeably for large pressurization ranges. Therefore, including the variation of thermophysical properties with temperature and pressure will extend the range of applicability of the models developed in this thesis.

9.2.5 Extend non-isobaric evaporation models to allow cryogenic mixtures

The non-isobaric evaporation models developed in this research showed a very good agreement with experimental data on pressure build-up. This quantity is of pivotal importance for mobility applications, such as LNG tanks used in trucks and heavy vehicles. In order to use the non-isobaric evaporation models to predict LNG weathering, a mixture thermodynamic sub-model must be included. This will allow to accurately predict LNG composition, vapour and liquid temperatures, and pressure build-up. The thermodynamic sub-model should be valid for the operating range of the storage tank of interest.

9.3 References

[1] F. Huerta and V. Vesovic, "A realistic vapour phase heat transfer model for the weathering of LNG stored in large tanks," *Energy,* vol. 174, pp. 280-291, 2019/05/01/ 2019, doi: https://doi.org/10.1016/j.energy.2019.02.174.

[2] M. Seo and S. Jeong, "Analysis of self-pressurization phenomenon of cryogenic fluid storage tank with thermal diffusion model," *Cryogenics,* vol. 50, no. 9, pp. 549-555, Sep 2010, doi: 10.1016/j.cryogenics.2010.02.021.

[3] M. Kang, J. Kim, H. You, and D. Chang, "Experimental investigation of thermal stratification in cryogenic tanks," *Exp. Therm. Fluid Sci.,* vol. 96, pp. 371-382, 2018/09/01/ 2018, doi: https://doi.org/10.1016/j.expthermflusci.2017.12.017.

List of publications and achievements

Publications

- Huerta, F. and Vesovic, V., 2021. CFD modelling of the isobaric evaporation of cryogenic liquids in storage tanks, *International Journal of Heat and Mass Transfer*, 176 (2021) 121419.
- Huerta, F. and Vesovic, V., 2019. Analytical solutions for the isobaric evaporation of pure cryogens in storage tanks. *International Journal of Heat and Mass Transfer*, *143*, p.118536.
- Huerta, F. and Vesovic, V., 2019. A realistic vapour phase heat transfer model for the weathering of LNG stored in large tanks. *Energy*, *174*, pp.280-291.

Conference presentations

- ICCHMT 2019: 12th International Conference on Computational Heat, Mass and Momentum Transfer 2019 (Rome, Italy, 03-06 September 2019). See Page.13 of the Book of Abstracts
- ECCE12: The 12th European Congress of Chemical Engineering (Florence, Italy, 15-19 September 2019). Oral Presentation: A realistic vapour phase heat transfer model for the weathering of LNG stored in large tanks**.** See Tuesday September 17th, 08:30 – 09:30, SYM/ENERGY AND CHEMICAL ENGINEERING.
- 7th ESI OpenFOAM Conference 2019 (Berlin, Germany, 15-17 October 2019). "A non-equilibrium evaporation model for pure cryogens stored in closed tanks".
- CFD2020 – Trondheim, Norway, 14-16 October 2020. "A non-equilibrium model for evaporation of liquefied natural gas stored in small vessels with pressure build-up"

Awards and Prizes

- John S. Archer Award for Research Excellence in Petroleum Geoscience and Engineering, 2019, Imperial College London.

Appendices

Appendix A

Fitting the overall heat transfer coefficient *U* to industrial boil-off rate data

The overall heat transfer coefficient for the vapour and liquid phases, $U = U_{\mathrm{L}} = U_{\mathrm{V}}$, has been obtained from Linde Cryogenic Standard Tanks technical specification [1]. The V60 storage tank with a net capacity of 6.37 m³ has been selected as a representative storage tank for mid-scale storage. The daily Boil-off rate (BOR) for liquid nitrogen (LN_2) in this tank filled at 95% of its capacity (P = 1 bar, T_{air} = 15°C) is 0.58% / d. The tank external and internal diameters are d_{o} = 1.6 m, d_{i} = 1.58 m. Assuming that the inner geometry of the storage tank is approximately a cylinder, the tank height is calculated through $H_{\mathrm{T}} = 4V_{\mathrm{T}}/\pi d_{\mathrm{i}}^2$ = 3.25 m. The evaporated mass after a day of storage can be calculated from the tank volume,

$$m_{\mathrm{evap}} = \rho_{\mathrm{L}} \times V_{\mathrm{T}} \times BOR\% = \frac{0.58}{100} \times 6.37\ \mathrm{m}^3 \times 806.6 \frac{kg}{m^3} = 29.78\ kg \qquad \text{(A.1)}$$

Assuming that the overall heat transfer coefficient is the same in the perlite insulation for both tank bottom and walls, the total liquid heat ingress is given by,

$$\dot{Q}_{\mathrm{L,tot}} = U_{\mathrm{L}}\left(A_{\mathrm{L}} + A_{\mathrm{T,o}}\right)(T_{\mathrm{air}} - T_{\mathrm{L}}) + \dot{Q}_{\mathrm{VL}}, \qquad \text{(A.2)}$$

where $A_{\mathrm{L}} = \pi d_{\mathrm{o}} V_{\mathrm{T}} LF$, $A_{\mathrm{T,o}} = \pi d_{\mathrm{i}}^2/4$ are the wet area and the external area of the tank bottom, respectively. It is further assumed that that the BOR data for isobaric conditions has been measured in pseudo-steady state. In this condition, the LN_2 is

stored at its saturation temperature, and all liquid heat ingress produces the evaporation of the stored LN_2. This allows us to estimate the total heat ingress as the total energy used to vaporise the nitrogen that left the tank in a day,

$$\dot{Q}_{\mathrm{L,tot}} \times \tau_s = m_{\mathrm{evap}} \times \Delta H_{\mathrm{LV}} \tag{A.3}$$

Where $\Delta H_{\mathrm{LV}} = 199{,}3$ kJ/kg is the latent heat of vaporisation of liquid nitrogen at P = 1 bar and τ_s is the storage period. For a storage period of 1 day, equivalent to 86,400 s, the total heat transfer rate to the liquid is $\dot{Q}_{\mathrm{L,tot}} = 68.69$ W. As the vapour to liquid heat transfer rate, $\dot{Q}_{\mathrm{VL}}$, is expected to be small and to contribute less than 0.5% of evaporation rates, it has been neglected in the estimation of U_{L}. Therefore, replacing the calculated value for $\dot{Q}_{\mathrm{L,tot}}$ in Eq. (A.2) gives an estimate of the overall heat transfer coefficient for LN_2 storage in the V60 storage tank,

$$U_{\mathrm{L}} \approx \frac{\dot{Q}_{\mathrm{L,tot}}}{\left(A_{\mathrm{L}} + A_{\mathrm{T,o}}\right)\left(T_{\mathrm{air}} - T_{\mathrm{L}}\right)} = \ 0.019 \ \mathrm{Wm^{-2}K^{-1}}. \tag{A.4}$$

References

[1] Linde, Cryogenic Standard Tanks LITS 2, Tacherting, Germany, 2019.

Appendix B

OpenFOAM implementation of the vapour-CFD model

Note: this appendix has been published as Supplementary Material in Huerta and Vesovic [2], and is reprinted without modification.

1. Introduction and Software Requirements

The following instructions are applicable for OpenFOAM-v2006. This version of OpenFOAM can be downloaded from the OpenFOAM official website, which also provides the Installation Guide for different operating systems. The code has been tested in OpenFOAM installations on two different operating systems: Linux Source and Microsoft Windows "Windows Subsystem for Linux". For post processing and visualizing the simulation results, ParaView 5.6 or superior is required. This software is automatically installed when following the Installation Guide of the "ThirdParty" open-source software that comes along with OpenFOAM. However, this part of the installation may fail. If this happens, ParaView can be installed separately from the ParaView official website. Python 3 is required to execute a number of scripts that facilitate the creation of the meshes and post processing the results. The meshes were generated using the Open-source mesh generator Gmsh 4.5.6, which can be downloaded from the Gmsh official website.

Summary of software requirements

- OpenFOAM-v2006 – open-source finite volume CFD Toolbox
- ParaView 5.6 or superior – open-source visualization software
- Python 3 – Interpreted programming language
- Gmsh 4.5.6 – open-source mesh generator

2. Description of simulation cases

In OpenFOAM, all the files required for a particular simulation are conventionally grouped into a folder denominated case. In Mendeley Data, four cases

are provided: LF_97_8m3, LF_30_8m3, LF_97_80m3 and LF_97_test. The first three cases correspond to Scenarios 1, 2 and 3, respectively, while the last case is a shortened version of Scenario 1 for testing purposes. The general structure of each case contains three folders, alongside several code utilities and scripts. The 0/ directory contains the initial and boundary conditions for all fields. The constant directory contains the thermophysical and transport properties of the cryogenic fluid, the gravitational constant, the turbulence properties, and a configuration file for the dynamic mesh. The system directory contains files to set-up the time and space discretization algorithms, the convergence criteria of the solvers, the domain decomposition dictionary and the runtime simulation control dictionary.

In what follows, the files that are present in all cases are examined. The Allclean script removes all the simulation results that have been written to files in serial and parallel simulations. The Allrun script contains a sequence of commands to create the mesh, decompose the domain (if necessary), run the simulation, and save the simulation log into the "cryogen_evaporation.log" file. The cyl_multi.geo file contains the code and parameters required to generate a hexahedral wedge mesh, which resembles the 2-D cylindrical geometry, using Gmsh. The update_mesh script calls a series of commands that take as an input the cyl_multi.geo file and outputs an OpenFOAM mesh. The rename_boundaries.py is called by the update_mesh script to ensure the consistency of the names of each boundaries every time the mesh is updated. Finally, the foam.foam file is a dummy file required to post process the simulation results using ParaView.

We start exploring the content of LF_97_8m3, corresponding to Scenario 1. This case provides the structure for all simulations of the isobaric evaporation of pure cryogens. All the other cases are based on LF_97_8m3, where the changes regarding the mesh parameters and tank size are located in the cyl_multi.geo, constant/polyMesh and constant/thermophysicalProperties files in each case.

2.1 Scenario 1: LF_97_8m3

This scenario corresponds to the isobaric evaporation of pure methane in an $8m^3$ storage tank filled at 97% of its capacity.

2.1.1 Directory 0/

This directory contains the initial and boundary conditions for all scalar and vector fields required by the overBuoyantPimpleDyMFoam solver.

The temperature (0/T) file contains the initial and boundary conditions for the vapour temperature. The units of temperature are K. The initial condition is stored in the internalField entry, while the boundary conditions are described in the boundaryField dictionary. Each sub dictionary corresponds to a boundary face of the compounded geometry. All the faces are of type "wedge", as this represents a 2-D axisymmetric mesh where the azimuthal direction is not resolved. The most relevant temperature boundary condition is the dynamic boundary condition in the tank_wall sub dictionary. The first two sub dictionaries, codeInclude and codeOptions, contain instructions to read all the libraries required by the customized code sub-dictionary. The code sub dictionary contains C++ / OpenFOAM code to implement the convection-conduction boundary condition.

The velocity (0/U) file contains the initial and boundary conditions for the vapour velocity. The units of velocity are m s^{-1}. An important difference between the U and T files is that U is a vector field while T is a scalar field. The roof and wall boundary conditions were set to no slip. The outlet velocity is "calculated" from the pressure boundary condition by means of the pressureInletOutletVelocity dynamic boundary condition. The most relevant boundary condition is U is the code below the "(bottom.*)" sub dictionary. This boundary condition was named surfaceEvaporationVelocity and calculates the vertical inlet velocity of the vapour at the interface based on the evaporation rate of the stored liquid. The code sub dictionary implements the liquid phase bulk model, described by Eqs. (1) – (4), (9).

The pointMotionUy file contains the initial and boundary conditions for the mesh velocity. The units of the mesh velocity are m s^{-1}. The roof and outlet boundary conditions are set to zero, as they are stationary boundaries. The tank_wall is set to slip, in order not to override the no slip boundary condition of the vapour velocity at the tank wall. The descendingLiquidVelocity dynamic boundary condition at the "(bottom.*)" sub dictionary represents the vapour-liquid interface displacement. In the code sub-dictionary of this customized boundary condition, Eq. (11) is implemented to

calculate the downwards velocity of the vapour-liquid interface. Note that in this implementation, this vapour inlet velocity is read in line 62. The zoneID file is an auxiliar file required by overBuoyantPimpleDyMFoam.

The 0/p_rgh file contains the initial and boundary conditions for modified pressure, defined as the pressure minus the hydrostatic pressure. The units of pressure are Pa. All boundary conditions except the outlet are fixedFluxPressure, which calculates the pressure from the velocity boundary condition. At the outlet, the modified pressure is set at 100 kPa as a boundary condition. The 0/p file contains the pressure initial and boundary conditions, which are all calculated based on the 0/p_rgh.

The remaining files in the 0/ directory represent initial and boundary conditions for scalar fields related to turbulence models. The 0/k file represents the turbulent kinetic energy, which has units of $m^2 s^{-2}$. The initial conditions, as well as the value of 0/k at the inlet are set to 10^{-7} based on the scaling of the turbulent kinetic energy with the size of the domain and the free stream velocity. It was observed that velocity and temperature results did not change more than 0.01% with a variation of three orders of magnitude on the initial and boundary conditions of the turbulent kinetic energy. The wall functions at the tank wall and roof were set to kqRWallFunction, which sets the gradient of the turbulent kinetic energy to zero in the specified boundaries.

The 0/nut file contains initial and boundary conditions for the turbulent viscosity. This is an auxiliar quantity used by the $k-\omega-SST$ and LES turbulence models that must be initialized at the value of zero. The boundary condition is set to nutkWallFunction, which calculates the turbulent kinematic viscosity ν_t based on the value of the turbulent kinetic energy and the dimensionless wall distance y^+. The 0/omega function contains the initial and boundary conditions for the specific turbulent dissipation rate ω in the $k-\omega-SST$ model. The initial value of ω is set to be consistent with the initial value of k. The boundary conditions are inletOutlet for all open boundaries. For the tank wall and roof, the omegaWallFunction has been selected, which switches the calculation of ω between the viscous and logarithmic region depending on the location y^+. A comprehensive description of the boundary conditions for turbulent quantities in OpenFOAM and their implementation can be found in Liu's work [3].

2.1.2 Directory *system*/

The controlDict file is a dictionary which enables the user the control of general parameters of the simulation. The endTime entry allows the user to indicate the duration of the simulation, in seconds. The writeInterval entry indicates how frequently simulation data will be saved. A lower writeInterval implies the storage of more data, which provides more details of the simulation at the expense of a higher use of disk space. The adjustTimeStep options enable the dynamic adjustment of the time step based on a threshold of the maximum Courant number in the simulation domain established in the maxCo entry. For all simulations, maxCo was set to 0.5 as this allowed a stable simulation without requiring an impractically small time-step. At the end of the controlDict file, a functions sub dictionary is specified to calculate the average vapour temperature and the derivative of the average vapour density by means of function objects. The function objects are OpenFOAM run-time postprocessing utilities which enable a more straightforward analysis of the results. The results produced by the function objects are stored in a directory named postProcessing, which is generated in the case directory when the simulation is executed.

The decomposeParDict specifies how the domain will be decomposed if the OpenFOAM decomposePar command is executed. In all the examples, 4 processors were selected to facilitate the implementation of the code. The simpleCoeffs sub dictionary specifies how many times the domain will be divided in each direction. In all cases, the domain was decomposed only in the vertical -y direction, which is the second coordinate of the n entry in the simpleCoeffs sub dictionary. The numberOfSubdomains entry must be consistent with the number after the flag -np of mpirun in line 20 of the Allrun script.

The fvSchemes file specifies the discretization schemes for the finite volume discretization of each term of the continuity, energy and Navier-Stokes equations. The backward time integration scheme, which is implicit and second order accurate in time, was required to keep the time integration error bounded. This is specified in the ddtSchemes sub dictionary. The fvSolution file specifies the solution algorithm and convergence criteria for each of the discretized partial differential equations that are

solved. On this file, the most important non-default parameter is the choice of the preconditioned bi-conjugate gradient PBiCGStab solver for all the modified pressure, density, enthalpy and velocity fields. Although this solver is more computationally expensive than the smoothSolver or multigrid methods, it provided better convergence for all the cases studied.

2.1.3 Directory constant/

The dynamicMeshDict file is a dictionary which loads the libraries required for the recalculation of the mesh at each time-step as the evaporation progresses. The diffusivity entry in this dictionary is a numerical artifact to ensure the convergence of the linear solver that calculates the position of each cell at each time-step, and it does not influence simulation results.

The thermophysicalProperties file contains three sub dictionaries. The thermoType establishes that the cryogenic vapour is modelled as an ideal gas through the equationOfState entry perfectGas. The mixture sub dictionary contains three further sub dictionaries. The specie dictionary contains the molar weight of methane. The thermodynamics sub-dictionary contains the thermodynamic properties of gaseous methane. The transport sub-dictionary contains the dynamic viscosity, Prandtl number and turbulent Prandtl number of gaseous methane. The dpdt entry is set to 'true' to account the compressibility effects in the energy equation. Finally, the tank sub-dictionary contains the physical properties of the cryogenic storage tank and the temperature of the surrounding air. The g file contains the acceleration of gravity in $m\ s^{-2}$, which is pointing in the negative vertical direction.

The turbulenceProperties file establishes the turbulence model to be used in the simulation. Two additional dictionaries are provided, turbulenceProperties_LES and turbulenceProperties_RANS which enables the quick selection of turbulence model. By default, the turbulenceProperties file contains the specification for the LES model. If the user wants to change the turbulence model, the only action required is to overwrite the turbulenceProperties file before running the simulation. Open a Unix terminal, navigate to the case directory, and execute:

```
cd constant
cp turbulenceProperties_RANS turbulenceProperties
cd ..
```

If the user wants to select the LES model, perform the same action but give the turbulenceProperties_LES as the first parameter of the cp UNIX shell command.

3. Running the scenarios

3.1 Test case: LF_97_test

The case LF_97_test is a copy of LF_97_8m3 configured to simulate 10 seconds of evaporation while saving the results after every second of simulated time. The objective of this case is to test the installation, mesh generation and dynamic boundary conditions. First, open a bash terminal in either using Linux or Windows Subsystem for Linux. Then, source the OpenFOAM environment in that terminal:

```
source $HOME/OpenFOAM/OpenFOAM-v2006/etc/bashrc
```

In the terminal, navigate to the folder where the case directories were downloaded, and change directory to the test directory,

```
cd LF_97_test
```

Execute the Allrun script by typing ./Allrun in the terminal to run the first 10 seconds of Scenario 1. Running this case in a single core of any modern processor should take no longer than 5 minutes. First, a new directory dynamicCode will be created, which contains a directory for each custom boundary conditions. The directory names are consistent with the name of the dynamic boundary conditions produced from the compilation of the 0/T, 0/U and 0/pointMotionUy, as discussed in subsection 2.1.1 of Supplementary Material S2. The successful creation of the dynamic boundary conditions can be tested using the ls -l dynamicCode command in the terminal, which should provide an output with four folders as below:

```
path/LF_97_test$ ls -l dynamicCode/
total 16
drwxrwxr-x 4 felipe felipe 4096 Jan 20 17:59 convection_Conduction
drwxrwxr-x 4 felipe felipe 4096 Jan 20 17:59 descendingLiquidVelocity
drwxrwxr-x 3 felipe felipe 4096 Jan 20 17:59 platforms
drwxrwxr-x 4 felipe felipe 4096 Jan 20 17:59 surfaceEvaporationVelocity
```

After the dynamic boundary conditions are compiled, the simulation will start as a new process named overBuoyantPimpleDyMFoam, which can be monitored using the top command in the terminal. As the test case runs in a single processor, only one process should appear. If mpirun is used to run a more complex case in parallel, a process will be created for each processor. As time progresses, OpenFOAM will write the directories 1, 2, ..., 10. These directories contain the simulation results of all the scalar and vector fields at the timestep which corresponds to the name of the directories. The directories are written after every second of simulated time, as the entry writeInterval is set to 1 in this test case. As soon as the directory 10 is written, the simulation will finish. The results can be then visualized using ParaView. After finishing the simulation, execute ParaView from the terminal and give foam.foam as an additional argument through:

```
path/LF_97_test$ paraview foam.foam &
```

Alternatively, open ParaView, go to File > Open, navigate to the case directory, select the empty file foam.foam and click OK. Both methods will load the case in ParaView. Then, click on the Properties > Apply button, and a pressure profile will be displayed. To complete the test, visualize the temperature profile after 10 seconds. In the upper part of the screen, go to the Time: dropdown list and select the last timestep (10). In the menu bar below, the first drop down list will display the pressure “p”, as from this list the scalar and vector fields can be chosen for visualization. Click on the dropdown list and select “T” to visualize the temperature field. This will show a buoyant plume rising from the boundary at the right of the domain and then moving inwards in the radial direction bellow the roof. The figure should look identical to Fig. S2.1.

Figure S2.1: Vapour temperature profile in the CFD simulation of the isobaric evaporation of methane for the test case, Scenario 1 (V_T = 8m³, LF = 0.97), after 10 seconds of simulation.

3.2 Scenario 1: LF_97_8m3

In this Scenario, the controlDict dictionary sets up a simulation of 4,800 seconds in the endTime entry and specifies that the results should be written each 60 s in the writeInterval entry. To run the simulation using 4 cores, navigate to the directory LF_97_8m3 and execute ./Allrun. This simulation took 20,000 s in an Intel® Core™ i7-7700K at 4.20GHz processor using 4 cores. If the simulation is intended to be executed in a single core, replace line 17 of Allrun with the serial execution code of overBuoyantPimpleDyMFoam:

```
overBuoyantPimpleDyMFoam > cryogen_evaporation.log &
```

This adaptation is also applicable for Scenarios 2 and 3. However, it is highly recommended running all scenarios in parallel with the domain decomposed in at least 4 processors. In the experience of the authors, the simulation times achieved with the parallel simulation were three times shorter than the single core simulations in all scenarios. Using 4 cores, this simulation was completed after 16 hours.

3.3 Scenario 2: LF_30_8m3

As most of the files in the case directory remain unchanged between Scenarios 1 and 2, only the files that have inputs specific for this case will be discussed. In this Scenario, the controlDict dictionary sets up an endTime 133,200 s and a writeInterval of 600 s. The cyl_multi_geo file specifies dr = dz = 0.01 m, LF = 0.3. These inputs condition the generation of the mesh for the vapour phase, as a larger mesh is required for an

initial liquid filling of LF = 0.3 of in Scenario 2, compared with LF = 0.97 in Scenario 1. To run the simulation using 4 cores, navigate to the directory LF_30_8m3 and execute ./Allrun. This simulation was completed after 36 hours.

3.4 Scenario 3: LF_97_80m3

In this Scenario, the controlDict dictionary sets up an endTime 10800 s and a writeInterval of 60 s. The cyl_multi_geo file specifies d*r* = 0.004 m, dz = 0.005 m, and a value of LF equals to 0.97. As Scenario 3 comprises an 80 m^3 storage tank, which is larger than the tanks in Scenarios 1 and 2, the radius and height in cyl_multi.geo are larger to be consistent with the dimensions of the large tank. Additionally, the tank sub dictionary in the constant/thermophysicalProperties file, the tank_height, R_T and radius_ext entries are also updated to be consistent with the larger tank. To run the simulation using 4 cores, navigate to the directory LF_97_80m3 and execute ./Allrun. This simulation was completed after 8 hours.

References

Appendix C

Coordinate transformation for a moving mesh

In order to include the interface displacement in the partial differential equation that defines the isobaric 1-D model, Eq. (3.20), a coordinate transformation is required. Defining ξ as the dimensionless length in the computational domain $\Omega_c$and t the time, the coordinate transformation:

$$z = z(\xi, t): \Omega_{c,1D} \equiv [0,1] \rightarrow \Omega_{1D} \equiv [0, l_V(t)] \tag{C.1}$$

defines the relationship between ξ, t and the vertical coordinate z in the physical domain Ω_{1D} that represents a location within the vapour phase. By discretising the vapour physical domain in N_z nodes in the vertical direction, the position of the grid point x_j in the physical domain will vary with time and it is given by,

$$z_i(t) = z(\xi_i, t), \quad i = 1, \dots, N_z, \tag{C.2}$$

where ξ_j is the position of the *j-th* grid point in the computational domain. Then, Eq. (3.20) is transformed considering that the vapour temperature is now a function of a spatial coordinate that varies with space and time,

$$\hat{T}_V(\xi, t) = T_V(z(\xi, t), t). \tag{C.3}$$

The relationship between spatial and temporal derivatives of $\hat{T}_V$ and the derivatives of T_V in the physical coordinates is obtained by applying the chain rule to Eq. (C.3),

$$\frac{\partial \hat{T}_V}{\partial \xi} = \frac{\partial T_V}{\partial z}\frac{\partial z}{\partial \xi}, \tag{C.4}$$

$$\frac{\partial \hat{T}_V}{\partial t} = \frac{\partial T_V}{\partial t} + \frac{\partial T_V}{\partial z}\frac{\partial z}{\partial t}, \tag{C.5}$$

$$\frac{\partial^2 \hat{T}_V}{\partial \xi^2} = \frac{\partial^2 T_V}{\partial z^2}\left(\frac{\partial z}{\partial \xi}\right)^2. \tag{C.6}$$

Defining the physical length scale for the isobaric evaporation as the vapour length, the mapping of the physical length into dimensionless length is given by,

$$\xi = \frac{z}{l_{\mathrm{V}}(t)} \rightarrow \frac{\partial \xi}{\partial z} = \frac{1}{l_{\mathrm{V}}(t)}. \tag{C.7}$$

Assuming that all mesh points move at the velocity of the interface, v_{int}, the time derivative of the physical vertical coordinate z is given by,

$$\frac{\partial z}{\partial t} = v_{\mathrm{int}} = \text{Eq. (3.17)} = -\frac{\dot{B}_{\mathrm{L}}}{\rho_{\mathrm{L}} \pi R_{\mathrm{T}}^2}, \tag{C.8}$$

where $\dot{B}_{\mathrm{L}}$ is the evaporation rate, ρ_{L} is the liquid density and R_{T} is the tank radius. Writing Eq. (3.20) in terms of $\hat{T}_{\mathrm{V}}$ and the dimensionless length in the computational domain, one obtains,

$$\frac{\partial \hat{T}_{\mathrm{V}}}{\partial t} = \alpha_{\mathrm{V}} \frac{\partial^2 T_{\mathrm{V}}}{\partial z^2} \left(\frac{\partial z}{\partial \xi}\right)^2 - \bar{v}_z \frac{\partial T_{\mathrm{V}}}{\partial z} \frac{\partial z}{\partial \xi} + \dot{S}_{\mathrm{w,V}} + \frac{\partial T_{\mathrm{V}}}{\partial z} \frac{\partial z}{\partial t}, \tag{C.9}$$

Replacing Eqs. (C.7) and (C.8) in Eq. (C.9), and noting that $\hat{T}_{\mathrm{V}} = T$, one obtains the 1-D vapour phase heat transfer model PDE in terms of the physical coordinates,

$$\frac{\partial T_{\mathrm{V}}}{\partial t} = \alpha_{\mathrm{V}} \frac{\partial^2 T_{\mathrm{V}}}{\partial z^2} \frac{1}{l_{\mathrm{V}}^2} - (\bar{v}_z - v_{\mathrm{int}}) \frac{\partial T_{\mathrm{V}}}{\partial z} \frac{1}{l_{\mathrm{V}}} + \dot{S}_{\mathrm{w,V}} \tag{C.50}$$

Therefore, the expansion of the domain is represented as a correction in the term for advective heat transfer, $(\bar{v}_z - v_{\mathrm{int}}) \frac{\partial T_{\mathrm{V}}}{\partial z} \frac{1}{l_{\mathrm{V}}}$. Finally, the spatial derivatives in Eq. (C.10) are discretised using finite differences to obtain an ODE for each node in the vapour phase,

$$\begin{aligned} \frac{\partial T_{\mathrm{V},i}}{\partial t} = \frac{\alpha_V}{l_{\mathrm{V}}^2} \left(\frac{T_{\mathrm{V},i+1} - T_{\mathrm{V},i-1}}{\Delta z^2}\right) - \frac{(\bar{v}_z - v_{\mathrm{int}})}{l_{\mathrm{V}}} \frac{T_{\mathrm{V},i+1} - T_{\mathrm{V},i-1}}{2\Delta \mathrm{z}} \\ + \frac{4U_{\mathrm{V}} d_o}{d_i^2} \left(T_{\mathrm{air}} - T_{\mathrm{V},i}\right), \qquad i = 1, \dots, N_z. \end{aligned} \tag{C.11}$$

The discretised form of the initial and boundary conditions in Eq. (3.21) are given

$$\begin{gathered} T_{\mathrm{V},i}(t=0) = T_{\mathrm{L}} = T_{\mathrm{sat}}(P) \\ T_{\mathrm{V},1} = T_{\mathrm{L}} = T_{\mathrm{sat}}(P) \\ \frac{\partial T_{\mathrm{V}}}{\partial z} \approx \frac{T_{\mathrm{V},i-1} - 4T_{\mathrm{V},i-1} + 3T_{\mathrm{V},i}}{2} = \frac{q_{\mathrm{roof}}}{k_{\mathrm{V}}(z = l_{\mathrm{V}})}, i = 1, \dots, N_z. \end{gathered} \tag{C.12}$$

where the first spatial derivative at the tank roof has been discretised using second order backward differences.

[1] Linde, "Cryogenic Standard Tanks LITS 2," Tacherting, Germany, 2019. [Online]. Available: https://www.linde-engineering.com/en/images/P_3_3_e_12_150dpi_tcm19-5774.pdf

[2] F. Huerta and V. Vesovic, "CFD modelling of the isobaric evaporation of cryogenic liquids in storage tanks," *Int. J. Heat Mass Transfer,* vol. 176, p. 121419, 2021/09/01/ 2021, doi: https://doi.org/10.1016/j.ijheatmasstransfer.2021.121419.

[3] F. Liu, "A thorough description of how wall functions are implemented in OpenFOAM," *Proceedings of CFD with OpenSource software,* pp. 1-33, 2016.

Appendix D

Implementation of the analytical solutions in Python 3

Note: this appendix has been published as Supplementary Material in Huerta and Vesovic [1] and is reprinted without modification.

This jupyter notebook accompanies the research article "Analytical solutions for the evaporation of pure cryogens in storage tanks" to provide software implementation of the developed analytical solutions. The notebook is organized in three subsections. In the first subsection, classes for storage tanks and cryogens are created and their attributes are listed. In the second subsection, the analytical solutions and auxiliary functions are de ned for both equilibrium and non-equilibrium models. After the definitions, a storage tank and a cryogen are initialized as an example, and examples of implemented classes and solutions are provided. The last section describes the numerical methods required to implement the solutions for (i) direct calculation, (ii) thermophysical iteration and (iii) sequential calculation.

Import required packages and libraries

```
# Import relevant packages
import numpy as np
import matplotlib.pyplot as plt
import copy # Copy constructor
%matplotlib inline
```

Classes definitions

To facilitate the implementation of the analytical solutions, two classes were defined.

Storage tank class

The storage tank class contains information on the geometrical and thermal properties of a vertical cylindrical storage tank

```
class Tank:
    """ Class to be used as a container for the
    evaporation of pure cryogens"""
    def __init__(self, d_i, d_o, V):
        """ Class constructor """
        # Compulsory parameters
        self.d_i = d_i # [m] Tank internal diameter
        self.d_o = d_o # [m] Tank external diameter
        self.V = V     # [m^3] Tank volume
        self.A_T = np.pi*d_i**2/4 # [m^2] Area of the surface
        # perpendicular to the vertical axis
        self.l = V/self.A_T # [m] Tank height
        self.roof_BC = 'Neumann' # Roof Temperature boundary conditi
on,
        # "Neumann" or "Robin"
        self.thermophysical_it =  False # Thermophysical iteration
        # switch for the non-eq model
        pass

    def set_HeatTransProps(self, U_L, U_V, Q_b, Q_roof, T_air):
        """Set separately tank heat transfer properties
        Usage: set_HeatTransProps(self, U_L, U_V, Q_b, Q_roof, T_air
)"""
        self.U_L = U_L # [W*m^-2*K^-1]Overall heat transfer coeffici
ent
        # for the liquid phase stored in the tank
        self.U_V = U_V # [W*m^-2*K^-1] Overall heat transfer coeffic
ient
        # for the vapour phase stored in the tank
        self.Q_b = Q_b # [W] Heat ingress through the bottom / W
        self.Q_roof = Q_roof # [W] Heat ingress through the roof
        self.T_air = T_air # [K] Temperature of the surrounding air
/K
        pass

    def set_LF(self, LF):
        """Update liquid filling and vapour length"""
        self.LF = LF # [-] set tank liquid filling
        self.l_V = self.l * (1-LF) # [m] sets vapour length
        pass

    def set_advective_v(self):
        """Update advective velocity with respect to tank liquid fil
ling"""
        # Area of the tank walls in contact with the liquid phase
        A_L = np.pi * self.d_o * self.l * self.LF
        # Initial wall heat ingress
        Q_L0 = self.U_V * A_L * (self.T_air-self.cryogen.T_sat)
        # Initial evaporation rate mol/s
```

```
        BL_0 = (Q_L0 + self.Q_b)/((self.cryogen.h_V-self.cryogen.h_L
))
        self.v_z = 4*BL_0/(self.cryogen.rho_V*np.pi*self.d_i**2)
        pass
```

Cryogen class definition

The cryogen class contains the thermophysical properties of a pure cryogen.

```
class Cryogen:
    """ Class which contains a cryogen thermodynamic
    and thermophysical properties """
    def __init__(self, name, P, T_sat, rho_L, rho_V, h_L, h_V, k_V,
cp_V):
        """Constructor"""
        self.name = name
        self.P = P # Pressure / Pa
        self.T_sat = T_sat # Saturation temperature / K
        self.rho_L = rho_L # Liquid Density / mol*m^-3
        self.rho_V = rho_V # Vapour density / mol*m^-3
        self.rho_V_sat = rho_V # Initialize vapour density at the in
terface
        self.h_L = h_L # Liquid enthalpy J/mol
        self.h_V = h_V # Vapour enthalpy J/mol
        self.k_V = k_V # Thermal conductivity of the vapour W/mK
        self.k_int = k_V # Thermal conductivity at the vapour-liquid
 interface
        self.cp_V = cp_V # Heat capacity at constant pressure / J/mo
lK
```

Analytical solutions and auxiliary functions

Equilibrium model

We can build the solutions from a selected storage tank

```
def equilibrium_sols(tank):
    """Calculates coefficients C and D in the analytical solution

    Return values:    C, D, V_L0    """
    C = -4*tank.d_o/tank.d_i**2 * \
    (tank.T_air - tank.cryogen.T_sat) / \
    (tank.cryogen.rho_L*(tank.cryogen.h_V - tank.cryogen.h_L)) * \
    (tank.U_L - tank.U_V)

    D = -1 /(tank.cryogen.rho_L*(tank.cryogen.h_V - tank.cryogen.h_L
)) * \
    ( 4*tank.d_o/tank.d_i**2 * (tank.T_air - tank.cryogen.T_sat) * \
    tank.U_V * tank.V + tank.Q_b )
```

```
    V_L0 = tank.V*tank.LF

    return C, D, V_L0

def V_L(t, C, D, V_L0):
    """Analytical solution for the liquid volume"""
    if (C != 0):
        V_L = D/C * ( np.exp(C*t)-1 ) + V_L0*np.exp(C*t)
    else:
        V_L = D*t + V_L0
    return V_L

# We can also define the BOG rate
def BOG(t, cryogen, C, D, V_L0):
    """BOG"""
    return (cryogen.rho_V - cryogen.rho_L) * ( C*V_L(t, C,D,V_L0) +
D)

def tau_evap(C,D,V_L0):
    """tau_evap(C,D,V_L0) estimates the evaporation time"""
    if C != 0:
        tau_evap = -1/C * np.log (1 + V_L0 * C/D)
    else:
        tau_evap = - V_L0/D
    return tau_evap
```

Initialize cryogens

```
# Cryogen thermophysical properties obtained from REFPROP 9.0

# Nitrogen

k_V = 7.1744e-3    #  W/(m2K)
k_V_roof = k_V # Assume k_V_roof = k_V
rho_V = 162.65316 # mol/m^3
rho_L = 2.8793e4  # mol/m^3
cp_V = 31.4624    # J/molK
T_L = 77.2435     # /K
h_V = 2.2045e3    # J/kgK
h_L = -3.3132e3   # J/kgK
P = 100000        # Pa

nitrogen = Cryogen("nitrogen", P, T_L, rho_L, rho_V, h_L, h_V, k_V,
cp_V)

# Methane
methane = Cryogen("methane", 116325, 113.2534, 2.6205e4, 128.1975, \
                  98.9155, 8.2684e3, 0.0117, 35.7950)
```

Initialize large tank

```
# Input tank properties
Q_roof = 0 # W
d_i = 76.4 # m
d_o = 80   # m
LF = 0.97
T_air = 293.15 # K
U_V = 0.0371 # W/m^2K
Q_b = 60000 # W, heat ingress from the bottom
V_tank = 165000 #m^3

# Initialize tank
large_tank = Tank(d_i, d_o, V_tank)
large_tank.set_HeatTransProps(U_V, U_V, Q_b, Q_roof, T_air)
large_tank.set_LF(LF)
large_tank.cryogen = methane
large_tank.set_advective_v()

# Build the analytical solutions
C, D, V_L0 = equilibrium_sols(large_tank)
```

Non-equilibrium model functions and solutions

Create the coefficients $\chi_{\pm,}$ c_1 and c_2

```
# PDE coefficients
def analytical_T_neq(tank):
    """ Calculates the parameters for the vapour temperature
    profile & vapour to liquid heat transfer rate

    Return values:
    chi_minus, chi_plus, c_1, c_2
    """
    name_BC = tank.roof_BC
    cryo = tank.cryogen
    H = cryo.rho_V*cryo.cp_V*tank.v_z
    S = 4*tank.U_V*tank.d_o/tank.d_i**2
    E = S*tank.T_air
    # Temperature gradient at the tank roof, if defined
    try:
        gradT_roof = tank.Q_roof/(tank.k_V_roof*tank.A_T)
    except:
        gradT_roof = tank.Q_roof/(cryo.k_V*tank.A_T)
    # Chi plus minus
    chi_plus = (H + np.sqrt(H**2+4*cryo.k_V*S))/(2*cryo.k_V)
    chi_minus = (H - np.sqrt(H**2+4*cryo.k_V*S))/(2*cryo.k_V)

    b_plus = np.exp(tank.l_V*chi_plus)
    b_minus = np.exp(tank.l_V*chi_minus)

    a_plus = chi_plus*b_plus
```

```
    a_minus = chi_minus*b_minus

    if(name_BC == "Neumann"):
        c_1 = (a_plus*(cryo.T_sat-tank.T_air) - gradT_roof)/(a_plus-
a_minus)
        c_2 = (a_minus*(tank.T_air-cryo.T_sat) + gradT_roof)/(a_plus
-a_minus)
    elif (name_BC == "Robin"):
        try:
            gamma = U_roof / k_V_roof
        except:
            gamma = tank.U_V / k_V_roof
        c_1 = (cryo.T_sat-tank.T_air)*(a_plus + gamma*b_plus)/ \
        ( (a_plus+gamma*b_plus)-(a_minus + gamma*b_minus))
        c_2 = (tank.T_air-cryo.T_sat)*(a_minus + gamma*b_minus) /\
        ((a_plus + gamma*b_plus) - (a_minus + gamma*b_minus))
    else:
        raise Exception("Unsupported BC, use Neumann or Robin")
    return chi_minus, chi_plus, c_1, c_2
```

Vapour temperature

```
def T_V(z, c_1, c_2, chi_minus, chi_plus, T_air):
    """Outputs the vapour temperature profile.
    z must be a length vector with 0 < z < l_V.
    The coefficients of the vapour T profile are also inputs"""
    TV = c_1*np.exp(z*chi_minus) + c_2 * np.exp(z*chi_plus) + T_air
    return TV
```

Vapour to liquid heat transfer rate

```
def Q_VL(tank):
    """Calculates the vapour to liquid heat ingress"""
    chi_minus, chi_plus, c_1, c_2 = analytical_T_neq(tank)
    Q = np.pi * tank.d_i **2/4 * tank.cryogen.k_int * (c_1*chi_minus
 + c_2*chi_plus)
    return Q
```

Average vapour temperature

```
def Tv_avg(tank):
    """Calculates the average vapour temperature
    for the non-equilibrium model"""
    chi_minus, chi_plus, c_1, c_2 = analytical_T_neq(tank)
    Tv_avg = tank.T_air + 1/tank.l_V * \
    (c_1/chi_minus * (np.exp(tank.l_V*chi_minus)-1) + \
     c_2/chi_plus * (np.exp(tank.l_V*chi_plus)-1))
    return Tv_avg
```

Non-equilibrium coefficients

```
def analytical_neq(tank):
    """Calculates C_neq and D_neq coefficients"""
    C_neq = -4*tank.d_o/tank.d_i**2 * \
    (tank.T_air - tank.cryogen.T_sat) / \
    (tank.cryogen.rho_L * (tank.cryogen.h_V - tank.cryogen.h_L))* \
    tank.U_L

    D_neq = - (tank.Q_b + tank.Q_VL)/\
    (tank.cryogen.rho_L * (tank.cryogen.h_V - tank.cryogen.h_L))
    return C_neq, D_neq

def Tv_plot(tank):
    """Function to plot vapour temperature profile"""
    zspan = np.linspace(0,tank.l_V,100)
    chi_minus, chi_plus, c_1, c_2 = analytical_T_neq(tank)
    plt.plot(zspan, T_V(zspan, c_1=c_1, c_2=c_2, chi_minus=chi_minus
, \
                        chi_plus = chi_plus, T_air = tank.T_air), 'r
')
    plt.xlabel("Height")
    plt.ylabel("Vapour Temperature")

# Example of usage of Tv_plot function
Tv_plot(large_tank)
```

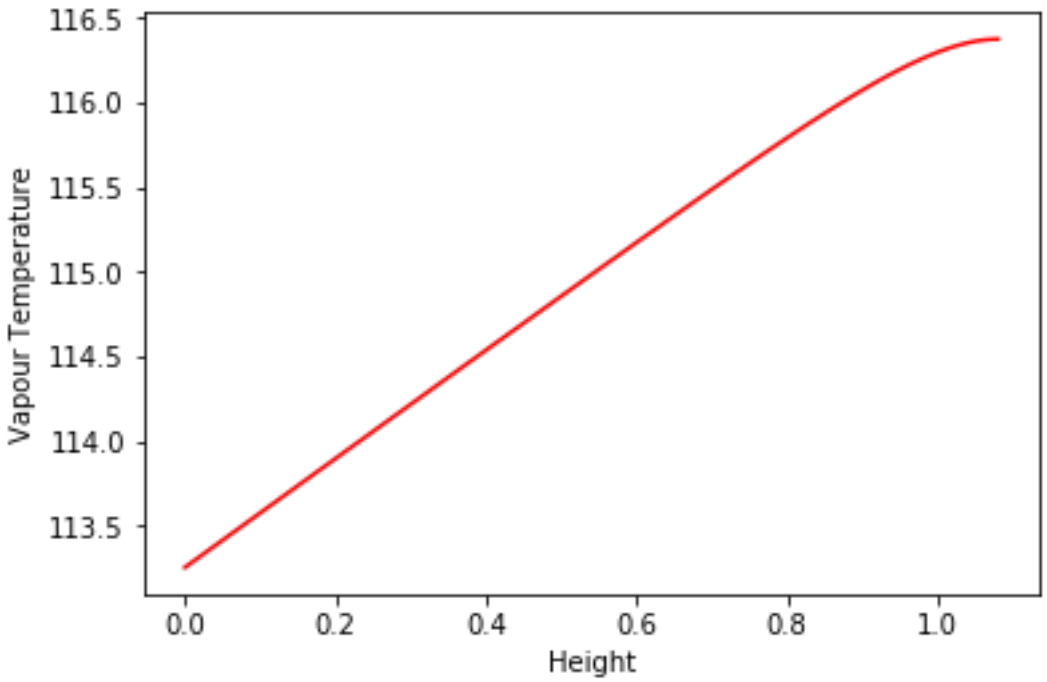

Initialize medium-size storage tank

```
# Tank properties
Q_roof = 0 # [W]
d_i = 2.8540 # [m]
d_o = 3.1480 # [m]
V_tank = 80.36 # [m^3]
LF = 0.97
T_air = 288.15 # [K]
U_V = 0.0110 # W/[m^2*K]
Q_b = 17.335 # [W], heat ingress from the bottom

mid_tank = Tank(d_i, d_o, V_tank)
mid_tank.set_HeatTransProps(U_V, U_V, Q_b, Q_roof, T_air)
mid_tank.set_LF(LF)
mid_tank.cryogen = nitrogen
mid_tank.set_advective_v()
mid_tank.Q_VL = 0
mid_tank.roof_BC = "Robin"
```

Numerical Methods

Direct calculation

```
def direct(tank, timespan):
    C_neq, D_neq = analytical_neq(tank)
    my_tank = copy.deepcopy(tank)
    V_L_direct = V_L(timespan, C=C_neq, D=D_neq, V_L0 = my_tank.V*my
_tank.LF)
    Q_VL_direct = np.zeros(len(V_L_direct))
    for i in range(0,len(V_L_direct),1):
        my_tank.set_LF(V_L_direct[i]/my_tank.V)
        # Get the temperature profile
        chi_minus, chi_plus, c_1r, c_2r = analytical_T_neq(my_tank)
        # Update Q_VL
        my_tank.Q_VL = Q_VL(my_tank)
        Q_VL_direct[i] = my_tank.Q_VL
        my_tank.set_advective_v()
        # Update advective velocity

    return V_L_direct, Q_VL_direct
```

Thermophysical iteration

This iteration updates the thermophysical properties of the vapour calculated at each timestep at the average temperature. In the original, publication the REFPROP 9.0 library was used to obtain the thermophysical properties of methane and nitrogen at different temperatures and pressures. In this Notebook, polynomials to evaluate c_p, k_V and ρ_V for methane and nitrogen are provided. For methane, the calculation is

performed at the operating pressure of the large tank, while for nitrogen the operating pressure of the small and medium sized tanks is used.

```
def T_vec(T):
    """ Utility to calculate polynomials of 6th degree"""
    return np.array([T**6, T**5, T**4, T**3, T**2, T, 1])

def k_V(T, cryogen_name):
    """Vapour thermal conductivity in W/[m*K]"""
    if cryogen_name == "nitrogen":
        coef = np.array([1.2891e-17,- 1.6853e-14, 8.9835e-12,\
                         - 2.4280e-9, 2.7918e-7, 8.4564e-5, - 1.8214
e-4])
    else:
        coef = np.array([1.05745348829032e-16,-1.66976160737431e-13,
\
                         1.06067666935673e-10,-3.42308423973392e-08,
\
                         5.92114833456723e-06, -0.000405925906877382
,\
                         0.0169054855927478])
    k_V = np.dot(T_vec(T),coef)
    return k_V

def rho_V(T, cryogen_name):
    """Vapour density in mol/[m^3]"""
    if cryogen_name == "nitrogen":
        # P = 100 kPa
        coef = np.array([4.023e-12, - 5.3256e-9, 2.9169e-6,\
                         - 8.5257e-4, + 0.1429, - 13.5159, 658.0484]
)
    else:
        coef = np.array([2.18499589355086e-12, -3.14564341280599e-09
,\
                         1.89240405227852e-06, -0.000614011250006166
,\
                         0.115248233542307,\
                         -12.3574905769077,681.411457371657])
    rho_V = np.dot(T_vec(T),coef)
    return rho_V

def cp_V(T, cryogen_name):
    """ Vapour specific heat capacity in J/[mol*K] """
    if cryogen_name == "nitrogen":
        coef = np.array([4.8391e-13, - 6.2028e-10,\
                         3.2526e-7, - 8.9351e-5,\
                         0.0136, - 1.0915, 65.8080])
    else:
```

```
        coef = np.array([8.79997426965283e-13, -1.21803356592957e-09
\
                         ,6.93498674769963e-07, \
                         -0.000207819771422151,\
                         0.0347286371956103,\
                         -3.08698360179143,\
                         148.487772497283])
    cp = np.dot(T_vec(T),coef)
    return cp

def thermophysprops(T,cryogen_name):
    return k_V(T,cryogen_name), rho_V(T, cryogen_name), cp_V(T, cryo
gen_name)

def thermophysical_iteration(tank):
    """Update k_V, rho_V and cp_V
    for a given liquid filling"""
    # Initialise old vapour temperature
    T_old = 0
    T_new = Tv_avg(tank)
    while abs(T_old-T_new) > 1e-2:
        T_old = T_new
        # Unpack thermophysical properties
        k, rho, cp = thermophysprops(T_old, tank.cryogen.name)
        # Update thermophysical properties
        tank.cryogen.k_V = k
        tank.cryogen.rho_V = rho
        tank.cryogen.cp_V = cp
        T_new = Tv_avg(tank)
```

Sequential numerical procedure

To improve the performance of the analytical solutions

```
def sequential_proc(tank, delta_t = 3600*24*7):
    """ Default timestep delta_t is a week
    delta_t must be in seconds

    Returns

    timespan: np.array, timestamps
    V_L_analytical: np.array, liquid volume
    Q_VL_analytical: np.array, vapour to liquid heat ingress
    T_V_analytical: np.array of i*j dimensions.
    T_V_analytical[i,j] corresponds to the
    temperature profile of the j node in the vapour
    at timespan[i], while     T_V_analytical[i,:]
    is the whole vapour temperature profile at timespan[i]
```

```
    """
    # Initialize Q_VL for the tank
    tank.set_advective_v()
    tank.Q_VL = Q_VL(tank)

    # Obtain C and D
    C_neq, D_neq = analytical_neq(tank)

    # Estimate evaporation time
    tau_neq = tau_evap(C_neq,D_neq,tank.V*tank.LF)

    # get n_timesteps approximating to
    # the highest nearest integer
    n_t = int(np.floor(tau_neq/(delta_t))+1)
    timespan = np.linspace(0,tau_neq,n_t)

    # Initialize V_L and Q_VL
    V_L_analytical = np.zeros(n_t)
    Q_VL_analytical = np.zeros(n_t)

    V_L_analytical[0] = tank.V*tank.LF
    Q_VL_analytical[0] = tank.Q_VL

    LF = copy.deepcopy(tank.LF)
    my_tank = copy.deepcopy(tank)

    # Initialize vapour temperature
    n_z = 100 # Number of nodes in the vapour domain
    T_V_analytical = np.zeros([n_t, n_z])
    chi_minus, chi_plus, c_1, c_2 = analytical_T_neq(my_tank)
    z = np.linspace(0,my_tank.l_V,n_z)
    T_V_analytical[0,:] = T_V(z, c_1, c_2, chi_minus, chi_plus, T_ai
r)


    for i in range(1, n_t,1):
        # Get V_L at t_0 + delta_t
        V_L_analytical[i] = V_L(delta_t, C=C_neq, D=D_neq,\
                                V_L0 = my_tank.V*my_tank.LF)
        # Update the liquid filling
        my_tank.set_LF(V_L_analytical[i]/my_tank.V)
        my_tank.set_advective_v()
        # If activated, update thermophysical properties
        if tank.thermophysical_it == True:
            thermophysical_iteration(my_tank)
        # Get the temperature profile for each time step
        chi_minus, chi_plus, c_1, c_2 = analytical_T_neq(my_tank)
        z = np.linspace(0,my_tank.l_V,n_z)
        T_V_analytical[i,:] = T_V(z, c_1, c_2, chi_minus, chi_plus,
```

```
T_air)
        # Update Q_VL
        my_tank.Q_VL = Q_VL(my_tank)
        Q_VL_analytical[i] = my_tank.Q_VL
        # Update C_neq, D_neq
        C_neq, D_neq = analytical_neq(my_tank)
    return timespan, V_L_analytical, Q_VL_analytical, T_V_analytical
```

Usage example

```
# We can set on or of the update of thermophysical properties

# Set Q_VL at the initial liquid filling
mid_tank.Q_VL = Q_VL(mid_tank)
C_neq, D_neq = analytical_neq(mid_tank)

# Thermophysical iteration and sequential procedure
mid_tank.thermophysical_it = True
timespan, V_L_analytical, Q_VL_analytical, T_V_analytical = \
sequential_proc(mid_tank, delta_t = 3600*24*7)

# Sequential procedure only
mid_tank.thermophysical_it = False
timespan, V_L_analytical_s, Q_VL_analytical_s, T_V_analytical_s = \
sequential_proc(mid_tank, delta_t = 3600*24*7)

# Direct calculation
V_L_direct, Q_VL_direct = direct(mid_tank, timespan)
```

References

[1] F. Huerta and V. Vesovic, "Analytical solutions for the isobaric evaporation of pure cryogens in storage tanks," *Int. J. Heat Mass Transfer,* vol. 143, p. 118536, 2019/11/01/ 2019, doi: https://doi.org/10.1016/j.ijheatmasstransfer.2019.118536.

Appendix E

Equations of the developed cryogen evaporation models

Geometry and heat transfer

$$A_{\mathrm{L}} = \frac{4V_{\mathrm{L}}d_{\mathrm{o}}}{d_{\mathrm{i}}^2} \tag{E.1}$$

$$A_{\mathrm{V}} = \frac{4(V_{\mathrm{T}} - V_{\mathrm{L}})d_{\mathrm{o}}}{d_i^2} \tag{E.2}$$

$$\dot{Q}_{\psi,\mathrm{in}} = U_{\psi}A_{\psi}\left(T_{\mathrm{air}} - \bar{T}_{\psi}\right), \quad \psi = \mathrm{L}\ or\ \mathrm{V} \tag{E.3}$$

Volume balance in the storage tank, valid for all models:

$$\frac{dV_V}{dt} = -\frac{dV_{\mathrm{L}}}{dt} \tag{E.4}$$

Equilibrium model for isobaric evaporation

$$-\dot{B}_{\mathrm{L}} = \rho_{\mathrm{L}}\frac{dV_{\mathrm{L}}}{dt} \tag{E.5}$$

$$-\dot{B} = -\dot{B}_{\mathrm{L}} + \rho_{\mathrm{V}}\frac{dV_{\mathrm{V}}}{dt} + V_{\mathrm{V}}\frac{d\rho_{\mathrm{V}}}{dt} \tag{E.6}$$

$$\dot{Q}_{\mathrm{L,tot}} = \dot{Q}_{\mathrm{L,in}} + \dot{Q}_{\mathrm{V,in}} + \dot{Q}_{\mathrm{bot}}, \tag{E.7}$$

$$T_{\mathrm{V}} = T_{\mathrm{L}} \tag{E.8}$$

$$\dot{Q}_{\mathrm{bot}} = U_{\mathrm{L}}A_{\mathrm{L}}(T_{\mathrm{air}} - T_{\mathrm{L}}) \tag{E.9}$$

$$\frac{dV_{\mathrm{L}}}{dt} = \frac{-\dot{Q}_{\mathrm{L,tot}}}{\rho_{\mathrm{L}}\left(h_{\mathrm{V}}(T_{\mathrm{L}}) - h_{\mathrm{L}}(T_{\mathrm{L}})\right)} = \frac{-\dot{Q}_{\mathrm{L,tot}}}{\rho_{\mathrm{L}}\Delta H_{\mathrm{LV}}} \tag{E.10}$$

$$\frac{dV_{\mathrm{V}}}{dt} = -\frac{dV_{\mathrm{L}}}{dt}, \tag{E.11}$$

Isobaric 1-D model

$$-\dot{B}_{\mathrm{L}} = \rho_{\mathrm{L}} \frac{dV_{\mathrm{L}}}{dt} \tag{E.12}$$

$$-\dot{B} = -\dot{B}_{\mathrm{L}} + \rho_{\mathrm{V}} \frac{dV_{\mathrm{V}}}{dt} + V_{\mathrm{V}} \frac{d\bar{\rho}_{\mathrm{V}}}{dt} \tag{E.13}$$

$$\dot{Q}_{\mathrm{L,tot}} = \dot{Q}_{\mathrm{L,in}} + \dot{Q}_{\mathrm{VL}} + \dot{Q}_{\mathrm{bot}}, \tag{E.14}$$

$$\dot{Q}_{\psi,\mathrm{in}} = U_{\psi} A_{\psi} \left(T_{\mathrm{air}} - T_{\psi}\right), \ \ \psi = \mathrm{L}\ or\ \mathrm{V} \tag{E.15}$$

$$\dot{Q}_{\mathrm{VL}} = \frac{\pi d_{\mathrm{i}}^2}{4} k_{\mathrm{V}}|_{z=0} \left.\frac{\partial T_{\mathrm{V}}}{\partial z}\right|_{z=0} \tag{E.16}$$

$$\dot{Q}_{\mathrm{bot}} = \ U_{\mathrm{L}} A_{\mathrm{L}} (T_{\mathrm{air}} - T_{\mathrm{L}}) \tag{E.17}$$

$$\frac{dV_{\mathrm{L}}}{dt} = \frac{-\dot{Q}_{\mathrm{L,tot}}}{\rho_{\mathrm{L}} \Delta H_{\mathrm{LV}}} \tag{E.18}$$

$$\dot{S}_{\mathrm{w,V}} = \frac{4 U_{\mathrm{V}} d_o}{d_i^2} (T_{\mathrm{air}} - T_{\mathrm{V}}) \tag{E.19}$$

$$\bar{v}_z = \frac{4\dot{B}_{\mathrm{L}}}{\pi d_{\mathrm{i}}^2 \bar{\rho}_{\mathrm{V}}} \tag{E.20}$$

$$\frac{\partial T_{\mathrm{V}}}{\partial t} = \bar{\alpha}_{\mathrm{V}} \frac{\partial^2 T_{\mathrm{V}}}{\partial z^2} - \bar{v}_z \frac{\partial T_{\mathrm{V}}}{\partial z} + \frac{\bar{\alpha}_{\mathrm{V}}}{\bar{k}_{\mathrm{V}}} \dot{S}_{\mathrm{w,V}}. \tag{E.21}$$

$$\begin{gathered} T_{\mathrm{V}}(t = 0, z) = T_{\mathrm{L}} = T_{\mathrm{sat}}(P) \\ T_{\mathrm{V}}(t, z = 0) = T_{\mathrm{L}} = T_{\mathrm{sat}}(P) \\ \frac{\partial T_{\mathrm{V}}}{\partial z}(t, z = l_{\mathrm{V}}) = \frac{q_{\mathrm{roof}}}{k_{\mathrm{V}}(z = l_{\mathrm{V}})} \end{gathered} \tag{E.22}$$

LNG weathering model

$$-\dot{B}_{\mathrm{L}} = \rho_{\mathrm{L}} \frac{dV_{\mathrm{L}}}{dt} + V_{\mathrm{L}} \frac{d\rho_{\mathrm{L}}}{dt} \tag{E.23}$$

$$-\dot{B}_{\mathrm{L}} x_i = \rho_{\mathrm{L}} V_{\mathrm{L}} \frac{dx_i}{dt} + \ \rho_{\mathrm{L}} x_i \frac{dV_{\mathrm{L}}}{dt} + V_{\mathrm{L}} x_i \frac{d\rho_{\mathrm{L}}}{dt} \ \text{ for } i = 1..n_{\mathrm{comp}} \tag{E.24}$$

$$-\dot{B} = -\dot{B}_{\mathrm{L}} + \rho_{\mathrm{V}} \frac{dV_{\mathrm{V}}}{dt} + V_{\mathrm{V}} \frac{d\rho_{\mathrm{V}}}{dt} \tag{E.25}$$

$$\dot{Q}_{\mathrm{L,tot}} = \dot{Q}_{\mathrm{L,in}} + \dot{Q}_{\mathrm{VL}} + \dot{Q}_{\mathrm{bot}} \tag{E.26}$$

$$\dot{Q}_{\mathrm{bot}} = U_{\mathrm{L}} A_{\mathrm{L}} (T_{\mathrm{air}} - T_{\mathrm{L}}) \tag{E.27}$$

$$\dot{Q}_{\mathrm{VL}} = \frac{\pi d_{\mathrm{i}}^2}{4} k_{\mathrm{V}}|_{z=0} \frac{\partial T_{\mathrm{V}}}{\partial z}\Big|_{z=0} \tag{E.28}$$

$$\dot{Q}_{\mathrm{L,tot}} = \dot{B}_{\mathrm{L}} \Delta H_{\mathrm{LV}}(P, \boldsymbol{x}, \boldsymbol{y}) + \rho_{\mathrm{L}} V_{\mathrm{L}} \frac{dh_{\mathrm{L}}}{dt}, \tag{E.29}$$

$$y_i = K_i x_i = \frac{\phi_i^{\mathrm{L}}}{\phi_i^{\mathrm{V}}} x_i \tag{E.30}$$

$$\dot{S}_{\mathrm{w,V}} = \frac{4 U_{\mathrm{V}} d_o}{d_i^2} (T_{\mathrm{air}} - T_{\mathrm{V}}) \tag{E.31}$$

$$\bar{v}_z = \frac{4\dot{B}_{\mathrm{L}}}{\pi d_{\mathrm{i}}^2 \bar{\rho}_{\mathrm{V}}} \tag{E.32}$$

$$\frac{\partial T_{\mathrm{V}}}{\partial t} = \bar{\alpha}_{\mathrm{V}} \frac{\partial^2 T_{\mathrm{V}}}{\partial z^2} - \bar{v}_z \frac{\partial T_{\mathrm{V}}}{\partial z} + \frac{\bar{\alpha}_{\mathrm{V}}}{\bar{k}_{\mathrm{V}}} \dot{S}_{\mathrm{w,V}}. \tag{E.33}$$

$$\begin{gathered} T_{\mathrm{V}}(t=0,z) = T_{\mathrm{L}}(P,x,t) = T_{\mathrm{sat}}(P,x,t) \\ T_{\mathrm{V}}(t=0,z) = T_{\mathrm{L}}(P,x,t) = T_{\mathrm{sat}}(P,x,t) \\ \frac{\partial T_{\mathrm{V}}}{\partial z}(t, z=l_{\mathrm{V}}) = \frac{q_{\mathrm{roof}}}{k_{\mathrm{V}}(z=l_{\mathrm{V}})} \end{gathered} \tag{E.34}$$

Vapour-CFD model

$$-\dot{B}_{\mathrm{L}} = \rho_{\mathrm{L}} \frac{dV_{\mathrm{L}}}{dt} \tag{E.35}$$

$$-\dot{B} = -\dot{B}_{\mathrm{L}} + \rho_{\mathrm{V}} \frac{dV_{\mathrm{V}}}{dt} + V_{\mathrm{V}} \frac{d\bar{\rho}_{\mathrm{V}}}{dt} \tag{E.36}$$

$$\dot{Q}_{\mathrm{L,tot}} = \dot{Q}_{\mathrm{L,in}} + \dot{Q}_{\mathrm{VL}} + \dot{Q}_{\mathrm{bot}}, \tag{E.37}$$

$$\dot{Q}_{\psi,\mathrm{in}} = U_{\psi} A_{\psi} \left(T_{\mathrm{air}} - T_{\psi}\right), \quad \psi = \mathrm{L}\ or\ \mathrm{V} \tag{E.38}$$

$$\dot{Q}_{\mathrm{VL}} = 2\pi k_{\mathrm{V}}(T_{\mathrm{L}}) \int_0^{R_{\mathrm{T}}} \frac{\partial T_{\mathrm{V}}}{\partial z}|_{z=0}\, r dr \tag{E.39}$$

$$\dot{Q}_{\mathrm{bot}} = U_{\mathrm{L}} A_{\mathrm{L}} (T_{\mathrm{air}} - T_{\mathrm{L}}) \tag{E.40}$$

$$\frac{dV_{\mathrm{L}}}{dt} = \frac{-\dot{Q}_{\mathrm{L,tot}}}{\rho_{\mathrm{L}}\Delta H_{\mathrm{LV}}} \tag{E.41}$$

$$\frac{\partial \rho_{\mathrm{V}}}{\partial t} + \nabla \cdot (\rho_{\mathrm{V}}\mathbf{v}) = 0 \tag{E.42}$$

$$\frac{\partial}{\partial t}(\rho_{\mathrm{V}}\mathbf{v}_{\mathrm{V}}) = -[\nabla \cdot \rho_{\mathrm{V}}\mathbf{v}_{\mathrm{V}}\mathbf{v}_{\mathrm{V}}] - \nabla P + \left[\nabla \cdot \left(\mu_{\mathrm{V}}\left(\mathbf{v}_{\mathrm{V}} + \mathbf{v}_{\mathrm{V}}^{\mathrm{T}}\right) - \frac{2}{3}\mu_{\mathrm{V}}(\nabla \cdot \mathbf{v}_{\mathrm{V}})\mathbf{I}\right)\right] + \rho_{\mathrm{V}}\mathbf{g} \tag{E.43}$$

$$\frac{\partial}{\partial t}\left(\frac{1}{2}\rho_{\mathrm{V}}|\mathbf{v}_{\mathrm{V}}|^2 + \rho_{\mathrm{V}}h_{\mathrm{V}}\right) = -\nabla \cdot \left(\frac{1}{2}\rho_{\mathrm{V}}|\mathbf{v}_{\mathrm{V}}|^2\mathbf{v}_{\mathrm{V}} + \rho_{\mathrm{V}}h_{\mathrm{V}}\mathbf{v}_{\mathrm{V}}\right) + k_{\mathrm{V}}\nabla^2 T_{\mathrm{V}} + \rho(\mathbf{v}_{\mathrm{V}} \cdot \mathbf{g}) + \frac{dP}{dt} \tag{E.44}$$

$$v_{\mathrm{V},z}|_{r,z=0} = \frac{\dot{B}_{\mathrm{L}}}{\rho_{\mathrm{V}}(T_{\mathrm{L}})\pi R_{\mathrm{T}}^2} \tag{E.45}$$

Boundary conditions for the vapour-CFD model

Field	Axis	Interface	Wall	Roof	Valve
P	$\frac{\partial P}{\partial r} = 0$	Calculated	Calculated	Calculated	10^5 Pa
$\mathbf{v}_{\mathrm{V}}$	$\frac{\partial v_{r,\mathrm{V}}}{\partial r} = 0$	$v_{z.\mathrm{V}}\|_{r,z=0}$, see Eq. (E.45)	(o o)	(o o)	Calculated
T_{V}	$\frac{\partial T_{\mathrm{V}}}{\partial r} = 0$	$T_{\mathrm{L}} = T_{\mathrm{sat}}(P)$	$\frac{\partial T_{\mathrm{V}}}{\partial r} = \frac{U_{\mathrm{V}}}{k_{\mathrm{V}}}(T_{\mathrm{air}} - T_{\mathrm{V}})$	$\frac{\partial T_{\mathrm{V}}}{\partial z} = 0$	$\frac{\partial T_{\mathrm{V}}}{\partial z} = 0$

Initial conditions for the vapour-CFD model

Field	Initial condition
P	$P_{\mathrm{valve}} + \rho_{\mathrm{V}}\|\mathbf{g}\|(l_{\mathrm{V}} - z)$
$\mathbf{v}_{\mathrm{V}}$	$(0, 0)$
T_{V}	$T_{\mathrm{L}} = T_{\mathrm{sat}}(P)$

Analytical solutions of the equilibrium model

$$\frac{dV_{\mathrm{L}}}{dt} = CV_{\mathrm{L}} + D, \tag{E.46}$$

$$C = -\frac{4d_{\mathrm{o}}}{d_{\mathrm{i}}^2}\frac{(T_{\mathrm{air}} - T_{\mathrm{L}})}{\rho_{\mathrm{L}}\Delta H_{\mathrm{LV}}}(U_{\mathrm{L}} - U_{\mathrm{V}}) \tag{E.47}$$

$$D = -\frac{1}{\rho_{\mathrm{L}}\Delta H_{\mathrm{LV}}}\left(\frac{4d_{\mathrm{o}}}{d_{\mathrm{i}}^2}(T_{\mathrm{air}} - T_{\mathrm{L}})U_{\mathrm{V}}V_{\mathrm{T}} + \dot{Q}_{\mathrm{bot}}\right) \tag{E.48}$$

$$-V_{\mathrm{L}} = \frac{D}{C}(\exp(Ct) - 1) + V_{\mathrm{T}}LF\exp(Ct), \qquad t \le \tau_{\mathrm{evap}} \tag{E.49}$$

$$\tau_{\text{evap}} = \frac{1}{C}\ln\left(1 + V_{\text{T}} LF\ \frac{C}{D}\right)^{-1} = -\frac{1}{C}\ln\left(1 + V_{\text{T}} LF\,\frac{C}{D}\right) \tag{E.50}$$

$$-\dot{B}_{\text{L}} = -\rho_{\text{L}}(CV_{\text{L}} + D), \tag{E.51}$$

$$\dot{B}(t) = (\bar{\rho}_{\text{V}} - \rho_{\text{L}})(CV_{\text{L}}(t) + D). \tag{E.52}$$

Analytical solutions for the isobaric 1-D model

$$\bar{v}_z = \frac{4\dot{B}_{\text{L}}}{\pi d_{\text{i}}^2 \bar{\rho}_{\text{V}}}, \tag{E.53}$$

$$\bar{k}_{\text{V}} \frac{d^2 T_{\text{V}}}{dz^2} - H\frac{dT_{\text{V}}}{dz} - ST_{\text{V}} = -E, \tag{E.54}$$

$$H = \bar{\rho}_{\text{V}} \bar{c}_{\text{p,V}} \bar{v}_z, \quad S = \frac{4U_{\text{V}} d_{\text{o}}}{d_{\text{i}}^2}, \quad E = ST_{\text{air}}\,, \tag{E.55}$$

$$\begin{aligned} T_{\text{V}}|_{z=0} &= T_{\text{L}}\,, \\ \left.\frac{dT_{\text{V}}}{dz}\right|_{z=l_{\text{V}}} &= \frac{q_{\text{roof}}}{k_{\text{V}}(z = l_{\text{V}})}\,. \end{aligned} \tag{E.56}$$

$$T_{\text{V}}(z) = c_1 \exp(z\chi_-) + c_2 \exp(z\chi_+) + T_{\text{air}}\,, \tag{E.57}$$

$$\chi_\pm = \frac{H \pm \sqrt{H^2 + 4\bar{k}_{\text{V}} S}}{2\bar{k}_{\text{V}}}. \tag{E.58}$$

$$\bar{T}_{\text{V}}(l_{\text{V}}) = T_{\text{air}} + \frac{1}{l_{\text{V}}}\left(\frac{c_1}{\chi_-}\left(\exp(l_{\text{V}}\chi_-) - 1\right) + \frac{c_2}{\chi_+}\left(\exp(l_{\text{V}}\chi_+) - 1\right)\right), \tag{E.59}$$

For a Neumann boundary condition at the tank roof, q_{roof} = constant:

$$c_1 = \frac{a_+(T_{\text{L}} - T_{\text{air}}) - \left.\frac{dT_{\text{V}}}{dz}\right|_{z=l_{\text{V}}}}{a_+ - a_-}, \quad c_2 = \frac{a_-(T_{\text{air}} - T_{\text{L}}) + \left.\frac{dT_{\text{V}}}{dz}\right|_{z=l_{\text{V}}}}{a_+ - a_-}, \tag{E.60}$$

$$a_\pm = \chi_\pm b_\pm\,, \tag{E.61}$$

$$b_\pm = \exp(l_{\text{V}}\chi_\pm), \tag{E.62}$$

$$\left.\frac{dT_{\text{V}}}{dz}\right|_{z=l_{\text{V}}} = \frac{q_{\text{roof,fixed}}}{k_{\text{V}}|_{z=l_{\text{V}}}}\,. \tag{E.63}$$

For a Robin boundary condition at the tank roof, $q_{roof} = U_{roof}(T_{air} - T_V(l_V))$:

$$c_1 = \frac{(T_\mathrm{L} - T_\mathrm{air})(a_+ + \gamma b_+)}{(a_+ + \gamma b_+) - (a_- + \gamma b_-)}, \quad c_2 = \frac{(T_\mathrm{air} - T_\mathrm{L})(a_- + \gamma b_-)}{(a_+ + \gamma b_+) - (a_- + \gamma b_-)}, \tag{E.64}$$

$$\gamma = \frac{U_\mathrm{roof}}{k_\mathrm{V}|_{z=l_\mathrm{V}}}, \tag{E.65}$$

$$\dot{Q}_\mathrm{VL} = \frac{\pi d_\mathrm{i}^2}{4} k_\mathrm{V}|_{z=0}(c_1\chi_- + c_2\chi_+)\,. \tag{E.66}$$

$$C_\mathrm{neq} = -\frac{4d_\mathrm{o}}{d_\mathrm{i}^2}\,\frac{(T_\mathrm{air} - T_\mathrm{L})}{\rho_\mathrm{L}(h_\mathrm{V} - h_\mathrm{L})} U_\mathrm{L}\,, \tag{E.67}$$

$$D_\mathrm{neq} = -\frac{\dot{Q}_\mathrm{bot} + \dot{Q}_\mathrm{VL}}{\rho_\mathrm{L}\Delta H_\mathrm{LV}(P)} \tag{E.68}$$

$$\frac{dV_\mathrm{L}}{dt} = C_\mathrm{neq}V_\mathrm{L} + D_\mathrm{neq} \tag{E.69}$$

$$-V_\mathrm{L} = \frac{D_\mathrm{neq}}{C_\mathrm{neq}}\left(\exp\left(C_\mathrm{neq}t\right) - 1\right) + V_\mathrm{T}LF\exp\left(C_\mathrm{neq}t\right), \qquad t \le \tau_\mathrm{evap} \tag{E.70}$$

$$\tau_\mathrm{evap} = \frac{1}{C_\mathrm{neq}}\ln\left(1 + V_\mathrm{T}LF\,\frac{C_\mathrm{neq}}{D_\mathrm{neq}}\right)^{-1} = -\frac{1}{C_\mathrm{neq}}\ln\left(1 + V_\mathrm{T}LF\,\frac{C_\mathrm{neq}}{D_{neq}}\right) \tag{E.71}$$

$$-\dot{B}_\mathrm{L} = -\rho_\mathrm{L}(C_\mathrm{neq}V_\mathrm{L} + D_\mathrm{neq}), \tag{E.72}$$

$$\dot{B}(t) = (\bar{\rho}_\mathrm{V} - \rho_\mathrm{L})\left(C_\mathrm{neq}V_\mathrm{L}(t) + D_\mathrm{neq}\right). \tag{E.73}$$

Non-isobaric equilibrium model

$$-\dot{B}_\mathrm{L} = \rho_\mathrm{L}\frac{dV_\mathrm{L}}{dt} + V_\mathrm{L}\frac{d\rho_\mathrm{L}}{dt} \tag{E.74}$$

$$\frac{d}{dt}(\rho_\mathrm{L}V_\mathrm{L} + \rho_\mathrm{V}V_\mathrm{V}) = -\dot{B}_\mathrm{L} + \rho_\mathrm{V}\frac{dV_\mathrm{V}}{dt} + V_\mathrm{V}\frac{d\rho_\mathrm{V}}{dt} = 0 \tag{E.75}$$

$$T_\mathrm{L} = T_\mathrm{V} = T_\mathrm{sat} \tag{E.76}$$

$$\dot{Q}_\mathrm{VI} - \dot{Q}_\mathrm{IL} = \dot{B}_\mathrm{L}\Delta H_\mathrm{LV}(P_\mathrm{sat}) \tag{E.77}$$

$$\dot{Q}_\mathrm{bot} = U_\mathrm{L}A_\mathrm{L}(T_\mathrm{air} - T_\mathrm{L}) \tag{E.78}$$

$$\dot{Q}_{\text{tot}} = \left((U_{\text{bot}} + U_{\text{roof}}) A_{\text{T}} + \frac{4 d_o}{d_i} \left(V_{\text{T}} U_{\text{L}} + V_{\text{V}} (U_{\text{V}} - U_{\text{L}}) \right) \right) (T_{\text{air}} - T_{\text{sat}}) \tag{E.79}$$

$$\frac{dT_{\text{sat}}}{dt} = \frac{\dot{Q}_{\text{tot}} - \dot{B}_{\text{L}} \Delta H_{\text{LV}}(P_{\text{sat}})}{\left(\rho_{\text{L}} c_{p,\text{L}} (V_{\text{T}} - V_{\text{V}}) + \rho_{\text{V}} c_{\text{p,V}} V_{\text{V}} \right)} \tag{E.80}$$

$$\phi_{\text{L}} = \phi_{\text{V}} \tag{E.81}$$

Non-isobaric 1-D model

$$-\dot{B}_{\text{L}} = \frac{d}{dt} (\bar{\rho}_{\text{L}} V_{\text{L}}) = \bar{\rho}_{\text{L}} \frac{dV_{\text{L}}}{dt} + V_{\text{L}} \frac{d\bar{\rho}_{\text{L}}}{dt}, \tag{E.82}$$

$$\frac{d}{dt} (\bar{\rho}_{\text{L}} V_{\text{L}} + \bar{\rho}_{\text{V}} V_{\text{V}}) = -\dot{B}_{\text{L}} + \bar{\rho}_{\text{V}} \frac{dV_{\text{V}}}{dt} + V_{\text{V}} \frac{d\bar{\rho}_{\text{V}}}{dt} = 0 \tag{E.83}$$

$$\dot{Q}_{\text{w,b}} = \eta_{\text{e,w}} \dot{Q}_{\text{L,in}} + \eta_{\text{e,b}} \dot{Q}_{\text{bot}} \tag{E.84}$$

$$\dot{B}_{\text{L}} = \frac{\left(\dot{Q}_{\text{VI}} - \dot{Q}_{\text{IL}} + \dot{Q}_{\text{w,b}} \right)}{\Delta H_{\text{LV}}} = \dot{B}_{\text{L,s}} + \dot{B}_{\text{L,w}} \tag{E.85}$$

$$\dot{Q}_{\text{VI}} = \pi R_{\text{T}}^2 \left(k_{\text{V}} \frac{\partial T_{\text{V}}}{\partial z} \right) \Big|_{z = l_{\text{L}}} \tag{E.86}$$

$$\dot{Q}_{\text{IL}} = \pi R_{\text{T}}^2 \left(k_{\text{L}} \frac{\partial T_{\text{L}}}{\partial z} \right) \Big|_{z = l_{\text{L}}} \tag{E.87}$$

$$\dot{S}_{\text{w,V}} = \frac{4 U_{\text{V}} d_{\text{o}}}{d_{\text{i}}^2} (T_{\text{air}} - T_{\text{V}}). \tag{E.88}$$

$$\dot{S}_c = \begin{cases} f_c (T_{sat} - T_{\text{V}}) & \text{if } T_{\text{V}} < T_{\text{sat}} \\ 0 & \text{otherwise} \end{cases} \tag{E.89}$$

$$\frac{\partial T_{\text{V}}}{\partial t} = \bar{\alpha}_{\text{V}} \frac{\partial^2 T_{\text{V}}}{\partial z^2} + \frac{\bar{\alpha}_{\text{V}}}{\bar{k}_V} \left(\dot{S}_{\text{w,V}} + \dot{S}_c \right). \tag{E.90}$$

$$\begin{gathered} T_{\text{V}}(t = 0,\ l_{\text{L}} < z < l_{\text{V}}) = T_{\text{sat}}(P_0), \\ T_{\text{V}}(t, z = l_{\text{L}}) = T_{\text{sat}}(P_{\text{I}}), \\ \frac{\partial T_{\text{V}}}{\partial z} (t, z = l_{\text{L}} + l_{\text{V}}) = \frac{q_{\text{roof}}}{k_{\text{V}}(z = l_{\text{L}} + l_{\text{V}})}, \end{gathered} \tag{E.91}$$

$$\dot{S}_{\text{w,L}} = \frac{4 U_{\text{L}} d_{\text{o}}}{d_{\text{i}}^2} (T_{\text{air}} - T_{\text{L}}). \tag{E.92}$$

$$\dot{S}_{\mathrm{e}} = \begin{cases} f_b(T_{\mathrm{L}} - T_{\mathrm{sat}}) & \text{if } T_{\mathrm{L}} > T_{\mathrm{sat}} \\ 0 & \text{otherwise} \end{cases} \tag{E.93}$$

$$\frac{\partial T_{\mathrm{L}}}{\partial t} = \bar{\alpha}_{\mathrm{L}} \frac{\partial^2 T_{\mathrm{L}}}{\partial z^2} + \frac{\bar{\alpha}_{\mathrm{L}}}{\bar{k}_{\mathrm{L}}} (\dot{S}_{\mathrm{w,L}} - \dot{S}_{\mathrm{e}}). \tag{E.94}$$

$$\begin{gathered} T_{\mathrm{L}}(t = 0, 0 < z < l_{\mathrm{L}}) = T_{\mathrm{sat}}(P_0), \\ T_{\mathrm{L}}(t, z = l_{\mathrm{L}}) = T_{\mathrm{sat}}(P_{\mathrm{I}}), \\ \frac{\partial T_{\mathrm{L}}}{\partial z}(t, z = 0) = \frac{q_{\mathrm{bot}}}{k_{\mathrm{L}}(z = 0)}, \end{gathered} \tag{E.95}$$

$$P_{\mathrm{int}} = P_{\mathrm{V}}(\bar{\rho}_{\mathrm{V}}, \bar{T}_{\mathrm{V}}) \, , \tag{E.96}$$

$$\phi_{\mathrm{L}}(z = l_{\mathrm{L}}, P_{\mathrm{int}}, T_{\mathrm{sat}}) = \phi_{\mathrm{V}}(z = l_{\mathrm{L}}, P, T_{\mathrm{sat}}). \tag{E.97}$$

Single phase CFD model for non-isobaric evaporation (CFD-SP)

$$\nabla \cdot \mathbf{v}_{\mathrm{L}} = 0 \tag{E.98}$$

$$\begin{aligned} \frac{\partial \mathbf{v}_{\mathrm{L}}}{\partial t} + \mathbf{v}_{\mathrm{L}} \cdot \nabla \mathbf{v}_{\mathrm{L}} = \; & -\nabla P_{\mathrm{rgh}} + \nabla \cdot \left(\nu_{\mathrm{L}} (\nabla \mathbf{v}_{\mathrm{L}} + (\nabla \mathbf{v}_{\mathrm{L}})^{\mathrm{T}}) \right) - \frac{2}{3} \nu_{\mathrm{L}} (\nabla \cdot \mathbf{v}_{\mathrm{L}}) \mathbf{I} \\ & + \rho_{\mathrm{k}} \mathbf{g} \end{aligned} \tag{E.99}$$

$$\frac{\partial T_{\mathrm{L}}}{\partial t} = \nabla \cdot (\alpha_{\mathrm{L}} \nabla T_{\mathrm{L}}) - \nabla \cdot (\mathbf{v}_{\mathrm{L}} T_{\mathrm{L}}). \tag{E.100}$$

$$\begin{gathered} T_{\mathrm{L}}|_{t=0} = T_{\mathrm{sat}}(P_{\mathrm{V}}|_{t=0}), \\ \left. \frac{\partial T_{\mathrm{L}}}{\partial z} \right|_{r=0,z} = 0, \\ T_{\mathrm{L}}|_{r,z=l_L} = T_{\mathrm{sat}}(P_{\mathrm{I}}), \\ k_{\mathrm{L}} \left. \frac{\partial T_{\mathrm{L}}}{\partial z} \right|_{r,z=0} = \dot{q}_b = (1 - \eta_{\mathrm{e,b}}) U_{\mathrm{L},b} \left(T_{\mathrm{air}} - T_{\mathrm{L}}|_{r,z=0} \right), \\ k_{\mathrm{L}} \left. \frac{\partial T_{\mathrm{L}}}{\partial r} \right|_{r=R_{\mathrm{T}},z} = (1 - \eta_{\mathrm{e,w}}) \dot{q}_{\mathrm{L,w}} = (1 - \eta_{\mathrm{e,w}}) U_{\mathrm{L}} \left(T_{air} - T_L|_{r=R_{\mathrm{T}},z} \right), \end{gathered} \tag{E.101}$$

$$P_{\text{int}} = P_{\text{V}}(\bar{\rho}_{\text{V}}, \bar{T}_{\text{V}}) \,, \tag{E.102}$$

$$\frac{d}{dt}(\bar{\rho}_{\text{L}} V_{\text{L}} + \bar{\rho}_{\text{V}} V_{\text{V}}) = -\dot{B}_{\text{L}} + \bar{\rho}_{\text{V}} \frac{dV_{\text{V}}}{dt} + V_{\text{V}} \frac{d\bar{\rho}_{\text{V}}}{dt} = 0 \tag{E.103}$$

$$\dot{Q}_{\text{V,in}} + \dot{Q}_{\text{roof}} - \dot{Q}_{\text{VI}} + \dot{B}_{\text{L}} h_{\text{V}}(T_{\text{sat}}) = \frac{d}{dt}\left(\bar{\rho}_{\text{V}} V_{\text{V}} \bar{h}_{\text{V}}\right). \tag{E.104}$$

$$\dot{Q}_{\text{w,b}} = \eta_{\text{e,w}} \dot{Q}_{\text{L,in}} + \eta_{\text{e,b}} \dot{Q}_{\text{bot}}. \tag{E.105}$$

$$\dot{B}_{\text{L}} = \frac{\left(\dot{Q}_{\text{VI}} - \dot{Q}_{\text{IL}} + \dot{Q}_{\text{w,b}}\right)}{\Delta H_{\text{LV}}} = \dot{B}_{\text{L,s}} + \dot{B}_{\text{L,w}}. \tag{E.106}$$

$$\dot{Q}_{\text{IL}} = 2\pi k_{\text{L}}(T_{\text{sat}}) \int_0^{R_{\text{T}}} \frac{\partial T_{\text{L}}}{\partial z}|_{z=l_{\text{L}}} r dr \,. \tag{E.107}$$

Closure for the vapour bulk model

$$\dot{Q}_{\text{VI}} = \dot{Q}_{\text{V,in}} + \dot{Q}_{\text{roof}} - \bar{\rho}_{\text{V}} V_{\text{V}} c_{\text{p,V}} \frac{d\bar{T}_{\text{V}}}{dt} \tag{E.108}$$

$$\frac{dP_{\text{V}}}{dt} = F\left(\dot{Q}_{\text{VI}} - \dot{Q}_{\text{IL}} + \dot{Q}_{\text{w,b}}\right) \tag{E.109}$$

$$F = \frac{\Delta H_{\text{LV}}}{V_{\text{V}}}\left(c_{\text{V,V}} T_{\text{sat}} + \left(\frac{\Delta H_{\text{LV}}}{R T_{\text{sat}}} - 1\right)\frac{\bar{\rho}_{\text{L}}}{\bar{\rho}_{\text{L}} - \rho_{\text{V}}}\left[\Delta H_{\text{LV}} - P_{\text{V}}\left(\frac{1}{\rho_{\text{V}}} - \frac{1}{\bar{\rho}_{\text{L}}}\right)\right]\right)^{-1} [1] \tag{E.110}$$

$$\phi_{\text{L}}(z = l_{\text{L}}, P_{\text{int}}, T_{\text{sat}}) = \phi_{\text{V}}(P_{\text{V}}, T_{\text{sat}}). \tag{E.111}$$

Closure for the Non-equilibrium 1-D vapour phase sub-model using analytical solutions.

The quantities $\chi_{\pm}$, c_1 and c_2 are given by Eqs. (E.) and (E.).

$$\bar{T}_{\text{V}}(l_{\text{V}}) = T_{\text{air}} + \frac{1}{l_{\text{V}}}\left(\frac{c_1}{\chi_-}\left(\exp(l_{\text{V}}\chi_-) - 1\right) + \frac{c_2}{\chi_+}\left(\exp(l_{\text{V}}\chi_+) - 1\right)\right), \tag{E.112}$$

$$\dot{Q}_{\text{VI}} = \frac{\pi d_{\text{i}}^2}{4} k_{\text{V}}|_{z=0}(c_1\chi_- + c_2\chi_+) \,. \tag{E.113}$$

$$\frac{dP_{\text{V}}}{dt} = \frac{R}{V_{\text{V}}}\left(\dot{B}_{\text{L}}\left[T_{\text{sat}} - \bar{T}_{\text{V}}\frac{\bar{\rho}_{\text{V}}}{\bar{\rho}_{\text{L}}}\right] + \frac{\dot{Q}_{\text{roof}} + \dot{Q}_{\text{V,in}} - \dot{Q}_{\text{VI}}}{c_{p,\text{V}}}\right). \tag{E.114}$$

$$\phi_{\text{L}}(z = l_{\text{L}}, P_{\text{int}}, T_{\text{sat}}) = \phi_{\text{V}}(z = l_{\text{L}}, P, T_{\text{sat}}). \tag{E.115}$$

Multiphase CFD model for non-isobaric evaporation (CFD-MP)

$$\frac{\partial(\rho_{\mathrm{L}}\alpha_{\mathrm{L}})}{\partial t}+\nabla\cdot(\rho_{\mathrm{L}}\alpha_{\mathrm{L}}\mathbf{v}_{\mathrm{L}})=-\Gamma_{\mathrm{LV}}\,, \tag{E.116}$$

$$\frac{\partial(\rho_{\mathrm{V}}\alpha_{\mathrm{V}})}{\partial t}+\nabla\cdot(\rho_{\mathrm{V}}\alpha_{\mathrm{V}}\mathbf{v}_{\mathrm{V}})=\Gamma_{\mathrm{LV}}\,, \tag{E.117}$$

$$\alpha_{\psi}=\frac{V_{\psi,\mathrm{cell}}}{V_{\mathrm{cell}}}\quad \text{for } \psi=\mathrm{L},\mathrm{V}, \tag{E.118}$$

$$\Gamma_{\mathrm{LV}}=\frac{h_{\mathrm{i,L}}a_{\mathrm{if}}(T_{\mathrm{L}}-T_{\mathrm{sat}})+h_{\mathrm{i,V}}a_{\mathrm{if}}(T_{\mathrm{V}}-T_{\mathrm{sat}})}{\Delta H_{\mathrm{LV}}}\,, \tag{E.119}$$

$$a_{\mathrm{if}}=\begin{cases}\dfrac{6\alpha_{\mathrm{V}}}{d_{\mathrm{s,d}}}, & \alpha_{\mathrm{V}}<0.5,\ \text{vapour bubbles dispersed in liquid}\\[2ex] \dfrac{6\alpha_{\mathrm{L}}}{d_{\mathrm{s,b}}}, & \alpha_{\mathrm{V}}\geq 0.5,\ \text{liquid droplets dispersed in vapour}\end{cases} \tag{E.120}$$

$$Nu_{\mathrm{i,L}}=\left(\frac{12}{\pi}Ja+\frac{2}{\sqrt{\pi}}\cdot k_{\mathrm{L}}Pe_{\mathrm{LV}}^{1/2}\right),\ [2] \tag{E.121}$$

$$Nu_{\mathrm{i,V}}=\left(\frac{12}{\pi}Ja+\frac{2}{\sqrt{\pi}}\cdot k_{\mathrm{V}}Pe_{\mathrm{VL}}^{1/2}\right)[2] \tag{E.122}$$

$$Pe_{\mathrm{LV}}=Re_{\mathrm{b}}Pr_{\mathrm{L}},\qquad Pe_{\mathrm{VL}}=Re_{\mathrm{d}}Pr_{\mathrm{V}} \tag{E.123}$$

$$Re_{\mathrm{b}}=\frac{\rho_{\mathrm{L}}|\mathbf{v}_{\mathrm{V}}-\mathbf{v}_{\mathrm{L}}|d_{\mathrm{s,b}}}{\mu_{\mathrm{L}}}\,,Re_{\mathrm{d}}=\frac{\rho_{\mathrm{V}}|\mathbf{v}_{\mathrm{L}}-\mathbf{v}_{\mathrm{V}}|d_{\mathrm{s,d}}}{\mu_{\mathrm{V}}} \tag{E.124}$$

$$\begin{aligned}\frac{\partial(\rho_{\mathrm{L}}\alpha_{\mathrm{L}}\mathbf{v}_{\mathrm{L}})}{\partial t}&=-\alpha_{\mathrm{L}}\nabla P+\ \nabla\cdot\left[\alpha_{\mathrm{L}}\mu_{\mathrm{L}}(\nabla\mathbf{v}_{\mathrm{L}}+(\nabla\mathbf{v}_{\mathrm{L}})^{\mathrm{T}})-\frac{2}{3}\alpha_{\mathrm{L}}\mu_{\mathrm{L}}(\nabla\cdot\mathbf{v}_{\mathrm{L}})\mathbf{I}\right]\\&-\nabla\cdot[\rho_{\mathrm{L}}\alpha_{\mathrm{L}}\mathbf{v}_{\mathrm{L}}\mathbf{v}_{\mathrm{L}}]\ +\alpha_{\mathrm{L}}\rho_{\mathrm{L}}\mathbf{g}+\Gamma_{\mathrm{LV}}(\mathbf{v}_{\mathrm{V}}-\mathbf{v}_{\mathrm{L}})+\mathbf{M}_{\mathrm{LV}}\frac{\partial T_{\mathrm{V}}}{\partial z}(t,z=l_{\mathrm{L}}+l_{\mathrm{V}})\end{aligned} \tag{E.125}$$

$$\begin{aligned}\frac{\partial(\rho_{\mathrm{V}}\alpha_{\mathrm{V}}\mathbf{v}_{\mathrm{V}})}{\partial t}=\ &-\alpha_{\mathrm{L}}\nabla P+\nabla\cdot\left[\alpha_{\mathrm{L}}\mu_{\mathrm{V}}(\nabla\mathbf{v}_{\mathrm{V}}+(\nabla\mathbf{v}_{\mathrm{V}})^{\mathrm{T}})-\frac{2}{3}\alpha_{\mathrm{V}}\mu_{\mathrm{V}}(\nabla\cdot\mathbf{v}_{\mathrm{V}})\mathbf{I}\right]-\\&\nabla\cdot[\rho_{\mathrm{V}}\alpha_{\mathrm{V}}\mathbf{v}_{\mathrm{V}}\mathbf{v}_{\mathrm{V}}]+\ \alpha_{\mathrm{V}}\rho_{\mathrm{V}}\mathbf{g}+\Gamma_{\mathrm{LV}}(\mathbf{v}_{\mathrm{L}}-\mathbf{v}_{\mathrm{V}})+\mathbf{M}_{\mathrm{VL}}\end{aligned} \tag{E.126}$$

$$\dot{S}_{\mathrm{e}}=\begin{cases}f_b(T_{\mathrm{L}}-T_{\mathrm{sat}}) & \text{if } T_{\mathrm{L}}>T_{\mathrm{sat}}\\ 0 & \text{otherwise}\end{cases} \tag{E.127}$$

$$\mathbf{M}_{\mathrm{LV}}=F_{\mathrm{D,LV}}+F_{\mathrm{L,LV}}+F_{\mathrm{W,LV}}+F_{\mathrm{VM,LV}}+F_{\mathrm{TD,LV}}. \tag{E.128}$$

$$F_{\mathrm{D,LV}}=\frac{1}{8}C_{\mathrm{D}}a_{\mathrm{if}}\rho_{\mathrm{L}}|\mathbf{v}_{\mathrm{V}}-\mathbf{v}_{\mathrm{L}}|(\mathbf{v}_{\mathrm{V}}-\mathbf{v}_{\mathrm{L}}) \tag{E.129}$$

$$P_{\text{int}} = P_{\text{V}}(\bar{\rho}_{\text{V}}, \bar{T}_{\text{V}}) \,, \tag{E.130}$$

$$C_{\text{D}} = \begin{cases} \frac{24\left(1+0.15\, Re_{\text{p}}^{0.687}\right)}{Re_{\text{p}}}, & Re_{\text{p}} \leq 1000 \\ 0.44\,, & Re_{\text{p}} > 1000 \end{cases} \quad [3] \tag{E.131}$$

$$Re_{\text{p}} = \frac{\rho_{\text{L}} |\mathbf{v}_{\text{v}} - \mathbf{v}_{\text{L}}| d_{\text{b}}}{\mu_{\text{L}}} . \tag{E.132}$$

$$F_{\text{L,LV}} = \frac{1}{8} C_{\text{L}} \alpha_{\text{V}} \rho_{\text{L}} (\nabla \times \mathbf{v}_{\text{L}}) \times (\mathbf{v}_{\text{V}} - \mathbf{v}_{\text{L}}), \tag{E.133}$$

$$F_{\text{LV,WL}} = \frac{\alpha_{\text{V}} \rho_{\text{L}} |(\mathbf{v}_{\text{V}} - \mathbf{v}_{\text{L}}) - [\mathbf{n}_{\text{w}} \cdot (\mathbf{v}_{\text{V}} - \mathbf{v}_{\text{L}})]\mathbf{n}_{\text{w}}|^2}{d_{\text{b}}} \left(C_{w1} + C_{w2} \frac{d_{\text{b}}}{x_{\text{w}}} \right) \mathbf{n}_{\text{w}}, \tag{E.134}$$

$$F_{\text{LV,VM}} = C_{\text{VM}} \alpha_{\text{V}} \rho_{\text{L}} \left(\frac{\text{D}\mathbf{v}_{\text{V}}}{\text{D}t} - \frac{\text{D}\mathbf{v}_{\text{L}}}{\text{D}t} \right), \tag{E.135}$$

$$F_{\text{LV,TD}} = -C_{\text{TD}} \left[\frac{1}{8} C_{\text{D}} a_{\text{if}} \rho_{\text{L}} |\mathbf{v}_{\text{V}} - \mathbf{v}_{\text{L}}| \right] \frac{\mu_{\text{V,t}}}{\rho_{\text{V}} Pr_{\text{t,b}}} \left(\frac{\nabla \alpha_{\text{V}}}{\alpha_{\text{V}}} - \frac{\nabla \alpha_{\text{L}}}{\alpha_{\text{L}}} \right), \tag{E.136}$$

$$\begin{aligned} \frac{\partial (\rho_{\text{L}} \alpha_{\text{L}} h_{\text{L}})}{\partial t} &= -\nabla \cdot (\rho_{\text{L}} \alpha_{\text{L}} \mathbf{v}_{\text{L}} h_{\text{L}}) + \nabla \cdot [\alpha_{\text{L}} k_{\text{L}} (\nabla T_{\text{L}})] + \alpha_{\text{L}} \rho_{\text{L}} (\mathbf{v}_{\text{L}} \cdot \mathbf{g}) \\ &\quad + \Gamma_{\text{LV}} (h_{\text{L}} - h_{\text{V}}) + \alpha_{\text{L}} \frac{dP}{dt} , \end{aligned} \tag{E.137}$$

$$\begin{aligned} \frac{\partial (\rho_{\text{V}} \alpha_{\text{V}} h_{\text{V}})}{\partial t} &= -\nabla \cdot (\rho_{\text{V}} \alpha_{\text{V}} \mathbf{v}_{\text{V}} h_{\text{V}}) + \nabla \cdot [\alpha_{\text{V}} k_{\text{V}} (\nabla T_{\text{V}})] + \alpha_{\text{V}} \rho_{\text{V}} (\mathbf{v}_{\text{V}} \cdot \mathbf{g}) \\ &\quad + \Gamma_{\text{LV}} (h_{\text{V}} - h_{\text{L}}) + \alpha_{\text{V}} \frac{dP}{dt} . \end{aligned} \tag{E.138}$$

Boundary conditions for multiphase model

Field	Axis	Bottom	Wall	Roof
P	$\frac{\partial P}{\partial r} = 0$	Calculated	Calculated	Calculated
$\mathbf{v}_{\text{L}}$	$\frac{\partial v_{r,\text{L}}}{\partial r} = 0$	(o o o)	(o o o)	(o o o)
$\mathbf{v}_{\text{V}}$	$\frac{\partial v_{r,\text{V}}}{\partial r} = 0$	(o o o)	(o o o)	(o o o)
T_{L}	$\frac{\partial T_{\text{L}}}{\partial r} = 0$	$\frac{\partial T_{\text{L}}}{\partial z} = \frac{U_{\text{bot}}}{k_{\text{L}}} (T_{\text{air}} - T_{\text{L}})$	$\frac{\partial T_{\text{L}}}{\partial r} = \frac{U_{\text{L}}}{k_{\text{L}}} (T_{\text{air}} - T_{\text{L}})$	$\frac{\partial T_{\text{L}}}{\partial z} = 0$
T_{V}	$\frac{\partial T_{\text{V}}}{\partial r} = 0$	$\frac{\partial T_{\text{V}}}{\partial z} = 0$	$\frac{\partial T_{\text{V}}}{\partial r} = \frac{U_{\text{V}}}{k_{\text{V}}} (T_{\text{air}} - T_{\text{V}})$	$\frac{\partial T_{\text{V}}}{\partial z} = \frac{U_{\text{roof}}}{k_{\text{V}}} (T_{air} - T_{\text{V}})$
α_{L}	$\frac{\partial \alpha_{\text{L}}}{\partial r} = 0$	$\frac{\partial \alpha_{\text{L}}}{\partial z} = 0$	$\frac{\partial \alpha_{\text{L}}}{\partial r} = 0$	$\frac{\partial \alpha_{\text{L}}}{\partial z} = 0$
α_{V}	$\frac{\partial \alpha_{\text{V}}}{\partial r} = 0$	$\frac{\partial \alpha_{\text{V}}}{\partial z} = 0$	$\frac{\partial \alpha_{\text{V}}}{\partial r} = 0$	$\frac{\partial \alpha_{\text{V}}}{\partial z} = 0$

Initial conditions for multiphase model

Field	Initial condition
P	$\rho_{\mathrm{V}} g \max(H_T - z, l_{\mathrm{V}}) + \rho_{\mathrm{L}} g \max(l_L - z, 0) + 10^5$
$\mathbf{v}_{\mathrm{L}}$	(0 0 0)
$\mathbf{v}_{\mathrm{V}}$	(0 0 0)
T_{L}	$T_{\mathrm{L}} = T_{\mathrm{sat}}(P_0)$
T_{V}	$T_{\mathrm{V}} = T_{\mathrm{sat}}(P_0)$
α_{L}	$\alpha_{\mathrm{L}} = 1$ if $z \leq l_{\mathrm{L}}$, $\alpha_{\mathrm{L}} = 0$ otherwise
α_{V}	$\alpha_{\mathrm{V}} = 1$ if $z > l_{\mathrm{L}}$, $\alpha_{\mathrm{V}} = 0$ otherwise

References

[1] C. H. Panzarella and M. Kassemi, "On the validity of purely thermodynamic descriptions of two-phase cryogenic fluid storage," *J. Fluid Mech.,* vol. 484, pp. 41-68, 2003, doi: 10.1017/s0022112003004002.

[2] K. Wolfert, " The simulation of blowdown processes with consideration of thermodynamic nonequilibrium phenomena," in *Proceedings of the Specialists Meeting of Transient Two-Phase Flow*, Toronto, ON, Canada, 3–4 August, 1976 1976: OECD/Nuclear Energy Agency.

[3] L. Schiller, "A drag coefficient correlation," *Zeit. Ver. Deutsch. Ing.,* vol. 77, pp. 318-320, 1933.

Appendix F

Simplified equilibrium model for the non-isobaric evaporation of a pure cryogen

In this appendix, a simplified model for the non-isobaric evaporation of pure cryogens is derived from the equilibrium model developed in section 6.2.1. The simplified model reduced the DAE system given by Eqs. (6.1) – (6.17) to a non-linear ordinary differential equations (ODE) system. Vapour and liquid temperatures are assumed spatially homogeneous and equal to the saturation temperature at the operating pressure, $T_{\mathrm{L}} = T_{\mathrm{V}} = T_{\mathrm{sat}}$. Under these assumptions, the global mass balance for the non-isobaric evaporation of a pure cryogen in a tank with no vent is given by,

$$\frac{d}{dt}(\rho_{\mathrm{L}} V_{\mathrm{L}} + \rho_{\mathrm{V}} V_V) = \rho_{\mathrm{L}} \frac{dV_{\mathrm{L}}}{dt} + V_{\mathrm{L}} \frac{d\rho_{\mathrm{L}}}{dt} + \rho_{\mathrm{V}} \frac{dV_{\mathrm{V}}}{dt} + V_{\mathrm{V}} \frac{d\rho_{\mathrm{V}}}{dt} = 0 \tag{F.1}$$

For short storage periods and small liquid thermal expansion coefficients, the liquid thermal expansion term in Eq. (F.1) is small, $V_{\mathrm{L}} d\rho_{\mathrm{L}}/dt \sim 0$, and will be neglected. The walls of the storage tanks have been assumed rigid. Thus, the volume of the tank is fixed and equal to the sum of the vapour and liquid volumes, $V_T = V_{\mathrm{V}} + V_{\mathrm{L}}$, which results in,

$$\frac{dV_L}{dt} = -\frac{dV_V}{dt}. \tag{F.2}$$

Combining Eqs. (F.1) and (F.2), the rate of change of liquid volume can be written as,

$$-\frac{dV_L}{dt} = \left(\frac{V_{\mathrm{T}} - V_{\mathrm{L}}}{\rho_{\mathrm{L}} - \rho_{\mathrm{V}}}\right) \frac{d\rho_{\mathrm{V}}}{dt}. \tag{F.3}$$

The vapour phase of the stored cryogen has been assumed to follow the ideal gas law,

$$\rho_{\mathrm{V}} = \frac{P}{R T_{\mathrm{sat}}}, \tag{F.4}$$

and its total time derivative can be computed using the quotient rule,

$$\frac{d\rho_{\mathrm{V}}}{dt} = \frac{1}{R T_{\mathrm{sat}}^2} \left(T_{\mathrm{sat}} \frac{dP}{dt} - P \frac{dT_{\mathrm{sat}}}{dt}\right). \tag{F.5}$$

For cryogenic fluids at typical storage conditions, the specific volume of the vapour phase is much higher than the specific volume of the liquid phase, $v_{\mathrm{V}} \gg v_{\mathrm{L}}$. This allows to neglect v_{L} in the Clausius equation, and write the phase boundary equation using the Clausius-Clapeyron relationship,

$$\frac{1}{P}\frac{dP}{dT} = \frac{\Delta H_{\mathrm{LV}}}{RT_{\mathrm{sat}}^2}, \tag{F.6}$$

The time derivative of pressure can be written as a function of the time derivative of the vapour temperature using the chain rule and Eq. (F.6),

$$\frac{dP}{dt} = \left(\frac{P\Delta H_{\mathrm{LV}}}{RT_{\mathrm{sat}}^2}\right)\frac{dT_{\mathrm{sat}}}{dt}. \tag{F.7}$$

Substituting Eqs. (F.5)-(F.7) in Eq. (F.3), one obtains an explicit ODE for the liquid volume,

$$\frac{dV_{\mathrm{L}}}{dt} = -\left(\rho_L - \frac{P}{RT_{\mathrm{sat}}}\right)^{-1}\frac{P(V_{\mathrm{T}} - V_{\mathrm{L}})}{RT_{\mathrm{sat}}}\left(\frac{\Delta H_{\mathrm{LV}}}{RT_{\mathrm{sat}}} - 1\right)\frac{dT_{\mathrm{sat}}}{dt}. \tag{F.8}$$

For simplicity, the function multiplying $-dT_{sat}/dt$ in Eq. (F.8) will be denoted F_1,

$$F_1 = \left(\rho_L - \frac{P}{RT_{\mathrm{sat}}}\right)^{-1}\frac{P(V_{\mathrm{T}} - V_{\mathrm{L}})}{RT_{\mathrm{sat}}}\left(\frac{\Delta H_{\mathrm{LV}}}{RT_{\mathrm{sat}}} - 1\right), \tag{F.9}$$

By performing a global energy balance in the storage tank, the change in liquid and vapour volumes are a function of the total heat ingress,

$$\frac{d}{dt}(\rho_{\mathrm{L}}V_{\mathrm{L}}h_{\mathrm{L}}) + \frac{d}{dt}(\rho_{\mathrm{V}}V_{\mathrm{V}}h_{\mathrm{V}}) = \dot{Q}_{\mathrm{tot}}\,, \tag{F.10}$$

where,

$$\dot{Q}_{\mathrm{tot}} = \left((U_{\mathrm{bot}} + U_{\mathrm{roof}})A_{\mathrm{T}} + \frac{4d_o}{d_i}\left(V_{\mathrm{T}}U_{\mathrm{L}} + V_{\mathrm{V}}(U_{\mathrm{V}} - U_{\mathrm{L}})\right)\right)(T_{\mathrm{air}} - T_{\mathrm{sat}}). \tag{F.11}$$

By assuming $U_{\mathrm{bot}} = U_{\mathrm{roof}} = U_{\mathrm{V}} = U_{\mathrm{L}} = U$, $h_{\mathrm{L}} = c_{\mathrm{v,L}}T_{\mathrm{sat}}$, $h_V = (c_{\mathrm{v,V}} + R)T_{\mathrm{sat}}$ and substituting Eq. (F.11) in Eq. (F.10), an ODE for the saturation temperature is obtained,

$$\frac{dT_s}{dt} = \frac{\dot{Q}_{\mathrm{tot}}}{F_2}. \tag{F.12}$$

The quantity F_2 is a function of the thermodynamic properties of the cryogenic liquid and its vapour,

$$F_2 = \rho_{\mathrm{L}} V_{\mathrm{L}} c_{\mathrm{v,L}} + \rho_{\mathrm{L}} F_1 T_{\mathrm{s}} \left(c_{\mathrm{v,V}} + c_{\mathrm{v,L}} + R \right) - \rho_{\mathrm{V}} V_{\mathrm{V}} (c_{\mathrm{v,V}} + R) \tag{F.13}$$

Replacing Eqs. (F.12) and (F.10) in Eq. (F.8), one obtains an explicit ODE for the liquid volume,

$$\frac{dV_{\mathrm{L}}}{dt} = -\frac{F_1}{F_2} \dot{Q}_{\mathrm{tot}}. \tag{F.14}$$

Eqs. (F.7), (F.12) and (F.14) constitute a non-linear ODE system for P, T_s and V_{L} that constitutes the simplified equilibrium model for non-isobaric evaporation of cryogenic liquids.